Transactions of the ASME®

Technical Editor, **T. H. OKIISHI (1998)**
Associate Technical Editors
Aeromechanical Interaction
R. E. KIELB (1999)
Gas Turbine (Review Chair)
A. KIDD (1997)
Heat Transfer
M. G. DUNN (1999)
N. NIRMALEN (2000)
Power
D. LOU (1998)
Turbomachinery
R. A. DELANEY (1998)
A. STRAZISAR (2000)

BOARD ON COMMUNICATIONS
Chairman and Vice-President
R. K. SHAH

OFFICERS OF THE ASME
President, **W. M. PHILLIPS**
Executive Director, **D. L. BELDEN**
Treasurer, **J. A. MASON**

PUBLISHING STAFF
Managing Director, Engineering
CHARLES W. BEARDSLEY
Director, Technical Publishing
PHILIP DI VIETRO
Managing Editor, Technical Publishing
CYNTHIA B. CLARK
Managing Editor, Transactions
CORNELIA MONAHAN
Production Coordinator
VALERIE WINTERS
Production Assistant
MARISOL ANDINO

Transactions of the ASME, Journal of Turbomachinery (ISSN 0889-504X) is published quarterly (Jan., Apr., July, Oct.) for $205.00 per year by The American Society of Mechanical Engineers, Three Park Avenue, New York, NY 10016. Periodicals postage paid at New York, NY and additional mailing offices. POSTMASTER: Send address changes to Transactions of the ASME, Journal of Turbomachinery, c/o THE AMERICAN SOCIETY OF MECHANICAL ENGINEERS, 22 Law Drive, Box 2300. Fairfield, NJ 07007-2300.
CHANGES OF ADDRESS must be received at Society headquarters seven weeks before they are to be effective. Please send old label and new address.
PRICES: To members, $40.00, annually; to nonmembers, $205.00.
To countries outside the United States and Canada, add $40.00 for surface postage and $60.00 for airmail postage.
STATEMENT from By-Laws. The Society shall not be responsible for statements or opinions advanced in papers or ... printed in its publications (B7.1, Par. 3).

INDEXED by Applied Mechanics Reviews and Engineering Information, Inc.
Canadian Goods & Services Tax Registration #126148048

Journal of Turbomachinery

Published Quarterly by The American Society of Mechanical Engineers

VOLUME 120 • NUMBER 4 • OCTOBER 1998

TECHNICAL PAPERS

625 **1997 Best Paper Award—Controls and Diagnostics Committee: Active Stabilization of Rotating Stall and Surge in a Transonic Single-Stage Compressor** (97-GT-411)
H. J. Weigl, J. D. Paduano, L. G. Fréchette, A. H. Epstein, E. M. Greitzer, M. M. Bright, and A. J. Strazisar

637 **Experiments in Active Control of Stall on an Aeroengine Gas Turbine** (97-GT-280)
C. Freeman, A. G. Wilson, I. J. Day, and M. A. Swinbanks

648 **Effects of Nonaxisymmetric Tip Clearance on Axial Compressor Performance and Stability** (97-GT-406)
M. B. Graf, T. S. Wong, E. M. Greitzer, F. E. Marble, C. S. Tan, H.-W. Shin, and D. C. Wisler

662 **Viscous Throughflow Modeling of Axial Compressor Bladerows Using a Tangential Blade Force Hypothesis** (97-GT-415)
S. J. Gallimore

671 **Inner Workings of Aerodynamic Sweep** (97-GT-401)
A. R. Wadia, P. N. Szucs, and D. W. Crall

683 **Effects of Stream Surface Inclination on Tip Leakage Flow Fields in Compressor Rotors** (97-GT-43)
M. Furukawa, K. Saiki, K. Nagayoshi, M. Kuroumaru, and M. Inoue

695 **The Influence of Wake–Wake Interactions on Loss Fluctuations of a Downstream Axial Compressor Blade Row** (97-GT-469)
G. J. Walker, J. D. Hughes, I. Köhler, and W. J. Solomon

705 **Reduction of Unsteady Blade Loading by Beneficial Use of Vortical and Potential Disturbances in an Axial Compressor With Rotor Clocking** (97-GT-86)
S. T. Hsu and A. M. Wo

714 **The Influence of Downstream Passage on the Flow Within an Annular S-Shaped Duct** (97-GT-83)
T. Sonoda, T. Arima, and M. Oana

723 **On the Design Criteria for Suppression of Secondary Flows in Centrifugal and Mixed Flow Impellers** (97-GT-393)
M. Zangeneh, A. Goto, and H. Harada

736 **Sound Generation by a Centrifugal Pump at Blade Passing Frequency**
M. Morgenroth and D. S. Weaver

744 **An Analysis Method for Multistage Transonic Turbines With Coolant Mass Flow Addition** (97-GT-183)
F. Mildner and H. E. Gallus

753 **Effect of Squealer Tip on Rotor Heat Transfer and Efficiency** (97-GT-128)
A. A. Ameri, E. Steinthorsson, and D. L. Rigby

760 **Unsteady Total Temperature Measurements Downstream of a High-Pressure Turbine** (97-GT-407)
D. R. Buttsworth, T. V. Jones, and K. S. Chana

768 **Aspects of Vane Film Cooling With High Turbulence: Part I—Heat Transfer** (97-GT-239)
F. E. Ames

777 **Aspects of Vane Film Cooling With High Turbulence: Part II—Adiabatic Effectiveness** (97-GT-240)
F. E. Ames

(Contents continued on p. 647)

This journal is printed on acid-free paper, which exceeds the ANSI Z39.48-1992 specification for permanence of paper and library materials.♾™

♻ 85% recycled content, including 10% post-consumer fibers.

(Contents continued)

785 **Effects of Very High Free-Stream Turbulence on the Jet–Mainstream Interaction in a Film Cooling Flow** (97-GT-121)
A. Kohli and D. G. Bogard

791 **Measurements in Film Cooling Flows: Hole *L/D* and Turbulence Intensity Effects**
S. W. Burd, R. W. Kaszeta, and T. W. Simon

799 **Detailed Film Cooling Measurements on a Cylindrical Leading Edge Model: Effect of Free-Stream Turbulence and Coolant Density** (97-GT-181)
S. V. Ekkad, J. C. Han, and H. Du

808 **Effect of Unsteady Wake on Detailed Heat Transfer Coefficient and Film Effectiveness Distributions for a Gas Turbine Blade** (97-GT-166)
H. Du, J. C. Han, and S. V. Ekkad

818 **Heat Transfer in a Rotating Cavity With a Peripheral Inflow and Outflow of Cooling Air** (97-GT-136)
I. Mirzaee, X. Gan, M. Wilson, and J. M. Owen

824 **The Effect of Turbulence on the Heat Transfer in Closed Gas-Filled Rotating Annuli** (97-GT-242)
D. Bohn and J. Gier

831 **Low-Aspect-Ratio Rib Heat Transfer Coefficient Measurements in a Square Channel** (97-GT-388)
M. E. Taslim and G. J. Korotky

839 **Prediction of the Becalmed Region for LP Turbine Profile Design** (97-GT-398)
V. Schulte and H. P. Hodson

847 **Direct Full Surface Skin Friction Measurement Using Nematic Liquid Crystal Techniques** (97-GT-397)
D. R. Buttsworth, S. J. Elston, and T. V. Jones

ANNOUNCEMENTS

670 **Change of address form for subscribers**

854 **Discussion of a previously published paper by F. A. Lyman**

1997 Best Paper Award—Controls and Diagnostics Committee

Active Stabilization of Rotating Stall and Surge in a Transonic Single-Stage Axial Compressor

H. J. Weigl

J. D. Paduano

L. G. Fréchette

A. H. Epstein

E. M. Greitzer

Gas Turbine Laboratory,
Department of Aeronautics and Astronautics,
Massachusetts Institute of Technology,
Cambridge, MA 02139

M. M. Bright

A. J. Strazisar

NASA Lewis Research Center
Cleveland, OH 44135

Rotating stall and surge have been stabilized in a transonic single-stage axial compressor using active feedback control. The control strategy is to sense upstream wall static pressure patterns and feed back the signal to an annular array of twelve separately modulated air injectors. At tip relative Mach numbers of 1.0 and 1.5 the control achieved 11 and 3.5 percent reductions in stalling mass flow, respectively, with injection adding 3.6 percent of the design compressor mass flow. The aerodynamic effects of the injection have also been examined. At a tip Mach number, M_{tip}, of 1.0, the stall inception dynamics and effective active control strategies are similar to results for low-speed axial compressors. The range extension was achieved by individually damping the first and second spatial harmonics of the prestall perturbations using constant gain feedback. At a M_{tip} of 1.5 (design rotor speed), the prestall dynamics are different than at the lower speed. Both one-dimensional (surge) and two-dimensional (rotating stall) perturbations needed to be stabilized to increase the compressor operating range. At design speed, the instability was initiated by approximately ten rotor revolutions of rotating stall followed by classic surge cycles. In accord with the results from a compressible stall inception analysis, the zeroth, first, and second spatial harmonics each include more than one lightly damped mode, which can grow into the large amplitude instability. Forced response testing identified several modes traveling up to 150 percent of rotor speed for the first three spatial harmonics; simple constant gain control cannot damp all of these modes and thus cannot stabilize the compressor at this speed. A dynamic, model-based robust controller was therefore used to stabilize the multiple modes that comprise the first three harmonic perturbations in this transonic region of operation.

1 Introduction

The concept of using rotating stall control to increase the stable compressor operating range has been demonstrated on several research compressors (Day, 1993; Paduano et al., 1993; Haynes et al., 1994; Behnken et al., 1995) and is now facing issues that will determine feasibility in modern full-scale devices. Whereas most experiments have been conducted on low-speed compressors, the three main issues addressed in this paper concern high-speed machines: (*i*) high-bandwidth, high-authority actuation, (*ii*) modeling compressible rotating stall dynamics, and (*iii*) demonstration of stabilization in a transonic compressor.

The issue of actuation is simply this: In a high-speed compressor, are there feasible approaches to forcing prestall waves with sufficient bandwidth and authority to stabilize these waves? Most previous studies, conducted at much lower Mach numbers, have not had as stringent actuator power and bandwidth requirements. This paper describes the first use of distributed inlet injection actuation to excite, identify, and stabilize prestall waves in a transonic compressor.

For low tip Mach number devices, a two-dimensional, linearized hydrodynamic stability model of rotating wave dynamics has proven useful for conceptualizing and implementing control systems (see Epstein et al., 1989; Hendricks and Gysling, 1994; Gysling and Greitzer, 1994). These studies have shown that stabilization of prestall waves, which grow into rotating stall, can be used to increase the compressor operating range by allowing operation at normally unstable conditions.

An important question is whether these modeling and control ideas carry over to modern high-speed devices, where compressibility is an important factor. In particular, we wish to know the character of the waves that lead to rotating stall when unstable, and the feasibility of actuating and stabilizing these waves to increase the stable operating range. In short, does this conceptual approach work in high-speed machines? These modeling and control questions have recently been answered theoretically; experimental demonstration of the theoretical predictions is the focus of this paper.

The actuators used in the present work are discrete jet injectors mounted on the compressor casing. The jet injectors are run with a steady mean blowing rate so that positive and negative unsteady actuation can be commanded. As will be shown, steady mean injection has a strong positive impact on the compressor stable operating range. This behavior has also been reported by Koch and Smith (1968) and Koch (1970), who investigated the impact of upstream blowing and downstream bleed on the stable operating range of a transonic compressor.

In the next section, we give a brief account of the theoretical developments that determine the requirements for successful control. Section 3 then describes the experimental setup used for the demonstrations, including the implementation and characterization of injection actuation. Section 4 compares the dynamic behavior of the high-speed compressor model to forced response measurements carried out in the transonic stage. Sec-

Contributed by the International Gas Turbine Institute and presented at the 42nd International Gas Turbine and Aeroengine Congress and Exhibition, Orlando, Florida, June 2–5, 1997. Manuscript received International Gas Turbine Institute February 1997. Paper No. 97-GT-411. Associate Technical Editor: H. A. Kidd.

tion 5 gives stabilization results using a constant-gain feedback control law at 70 percent speed. This section also includes a brief overview of the robust H_∞ control law design used at 100 percent speed followed by experimental results. Discussion and conclusions are presented in Section 6.

2 Prestall Wave Dynamics in High-Speed Compressors

The two-dimensional, linearized stability model of Moore and Greitzer (1986) has been extended by Bonnaure (1991) and Hendricks et al. (1993) to the compressible flow regime. The analysis has been further modified to include actuation by Feulner et al. (1996), who also converted the model to a form compatible with control theory. The analysis describes prestall compressor eigenmodes: their circumferential (θ) and axial shape, rotation frequency, and growth rate (stability). Here we discuss the nature of the "compressible" modes, and the implications for active control. See Fréchette (1997) for a physical explanation of these modes.

A qualitative difference in the prestall dynamics that is due to compressibility is the introduction of new modes with axial structure. In *in*compressible stability theory the modal perturbations vary in θ (sinusoidally), but at a given θ location the axial velocity perturbations are uniform through the compressor. In compressible stability theory, on the other hand, the modes have not only a sinusoidal circumferential shape but also axial structure so the axial velocity and mass flow vary with θ and with axial position in the compressor. We thus refer to the modes in terms of two wave numbers, a circumferential and an axial one. The modes denoted [0, 0], [1, 0], [2, 0], . . . [n, 0] are like those originally described by Moore and Greitzer for incompressible flow, and those denoted [n, −1], [n, 1], [n, 2], etc., have an nth harmonic shape in θ and various shapes axially. We refer to the latter as "compressible modes."

Compressible modes would not interest us if they remained stable and their frequency remained outside the bandwidth of control. However, the theory predicts these modes to be critical in high-speed compressors, both in frequency and stability. The frequency is set by axial length rather than rotor frequency, because axial structure is primarily set by acoustic considerations. The incompressible (e.g., [1, 0]) mode frequency, in contrast, is set by rotor frequency (typically [1, 0] rotates at between 0.2E and 0.6E). Thus, for instance, the [1, 0] and [1, 1] modes become closer as rotor frequency increases. At design speed in a modern high-speed compressor, the [1, 1] mode generally rotates at about 1E.

This mode has been identified as a likely cause of instability in various high-speed compressors by Tryfonidis et al. (1995). Another concern is that excitations, such as 1E excitation or feedback from active control systems, can cause large resonances that can drive the system into rotating stall.

The set of first harmonic modes (. . . [1, −1], [1, 0], [1, 1], . . .) are decoupled from the set of second harmonic modes (. . . [2, −1], [2, 0], [2, 1], . . .) because they are spatially orthogonal. Thus we do not expect these sets of modes to interact if we actuate the harmonics independently. However, all of the lightly damped modes with the same circumferential wave number affect the prestall dynamics. When actuating the first harmonic, for instance, the control law must properly account for the actuation effects on both the [1, 0] and the [1, 1] mode.

As shown in Section 4, predictions from the compressible rotating stall theory are not yet accurate enough for *a priori* control law design. The model's qualitative behavior does, however, drive the control system implementation and design. Because the [1, 1] mode appears to be important to compressor stability, actuator bandwidth must be sufficient to stabilize this and other lightly damped high-frequency compressible modes. In addition, identification of the compressor behavior is needed to characterize the incompressible and compressible modes. Frequency shaping in the control law is then needed simultaneously to stabilize (for instance) the [1, 0] mode, while avoiding instability in the [1, 1] and higher modes.

3 Experimental Setup

The experiments described here were conducted in the NASA Lewis Research Center's Single-Stage Axial Compressor Test Facility, an open circuit facility for testing advanced compressor stages. A new casing for the compressor was designed and built to accommodate the actuators and sensors required for rotating stall control as illustrated in Fig. 1. Some of the basic considerations in the experimental setup are discussed here; for a complete description of the injection actuation development, see Berndt (1995) and Berndt et al. (1995).

The test compressor, designated NASA Stage 35, was originally designed as an inlet stage of an eight-stage 20:1 pressure ratio core compressor (Reid and Moore, 1978a). The design conditions are a total pressure ratio of 1.82, a mass flow of 20.2 kg/s, a rotor tip speed of 455 m/s, and a rotation frequency of 286 Hz. The blade tip diameter is approximately 50 cm with a hub-to-tip radius ratio of 0.7. The mean-line rotor and stator chord lengths are 56 mm and 40 mm. A detailed description of performance measurements from Stage 35 is given by Reid and Moore (1978b).

Data acquisition and control are performed by a 90 MHz Pentium PC computer system, with 64 input and 16 output channels. The sample rate used is 3 kHz, or roughly 10E, to insure that controller delays will not adversely affect performance. The optimized control loop can implement linear control laws with up to 60 states at 3 kHz, while acquiring data in a circular buffer of up to 45 seconds in length (limited only by RAM). Inputs to the control computer include high-response pressure transducer measurements, position sense signals from the actuators, and low-frequency compressor performance measurements (mass flow, pressure rise, and throttle position). High-response sensors are distributed circumferentially (8–12 wall static pressure ports at each axial station) to allow decomposition of perturbations into harmonics. The array of sensors immediately upstream of the rotor provided the cleanest traveling wave measurements and were therefore used for forced response and control testing.

The outputs of the control computer are 12 independently commanded mass flow injection rates. Figure 1 shows the location of a circumferential array of 12 jet actuators placed 1.1 rotor chord lengths (63 mm) upstream of the compressor face. This axial distance is chosen to be as small as mechanically feasible, to reduce the convective time delay between actuator fluid injection and compressor response. Measurement of the dynamics of fluid forcing indicate that this delay is one of the major dynamic effects which must be minimized. Berndt (1995) gives a complete description of the actuator design requirements; other important issues are briefly discussed below.

The actuators were designed to deliver a relatively high mass flow (they are capable of delivering 5.8 percent of the design compressor mass flow when supplied with 100 psi air). The actuators must also have sufficient bandwidth to stabilize the lightly damped modes of interest. These actuators, developed by Moog Inc. and MIT and described by Berndt, have a large signal bandwidth of 400 Hz. It should be noted that this is only 1.4E, and that the theory predicts there are lightly damped modes traveling significantly faster. The actuators have performed reliably over three months of extensive testing which was a primary concern in such a harsh test environment.

Two different injector geometries were used in this study (see Berndt, 1995). The injector is the portion of the actuator that directs flow, modulated by a servomotor driven valve, from the actuator to the compressor face. Its shape is critical to the injection characteristics. After extensive wind tunnel testing, two types of injector were designed for testing in this program.

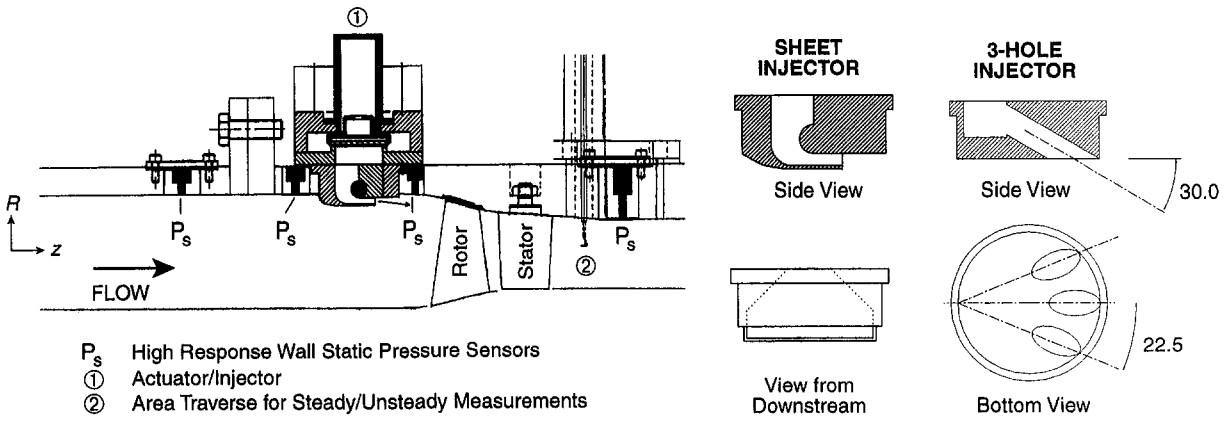

Fig. 1 Stage 35 actuation and instrumentation schematic

The first type attempts to provide a radially well-mixed axial momentum flux at the compressor face. There are three holes in the injector as shown in the inset in Fig. 1. Each hole is at an angle of 30 deg relative to the casing wall in the $R-z$ plane. The objective is to inject over a significant portion of blade span because previous stall control experiments have been conducted with variable-pitch IGVs, which affect the entire blade span. The resulting injection profile covers the upper 40 percent of the annulus height. This injector is flush with the casing wall; that is, it does not protrude into the flow.

The second injector geometry, shown in the inset in Fig. 1, was designed to inject a sheet of high-momentum air along the casing wall into the rotor tip region. The objective of the sheet injector is to provide maximum control authority taking advantage of the fact that Rotor 35 is tip critical. Berndt found that a large radius of turning was required to accomplish this, so the injector protrudes into the flow by 7 percent of the rotor inlet span. As with the three-hole injector, the exit area must be sufficiently large to prevent mass storage, which results in delay, in the valve body. About 50 percent of the circumference over the outboard 15 percent of the span is affected by the injected sheets from the twelve actuators.

3.1 Steady State Injection Characteristics. The actuators were designed so that the injection yaw angle (incidence angle with respect to the rotor) can be varied in 15 deg increments by rotating the injector on the valve body. Injector type and injection yaw angle thus form a matrix of possible injection configurations. The configuration providing the largest increase in pressure rise and operating range was determined experimentally, using steady injection with a fixed supply pressure of 100 psi and 0, 50, and 100 percent valve opening. Unless otherwise noted, all future references to "50 percent blowing" imply a 100 psi supply pressure with a 50 percent valve opening.

All of the compressor speedlines presented in this paper include the combined effects of steady injection and of the compressor itself. The inlet pressure is measured upstream of the actuators and the total corrected mass flow (kg/s) is the sum of the inlet flow rate measured by an orifice far upstream of the compressor and the injection mass flow rate measured by a separate venturi meter.[1] Total-to-total pressure ratio maps and inlet total-to-exit static pressure ratio maps were both constructed. The exit static pressure was determined by averaging inner and outer wall static pressure downstream of the stage. Exit total pressure was determined by mass-averaging data acquired with seven-element pressure and temperature rakes located downstream of the stage. The total-to-static pressure ratio is plotted since its slope is analogous to the slope of total-to-static pressure rise coefficient which is a relevant parameter for rotating stall in low-speed machines:

Low-speed:

$$\frac{P_{s_{\text{exit}}} - P_{t_{\text{inlet}}}}{\rho U^2}$$

High-speed:

$$\frac{P_{s_{\text{exit}}} - P_{t_{\text{inlet}}}}{P_{t_{\text{inlet}}}} = \frac{P_{s_{\text{exit}}}}{P_{t_{\text{inlet}}}} - 1$$

The results of the injector configuration study are summarized in Figs. 2 and 3. For active control, we are primarily interested in modulating pressure rise at fixed mass flow, that is we would like the speedlines to be separated vertically. The sheet injector directed 15 deg against rotor rotation provided the largest and most consistent separation. Figure 2(*a*) shows the total-to-total pressure ratio maps for a solid casing and for this injector configuration with 50 percent of the maximum blowing rate (3.6 percent of the design compressor mass flow). Significant range extension is obtained with this amount of steady blowing, which is the mean blowing level at which all of the control experiments are conducted. Mean blowing is introduced so that positive and negative actuation can be commanded (similar to the injection scheme used by Gysling and Greitzer, 1994).[2] The pressure rise delivered by the compressor is increased by a substantial fraction. Figures 2(*b*) and 2(*c*) detail the inlet total-to-exit static pressure ratio for various levels of steady blowing with the same injector configuration.

Figure 3 shows a summary of the injector configuration study; in this figure the total-to-total pressure ratio is plotted to highlight the differences for the four injector configurations. All speedlines are for 100 percent steady blowing. The sheet injector at −15 deg yaw yields a higher total pressure ratio than both the sheet at −30 deg yaw and the three-hole injector. At 0 deg yaw, the sheet injector provides higher total pressure ratio, but the mass flow could not be increased above 20 kg/s corrected flow. This was thus not considered an acceptable configuration. Detailed investigation of the effect of steady injection on the compressor performance is currently being conducted as part of this research program.

[1] The upstream orifice mass flow is corrected based on total pressure and temperature measured far upstream of the compressor; the corrected injected mass flow is based on total pressure and temperature measurements in the injector.

[2] As discussed in Section 5.3, preliminary results indicate that the compressor can be successfully stabilized using only "one-sided" actuation (only adding injector mass flow).

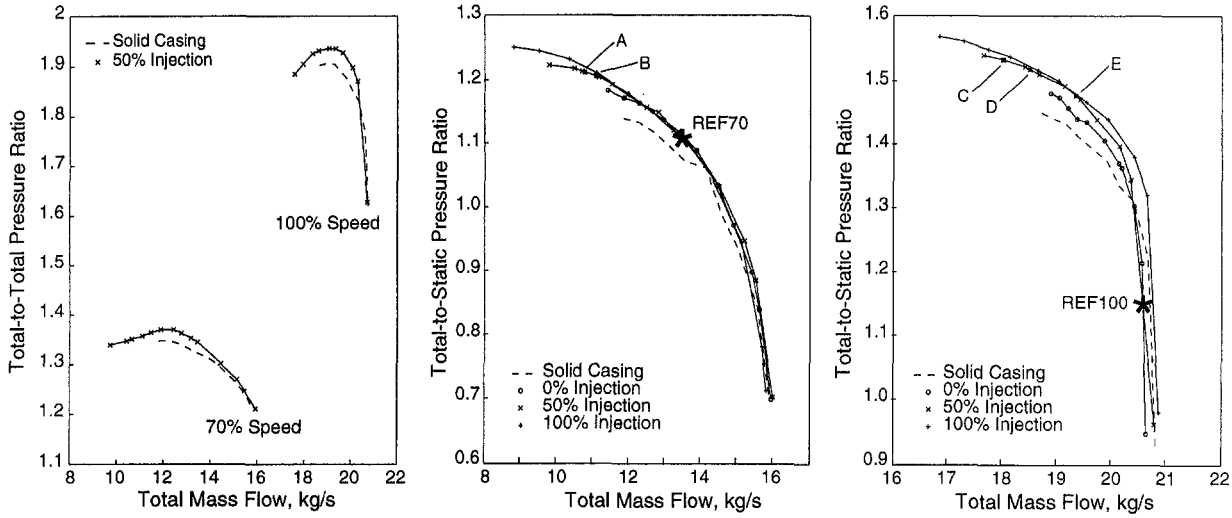

(a) Pressure ratio at 70% and 100% speed. (b) Pressure ratio at 70% speed. (c) Pressure ratio at 100% speed.

Fig. 2 Compressor characteristics for steady blowing with sheet injectors at −15 deg yaw angle

4 Open-Loop Dynamics

In this section we compare qualitative and quantitative predictions of the compressible rotating stall model to forced response results obtained with unsteady injection. Our purpose is to demonstrate that compressibility has a significant effect on the dynamic behavior of compressors, and that the theory correctly accounts for the differences between incompressible and compressible rotating stall dynamics.

It should be noted that all of the root loci and transfer functions presented in the following sections are for complex coefficient models. The output is a complex spatial Fourier coefficient (SFC) of the nth harmonic pressure perturbation; the input is the corresponding nth SFC of the injection. Since the $n \neq 0$ models are complex, the root loci and transfer functions are not symmetric for positive and negative frequencies, which determine the direction of wave rotation.

4.1 Comparison of Predicted and Measured Dynamics. Figure 4 compares the forced response behavior of the low-speed compressor used by Haynes et al. (1994) and Vo (1997) (with a relative tip Mach number of 0.25) to that of the current compressor at 70 and 100 percent design speed (M_{tip} of 1.0

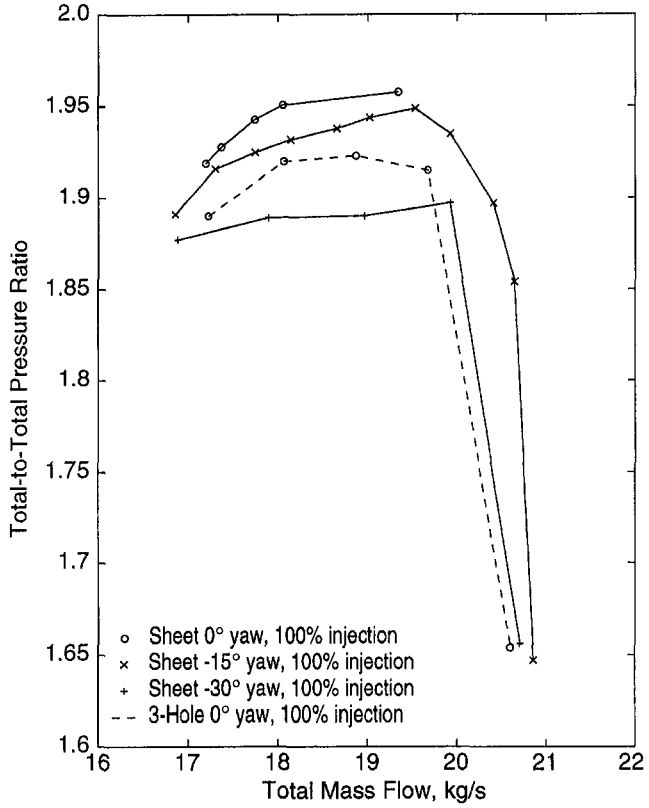

Fig. 3 Pressure ratio characteristics for steady blowing with four injector configurations at 100 percent speed

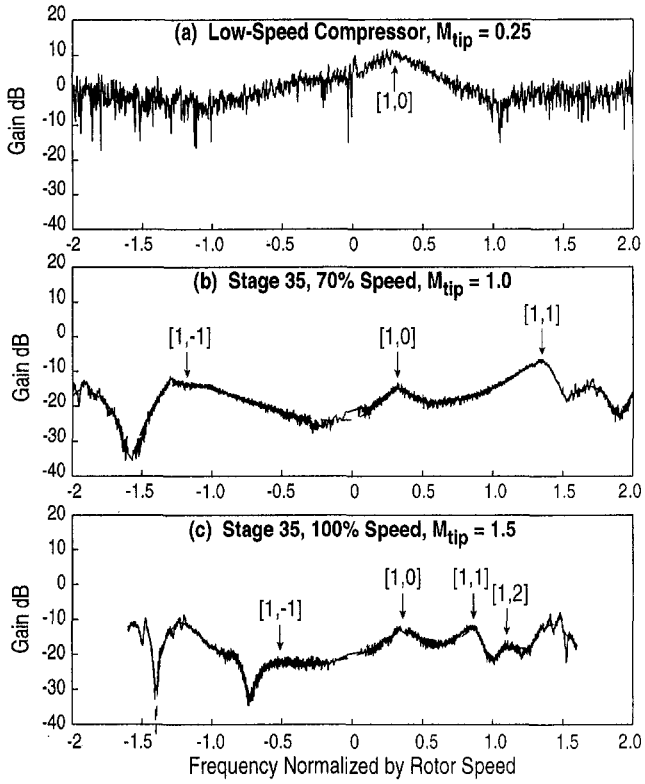

Fig. 4 Transfer functions for low and high-speed compressors: —— measured, – – – model fit

and 1.5, respectively). The latter responses were obtained by exciting the system with a rotating sinusoidal wave of actuation, superimposed on the nominal 3.6 percent injection rate. The frequency of rotation was swept from 10 Hz to 500 Hz in both directions of rotation. Standard spectral analysis procedures yielded the transfer function estimates shown. The measured input/output coherence was typically above 0.8, resulting in accurate transfer function estimates. Figures 4(*b*) and 4(*c*) also include a fit using eigenvalues and zeros (indicated by a dashed line). Note that this is not the model described in Section 2; this is an identified model based on the experimental measurements. In both the low and high-speed compressor tests, the actuation was inlet injection, although the details of the injection and measured response differ somewhat. However, the goal here is to compare eigenmodes, which are independent of the forcing details.

The transfer functions exhibit peaks at the natural eigenfrequencies of lightly damped modes. As predicted by the incompressible theory, Fig. 4(*a*) shows that the low-speed compressor exhibits only one such peak in the first harmonic response. The compressible theory, on the other hand, predicts that multiple eigenfrequencies exist for each spatial harmonic. Furthermore, while the incompressible mode frequency scales with the rotor frequency, the frequencies of the remaining (compressible) modes are set by the geometry of the compression system rather than the rotor speed. As the rotor frequency (tip Mach number) increases, the frequencies of the compressible modes decrease with respect to the rotor frequency, as shown by the second peak in Figs. 4(*b*) and 4(*c*). At a M_{tip} of 1.0, the [1, 1] peak appears at 1.38 times the rotor frequency, or 280 Hz in dimensional units. For $M_{tip} = 1.5$, this peak appears at 0.89 times the rotor frequency, or 260 Hz. The dimensional frequency is thus relatively constant. The frequency of the [1, 0] mode scales primarily with rotor frequency for all three cases (0.32E for the low-speed compressor, 0.32E for the low-speed Stage 35 test, and 0.28E at the design speed). Note also that the Stage 35 forced response measurements include other lightly damped modes traveling with and against the rotor direction (peaks at positive and negative frequencies) at up to 2E, which is consistent with the theory.

Figure 4 shows that detailed dynamic information can be obtained through spatially distributed forced response testing; transfer functions similar to those shown in Fig. 4 have been measured for the 0th, 1st, and 2nd circumferential harmonics. Using these data, at least 20 dynamic modes of the system have been identified. Table 1 gives the identified frequencies of the lowest five first harmonic rotating stall modes at 100 percent speed, and compares them to the theory described in Section 2. The comparison is shown for the operating point D in Fig. 2(*c*), where the most coherent near-stall transfer function estimate was obtained.

Feulner's model has been extensively refined in order to model Stage 35 with steady 3.6 percent mean injection rate; this is the first time that the compressible model has been directly compared to forced response data (see Weigl, 1997, and Fréchette, 1997, for details). The inputs to the dynamic model are the mean-line flow quantities at 70 and 100 percent speed. Since standard correlations for total pressure loss and deviation do not apply to this compressor due to the tip injection from the actuators, the steady flow field could not be obtained from standard correlations. These steady flow fields have therefore been derived from a mean-line data fit procedure based on total temperature, total pressure, and static pressure measurements at various axial locations through-out the compressor. The equivalent loss and deviation for each blade row are determined from the mean-line calculation. Using a constrained optimization algorithm, the values of loss and deviation were changed iteratively within experimental error until the computed flow field matched the temperature and pressure measurements for each blade row. The optimization was augmented to match the measured *dynamics* (eigenvalue locations) as well as the steady temperature and pressure.

Table 1 shows that the rotation frequencies of the theoretical and measured eigenvalues are in general agreement. As might be expected from the fact that geometry is the primary influence on frequency, the theoretical frequencies do not depend strongly on the aerodynamic and performance inputs to the model. Growth rate comparisons are much more sensitive to these parameters, and are less accurate. For example, the growth rate of the [1, 0] mode is underestimated by 27 percent at this operating point. This error in stability translates into an error in predicted stalling mass flow of 7 percent.

Figure 5 combines the frequency information in Table 1 with growth rate information, for both the measured and calculated eigenvalues at operating point D in Fig. 2(*c*). The frequencies of the measured eigenvalues are captured well. However, there is a significant difference in the growth rates, which is primarily due to the sensitivity in stability to the steady model inputs. Furthermore, comparison of the measured and theoretical transfer function indicates that the model does not capture the zeroes accurately. We believe that the source of error in modeling the zeros is that the two-dimensional model ignores the spanwise nonuniformity of the tip injection.

Near −1E and 1.2E, two additional eigenvalues (marked by arrows in Fig. 5) are predicted, which were not identified from the forced response tests. It is unclear whether these eigenmodes are indeed erroneous. Detailed examination of the measured transfer functions indicate that there are closely spaced eigenvalues and zeros above 1E (see for example Fig. 4(*c*) near 1.5E), which are not included in the experimental fit.[3] These eigenvalues and zeros are so well damped and closely spaced that they contribute only a small change in magnitude and phase to the transfer function. The magnitude of some of these eigenvalue/zero peaks is indistinguishable from the noise in the transfer function estimate.

The results shown in Table 1 and Fig. 5 indicate that the main features of the measured modal dynamics, such as number, frequency and, to a lesser degree, stability of the dominant eigenvalues, are captured by the compressible stall inception theory. Comparable results were also found for the measured dynamics at 70 percent of design speed. The theory is not yet an *a priori* tool for stall prediction and control system design since the model inputs were derived from experimental measurements and the error in modal growth rate is significant.

Table 1 Measured and theoretical first harmonic rotational frequencies

Mode	Measured Frequency/ Rotor Frequency	Theoretical Frequency/ Rotor Frequency
[1, 0]	0.36	0.49
[1, 1]	0.89	0.80
[1, 2]	1.13	1.10
[1, -1]	-0.72	-0.59
[1, -2]	-0.88	-0.83

4.2 Critical Mode for Instability. The theory predicts that both the [1, 0] mode and the compressible modes can become lightly damped as the compressor mass flow is reduced, and this has important implications for active stabilization. To show the experimental trends of the eigenvalues, their frequencies and growth rates were found from the identified models at various mass flows: points A and B in Fig. 2(*b*) and points C,

[3] The closely spaced poles and zeros do not play an important role for control (since these modes are effectively uncontrollable). They have therefore been omitted to simplify the experimental fit procedure by fitting a lower order model.

D, and E in Fig. 2(*c*). Figure 6 shows the measured eigenvalue migrations as stall is approached.

As the throttle is closed at design speed, several modes migrate toward instability. The large change in stability of the [1, 0] mode with mass flow indicates that it is the critical mode for stall inception (this is indeed the case as discussed in Section 5.3). The [1, 1] mode is also of concern since it is lightly damped and has a frequency close to 1E, and can be driven unstable by an 1E excitation (Tryfonidis et al., 1995). Figure 6(*b*) indicates that there are *several* lightly damped modes up to ±1.5E. Since this is the bandwidth limit of the actuator, there is more uncertainty in the exact location of these high-frequency modes. At 70 percent speed, the [1, 1] and other compressible modes are more stable, and do not move much as the compressor mass flow is decreased. The [1, 0] mode determines the stability of the first harmonic at this speed.

For this particular compressor, the [1, 1] and other compressible modes do not become unstable at the mass flows we have reached with and without control, unlike some of the cases presented by Tryfonidis et al. (1995). However, at 100 percent speed, the lightly damped compressible modes play an important role in compressor stabilization as discussed in the following section.

5 Active Control

Discussion of the active stabilization results will be presented in several parts to illustrate how the alteration in dynamics as rotor speed is increased affects the control problem. We first present the results of constant-gain feedback at 70 percent speed with a tip Mach number of 1.0. We also present the results of reducing the supply pressure to the injectors to demonstrate that the control power requirements for stabilization are not prohibitive. We then describe results at 100 percent speed where a simple constant-gain control law is not sufficient to stabilize the various modes that can lead to stall and surge. We thus introduce the design of a model-based H_∞ control law, which successfully stabilized the compressor. Results are then given showing the range extension achieved and details of the controlled behavior. Finally, we illustrate the robustness of the controlled compressor by demonstrating recovery from a growing rotating stall disturbance and from fully developed surge. Only the main results are presented here; a complete overview of the control experiments including control design trade-offs and limitations, and detailed prestall transient and spectral analysis can be found in Weigl (1997).

In Sections 5.1 and 5.3 we present the percentage decrease in stalling mass flow referenced to the stalling mass flows at 70 percent and 100 percent speed with a solid casing (no injectors installed). Table 2 in Section 6 summarizes these results and also lists the improvement in stall margin for each of the following cases.

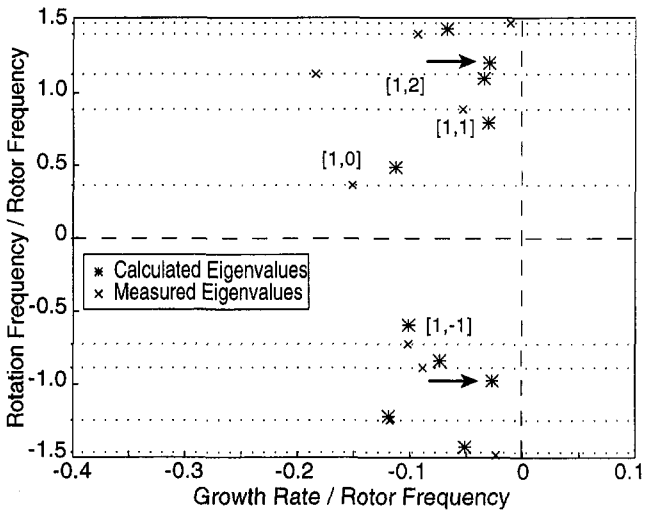

Fig. 5 Calculated and measured eigenvalues at 100 percent speed

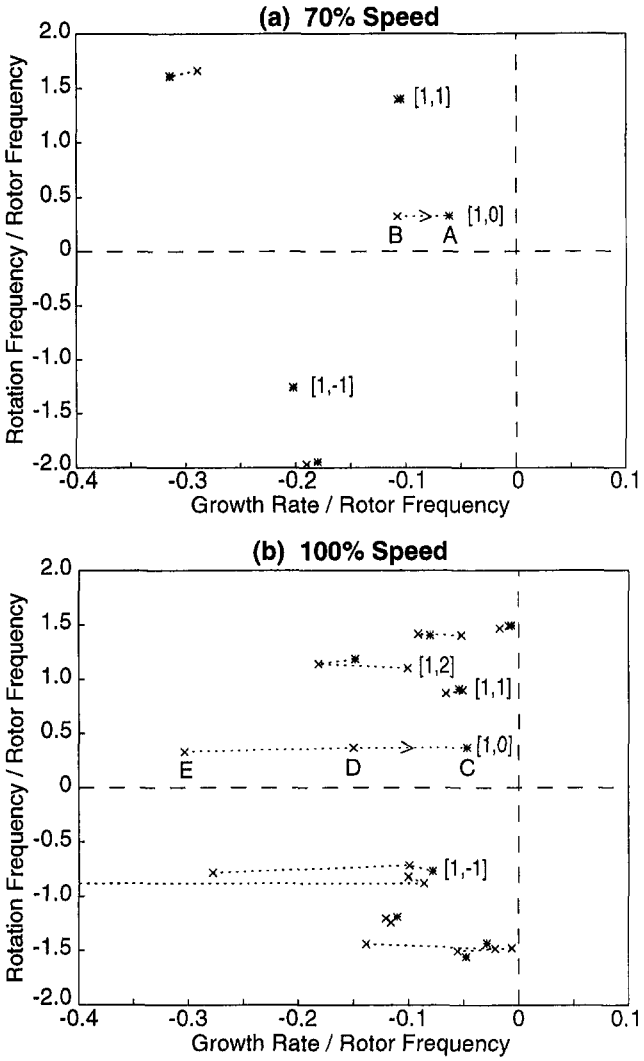

Fig. 6 Migration of eigenvalues with decreasing mass flow (*indicates eigenvalues at lowest measured mass flow)

5.1 Rotating Stall Stabilization at 70 Percent Speed. Figure 7 shows the 70 percent speed total-to-static pressure ratio characteristic. The solid line corresponds to steady injection at 50 percent of full blowing, while the dashed line shows the baseline characteristic without injectors (solid casing). Steady blowing without feedback extends the stable operating range of the compressor by 17.4 percent. A simple constant gain feedback control, like those used by Paduano et al. (1993) and Haynes et al. (1994), was implemented on the measured first harmonic. This feedback law has the following form:

$$\tilde{u}_1 = -Z\tilde{p}_1.$$

where $\tilde{p}_1$ is the first spatial Fourier coefficient (SFC) of the static pressure perturbations measured at the sensor location 44 percent of chord upstream of the rotor as shown in Fig. 1, and $\tilde{u}_1$ is the corresponding first SFC of the injection wave, which is introduced as a first harmonic sinusoidal wave. Z, the proportionality constant between the measured and actuated wave, is a complex number. The amplitude of Z determines the feedback gain of the control law, and the phase of Z determines the spatial phase shift (in rad) between the measured and actuated wave.

Table 2 Summary of steady blowing and control experiments

Configuration	Mass Flow at Stall	% Decrease Mass Flow at Stall	Pressure Ratio at Stall	Stall Margin %
70% Speed				
Solid casing	11.86	—	1.3450	14.2
1.5% blowing, no control	11.53	2.8	1.3370	16.8
3.6% blowing, no control	9.80	17.4	1.3370	37.4
5.8% blowing, no control	8.83	25.5	1.3640	55.7
1.5% blowing, 1st, 2nd control*	10.22	13.8 (+11.0)	1.2940	27.5 (+10.7)
3.6% blowing, 1st harmonic control*	8.81	25.7 (+8.3)	1.3370	51.1 (+13.7)
100% Speed				
Solid casing	18.73	—	1.9010	12.2
3.6% blowing, no control	17.92	4.3	1.8850	17.9
5.8% blowing, no control	16.86	10.0	1.8910	24.0
3.6% blowing, 0th, 1st, 2nd control*	17.27	7.8 (+3.5)	1.8650	19.4 (+1.5)
3.6% blowing, 1-sided actuation*	17.16	8.4 (+4.1)	1.8670	20.3 (+2.4)

* The values in parentheses indicate the portion of the total stall margin improvement due to active control.

Z was experimentally optimized to the value $Z = 2e^{j*2.36}$ for the results in Fig. 7. Constant-gain feedback control of the first mode increased the stable operating range of the compressor an additional 8.3 percent above steady blowing, for a total range increase of 25.7 percent. The compressor characteristic was extended smoothly without a drop in pressure rise.

The control activity required to obtain the results in Fig. 7 with a 100 psi injector supply pressure was approximately ±5 percent of the available ±50 percent valve motion. The small valve motion motivated an experiment in which the supply pressure to the valves was reduced to 30 psi and the mean blowing rate was 1.5 percent of the design compressor mass flow. This pressure was the minimum value that could be used effectively in the valve, and represented roughly the supply pressure available from downstream of the compressor at design speed. Figure 8 shows the constant gain feedback stabilization results for this experiment. Reducing the steady injection rate changes the compressor characteristic dramatically, which in turn alters the stall inception dynamics. The constant gain control law was therefore retuned experimentally to provide the range extension shown.

The compressor characteristic with mean blowing is shifted only slightly from the characteristic with no blowing. Steady blowing extends the operating range by about 2.8 percent. Feeding back the first Fourier coefficient extends the stable operating

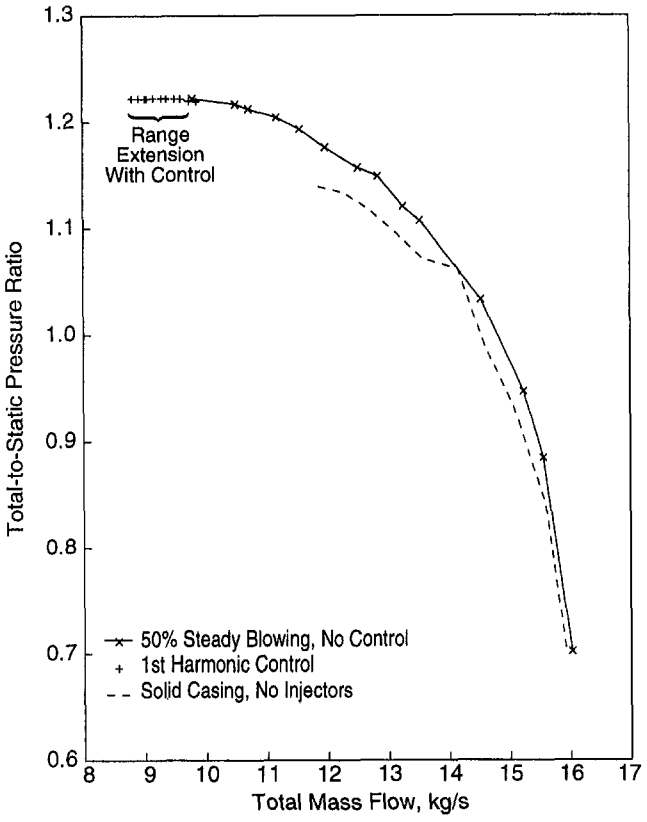

Fig. 7 Stabilized compressor characteristic at 70 percent speed with 3.6 percent injected mass flow rate

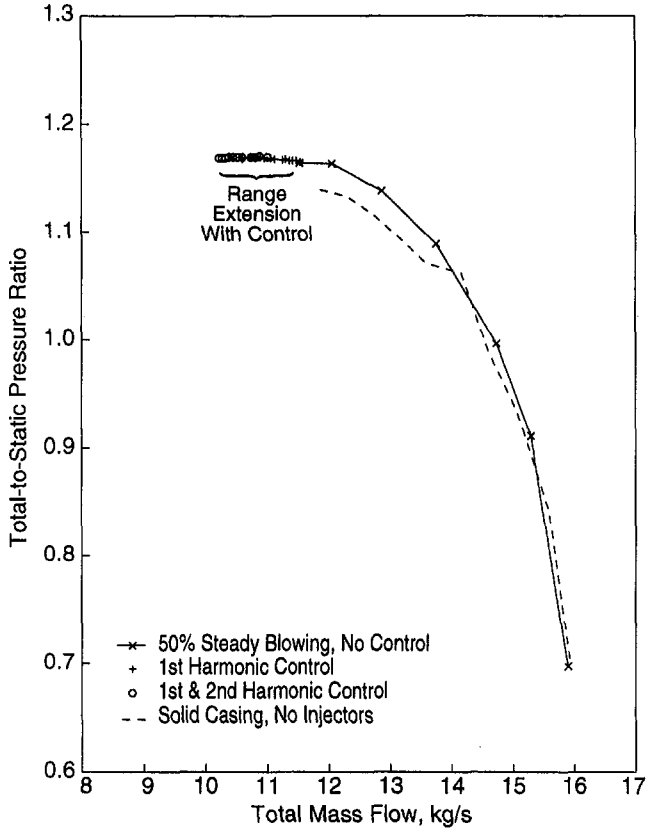

Fig. 8 Stabilized compressor characteristic at 70 percent speed with 1.5 percent injected mass flow rate

range by an additional 7 percent, and first and second SFC feedback extends the range 4 percent more, for a total of 13.8 percent range extension. In this case, the feedback gains for the first and second harmonics are $Z_1 = 4e^{j*2.36}$ and $Z_2 = 4e^{j*4.10}$.

These results show that constant gain control can achieve a range improvement for this high-speed compressor at 70 percent speed. The results are similar to those obtained by Paduano et al. (1993) and Haynes et al. (1994) on much lower speed compressors in that stabilizing the incompressible-type modes increases the operating range. At this rotor speed the compressible modes, such as the [1, 1] and [2, 1] mode, are sufficiently stable that stabilizing only the [1, 0] and [2, 0] mode with constant gain feedback provides significant range extension.

Study of the prestall waves at the limit of stabilization indicates that the compressible [2, 1] mode becomes lightly damped with constant gain control, and that additional compensation for the [0, 0] and [1, 0] modes may further increase the stable range at 70 percent rotor speed. Rather than refining this control design, however, our investigation turned to control at 100 percent design speed. At this speed, no range extension was achieved with constant gain feedback on the zeroth and first spatial Fourier coefficients. The reason is that both the [1, 0] and the [1, 1] mode are lightly damped at the stall point and a constant-gain controller cannot stabilize both modes simultaneously. A dynamic controller, which can introduce the proper gain and phase at different frequencies, is thus required.

5.2 H_∞ Control Law Design With Eigenvalue Perturbations. Using the identified models presented in Section 4, a robust, linear, dynamic control law was designed to stabilize the compressor at 100 percent speed. This section briefly describes some of the challenges faced and highlights the use of a new design technique to address eigenvalue uncertainty. Details of the control law are left for a future article (see also Weigl, 1997). The reader can refer to Kwakernaak (1993) for a tutorial on H_∞ control law design. The theoretical development of the new eigenvalue perturbation procedure is presented in Smith (1995); Smith et al. (1994) describe the application of the technique to control of a flexible structure. Although the zeroth, first, and second harmonics have been stabilized, we will again focus our discussion on the first harmonic. The design issues and procedure carry over directly to the zeroth and second harmonics. A separate H_∞ control law was implemented for each of these decoupled harmonics.

The reason that constant gain control cannot stabilize the first harmonic is straightforward: The particular gain and phase that damp the [1, 0] mode destabilize the higher frequency modes. To damp all of the dominant modes simultaneously, a dynamic controller tuned to provide different gain and phase at various frequencies is required. Such a dynamic control law can only be designed based on a model of the dynamics to be controlled (the two parameters of the constant gain control law were simply tuned experimentally). Unfortunately, we do not have an accurate model of the *unstable* stall inception dynamics for two reasons. First, the theoretical model discussed in Section 2 is not yet accurate enough for control design. Second, it is difficult to measure the unstable dynamics experimentally even when the compressor has been effectively stabilized. We therefore estimated the unstable dynamics from the identified stable dynamics by extrapolating the stable eigenvalue (and zero) locations shown in Fig. 6(*b*) to a lower mass flow for which the [1, 0] mode is unstable.

This method of estimating the unstable dynamics introduces uncertainty in the control design model. However, the main attribute of many modern control design algorithms, such as H_∞ control, is *robustness* to errors in the control design model: to meet the control specifications effectively despite modeling errors. In this case, the goal is to damp all of the dominant first harmonic modes even though their precise stability and rotation frequency are not known. To address uncertainty directly in the eigenvalue locations, a new technique developed by Smith (1995) and Smith et al. (1994) was used within the H_∞ control design framework. This procedure designs to a *range* of eigenvalue locations as illustrated in Fig. 9. The estimated eigenvalue locations are shown by the x's; note that only the [1, 0] mode is assumed to be unstable based on the identified modes in Fig. 6(*b*). The circles represent uncertainty in the eigenvalue locations; the control law will stabilize the compressor as long as the actual first harmonic eigenvalues lie within these uncertainty areas. [Note that only circular uncertainty regions can be implemented, though the scale in Fig. 9 makes them appear to be ellipses.] The large [1, 0] mode disk ensures that the controller will not destabilize the system at higher mass flows when the compressor is open-loop stable, yet will stabilize the [1, 0] mode at lower mass flows where the dynamics have been estimated. The smaller circles around the lightly damped high-frequency modes account for changes in these eigenvalue locations as the compressor mass flow changes, although these perturbations do not allow for unstable high-frequency modes.

This H_∞ control design has been used to stabilize the first three harmonic perturbations at 100 percent speed. The following section presents the results for the nominal control configuration. We have found that the control design is also robust to moderate changes in the steady-state operating point of the compressor. This was verified by testing the control law with less injected air and at a 95 percent speed as discussed in Weigl (1997). The controlled compressor has also proven to be robust to large amplitude disturbances as shown below.

5.3 Rotating Stall and Surge Stabilization at 100 Percent Speed. The range extension achieved at 100 percent speed is shown in Fig. 10. As in Fig. 7, the total-to-static pressure ratio map is presented for the nominal 3.6 percent injection mass flow rate along with the original speedline. This figure also shows the results of four different control runs, which demonstrate the importance of controlling the 0th and 1st harmonic simultaneously. Controlling either the 0th harmonic or 1st harmonic *alone* results in almost no further range extension. With 50 percent steady injection, the stalling mass flow is reduced by 4.3 percent. With both 0th and 1st harmonic control, about 3.0 percent range extension is achieved; an additional 0.5 percent is gained by stabilizing the 2nd harmonic.

To illustrate that instability in any of these harmonics (0th, 1st, or 2nd) can lead to stall, stall inception transients were recorded with various combinations of harmonics stabilized. The harmonic left uncontrolled is always the one responsible for stall inception. Figure 11 shows the evolution of three wall

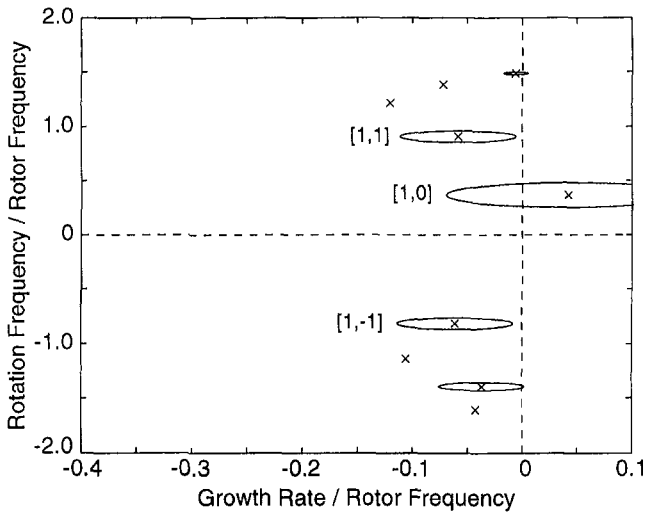

Fig. 9 Eigenvalue perturbations for first harmonic control design

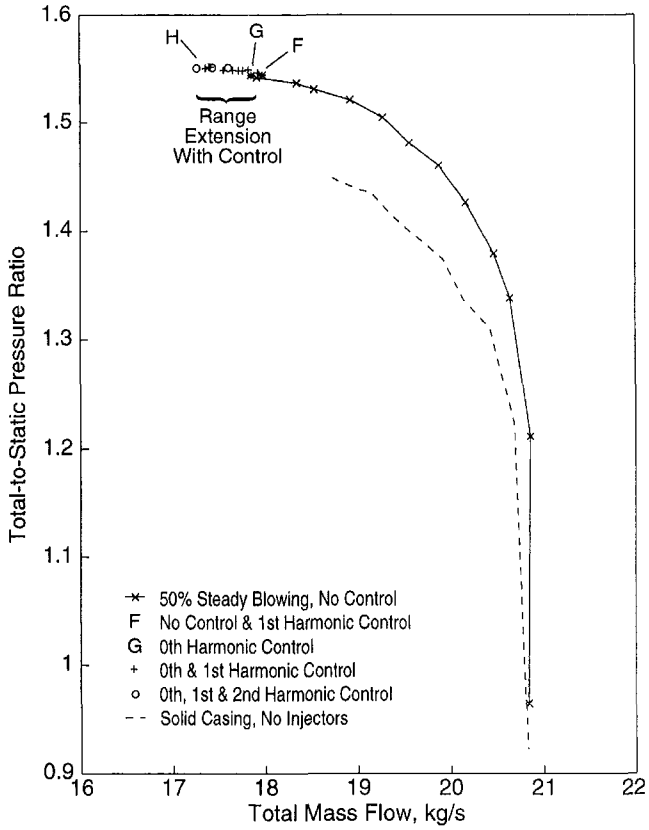

Fig. 10 Stabilized compressor characteristic at 100 percent speed with 3.6 percent injected mass flow rate

static pressure traces at the different stall inception points shown in Fig. 10: (*a*) F: no control, (*b*) F: 1st harmonic control only, (*c*) G: 0th harmonic control only, and (*d*) H: 0th and 1st harmonic control combined. Note that the mass flow is different in each case, corresponding to the mass flow at which *the most unstable uncontrolled harmonic* goes unstable. The pressure perturbations have been nondimensionalized by a measure of the mean dynamic head in the inlet duct ($P_{t_{\text{inlet}}} - P_{s_{\text{inlet}}}$). In all four cases, large-scale instability is initiated by approximately 10 rotor revolutions of rotating stall followed by classic surge cycles. During the large amplitude rotating stall, the peak-to-peak amplitude of the nondimensional pressure perturbations is approximately 4.

Figure 11(*a*) shows that both 0th and 1st harmonic perturbations exist in uncontrolled prestall traces indicating lightly damped 0th and 1st harmonic modes. In Fig. 11(*b*), the 1st harmonic prestall perturbations have been effectively damped, leaving 0th harmonic perturbations, which eventually initiate rotating stall; no operating range extension is achieved. In Fig. 11(*c*), a small range extension is achieved by controlling only 0th harmonic perturbations; here prestall perturbations contain only the 1st harmonic. As discussed by Hendricks et al. (1997), both the 0th and 1st harmonics need to be damped to extend the transonic compressor operating range. Figure 11(*d*) shows stall inception with 0th plus 1st harmonic control; a 2nd harmonic perturbation is now evident prior to stall. Stabilizing the 2nd harmonic provides a little more range extension. Spectral analysis of the stall inception for these four cases (as in Tryfonidis, 1995) indicates that the low-frequency *incompressible,* uncontrolled modes ([0, 0], [1, 0], or [2, 0]) become unstable in this compressor. For the control laws that have been tested, some resonating high-frequency modes are also evident but do not appear to be the cause of instability.

Control tests were also conducted with "one-sided" actuation where the valves were thresholded to only move from 50–100 percent open by clipping the negative portion of the sinusoidal command. With this one-sided unsteady valve motion, the time-averaged injected mass flow rate did increase from 3.6 to 4.0 percent so that the controlled speedline shifted to a slightly higher pressure rise. Roughly the same additional range extension (4.1 percent) was achieved with one-sided actuation as with two-sided, suggesting that it may be possible to stabilize the compressor without adding a large steady amount of injected mass flow. Such a test, allowing the actuators to open from 0–50 percent unsteadily, has not yet been attempted on Stage 35.

We have discussed the robustness properties of the control law with respect to design model inaccuracies. Another form of robustness that has received much attention is disturbance rejection (Eveker et al., 1995). Fundamentally, disturbances drive the system away from its equilibrium, requiring the controller to exert extra effort to recover stable operation. To test robustness, the mass flow was reduced below the open-loop neutral stability point with the control activated. Control was then switched off for some time. During the period with no control, the unstable perturbations grew to large amplitude. When the controller was switched back on, it was required to restabilize with large initial conditions, thereby approximating the effect of a large amplitude disturbance.

Figure 12 shows the results of the disturbance rejection tests. In Fig. 12(*a*), rotating stall perturbations are recovered, and in Fig. 12(*b*), a fully developed surge is recovered. The top trace is the wall static pressure from one sensor and the bottom trace is the measured valve position from one actuator. The accompanying Lissajous figures, 12(*c*) and 12(*d*), plot 0th against 1st harmonic amplitude, to show the trajectory of the system state back toward equilibrium. The units of pressure are ($P_{t_{\text{inlet}}} - P_{s_{\text{inlet}}}$) so that the perturbations can be seen to be a substantial fraction of the mean inlet dynamic pressure. The first point on these plots is the amplitude of the perturbations *at the instant of control reinitiation;* this is the relevant measure of disturbance rejection. In the first case, a primarily 1st harmonic initial condition is stabilized; in the second the 0th harmonic is also large.

6 Discussion and Conclusions

This machine is the first high-speed compressor with circumferentially distributed actuation of sufficient authority and bandwidth to excite and control the modal system dynamics. We have described for the first time the impact of unsteady blowing on compressor performance. The flexibility to excite distributed modal dynamics enabled the first detailed look at rotating stall fluid mechanics in a high-speed environment. We have demonstrated active stabilization of rotating stall and surge in a transonic compressor and achieved a significant extension of the operating range. Finally, these results demonstrate the effectiveness of inlet injection for forcing and controlling high-speed compressor dynamics.

Table 2 summarizes the operating range improvement for the cases we have presented in terms of the change in stalling mass flow referenced to the stall points without injectors. We also tabulate the increase in the NASA standard stall margin as defined by Reid and Moore (1978b):

$$SM = \left[\frac{\text{Total Pressure Ratio (stall)}}{\text{Total Pressure Ratio (ref)}} \frac{\text{Mass Flow (ref)}}{\text{Mass Flow (stall)}} - 1 \right] \times 100$$

For 70 and 100 percent speeds, the peak efficiency points with a steady 3.6 percent injection rate (the nominal configuration for control) have been chosen as the reference points. These reference operating points are labeled as REF70 and REF100

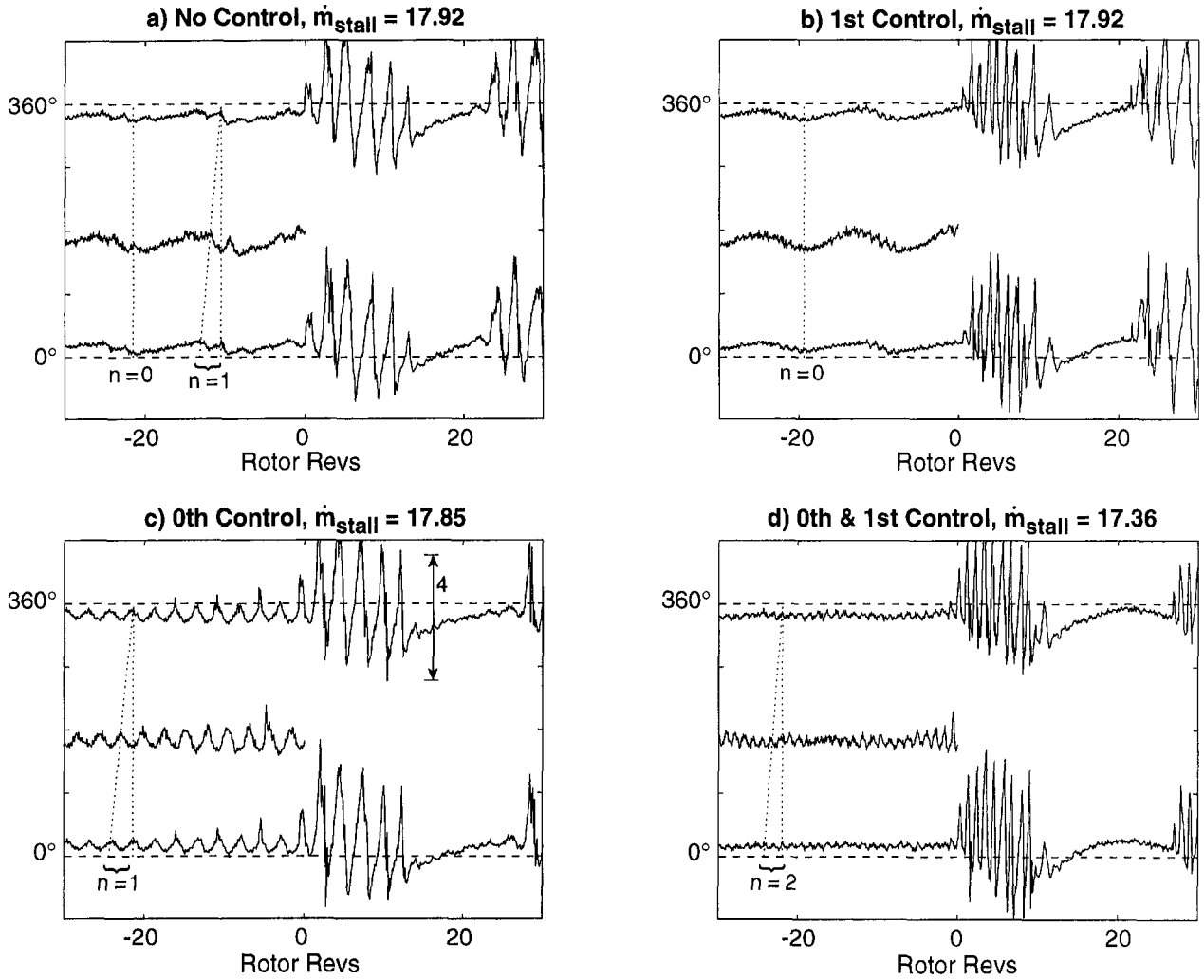

Fig. 11 Wall static pressure perturbations nondimensionalized by ($P_{t_{inlet}} - P_{s_{inlet}}$) at 100 percent speed

in Figs. 2(*b*) and 2(*c*). Although this choice of reference points is somewhat arbitrary, we are not so much interested in the absolute value of stall margin as we are in comparing the changes in stall margin due to steady and controlled injection.

Injection can influence the overall behavior of the compressor in two ways. The first is simply the additional momentum added by the jets, which increases the total pressure at the rotor inlet. The second effect is a change in compressor performance, which increases the pressure rise across the stage. In order to separate the two effects, we have also calculated the stall margin based on the total pressure ratio from the rotor inlet to the compressor exit. To estimate the total pressure at the rotor inlet (with the added jet momentum), the inlet total pressure and injector total pressure were mass-averaged. This conservative estimate assumes that the injected fluid does not mix with the primary inlet flow. Recalculating the stall margin in this manner indicates that the additional momentum contributes approximately 2 percent of the stall margin improvements shown in Table 2, while the change in compressor performance is only about 0.5 percent.

Perhaps the most promising aspect of these experiments is that the prestall dynamics behaved qualitatively as expected from hydrodynamic stability theory, adapted for active control work. Although gaps still exist in *ab initio* predictive capability, the theoretical framework for modeling and control captures the physical processes, and provides guidance in selecting actuator and sensor type, number and placement, bandwidth requirements, and control law design procedures. Neither the predictive capability nor the accuracy of the model is currently sufficient for direct control law design.

Using distributed inlet injection actuators allows us to validate the modeling concepts and proposed physical mechanisms for stall initiation when compressibility is a factor. In particular, we have directly verified that eigenmodes that rotate at a frequency near the rotor frequency exist and become lightly damped near the peak of the pressure-rise map. The existence of these modes was strongly supported by the unforced data and calculations of Tryfonidis et al. (1995), but room for conjecture remained because these modes are close to the rotor frequency. With forced response experiments, we are able to make the following additional statements about the linearized dynamic model of Bonnaure (1991), Hendricks et al. (1993), and Feulner et al. (1996):

- The primary physical mechanisms associated with prestall dynamics in high-speed compressors are captured by the compressible model. This is verified by eigenvalue analysis of data.
- Control design based on the understanding afforded by the theory is effective for stabilization of rotating stall. The theoretical model is validated from a conceptual standpoint although more work is needed for it to be usable as a stall prediction and control design tool.

A useful way to summarize the results is to compare and contrast stabilization of this compressor to stabilization of low-

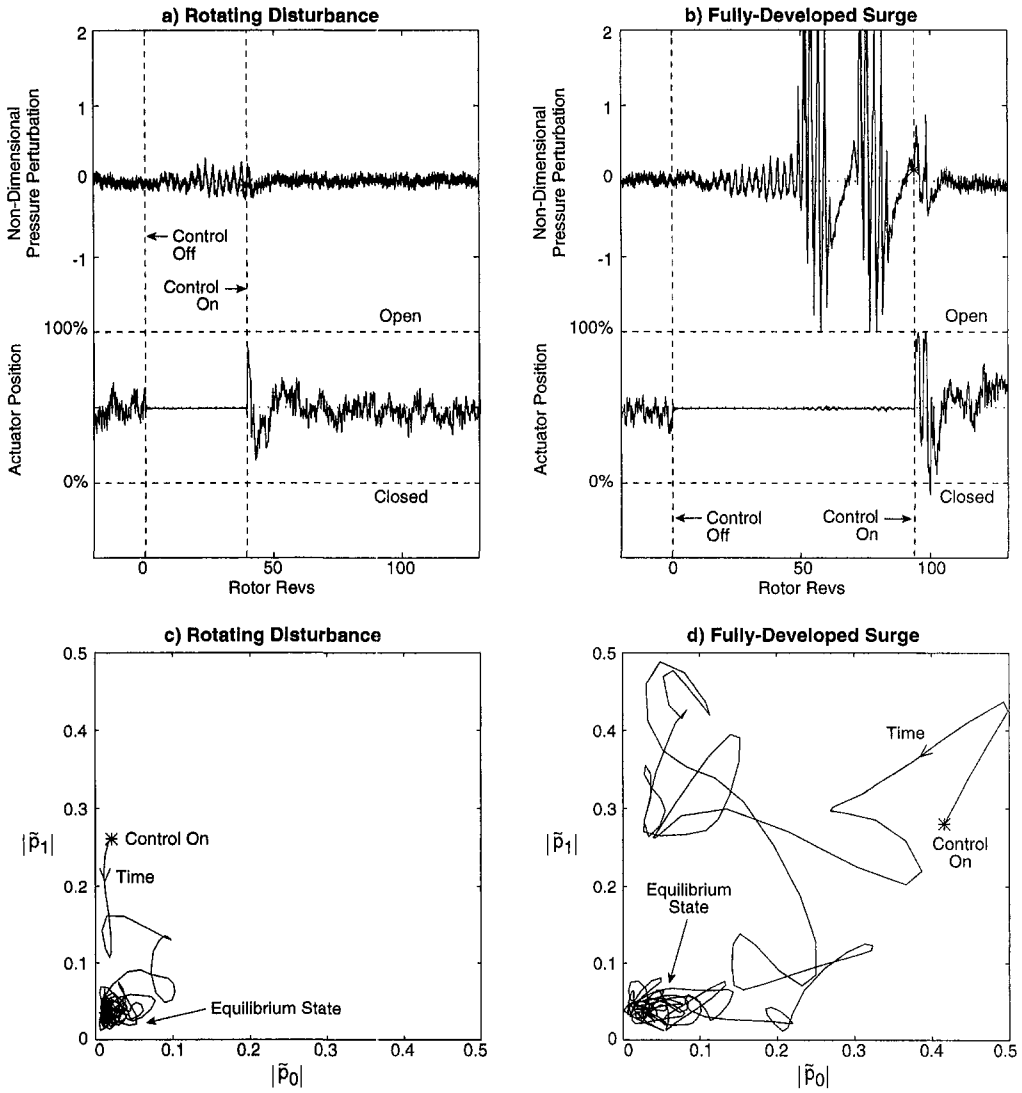

Fig. 12 Recovery from large-amplitude disturbance (pressure perturbations are nondimensionalized by ($P_{t_{inlet}} - P_{s_{inlet}}$))

speed compressors by similar means, reported in Paduano et al. (1993), Haynes et al. (1994), and Gysling and Greitzer (1994). Control results are the same in the following ways:

- Significant range extension can be obtained through stabilization of small amplitude, prestall waves.
- The incompressible modes observed in low-speed compressors are the first to become unstable in this high-speed compressor, although this may not be the case in general, as shown by Tryfonidis et al. (1995).
- With a circumferentially uniform background flow, the dynamics of the circumferential harmonics are decoupled and can be treated as separate entities for the purpose of control.
- As more eigenmodes of the system are stabilized, more range extension is obtained. Instability typically results when an eigenmode that is not being stabilized goes unstable.
- Active stabilization extends the compressor characteristic smoothly, without a sharp drop in pressure rise.

The *differences* between high and low-speed applications are:

- Although circumferential harmonics are decoupled, multiple eigenmodes exist for each circumferential mode due to compressibility effects. Understanding the "compressible modes" is critical to designing effective control laws at high speed.
- Because of the multimodal nature of the dynamics, simple proportional gain feedback is not always sufficient to stabilize the dynamics associated with a given circumferential harmonic. In this study, a dynamic control law using eigenvalue perturbations achieved good results.

Finally, several conclusions were reached concerning the actuation mechanism itself. This experiment constitutes the first demonstration that unsteady injection provides effective and reliable actuation in a high-speed compressor (previous injection studies such as Day, 1993, Behnken et al., 1995, and Vo, 1997, have been done on low-speed compressors). Injecting high-momentum flow near the tip region of the rotor was found to have a significant effect on the steady-state performance of the compressor, increasing its pressure rise and range of operation, as previously reported by Koch and Smith (1968). Further work is needed to investigate the trade-offs between steady injection and active control. Steady blowing requires a large amount of injected air. Active stabilization requires a feedback control law with high-bandwidth sensing and actuation. One must also study the performance impact of both stabilization

schemes before considering any implementation in an engine. In addition, work directed toward developing robust (durable) actuators for engine environments is a necessity if active control is to become a viable technology.

We also note that forced response testing with high-authority, high-bandwidth, distributed actuation provides valuable information that cannot be obtained in other ways. By applying system identification methods to input–output data, we are able to identify the modal content of the wave dynamics of a high-speed compressor. Prior to these studies, compressor wave dynamics were thickly veiled by noise, turbulence, and secondary sources of forcing (rotor–stator interaction noise, excitation at multiples of the rotor frequency, wake noise, etc.). Regardless of the implications for control of rotating stall, the value of this type of experimental setup for the investigation of the compressor dynamics that lead to rotating stall is apparent.

Acknowledgments

This project is a collaboration between NASA Lewis and MIT. The authors would like to thank D. Williams, B. Piendl, M. Goin, D. Van Zante, and R. Bruckner for their help during compressor testing, as well as V. Dubrowski, J. Letendre, and M. Hellwig for their assistance developing the experimental hardware. We would also like to thank H. D. Vo for providing low-speed compressor forced response data. Special thanks also to D. Park for preparing this manuscript. This work was conducted under NASA grant No. NAG3-1457.

References

Behnken, R. L., D'Andrea, R., and Murray, R. M., 1995, "Control of Rotating Stall in a Low-Speed Axial Flow Compressor Using Pulsed Air Injection: Modeling, Simulations, and Experimental Validation," presented at the 34th IEEE Conference on Decision and Control, New Orleans, Dec. 13–15.

Berndt, R. G., 1995, "Actuation for Rotating Stall Control of High Speed Axial Compressors," M. S. Thesis, MIT Department of Aeronautics and Astronautics.

Berndt, R. G., Weigl, H. J., Paduano, J. D., and Epstein, A. H., 1995, "Experimental Techniques for Actuation, Sensing, and Measurement of Rotating Stall Dynamics in High-Speed Compressors," presented at the SPIE International Symposium on Aerospace/Defense Sensing and Dual-Use Photonics, Apr. 17–18, Orlando, FL.

Bonnaure, L. P., 1991, "Modeling High Speed Multistage Compressor Stability," M.S. Thesis, MIT Department of Aeronautics and Astronautics.

Day, I. J., 1993, "Active Suppression of Rotating Stall and Surge in Axial Compressors," ASME JOURNAL OF TURBOMACHINERY, Vol. 115, pp. 40–47.

Epstein, A. H., Ffowcs-Williams, J. E., and Greitzer, E. M., 1989, "Active Suppression of Aerodynamic Instabilities in Turbomachines," *Journal of Propulsion,* Vol. 5, No. 2, pp. 204–211.

Eveker, K. M., Gysling, D. L., Nett, C. N., and Sharma, O. P., 1995, "Integrated Control of Rotating Stall and Surge in a Low-Speed Axial Compression System," presented at the SPIE International Symposium on Aerospace/Defense Sensing and Dual-Use Photonics, Apr. 17–18, Orlando, FL.

Fréchette, L. G., 1997, "Implications of Stability Modeling for High-Speed Axial Compressor Design," M. S. Thesis, MIT Department of Aeronautics and Astronautics.

Feulner, M. R., Hendricks, G. J., and Paduano, J. D., 1996, "Modeling for Control of Rotating Stall in High Speed Multi-Stage Axial Compressors," ASME JOURNAL OF TURBOMACHINERY, Vol. 118, pp. 1–10.

Gysling, D. L., and Greitzer, E. M., 1994, "Dynamic Control of Rotating Stall in Axial Flow Compressors Using Aeromechanical Feedback," ASME Paper No. 94-GT-292.

Haynes, J. M., Hendricks, G. J., and Epstein, A. H., 1994, "Active Stabilization of Rotating Stall in a Three-Stage Axial Compressor," ASME JOURNAL OF TURBOMACHINERY, Vol. 116, pp. 226–239.

Hendricks, G. J., Bonnaure, L. P., Longley, J. P., Greitzer E. M., and Epstein A. H., 1993, "Analysis of Rotating Stall Onset in High-Speed Axial Flow Compressors," AIAA Paper No. 93-2233.

Hendricks, G. J., and Gysling, D. L., 1994, "A Theoretical Study of Sensor-Actuator Schemes for Rotating Stall Control," *Journal of Propulsion and Power,* Vol. 10, No. 1.

Hendricks, G. J., Sabnis, J. S., and Feulner, M. R., 1997, "Analysis of Instability Inception in High-Speed Multi-Stage Axial-Flow Compressors," ASME JOURNAL OF TURBOMACHINERY, Vol. 119, pp. 714–722.

Koch, C. C., and Smith, L. H., 1968, "Experimental Evaluation of Outer Case Blowing or Bleeding of Single Stage Axial Flow Compressor. Part III—Performance of Blowing Insert Configuration No. 1," NASA CR-54589, GE R68AEG318.

Koch, C. C., 1970, "Experimental Evaluation of Outer Case Blowing or Bleeding of Single Stage Axial Flow Compressor. Part IV–Final Report," NASA CR-54592, GE R69AEG256.

Kwakernaak, H., 1993, "Robust Control and Hinf-Optimization—Tutorial Paper," *Automatica,* Vol. 29, No. 2, pp. 255–273.

Longley, J. P., 1994, "A Review of Non-steady Flow Models for Compressor Stability," ASME JOURNAL OF TURBOMACHINERY, Vol. 116, pp. 202–215.

Moore, F. K., and Greitzer, E. M., 1986, "A Theory of Post-Stall Transients in Axial Compression Systems, Part I—Development of Equations; Part II—Application," ASME *Journal of Engineering for Gas Turbines and Power,* Vol. 108, pp. 68–97.

Paduano, J. D., Epstein, A. H., Valavani, L., Longley, J. P., Greitzer, E. M., and Guenette, G. R., 1993, "Active Control of Rotating Stall in a Low-Speed Axial Compressor," ASME JOURNAL OF TURBOMACHINERY, Vol. 115, pp. 48–56.

Paduano, J. D., Valavani, L., Epstein, A. H., and Greitzer, E. M., 1994, "Modeling for Control of Rotating Stall," *Automatica,* Vol. 30, No. 9, Sept.

Reid, L., and Moore, R. D., 1978a, "Design and Overall Performance of Four Highly Loaded, High Speed Inlet Stages for an Advanced High Pressure Ratio Core Compressor," NASA TP-1337.

Reid, L., and Moore, R. D., 1978b, "Performance of Single-Stage Axial-Flow Transonic Compressor With Rotor and Stator Aspect Ratios of 1.19 and 1.26, Respectively, and With Design Pressure Ratio of 1.82," NASA TP-1338.

Setiawan, J. D., 1996, "Distortion Tolerance of Stall/Surge Controllers in Axial Compression Systems," M. S. Thesis, MIT Department of Aeronautics and Astronautics.

Smith, R. S., Chu, C., Fanson, J. L., 1994, "The Design of Controllers for an Experimental Non-collocated Flexible Structure Problem," *IEEE Trans. on Control Systems Technology,* Vol. 2, No. 2, pp. 101–109.

Smith, R. S., 1995, "Technical Notes and Correspondence: Eigenvalue Perturbation Models for Robust Control," *IEEE Trans. on Automatic Control,* Vol. 40, No. 6, pp. 1063–1066.

Tryfonidis, M., Etchevers, O., Paduano, J. D., Epstein, A. H., and Hendricks, G. J., 1995, "Pre-stall Behavior of Several High-Speed Compressors," ASME JOURNAL OF TURBOMACHINERY, Vol. 117, pp. 62–80.

Vo, H. D., 1997, "Active Control of Rotating Stall in a Three-Stage Axial Compressor With Jet Actuators," M.S. Thesis, MIT Department of Aeronautics and Astronautics.

Weigl, H. J., 1997, "Active Stabilization of Rotating Stall and Surge in a Transonic Single Stage Axial Compressor," Ph.D. Thesis, MIT Department of Aeronautics and Astronautics.

Experiments in Active Control of Stall on an Aeroengine Gas Turbine

C. Freeman

A. G. Wilson

Rolls-Royce plc,
Derby, United Kingdom

I. J. Day
Whittle Laboratory,
Cambridge University,
Cambridge, United Kingdom

M. A. Swinbanks
MAS Research Ltd.,
8 Pentlands Court,
Pentlands Close,
Cambridge, United Kingdom

This paper describes work carried out between 1989 and 1994 to investigate the application of "Active Stall Control" to a Rolls-Royce Viper turbojet. The results demonstrate that stall control is feasible and can increase the stable operating range by up to 25 percent of pressure rise. Stall disturbances were detected using rings of high response pressure transducers positioned at different axial planes along the compressor, and processed using a PC-based data acquisition and control system. Actuation was provided by six hydraulically operated sleeve valves positioned to recirculate air over all or part of the compressor. Stall was artificially induced using combinations of in-bleed into the combustor outer casing, fuel spiking, hot gas ingestion, and inlet pressure spoiling, thus replicating many of the transient conditions commonly observed to make a compressor prone to stall. Results are compared from a number of stall control strategies including those demonstrated at low speed by Paduano et al. (1993) and Day (1993). Best results were obtained with detection of nonaxisymmetric disturbances coupled with axisymmetric control action. A control system of this type is demonstrated to be capable of extending the stable engine operating range at all speeds and with each method of inducing stall.

Introduction

Adequate surge margin is a primary requirement of every aeroengine compressor design. Conventional methods of ensuring sufficient margin (increasing blade numbers, variable guide vanes, handling bleed) all carry implicit penalties in terms of compressor weight, cost, complexity, and/or efficiency. The search for an alternative means of achieving sufficient margin is as old as the gas turbine. Condition monitoring and subsequent bleed valve opening were studied in the 1960s. Stall cell triggered blowing (Ludwig and Nenni, 1978), and feedback control of surge in centrifugal compressors (Ffowcs Williams and Huang, 1989) were examined in the 1970s and 1980s. The most important advance since the 1960s has been the advent of microprocessors, which enable many detectors to be monitored simultaneously and rapid actuator movements to be accurately controlled. In the early 1990s control of rotating stall was theoretically examined and demonstrated on low-speed compressors by Paduano et al. (1993) and by Day (1993). Over the last decade many studies have been made too of stall inception in axial flow compressors at low and high speed.

The objective of the work described in this paper was to apply active stall control directly to an aeroengine. The intention was not to produce a flight-worthy active control system, but rather to explore what gains could be achieved with current technology, what new technology might be needed in the future, and what the potential benefits might be.

Aeroengines in service experience a number of conditions that can make them prone to stall. These can be categorized as follows:

1 *Raised Working Line.* The working line can be raised by throttle transients, nonequilibrium clearance changes, nonequilibrium heat transfer, and unsteady inlet flow. These are all transient conditions and typically last for a few seconds. Rubs, erosion, corrosion, foreign object damage, and bill of material damage also raise the working line and are irreversible without a shop visit.

2 *Lowered Surge Line.* The surge line can be lowered transiently by inlet distortion, nonequilibrium clearance changes, and unsteady gas ingestion. Irreversible changes are produced by shaft out of balance, foreign object damage, bill of material damage, and rubs.

Any successful stall control system has to be capable of dealing with short-duration movements in both the working line and the stall line; monitoring the working line alone is not sufficient. Similarly, any experimental investigation of active control techniques must allow both types of surge margin deterioration to be investigated.

Equipment

Viper Engine. The VIPER was originally designed in the late 1940s as an expendable engine for unmanned air vehicles. Since that time it has been progressively developed and uprated, and is now used on a number of aircraft types. The research vehicle has an eight-stage axial flow compressor, a single-stage turbine, an annular vaporizer combustor, and a single shaft with three bearings. The overall design pressure ratio is 5.25, with a mass flow of 23 kg/s and a turbine entry temperature of 1200 K. Early designs had a seven-stage compressor. Later versions were upflowed with a "0" stage; the stages are therefore numbered from 0 to 7. The compressor has fixed inlet guide vanes and a stage 4 bleed through the stator outlet platforms into a bleed manifold. This is used for starting and low-speed handling. At exit from the compressor there is a two-row outlet guide vane arrangement and a diffuser split into six segments by the center bearing support structure. For these tests the fuel flow rate was controlled manually. The VIPER was chosen as it is both simple and robust, while sharing many of the aerodynamic characteristics of more complex engines. The particular engine used for the experiments is an old mark, being time-expired after several thousand hours of flight.

The engine is shown in Fig. 1, with the stall control equipment fitted.

Contributed by the International Gas Turbine Institute and presented at the 42nd International Gas Turbine and Aeroengine Congress and Exhibition, Orlando, Florida, June 2–5, 1997. Manuscript received at ASME Headquarters February 1997. Paper No. 97-GT-280. Associate Technical Editor: H. A. Kidd.

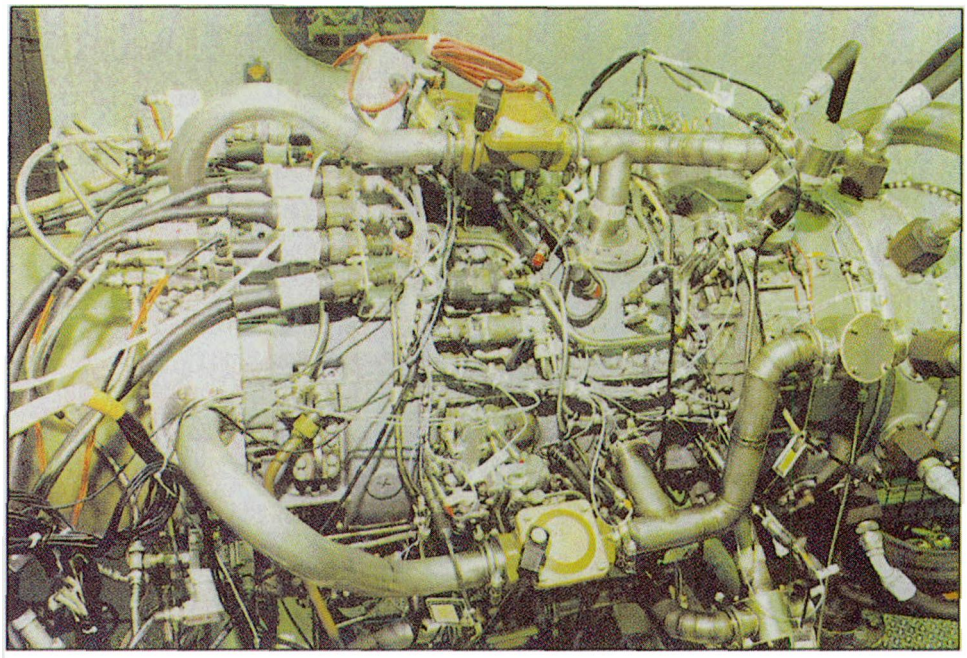

Fig. 1 Rolls-Royce VIPER engine with stall control equipment fitted

Control Bleed Recirculation. The actuation system adopted for most of the experiments described in this paper was bleed air recirculation. High-pressure air was taken from a downstream position and re-injected through the compressor casing. The control mechanism thus had the combined effect of upstream-injected flow, such as used by Day (1993), and downstream bleed-off. The recirculated air was ducted forward through six pipes positioned around the annulus. These pipes were not symmetrically spaced around the engine because of the inevitable complexity of a real engine geometry (Fig. 1).

The axial position at which control action is required can move with engine speed as a result of changes in stage matching (Wilson and Freeman, 1994; Day and Freeman, 1994). In order to accommodate this, a flexible arrangement was devised whereby air could be recirculated from the exit of the compressor to stage 4, from stage 4 to compressor inlet, or around the whole compressor from exit to inlet. Provision was thus made for six bleeds from stage 4 by segmenting the bleed manifold, and for a similar number from the exit diffusers. Re-injection at inlet was through discrete adjustable area injector nozzles upstream of the inlet guide vanes, and at stage 4 through stator outer wall bleed holes. In each case nozzles were designed to inject the flow broadly parallel to the free-stream direction. The nozzles were sized such that the maximum flow rate was 8 percent of inlet flow when recirculating around the whole compressor, and 5 percent of inlet flow when recirculating around the rear of the machine.

Control Valves. The flow through each of the recirculation pipes was independently controlled using an injector unit consisting of a sleeve valve inside a duct (Fig. 2) with an adjustable nozzle in the compressor casing. A form of flapper valve as the nozzle would have been more aerodynamically efficient, but was not used because of the risk of damage to the engine through uncontained valve failure. The sleeve valves were generally placed just upstream of the reinjection point, but could also be positioned at the far end of the recirculation duct.

Each of the sleeve valves was designed to pass a flow comparable to one sixth of the bleed required for starting and was capable of operation at up to 300 Hz. For comparison rotating stall cell frequency at design engine speed is 106 Hz, and so the valves were capable of tracking the second harmonic of a developing stall cell. Some loss of performance would be expected for a rapidly changing second harmonic signal at high engine speeds, where the amplitude and phase changes can introduce higher frequencies into the signal. Higher frequency response could have been achieved by using larger numbers of smaller valves, but the complexity of the engine geometry made this impractical.

Alternative Actuation Techniques. Two alternative actuation techniques were investigated in addition to bleed air recirculation. High-response bleed-off from the rear of the compressor was effected using the same control valves as for the recirculated bleed. Fuel modulation was also investigated by coupling a high response fuel dipper unit into the manifold supply line.

Inducing Stall. The VIPER is a robust engine, which does not stall under normal test conditions. In order to carry out the experiments described in this paper, stall had to be artificially induced using combinations of inbleed into the combustor outer casing, fuel spiking, hot gas ingestion, and inlet pressure spoiling.

Combustor inbleed air was taken from a large external tank pressurised to 25 atm by means of a standard commercial air compressor. Air was fed from the tank into a manifold around the engine and from there into the combustion chamber through

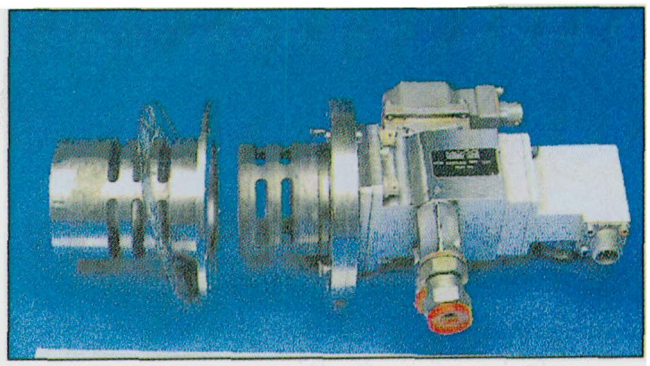

Fig. 2 Sleeve valve assembly

12 adjustable nozzles. The air flow was controlled by an on/off valve coupled with a pressure control valve, which compensated for falling supply pressure as the tank emptied.

For the hot gas ingestion tests, a mixture of exhaust gas and bleed air was taken from a small Palouste gas turbine. A flapper valve (Fig. 3) was used to direct the hot gas either into a sector of the inlet or into the detuner downstream of the VIPER engine. The Palouste had two speed settings, idle and max. Hot gas ingestion was therefore off, low, or high with no settings in between. For these tests the normal airmeter was replaced by a metal inlet capable of withstanding the higher temperature inlet gas.

The normal fuel control system was replaced by a manual system, which allowed fuel injection at a rate sufficient to stall the engine. Fuel spiking was only effective at low engine speeds as the fuel flow rate could not be increased above the normal maximum.

Instrumentation. High-response Kulite pressure transducers were placed in rings of five or six around the compressor casing at stage 0 inlet, stage 2, stage 3, stage 4, stage 6, and stage 7 exit. A smaller number of transducers were placed at stages 1 and 5 where access is limited. The overall pressure ratio and mass flow were measured by lower response probes. Additional vibration monitors, compressor exit thermocouples, and shaft speed detectors were also fitted. The pipes linking the bleed off and re-injection ports were equipped with mass flow meters.

Control Computer and Associated Hardware. A dedicated data acquisition and control system was constructed specifically for the work described in this paper. For the main series of tests a 32 input, 16 output digital signal processing unit was used based on a Motorola 96000 floating point-processor and associated mass-RAM storage. Data were sampled at 4 kHz per channel and captured in the local high-speed RAM. This unit was interfaced to a 386/25 PC for subsequent data download and high-level data analysis. This enabled a wide range of real-time control algorithms to be implemented, while at the same time permitting the capture and storage of all input and output data during the course of a stall event. Immediately after an event had been captured, data were automatically downloaded to the host PC, permitting on-line analysis of the results.

For some of the later tests, a second 48 channel data acquisition unit operating to similar conventions was interfaced to the first via a networked 486/66 PC. The units were externally synchronized to permit the accurate acquisition of up to 80 channels, but with the capability to perform more detailed higher-rate sampling on the second unit.

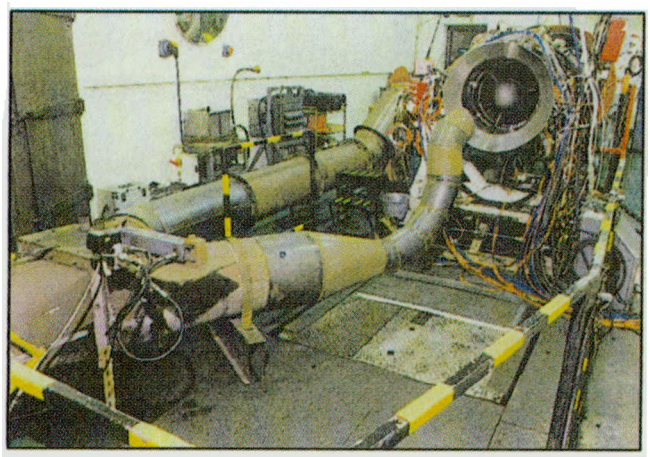

Fig. 3 Hot gas ingestion unit (flapper valve on far left)

Control algorithms could be selected using appropriate menus to configure the operating setup and parameters. The algorithm and configuration parameters were automatically stored along with the acquired data to give a comprehensive record of each test condition.

System Evaluation

Stall Inception Behavior Without Control Action. The "natural" stalling behavior of a compressor (that is, the behavior without any control action present) can have a large impact on the design of an effective control strategy. The VIPER engine compressor exhibits a wide variety of behavior dependent on engine speed and the method used to induce stall.

The stall inception behavior of the VIPER engine with fuel spiking and combustor inbleed has already been extensively analyzed and modeled (Wilson and Freeman, 1994; Day and Freeman, 1994; Freeman and Wilson, 1993; Wilson, 1996), and is therefore only summarized here. Up to 75 percent speed (without the usual handling bleed) the compressor operates in permanent three or four-cell "tip stall" of stage 0. This stall is benign in the sense that it does not inhibit normal engine operation and disappears as the speed is increased. As the surge line is crossed one of the cells grows, leading to single cell "locked-in" stall. Between 70 and 87 percent locked-in stall is initiated by a single short circumferential length scale "spike" at the front of the machine. Between 90 and 100 percent speed stall/surge is initiated by a disturbance covering a third of the annulus downstream of stage 4, which stays in a fixed circumferential location for three to four rotor revolutions before starting to rotate. A "modal" stall inception pattern has recently been detected in the VIPER engine, but only in the narrow speed range between 85 and 87 percent speed.

During these tests hot gas ingestion was also used to stall the engine, giving somewhat different stalling behavior. The surge line with hot gas ingestion is compared to the clean inlet flow surge line in Fig. 4, and for this extreme level of distortion shows a complete loss of surge margin at high speed. At part speed some additional combustor inbleed in addition to the hot gas ingestion was required to induce stall. Pressure traces from the individual transducers at compressor inlet, stage 3 and exit are compared in Fig. 5 for a hot gas ingestion stall event and a combustor inbleed event, both at high speed. The pressure spikes at compressor inlet and stage 3 and corresponding troughs at compressor exit seen at around 0.07 s in Fig. 5(a) represent short circumferential length scale stall cells that extend almost axially through the compressor. The cells quickly die out as they move around the annulus, until at around 0.17 s a cell is produced that travels around the circumference and leads to surge.

At each axial position the red trace in figure 5 represents the transducer nearest top dead center. The green trace represents the next position in the direction of rotor rotation, followed by the purple and light blue traces. The disturbances at around 0.07 s in Fig. 5(a) are visible on the red trace at stage 3, but are most strongly pronounced on the green traces, indicating that the cells are strongest just after top dead center, that is, out of phase with the circumferential position of the distortion, which was centered at 225 deg from top dead center in the direction of rotation. This phase difference can be compared with the distortion theory of Hynes and Greitzer (1987), which predicts that the maximum growth of stall disturbances will occur toward the end of the distorted region in the direction of rotor rotation.

The spike stall inception pattern observed with hot gas ingestion at high speed is thought to be due to the change in corrected speed. The peak inlet temperature in the distorted region is around 200°C, which drops the inlet corrected speed such that 98 percent mechanical speed becomes 75 percent corrected speed locally. Spikes were observed in the clean compressor at this speed. Inlet pressure distortion generated by a spoiler gauze

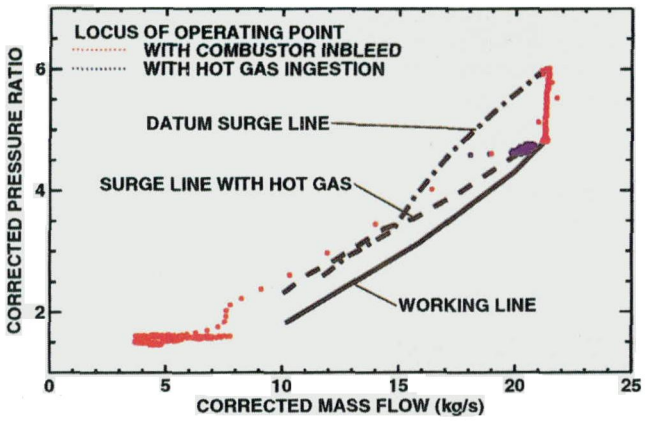

Fig. 4 Comparison of hot gas and inbleed surge lines

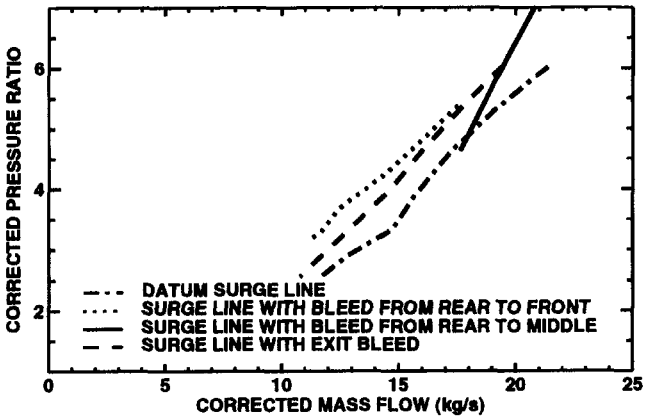

Fig. 6 Effect of steady-state recirculated bleed on the surge line compared with the effect of an equivalent amount of exit bleed

gave similar part-circumference stall cells, generated at random intervals, that eventually travel around the circumference followed by stall. It did not, however, produce spikes at high shaft speed as the corrected speed was unchanged.

Effect of Steady-State Recirculation. The surge line of the compressor was measured with steady-state recirculation from compressor exit to inlet and from exit to stage 4, using combustor inbleed to induce stall. The results are compared in Fig. 6 with the datum surge line (no recirculation). The effect on the surge line of conventional exit bleed is also shown, plotted on a net flow (after bleed) basis. This is not a measured surge line, but is simply calculated from the datum performance, neglecting movements in the steady-state operating point due to efficiency changes. The quantity of bleed air taken (8 percent) is the same for the conventional exit bleed case as when recirculating bleed around the whole compressor.

At low speeds recirculating air from the rear of the compressor to the front removes the permanent rotating stall and there is a net gain in surge margin. The recirculation at high speed from compressor exit to stage 4 shows a sizable gain in high speed pressure ratio, which is consistent with stage stacking studies carried out on the compressor. Figure 6 shows that over most of the speed range steady-state gains in surge margin can be achieved by appropriate use of bleed air recirculation.

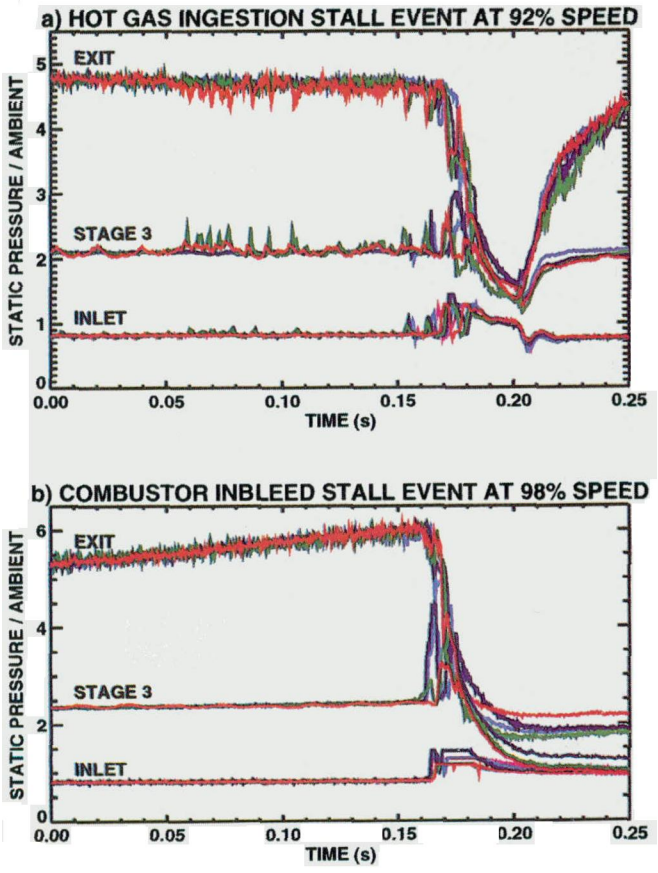

Fig. 5 Comparison of two high-speed stall events

Valve Calibration. There are two elements of the performance of the valves requiring calibration: the mechanical movement in response to the electrical demand and the aerodynamic response to the mechanical movement. In order to determine the mechanical response of the valves a swept frequency signal to 300 Hz was applied as the demand signal with the valve motion monitored by linear velocity displacement transducers (LVDTs). The response amplitude was flat up to 200 Hz with a mean time lag of 3.1 ms. Above 200 Hz a reduced response was measured. In operation this was corrected by a frequency-dependent gain in the control software. In practice the linearity of the actuation system was compromised above 200 Hz by the aerodynamic response of the ducting.

The aerodynamic response to the movement of the valves was determined by applying a square wave demand signal to the valves and comparing the downstream nozzle drive pressure with the feed pressure and the valve opening. The duct/valve combination was observed to give 75 percent pressure recovery when fully open and 37.5 percent when 30 percent open. The ducting, up to 1 m from inlet to outlet, imposed a further lag of up to 3 ms (depending on temperature) when recirculating around the whole machine and 1 ms when recirculating from compressor exit to stage 4. For a rotating wave input signal (that is, a sinusoidal input signal opening each valve in turn around the compressor) this time lag represents a phase shift between the effect of bleed-off at the rear of the recirculation region and mass flow injection at the front. The phase shift is 45 deg for a typical cell speed when recirculating from the rear of the compressor to stage 4, and 150 deg for a stall cell at the front with recirculation around the whole compressor. This phase shift proved significant during the stall control tests and is considered further below.

System Response and Actuator/Detector Interaction. Attempts were made to characterize the dynamic response of the system using frequency swept rotating input signals. Figure 7 shows the response of a stage 3 transducer to frequency sweeps from 50 to 150 Hz with recirculation from compressor exit to stage 4 during a 90 percent speed combustor inbleed event, and

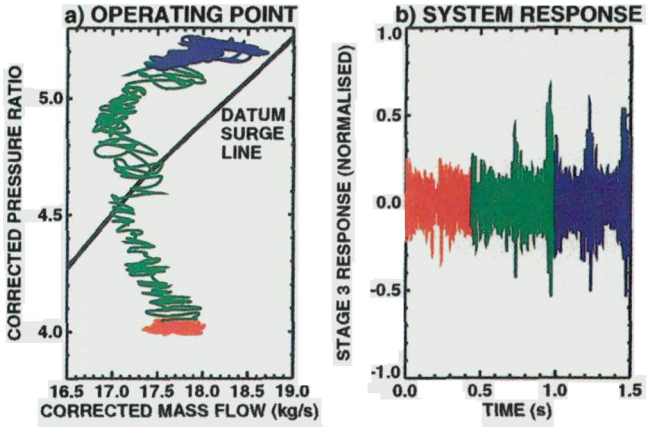

Fig. 7 Response to injected signals versus proximity to surge. First harmonic rotating wave, frequency swept 50–150 Hz every 0.25 s. Colors relate equivalent periods on each graph.

shows that the response is dependent on the position of the operating point relative to the surge line; away from the surge line (marked in red on Fig. 7) the response is relatively small. As the pressure ratio rises (green) the response increases in amplitude. Above the datum surge line (blue; operation here is made possible by the steady-state effect of the recirculated bleed air) the response remains at its maximum level. Further investigation showed that the response is also dependent on detector position (axial and circumferential), actuator position, shaft speed, and the test waveform. In these circumstances a constant linear characterization is not possible.

For the engine/control system configurations described in this paper, the objective was to achieve feed forward control (simple conventional feedback control was not considered appropriate due to the extended, distributed nature of the system, the inherent system delays, and the nonlinear operating characteristics). With control systems of the feed forward type the most tractable performance is achieved by minimizing interactions between actuator and detector. A study was therefore undertaken to determine the best axial position for the detector signals, defined as the position showing the highest amplitude stall inception signals relative to the response to actuator movement. At high speed with recirculation from compressor exit to stage 4 the optimal position was found to be stage 3, as illustrated in Fig. 8. Note that the amplitude of the stall signal changes continuously over the inception period, and so the scaling for the line representing the stall signal is necessarily arbitrary. Below 86 percent speed stage 0 showed the highest amplitude stall inception signals, but also the greatest response to the actuators, and again stage 3 was found to be optimal. The control experiments presented in this paper were all performed using the stage 3 transducers for stall detection, although similar experiments were performed using the transducers at compressor inlet, stage 2, and stage 6.

Fuel Dipper and Exit Bleed Frequency Response. The response of the fuel dipper unit was tested using a square wave test signal. The fuel manifold pressure responded to the injected test signal with a delay of only 3 ms. The combustor pressure, however, responded only slowly to the change in fuel pressure, with a further 40 ms delay before it started to fall. This delay was due to the vaporizer dwell (air spray burners have much lower dwell times), and rendered fuel dipping ineffective as a stall control actuator mechanism.

The exit bleed-off system was also slow in dropping compressor delivery pressure. A time of 3 ms was required for the valve opening and a further 7 ms for an adequate pressure response. Again this was found to be too slow for stall control purposes. A relatively faster response would be expected in higher pressure ratio engines, which have in general a smaller air mass at compressor delivery pressure relative to the mass flow rate.

The conclusions given above relate to active control in the sense of eliminating or avoiding high-amplitude rotating stall. Stall control experiments have been performed using exit bleed as an actuation device (Ludwig and Nenni, 1978; Eveker et al., 1995). In these experiments significant improvements were recorded in the stalled behavior of the compression system. In neither case, however, did the system prove sufficient (in general) to prevent the growth of rotating stall to significant amplitudes.

Stall Control Experiments

In the following sections three active control techniques are described, which were applied to the VIPER engine; linear modal control, threshold control with nonaxisymmetric actuation (''threshold sequential''), and threshold control with axisymmetric actuation (''threshold simultaneous''). The threshold techniques proved most effective. In particular, the threshold simultaneous technique proved a robust method capable of extending the stable engine operating range at all speeds. A subsequent section describes the use of nonaxisymmetric recirculated bleed to recover surge margin lost due to inlet distortion.

Linear Rotating Stall/Surge Modal Control. Paduano et al. (1993) used a low-speed compressor to demonstrate a linear modal stall control system in which measured flow disturbances were decomposed into circumferential harmonics and fed to the actuators (in their case fast-moving inlet guide vanes) with a preset gain and phase adjustment. The compressor they used showed a modal stall inception pattern, and a significant improvement in surge margin was recorded controlling only the first two harmonics of the disturbance. The VIPER engine, however, exhibits a short circumferential length scale (''spike'') inception pattern (Day and Freeman, 1994), with no significant period of growing prestall modal waves (Wilson, 1996). Even in the early stages of development where linear control might be appropriate, the waveform of these short length scale disturbances could not be matched by the actuation system: the spikes had significant signal content up to the eighth circumferential harmonic, whereas control action was limited to the first two harmonics by the frequency response of the control valves. Scaling valves to operate with equal stress and drive pressure means the number of valves required to pass a given flow rate rises as the square of the frequency response, and ten times as many valves would be required to match the waveform of the stall cells early on in the event.

In view of the above, it was not expected that a linear modal control system would be applicable to the VIPER engine. This

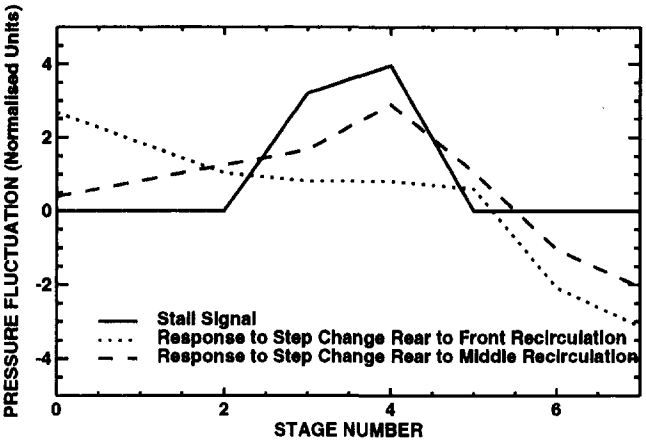

Fig. 8 Actuator detector interaction. Stall inception signal at stage 3 compared with response to actuator movement.

was verified experimentally using a system similar to that of Paduano et al., but using recirculated bleed as the control mechanism. The pressure signals from a ring of transducers at a given axial plane were first of all resolved into first and second circumferential harmonics (together with a mean level), and then filtered to pass only rotating stall signals in a given frequency band. The results were adjusted in accordance with a preset gain and phase setting before being sent to the control valves. At high speed the growth rate of the stall disturbance was such that the numerical filters in the control algorithm did not respond until the stall was too far developed to be stopped. At middle speeds some improvement in surge margin was recorded, but detailed investigation showed the improvement to be largely independent of phase. This indicates that the improvement was not due to true "modal control," but rather to the mean level of valve opening.

Although largely independent of phase, the surge margin improvement at middle speeds was heavily dependent on the gain setting. Data from a series of stall events with various gain settings are shown in Fig. 9. In each case inbleed was introduced into the combustion chamber at 90 percent speed at a rate insufficient to stall the engine. The engine was then decelerated until it could no longer support the increased pressure rise due to the inbled air. The events with high gain settings, and therefore high levels of recirculation, show stable operation to lower flows as the engine decelerates.

In view of the results described above, a simpler control system was developed using the modal stall detection system but with axisymmetric actuation. This new system worked well at low and middle speeds, with comparable results to those obtained using the threshold simultaneous control system described later.

Threshold Sequential Control. The "threshold sequential" control technique is similar to that used by Day (1993). Each valve is effectively controlled by a single pressure transducer. The AC coupled pressure signal measured by each transducer is compared to a threshold level. If this level is exceeded, then appropriate valves are opened (depending on the preset phase relationship) until the measured pressure level falls below the threshold level. It is then held open for a further predefined time interval before being closed. The nonuniform spacing of the valves and transducers and the requirement of an arbitrary phase relationship between the two was catered for by assuming that the valve demand waveform was sinusoidal around the circumference and opening each valve in proportion to the positive part of the wave. The valves opened were not necessarily close to the transducer detecting the disturbance. With recirculation from compressor exit to stage 4 the response time of the control system is 4 ms, whereas at high speed a stall cell takes 8 ms to rotate around the annulus, and so the valve to be opened

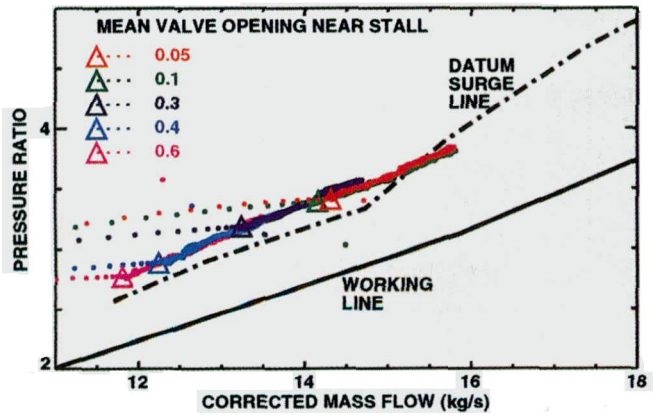

Fig. 9 Modal control: stall point as a function of mean valve opening

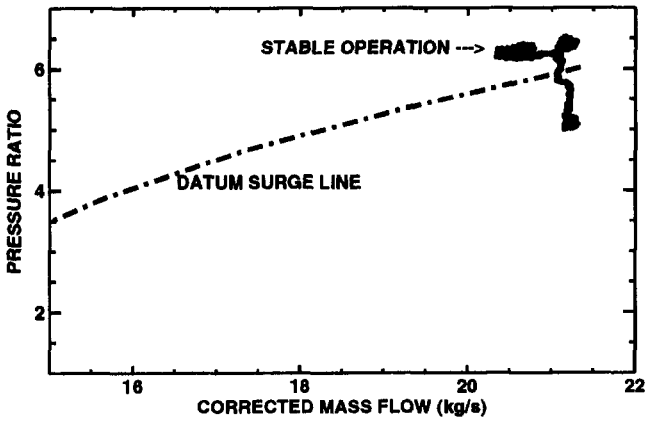

Fig. 10 Threshold sequential control at 98 percent speed

in this case is diametrically opposite the transducer detecting the disturbance. In practice a range of phase relationships and threshold levels was tested at each engine speed.

At high speed, stall in the VIPER engine is initiated toward the rear of the compressor (Wilson and Freeman, 1994; Day and Freeman, 1994), and recirculation from the rear of the compressor to the middle can be used as a control mechanism. Figure 10 shows a typical combustor inbleed event at 98 percent speed with stall control. Here the valves are controlled using the stage 3 transducers at the optimum phase angle (180 deg), and the engine is shown to operate stably above the pressure ratio at which it had previously stalled, with a gain in surge margin of at least 11 percent of the pressure rise. At this speed the engine could not be stalled by inbleed with the control system in operation as the industrial compressor used to pump up the air tank was on its limit.

The threshold level used for the control experiments ensured that the valves were closed for normal engine operation below the surge line. As the surge line was crossed, the threshold nature of the system meant that most of the time some low level of stall was present, continuously growing, then being removed and starting again. As the pressure level moved significantly above the surge line, the level of activity increased such that the valves were kept mostly open. Close to the surge line, the valves were opening and closing individually, and consequently the amount of air recirculated when operating in this form was relatively small.

Without control, the stalling behavior shows a clear circumferential bias, being concentrated around top dead center. With control at the optimal phase setting, the maximum transducer activity was seen after top dead center and the maximum valve activity prior to top dead center (Fig. 11). A degree of asymmetry is present in all aeroengines, and hence this type of behavior, with activity levels distributed asymmetrically around the compressor, is to be expected.

The control system with the same gain and phase settings and recirculation from the rear to the middle of the compressor was also used to control stall events induced by hot gas ingestion at high speed. Without control the compressor stalled with hot gas ingestion and no inbleed; with threshold sequential control there was an improvement equal to half the loss of surge margin.

The control technique was also tested with recirculation from the rear of the compressor to the front. The results in this case were less impressive. At 92 percent speed there was an improvement in the surge margin of 6 percent of pressure rise at the optimum phase angle (180 deg), as shown in Fig. 12. Furthermore, the threshold levels were required to be lower than for the simultaneous control described in the next section.

The recirculating bleed actuation system relies on the double beneficial effect of bleed off at the back of the compressor and mass flow injection at the front. One reason for the relatively

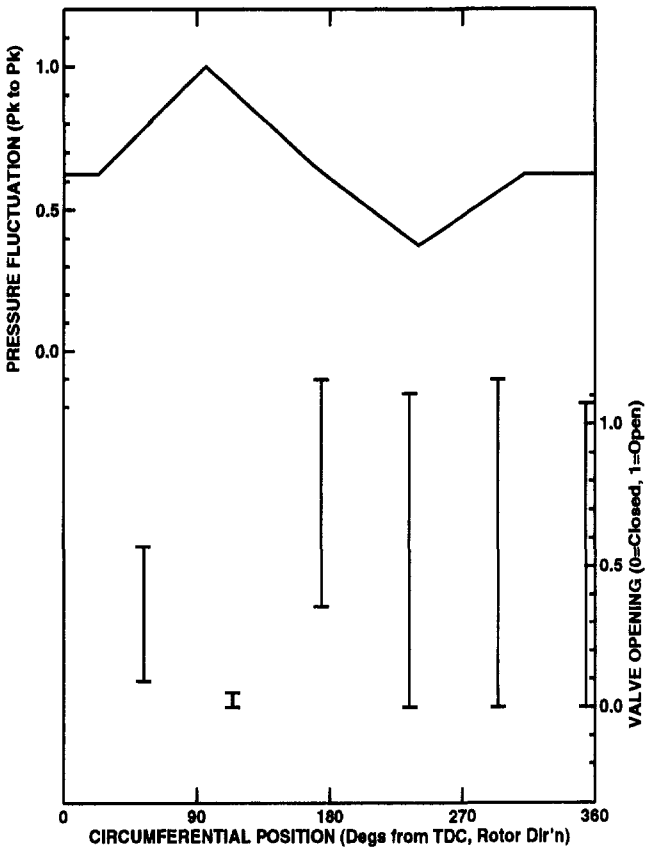

Fig. 11 Threshold sequential control at 98 percent speed. Control bleed air recirculated rear to middle.

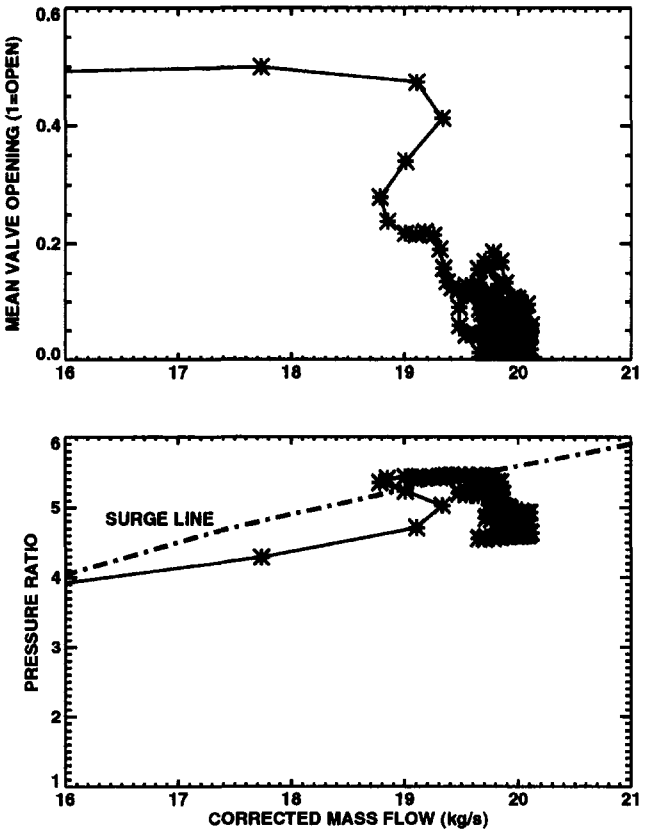

Fig. 12 Threshold sequential control at 92 percent speed with recirculation from rear to front

poor performance with recirculation around the whole compressor is that the total gas path length for the control air is up to 2 m, with a resulting time lag of 6 ms. With this time lag the pressure signal resulting from the bleed-off at the rear of the compressor is out of phase with the signal from the mass flow injection at the front. Furthermore, it is impossible with a fixed geometry to ensure that the two effects are in phase across the entire operating speed range.

Threshold Control of All Valves Simultaneously. The two stall control techniques described above, which were based on nonaxisymmetric actuation, gave only limited benefits in terms of stall margin at low to middle speeds where recirculation was required around the whole compressor. For this reason a simpler control strategy was developed, in which all of the valves were triggered simultaneously in response to any pressure signal exceeding a threshold level. This technique was investigated for stall events induced by inbleed, hot gas, and combinations of the two over the entire speed range, with recirculation from the rear of the compressor to the front and from the rear to the middle.

For successful control, the threshold level must lie between upper and lower limits, as illustrated in Fig. 13, which shows pressure traces as recorded by the transducers at stage 3 during a stall event without control at 98 percent speed. The first clear sign of impending stall is the slow rise in pressure on the green and red signals at 9 rotor revs. The leftmost vertical line marks the point at which a stall detection signal would be too late to reverse the growing stall cell, after accounting for the time delay introduced by the actuation signal. The threshold level must therefore be below the maximum pressure level reached prior to this point. At the same time it must be above the level (marked by the horizontal line) of the background noise to prevent false alarm signals away from stall.

A picture similar to Fig. 13 could be drawn for each of the methods used to precipitate stall. It is possible that a very fast stalling disturbance, of the order of the stall inception time, would give a different picture, but such disturbances were not modeled in the present tests.

Detailed testing over the speed range established the upper and lower limits on threshold values which proved effective. The limits are shown in Fig. 14 for control using the stage 3 transducers. Within these limits the control technique proved able to prevent or delay the onset of stall at all speeds, with each of the methods used to induce stall.

During each controlled event the valves opened in response to a growing stall disturbance. With the valves open, the com-

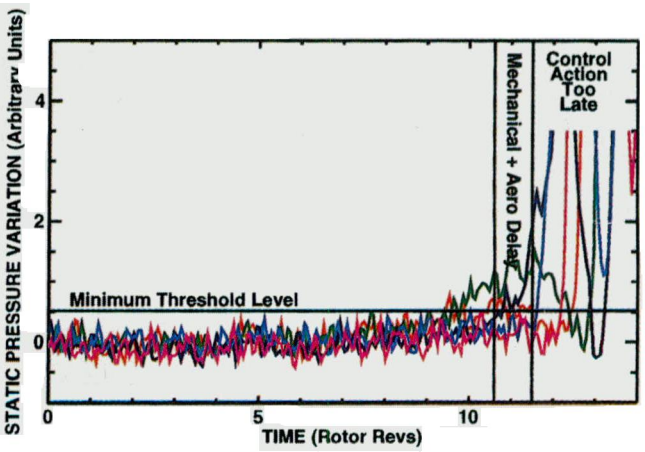

Fig. 13 Stall event at 98 percent speed without control, demonstrating limits on threshold level

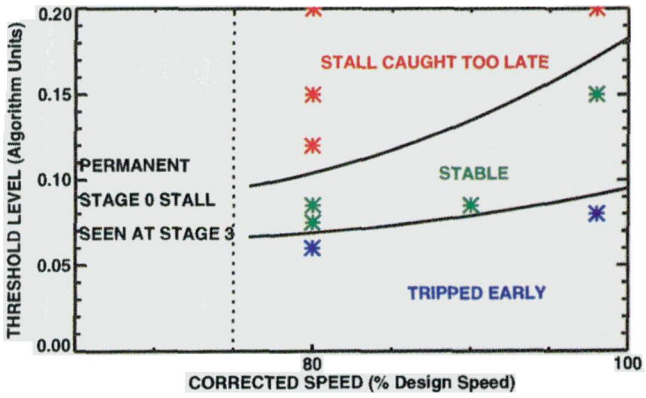

Fig. 14 Threshold simultaneous control: stability with hot gas ingestion. Control bleed air recirculated rear to middle, controlled from stage 3 kulites.

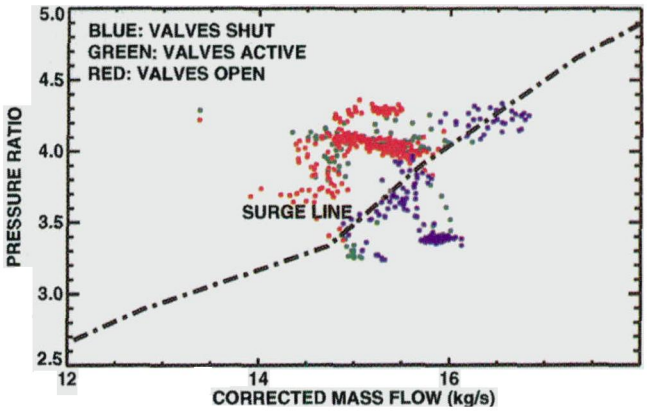

Fig. 16 Threshold simultaneous control at middle speeds. Control bleed air recirculated rear to front, controlled from stage 3 kulites.

pressor had the improved steady-state surge lines shown earlier. Once the stall disturbance had been eliminated, however, the valves closed again, and the surge line returned to the datum, that is below the new operating point. The compressor would then immediately move to stall again. The more rapidly the valves closed, the more rapidly a stall disturbance developed and the more difficult it was to reverse its effects. This problem was overcome by slowing the rate at which the valves closed, such that subsequent stalls were no more rapid in development than the natural stall. The required closure rate was determined by experiment. Short closure times of 5 ms always led to stall. Extending the time eventually resulted in stable operation with operating limits as shown in Fig. 15. The requirement to re-establish normal behavior slowly is a key element of this type of control.

An example of the effectiveness of threshold simultaneous control is shown in Fig. 16. Four combustor inbleed events are overlaid, with recirculation from the rear to the front of the compressor at 80 percent speed. The mean valve opening is shown by the color of the data points, and shows that the valves remain closed up to the normal surge line. On crossing the surge line, the valves open automatically, giving an improvement in the surge line of over 25 percent of pressure rise. The high-pressure air used to raise the working line is taken from an external tank. As the pressure in this tank falls, the operating point moves below the surge line again and the valves close automatically.

The effect of opening the bleed valves can be decomposed into a steady-state and a dynamic effect. The former is related to the adjustment of the flow to the new steady-state conditions with the valves open. The latter corresponds to the transiently reduced pressure at the bleed-off port, the transiently increased pressure at the bleed-in port, and the transiently increased pressure at inlet due to the inertia of the fluid in the inlet duct. This last effect is particularly strong: With the valves open for recirculation, there is a reduction in the net flow requirement through the inlet duct. The deceleration of the fluid in the duct is brought about by a high static pressure at the compressor face, which initially overshoots the equilibrium change in inlet pressure (due to the reduced dynamic head) by a factor of approximately two. The slow closure of the valves prevents the opposite detrimental effect happening when the valves close.

The dynamic effect of opening the bleed valves cannot be ignored. At high speed the surge margin improvement with steady-state recirculation around the whole compressor is comparable to that obtained with conventional exit bleed (Fig. 6). As an actuation device in a stall control system, however, recirculation proved capable of damping out incipient stall cells, whereas fast acting exit bleed was found to be totally ineffective.

Recovery of Loss of Stall Margin Due to Inlet Distortion. Nonaxisymmetric inlet flow is a well-known cause of stall and surge. A simple experiment was performed to investigate the use of steady nonaxisymmetric recirculation to recover the loss of surge margin. The engine was set up at 90 percent speed with hot gas fed into a sector of the inlet as illustrated in Fig. 17. Various combinations of valves were opened, allowing recirculation from the rear to the front of the compressor. The combustor inbleed was activated and the stall point determined (Fig. 17). With all of the valves closed, no inbleed was required

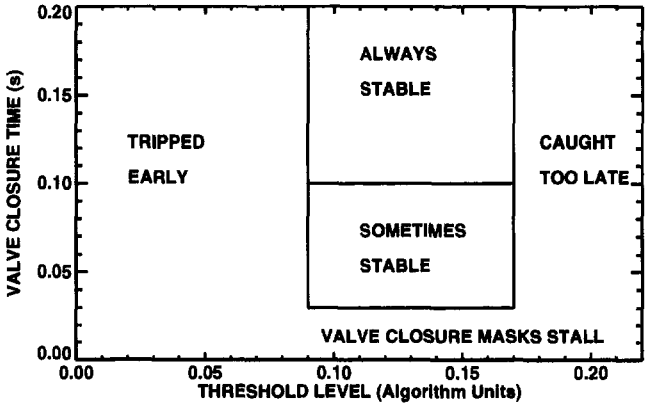

Fig. 15 Threshold control parameter limits versus valve closure rate at 98 percent speed

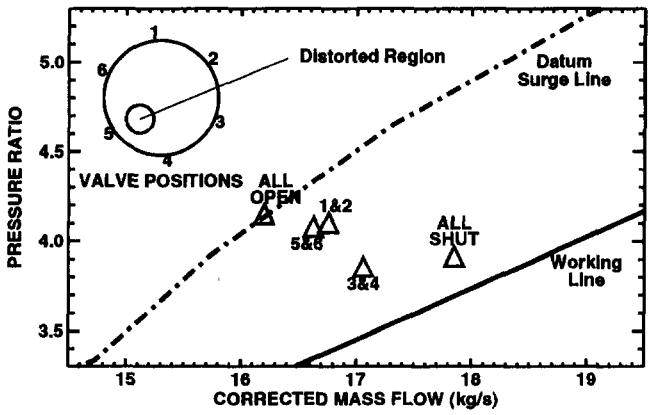

Fig. 17 Hot gas ingestion with asymmetric recirculated bleed. Surge points with different combinations of valves open.

to stall the engine. 30 percent of the margin could be recovered with just valves 3 and 4 open, 75 percent of the margin with valves 1 and 2, and a similar amount with valves 5 and 6 open. With all the valves open, the surge line was restored to that with undistorted inflow. The most effective valves were the ones in the region where the uncontrolled stall cell was observed to grow most rapidly.

The principle is thus demonstrated that the loss of stall margin due to asymmetric flow can be recovered with asymmetric recirculation. As a further refinement, the level of recirculation was set automatically by driving the valves from the measurements at stage 3 using a threshold technique similar to that described above, applying a phase shift to move from the position of maximum signal (just after top dead center) to the position where the distortion was introduced. This method proved equally effective in cancelling the surge margin deterioration.

Summary of Results. The experiments discussed above represent only a subset of the tests performed, which included detailed parametric studies of a number of possible control strategies. The threshold simultaneous control strategy outlined above, recirculating air axisymmetrically from the rear to the front of the compressor controlled by the stage 3 pressure measurements, was found to be effective across the whole operating speed range, regardless of the method used to induce stall, and in spite of the wide variety of stalling behavior observed. Control using the pressure measurements at inlet was possible at middle speeds, but was sometimes rendered ineffective by actuator/detector interaction effects. At high speeds, where stall starts toward the back of the machine, more effective control could be obtained by recirculating air over only the rear of the compressor.

The threshold sequential control method was effective at high speed when recirculating air around the rear of the compressor, and was more efficient than the threshold simultaneous method in terms of the amount of bleed air required. At middle speeds, recirculating air around the whole compressor, control was less effective than the threshold simultaneous method due to the phase shift between the bleed-off and bleed re-injection effects.

The low circumferential harmonic modal stall control method demonstrated at low speed by Paduano et al. (1993) was ineffective due to the fact that the long length scale disturbances for which this system was designed did not exist in the VIPER engine outside of the 85–87 percent speed range.

Experiments were performed concerning the use of conventional bleed-off and fuel modulation at high response rates as alternative actuation mechanisms; these proved too slow for stall control purposes.

Further experiments were carried out with inlet distortion. A system to restore the surge margin based on the controlled recirculation of bleed air is outlined in the previous section.

Discussion

The threshold simultaneous control system described earlier was found to be a reliable method of eliminating incipient stall cells. The system relies on both a dynamic effect as the control valves are opened and the beneficial steady-state effect on surge margin of recirculating bleed air. In this respect it is different from linear modal control, which relies on changing the dynamic response of the system with no change in the steady-state performance of the compressor. The steady-state effect alone, however, would be insufficient for successful stall control; conventional exit bleed can give a similar steady-state improvement, but was found to be too slow for use as an actuation mechanism.

This type of control, with axisymmetric response to nonaxisymmetric disturbances, uses the disturbances present during stall inception to initiate a change to a more stall tolerant but less efficient machine, in a similar manner to that demonstrated by Ludwig and Nenni (1978). In the present case, however, the control system reacts to the initial stages of stall development, and does not wait for rotating stall to develop first. Furthermore, the control system has been demonstrated to be effective across the entire operating range of the engine, whereas the system described by Ludwig and Nenni was demonstrated only at low engine speeds.

The gradual loss of stall margin due to irreversible damage during the life of an engine creates the requirement that a control system would need a reliability and life at least as good as the basic engine. While it has been demonstrated that surge can be held at bay substantially more efficiently than with conventional bleed valves, the type of actuators used in these investigations are not compatible with the life and cost requirements of an aeroengine. Further developments in the design of actuators are needed before active control can be applied to a flightworthy aeroengine. Ideally actuation would be provided by the mechanical equivalent of transistors, cheap, usable in large numbers, allowing air flow or not according to electronic control.

Control System Effectiveness. The thermodynamic efficiency of the compressor with stall control in operation was not measured directly. Nonetheless, significant conclusions can be drawn as to the effectiveness of the control systems. In this section the threshold control systems presented earlier are compared with conventional exit bleed and with an idealized linear control system. The threshold control systems are shown to be similarly effective to the idealized system. A more thorough comparison of the effectiveness of different control systems requires a full engine cycle analysis, yielding results that are heavily dependent on the particular engine application. Such a study is beyond the scope of this paper.

The threshold control systems described earlier provide a more efficient method of increasing surge margin than conventional exit bleed. There are three reasons for this. The major efficiency benefit derives from the fact that no operation is required below the normal surge line, whereas conventional bleed has to be scheduled to come into operation on the stable side of the surge line. This benefit is independent of the type of control system used. The second benefit concerns the steady-state effect of recirculated bleed compared to pure exit bleed. Figure 18 shows the effect of steady-state recirculated bleed on surge margin when compared with an equivalent amount of exit bleed, and shows considerable improvement over most of the operating speed range. Although the thermodynamic efficiency of the compressor with recirculating bleed was not measured directly, the fact that less air is required suggests that the effi-

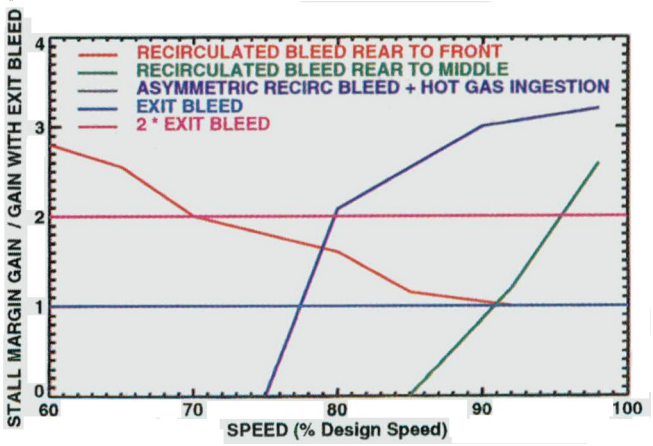

Fig. 18 Effect on surge margin of steady-state recirculated bleed. Normalized by effect of equivalent amount of exit bleed.

ciency penalty is likely to be lower for a given surge margin requirement.

The third efficiency benefit of the threshold control systems when compared to conventional exit bleed relates to the control system itself; how effective the control system is at using the available bleed capability. The threshold systems are designed to operate only when a stall disturbance is present. Even above the normal surge line stall disturbances are not continuously present, and so the valves close for part of the time, giving an efficiency advantage over continuous bleed. In practice this improvement is tempered by an inability to match precisely the amount of bleed required using the threshold system. Figure 19 shows the operating point relative to the normal surge line against valve opening (and therefore bleed rate) for a high-speed event with threshold sequential control. This figure shows too the average valve opening for four nominally similar middle speed events with threshold simultaneous control. Also marked is the surge line, which would be obtained with an equivalent amount of exit bleed for a given valve opening. The sequential control case shows a lower bleed rate for a given improvement in surge margin than with simultaneous control and an effectiveness of up to two times that of exit bleed. Operations at higher back pressures were not possible due to the limits on the combustor inbleed pressure, and so the ultimate performance was not known.

When the valves are predominantly open (the right-hand side of Fig. 19) the simultaneous control case shows stable behavior at substantially higher pressure ratios than with conventional exit bleed. At lower pressure ratios, however, just above the surge point, the nature of the control system is such that on average the valves are half open. In this case more air is being bled than required, and an equivalent improvement in operating range could have been obtained with a smaller amount of conventional bleed-off. The valve opening seen below the surge line in Fig. 19 is not due to premature opening on the stable side of the normal surge line, but is a result of the slow closure rate of the valves (0.25 s) as the operating point fell below the surge line at the end of each event.

It is commonly assumed that the ideal stall control system would be a form of linear control, which would allow stable operation at ever-lower compressor flows with negligible energy input. In well-matched core compressors, however, compressor efficiency falls as the flow is reduced even before the natural surge line is reached, and it is undesirable to operate the compressor near the surge line for any length of time. In the VIPER compressor the efficiency drops by approximately 1 percent for 2 percent of flow as stall is approached; this figure thus represents the maximum efficiency of a linear stall control system. In practice, with a limited number of stages of bleed-off and re-injection, the axial movement of the position of stall inception from the front to the rear with increasing engine speed cannot be tracked exactly. Hence the stall cell will have grown prior to actuator movement, and some level of energy input would be required to restore axisymmetric operation. Thus the efficiency of a practical linear control system would be some way below this maximum value.

If a control system could be devised that scheduled exactly the amount of exit bleed required to keep the compressor stable, there would be a 2 percent efficiency penalty for achieving a 2 percent lower net flow. The earlier discussion suggested that the threshold control systems described in this paper are more efficient than pure exit bleed, and hence the efficiency is likely to be comparable to that of more complex systems designed to allow stable compressor operation at very low flows.

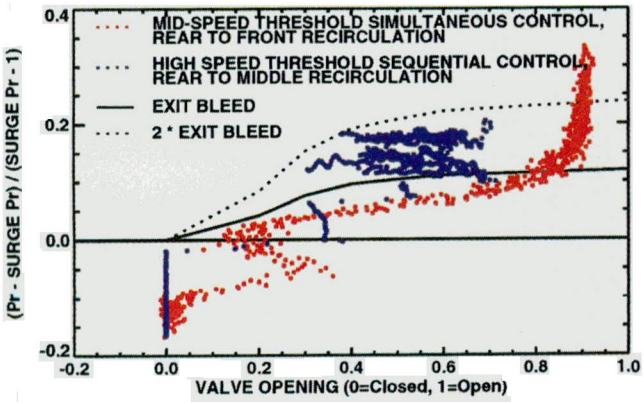

Fig. 19 Mean valve opening versus surge margin with threshold control

Conclusions

1. Results have been presented from a number of active stall control experiments on a VIPER aeroengine using high response valves to control bleed air recirculation around all or part of the compressor.
2. Best results were obtained with detection of nonaxisymmetric disturbances coupled with axisymmetric control action. Such a control system ("threshold simultaneous") has been developed that is capable of extending the stable engine operating range at all speeds.
3. The operating envelope extension was effective for stalls induced by raising the working line as well as lowering the surge line with inlet distortion.
4. The change in net flow stall margin with controlled recirculation was up to 3.5 times that obtained by steady state exit bleed.
5. The efficiency penalty associated with the threshold simultaneous control system is comparable to that which proprietary data suggests would be obtained by running the compressor at very low flows using a more complex control strategy.
6. Nonaxisymmetric actuation with threshold control gave some improvement in efficiency over part of the speed range in terms of the amount of bleed air required, but at the expense of a considerably more complex control system.
7. Nonaxisymmetric linear control of the initial stall disturbances was not possible because the long length scale disturbances for which this type of control was designed do not appear in the VIPER compressor, except over a very narrow speed range.
8. Fuel dipping and exit bleed-off were found to be too slow to prevent stall when triggered by the first appearance of a stall cell.
9. Nonaxisymmetric steady-state recirculated bleed can be used to restore stall margin lost due to inlet distortion. Using threshold detection, the system can be automated so that it only operates when required.

Acknowledgments

The authors would like to thank Rolls-Royce plc for permission to publish this paper. Thanks are also due to the Department of Trade and Industry, the Ministry of Defence and the Defence Research Agency, Pyestock, for partially funding the work.

References

Day, I. J., 1993, "Active Suppression of Rotating Stall and Surge in Axial Compressors," ASME JOURNAL OF TURBOMACHINERY, Vol. 115, pp. 40–47.

Day, I. J., and Freeman, C., 1994, "The Unstable Behavior of Low and High-Speed Compressors," ASME JOURNAL OF TURBOMACHINERY, Vol. 116, pp. 194–201.

Eveker, K. M., Gysling, D. L., Nett, C. N., and Sharma, O. P., 1995, "Integrated Control of Rotating Stall and Surge in Aeroengines," SPIE Vol. 2494 (*Proc. Conference "Sensing, Actuation and Control,"* Orlando, FL, Apr. 17–18), pp. 21–35.

Ffowcs Williams, J. E., and Huang, X. Y., 1989, "Active Stabilisation of Compressor Surge," *Journal of Fluid Mechanics,* Vol. 204, pp. 245–262.

Freeman, C., and Wilson, A. G., 1993, "Stall Inception and Post Stall Transients in an Aero Engine Axial Flow Compressor," presented at IMechE Seminar on Turbo Compressor and Fan Stability, London, Apr. 8.

Hynes, T. P., and Greitzer, E. M., 1987, "A Method for Assessing the Effects of Inlet Flow Field Distortion on Compressor Stability," ASME JOURNAL OF TURBOMACHINERY, Vol. 109, pp. 371–379.

Ludwig, G. R., and Nenni, J. P., 1978, "A Rotating Stall Control System of Turbojet Engines," ASME Paper No. 78-GT-115.

Paduano, J., Epstein, A. H., Valavani, L., Longley, J. P., Greitzer, E. M., and Guenette, G. R., 1993, "Active Control of Rotating Stall in a Low-Speed Axial Compressor," ASME JOURNAL OF TURBOMACHINERY, Vol. 115, pp. 48–56.

Wilson, A. G., and Freeman, C., 1994, "Stall Inception and Development in an Axial Flow Aeroengine," ASME JOURNAL OF TURBOMACHINERY, Vol. 116, pp. 217–225.

Wilson, A. G., 1996, "Stall and Surge in Axial Flow Compressors," PhD Thesis submitted to Cranfield University.

Effects of Nonaxisymmetric Tip Clearance on Axial Compressor Performance and Stability

M. B. Graf

T. S. Wong

E. M. Greitzer

F. E. Marble

C. S. Tan

Gas Turbine Laboratory,
Massachusetts Institute of Technology,
Cambridge, MA 02139

H.-W. Shin

D. C. Wisler

Aero Technology Laboratories,
GE Aircraft Engines,
Cincinnati, OH 45215

The effects of circumferentially nonuniform tip clearance on axial compressor performance and stability have been investigated experimentally and analytically. A theoretical model for compressor behavior with nonaxisymmetric tip clearance has been developed and used to design a series of first-of-a-kind experiments on a four-stage, low-speed compressor. The experiments and computational results together show clearly the central physical features and controlling parameters of compressor response to nonaxisymmetric tip clearance. It was found that the loss in stall margin was more severe than that estimated based on average clearance. The stall point was, in fact, closer to that obtained with uniform clearance at the maximum clearance level. The circumferential length scale of the tip clearance (and accompanying flow asymmetry) was an important factor in determining the stall margin reduction. For the same average clearance, the loss in peak pressure rise was 50 percent higher for an asymmetry with fundamental wavelength equal to the compressor circumference than with wavelength equal to one-half the circumference. The clearance asymmetry had much less of an effect on peak efficiency; the measured maximum efficiency decrease obtained was less than 0.4 percent compared to the 8 percent decrease in peak pressure rise due to the asymmetric clearance. The efficiency penalty due to nonaxisymmetric tip clearance was thus close to that obtained with a uniform clearance at the circumferentially averaged level. The theoretical model accurately captured the decreases in both steady-state pressure rise and stable operating range which are associated with clearance asymmetry. It also gave a good description of the observed trends of: (i) increasing velocity asymmetry with decreasing compressor flow, and (ii) decreasing effect of clearance asymmetry with decreasing dominant wavelength of the clearance distribution. The time-resolved data showed that the spatial structure of the prestall propagating disturbances in the compressor annulus was well represented and that the stability limiting process could be linked to the unsteady structure of these disturbance modes. The model was also utilized for parametric studies to define how compressor performance and stability are affected by the circumferential distribution of clearance, steady-state compressor pressure-rise characteristic, and system dynamic parameters. Sensitivity to clearance asymmetry was found to fall off strongly with the (asymmetry-related) reduced frequency and to increase with peak pressure rise and increasing curvature of the characteristic near the peak.

1 Problem Description, Motivation, and Scope of the Paper

It is well known that tip clearance has an important effect on the performance of axial compressors. Such aspects as peak pressure rise, peak efficiency, and stall margin all tend to be degraded as clearance is increased. Circumferential variations in tip clearance, such as those due to casing distortion or rotor eccentricity, present additional operating problems for gas turbine engines. Although it is recognized that such situations can affect performance in an adverse manner, almost all studies of tip clearance in the literature have focused on axisymmetric rather than nonaxisymmetric clearance, so that the impact of the latter is much less understood. The present paper addresses this topic.

It is useful to assign clearance nonuniformities into two broad categories: stationary and rotating asymmetries. Stationary asymmetries are steady when viewed in the absolute (stationary) reference frame. They can be caused by relative displacement between the rotor and the casing (e.g., an off-centered rotor) or by deformation of the casing (e.g., casing ovalization), as illustrated in Fig. 1. Compressors with such asymmetry have regions of small clearance and regions of large clearance relative to the design clearance, although the average clearance remains unchanged from the design value. Rotating asymmetries exhibit unsteady circumferential clearance variations when viewed in the absolute frame. They can be generated by nonuniform rotor blade heights, by a whirling rotor, or by a "bowed rotor" in which there is mechanical bending or shaft deflection due to temperature nonuniformity. The focus of the present investigation is primarily on effects associated with stationary asymmetry, but a simple description of the behavior with a rotating asymmetry will be also be given.

The paper is organized as follows. In Section 2 we present a qualitative description of the phenomena associated with compressor operation with nonaxisymmetric clearance. As background to this, we will briefly summarize the effects of tip clearance on compressor performance and stability in an axisymmetric situation. Section 3 describes the modeling approach and gives selected numerical results to illustrate main trends. In Section 4 the approach to, and the design of, the experiments

Contributed by the International Gas Turbine Institute and presented at the 42nd International Gas Turbine and Aeroengine Congress and Exhibition, Orlando, Florida, June 2–5, 1997. Manuscript received International Gas Turbine Institute February 1997. Paper No. 97-GT-406. Associate Technical Editor: H. A. Kidd.

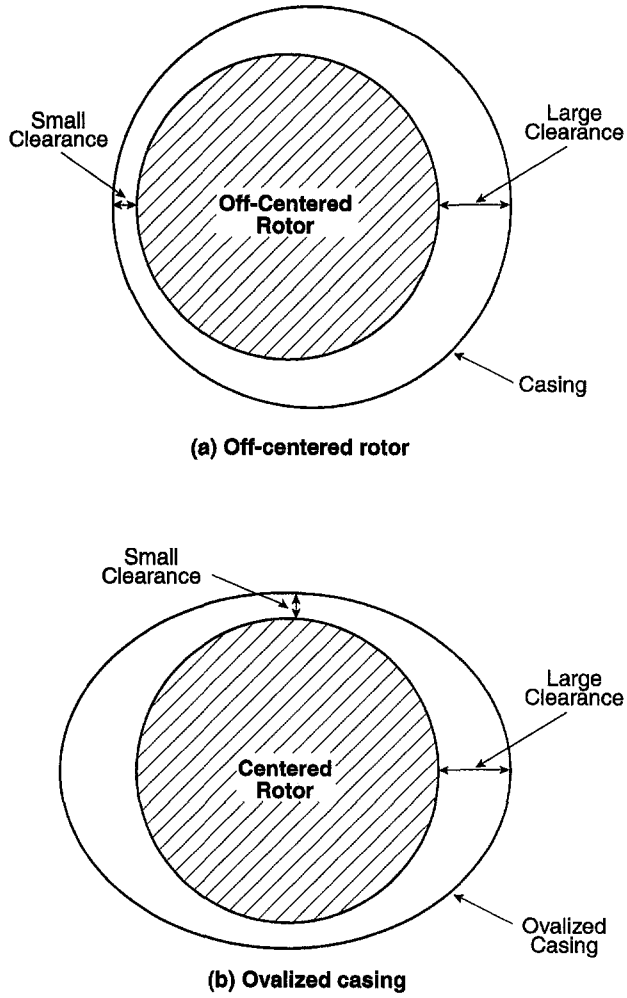

Fig. 1 Nonaxisymmetric tip clearance caused by: (*a*) off-centered rotor, and (*b*) ovalized casing

is discussed, followed by a short description of the compressor facility used to conduct the experiments in Section 5. The experimental results and the comparison with theory are then presented in Section 6 as overall results, time mean flow field, and unsteady behavior and instability onset. The parametric studies of Section 7 then show the influence of different design and system dynamic parameters on compressor sensitivity to asymmetric clearance. Section 8 gives the summary and conclusions.

2 Compressor Fluid Dynamic Features With Asymmetric Clearance

2.1 Background-Compressor Performance With Axisymmetric Tip Clearance. There is a large number of data that show effects of clearance on performance and stable flow range. An early compilation of experimental information, which demonstrated the importance of rotor tip clearance on compressor pressure rise capability, is that of Smith (1958). He showed that for a number of compressors with clearances between 1.5 and 8 percent of chord, a 1 percent increase in clearance produced approximately a 5 percent decrease in peak pressure rise. The trend illustrated by Smith (1958) has since been corroborated and extended by data from other sources including Koch (1981), Wisler (1985a), and Baghdadi (1996). Clearance effects on peak efficiency are well illustrated, also by Smith, in his landmark paper of 1970 (see also Koch and Smith, 1976) and by Wisler (1985b). Efficiency penalties range from 1 to 2 points for each 1 percent increase in the stage average clearance/blade height, depending upon the design.

2.2 Compressor Behavior With Asymmetric Tip Clearance. Although tip clearance asymmetry exists in all compressors to some extent (with the severity depending on both mechanical design and machine operating condition), published works on the impact of this phenomenon are sparse. Some data given by Freeman (1985) indicate that the stability margin is worsened compared to a machine with uniform clearance at the average level, and this seems anecdotally to be a general industry experience. However, there appear to be no rigorous methods for predicting the performance decrease and the flow field due to clearance asymmetry and it is thus of interest to define quantitatively how stability and performance for a multistage compressor are affected by the distribution of clearance around the annulus.

In a compressor with asymmetric tip clearance, regions having smaller tip clearance produce increased pressure rise compared to those having larger clearance, resulting in a pressure rise and an axial velocity that vary around the circumference. The response of the compressor flow field to the clearance asymmetry can be viewed as somewhat analogous to a compressor operating with circumferential inlet distortion, although the flow nonuniformity is induced by a geometric variation within the compressor rather than by upstream conditions.

The approach taken here is to consider a compressor with nonaxisymmetric clearance as a distribution of different compressors around the annulus, each with a pressure rise characteristic that corresponds to the local level of tip clearance. While this approach has a connection with the parallel compressor concept for circumferential inlet distortion, there is a difference

Nomenclature

AR = blade aspect ratio
b_x = blade axial chord
B = B-parameter, or a constant
n = spatial harmonic number
P = pressure
r = radius
t = time
U = rotor wheel speed
x = axial coordinate
γ = blade stagger angle
δ = perturbation quantity or boundary layer thickness
ϵ = tip clearance nondimensionalized by chord
η = efficiency
θ = circumferential coordinate
λ = parameter representing inertia of fluid in rotor
μ = parameter representing inertia of fluid in compressor
ϕ = flow coefficient
Φ = velocity potential function
ρ = density
ψ = total-to-static pressure rise coefficient
ω = radian frequency

Subscripts

d = design point
exit = compressor exit
h, t = hub, tip
IGV = inlet guide vane
inlet = compressor inlet
rot = rotor
stat = stator
t = total
ts = total-to-static
x = axial component

Superscripts

$\bar{}$ = time mean value

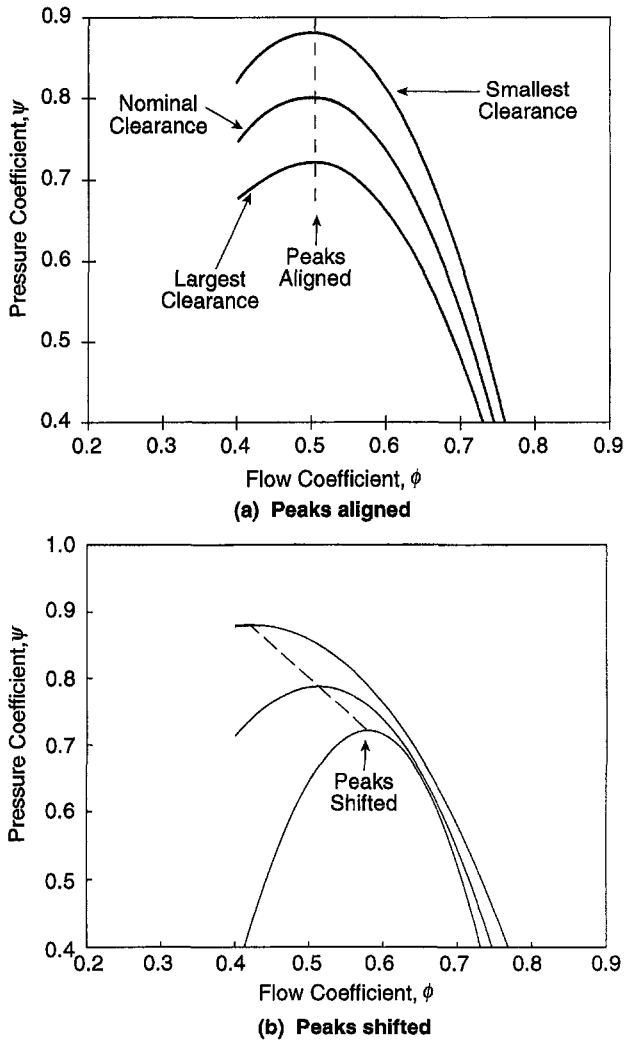

Fig. 2 Possible pressure rise characteristics for an axial compressor at three different axisymmetric clearances: (*a*) peaks in pressure aligned, (*b*) peaks in pressure shifted

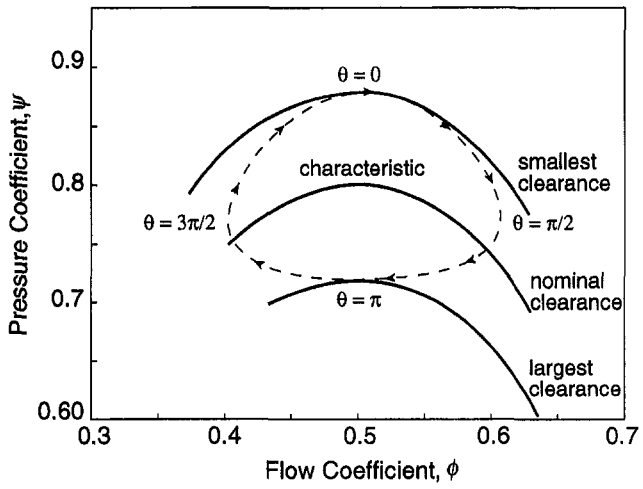

Fig. 3 Locus of operating points around the annulus for the compressor in Fig. 2(*a*) with nonaxisymmetric clearance variation operating at peak pressure rise conditions

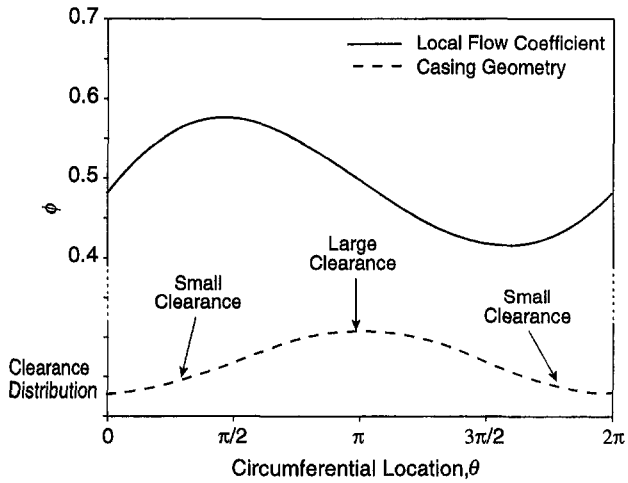

Fig. 4 Distribution of inlet flow coefficient around the annulus of the compressor with nonaxisymmetric tip clearance, characteristics of Fig. 2(*a*), operating at peak pressure

in that locally the compressors are viewed as operating along *different* pressure rise characteristics.

We can illustrate the concept using Fig. 2, which shows the total-to-static pressure rise characteristic for an axial compressor at three different, circumferentially uniform, clearances. For reference, the values are based on a three-stage compressor (Haynes et al., 1994) with nominal clearance of 3 percent of chord, but the arguments to be given are quite general. Two situations are shown. In Fig. 2(*a*), the effect of clearance on the local pressure rise characteristic is a decrease in peak pressure rise. The peaks remain aligned at the same flow. In Fig. 2(*b*), a more general situation is shown in which not only have the values of the peak decreased, but their locations have shifted to higher flow.

As a basic example, consider the compressor in Fig. 2(*a*) with a cosine-shaped casing asymmetry having an amplitude equal to 2 percent of chord. The compressor will have minimum and maximum clearance-to-chord of 1 and 5 percent, respectively. If we assume that the pressure rise behaves locally as with uniform clearance, the peak pressure rise will vary around the annulus from 10 percent below nominal to 10 percent above nominal and, at a particular circumferential position, will depend upon the level of clearance at that location.

For this compressor operating at peak pressure rise, the cosine-shaped clearance asymmetry will produce a circumferential variation in flow and pressure rise illustrated by the locus of points shown in Fig. 3. At this condition, approximately half the points around the annulus are operating on positively sloped portions of the local compressor characteristics and half are operating on the negatively sloped portions. Figure 4 gives a different view of the situation and shows the magnitude and relative phase of the flow coefficient distribution at inlet to the compressor.[1]

3 Modeling Approach

With Section 2 as background, we now describe the modeling approach in more detail. The nonaxisymmetric tip clearance model described (Graf, 1996; Graf et al., 1997) is an extension of the conceptual framework utilized by Hynes and Greitzer (1987) to assess effects of circumferentially nonuniform inlet flow on compressor performance and stability. The goal of the analysis is to provide information about the overall behavior of the compressor and compression system, including stability and decrease in peak efficiency, rather than to capture the detailed

[1] The results in Figs. 3 and 4 were obtained using the model to be described in Section 3. Although the results are mainly meant to be illustrative, they do provide a quantitative indication of the level of flow and pressure nonuniformity that can be expected.

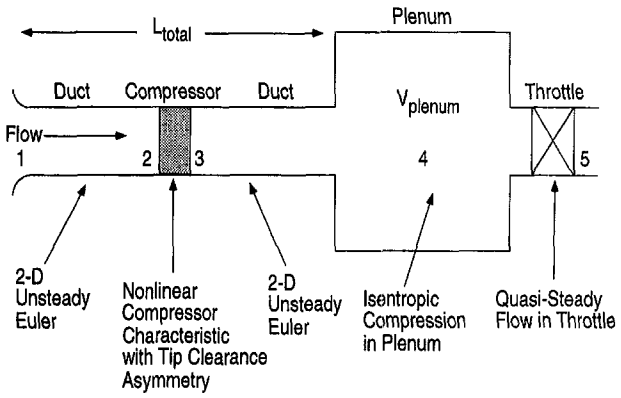

Fig. 5 Schematic of compression system

fluid mechanics of the clearance flow. A schematic of the system considered is shown in Fig. 5. There is a compressor that pumps flow to a plenum, which exhausts through an exit throttle. The compressor is assumed to have high hub-to-tip ratio so that the flow can be represented on a two-dimensional or meanline basis; the variations considered are in the axial and circumferential directions. The flow external to the compressor is taken as inviscid. The compressor and throttle are modeled as actuator disks, each of which has a nonlinear constitutive relation that includes a rudimentary description of blade row unsteady response. Finally, the compressor ducting is taken to be long enough so that there are no nonaxisymmetric pressure field interactions with the inlet and exit duct terminations. [This is not a fundamental limitation of the model, but was done to (slightly) decrease algebraic complexity.] The relevant Mach numbers are assumed to be low enough that compressibility effects can be neglected in the compressor and in the ducts. Density changes in the plenum, where effects of compressibility are important, are related to pressure changes through an isentropic relationship.

The stability analysis consists of two distinct steps. The first involves the solution of the governing equations for the steady state background flow through the compression system. As is typical of hydrodynamic stability problems, this solution can be obtained whether or not such a flow would be stable in practice. The second step then involves adding a small perturbation to the background flow and determining from a linearized stability analysis whether or not such a disturbance grows or decays in time. The eigenvalues of the resulting system of linearized differential equations determine this and are the indications of stability. The two steps will be briefly described below.

3.1 Description of Steady Flow Analysis. In this section, we present only a summary of the analysis. Further details are given by Hynes and Greitzer (1987), Longley (1994), and Haynes et al. (1994). The first of these references develops an equation for nonaxisymmetric steady flow through a compressor:

$$\frac{P_{\text{exit}} - P_{t,\text{inlet}}}{\rho U^2} = \psi(\phi) - \lambda \frac{d\phi}{d\theta} \tag{1}$$

The physical content of this equation is that the local pressure difference across the compressor (exit static minus inlet total) is given by the local uniform flow compressor pumping characteristic plus a correction to account for the fact that the flow in the rotors, which move through a circumferentially nonuniform flow, is unsteady. In Eq. (1) the compressor characteristic utilized is the axisymmetric nondimensional total-to-static pressure rise coefficient, ψ, as a function of flow coefficient, ϕ. The parameter λ represents the inertia of the fluid in the rotor passages and is defined as

$$\lambda = \frac{b_x}{r \cos^2 \gamma} \tag{2}$$

With a nonaxisymmetric clearance, we now view the compressor as having a local pressure rise characteristic, which is a function of the local tip clearance as well as the local flow coefficient. It is through modification of the characteristic that the effects of clearance asymmetry are included. The steady state performance of the compressor with nonuniform clearance is thus given by,

$$\frac{P_{\text{exit}} - P_{t,\text{inlet}}}{\rho U^2} = \psi(\phi, \epsilon) - \lambda \frac{d\phi}{d\theta} \tag{3}$$

where ϵ is the nondimensional tip clearance (normalized by chord). The asymmetric background flow is obtained by solving Eq. (3), which is a nonlinear equation for ϕ as a function of θ, along with an equation that determines the annulus average flow through the compression system.

The background flow model as applied is nonlinear, but it is helpful to present a simplified linear description to illustrate some basic parametric dependencies. For small variations from a uniform tip clearance (in which $\delta\epsilon = \delta\phi = 0$), Eq. (3) can be linearized to obtain the following expression for the steady flow nonuniformities in pressure and flow:

$$\frac{\delta P_{\text{exit}} - \delta P_{t,\text{inlet}}}{\rho U^2} = \frac{\partial \psi}{\partial \phi} \delta\phi + \frac{\partial \psi}{\partial \epsilon} \delta\epsilon - \lambda \frac{d\delta\phi}{d\theta} \tag{4}$$

In Eq. (4), δ signifies the circumferential nonuniformity and $\partial\psi/\partial\phi$ and $\partial\psi/\partial\epsilon$ are the derivatives of the pressure rise characteristics with respect to axial flow coefficient and tip clearance. Since no losses are generated upstream of the compressor, the *total* pressure is circumferentially uniform at the inlet. Further, because the flow is assumed to exit the last stator axially, the *static* pressure at the compressor outlet is uniform. The quantities $\delta P_{t,\text{inlet}}$ and δP_{exit} are thus zero. Equation (4) thus reduces to a linear first-order equation for $\delta\phi$ in terms of the (specified) clearance variation, $\delta\epsilon$,

$$\lambda \frac{d\delta\phi}{d\theta} - \left(\frac{\partial \psi}{\partial \phi}\right)\delta\phi = \left(\frac{\partial \psi}{\partial \epsilon}\right)\delta\epsilon \tag{5}$$

The flow coefficient and clearance variation can be expressed in terms of Fourier series representations,

$$\delta\phi = \sum_{n=-\infty}^{\infty} A_n e^{in\theta}, \quad \delta\epsilon = \sum_{n=-\infty}^{\infty} B_n e^{in\theta} \tag{6}$$

Substituting Eqs. (6) into (5), the variation in flow coefficient is found to be

$$\delta\phi = \sum_{n=-\infty}^{\infty} B_n e^{in\theta} \cdot \frac{\dfrac{\partial \psi}{\partial \epsilon}}{in\lambda - \dfrac{\partial \psi}{\partial \phi}} \tag{7}$$

Equation (7) shows the central features governing the flow nonuniformity. The axial velocity variations around the annulus depend on: (1) the harmonic content of the clearance variation B_n, (2) the flow inertia parameter λ, (3) the sensitivity of compressor pressure rise to axisymmetric clearance changes $\partial\psi/\partial\epsilon$, and (4) the local slope of the pressure rise characteristics $\partial\psi/\partial\phi$. A more negatively sloped compressor characteristic, a larger inertia parameter, a higher harmonic content of the clearance variation, and a decreased sensitivity to axisymmetric clearance changes all promote smaller variations in flow coefficient, and thus, presumably, create less of an adverse effect on overall compressor performance and stability.

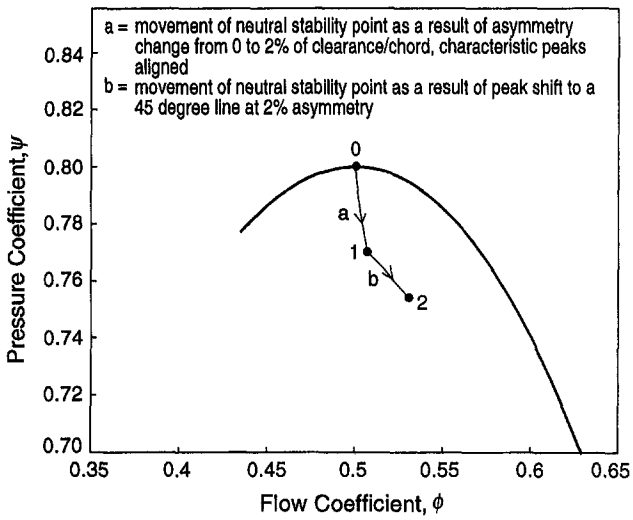

Fig. 6 Locus of instability points for different levels of nonaxisymmetric clearance

3.2 Stability Analysis. Once the steady flow is obtained using Eq. (3), the stability of the compression system can be assessed by adding a small, arbitrary, unsteady perturbation to the steady flow and determining whether it grows or decays in time. The behavior of such perturbations is described by a coupled set of linearized equations. Stability is linked to unsteady flow processes in the system and cannot be predicted using only steady-state analyses.

In the present situation, there is an interaction between the steady flow nonuniformity and the unsteady disturbances. This interaction is included in the description of the upstream flow field and (most critically) the compressor, but is neglected in the downstream region. Physically, this corresponds to the neglect of the convection of mean flow vorticity by the disturbance velocity field. The goodness of this approximation has been demonstrated in several similar problems, namely circumferential inlet distortion (Hynes and Greitzer, 1987) and rotating stall (Lavrich, 1988), in both of which the velocity nonuniformities, and hence the demands on the approximations, are larger than encountered here. (Put another way, we adopt here an approximation for the downstream flow field impedance, which has been shown to be adequate in situations that tax it more severely than the present application.) Further discussion of this point can be found in the above-mentioned two references.

The primary result of interest is the condition (i.e., the annulus averaged pressure rise and flow) at which the compressor experiences the onset of rotating stall, which we associate with the growth of traveling wavelike disturbances. Development and growth of such disturbances has been reported by Haynes et al. (1994) and Garnier et al. (1991), and was also observed in the present investigation.

As an example of the change in stability associated with clearance asymmetry, calculations have been carried out for the three-stage compressor geometry mentioned previously. The configuration used had a mean clearance equal to 3% of the rotor chord and nominal pressure rise characteristics shown in Fig. 2(a), with the peaks of the pressure rise characteristics aligned. The clearance nonuniformity examined was cosine shaped. The amplitudes of the clearance nonuniformity about the uniform clearance ranged from 0 to 2 percent of the rotor chord, so the average clearance was always equal to 3 percent of chord, although the level of clearance variation was varied. The results of the calculations are shown in Fig. 6. As the amplitude of the asymmetric clearance increases from 0 to 2 percent of clearance/chord, the neutral stability point moves along curve "a" from point "0" to reduced pressure rise and higher flow coefficient at point "1." Compared to the uniform-clearance stability point, which is at the peak of the nominal characteristic at point "0," the flow coefficient at stall at point "1" has increased 1.4 percent and the pressure rise coefficient has decreased 3.7 for 2 percent clearance asymmetry.

Figure 6 also contains results of calculations carried out to show the effect of shifting the peak pressure rise to a higher flow rate as tip clearance is increased (as in Fig. 2(b)), since this is generally the trend seen in practice. Thus, for 2 percent clearance asymmetry, the peaks of the local pressure rise characteristics that make up the family shown in Fig. 2(b) were shifted horizontally. The shift for this example corresponded to a 38 percent change in flow coefficient between the peaks for minimum and maximum clearances. The stability onset point now moves along segment (b) shown in Fig. 6 to point 2; this gives an increase in flow coefficient at stall of 6.2 percent and a decrease in pressure rise coefficient of 5.8 percent. Once again, for all the calculations shown in Fig. 6, *the mean clearance remains unchanged,* so the instability point is directly affected by the presence of the clearance asymmetry and the corresponding geometry-induced flow nonuniformity. The mechanism associated with the change in stall point will be discussed in greater detail in later sections.

4 Experimental Design

To assess the basic theoretical framework, a set of experiments was designed and performed (Wong, 1996; Graf et al., 1997). This included compressor performance information at several different operating conditions, to assess the ability of the model to capture trends with compressor operating point, and steady and unsteady flow field measurements. The experiments were performed at the General Electric Aerodynamics Research Laboratory using the Low-Speed Research Compressor (LSRC) test facility (Wisler, 1985a).

The experiments were divided into two sets. In the first set, characteristics of the compressor with different axisymmetric clearance levels were obtained; these served as input to the analytical model. Three clearances were tested corresponding to 1.5, 2.9, and 4.3 percent of annulus height. The performance of the 2.9 percent clearance configuration served as the baseline or nominal case.

For reference, typical levels of clearance-to-annulus height in the rear block of compressors in modern commercial engines are about 1.5 to 2.0 percent. Average levels of clearance for the whole compressor are often quoted at about 1 percent; however, the rear block levels are larger than average because annulus heights are smaller. The low-speed test geometry for our experiments is meant to model the middle and rear blocks of HP compressors, and clearance variations were used that bounded typical rear block engine levels.

The second set of experiments involved two different asymmetric clearance distributions. The analysis showed that the circumferential harmonic content of the clearance variation had a significant influence on the severity of asymmetric clearance effects, and the test series thus included configurations with a single lobe (first-harmonic) and a two-lobed (second-harmonic) clearance variation.

A summary of the axisymmetric and nonaxisymmetric test configurations examined is provided in Table 1.

5 Facility Description

5.1 Low-Speed Research Compressor. The low-speed research compressor blading used was representative of modern multistage blade design. The compressor has four identical (or repeating) stages. There are fifty-three inlet guide vanes. Each stage has 54 rotor blades and 74 stator vanes. Blade Reynolds number was 3.5×10^5 based on rotor chord length and midspan blade velocity. Tip Mach number was 0.2, so the flow can be

Table 1 Summary of test cases

Test	Configuration	Average Clearance to Annulus Height	Clearance Asymmetry to Annulus Height	Wavelength of Asymmetry
	Axisymmetric			
1	Small	1.5%	0	0
2	Baseline	2.9%	0	0
3	Large	4.3%	0	0
	Non-Axisymmetric			
4	One-lobed	2.9%	±1.4%	circumference
5	Two-lobed	2.9%	±1.4%	1/2 circumference

considered incompressible for modeling purposes, and the degree of reaction was 67 percent. Some geometric information is given in Table 2.

Steady-state aerodynamic data were obtained using circumferential arrays of eleven casing static taps located at a flow measurement plane roughly 0.8 radii upstream of the IGVs, upstream of the first-stage rotor, and at the compressor exit, and eleven midspan Kiel probes placed uniformly around the circumference at the compressor inlet and exit. High response measurements were obtained from eight casing pressure transducers placed uniformly around the circumference just above the first-stage rotor. Overall efficiency was obtained from shaft speed and torque measurements. Accuracy of the measurements was ±0.025 percent of full scale (2 psi) for all pressures, ±0.10 percent for pressure coefficient, ±0.12 percent for overall flow coefficient, and ±0.15 points for overall efficiency. Further details of the experimental configuration and instrumentation utilized in this study will be referred to as needed and a thorough description of the LSRC can be found from Wisler (1985a).

5.2 Description of Asymmetric Casing Geometry. The casing of the compressor is comprised of Plexiglas windows mounted on steel frames. There are twelve windows in each of four stages. These were moved radially using shims to provide the nonuniform clearance variation. The two clearance configurations tested are illustrated schematically in Fig. 7. Each long dashed segment in the figure corresponds to a window in each stage. Both the one-lobed and the two-lobed configurations had an average tip clearance equal to 2.9 percent of rotor height, the same as the baseline configuration. In the experiments, the windows in all four stages were moved the same amount.

Table 2 Four-stage compressor design parameters

IGV chord (mm)	84
IGV aspect ratio	1.36
IGV pitchline solidity	1.00
IGV midspan stagger	+3.6°
Rotor chord (mm)	91
Rotor aspect ratio	1.25
Rotor pitchline solidity	1.11
Rotor midspan stagger	47°
Stator chord (mm)	79
Stator aspect ratio	1.45
Stator pitchline solidity	1.32
Stator midspan stagger	14.1°
Blade height (mm)	114

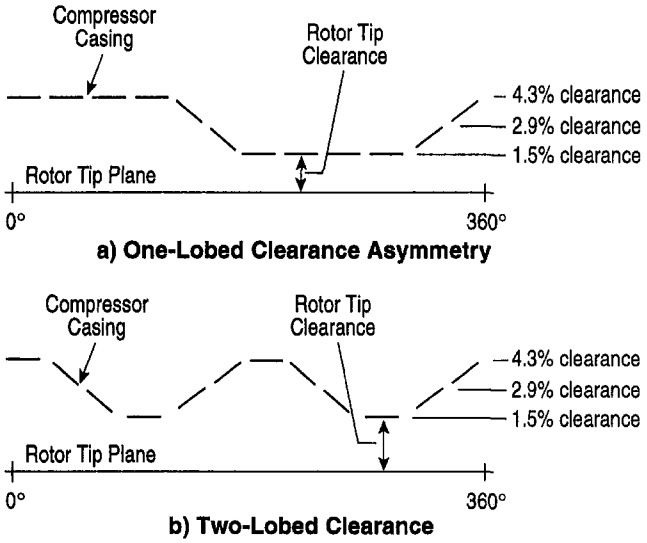

Fig. 7 Clearance geometries tested in the LSRC. Each long-dashed segment in the compressor casing represents one window of the twelve windows per stage.

6 Experimental Results and Comparison With Theory

6.1 Compressor Pressure Rise and Efficiency With Axisymmetric Tip Clearance. Figure 8(*a*) shows the overall total-to-static pressure rise characteristics of the compressor with different *axisymmetric* clearance values. Increased tip clearance causes a decrease in peak pressure rise and an increase in stalling mass flow. The clearance increase from 1.5 to 2.9 percent of blade height caused considerably smaller changes than that from 2.9 to 4.3 percent, implying that the machine may be hub critical at tight clearance.

Efficiency characteristics for the three different levels of clearance are shown in Fig. 8(*b*). The efficiency is presented as changes from the peak (design point) value for the nominal clearance. The data indicate roughly 2 percent change in peak efficiency for a change in tip clearance of 1.5 percent blade height.

6.2 Compressor Pressure Rise and Efficiency With Nonaxisymmetric Clearance. Compressor pressure rise characteristics with *nonaxisymmetric* clearance are shown in Fig. 9(*a*) as the data points. The axisymmetric results of Fig. 8(*a*) are indicated by the dashed lines. The 2.9 percent clearance axisymmetric data (the middle dashed line) can be compared with the nonaxisymmetric data, all of which are for an average clearance of 2.9 percent. There is a substantial degradation in pressure rise and flow range with the nonaxisymmetric clearance.

Several other points can also be noted. First, at high flow coefficients (say design point or above), the characteristics with nonaxisymmetric clearance are close to those of the axisymmetric baseline; it is at low flow that the difference in performance between the configurations becomes large. Secondly, the degradation in compressor performance is less when the wavelength of the clearance is cut in half, as seen by comparing the two-lobed clearance asymmetry data with the one-lobed data in Fig. 9(*a*). This is an effect of flow unsteadiness because the reduced frequency of the nonuniform flow increases by a factor of two, as will be discussed later. Finally, the theoretical results, shown as solid lines in Fig. 9(*a*), capture the effects of both asymmetry and reduced frequency, not only for pressure rise but also for flow coefficient at stall.

Measured compressor efficiencies for one-lobed and two-lobed nonaxisymmetric configurations are shown in Fig. 9(*b*) as the data points. Again, the data of Fig. 8(*b*) for axisymmetric

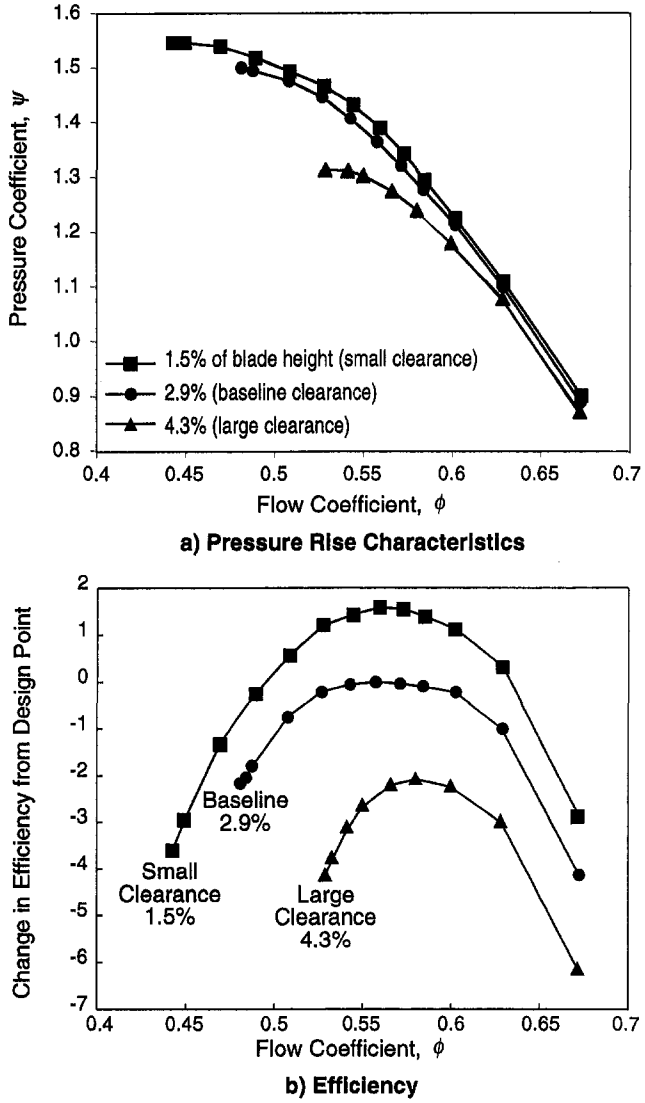

Fig. 8 Measured compressor performance with different axisymmetric clearances

clearance are given as dashed lines. The peak efficiencies for the two nonaxisymmetric configurations are close to that for the baseline 2.9 percent axisymmetric clearance configuration, indicating that clearance asymmetry has only a small impact on *peak* efficiency. This is consistent with the pressure rise characteristics, which show only small differences between axisymmetric and nonaxisymmetric clearance configurations at flows near design. At lower flow coefficients in Fig. 9(*b*), effects of asymmetry on efficiency become apparent as efficiency levels now lie between those for the baseline and large clearance. Figure 9(*b*) also shows excellent agreement between theory and data, as far as effects of both asymmetry and reduced frequency.

To assess in more detail the relative changes in stall margin produced by the various clearance configurations, we compare differences in performance at the stall point using bar charts. The differences in stalling pressure rise coefficient and stalling flow coefficient are shown in Figs. 10(*a*) and 10(*b*), respectively, as deltas relative to the level of performance obtained for the baseline configuration with 2.9 percent axisymmetric clearance. The left-hand portion of each figure shows how performance changes when axisymmetric clearance levels are decreased and increased relative to that of the baseline level. This indicates how axisymmetric clearance levels affect stability. The right-hand portion of each figure shows how performance changes when the *average* clearance level remains unchanged relative to the baseline level but the clearance configuration becomes nonaxisymmetric. This shows how nonasymmetric clearance affects stability.

The data for two nonasymmetric clearances in Fig. 10 clearly show the following: (1) The theoretical model does well in capturing the effects of both clearance asymmetry and reduced frequency on performance at stall; (2) nonaxisymmetric clearance has a negative impact on both stalling pressure rise and flow, with the effects being similar to those obtained for symmetric clearance levels that are larger than the nonaxisymmetric average; (3) the negative effects of nonaxisymmetric clearance decrease as the wavelength of the clearance decreases.

Figure 11 gives a similar bar chart comparison for the measured change in peak efficiency with axisymmetric and nonaxisymmetric clearance variation. The flow conditions correspond to the peak efficiency points in Fig. 9(*b*); these can be characterized as near design. Theory and data indicate that the circumferential variation in flow coefficient near design conditions is much smaller than that near stall. Hence the overall efficiency penalty associated with clearance asymmetry, which depends quadratically on the amount the local compressor operating point differs from the peak efficiency point, is also small. Differ-

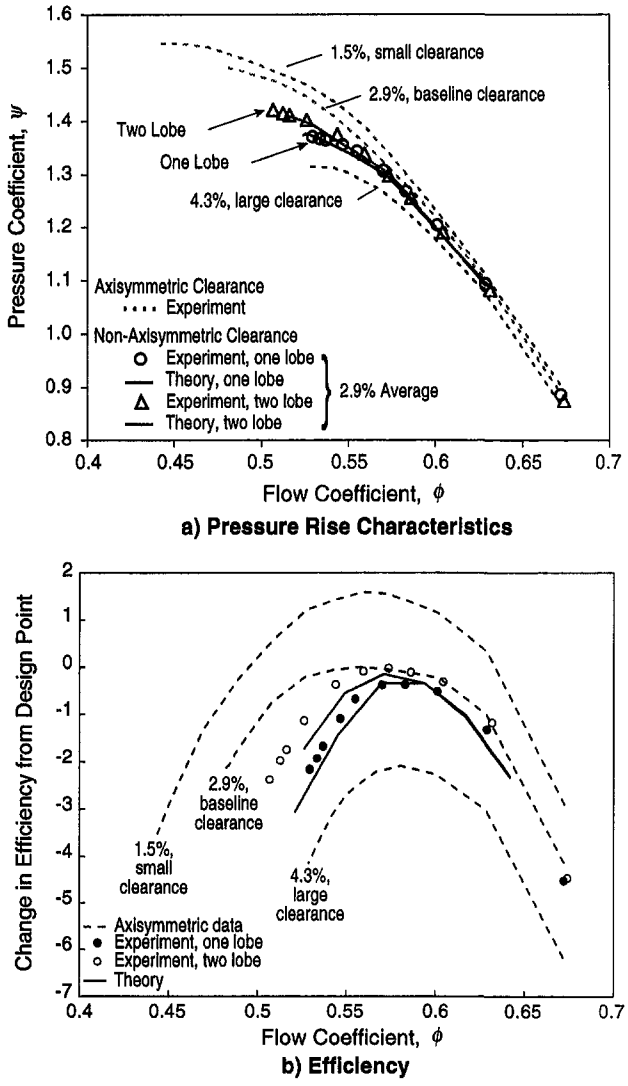

Fig. 9 Measured compressor performance with nonaxisymmetric clearance compared with that for axisymmetric clearance

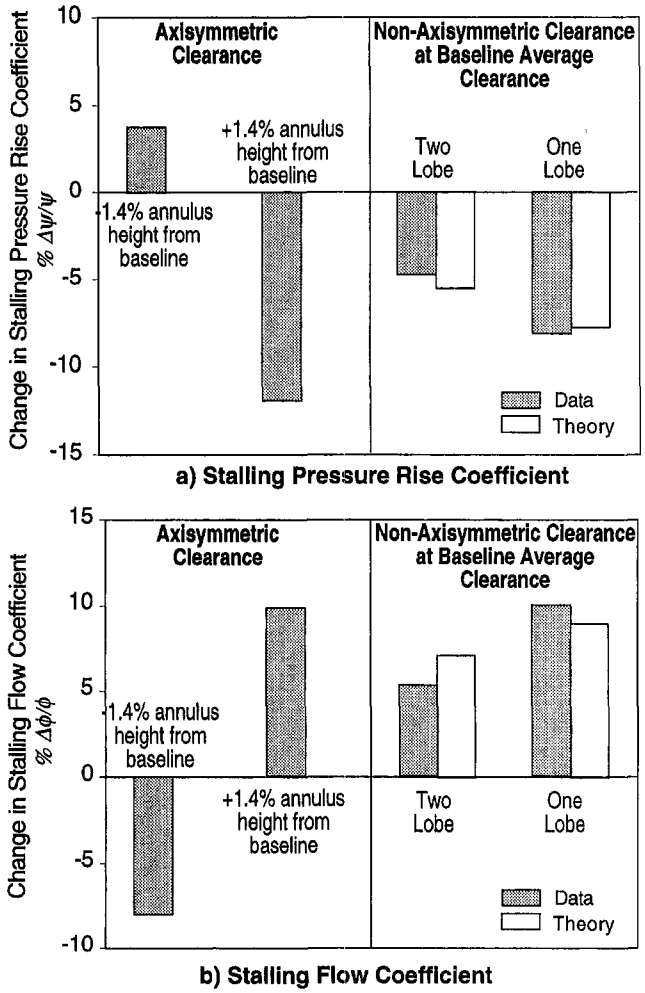

Fig. 10 Changes in stalling pressure rise and flow coefficients with axisymmetric and nonaxisymmetric clearance; (*a*) stalling pressure rise, (*b*) stalling flow coefficient. All data shown are presented as differences from values obtained at 2.9 percent baseline axisymmetric clearance.

ences in efficiency, like those in pressure rise, thus only become appreciable away from design.

6.3 Circumferential Distribution of Time-Mean Flow. Measured distributions of time-mean inlet axial velocity around the circumference of the compressor are shown in Fig. 12 for both one-lobed and two-lobed asymmetry. The nonuniformity in axial velocity is seen to increase as the compressor is throttled to lower flow, and thus the slope of the compressor pressure-rise characteristic decreases. This was implied by the introductory discussion in Section 3. Further, if we regard the compressor as operating along a characteristic corresponding to the local level of clearance, the characteristics for axisymmetric clearance are farther apart near stall than near design. Both of these conditions cause flow field variations to be greater at low flow than at high flow.

The results from theory, using the nonlinear model, are also shown in Fig. 12. The theory captures the trend with flow as well as the shape of the axial velocity distribution with good accuracy for all cases. In Fig. 12(*b*) the circumferential length scale of the flow field variation has been reduced by a factor of 2 and the amplitude of the axial velocity variation has decreased at low flow. One way to view this behavior is by analogy with one-dimensional unsteady flow in a duct. For inviscid flow in a duct with a fixed driving pressure difference, the amplitude of the corresponding velocity perturbation decreases as the re-

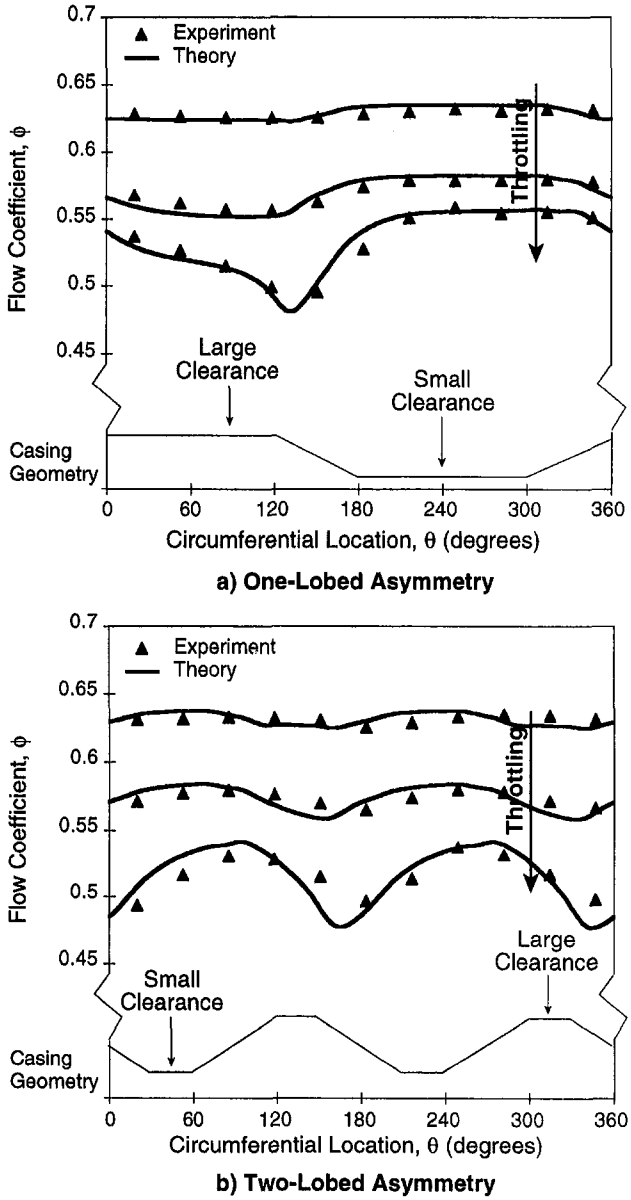

Fig. 12 Circumferential distribution of flow coefficient for one-lobed and two-lobed clearance asymmetry

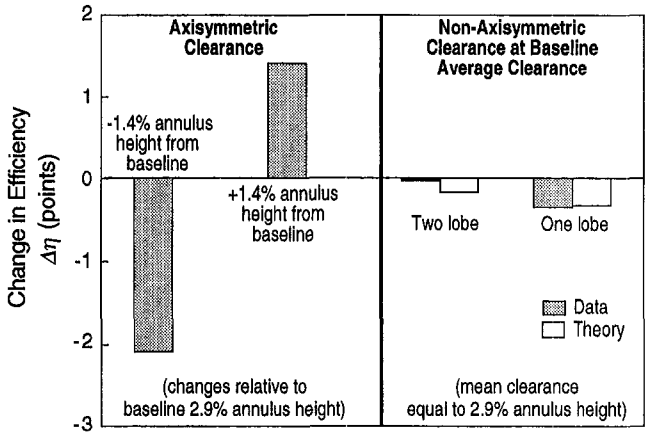

Fig. 11 Changes in peak efficiency with asymmetric and nonaxisymmetric clearance. All data shown are presented as differences from values obtained at 2.9 percent baseline axisymmetric clearance.

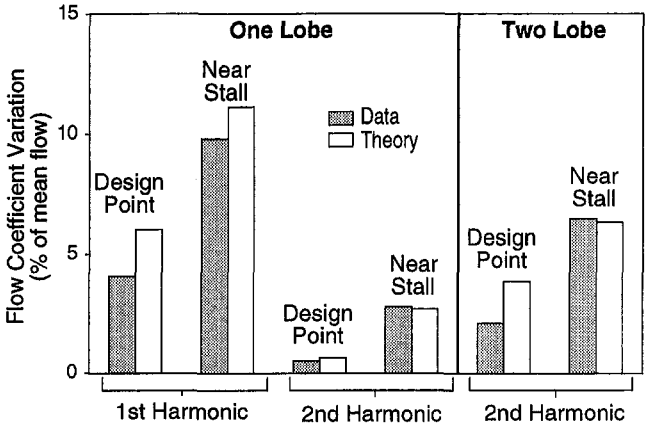

Fig. 13 Spatial harmonics of steady flow variation

duced frequency increases. The situation with clearance nonaxisymmetry corresponds roughly to a fixed variation in driving pressure, and as the length of the nonuniform region decreases and the reduced frequency associated with the nonuniformity increases, the amplitude of the axial velocity nonuniformity decreases.

The trends with operating point and lobe number are summarized in Fig. 13, which shows the calculated and experimentally measured amplitudes of the flow variation at the design and near-stall points. For the one-lobed clearance distribution, the amplitudes of the first and second harmonics of the variation are shown; for the two-lobed distribution, only the second harmonic is considered. The data show an increase in amplitude as the overall flow is throttled from design conditions to near stall. The effect of flow unsteadiness mentioned above is also seen in comparing the results for one- and two-lobed asymmetries; higher harmonics result in reduced amplitude of axial velocity nonuniformity. Finally, note that the ratio of second harmonic to first harmonic is nearly twice as large near stall as at design, indicating a greater role of nonlinearity at the former conditions.

6.4 Unsteady Results and Stability

6.4.1. Circumferential Variation of Flow Unsteadiness. We now examine the unsteady flow processes that limit stability. With nonaxisymmetric clearance, the steady flow field entering the compressor is nonaxisymmetric. The effect of this nonuniformity on the unsteady behavior is seen in Fig. 14(a), which shows the shape of the least stable eigenmode of the compression system at several different times during a period. The wave changes shape as it travels around the annulus. The level of the velocity fluctuation that a stationary sensor, such as a hot wire, would see thus differs at different points around the annulus because the propagating disturbances, i.e., the eigenmodes of the system, are nonsinusoidal. The example in Fig. 14(a), which is based on the results with the single-lobed clearance, shows regions of large and small velocity amplitude roughly in quadrature with the clearance variation.

The regions of wave growth and decay can be directly linked to the sections of the annulus where the compressor is locally operating on either the unstable (positive slope) or stable (negative slope) portion of the pressure rise characteristic. To see this, the calculated local value of the slope of the compressor characteristic, $\partial\psi/\partial\phi$, is shown in Fig. 14($b$). Comparison of Figs. 14(a) and 14(b) shows that the region of positive slope corresponds to wave amplification while the region with negative slope produces attenuation. Gysling and Greitzer (1995) used the product of the pressure rise perturbation and mass flow perturbation, nondimensionally $\delta\psi \cdot \delta\phi$ or $(\delta\phi^2)\cdot(\partial\psi/\partial\phi)$ as an indication of the unsteady energy input associated with dynamic instability. Wave growth or decay in a particular portion of the annulus is associated with the addition or dissipation of perturbation mechanical energy by the compressor in that region. It is this mechanism that produces the change in stability associated with nonaxisymmetric clearance.

The spatial Fourier harmonic content of the traveling wave has been analyzed (Graf et al., 1997) for the one-lobe, nonaxisymmetric clearance. Although the first spatial harmonic is dominant, the second and third spatial harmonic amplitudes are a significant fraction of the first. Thus, the clearance asymmetry and resulting asymmetric flow give the eigenmodes of the system a richer spatial harmonic content than with an axisymmetric clearance, which has only a single harmonic.

The calculated wave envelope described above indicates that the amplitude of the velocity and pressure fluctuations will vary circumferentially. To investigate this, eight equally spaced high-response pressure transducers were used to measure the level of unsteadiness around the compressor. The normalized root-mean-square values of the static pressure fluctuation measured above the first-stage rotor operating at near stall are shown in Fig. 15, along with the corresponding pressure perturbation wave envelope calculated by the model. The equations for the

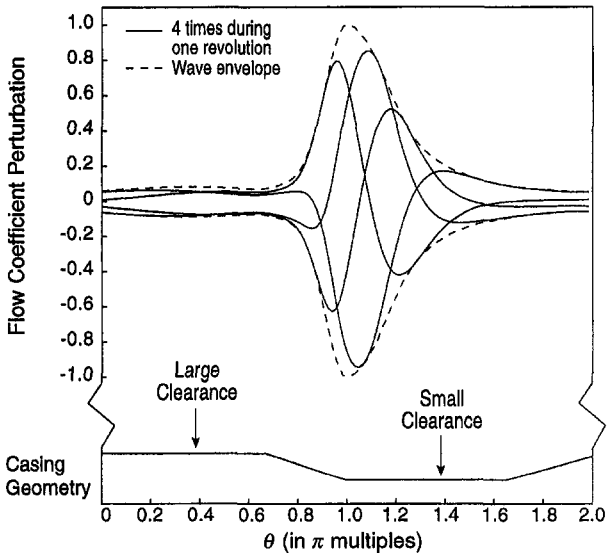

a) Traveling wave disturbance at different times (least stable eigenmode of the compression system) at neutral stability point.

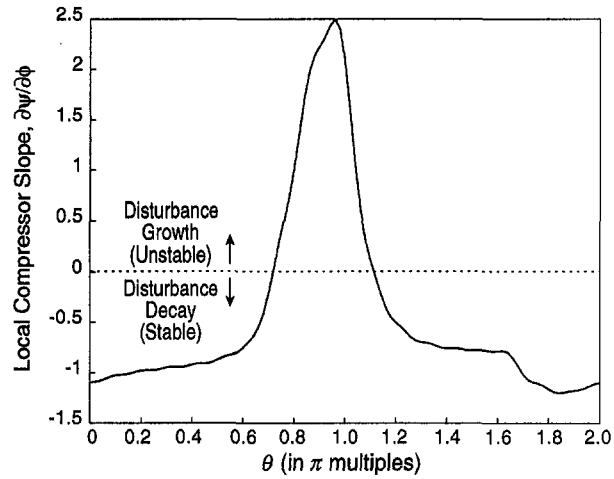

b) Predicted variation in pressure rise characteristic slope.

Fig. 14 Circumferential variation of flow unsteadiness for one-lobed nonaxisymmetric clearance

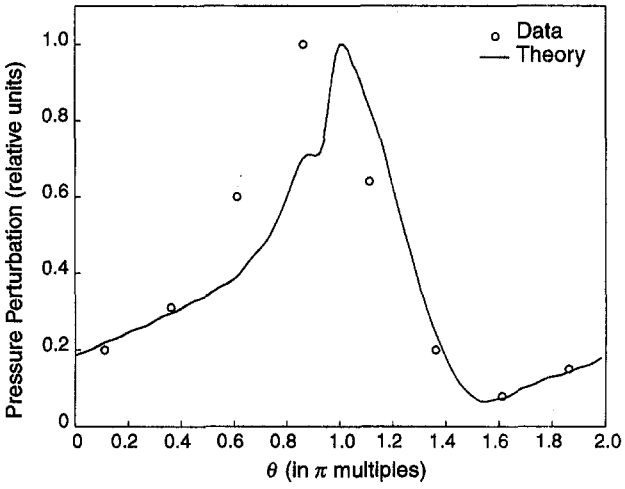

Fig. 15 Amplitude of static pressure disturbance above the first-stage rotor

perturbations are linear and homogeneous so that the amplitude is arbitrary. The relative level has thus been set by matching the peak values. The data indicate a varying fluctuation level, with the overall shape of the amplitude distribution agreeing well with the theoretical result. The trend of the maximum occurring near the edge of the large tip clearance region was also previously observed by Silkowski (1995).

6.4.2 Circumferential Position of Stall Onset. The theory asserts that the onset of stall is characterized by a rapid increase in perturbation amplitude due to the growth of an underdamped circumferentially traveling disturbance. This concept was examined by measuring unsteady static pressure during a stall transient using fast-response pressure transducers located above the first stage rotor. The results are shown in Fig. 16 for axisymmetric and nonaxisymmetric clearances. The abscissa is time in units of rotor revolutions and the ordinate is the circumferential positions of the eight transducers.

Prior to stall, say for the ten revolutions before, all eight traces in Fig. 16(a) look roughly similar for the axisymmetric clearance. Further, although the origin of the stall cell can be traced back to a location near 250 deg, once identified, the traveling wave grows similarly over the annulus, increasing in amplitude as it travels around.

With nonaxisymmetric clearance, the results in Fig. 16(b) are quite different. As mentioned for Fig. 15, the measured level of fluctuation is much higher at locations near 150 deg and the stall cell can be traced back to approximately this location. The cell begins to grow at the 150 deg location and its amplitude increases as it reaches the 200 deg location. From 250 deg back around to 50 deg, however, the amplitude decreases. There is thus disturbance growth at some locations and decay at others, in line with the previous arguments about the local value of the compressor characteristic slope and the unsteady energy input.

Examination of the location of stall cell inception for different test runs for both the baseline axisymmetric configuration and the one-lobe asymmetric configuration is instructive. As a quantitative criterion, we define the stall inception points by the observation of a specific value of the rms pressure fluctuation amplitude, say $\delta\psi = 0.1$. A histogram of the stall cell inception locations defined in this manner (Graf et al., 1997) reveals that the compressor with axisymmetric clearance does not appear to have a preferred location from which the stall cells emerge. Stall inception in the asymmetric compressor, however, always appears at the location where the flow field unsteadiness is the highest, around 160 deg in Fig. 16(b).

7 Parametric Study

The agreement between theory and experiment described in Section 6 gives confidence that the model captures the overall flowfield response and the relevant parametric trends. It is thus instructive to use the model to determine the effects of several design parameters on the stability of compressors operating with asymmetric tip clearance. The baseline used for this parametric study was the nominal characteristic shown in Fig. 2 with parameters of the three-stage compressor studied by Haynes et al. (1994). Design variables were modified to assess the impact of: (a) compressor characteristic curvature, (b) compressor peak pressure rise, (c) clearance distribution, and (d) compressor/compression system coupling. A simplified linearized analysis for a rotating clearance asymmetry is also described and used to show the relative effects of stationary and rotating clearances.

7.1 Effect of Compressor Characteristic Curvature. We first assess the effect on stability of changes in the radius of curvature at the peak of the pressure rise characteristic. Generally, altering the radius of curvature at the peak changes the width of the compressor operating map. Three different levels of peak radius of curvature were examined: (i) baseline case, (ii) half the radius of the baseline case, and (iii) twice the radius of the baseline case. In all calculations, the clearance

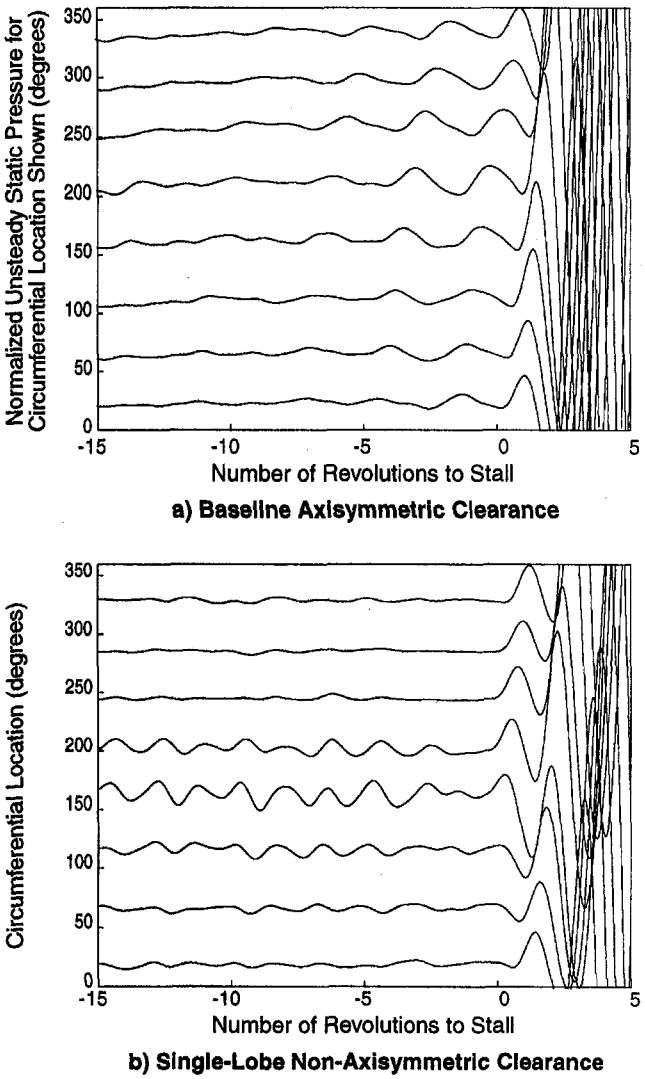

Fig. 16 Time traces of casing static pressure measured for stall transients

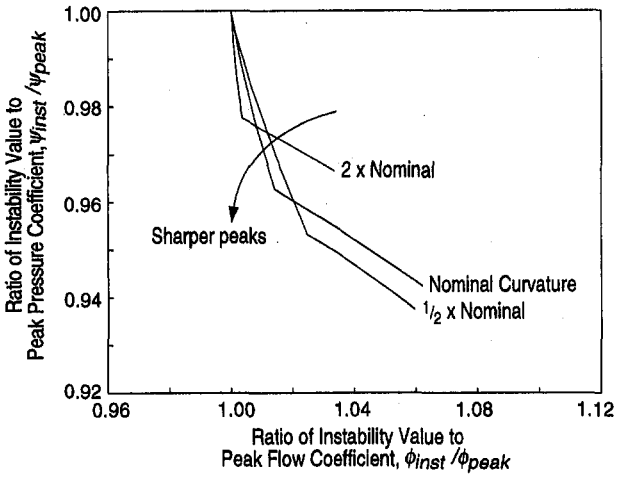

Fig. 17 Loci of neutral stability points showing how compressor stability is affected by the magnitude of the radius of curvature at the peak of the pressure rise characteristic

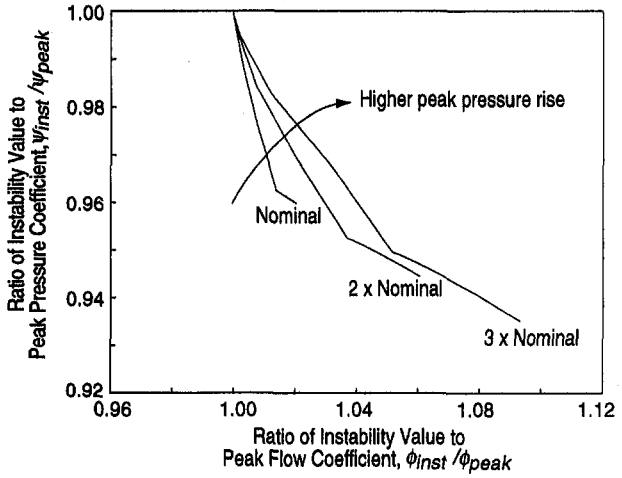

Fig. 18 Loci of neutral stability points showing how compressor stability is affected by the magnitude of the peak pressure rise

asymmetry was cosine shaped with an amplitude of 2 percent of rotor chord.

The loci of the neutral stability points for the three different peak curvature cases are shown in Fig. 17. Stall margin is reduced if the loci of points in the figure move to lower pressures and/or higher flows. As the peak radius of curvature is reduced, the data in Fig. 17 show that the loss in stall margin increases for a given level of clearance asymmetry or peak shift; that is, characteristics with sharper peaks have increased sensitivity to clearance asymmetry.

To understand why the sensitivity is increased, we can refer back to the discussion of Fig. 2. Calculation of the loci of operating points at neutral stability in Fig. 3 showed that approximately half the points around the annulus are in the positive slope region of the compressor map. As the radius of curvature is reduced (sharper peaks), the variations in pressure rise and slope encountered around the annulus become larger. Regions of lower pressure rise and increased (steeper) positive slope are thus accessed, causing the onset of instability at a higher annulus averaged flow coefficient.

7.2 Effect of Compressor Peak Pressure Rise. The baseline three-stage compressor had a peak pressure rise of $\psi = 0.8$. To determine the effect of increasing this peak pressure rise, it is useful to think in terms of adding repeating stages to the baseline compressor. The compressor map width was set to be the same regardless of the number of stages so that increasing the peak height for fixed map width also results in a reduction of the peak radius of curvature. Three levels of peak pressure rise were evaluated: nominal, two times nominal, and three times nominal. These represent three, six, and nine stage machines of the same map width but with a 2 percent clearance asymmetry.

The loci of the movement of the neutral stability point for the three cases having different map heights are shown in Fig. 18. The results are normalized by the peak quantities to allow direct comparison. As the maximum pressure rise increases, the loss in stall margin (pressure rise and flow) also increases for a given level of clearance asymmetry or peak shift. This occurs for reasons directly analogous to those given in Section 7.1 for changes in peak curvature.

7.3 Effect of Tip Clearance Distribution. As shown both theoretically and experimentally, the number of lobes of the clearance asymmetry has a direct influence on the performance penalty paid by the compressor. To illustrate the impact of tip clearance geometry on stability further, we examine four different casing profiles: (1) cos θ, (2) cos 2θ, (3) cos 4θ, and (4) two 90 deg square notches, one above and one below the nominal clearance, separated by 90 deg. The first three are continuous clearance variations, which contain only a single spatial harmonic, while the fourth, in theory, contains an infinite number of harmonics. The average clearances of the four cases were specified to be the same and equal to that of the baseline.

The locus of neutral stability points for each of the clearance geometries is shown in Fig. 19. As with the experiment, the clearance variations with the longest wavelength produced the greatest loss in stall margin, as seen by curve 1. For the discrete notches seen as curve 4 in Fig. 19, the movement of the neutral stability point is similar to that of the cos θ asymmetry in curve 1 because this nonuniformity has a dominant first harmonic. These trends are also similar to those obtained for the effects of the spatial extent of circumferential inlet distortions. That is, distortions with larger circumferential extent produced larger losses in stall margin.

The four clearance asymmetries in the example given above were specified to maintain the same minimum, average, and maximum clearance, which is the way the experiments were carried out. This implies that the arc lengths of the two-lobed and four-lobed casings necessary to generate the asymmetry were longer than for the single-lobed casing. A more realistic

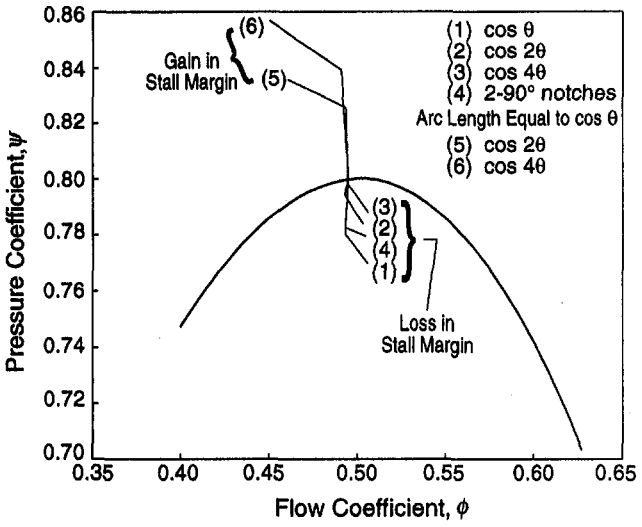

Fig. 19 Effect of circumferential clearance distribution and amplitude on compressor instability point

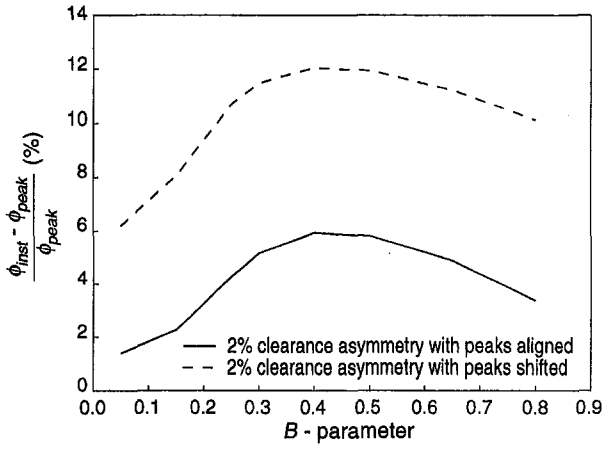

Fig. 20 Change in flow coefficient at instability with *B*-parameter

scenario is one in which the casing arc length with nonaxisymmetric clearance would deviate little from the axisymmetric value.[2] Thus, two-lobed and four-lobed asymmetries that had arc lengths the same as the single-lobed asymmetry were also examined. This means that the *average* clearance of the asymmetries *decreased* as the number of lobes increased. The loci of stall points for constant arc length cases with cos 2θ (case 5) and cos 4θ (case 6) are also shown in Fig. 19. These cases lie above and to the left of the baseline characteristic, and thus indicate an increase in stall margin. This occurs because, for constant arc length, the average clearance decreases as lobe number increases.

7.4 Effect of Compressor/Compression System Coupling. A nondimensional parameter that characterizes the dynamic behavior of a compression system is

$$B = \frac{U}{2\omega L} \tag{8}$$

where L is the characteristic length of the compressor for one-dimensional (surge-type) oscillations and ω is the Helmholtz frequency of the system. We can write this parameter as the ratio of two characteristic frequencies in the form

$$B = \frac{(U/r)}{\omega}\left(\frac{r}{2L}\right) \tag{9}$$

where $r/2L$ represents the geometry of the compressor. The characteristic frequency of a propagating disturbance will scale with U/r, whereas the frequency associated with surgelike disturbances does not scale with rotor speed, but rather, is related to the Helmholtz resonator frequency, ω. Therefore, as the B-parameter is varied, there will be some value at which surge-type frequencies and propagating disturbance frequencies come together, giving possibilities for resonance, increased sensitivity to perturbations, and hence a decreased stability. An analogous situation occurs with the asymmetry due to inlet distortion, where Chue et al. (1989) have presented a description of the physical mechanism that couples propagating disturbances and surgelike disturbances. For small amplitude disturbances, this type of coupling will only occur if the mean flow is nonaxisymmetric.

To investigate the effect of compressor–compression system coupling, we have carried out computations using a cosine-shaped clearance asymmetry with B-parameters from 0.05 to 0.8. The upper limit of 0.8 was chosen because B greater than this caused the zeroth ("surgelike") mode to become unstable before the first ("stall-like") mode. Figure 20 shows the results for the 2 percent clearance asymmetry with the peaks of the characteristics first aligned and then shifted, as described in Section 3.2. With peaks shifted, there is an increase in stalling flow coefficient over a range of values of B, with a broad peak at roughly $B = 0.4$.

7.5 Effect of Rotating Clearance Asymmetry. Throughout this investigation the focus has been on stationary clearance nonuniformities. It is useful, however, to give some discussion of the effect on the compressor flow field of rotating clearance asymmetries, which can also be encountered in practice.

One difference between stationary and rotating asymmetries is the response of the flow fields upstream and downstream of the compressor. For the stationary asymmetry, the inlet static pressure is spatially nonuniform. At the compressor exit (assuming constant exit flow angle), the static pressure is circumferentially uniform. With a rotating asymmetry, the inlet total pressure is also nonuniform, and the asymmetry will rotate at the shaft frequency. In addition, the exit of the compressor will also experience temporal variations in static pressure as the geometry-induced flow asymmetry rotates around the annulus, so a compressor with a rotating clearance asymmetry generates an unsteady flow at inlet and exit.

The appendix describes a linearized model of the compressor response to a rotating clearance asymmetry similar to that presented in Section 3. One result is an expression for the axial flow variation induced by a rotating asymmetry,

$$\delta\phi_{\text{rot}} = \frac{\dfrac{\partial\psi}{\partial\epsilon}\,\delta\epsilon}{in(\lambda + \mu) + 2i - \dfrac{\partial\psi}{\partial\phi}} \tag{10}$$

Comparing Eq. (10) with Eq. (7) for a stationary clearance asymmetry, it is observed that given the same clearance nonuniformity $\delta\epsilon$, the flow nonuniformity will be smaller for the rotating asymmetry than for the stationary. This effect is due to the additional terms present in the denominator of Eq. (10), which account for flow unsteadiness both external to and within the compressor. To illustrate the difference, Fig. 21 gives the magnitude of the axial velocity variation, normalized by clearance variation, for stationary and rotating clearance asymmetries as a function of the compressor characteristic slope (i.e., operating point). The sensitivity to slope changes is substantially greater for the compressor with the stationary asymmetry.

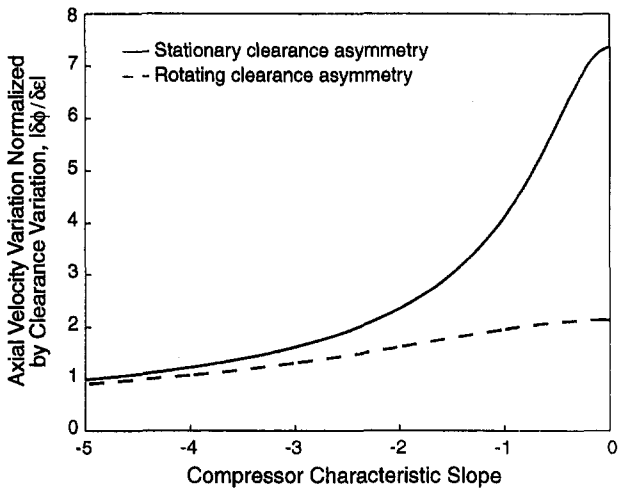

Fig. 21 Magnitude of flow nonuniformity induced by stationary and rotating clearance asymmetries. Parameters of baseline three-stage compressor.

[2] We thank Professor A. H. Epstein for this suggestion.

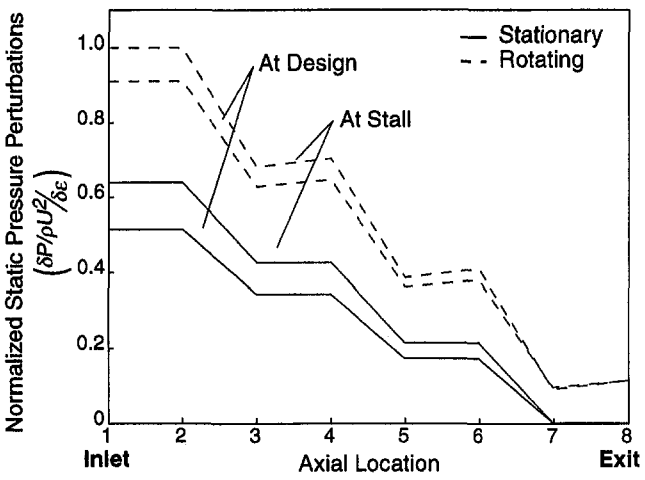

Fig. 22 Static pressure perturbation in a three-stage compressor with stationary and rotating clearance asymmetries

In Fig. 22, we examine the axial distribution of the pressure field within the compressor. The amplitude of the static pressure perturbations have been normalized by the inlet static pressure nonuniformity at stall with the rotating asymmetry. Results are shown for design and peak pressure rise conditions. As one might expect, the pressure disturbances decrease in amplitude through the machine but the change in amplitude with operating point is greater with the stationary asymmetry. Also, the static pressure disturbances go to zero at the compressor exit with the stationary asymmetry, while they remain nonzero for the rotating asymmetry, because the flow is unsteady at the compressor exit when the asymmetry rotates.

8 Summary and Conclusions

The effect of tip clearance asymmetry on multistage compressor performance and stability has been studied theoretically and experimentally.

A theoretical model was developed to describe the steady and unsteady flow response of an axial compressor with asymmetric tip clearance. Clearance asymmetry was analyzed by viewing each circumferential location as operating along a pressure rise characteristic corresponding to the local level of clearance. The present work gives the first nonlinear treatment of the steady flow with clearance asymmetry and the first analysis of the effect on compressor stability.

Experiments were conducted on a four-stage, low-speed compressor to establish the impact of asymmetric tip clearance on multistage compressor performance and stability, and to verify the theoretical model. The experiments were designed and performed on a four-stage, low-speed compressor. Specific findings were:

1 The theory accurately describes the steady and unsteady behavior of the measured flow field. The effects of clearance asymmetry and of reduced frequency were captured for pressure rise, for flow coefficient at stall, and for efficiency.
2 Nonaxisymmetric tip clearance resulting from casing distortion can significantly reduce the levels of compressor peak pressure rise and stable flow range relative to the levels obtained for an equivalent average axisymmetric clearance. As shown by both analysis and experiment, the decrease in stability (stall margin) for asymmetric clearance was closer to that obtained for averaged clearances equal to the maximum asymmetric clearance. Thus, peak pressure and stable flow range degrade in proportion to the increase in maximum level of the clearance asymmetry.
3 The reduction in *peak* efficiency due to clearance asymmetry was roughly equal to that obtained for an equivalent average axisymmetric clearance. Thus, peak efficiency degrades in proportion to the increase in average level of the clearance asymmetry.
4 The spatial harmonic content of the clearance asymmetry is an important factor in determining the severity of the impact on compressor performance and stability. Asymmetries with lower harmonics are more detrimental than asymmetries with higher harmonics. The most severe effects are produced by clearance asymmetries with dominant wavelength equal to that of the compressor circumference. This effect was also captured by the theory.
5 Unsteady flow measurements with asymmetric clearance showed that the variation in rms unsteadiness around the annulus is related to stall cell inception location and to the disturbance wave structure. The measured location of maximum flow field unsteadiness corresponded to the end of the large clearance sector and the theoretical location of maximum disturbance growth. The theoretical results imply that the stability of a compressor with clearance asymmetry can be linked to unsteady flow processes driven by the casing variation.
6 For a given clearance nonuniformity, the circumferential variation in velocity is reduced if the asymmetry is rotating as opposed to stationary.
7 A parametric study was conducted to explore the effects of asymmetric clearance on compressor performance and stability. The results of the study were:

- There is an increased sensitivity to clearance asymmetry for compressors with characteristics that are steep, have high peak pressure rise, narrow map width, and a sharp drop in pressure rise after the peak.
- Decreasing the wavelength of the clearance nonuniformity (i.e., increasing the reduced frequency) decreases the effect of clearance asymmetry on stall margin. There is virtually no further penalty due to asymmetry when the asymmetry has four or more lobes.
- For a given compressor, sensitivity to clearance asymmetry is only a weak function of compressor–compression system coupling.

Acknowledgments

This work has been supported by the Air Force Office of Scientific Research, Dr. James McMichael, Program Manager. This support is gratefully acknowledged. Support for M. Graf was provided under the Air Force Research in Aero Propulsion Technology (AFRAPT) Program; this assistance is also appreciated. The authors would like to thank GE Aircraft Engines for support and permission to publish the results. We also acknowledge the indispensible efforts of Mr. Donald Menner of GE Aircraft Engines in helping carry out the experiments, and of Dr. C. Van Schalkwyk for facilitating implementation of the computational work. Thanks also to Mr. K. Gordon for pointing out a minor mistake in the appendix. Finally, we are most pleased to acknowledge the patience and understanding shown by Ms. D. Park to the authors during the manuscript preparation process.

References

Baghdadi, S., 1996, "Modeling tip clearance effects in multistage axial compressors," ASME JOURNAL OF TURBOMACHINERY, Vol. 118, pp. 697–705.

Chue, R., Hynes, T. P., Greitzer, E. M., Tan, C. S., and Longley, J. P., 1989, "Calculations of inlet distortion induced compressor flow field instability," *Int. J. Heat Fluid Flow*, Vol. 10, pp. 211–223.

Freeman, C., 1985, "Effect of tip clearance flow on compressor stability and engine performance," von Karman Institute for Fluid Dynamics, Lecture Series 1985-05.

Garnier, V. H., Epstein, A. H., and Greitzer, E. M., 1991, "Rotating waves as a stall inception indication in axial compressors," ASME JOURNAL OF TURBOMACHINERY, Vol. 113, pp. 290–301.

Graf, M. B., 1996, "Effects of asymmetric tip clearance on compressor stability," Master's Thesis, MIT Department of Aeronautics and Astronautics.

Graf, M. B., et al., 1997, "Effects of Non-axisymmetric Tip Clearance on Axial Compressor Performance and Stability," MIT Gas Turbine Laboratory Report No. 225.

Greitzer, E. M., 1981, "The stability of pumping systems—The 1980 Freeman Scholar Lecture," ASME *Journal of Fluids Engineering*, Vol. 103, pp. 193–242.

Gysling, D. L., and Greitzer, E. M., 1995, "Dynamic control of rotating stall in axial flow compressors using aeromechanical feedback," ASME JOURNAL OF TURBOMACHINERY, Vol. 117, pp. 307–319.

Haynes, J. M., Hendricks, G. J., and Epstein, A. H., 1994, "Active stabilization of rotating stall in a three-stage axial compressor," ASME JOURNAL OF TURBOMACHINERY, Vol. 116, pp. 226–239.

Hynes, T. P., and Greitzer, E. M., 1987, "A method for assessing effects of inlet flow distortion on compressor stability," ASME JOURNAL OF TURBOMACHINERY, Vol. 109, pp. 371–379.

Koch, C. C., and Smith, L. H., 1976, "Loss sources and magnitudes in axial-flow compressors," ASME *Journal of Engineering for Power*, Vol. 98, pp. 411–424.

Koch, C. C., 1981, "Stalling pressure rise capability of axial flow compressor stages," ASME *Journal of Engineering for Power*, Vol. 103, pp. 645–656.

Lavrich, P. L., 1988, "Time Resolved Measurements of Rotating Stall in Axial Flow Compressors," MIT Gas Turbine Laboratory Report No. 194.

Longley, J. P., 1994, "A review of non-steady flow models for compressor stability," ASME JOURNAL OF TURBOMACHINERY, Vol. 116, pp. 202–216.

McDougall, N. M., Cumpsty, N. A., and Hynes, T. P., 1990, "Stall inception in axial compressors," ASME JOURNAL OF TURBOMACHINERY, Vol. 112, pp. 116–125.

Silkowski, P. D., 1995, "Measurements of Rotor Stalling in a Matched and a Mismatched Multistage Compressor," MIT Gas Turbine Laboratory Report No. 221.

Smith, L. H., Jr., 1958, "The effect of tip clearance on the peak pressure rise of axial-flow fans and compressors," *ASME Symposium on Stall*, pp. 149–152.

Smith, L. H., Jr., 1970, "Casing boundary layers in multistage axial flow compressors," in: *Flow Research on Blading*, L. S. Dzung, ed., Elsevier Publishing Co.

Wisler, D. C., 1985a, "Loss reduction in axial-flow compressors through low-speed model testing," ASME *Journal of Engineering for Gas Turbines and Power*, Vol. 107, pp. 354–363.

Wisler, D. C., 1985b, "Advanced compressor and fan systems," General Electric Aircraft Engine Business Group Publication, Cincinnati, OH.

Wong, T. S., 1996, "Effects of asymmetric tip clearance on compressor performance and stability," Master's Thesis, MIT Department of Aeronautics and Astronautics.

APPENDIX

Analysis of Rotating Clearance Asymmetry

In this appendix, a linearized description is given of the response of a compressor to a rotating clearance asymmetry.

Upstream Duct. As a result of the rotating clearance nonuniformity, the total pressure upstream of the compressor will vary in time. The unsteady changes in inlet total pressure can be expressed as (Hynes and Greitzer, 1987)

$$\frac{\delta P_{t,\text{inlet}}}{\rho U^2} = -\frac{1}{|n|}\frac{r}{U}\frac{\partial \delta\phi}{\partial t} \tag{A.1}$$

with the nth harmonic of $\delta\phi$ given by

$$\delta\phi_n = \frac{|n|}{r} a_n e^{|n|(x/r)+i(n\theta-\omega t)} \tag{A.2}$$

so that

$$\frac{\delta P_{t,\text{inlet}}}{\rho U^2} = +\frac{i\omega r}{|n|U}\delta\phi_n \tag{A.3}$$

where ω is the disturbance frequency associated with the corotating asymmetry. For an n-lobed rotating asymmetry,

$$\omega = n\frac{U}{r} \tag{A.4}$$

Substituting Eq. (A.4) into Eq. (A.3) gives

$$\frac{\delta P_{t,in}}{\rho U^2} = +i\delta\phi_n \tag{A.5}$$

Downstream Duct. The pressure distribution downstream of the compressor will also vary in time. Using the exit condition of constant leaving angle, one can write the unsteady static pressure variation as

$$\frac{\delta P_{\text{exit}}}{\rho U^2} = \frac{1}{|n|}\frac{r}{U}\frac{\partial \delta\phi}{\partial t} \tag{A.6}$$

and using Eqs. (A.2) and (A.4), one obtains

$$\frac{\delta P_{\text{exit}}}{\rho U^2} = -i\delta\phi_n \tag{A.7}$$

Compressor. The linearized equation for the compressor response with a rotating clearance asymmetry is Eq. (4) with an additional term related to the unsteady response of the compressor flow field:

$$\frac{\delta P_{\text{exit}} - \delta P_{t,\text{inlet}}}{\rho U^2} = \frac{\partial\psi}{\partial\phi}\delta\phi + \frac{\partial\psi}{\partial\epsilon}\delta\epsilon - \lambda\frac{\partial\delta\phi}{\partial\theta} - \frac{\mu r}{U}\frac{\partial\delta\phi}{\partial t} \tag{A.8}$$

Substituting the inlet and exit duct Eqs. (A.5) and (A.7) gives

$$\lambda\frac{\partial\delta\phi}{\partial\theta} + \frac{\mu r}{U}\frac{\partial\delta\phi}{\partial t} - \frac{\partial\psi}{\partial\phi}\delta\phi - 2i\delta\phi = \frac{\partial\psi}{\partial\epsilon}\delta\epsilon \tag{A.9}$$

and using Eqs. (A.2) and (A.4),

$$\delta\phi\left\{in(\lambda-\mu) - 2i - \frac{\partial\psi}{\partial\phi}\right\} = \frac{\partial\psi}{\partial\epsilon}\delta\epsilon \tag{A.10}$$

or,

$$\delta\phi = \frac{\dfrac{\partial\psi}{\partial\epsilon}\delta\epsilon}{in(\lambda-\mu) - 2i - \dfrac{\partial\psi}{\partial\phi}} \tag{A.11}$$

Equation (A.11) gives the flow nonuniformity ($\delta\phi$) induced by a rotating asymmetry ($\delta\epsilon$). As compared to Eq. (7) for the stationary asymmetry, new terms have been introduced in the denominator; one is related to unsteady flow in the compressor and the other to the unsteady flow in the inlet and exit ducts. By taking the ratio of Eq. (7) to Eq. (A.11) and assuming that the sensitivity to clearance change ($\partial\psi/\partial\epsilon$) and the clearance variation ($\delta\epsilon$) are the same for the rotating and stationary asymmetries, we obtain

$$\frac{\delta\phi_{\text{stat}}}{\delta\phi_{\text{rot}}} = \frac{in(\lambda-\mu) - 2i - \dfrac{\partial\psi}{\partial\phi}}{in\lambda - \dfrac{\partial\psi}{\partial\phi}} \tag{A.12}$$

Near the peak of the characteristic ($\partial\psi/\partial\phi \approx 0$), this can be approximated as

$$\frac{\delta\phi_{\text{stat}}}{\delta\phi_{\text{rot}}} = \frac{n(\lambda-\mu) - 2}{n\lambda} \tag{A.13}$$

These results show that a stationary clearance asymmetry induces a greater axial velocity nonuniformity than that obtained if the asymmetry were rotating, for

(i) $\mu > \lambda$

(ii) n low ($n < 5$, say).

Viscous Throughflow Modeling of Axial Compressor Bladerows Using a Tangential Blade Force Hypothesis

S. J. Gallimore
Rolls-Royce Plc,
Derby, United Kingdom

This paper describes the modeling of axial compressor blade rows in an axisymmetric viscous throughflow method. The basic method, which has been reported previously, includes the effects of spanwise mixing, using a turbulent diffusion model, and endwall shear within the throughflow calculation. The blades are modeled using a combination of existing two-dimensional blade performance predictions for loss and deviation away from the annulus walls and a novel approach using tangential blade forces in the endwall regions. Relatively simple assumptions about the behavior of the tangential static pressure force imposed by the blades allow the secondary deviations produced by tip clearance flows and the boundary layer flows at fixed blade ends to be calculated in the axisymmetric model. Additional losses are assigned in these regions based on the calculated deviations. The resulting method gives realistic radial distributions of loss and deviation across the whole span at both design and off-design operating conditions, providing a quick method of estimating the magnitudes of these effects in the preliminary design process. Results from the method are compared to measured data in low and high-speed compressors and multistage three-dimensional viscous CFD predictions.

Introduction

Despite the recent advances in three-dimensional multistage viscous calculations (Rhie et al., 1998; LeJambre et al., 1998) the axisymmetric throughflow calculation remains a valuable tool in the design of axial flow compressors. Apart from its role in the setting up of the basic air angle design, these methods also lend themselves to the rapid performance prediction of machines both in the preliminary design phase and later on in the process. Any improvement in the modeling of the compressor flow in the throughflow environment will therefore make a significant contribution to the design system.

The modern era of throughflow calculations can be said to have started with the inclusion of the effects of spanwise mixing into the calculations by Adkins and Smith (1982). Their method was based on deterministic secondary flows. An alternative approach based on a turbulent type diffusion process was suggested later by Gallimore and Cumpsty (1986) and Gallimore (1986), which produced similar improvements in the predictions relative to test data. A logical extension to this latter method was to include the effects of endwall shear into the calculations (Howard and Gallimore, 1993), to produce more realistic radial predictions of the flow properties. The work of Dunham (1995, 1996) has combined two-dimensional blade performance correlations with the effects of spanwise mixing, secondary flow theory, and an integral annulus wall boundary layer method into a throughflow method.

The method described in this paper is based on the viscous throughflow model of Howard and Gallimore (1993), which has been extended to include two-dimensional blade performance calculations and a simple tangential blade force model to calculate the extra loss and deviations associated with the tip clearance and endwall flows. The important role of the tangential blade force in controlling the behavior of axial flow compressors has long been recognized and it is this part of the modeling, in particular the radial variation of tangential blade static pressure force, that is fundamental to the method and will be concentrated on in this paper. It is recognized that the real flow in axial flow compressors is unsteady, viscous, and three-dimensional, and that an axisymmetric method cannot include all the physics present in the complicated flow. The results presented here, however, show that significant features of the flow, such as endwall boundary layers, tip clearance flows, and the over and underturning due to secondary flows at fixed blade ends, can be successfully calculated to a level of accuracy that is more than sufficient for preliminary design and performance prediction purposes. The method is suitable and convenient for preliminary design calculations because it is quick and the only inputs required are some basic blade properties such as pitch to chord ratio. This is very different from a multistage three-dimensional viscous calculation where a full definition of the blade profiles is needed. The calculation does not deal with endbent blades or blades with significant deviation from a radial stacking line (e.g., bowed stators), but it is felt that these omissions are not crucial in the application of the method early on in the design process before such sophisticated blading techniques are introduced later in the design.

In the next two sections of the paper tangential blade force definitions are presented and observations are made on the behavior of the tangential blade force in axial flow compressors. This leads to a tangential blade force hypothesis suitable for an axisymmetric flow calculation. The implementation of this model into the throughflow method is then described, to be followed by some results from the method, a discussion, and finally, conclusions.

Tangential Blade Force Definitions

Two tangential forces may be defined for a blade row, one describing the pressure force imposed by the blade on the flow (P_θ) and the other derived by considering the tangential momen-

Contributed by the International Gas Turbine Institute and presented at the 42nd International Gas Turbine and Aeroengine Congress and Exhibition, Orlando, Florida, June 2–5, 1997. Manuscript received at ASME Headquarters February 1997. Paper No. 97-GT-415. Associate Technical Editor: H. A. Kidd.

tum change of the flow across the blade row (F_θ). The tangential momentum change is a result of the pressure force imposed by the blade and the other forces caused by the effects of endwall shear and shear within the flow field and in general F_θ will therefore differ from P_θ. Figure 1 shows a schematic meridional view of a streamtube passing through a blade row. In the viscous throughflow model the streamtube has a force due to tangential shear in the flow acting upon it on the top and bottom surfaces, denoted here as T_θ. It also assumes no momentum transport out of the top and bottom of the control volume due to radial secondary flows. Taking the streamtube height variation into account gives the following relationship between the pressure force and the tangential momentum change:

$$F_\theta = P_\theta + T_\theta \tag{1}$$

where:

$$F_\theta = \frac{2\rho_1 V_{m1} s_1 (r_1 V_{\theta 1} - r_2 V_{\theta 2})}{\bar{r}(1 + h_2/h_1)} \tag{2}$$

The definitions just described take into account the streamtube height ratio and radius change across the blade row but data derived directly from test data often does not. An example of this is the data reported by Dring (1993), which will be used later, where forces derived from measurements made at constant radii are used. For comparisons with these data, the results from the calculations described later have been evaluated in a similar way to the test data, i.e.,

$$F_\theta = s(\rho_2 V_{x2} V_{\theta 2} - \rho_1 V_{x1} V_{\theta 1}) \tag{3}$$

The force derived from the blade pressure field in the calculations of Dring's compressor has also been re-evaluated in the comparisons with test data to give the blade force at a constant radius.

Some Observations on Tangential Blade Forces

Measurements of the blade static pressure force in axial flow compressors have been reported by Dring (1993) and additional data are available to the author. Examination of these data reveals that the tangential static pressure blade force tends to be smoothly varying across the span and does not exhibit rapid changes as the endwalls are approached. This seems a reasonable observation for blades with a predominantly radial stacking axis where there is little reason for significant variations of the radial distribution of static pressure along the blade span to

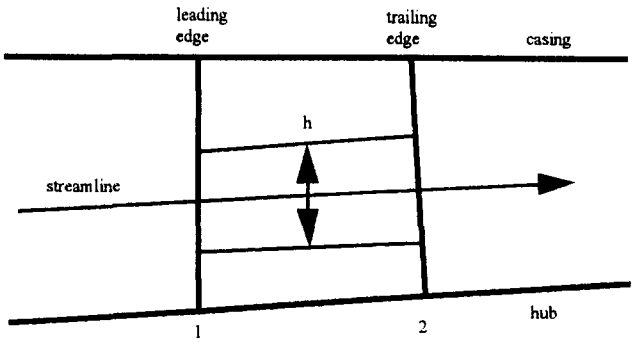

Fig. 1 Meridional view of streamtube passing through a blade row

exist. This smooth variation is in contrast to the blade forces deduced from measurements of the blade inlet and exit velocity fields (F_θ), for example Smith (1970) and Dring (1993), which show quite large variations near the endwalls that do not seem to behave in a predictable way. Figure 2 shows examples of this taken from Dring for a two-stage low-speed compressor at near-stall conditions. While the radial variation of F_θ is seen to vary quite dramatically for both the rotor and the stator, the radial variation in P_θ would seem to vary in a more controlled and predictable manner. It was these types of observed variations in F_θ that gave rise to the introduction of the tangential blade force deficit. This proved to be a particularly difficult quantity to predict or correlate and was one of the prime reasons for the failure of the integral boundary layer methods widely tried in the 1970s and 1980s (e.g., Hirsch and de Ruyck, 1981). The assumption of how the blade force varied through the boundary layer dictated the results.

The difference between P_θ and F_θ is due to radial redistribution of the flow and to tangential shear forces acting within the flow and on the endwalls and it is these that produce the unpredictable behavior in F_θ. In the viscous throughflow method used here, the effects of tangential shear are included directly in the flow calculation, which should therefore be able to calculate some of the unpredictable behaviour in F_θ. This allows the blades to be modeled using P_θ in the current method. It is this concept that is the underlying hypothesis in the current model.

Basic Viscous Throughflow Method

The basic viscous throughflow method is that described by Howard and Gallimore (1993). This includes the effects of spanwise mixing using a turbulent diffusion type model and explicitly includes the effects of the annulus wall boundary

Nomenclature

C = blade chord
DH = De Haller number = V_2/V_1
DR = diffusion ratio = V_{max}/V_2
F_θ = tangential blade force based on momentum change
H = blade height
h = streamtube height
LC = loading coefficient (Eq. (4))
p = static pressure
P_0 = total pressure
P_θ = tangential blade force due to blade static pressure field
r = radius
s = blade pitch
T_θ = tangential force due to flow shear
U = blade speed
V = flow velocity
V_τ = friction velocity
y = distance from the wall
$y^+ = yV_\tau/\nu$
ν = kinematic viscosity
ρ = density
ϕ = flow coefficient
ω = pressure loss coefficient = $(P'_{02is} - P'_{02})/(P'_{01} - p_1)$

Subscripts

1 = blade inlet
2 = blade exit
2d = calculated from two-dimensional calculations
in = input to next throughflow iteration
is = isentropic process value
m = meridional direction
max = maximum value on blade suction surface
mid = midspan value
min = minimum value on blade suction surface
tip = value at outer casing
x = axial direction
θ = tangential direction

Superscripts

$\bar{}$ = average of blade inlet and exit values
$'$ = relative value

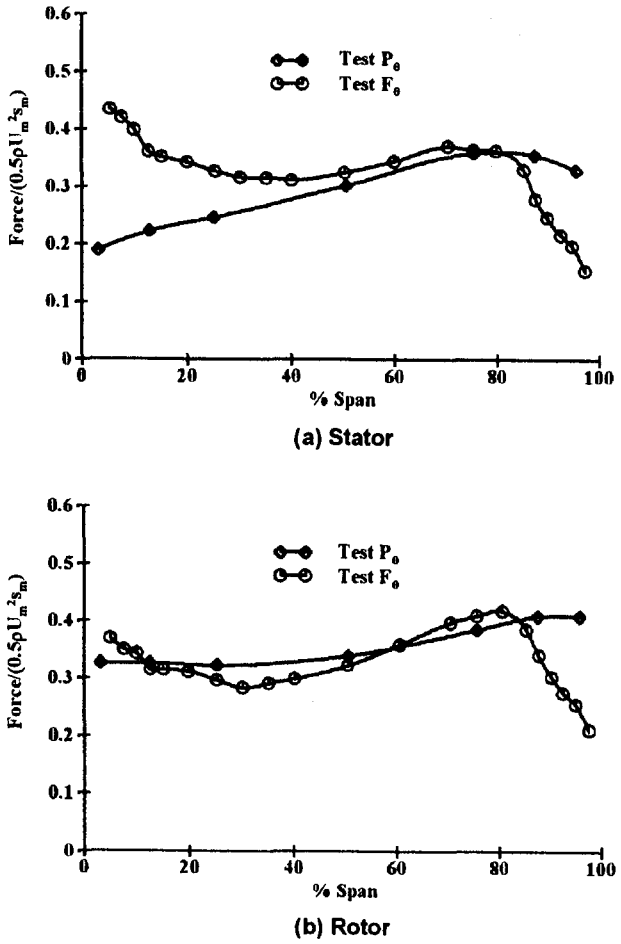

Fig. 2 Stator and rotor tangential forces from Dring (1993): $\phi = 0.45$

layers by specifying a no-slip condition on the endwalls. The mixing levels are calculated using the method described by Gallimore and Cumpsty (1986) and these are modified close to the annulus walls to drop to the laminar level of viscosity at the edge of the laminar sublayer, taken here at $y^+ = 12.5$. In the previous work of Howard and Gallimore, the blades were modeled by including empirical radial distributions of loss and relative exit angle based on correlations. It is this modeling of the blade rows that has been changed in the current work to give a more general model for the blades using the tangential blade static pressure force (P_θ) and loss as input. However, because of the need to represent the complicated real flow pattern in an axisymmetric environment some element of correlation and empiricism remains in the method.

Tangential Blade Force Modeling

Introduction. The starting point for modeling the blades is the two-dimensional performance. Any suitable method available could be used for this part of the process including correlations, blade-to-blade calculations, or even the specified design values. Whatever the approach adopted, these input values are based on two-dimensional blade sections and they become invalid as the endwalls are approached and the flow properties change in what can be termed the annulus wall boundary layer. In these regions the new approach is adopted based on the observations of how the tangential static pressure blade force varies in real machines.

The two-dimensional performance calculation is used to obtain an initial estimate of the blade exit air angles all the way across the span. By assuming the axial velocity distributions from the previous throughflow iteration, this turning is used to calculate the tangential momentum change across the blade row. At this point it is assumed that this momentum change is equal to the tangential blade pressure force ($P_{\theta 2d}$), which is equivalent to stating that the two-dimensional performance calculations give a first estimate of the blade pressure field that is applied to the flow. Near the blade ends, where the two-dimensional correlations are not valid and the axial velocity varies rapidly with radius, this can result in quite rapid changes in the radial distribution of the blade force.

Once the $P_{\theta 2d}$ variation has been calculated it is then modified near the endwalls, in a two-step procedure, to produce a different, smooth, variation (P_θ) that is then used in the throughflow calculation. For the work described in this paper, the regions near the endwalls are defined as extending spanwise by one blade axial chord away from each of the annulus walls. This is a rather arbitrary value but does recognize the likely spanwise extent of endwall and secondary flow effects. No doubt more sophisticated criteria could be developed, but it was found that this simple definition gave reasonable agreement with test data over the range of cases considered in this study. For low-aspect-ratio blading, the defined endwall regions will meet and overlap at the blade midheight section, which reflects the observation that it is often not possible to define the edge of the annulus wall boundary layers in the rear stages of multistage axial flow compressors where the aspect ratios are low. For these cases the endwall regions are limited to extending just less than half the blade span away from the annulus walls so that the midspan value of $P_{\theta 2d}$ is not altered by the procedures described below. It should also be noted that $P_{\theta 2d}$ is only modified in the endwall regions if it is required by the procedures defined below and so it is quite possible that the radial extent over which the modifications are made is less than that of the endwall regions defined.

First Step in Modifying Blade Force. The first step in the modification of $P_{\theta 2d}$ is to apply a limiting loading criterion within the defined endwall regions. The criterion is based on the pressure diffusion on the suction surface of the blade assuming a triangular loading distribution, Fig. 3, which is taken as a simplified representation of an aerofoil section near stall. The loading coefficient (LC) is defined by:

$$\mathrm{LC} = \frac{(p_2 - p_{\min})}{\frac{1}{2}\rho_1 V_1^2} \tag{4}$$

and, for the simple triangular loading distribution, is related to the blade tangential force by:

$$\mathrm{LC} = \frac{2P_\theta}{\frac{1}{2}\rho_1 V_1^2 C_x} \tag{5}$$

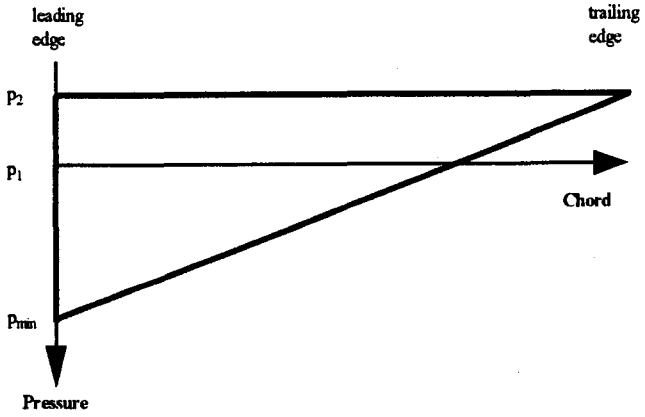

Fig. 3 Assumed blade surface static pressure distribution

The maximum diffusion that the endwall flow has to undergo is in the endwall suction surface corner of the blade passage and its ability to achieve this diffusion is dependent on the inlet dynamic head. LC is designed to reflect this. It is recognized that the coefficient has a two-dimensional type derivation, assuming that the flow travels along the axisymmetric streamlines, whereas it is actually three-dimensional. However, comparison of results from viscous and inviscid three-dimensional CFD, for the same geometry, do indicate that the peak suction surface diffusion that would be achieved near the endwalls in an inviscid calculation is a good indication of the amount of separation predicted in the viscous calculation: more separation is implied by a required higher diffusion.

LC is first evaluated at the spanwise position of the blade that has the highest meridional velocity entering the blade row and is also outside the endwall regions. The purpose of this is to obtain a value of LC that can be attained by the design away from most of the influence of endwall effects. This value of LC is taken as a limit in the endwall regions unless it is below 1.13, in which case 1.13 is taken as the limiting level. The value of 1.13 was derived from numerical experiments to give a reasonable data fit and can be related to the more conventional loading criteria using some algebra. For example, LC can be related to the De Haller number ($DH = V_2/V_1$) and diffusion ratio ($DR = V_{max}/V_2$) by:

$$\mathrm{LC} = DH^2(DR^2 - 1) \tag{6}$$

A value of LC = 1.13 can be obtained with $DR = 1.9$ and $DH = 0.68$, both quite close to the values traditionally used for stall, 2.2 and 0.6, respectively. If the limiting level of LC is exceeded on a streamline in the endwall regions the value of P_θ is locally reduced using Eq. (5), so that LC is on the limit.

Second Step in Modifying Blade Force. Once the loading criterion just described has been applied to every streamline in the endwall regions, and the values of P_θ recalculated as required, the updated values of P_θ are further adjusted as follows. The procedure is to evaluate the radial gradient of P_θ between the streamlines in the endwall regions, starting with the streamline at the edge of the endwall region and the next one toward the annulus wall. If the gradient is outside a specified limit (described below) then the value of P_θ on the streamline nearer the annulus wall is set to a new value that brings the gradient back to the limit. The procedure is then repeated using this new value of P_θ and the value on the next streamline toward the annulus wall until the wall streamline has been adjusted.

The controls described here were arrived at empirically and are based on the observation made earlier that the pressure force tends to be smoothly varying in the endwall regions and does not have large excursions. The actual values of the controls were derived from observations of experimental data, such as that of Dring (1993), and some data matching of the results of the throughflow calculations with the experimental results for a range of test cases.

A blade end with tip clearance can maintain relatively high levels of loading all the way along the blade span without separation. This fact was used by Wisler (1985) to change the work input into the flow at the tip of a rotor blade. Locally near the tip the work of Lakshminarayana and Horlock (1962) and Storer and Cumpsty (1991) showed that for a cascade there was some reduction in blade force near the tip leading to shed vorticity in the blade gap. During the present work it was found that this modification was not required in order to get good agreement in relative exit tangential velocities with test data. Furthermore data from rotor measurements (e.g., Dring (1993) and Fig. 2) support the assumption of maintaining a constant force until extremely close to the end of the blade. Therefore, at a blade end with tip clearance, the absolute value of the radial gradient of blade force is limited to $\leq 0.2\ P_{\theta\,\mathrm{mid}}/H$. In addition over a distance of ten times the tip clearance from the annulus wall, the blade force is kept constant at the value at ten times the clearance away from the wall, except in the blade gap where it is set to zero.

At fixed blade ends it is assumed that the blade force can decrease more in the spanwise direction than at blade ends with tip clearance. An increase in blade force is allowed at rotor hubs as a reflection of the observed ability of these regions to sustain more turning, perhaps due to the thinning of the boundary layer produced by the centrifugal force causing some radially outward flow within the blade boundary layers. Therefore, at fixed blade ends, the tangential force gradient between streamlines is not allowed to be less than $-0.8P_{\theta\,\mathrm{mid}}/H$. No positive blade force gradient is permitted, except at rotor hubs where a gradient of up to $+0.2P_{\theta\,\mathrm{mid}}/H$ is allowed.

An Example of Blade Force Modeling. An example of the results of these modifications is given in Fig. 4, which shows the radial variations of the tangential forces for the rotor of the four-stage compressor case described later. The curve of $P_{\theta 2d}$, based on the two-dimensional performance calculations, shows unrealistically large variations in gradient and level, particularly at the hub. These are removed by the procedures described above to give the smooth distribution of P_θ shown, which is used as input to the throughflow calculation. The value of F_θ deduced from the resulting flowfield calculated in the method is different from P_θ, because of the effect of the shear stresses and spanwise mixing in the viscous throughflow method (Eq. (1)), and is quite close to the values deduced from the measured data. F_θ drops to a significantly lower level than P_θ toward the hub. This indicates that the true tangential pressure force exerted by the blade does not decrease as much in this region as would have been deduced solely from measurements of F_θ. At the casing the effect of setting $P_\theta = 0$ in the tip gap is spread out radially by the spanwise mixing in the method and can be seen in the reduction in F_θ over the last 10 percent of the span.

Blade Loss Modeling

The initial estimate of the spanwise variation of blade loss (ω_{2d}) is taken from two-dimensional performance calculations using the flowfield calculated in the previous throughflow iteration. The loss could be taken from any suitable method such as correlations, blade-to-blade calculations, or even specified design values. These values are then modified in the regions where P_θ has been calculated to be different from $P_{\theta 2d}$ in the tangential blade force model described above. The method for modifying the losses to obtain the values input into the next throughflow iteration (ω_{in}) is described next.

Removing the blade force in the tip gap results in underturning of the flow in that region, which in turn creates some loss due to the tangential shear within the viscous throughflow

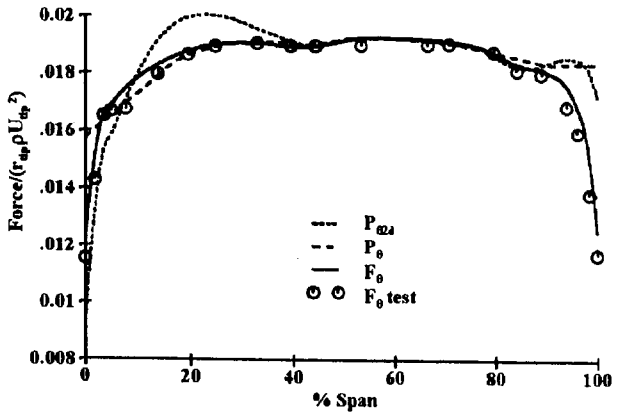

Fig. 4 Example of tangential blade forces for rotor 3 of low-speed four-stage compressor: design flow coefficient

method. The empirical loss from the two-dimensional performance calculations is ignored in this region, but additional loss is specified similar to the model of Storer and Cumpsty (1994) but modified to be suitable for an axisymmetric representation of the flow. It is assumed that the flow through the tip gap is inviscid and so picks up dynamic head equivalent to the blade pressure force at the tip as it passes through the gap. This extra dynamic head of the flow that passes through the gap is assumed to be destroyed and is accounted as a loss input. Most of this loss is radially specified in the tip gap but 20 percent is spread beyond the gap as shown in Fig. 5 to give a smoother input to the calculation.

Where P_θ has been decreased below $P_{\theta 2d}$, at radii away from the tip gap, underturning and extra deviation must occur. The magnitude of the extra deviation is calculated from the change of tangential momentum across the blade row given by the difference between P_θ and $P_{\theta 2d}$ using the axial velocity distributions from the previous throughflow iteration. Examination of test data and existing correlations for secondary loss and deviation (e.g., Roberts et al., 1986, 1988) shows that secondary deviation and loss occur together and to model this the relationship between off-design loss and deviation deduced from the two-dimensional performance correlations of Miller and Wasdell (1987) and Wright and Miller (1991) is used to determine the secondary loss. This relationship is shown in Fig. 6. It is appreciated that this is at best a simplification of the flow physics in this region, where there is evidence that secondary flow can move the endwall boundary layer fluid radially along the blade, but it seems reasonable that there is some link between the secondary loss and deviation.

In regions where the modified blade force implies reduced deviation relative to the two-dimensional correlation values ($P_\theta > P_{\theta 2d}$) the blade losses are taken to be unchanged from the correlation values. Again this is based on observations of experimental data where overturning does not seem to increase the measured blade losses.

An example of the blade losses produced by this technique is shown in Fig. 7, which is taken from the four-stage low-speed compressor calculation presented below. For this case the initial estimate of the profile loss (ω_{2d}) was taken as the two-dimensional design profile loss. The method described above to calculate ω_{in} has produced extra loss above ω_{2d} between about 5 and 50 percent span, similar to the test data, and again toward the blade tip. The final losses deduced from the throughflow results are different from ω_{in} because they include the effects of spanwise mixing and endwall shear. They show similar trends to the test data except very close to the hub, between 0 and 2 percent of span, where the predicted increase in loss is not present in the measurements. However, there is some uncertainty over the test results in this region. The plotted results are taken from a throughflow analysis of the test data derived from traverse measurements that do not extend all the way to the annulus wall and consequently the losses calculated on the wall rely on extrapolation from the measured data. The details of the analysis are described in detail by Howard et al. (1994). Other data for the same rotor running at a larger tip clearance are also presented by Howard et al. in their paper and these show deduced test loss distributions close to the rotor hub that resemble the viscous throughflow results, with the loss rising very close to the hub annulus wall.

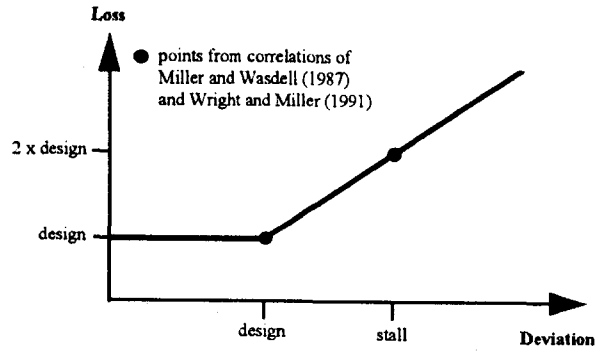

Fig. 6 Relationship between off-design loss and deviation

Evaluation of the Viscous Throughflow Method

Results are presented for two low-speed research compressors and a high-speed aero-engine compressor. The results are compared to measured test data and, in two cases, multistage three-dimensional viscous CFD calculations.

Low-Speed Four-Stage Compressor. This large-scale low-speed compressor consists of four stages of identical blading of controlled-diffusion aerofoils designed to replicate typical loadings and flow distributions found in high-speed multistage compressors. The compressor is described in some detail by Howard et al. (1994) together with the experimental results. Detailed experimental data are available at several axial stations but for this paper only the third stage, which is effectively a repeating stage, is considered. The experimentally measured inlet conditions to rotor 3 were used as input to the viscous throughflow calculation in order to isolate the effects of the modeling by giving it accurate inlet conditions. In the two other evaluations described later, the complete compressors were calculated so that the inaccuracies in the calculation could build up through the machines. The two-dimensional blade performance was calculated using the design levels of profile loss and deviation, which were corrected for off-design incidence using the method of Miller and Wasdell (1987) and Wright and Miller

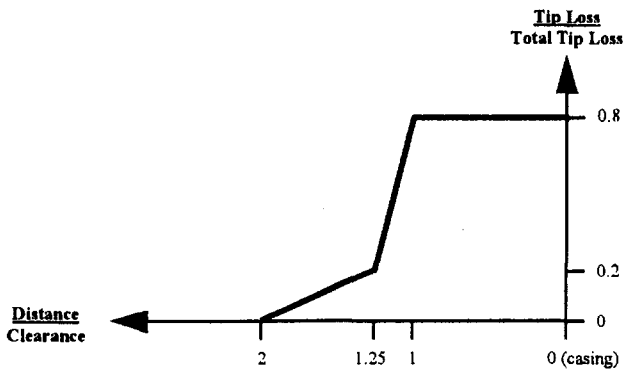

Fig. 5 Input radial distribution of tip clearance loss

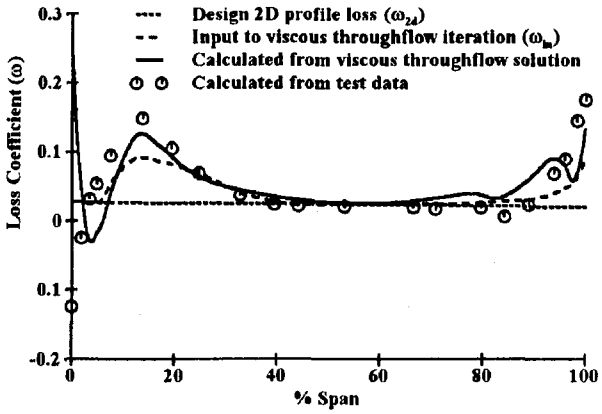

Fig. 7 Example of losses for rotor 3 of low-speed four-stage compressor: design flow coefficient

(1991). For comparison the results from a slightly modified version of the multistage three-dimensional viscous CFD method described by Denton (1992) are also presented. (The CFD calculations were made with the compressor run with a higher blade speed than the real machine, so that the free-stream Mach numbers were about 0.3, to allow the time marching calculation to converge properly. This is a usual technique in these types of cases, but experience has shown that this does not lead to significant inaccuracy.) The CFD predicted a slightly higher flow than that measured at the design pressure rise, which explains the generally higher levels of velocity for these data. The purpose of presenting the CFD data is to provide an additional comparison with the throughflow method and not to speculate on the accuracy of the CFD method, which in itself is a major topic of investigation.

The tangential blade forces and losses for rotor 3 have already been presented in Figs. 4 and 7 as part of the description of the viscous throughflow method. These showed good agreement with the values deduced from the measurements and this is reflected in the results for the rotor relative exit air angles and axial velocities, Figs. 8 and 9. Also shown for comparison are the design air angles, the predicted axial velocities from a conventional throughflow calculation using the design losses and turning, and the results of the CFD calculations. The viscous throughflow method has successfully calculated the underturning due to the rotor tip clearance as well as the more complicated over and underturning at the hub and gives results very similar to the CFD calculation. At midheight the CFD has not predicted the deviation correctly, whereas the viscous throughflow method has been fixed at the design level here, which lines up with the test in the midheight regions. The rotor exit axial velocity distribution is also well modeled by the method and again gives results of comparable accuracy to the CFD, which predicts a thicker casing boundary layer. The accuracy of the calculations is similar at stator exit and is illustrated by the radial distributions of absolute flow angle shown in Fig. 10. At the hub the underturning is caused by the clearance of the cantilevered stator, while at the casing there is both under and overturning in a similar form to the rotor hub.

To test further the accuracy of the tip clearance modeling, the viscous throughflow calculation was repeated at the larger tip clearance tested (increased from 1.2 to 3.0 percent clearance/tip chord) and the rotor relative exit angles for both cases are presented in Fig. 11. The increased tip deviation at the larger clearance is modeled quite well. The calculated loss in efficiency for increasing the clearance was 0.5 percent, which is very similar to the measured value of 0.7 percent.

Low-Speed Two-Stage Compressor. The second low-speed case presented is the two-stage compressor of conventional blading with a shrouded stator design that has been extensively measured and reported, for example by Joslyn and Dring (1985). The complete two stages of the machine were calculated. The correlations of Miller and Wasdell (1987) and Wright and Miller (1991) were again used to obtain the two-dimensional blade performance. CFD predictions have not been made for this case. The reported experimental data from the machine indicate that the predominant feature of this machine is the large amount of stator hub separation present as stall is approached, which gives a severe test of an axisymmetric method and in itself has provoked considerable effort in throughflow methodology to try and model the measured flowfield (Dring and Oates, 1990).

Data from this machine have been used to investigate the tangential blade forces, as described earlier and presented in Fig. 2. The largest reported difference between the measured F_θ and P_θ was for the second stator at near stall conditions. The stator data from Fig. 2 are reproduced in Fig. 12 where they are compared to the equivalent quantities deduced from the viscous throughflow calculation. At midheight there is some discrepancy between the measured and calculated values, which is partly a result of inaccuracies in the two-dimensional correlations in the method. What is of interest, however, is the difference between P_θ and F_θ for the two sets of results. Close to the casing the calculations show F_θ to be significantly less than P_θ, a difference reflected in the measurements. Indeed the calculated profiles of both P_θ and F_θ in this region are very similar to those measured although at a different absolute level. Toward the hub the measurements show that F_θ is greater than P_θ over a considerable portion of the span. This trend is also present in the calculations, though only in a region closer to the hub, but

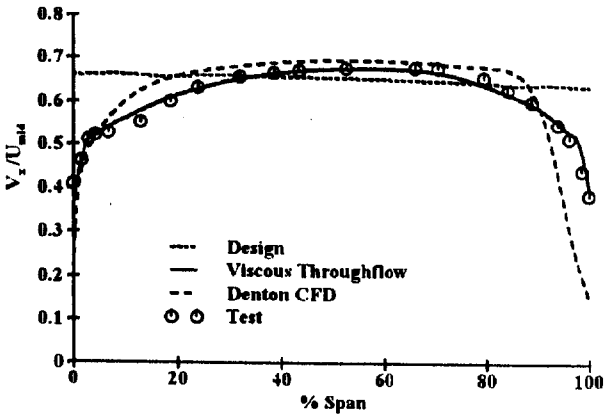

Fig. 9 Rotor 3 exit V_x/U_{mid} of low-speed four-stage compressor: design flow coefficient

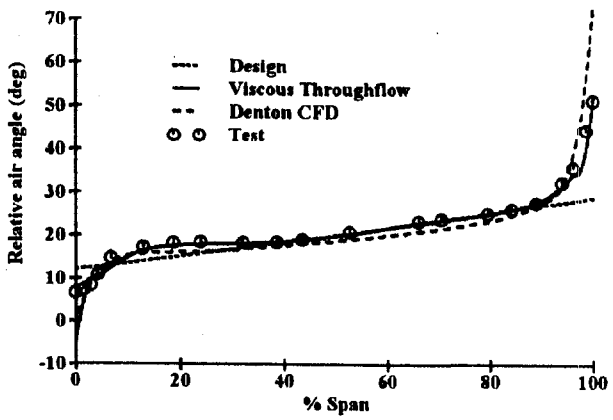

Fig. 8 Rotor 3 exit air angles of low-speed four-stage compressor: design flow coefficient

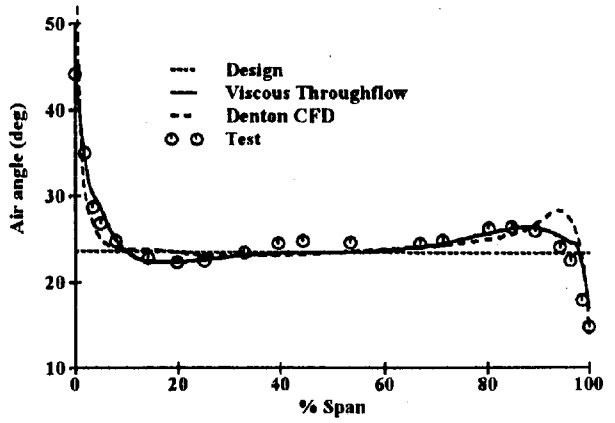

Fig. 10 Stator 3 exit air angles of low-speed four-stage compressor: design flow coefficient

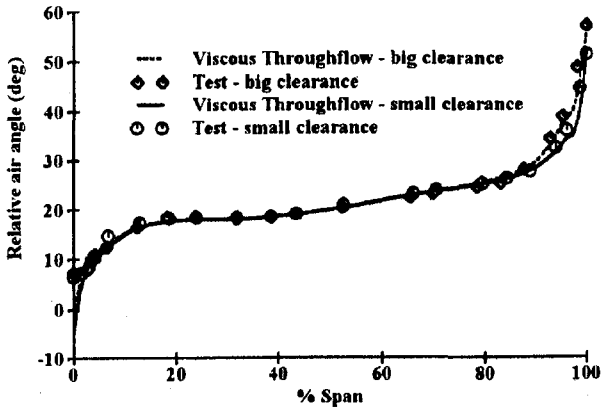

Fig. 11 Effect of tip clearance on rotor 3 exit air angles of low-speed four-stage compressor: design flow coefficient

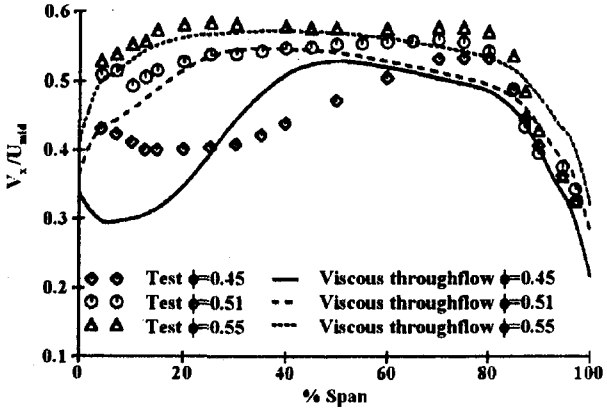

Fig. 13 Stator 2 inlet V_x/U_{mid} of low-speed two-stage compressor

it is significant that the method can show this effect. It must be remembered that the exit traverse data showed large regions of hub corner separation in this blade row extending radially beyond midheight, indicating a significant deviation of the flow from that which an axisymmetric model could be reasonably expected to predict. Despite this, the current method, which assumes that the midheight section of the blade is behaving in a two-dimensional way (clearly not the case here), has captured some of the significant features of the blade behavior.

The calculated axial flow velocities at inlet and exit to the second stator row reflect this discrepancy in the blade forces at stall. Results are presented at three flow coefficients ranging from a wide-open throttle position ($\phi = 0.55$), through design ($\phi = 0.51$), to near stall ($\phi = 0.45$) for a single rotor tip clearance in Figs. 13 and 14. At the near-stall condition the measurements show a greater region of reduced axial velocity extending radially outward from the hub than the calculations, which is again partly due to the assumption in the method that the midspan sections of the blade are not stalled. At higher flow coefficients the measured area of stator separation decreases so that the midspan of the blade unstalls and for this case the calculations give better results in the lower half of the blade. The trend at the hub, however, is correctly modeled by the method and had it been applied at the preliminary design stage would have identified that this is likely to be a problem area in the design. Because of the large hub separation the outer portion of the stator is off-loaded as stall is approached, which gives rise to the relatively high axial velocities measured in this region. Because the magnitude of the hub separation is underestimated by the method, the calculated velocities are lower than the measurements away from the hub. At stator inlet, where the flow conditions are more determined by the upstream rotor, the results show a generally satisfactory resemblance to the test data toward the casing. This indicates that the effect of the rotor tip clearance has been modeled accurately. There are signs that the method does not calculate the radial extent of the low axial velocities at rotor exit for the near-stall operating point. This may be due to both the rotor modeling and the inlet conditions it is accepting from the first stator. It is likely that the calculated rotor inlet conditions do not line up with the actual flow conditions and, based on the observations at the exit to the second stator, one can suppose that the radial extent of low axial velocity at the hub has been undercalculated. This error in the inlet conditions will influence the calculation through the rotor so that the rotor exit conditions will not be calculated correctly.

High-Speed Compressor. Some results are now presented for an early development rig test of the eight-stage intermediate pressure compressor for the Trent engine. For these viscous throughflow calculations, the two-dimensional blade performance was again based on the design deviations and losses and the off-design correlations of Miller and Wasdell (1987) and Wright and Miller (1991). The multistage CFD method of Denton (1992) has also been used to analyze this machine and these results are also presented.

Because of the rig design only stator leading edge measurements of total pressure and temperature can be used to compare directly with the calculations. The comparisons are made at inlet to the last stator, in order to maximize the opportunity for errors in the calculations to build up through the previous stages, and at 95 percent of design speed on the engine working line.

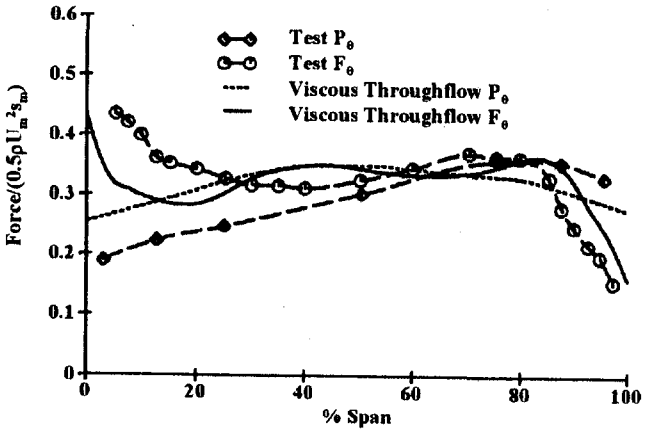

Fig. 12 Stator 2 tangential forces of low-speed two-stage compressor: $\phi = 0.45$

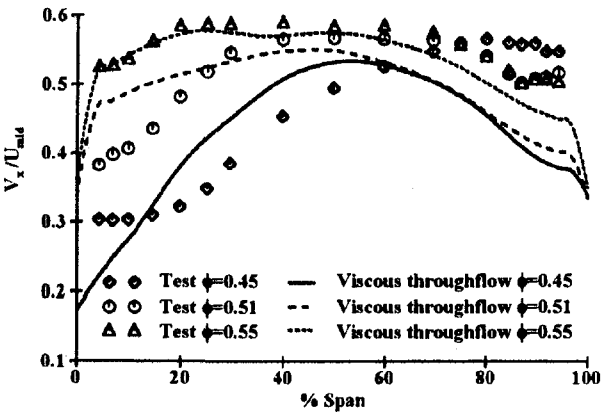

Fig. 14 Stator 2 exit V_x/U_{mid} of low-speed two-stage compressor

The level of agreement between the calculation and the test data shown is typical of that obtained at the other stator leading edge stations in the compressor. The radial distributions of the total pressure and temperature are presented in Fig. 15. The agreement between both calculation methods and the test data is quite good and in fact the viscous throughflow method seems to give better agreement with the test temperatures in the casing region. This may be due to the higher mixing levels in the throughflow method, which are not included in the turbulence modeling in the CFD calculation. The throughflow method also calculates a slightly thicker casing boundary layer, more in line with the test data. In general it can be said that the viscous throughflow calculation gives results of comparable accuracy to the fully three-dimensional viscous multistage CFD.

Discussion

The results presented above have shown that the blade force modeling employed in the viscous throughflow calculation method can give realistic radial flow distributions of flow properties across the whole span at a range of operating conditions for axial flow compressors. The throughflow results were less good when compared to measurement of the Joslyn and Dring case that was dominated by a large stator hub separation, but even there it demonstrated the correct trends. The method successfully captures the effect of tip clearance on the flow angle and can detect the effects of changes in the tip clearance on loss. Results at the fixed ends of blades are not quite as good, but again the over and underturning of the flow in these regions can be captured by the model. In general the method is sufficiently accurate to be used during the preliminary design phase of multistage compressors to identify areas of weakness in proposed designs, for example the trend toward hub stall just mentioned. The accuracy of the results is comparable to that obtained from a fully three-dimensional viscous multistage CFD calculation where comparisons were made. The computational time for the viscous throughflow for the case of the high-speed compressor was about 1 percent of that for the CFD. Once the final stages of the design process are reached the fully three-dimensional CFD methods now available are more appropriate to allow the effect of end-bends and nonradial stacking of the blades to be included.

The fact that the model gives reasonable results indicates that the physical understanding of the blade behavior and the flow physics that underlie the method are realistic and sensible. The effects of endwall shear and spanwise mixing on the flow mean that deducing the tangential blade forces from the momentum changes across the blade row can give misleading results. This explains the difficulty in using the tangential force deficit deduced from these data to predict the endwall flow behavior. The complicated behavior is caused by the flow itself and not by the blade pressure field imposed on the flow, which would seem to behave in a far more controlled way and is therefore more predictable. It would seem that blades with a predominantly radial stacking axis cannot have large radial variations in their surface static pressure and that the maximum suction surface diffusion that can be sustained at a spanwise position is dependent on the inlet dynamic head to the blade. It is recognized that some of the real flow physics cannot be modeled in the throughflow environment and that these effects have been included in the method via some of the empirically derived inputs.

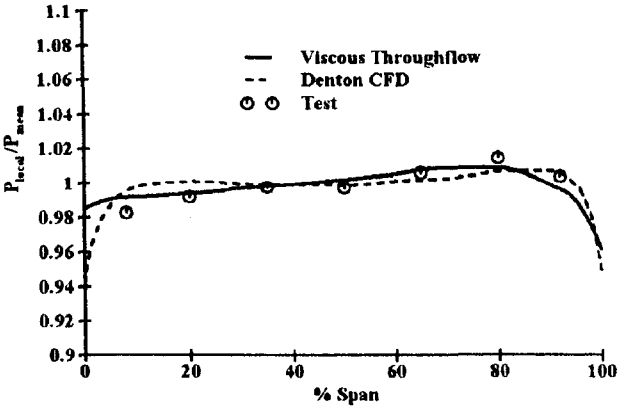

(a) Inlet total pressure

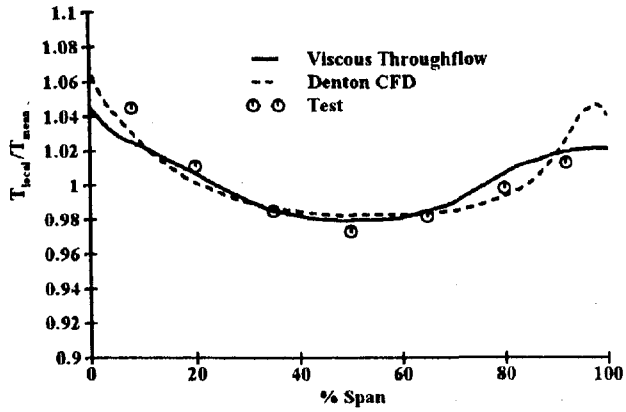

(b) Inlet total temperature

Fig. 15 High-speed compressor stator 8 inlet pressure and temperature profiles

Conclusions

An axisymmetric viscous throughflow method that includes the effects of spanwise mixing and endwall shear has been modified to represent the blades using a tangential blade force hypothesis. This hypothesis is based on experimental observations of the radial distribution of the tangential static pressure force imposed by the blades. The method gives realistic calculations of the spanwise distributions of flow properties for multistage axial flow compressors including the effects of tip clearance and the over and underturning of the flow at fixed blade ends. The results are of comparable accuracy to those obtained from three-dimensional viscous multistage CFD calculations, at a fraction of the computing effort, which means that the method is suitable for use in the preliminary design phase of compressors.

Acknowledgments

The author would like to thank Rolls-Royce Plc for permission to publish this work and Mr. J. Place for providing the CFD results for the four-stage low-speed compressor.

References

Adkins, G. G., Jr, and Smith, L. H., Jr, 1982, "Spanwise Mixing in Axial Flow Turbomachines," ASME *Journal of Engineering for Power,* Vol. 104, p. 97.

Denton, J. D., 1992, "The Calculation of Three Dimensional Viscous Flow Through Multistage Turbomachines," ASME JOURNAL OF TURBOMACHINERY, Vol. 114.

Dring, R. P., and Oates, G. C., 1990, "Through Flow Theory for Nonaxisymmetric Turbomachinery Flow: Part I—Formulation, Part II—Assessment," ASME JOURNAL OF TURBOMACHINERY, Vol. 112, p. 320.

Dring, R. P., 1993, "Radial Transport and Momentum Exchange in an Axial Compressor," ASME JOURNAL OF TURBOMACHINERY, Vol. 115, p. 477.

Dunham, J., 1995, "A New Endwall Model for Axial Compressor Throughflow Calculations," ASME JOURNAL OF TURBOMACHINERY, Vol. 117, p. 533.

Dunham, J., 1996, "Compressor Off-Design Performance Prediction Using an Endwall Model," ASME Paper No. 96-GT-62.

Gallimore, S. J., and Cumpsty, N. A., 1986, "Spanwise Mixing in Multi-Stage Axial Flow Compressors: Part I—Experimental Investigations," ASME JOURNAL OF TURBOMACHINERY, Vol. 108, p. 2.

Gallimore, S. J., 1986, "Spanwise Mixing in Multi-Stage Axial Flow Compressors: Part II—Throughflow Calculations Including Mixing," ASME JOURNAL OF TURBOMACHINERY, Vol. 108, p. 10.

Hirsch, C., and de Ruyck, J., 1981, "Throughflow Calculations in Axial Turbomachines," AGARD AR 175, Chap. II.2.3.

Howard, M. A., and Gallimore, S. J., 1993, "Viscous Throughflow Modeling for Multi-Stage Compressor Design," ASME JOURNAL OF TURBOMACHINERY, Vol. 115, p. 296.

Howard, M. A., Ivey, P. C., Barton, J. P., and Young, K. F., 1994, "Endwall Effects at Two Tip Clearances in a Multi-Stage Axial Flow Compressor With Controlled Diffusion Blading," ASME JOURNAL OF TURBOMACHINERY, Vol. 116, p. 635.

Joslyn, H. D., and Dring, R. P., 1985, "Axial Compressor Stator Aerodynamics," ASME *Journal of Engineering for Gas Turbines and Power,* Vol. 107, p. 485.

Lakshminarayana, B., and Horlock, J. H., 1962, "Tip-Clearance Flow and Losses for an Isolated Compressor Blade," ARC R&M No 3316.

LeJambre, C. R., Zacharias, R. M., Biederman, B. P., Gleixner, A. J., and Yekta, C. J., 1998, "Development and Application of a Multistage Navier–Stokes Solver: Part II—Application to a High Pressure Compressor Design," ASME JOURNAL OF TURBOMACHINERY, Vol. 120, pp. 205–214.

Miller, D. C., and Wasdell, D. L., 1987, "Off-Design Prediction of Compressor Blade Losses," *I.Mech.E Conference Proc. CP* 1987-6, paper C279/87.

Rhie, C. M., Gleixner, A. J., Spear, D. A., Fischberg, C. J., and Zacharias, R. M., 1998, "Development and Application of a Multistage Navier–Stokes Solver: Part I—Multistage Modelling Using Bodyforces and Deterministic Stresses," ASME JOURNAL OF TURBOMACHINERY, Vol. 120, pp. 215–223.

Roberts, W. B., Serovy, G. K., and Sandercock, D. M., 1986, "Modelling the 3D Flow Effects on Deviation Angle for Axial Compressor Middle Stages," ASME *Journal of Engineering for Gas Turbines and Power,* Vol. 108, p. 131.

Roberts, W. B., Serovy, G. K., and Sandercock, D. M., 1988, "Design Point Variation of Three-Dimensional Loss and Deviation for Axial Compressor Middle Stages," ASME JOURNAL OF TURBOMACHINERY, Vol. 110, pp. 426–433.

Smith, L. H., Jr., 1970, "Casing Boundary Layers in Multi-Stage Axial Flow Compressors," Brown Boveri: *Flow Research in Blading,* L. S. Dzung, ed., Elsevier, Amsterdam.

Storer, J. A., and Cumpsty, N. A., 1991, "Tip Leakage Flow in Axial Compressors," ASME JOURNAL OF TURBOMACHINERY, Vol. 113, p. 252.

Storer, J. A., and Cumpsty, N. A., 1994, "An Approximate Analysis and Prediction Method for Tip Clearance Loss in Axial Compressors," ASME JOURNAL OF TURBOMACHINERY, Vol. 116, pp. 648–656.

Wisler, D. C., 1985, "Loss Reduction in Axial Flow Compressors Through Low Speed Model Testing," ASME *Journal of Engineering for Gas Turbines and Power,* Vol. 107, p. 354.

Wright, P. I., and Miller, D. C., 1991, "An Improved Compressor Performance Prediction Model," *I.Mech.E Conference Proc.,* CP 1991-3, Paper No. C423/028.

Inner Workings of Aerodynamic Sweep

A. R. Wadia

P. N. Szucs

D. W. Crall

GE Aircraft Engines,
Cincinnati, OH 45215

The recent trend in using aerodynamic sweep to improve the performance of transonic blading has been one of the more significant technological evolutions for compression components in turbomachinery. This paper reports on the experimental and analytical assessment of the pay-off derived from both aft and forward sweep technology with respect to aerodynamic performance and stability. The single-stage experimental investigation includes two aft-swept rotors with varying degree and type of aerodynamic sweep and one swept forward rotor. On a back-to-back test basis, the results are compared with an unswept rotor with excellent performance and adequate stall margin. Although designed to satisfy identical design speed requirements as the unswept rotor, the experimental results reveal significant variations in efficiency and stall margin with the swept rotors. At design speed, all the swept rotors demonstrated a peak stage efficiency level that was equal to that of the unswept rotor. However, the forward-swept rotor achieved the highest rotor-alone peak efficiency. At the same time, the forward-swept rotor demonstrated a significant improvement in stall margin relative to the already satisfactory level achieved by the unswept rotor. Increasing the level of aft sweep adversely affected the stall margin. A three-dimensional viscous flow analysis was used to assist in the interpretation of the data. The reduced shock/boundary layer interaction, resulting from reduced axial flow diffusion and less accumulation of centrifuged blade surface boundary layer at the tip, was identified as the prime contributor to the enhanced performance with forward sweep. The impact of tip clearance on the performance and stability for one of the aft-swept rotors was also assessed.

Introduction

Swept wing theory has been used extensively to delay drag rise due to shock formation on aircraft wings over the last 50 years. However, workable swept blading applications in compressive turbomachinery design have only recently come of age, the reason for the delay being structural difficulties and the inadequacy of the aerodynamic design codes.

A series of attempts were made to exploit the concept of aerodynamic sweep for compressor blading between 1950 and 1970 by Beatty et al. (1954), Goodwin (1957), Smith and Yeh (1963), and Lewis and Hill (1971). All these efforts were strictly analytical or confined to very low-speed compressor testing with blades that contained linearly aft-swept leading edges. During the same time period (1966–1968), internally within GE Aircraft Engines, two swept blades for a TF39 outer panel application, one with aft sweep and one with forward sweep, were designed to explore the impact of aerodynamic sweep on transonic blading. The leading edges were swept in a linear manner. The aft-swept blade was tested and showed no noticeable improvement in efficiency relative to the unswept TF39 fan rotor as reported by Gostelow and Smith (1968). The forward-swept rotor was not tested because of low confidence in the structural integrity of the blades.

In the mid-seventies, NASA sponsorship resulted in the design and testing of the QF-12 swept fan stage as reported by Bliss et al. (1976), Lucas et al. (1978) and Hayden et al. (1978). The preferred direction of sweep selected for the NASA program was aft-sweep. The measured aerodynamic performance was disappointing as the fan rotor was unable to achieve the flow, pressure ratio and efficiency goals. However, some acoustic MPT (multiple pure tone) noise improvements were measured with the aft-swept fan but they were still below design expectations.

In 1986, as a continuation of an experimental program initiated in 1971 by the Compressor Aerodynamic Research Laboratory (CARL) at Wright Patterson Air Force Base (WPAFB), the Air Force designed and tested an aft-swept rotor (Rotor 6) to evaluate the effect of sweep on the performance of transonic low aspect ratio compressor blades. The results were reported by Puterbaugh, Copenhaver, Hah and Wennerstrom (1996). Some additional results have also been reported by Hah and Wennerstrom (1991).

While the aft-swept Rotor 6 showed significant improvement in peak efficiency relative to the baseline rotor (Law and Wadia, 1993), its peak efficiency at design speed occurred at stall and the stall line fell significantly below the stall limit of the baseline rotor. Differences in levels and trends of speed-flow and efficiency-flow characteristics noted with Rotor 6 relative to the results with the baseline rotor suggested that perhaps more than just effects due to aerodynamic sweep were being encountered here. In fact, an internal analysis of the swept design showed this rotor to have less trailing edge effective camber. This suspicion was confirmed by test results from Rotor 4 (Wadia and Copenhaver, 1996), an unswept rotor designed by GE Aircraft Engines under USAF contract to achieve the baseline rotor's mass flow and pressure ratio specification, but having smaller throat area. Rotor 4 attained a design speed peak efficiency level matching that of the aft-swept Rotor 6 without any penalty being incurred by the stall line.

About the same time that this data set was being disseminated to the gas turbine industry within the United States by the Air Force, two other independent sets of data on high-speed, low-aspect-ratio aft-swept rotors were also becoming available to the compressor design community.

The first design and test data set was published by Neubert et al. (1990) and Rabe et al. (1991) on the Navy funded NAFCOT program specifically aimed at quantifying the effects of aft-swept rotors on high-pressure-ratio transonic fan stages. The

Contributed by the International Gas Turbine Institute and presented at the 42nd International Gas Turbine and Aeroengine Congress and Exhibition, Orlando, Florida, June 2–5, 1997. Manuscript received International Gas Turbine Institute February 1997. Paper No. 97-GT-401. Associate Technical Editor: H. A. Kidd.

fan was designed to be shock free by sweeping the leading edges aft beyond the Mach cone angle. The rotor was to achieve the same pressure ratio of 2.20 as an unswept baseline rotor having an inlet tip relative Mach number of 1.60. The test results of Rabe et al. (1991) were disappointing, indicating no improvement in spanwise mass-averaged efficiency with the aft-swept rotor yet demonstrating a significant reduction in the stall line relative to the unswept baseline rotor. The reduction in stall line implies that at a given mass flow, the stalling pressure ratio is lower.

The second set of data available only to the United States gas turbine establishments included the design and testing of two aft-swept blades; the first for GE Aircraft Engines Joint Technology Demonstrator Engine and the other for a high-tip-speed, high-pressure-ratio multistage compressor. Results from both these tests once again re-emphasized the notion that aft-sweep for rotors with high tip loadings has an adverse impact on stall margin.

Up to this point, application of aerodynamic sweep in transonic blading was done with the intent to achieve performance gains by reducing the bow and passage shock strengths. The aerodynamic sweep can be used effectively to reduce the losses through the weaker detached leading edge bow wave. However, from a one-dimensional perspective, it is the shock-boundary layer interaction phenomenon, the required static pressure rise, and the streamwise passage area variation and not the level of aerodynamic sweep that sets the passage shock strength in transonic blading. This pre-occupation with trying to reduce the passage shock strength tended to omit from consideration the aerodynamic sweep benefits derivable from radial flow migration and boundary layer centrifugation. Mohammed and Prithviraj (1977) and later Yamaguchi et al. (1991) experimentally demonstrated this type of benefit with forward sweep in a very low-speed environment.

Prompted by the results with the unswept Rotor 4, a shift of focus away from the passage shock strength reduction, with the consequent, persistent trend of losing stall capability with aerodynamic aft-sweep, the Air Force and GE Aircraft Engines mutually agreed to a cooperative research arrangement in 1988 to quantify the benefits of aerodynamic sweep through tests with three swept rotors, aerodynamically equivalent to Rotor 4. Most of this paper deals with the results and insights gained from these single-stage tests. To the best of our knowledge, the results with forward sweep, reported in this paper, are unique in the open literature on transonic blading.

Single-Stage Rotor Designs

The aforementioned unswept Rotor 4 configuration, having excellent aerodynamic performance and stability, was selected as the technology base to be improved on by employing aerodynamic sweep technology. The design and test results of Rotor 4 have been reported in great detail by Copenhaver et al. (1993) and by Wadia and Copenhaver (1996).

In addition to keeping the tip speed, inlet corrected flow, and pressure ratio requirements the same, the swept blading was designed to retain the passage area distribution qualities of Rotor 4 in terms of throat margin, start margin, and effective camber (Wadia and Copenhaver, 1996) to ensure that the perceived performance changes with the new blading is a consequence of aerodynamic sweep only. As part of imparting aerodynamic sweep into the blading and due to the mechanical constraints in executing the various sweep configurations, the chords, hence solidity (with constant blade count), the airfoil section edge, and maximum thicknesses together with the axial location of maximum thickness could not be held fixed. These differences were viewed as essential and their performance impact, favorable or adverse, was considered to be the direct consequence of the particular "sweep package."

Table 1 Rotor 4 key design parameters

Parameter	
Specific Flow	43.61 lbm/sec-ft^2
Corrected Tip Speed	1500 ft/sec
Stage Pressure Ratio	1.92
Inlet Corrected Flow	61.81 lb/sec
Measured Stage Efficiency	0.8764
Inlet Radius Ratio	0.312
Tip Diameter	17 in
Number of Rotors/Stators	20/37
Mean Aspect Ratio (Rotor/Stator)	1.32/1.26
Average Solidity (Rotor/Stator)	2.3/1.68

An aerodynamic synthesis of Rotor 4 test data served as the basis for the vector diagrams used to design the blading for the swept rotors. The detailed design procedure was identical to that used to design the unswept rotors and is presented in the paper by Wadia and Law (1993). In addition, a three-dimensional inviscid code coupled with a simple boundary layer analysis, available at the time of the design of the swept rotors in the late eighties, was used extensively in the design of the three swept rotors. The stator inlet conditions were held constant with each sweep configuration so that no major adverse or beneficial impact occurred to the overall performance of the stage. Minor adjustments to the rotor exit radial total pressure profile were made, when required, to accomplish this.

Table 1 summarizes the salient geometric and aerodynamic features of the baseline unswept Rotor 4.

Figure 1 compares the meridional views of the swept rotors relative to the unswept Rotor 4. The rotor inlet and exit hub and casing radii were retained such that on a one-dimensional basis the specific flow into the rotor and the following stator was constant among the configurations.

Rotor 8 was swept aft through a combination of barreling the chord in the pitch region and leaning the blade tangentially opposite to the direction of rotation. Tangentially leaning the blade in the direction opposite to that of rotation imparts aft sweep to the rotor. Rotor 9 was swept forward using both chord barreling and tangential lean in the direction of rotation. Sweeping the blades with chord barreling increases both axial length and weight. To alleviate these two issues, and to assess sweep technology available for imbedded stages, another aft-swept blade, Rotor 10, was designed within the same planform as Rotor 4 imparting aft-sweep through tangential lean alone. The spanwise distribution of the normalized leading edge aerody-

Nomenclature

D-Factor = diffusion factor
IMM = radial immersion (0 = tip, 1 = hub)
LE = leading edge
PR = pressure ratio on an operating line
PRS = pressure ratio at stall
PS = pressure surface
SM = stall margin
SS = suction surface
TE = trailing edge
TLE = leading edge thickness
TMAX = maximum thickness
W = inlet corrected flow on an operating line
WS = inlet corrected flow at stall
Δ = change in clearance or efficiency relative to Rotor 4

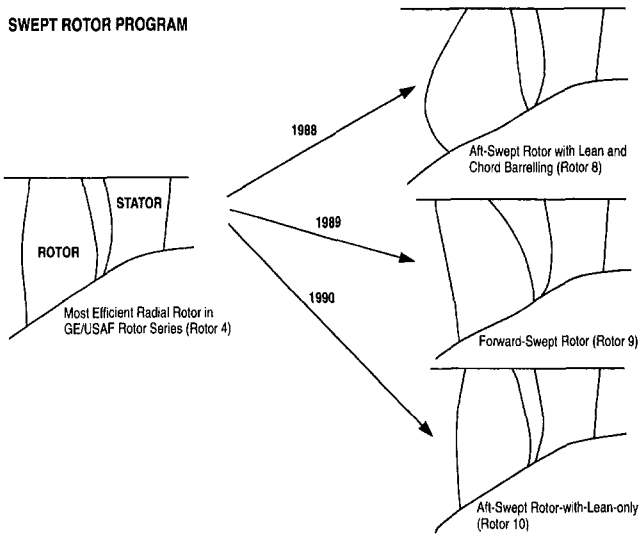

Fig. 1 Comparison of rotor planforms for the unswept Rotor 4, the aft-swept Rotor 8, the forward-swept Rotor 9, and the aft-swept Rotor 10

namic sweep is shown in Fig. 2(*a*). The leading edge aerodynamic sweep shown in Fig. 2(*a*) was calculated using the method described by Smith and Yeh (1963) and further nondimensionalized with the local value of the sweep at the tip of Rotor 4. Area ruled flowpath contouring to offset some of the metal blockage present was applied at the hub for all the rotors.

Figures 2(*b–e*) compare the resulting solidity and normalized section thicknesses for the rotor blading. Rotor 10's geometric parameters were similar to that for Rotor 4 and hence are not shown in these figures. Mechanically, as can be deduced from the section thickness plots in Fig. 2, the swept blading presented differing design challenges. The swept forward Rotor 9 presented the most and the swept through lean only Rotor 10 the least. The two main issues with the swept forward configuration were that its lean increased the blade length, which required added root thickness to hold the flexural frequency, and its forward shifted tip sections required increased edge thicknesses to control the leading edge stresses. Conversely, sweeping aft with chord barrelling reduced the leading edge stresses. Although the trailing edge stresses increased, these were less of a concern from a FOD (Foreign Object Damage) point of view. For future product applications, development of the "Laser Shock Peening" process that reduces residual stresses in the leading edge or leading edge treatments such as protective coverings (Wadia et al., 1996) could greatly reduce this disadvantage for forward-swept blading.

Table 2 Mechanical design parameter summary

Parameter	Rotor 4	Rotor 8	Rotor 9	Rotor 10
Material	Ti6-4	Ti6-4	Ti17	Ti6-4
.2% Min Yield Strength (Ksi)	105	105	130	105
Weight (lbs/blade)	0.431	0.566	0.544	0.466
Tip Radial Growth (in)	0.012	0.020	0.015	0.013
Tip Chord (in)	4.05	4.05	4.05	4.05
Pitch Chord (in)	3.84	4.72	4.24	3.96
Hub Chord (in)	3.46	3.76	3.76	3.36

Table 2 presents the mechanical configuration comparison for the rotors. As a disadvantage, both the aft-swept Rotor 8 and the forward-swept Rotor 9 represented significant weight increases over the base unswept Rotor 4. While the aft sweep technology of Rotor 10 limited the achievable level of sweep, its weight and space impact was much less. A similar savings in weight and space would be available with a forward-swept version of Rotor 10. Although hollow blade technology is available to trade weight for expense, preliminary studies have shown the weight benefits from hollow construction are about the same for the radial and swept configurations, so the weight penalty for sweep would remain. Table 2 also shows that in addition to thickness increases, the forward-swept Rotor 9 re-

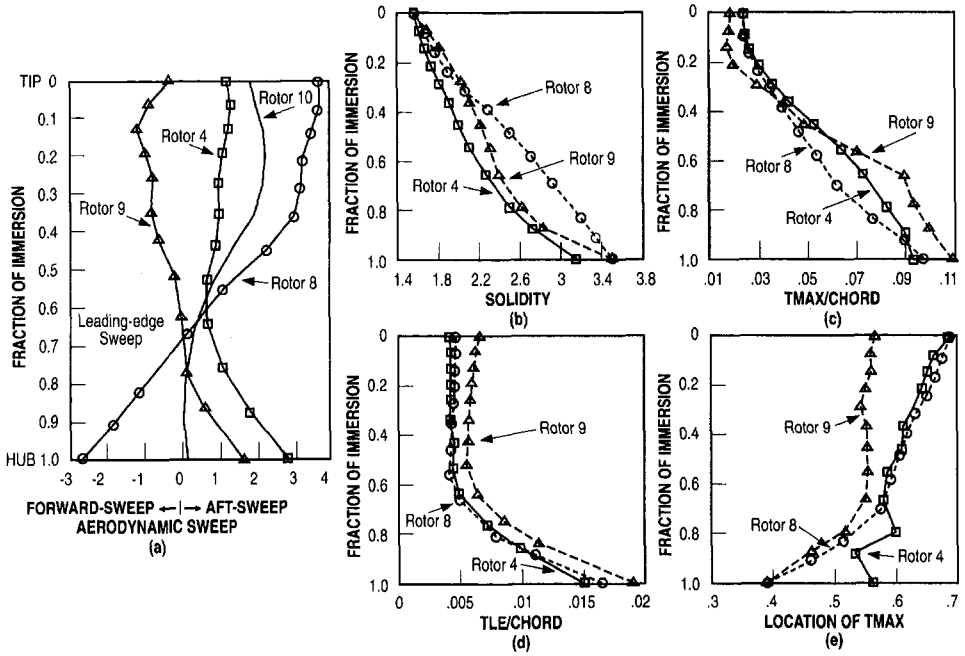

Fig. 2 Comparison of the spanwise distribution of: (*a*) nondimensionalized leading-edge aerodynamic sweep, (*b*) solidity, (*c*) ratio of maximum thickness to chord, (*d*) ratio of leading-edge thickness to chord, and (*e*) fraction of location of maximum thickness from the leading edge

quired a material change to Ti17 that has superior mean stress capability and higher cost. Although beyond the scope of this paper, the information in Table 2 could be used to evaluate the DOC (Direct Operating Cost) of aerodynamic sweep technology by rating its performance impact against its weight and cost adder.

Another unique mechanical design feature observed with the forward-swept Rotor 9 was related to its "hot-to-cold" untwist characteristic, especially of the tip sections. While the unswept and the aft-swept rotors showed the airfoil tip sections twisting in the closed direction (conventional) as the rotational speed was reduced, the forward-swept Rotor 9 showed the tip sections twisting open as the speed was reduced. Simultaneously, as a consequence of this twist difference between the forward-swept rotor and the other rotors, the tip sections deflected axially aft as the rotational speed was increased with Rotor 9, while the deflection was axially forward in the case of the other rotors. These untwist differences have been documented by Wadia et al. (1992).

Test Setup and Instrumentation

The tests were conducted by the Air Force in the 2000-hp Compressor Aerodynamics Research Laboratory (CARL) at Wright Field. The single-stage test vehicle has no inlet guide vanes and uses a cantilevered rotor to allow easy exchange of rotor designs with no impact on instrumentation. The rotors were of integral construction machined from single forgings.

Aerodynamics instrumentation consisted of 10 total temperature and 10 total pressure stator-exit radial rakes, each with 8 measurements at centers of equal area. The rakes were distributed around the circumference and spaced to divide a single vane exit passage into ten equal parts. Vane leading edge total pressure and total temperature instrumentation was also available and used to calculate the rotor-alone performance. Static pressure taps were located on the inner and outer endwalls at the inlet and exit plane of the stator. Dynamic pressure measurements and steady-state static pressures along the casing over the blade tip were also acquired at key operating points. Inlet total pressure, total temperature, rotor speed, and mass flow rate were also measured. All test data were acquired with some degree of depressed inlet pressure and later corrected to standard day inlet conditions as reported herein. Further details on the test setup, instrumentation, and experimental precision error are described by Law and Wadia (1993).

The average measured (leading and trailing edge) running clearance for the baseline unswept Rotor 4 and the swept rotors is shown in Table 3. The forward-swept rotor's clearance is based on a single measurement at midchord.

Aft-swept Rotor 10 data were obtained at two tip clearance levels and is presented later in the paper. Rotor 10 had the larger tip clearance and this rotor with the smaller tip clearance was designated as Rotor 10N. The correction in the stage efficiency at design speed due to the differences in tip clearance amongst the rotors was estimated using this data. The efficiency corrections (ΔEFFICIENCY, defined as the difference between the expected percent efficiency with Rotor 4's clearance and the percent measured test efficiency) are shown in Table 4.

Table 3 Average rotor clearance at design speed

Unswept Rotor 4	0.025 in
Aft-swept Rotor 8	0.030 in
Forward-swept Rotor 9	0.022 in
Aft-swept Rotor 10 (large clearance)	0.080 in
Aft-swept Rotor 10N (small clearance)	0.011 in

Table 4 Efficiency corrections for clearance variations at 100 percent speed

ROTOR	ΔCLEARANCE	ΔEFFICIENCY
Rotor 4	0.000	0.00
Rotor 8	+0.005	+0.44
Rotor 9	-0.003	-0.26
Rotor 10N	-0.014	-1.22

Comparison of Measured Stage Performances

The overall performance of the swept rotors is compared with the performance of the unswept Rotor 4 in the following paragraphs. The efficiency and pressure ratio were determined through mass weighted averages of the measured exit pressures and temperatures. The most throttled-up data point for each speed shown on the compressor maps represents the last steady state data point acquired very near to where the stage stalled.

Figure 3 shows the comparison of the measured stage performance of the aft-swept Rotor 8 and the unswept Rotor 4. The speed-flow trends along an operating line that passes through the design point are identical between both rotors except for the 1.8 percent increase in mass flow for Rotor 8 at design speed. This confirms the aerodynamic design equivalence between the two rotors. The peak efficiencies achieved by both rotors at design speed were approximately the same. The aft-swept Rotor 8, however, shows an 8 percent reduction in the clean inlet stall line relative to Rotor 4.

The comparison of the measured stage performance between the forward-swept Rotor 9 and the unswept Rotor 4 is illustrated in Fig. 4. Rotor 9 like Rotor 8 achieved about 1.5 percent higher mass flow rate at design speed. However, contrary to the trends at lower speeds observed with Rotor 8 (see Fig. 3), the forward-

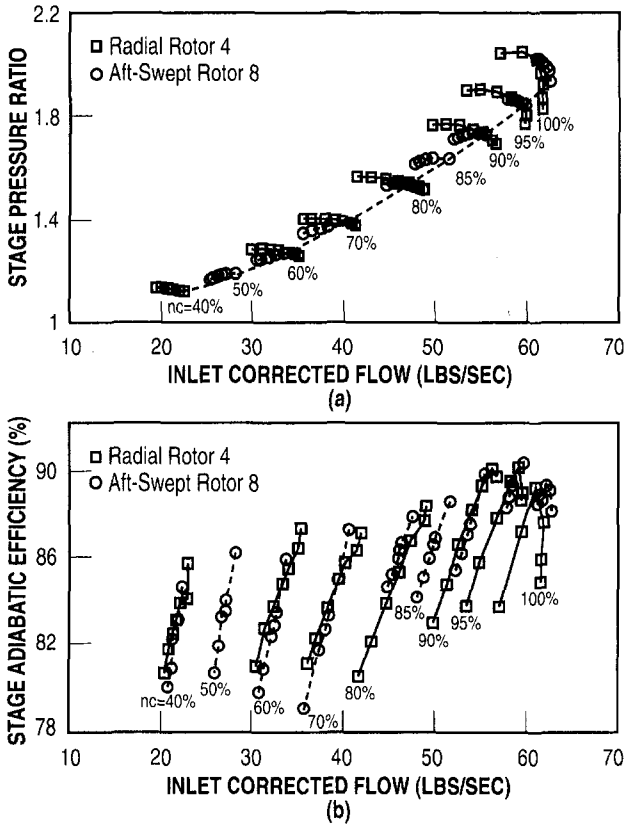

Fig. 3 Comparison of measured stage performance for unswept Rotor 4 and aft-swept Rotor 8

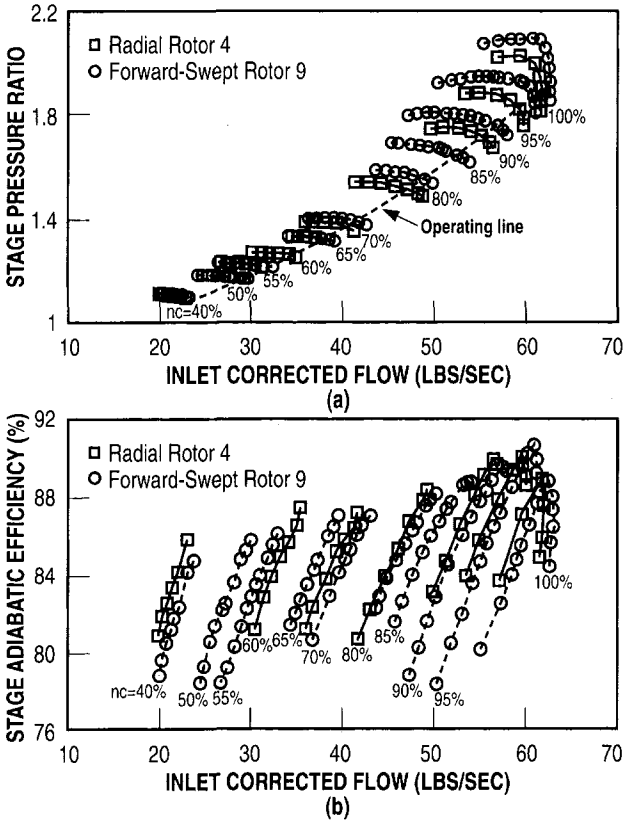

Fig. 4 Comparison of measured stage performance for unswept Rotor 4 and forward-swept Rotor 9

swept rotor flowed significantly more than Rotor 4 along the nominal operating line. This improvement in the flow pumping with forward sweep could be attributed to a number of things, including its untwist characteristic (i.e., the airfoil sections twist open as the speed is reduced), lower effective specific flow (i.e., the blading is swept forward into a larger annulus area region) and reduced shock/boundary layer interaction losses in the blade outer panel. While the peak stage efficiencies at design speed were approximately the same for both rotors, the peak efficiency attained by Rotor 9 at 95 percent speed was 0.9 points higher relative to the unswept Rotor 4. Rotor 9 testing showed a significantly improved total pressure ratio characteristic when throttled, resulting in an 8 percent improvement in its stall line at constant flow relative to Rotor 4 at high speeds. Together with this flow pumping improvement at high speeds came significantly higher flow rollback.

At part speed (50 to 60 percent inlet corrected speed), a stall-flutter aeromechanical limit boundary was reached before the aerodynamic stall for Rotor 9. However, at these speeds the boundary was very near to the stall limit of Rotor 4. Also, relative to Rotor 4, at 70 and 80 percent speed, where Rotor 9 had no aeromechanical instabilities, the stall line remained unchanged with forward sweep. This was most likely due to Rotor 9's unconventional untwist, which opens the airfoil sections at part speed. This structural untwist characteristic for Rotor 9 results in its shock being unstarted, forcing the tip leading edge incidences to higher levels at part speed.

Figure 5 shows the comparison of the measured stage performance for the aft-swept Rotor 10N (with the smaller clearance) and the unswept Rotor 4. Recall that this rotor has approximately half the level of leading edge sweep at the tip as Rotor 8. Similar to the other swept rotors, the design flow achieved by Rotor 10N was approximately 1.8 percent higher relative to Rotor 4, and the part-speed mass flow pumping characteristic remained the same. The peak efficiencies for Rotor 10N were 0.8 and 1.0 points higher relative to Rotor 4 at 95 and 100 percent inlet corrected speeds, respectively. Consistent with other aft-swept rotor trends, the measured stall line was approximately 6 percent lower with the aft-swept Rotor 10N compared to Rotor 4's stall line.

The experimental data presented in Figs. 3, 4, and 5, discussed above, suggests some possible minor improvement in stage efficiency with the aft-swept rotors but at a considerable loss in stall margin relative to the unswept Rotor 4. On the other hand, the forward-swept rotor, while basically retaining the stage efficiency, significantly increased the high-speed stall line. Figure 6 shows the variation of the stage adiabatic efficiency with stall margin at design speed to further clarify the design implications of the data for practical applications with the swept rotors. The stall margin shown in Fig. 6 was defined as:

$$SM = ((PRS/PR) \times (W/WS) - 1.0) \times 100 \text{ percent} \quad (1)$$

where each operating line point (for PR and W in Eq. (1)) is the corresponding steady-state data point obtained along the 100 percent speed line. The peak efficiencies for Rotors 4, 8, 10N, and 9 occur at 9, 4, 7, and 13.5 percent stall margin, respectively. Generally, some (5–10 percent) stall margin is consumed by throttle transients, inlet distortion, etc., in aircraft engine operation. The data in Fig. 6 shows that peak efficiencies with aft-swept rotors occur too close to the stall line to be of practical use.

At part speed, the single-stage test facility throttle opening (i.e., discharge valve fully open) limitations prevented attainment of the peak efficiency condition. As a result, no conclusive

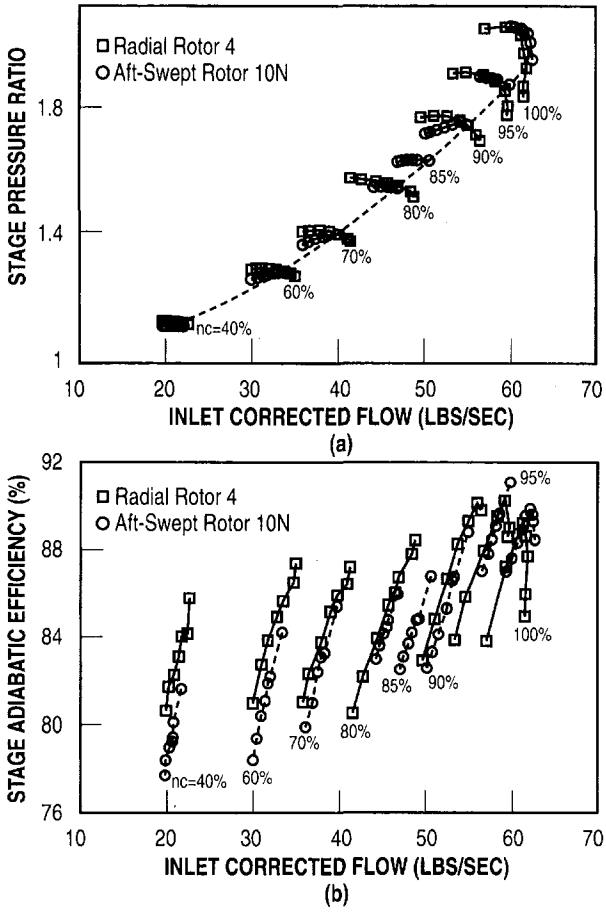

Fig. 5 Comparison of measured stage performance for unswept Rotor 4 and aft-swept Rotor 10N

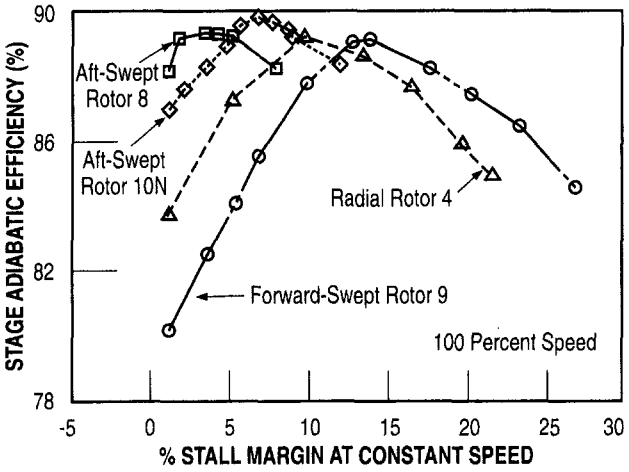

Fig. 6 Comparison of the stage adiabatic efficiency versus stall margin for the baseline and swept rotors at design speed

assessment of the preferred direction of sweep at low corrected speed conditions with regard to efficiency could be made.

Comparison of Measured Rotor Performances

Further assessment of the performance of the rotors was obtained by calculating the adiabatic efficiency for the rotor only using the measured stator leading edge values of total pressure and total temperature. The measured test data without any corrections for rotor tip clearance differences is presented in Figs. 7 and 8 for Rotors 8 and 9, respectively. The correction in rotor-alone efficiencies due to the differences in tip clearance amongst the rotors would be similar to that shown in Table 4 for the stage efficiencies.

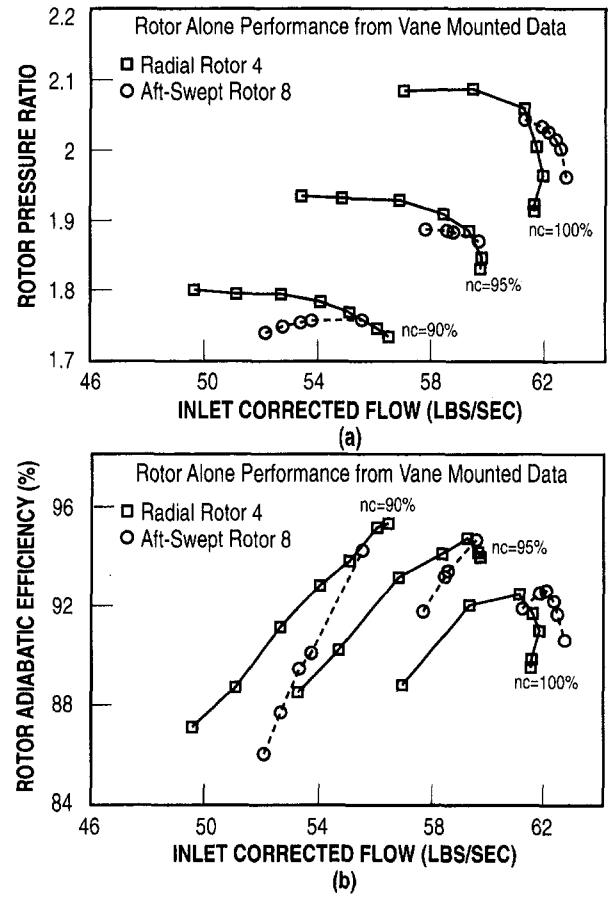

Fig. 7 Comparison of rotor (alone) performance: (*a*) pressure ratio, (*b*) adiabatic efficiency; for the unswept Rotor 4 and aft-swept Rotor 8

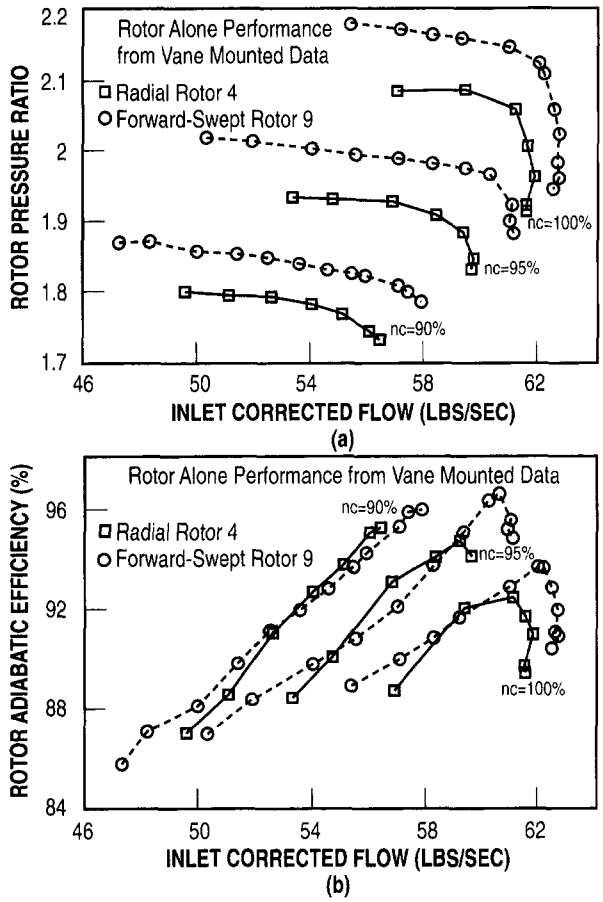

Fig. 8 Comparison of rotor (alone) performance: (*a*) pressure ratio, (*b*) adiabatic efficiency; for the unswept Rotor 4 and forward-swept Rotor 9

The peak rotor efficiencies for the aft-swept Rotor 8 and the unswept Rotor 4 are approximately equal as shown in Fig. 7(*b*). Similar trends in peak stage efficiency between the aft-swept and the unswept rotors were observed as shown in Fig. 3(*b*). However, the forward-swept Rotor 9 shows approximately 1 to 2 points improvement in peak rotor efficiency relative to Rotor 4 as shown in Fig. 8(*b*). The comparison of the peak stage efficiencies, shown in Fig. 4(*b*), shows this relative improvement to be less, suggesting that the stator losses could be higher with the forward-swept rotor. The larger gap between the rotor trailing edge and the stator leading edge, especially in the outer span, with the forward-swept rotor could be partly responsible for the higher stator losses.

The test results presented so far with these aerodynamically equivalent swept rotors suggest a significant impact of aerodynamic sweep on the stall line with major rotor efficiency benefit with forward sweep. The efficiency benefit, however, is certainly not the several points in magnitude expected if the passage shock strength reduction proportional to the local aerodynamic sweep alone was the source of the improvement.

Comparison of Stage Exit Radial Profiles

Figure 9 shows the comparison of the spanwise distribution of the stage exit total pressure between the swept Rotor 8 and Rotor 9 and the unswept Rotor 4. The effects of throttling are included in each figure. All data have been corrected to standard day conditions.

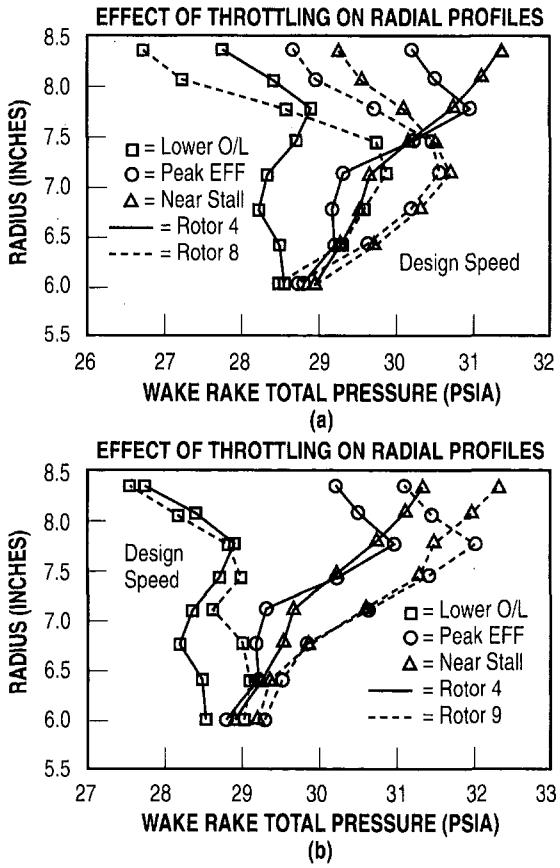

Fig. 9 Comparison of the effect of throttling on the radial profiles of total pressure at design speed for (*a*) the unswept Rotor 4 and the aft-swept Rotor 8 and (*b*) the unswept Rotor 4 and forward-swept Rotor 9

The total pressure radial profiles for Rotor 4 show the normal behavior with throttling in low radius ratio machines where the response at the tip is more than at the hub. In comparison, consistent with its lower stall line, the aft-swept Rotor 8's spanwise total pressure profile indicates a distinct weakness at the tip.

The measured efficiency profile comparison at the map peak efficiency condition at 95 percent speed is presented in Fig. 10. There is an indicated improvement in efficiency near the tip with the forward-swept Rotor 9 and loss in efficiency with the aft-swept Rotor 8 relative to Rotor 4 in the tip region where the sweep is the largest. Ironically, the largest gain in efficiency with the aft-swept rotor is in the inner region where the chord flaring is the most, and the leading edge sweep is at or near zero. Again, the indication from this is that phenomena other than the conventional compressibility benefits that are customarily associated with aerodynamic sweep are at play here.

Although not shown, the radial profiles of both the total pressure and efficiency for Rotor 10N, the aft-swept rotor through lean only, showed trends very similar to that for Rotor 4.

Data Analyses

The analytical results presented in this section are for the sole purpose of gaining an engineering understanding and interpretation of the test results regarding the inner workings of aerodynamic sweep and not for code validation purposes. While a much larger and more detailed body of work exists internally within GE Aircraft Engines, only selected supporting analytical results are presented in the paper. To streamline things further, the discussions in this section were limited to Rotors 4, 8 and 9 as representatives of the unswept, aft-swept, and forward-swept aerodynamic technologies. In most cases, the observations noted concerning Rotor 8 also applied to Rotor 10N. In addition, more information is available regarding Rotor 10N's results in the paper by Copenhaver et al. (1996).

To gain insights into the aerodynamic loading characteristics of the rotors, datamatch results employing a two-dimensional axisymmetric throughflow analysis with models for secondary flow and mixing at design speed near the stall condition are presented in Fig. 11. The comparisons of the spanwise distributions of the inlet and exit meridional velocities and the diffusion factor are illustrated in this figure. In interpreting these results, it must be remembered that the compressor map location of each of these near stall conditions are quite different in mass flow and attained pressure ratio. For example, the diffusion factor levels are significantly lower and the meridional velocity levels significantly higher relative to what is shown for Rotor 9 at the much lower throttle level (throttle level defined as pressure ratio/inlet corrected flow) that corresponds to the near stall condition for Rotor 8.

The spanwise distribution of the diffusion factor for Rotor 4 shown in Fig. 11(*c*) indicates that with respect to aerodynamic loading, the machine is tip limited, and is getting more so with aft sweep and less tip limited with forward sweep. As would be expected, the relative poorness in the measured stall lines is proportional to the magnitude of radial nonuniformity in the aerodynamic loading. The significantly more uniform loading distribution attained with the forward-swept blading (that is to say that the aerodynamic loading levels for the inboard sections are closer in level to the limiting tip value) allows this rotor to reach nearer its ultimate loading potential, while exactly the opposite is true with the aft-swept blading. The localized high loading level at the tip with Rotor 8 explains this rotor's tendency to reach a rotating stall type of stability limit (based on Kulite data), while the more balanced loading levels with Rotor 9 result in a surge type of stability limit at high speeds. The meridional velocities shown in Figs. 11(*a*) and 11(*b*) also suggest more nonuniformity with the aft-swept rotor and less with the forward-swept blade. The aft-swept rotor pulls the flow away from the tip, while forward sweep tends to move the flow out toward the tip as originally observed in the low-speed experiments of Mohammed and Prithviraj (1977). In addition to the increased meridional velocity nonuniformity with aft sweep, the meridional velocity diffusion from inlet to exit increases as well, contributing greatly to the earlier noted radial unbalance in the rotor diffusion factor.

Another adverse consequence of the large meridional velocity nonuniformity with the aft-swept rotor is the requirement on the resulting blade twist distribution. The rapid fall-off in merid-

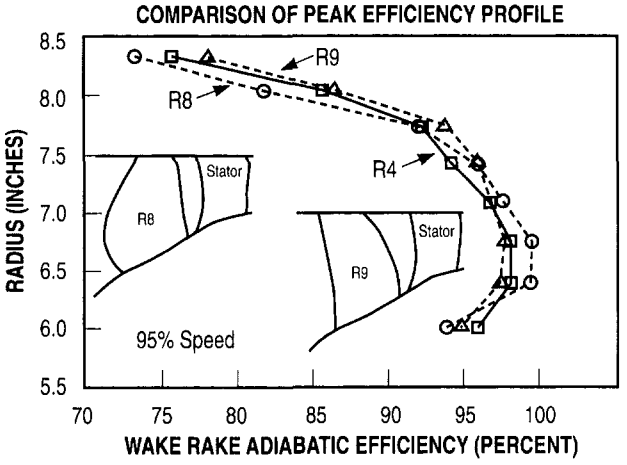

Fig. 10 Comparison of the spanwise variation of adiabatic efficiency at 95 percent speed for Rotor 4, Rotor 8, and Rotor 9

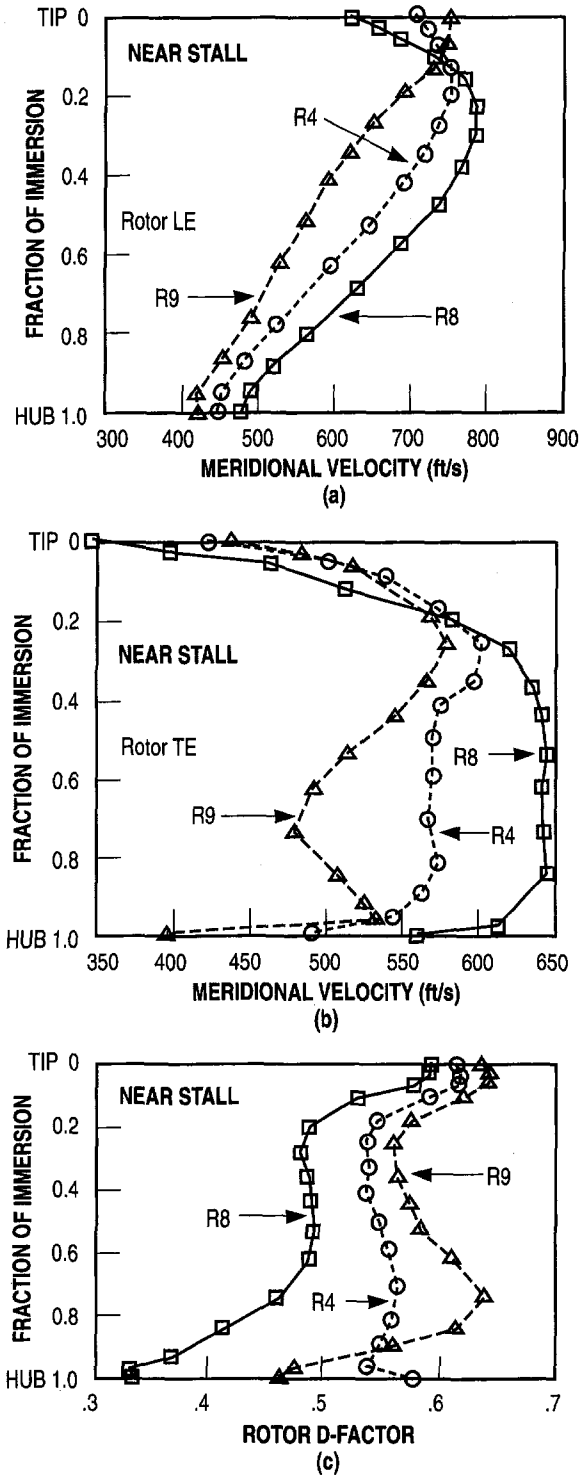

Fig. 11 Comparison of the spanwise distribution of: (*a*) rotor leading-edge meridional velocity; (*b*) rotor trailing-edge meridional velocity; (*c*) rotor diffusion factor for Rotors 4, 8, and 9 at design speed near stall

ional velocity toward the tip demands that a rapid twist closure toward the tip be implemented in the blading. As a result, the aft-swept rotor has very large acute dihedral angle (as defined in the paper by Smith and Yeh, 1963) at the tip along the suction side in the front half of the blading, while in contrast the forward-swept rotor with much less twist operates with near zero suction side dihedral angles at the tip. Acute dihedral angles are known to be adverse for endwall boundary layer flows, and this aspect is probably one of the major contributors to the poor aerodynamic stability and tip performance with aft-swept blading such as Rotor 8.

The throughflow analysis results at design speed, near stall were reported in the paragraphs above. After a similar throughflow analysis, the measured peak efficiency condition at design speed for the respective rotors was selected for further three-dimensional analysis to probe the internal flow quality differences and provide added insights into the inner workings of aerodynamic sweep. It is worth noting that as indicated in Figs. 3 and 4, the corrected mass flow levels are identical for Rotors 8 and 9 at this condition. Also, in the case of Rotor 8 the peak efficiency condition is very near to its stall limit condition.

The details of the three-dimensional viscous code used, and which has found wide usage within General Electric Company for compressor and turbine design, has been reported by Jennions and Turner (1993). The inlet boundary conditions for the analysis consisted of uniform inlet total pressure and temperature and tangential flow velocity (zero in this case). The exit boundary condition consisted of prescribing a radial distribution of the circumferentially averaged static pressure determined by the throughflow analysis of the data at the stator inlet.

The three-dimensional analysis computed flows were 0.5 to 1.0 percent higher than those measured in the rig test for all the rotors analyzed. The agreement between the measured and calculated radial profiles of total pressure and temperature was good. The calculated axial distribution of the circumferentially averaged static pressure and the blade-to-blade contours of static pressure along the tip endwall were in good agreement with the static pressure and kulite data for all the rotors.

The resulting isobar contours on the suction surface for the three rotors are shown in Fig. 12. The dense gradient in the isobars defines the shock intersections on the suction side, indicating a shock front that is nearly radial with the forward-swept Rotor 9 and slanted aft for Rotors 4 and 8. Although Rotor 4 is referred to as being unswept, its shock front indicates a small degree of inherent aft sweep resulting from its blade twist distribution. The most interesting isobar pattern results are with the highly swept Rotor 8. Contrary to the earlier reasoning regarding the influence of sweep on the passage shock strength from a one-dimensional viewpoint, Figure 12(*b*) illustrates a shock front for Rotor 8 that has been considerably diffused/eliminated in the blade's inner region, but then coalesces into a near normal strong shock front near the tip in agreement with the one-dimensional model described in the Introduction. From a three-dimensional viewpoint, the highly skewed and considerably diffused shock front with Rotor 8 is attainable because of radial equilibrium considerations and the selection of proper blade chordwise camber distribution, aided in the case of Rotor 8 by the longer (barreled) chords in the blade inner region. The assistance from radial equilibrium comes as a result of the skewed shock's downstream static pressure conditions in the blade's inner region being governed by the shock upstream region static pressures at the tip. These results support the radial trends in stage efficiency shown in Fig. 10 that credited Rotor 8 with achieving the highest performance levels in the pitch region and below, and, consistent with its strong near normal shock front at the tip, had shown its tip performance level as the worst.

Added confirmation regarding Rotor 8's diffused shock front on the suction surface is provided in Fig. 13. The surface isentropic Mach number distributions are compared among the three rotors at 30 percent immersion from the tip toward the hub. Compared to the suction side trends for Rotor 4 and 9, Rotor 8 indicates a shock free deceleration, albeit with a significantly high Mach number diffusion ratio (i.e., the ratio of the peak suction surface Mach number to the trailing edge Mach number) that the barreled chords of Rotor 8 help or are perhaps required to tolerate without separation.

To get an insight to the boundary layer health and migration, Fig. 14 compares the suction surface velocity vectors for the

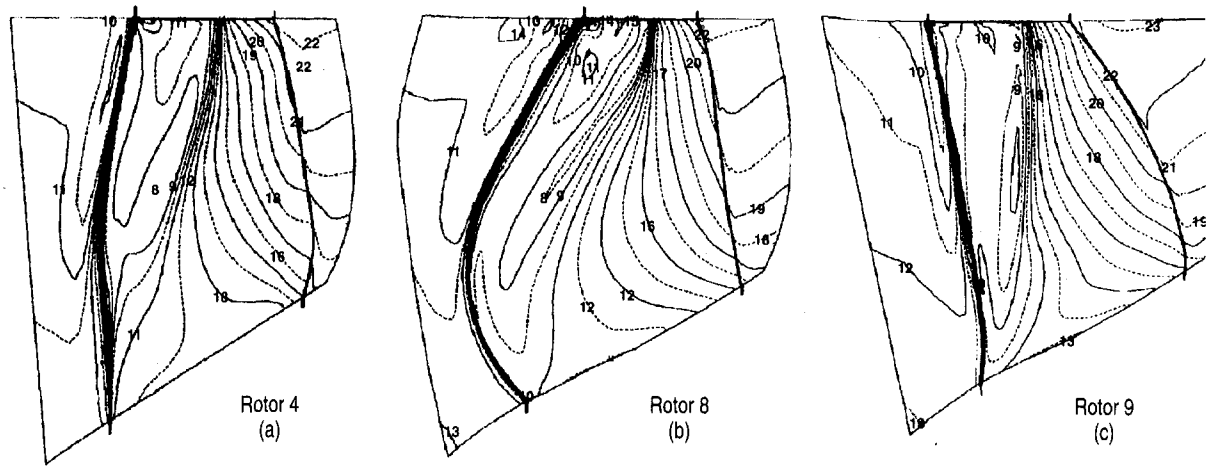

Fig. 12 Comparison of the calculated contours of static pressure on the suction surface at design speed near peak efficiency for (*a*) unswept Rotor 4, (*b*) aft-swept Rotor 8, and (*c*) forward-swept Rotor 9

aft-swept Rotor 8 and the forward-swept Rotor 9 one grid off the airfoil surface representing a $y+$ of 10. Ironically, as shown in Fig. 14(*a*), the aft sweep of the blade leading edge combined with the radially increasing static pressure on the blade surface turns the flow into the shock front. The boundary layer health ahead of the shock appears to be good, as otherwise a radially outward pointing velocity vector indicative of centrifuged wake fluid would result. The same is indicated for the forward-swept rotor in Fig. 14(*b*).

However, when comparing the exit portion of the blading's suction surface velocity vectors, the results are significantly different between the two modes of aerodynamic sweep. Even behind the diffused portion of the shock front in Rotor 8, Fig. 14(*a*) indicates a large deterioration/thickening of the boundary layer. The thickened boundary layer is shown to be centrifuged radially outward, adding in the outer region to the even more deteriorated conditions behind the strong portion of the suction side shock front, and then collecting at the outer casing. Due to this collection of low-energy fluid at the tip, the weakened boundary layer cannot support the added diffusion that would be required of it had the shock front remained swept. Hence the shock front has to assume all of the required diffusion and it becomes normal.

With the forward-swept Rotor 9, Fig. 14(*b*) shows a much healthier downstream boundary layer, even though its shock front, in the pitch region at least, is stronger relative to that of Rotor 8. It should be recalled, however, that in this region, according to Fig. 10, Rotor 8's performance is superior to Rotor 9's. There is no indication of radially outward boundary layer centrifugation at all in the pitch region, and the centrifuged boundary layer accumulation at the tip appears to be much less relative to that with the aft-swept blading. It is also evident that with the swept-forward blading arrangement of shifting the tip sections forward, there is less tendency to collect the centrifuged boundary layer at the casing.

In the pitch region, the comparison of the trailing edge velocity vectors within the boundary layer indicating more wake fluid centrifugation with Rotor 8 as shown in Fig. 14, suggests that from an aerodynamic stability viewpoint, for certain static pres-

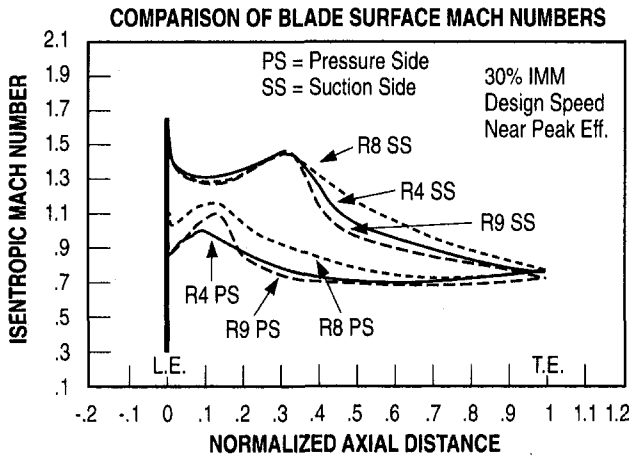

Fig. 13 Comparison of rotor surface isentropic Mach number distribution at 30 percent immersion at design speed at peak efficiency

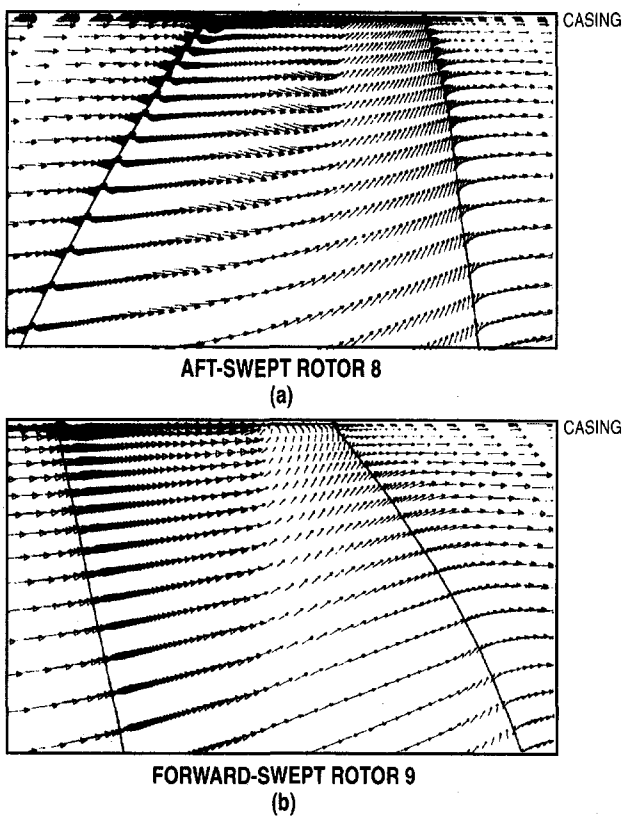

Fig. 14 Comparison of the velocity vectors one grid line away ($y\dagger$ = 10) from the blade suction surface from pitchline to the casing at design speed near peak efficiency for (*a*) Rotor 8 and (*b*) Rotor 9

sure rise levels, it is preferable to achieve the static pressure rise through a combination of shock plus downstream diffusion rather than through shock-free diffusion. Although the performance is indicated to be better with the latter, the added centrifuged wake fluid's contribution toward lower aerodynamic stability, as is the case with Rotor 8, might not make its use worthwhile.

The tip section blade-to-blade solutions and the surface isentropic Mach number distributions are compared in Fig. 15. As expected, Rotor 9 looks best with a clean started inlet shock system resulting in a good incidence level. The aft-swept Rotor 8 is the worst, with the collected wake fluid blockage forcing an unstarted passage shock system that results in a high leading edge incidence level. The relative tip region performances indicated in Fig. 10 are not hard to justify from Fig. 15's results. Also, in addition to the collection of wake fluid at the casing with the aft-swept Rotor 8, the large acute dihedral angles along the suction side at the tip leading edge region are probably a major contributor to this rotor's endwall flow weakness, causing its performance and aerodynamic woes at the tip.

Effect of Tip Clearance on Performance

The effect of tip clearance on the performance of transonic low-aspect-ratio rotors was investigated using the aft-swept Rotor 10 at two clearance levels shown in Table 3. Rotor 10 has the larger clearance with average clearance to blade height of 1.6 percent and average clearance to tip chord of 2 percent. Rotor 10N had the smaller clearance with an average clearance to blade height of 0.22 percent and average clearance to tip chord of 0.28 percent.

Figure 16 shows the comparison of the measured stage performance for the rotors at the two clearance levels. The average loss in design flow and stall margin with Rotor 10 was about

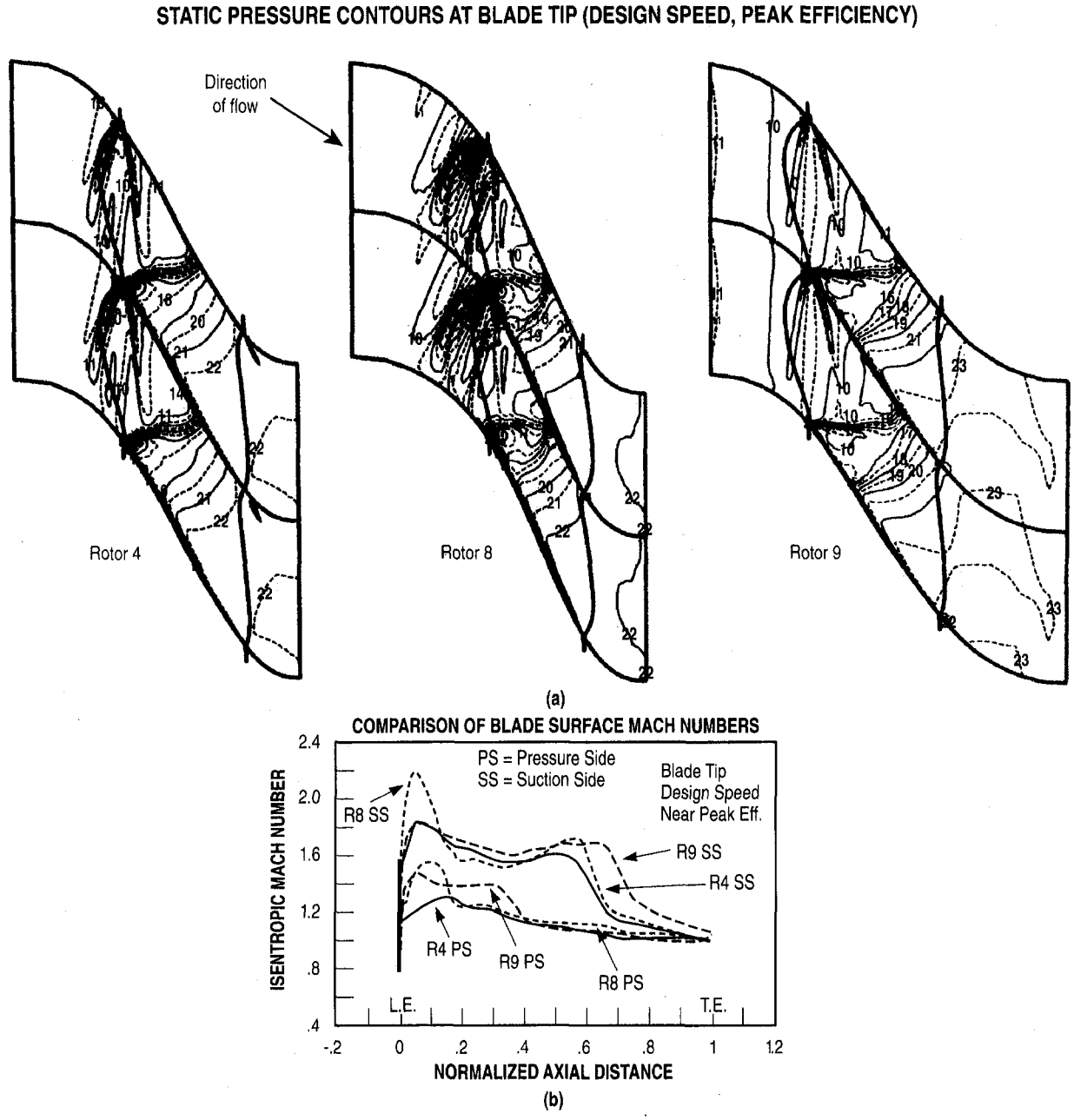

Fig. 15 Comparison of the calculated (a) blade-to-blade contours of static pressure and (b) blade surface isentropic Mach number distribution at the blade tip at design speed near peak efficiency

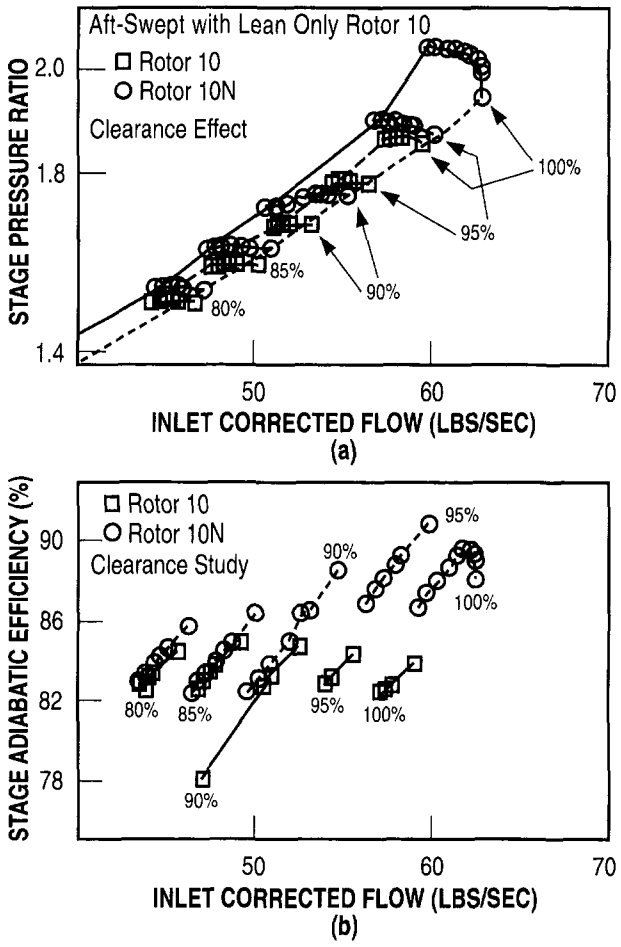

Fig. 16 Comparison of measured stage performance for aft-swept Rotor 10 with small and large tip clearance

5.6 and 2.8 percent, respectively relative to Rotor 10N. The loss in design speed peak efficiency was about 6 points with the larger clearance rotor. The flow and efficiency derivatives with Rotor 10 for a given change in clearance over blade height is much larger than is usual with the more generally available conventional subsonic blading. This large reduction in efficiency is mainly attributed to the endwall shock/boundary interaction as shown by Copenhaver et al. (1996). But this strong, detached shock at the very tip of this blade may be an inescapable consequence of the aft sweep, and suggests that tip-weak, aft-swept blades may be inherently more sensitive to clearance variations.

Figure 17 shows the comparison of the spanwise distribution of the measured total pressure and stage efficiency for the two clearance levels at design speed and peak efficiency. The effect of the larger clearance is felt across the entire span and results in a significantly lower value of the total pressure at the tip. The reduction in efficiency is observed up to 65 percent immersion from the tip. While the "tip weak" exit profile of total pressure from the rotor also produced a slightly higher loss in the downstream stator, the increase in the rotor loss was the predominant driver in reducing the stage efficiency with the larger tip clearance.

Concluding Remarks

Both detailed experimental and analytical results of a study on the influence of sweep on transonic fan or compressor performance have been presented. The results for single-stage applications are reported.

On an aerodynamic equivalent basis, the magnitude of stage performance improvement directly attributable to aerodynamic sweep was indicated to be upward of one point in efficiency for the relative Mach number range of 1.5 to 1.6 investigated.

For the single-stage fans examined, the comparison of the measured performance shows that forward sweep can result in improvements in both efficiency and stall margin, a unique combination. The better performance of the forward-swept rotor, as explained with the support of three-dimensional viscous analysis, is attributed to the reduced shock/boundary layer interaction resulting from reduced axial flow diffusion, lower acute suction side dihedral angle in the leading edge, and less accumulation of the blade surface boundary layer at the blade tip.

The penalty in the stall capability with aft-swept rotors, as determined in the single-stage rig tests, appears to be a direct consequence of a locally high diffusion loading requirement at the tip being imposed on a weak endwall flow. The locally high loading requirement comes as a result of the aft sweep induced flow shift away from the tip, while the weak tip endwall flow results from the accumulation of the centrifuged suction side wake fluid and corner flows generated by the large acute suction side dihedral angles. While aft-swept blades achieve lower shock strength and better performance in the inboard sections, this comes at the expense of thickened trailing edge region boundary layers, which are centrifuged and are likely to contribute to the aft-swept blades poor stall capability. In the case with forward sweep, however, the radial distribution in aerodynamic loading is much more uniform, and the endwall flow is much healthier due to less collection of wake fluid and the near-zero

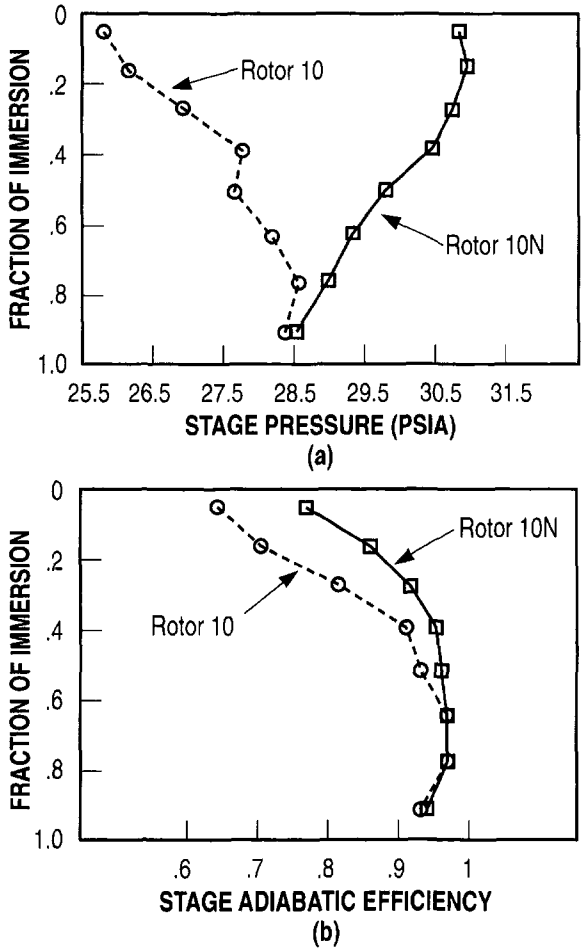

Fig. 17 Comparison of spanwise variation of (*a*) stage pressure ratio, (*b*) stage adiabatic efficiency for aft-swept Rotor 10 with small and large tip clearance at design speed at peak efficiency

tip suction side dihedral angles. All together, this results in the entire blade span performing nearer to the limiting loading capability at stall, and hence the superior stall line results at high speeds with forward sweep.

At part speed, the speed at which the blade reaches the shock "unstart" condition and below, no advantage in the aerodynamic stability limit is evident with either forward or aft-sweep. Also at part speed, the single-stage test facility limitations prevented conclusive assessment of the preferred direction of sweep with regard to efficiency.

After assessing the impact associated with each direction of sweep in a single-stage environment, the study was expanded to include the effects of forward sweep in a two-stage fan where inlet distortion tolerance was also assessed. An investigation has been completed on a back-to-back basis using an unswept and a forward-swept stage 1 blade in the two stage configuration and the data will be reported at a later date. Some highlights of the results of this study obtained with the forward-swept rotor with inlet distortion has been reported by Kandebo (1996) and Ashley (1996).

The aerodynamic implications with aft and forward-swept blading have been explored in great detail on a back-to-back basis. The overall experimental results and the complementary three-dimensional viscous analyses suggest some unique improvements to efficiency and stall margin with forward-swept blading for tip loading limited transonic stages. Further studies are now underway to determine reduced-weight configurations that can utilize the advantages of forward-swept blading presented in this paper.

Acknowledgments

The authors would like to acknowledge the following individuals at Wright Patterson AFB for their excellent support in obtaining the data: Dr. Herb Law, Dr. Steve Puterbaugh, Dr. William Copenhaver, and Mr. Bob DeRose. We also thank Dr. Art Wennerstrom, Mr. John Lueke, Mr. Marvin Stibich of the USAF, and Pamela Battle, David Chang, and Pat Niskode of GE for their support during the course of this investigation. We would also like to acknowledge Dr. Chunill Hah for performing all the pre-test 3D calculations at NASA and for providing us with an accurate assessment of the performance of the swept blades before the rig test. We are grateful to the management at GE and USAF for giving us permission to publish the single-stage results of our investigation with swept blading.

References

Ashley, S., 1996, "Forward-Swept Fan Moves Ahead," *Mechanical Engineering,* Jan., p. 142.

Beatty, L. A., Savage, M., and Emery, J. C., 1954, "Low Speed Cascade Tests of Two 45 Degree Swept Compressor Blades With Constant Spanwise Loading," NACA Research Memorandum, L53L07.

Bliss, D. B., Hayden, R. E., Murray, B. S., and Schwer, P. G., 1976, "Design Considerations for a Novel Low Source Noise Transonic Fan Stage," AIAA Paper No. 76-577.

Copenhaver, W. W., Hah, C., and Puterbaugh, S. L., 1993, "Three-Dimensional Flow Phenomena in a Transonic, High-Through-Flow, Axial-Flow Compressor Stage," ASME JOURNAL OF TURBOMACHINERY, Vol. 115, pp. 240–248.

Copenhaver, W. W., Mayhew, E. R., Hah, C., and Wadia, A. R., 1996, "The Effect of Tip Clearance on a Swept Transonic Compressor Rotor," ASME JOURNAL OF TURBOMACHINERY, Vol. 118, pp. 230–239.

Goodwin, W. R., 1957, "Effect of Sweep on Performance of Compressor Blade Sections as Indicated by Swept Blade Rotor, Unswept Blade Rotor and Cascade Tests," NACA TN 4062.

Gostelow, J. P., and Smith, L. H., 1968, "Aerodynamic Design and Performance of a Swept Back Rotor SW-1," GE Internal Report, 68-AEG-175.

Hah, C., and Wennerstrom, A. J., 1991, "Three-Dimensional Flowfields Inside a Transonic Compressor With Swept Blades," ASME JOURNAL OF TURBOMACHINERY, Vol. 113, pp. 241–251.

Hayden, R. E., Bliss, D. B., Murray, B. S., Chandiramani, K. L., Smullin, J. I., and Schwaar, P. G., 1978, "Analysis and Design of a High Speed Low Noise Aircraft Fan Incorporating Swept Leading Edge Rotor and Stator Blades," NASA CR-135092.

Jennions, I. K., and Turner, M. G., 1993, "Three-Dimensional Navier–Stokes Computations of Transonic Fan Flow Using an Explicit Flow Solver and an Implicit K-E Solver," ASME JOURNAL OF TURBOMACHINERY, Vol. 115, pp. 261–272.

Kandebo, S., 1996, "General Electric Tests Forward-Swept Fan Technology," *Aviation Week and Space Technology,* Sept. 23, p. 32.

Law, C. H., and Wadia, A. R., 1993, "Low Aspect Ratio Transonic Rotors, Part I: Baseline Design and Performance," ASME JOURNAL OF TURBOMACHINERY, Vol. 115, pp. 218–225.

Lewis, R. I., and Hill, J. M., 1971, "The Influence of Sweep and Dihedral in Turbomachinery Bladerows," *Journal of Mechanical Engineering Science,* Vol. 13, No. 4.

Lucas, R. G., Woodard, R. P., and MacKinnon, M. J., 1978, "Acoustic Evaluation of a Novel Swept-Rotor Fan," AIAA Paper No. 78-1121.

Mohammed, K. P., and Prithviraj, D., 1977, "Investigation on Axial Flow Fan Impeller With Forward-Swept Blades," ASME Paper No. 77-FE-1.

Neubert, R. J., Hobbs, D. E., and Weingold, H. D., 1990, "Application of Sweep to Improve the Efficiency of a Transonic Fan: Part 1—Design," AIAA Paper No. 90-195.

Puterbaugh, S. L., Copenhaver, W. W., Hah, C., and Wennerstrom, A. J., 1996, "Investigation of an Aft-Swept Transonic Compressor Rotor," ASME Paper No. 96-GT-354; published as "A Three-Dimensional Shock Loss Model Applied to an Aft-Swept, Transonic Compressor Rotor," ASME JOURNAL OF TURBOMACHINERY, Vol. 119, 1997, pp. 452–459.

Rabe, D., Hoying, D., and Koff, S., 1991, "Application of Sweep to Improve Efficiency of a Transonic Fan: Part II—Performance and Laser Test Results," AIAA Paper No. 91-2540.

Smith, L. H., and Yeh, H., 1963, "Sweep and Dihedral Effect in Axial Flow Turbomachinery," ASME *Journal of Basic Engineering,* Vol. 85.

Wadia, A. R., Szucs, P. N., Niskode, P. N., Battle, P. M., 1992, "Forward-Swept Rotor Blade," US Patent No. 5,167,489.

Wadia, A. R., and Law, C. H., 1993, "Low Aspect Ratio Transonic Rotors: Part 2: Influence of Location of Maximum Thickness on Transonic Compressor Performance," ASME JOURNAL OF TURBOMACHINERY, Vol. 115, pp. 226–239.

Wadia, A. R., and Copenhaver, W. W., 1996, "An Investigation of the Effect of Cascade Area Ratios on Transonic Compressor Performance," ASME JOURNAL OF TURBOMACHINERY, Vol. 118, pp. 760–770.

Wadia, A. R., Crall, D. W., Prentice, I., and Koch, C. C., 1996, "Forward-swept Turbofan Blade With Non-structural Leading Edge Extension," US Patent Filed, GE Aircraft Engines Patent Docket 13DV-12419.

Yamaguchi, N., Tominaga, T., Hattori, S., and Mitsuhashi, T., 1991, "Secondary-Loss Reduction by Forward-Skewing of Axial Compressor Rotor Blading," presented at 1991 Yokohama International Gas Turbine Congress.

Effects of Stream Surface Inclination on Tip Leakage Flow Fields in Compressor Rotors

M. Furukawa

K. Saiki

K. Nagayoshi

M. Kuroumaru

M. Inoue

Department of Energy and Mechanical Engineering, Kyushu University, Fukuoka 812-8581, Japan

Experimental and computational results of tip leakage flow fields in a diagonal flow rotor at the design flow rate are compared with those in an axial flow rotor. In the diagonal flow rotor, the casing and hub walls are inclined at 25 deg and 45 deg, respectively, to the axis of rotation, and the blade has airfoil sections with almost the same tip solidity as that of the axial flow rotor. It is found out that "breakdown" of the tip leakage vortex occurs at the aft part of the passage in the diagonal flow rotor. The "vortex breakdown" causes significant changes in the nature of the tip leakage vortex: disappearance of the vortex core, large expansion of the vortex, and appearance of low relative velocity region in the vortex. These changes result in a behavior of the tip leakage flow that is substantially different from that in the axial flow rotor: no rolling-up of the leakage vortex downstream of the rotor, disappearance of the casing pressure trough at the aft part of the rotor passage, large spread of the low-energy fluid due to the leakage flow, much larger growth of the casing wall boundary layer, and considerable increase in the absolute tangential velocity in the casing wall boundary layer. The vortex breakdown influences the overall performance, also: large reduction of efficiency with the tip clearance, and low level of noise.

Introduction

Tip leakage flow fields in axial flow compressors have been studied by many researchers since Rains' work (1954), because of their impact on compressor stability and performance (Smith, 1970). They have been especially highlighted over the last decade, and the complex flow mechanism is getting more and more clarified by numerous experimental and numerical works (Inoue et al., 1986; Hah, 1986; Murthy and Lakshminarayana, 1986; Dawes, 1987; Inoue and Kuroumaru, 1989; Chen et al., 1991; Storer and Cumpsty, 1991; Moyle et al., 1992; Adamczyk et al., 1993; Stauter, 1993; Lakshminarayana et al., 1995; Zierke et al., 1995; Foley and Ivey, 1996; Suder and Celestina, 1996; Kang and Hirsch, 1996). The distinctive feature of the flow structure is the rolling-up of the tip leakage vortex and its interaction with secondary flows.

On the other hand, one of the authors has once studied the possibility of a diagonal flow compressor rotor as a first stage of a multistage compressor, because its loading coefficient can be about one and a half times as high as that of an axial flow rotor. On the basis of the quasi-three-dimensional design method proposed by Inoue et al. (1980), a diagonal flow rotor with NACA 65 series profile was designed and tested (Inoue et al., 1984). The blade solidity at the tip was almost the same as that of the axial compressor rotor which the authors used to investigate the structure of the tip leakage flow (Inoue et al., 1986). The high loading coefficient required was obtained notwithstanding the small number of blades, and the noise level was considerably low, compared with the axial flow rotor. However, an effect of the tip clearance on the rotor performance was much larger in comparison with the axial rotor case: The reduction of efficiency with the tip clearance was about three times as large as that of the axial flow rotor. Recently, the authors reassembled the diagonal flow rotor in the low-speed rotating cascade equipment of Kyushu University, and surveyed the internal flow field to examine a cause of the large reduction of efficiency with the tip clearance (Furukawa et al., 1995a). The phase-locked flow fields measured just behind the rotor indicated that there was no vortex rolling-up even in the case of a large tip clearance.

Goto (1992a, b) studied internal flows in a mixed-flow pump impeller with various tip clearances by experiments and numerical simulations. His results showed that there was substantial difference in the secondary flow field between axial-flow and mixed-flow impellers.

In this study the tip leakage flow fields at the design flow rate are compared between the axial and the diagonal flow rotor, which have similar blade solidities at the tip section, to clarify the reason why the reducing rate of efficiency with the tip clearance is much larger and the noise level is much less for the diagonal flow rotor. The experimental data used in the comparison are tangentially averaged velocity distributions, phase-locked averaged velocity distributions just downstream of the rotors, and phase-locked averaged pressure distributions on the casing walls. Three-dimensional viscous flow simulations are carried out by a high-resolution upwind scheme based on a TVD formulation with a cell-centered finite volume method, to investigate the detailed behavior of the tip leakage flows.

Experimental Apparatus and Procedure

Diagonal Flow Rotor. The experimental investigation was performed using the diagonal flow rotor with high specific speed shown in Fig. 1. Design specifications of the rotor are summarized in Table 1 where the flow coefficient, ϕ, and the total pressure rise coefficient, ψ, are defined as

$$\phi = \frac{Q}{U_t \pi (D_t^2 - D_h^2)/4} \tag{1}$$

$$\psi = \frac{\Delta P}{\rho U_t^2/2} \tag{2}$$

where Q is the volume flow rate, ΔP is the total pressure rise,

Contributed by the International Gas Turbine Institute and presented at the 42nd International Gas Turbine and Aeroengine Congress and Exhibition, Orlando, Florida, June 2–5, 1997. Manuscript received International Gas Turbine Institute February 1997. Paper No. 97-GT-43. Associate Technical Editor: H. A. Kidd.

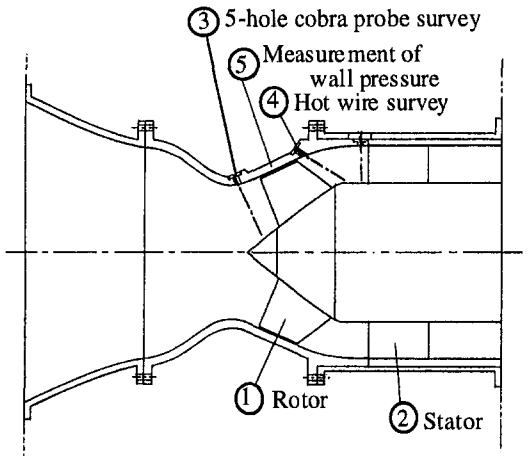

Fig. 1 Meridional view of diagonal flow rotor

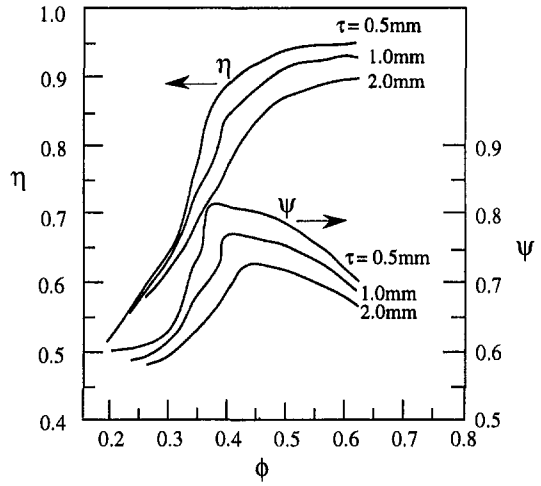

Fig. 2 Stage performance of diagonal flow rotor

U_t is the blade tip speed at the rotor exit, ρ is the density, D_t and D_h denote the tip and hub diameters at the rotor exit, respectively. In the rotor the shapes of the hub and casing walls were cones with inclinations of 45 deg and 25 deg, respectively, to the axis of rotation. The design vortex type of the rotor was a free vortex with an axial inlet condition. The equivalent diffusion ratio in Table 1 is based on an extension of that of Lieblein to include changes in radius and axial velocity through the blade row derived by Klapproth (1959).

Blades of the rotor were made up of NACA 65 series airfoil sections designed by the quasi-three-dimensional method of Inoue et al. (1984). In the design method, a meridional throughflow was first solved by a streamline curvature method to determine averaged stream surfaces, and then the stream surfaces were transformed conformally into two-dimensional planes on which blade elements were selected by means of a two-dimensional cascade data. Cascade geometries of the blade elements were corrected theoretically by taking account of effects due to the stream surface inclination and the stream surface thickness variation. Lastly the blade elements on the two-dimensional planes were retransformed into the physical space.

The blade tip clearance was varied by moving the rotor in the axial direction. Experiments were performed for three blade tip clearances of τ = 0.5, 1.0, and 2.0 mm, which corresponded to 0.3, 0.6, and 1.3 percent of tip chord, respectively. Figure 2 shows the stage performance of the diagonal flow rotor. In the case of the minimum clearance, the performance satisfied the design point, and the efficiency was 95 percent at the design flow rate.

Table 1 Design specifications of diagonal flow rotor

Flow coefficient	ϕ = 0.563
Total pressure rise coefficient	ψ = 0.75
Vortex design	Free vortex
Tip diameter	D_t = 400 mm (rotor exit)
Hub-tip ratio	ν = 0.75 (rotor exit)
Blade profile	NACA 65 series
Number of blades	6
Blade thickness	10%(root), 4%(tip)
Solidity at tip	1.054
Chord length at tip	157 mm
Equivalent diffusion ratio at tip	D_{eq} = 1.64
Hub inclination	45°
Casing inclination	25°

Flow fields upstream and downstream of the rotor and pressure distributions on the casing wall were measured, as shown in Fig. 1, at the design flow rate (ϕ = 0.563) for the three different tip clearances. The flow measurements were made at a rotor rotational speed of 1300 rpm. Upstream of the rotor the survey of a five-hole cobra probe was carried out. In all the experiments the meridional displacement thickness of the casing wall boundary layer was 0.3 percent of tip chord upstream of the rotor. On the other hand, downstream of the rotor phase-locked flow fields were obtained by a constant temperature hot-wire anemometer and a periodic multisampling and averaging technique with a computerized data acquisition system (Kuroumaru et al., 1982). The hot-wire sensor was a slanted single tungsten wire with a diameter of 5 μm, an effective length of 1 mm, and a slant angle of 45 deg. The hot-wire measurements were made at 23 spanwise positions. In each spanwise position, the hot-wire signals were sampled at 300 tangential points relative to the rotor. The 300 tangential points covered three successive blade passages. Phase-locked pressure distributions on the casing wall were obtained by also applying the periodic multisampling and averaging technique to pressure measurements using a high response pressure sensor. The pressure sensor was installed on the casing wall in a similar manner to that used in the previous study (Inoue and Kuroumaru, 1989). The casing wall pressure measurements were performed at 13 axial positions, and pressure samplings in each axial position were made at 200 tangential points corresponding to two successive blade passages.

Axial Flow Rotor. Experimental results for the diagonal flow rotor were compared with those for the axial flow rotor presented in the previous papers (Inoue et al., 1986; Inoue and Kuroumaru, 1989). The axial flow rotor had design specifications given in Table 2. The hub and casing walls were cylindrical, that is, had no inclination to the axis of rotation.

Experiments were performed for five different tip clearances of τ = 0.5, 1.0, 2.0, 3.0, and 5.0 mm (0.4, 0.8, 1.7, 2.6, and 4.3 percent of tip chord, respectively). Phase-locked velocity fields downstream of the rotor (Inoue et al., 1986) and phase-locked pressure fields on the casing wall (Inoue and Kuroumaru, 1989) were measured at the design flow condition with a rotor rotational speed of 1300 rpm in the same way as the diagonal flow rotor. The displacement thickness of the casing wall boundary layer at the inlet was 0.6 percent of tip chord in all the experiments.

Numerical Analysis

Numerical Scheme. We performed numerical flow simulations in order to investigate the tip leakage flow field inside the

Table 2 Design specification of axial flow rotor

Flow coefficient	$\phi = 0.5$
Total pressure rise coefficient	$\Psi = 0.4$
Vortex design	Free vortex
Tip diameter	D_t =449 mm
Hub-tip ratio	$\nu = 0.6$
Blade profile	NACA 65 series
Number of blades	12
Blade thickness	10%(root), 6%(tip)
Solidity at tip	1.00
Chord length at tip	117.5 mm
Equivalent diffusion ratio at tip	$D_{eq} = 1.43$

rotor passage, which could not be measured by our experimental apparatus. In the numerical simulations the compressible Navier–Stokes equations were solved by an unfactored implicit upwind relaxation scheme (Furukawa et al., 1995b). The numerical method used is outlined in the following.

The three-dimensional, Reynolds-averaged Navier–Stokes equations were discretized in space using a cell-centered finite volume formulation and in time using the Euler implicit method. To capture the tip leakage vortex sharply near the casing wall, the inviscid fluxes were evaluated by a high-resolution upwind scheme based on a TVD formulation (Furukawa et al., 1991; Inoue and Furukawa, 1994) where a Roe's approximate Riemann solver of Chakravarthy (1986) and a third-order accurate MUSCL approach of Anderson et al. (1986) with the Van Albada limiter were implemented. Most numerical flow solvers for turbomachinery problems, however, are based on artificial dissipative schemes in which the inviscid terms are discretized in central differencing manners with artificial dissipation terms. According to studies on the application of high-resolution upwind schemes to the Navier–Stokes equations by van Leer et al. (1987), and Swanson and Turkel (1993), it is found that built-in numerical dissipation terms introduced by the high-resolution upwind schemes using Riemann solvers such as Roe's (1981) and Osher and Chakravarthy's (1983) automatically become much smaller in boundary layers than those introduced by the artificial dissipative schemes so as not to mask the physical diffusion in the boundary layers. It should be noted that the high-resolution upwind schemes based on the Riemann solvers have excellent shear-layer capturing capability as well as shock-wave capturing one. In the present scheme, the viscous fluxes were determined in a central differencing manner with Gauss's theorem, and the algebraic turbulence model of Baldwin and Lomax (1978) was employed to estimate the eddy viscosity. The boundary layer transition was determined in accordance with an original criterion of transition in the Baldwin and Lomax model. Unfactored implicit equations derived with no approximate factorization were solved by a point Gauss–Seidel relaxation method. The present scheme was stable up to a Courant number of about 100.

The present scheme has been already applied to calculations of a trailing edge vortex shedding in a transonic turbine cascade (Furukawa et al., 1992) and a three-dimensional flow in a diagonal flow rotor with a vortex type of a constant tangential velocity (Furukawa et al., 1995b). In these previous studies the validity of the scheme has been presented by comparing numerical results with experimental ones.

Computational Grids. A composite grid system with structured **H**-type grids was used to simulate the tip leakage flow accurately. A computational domain was divided into two zones. One zone was a main flow region outside the blade tip clearance, and the other was the tip clearance region. In each zone a structured **H**-type grid was generated as shown in Fig. 3. The main grids for both the diagonal and axial flow rotors consisted of 80 cells in the streamwise (I) direction (52 cells on the blade), 64 cells in the spanwise (J) direction, and 64 cells in the pitchwise (K) direction, as shown in Fig. 4. In order to capture the tip leakage vortex sharply, grid resolution was kept high even at the midpitch near the casing, as seen in Fig. 4(b). The grid embedded in the blade tip clearance consisted of $52 \times 32 \times 16$ cells in the chordwise, pitchwise, and spanwise directions, respectively, for both rotors. The whole grid system had 354,304 cells. The ratio of the minimum grid spacing on solid walls to the blade tip chord length was under 5×10^{-5} to evaluate the viscous fluxes at the walls by applying the no-slip and adiabatic conditions with no wall function method.

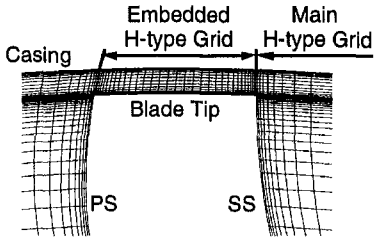

Fig. 3 Typical cross-sectional view of computational grid near blade tip

Boundary and Computational Conditions. Boundaries of the computational domain are formed by cell interfaces for the cell-centered finite volume approach. Hence, the boundary conditions must be imposed by the fluxes through the boundaries. In the present scheme, fictitious cells were introduced just outside all the boundaries, and values of conserved variables satisfying boundary conditions were given at the fictitious cells. Using the fictitious cells, numerical fluxes through the boundaries were evaluated in the same way as interior cell interfaces. This treatment of the boundary conditions prevented nonphysical reflections at the inflow and outflow boundaries, because the inviscid fluxes through the boundaries were evaluated according to the approximate Riemann solver in which the signal propagation properties of the Euler equations were simulated.

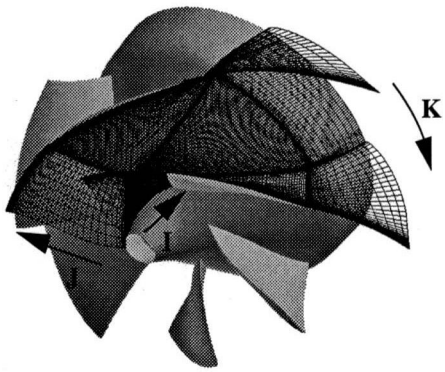

(a) Perspective view

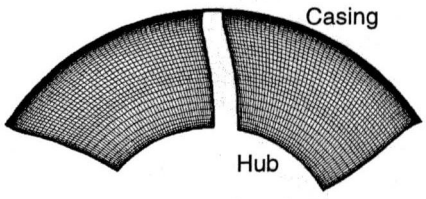

(b) Cross-sectional view

Fig. 4 Computational grid for diagonal flow rotor

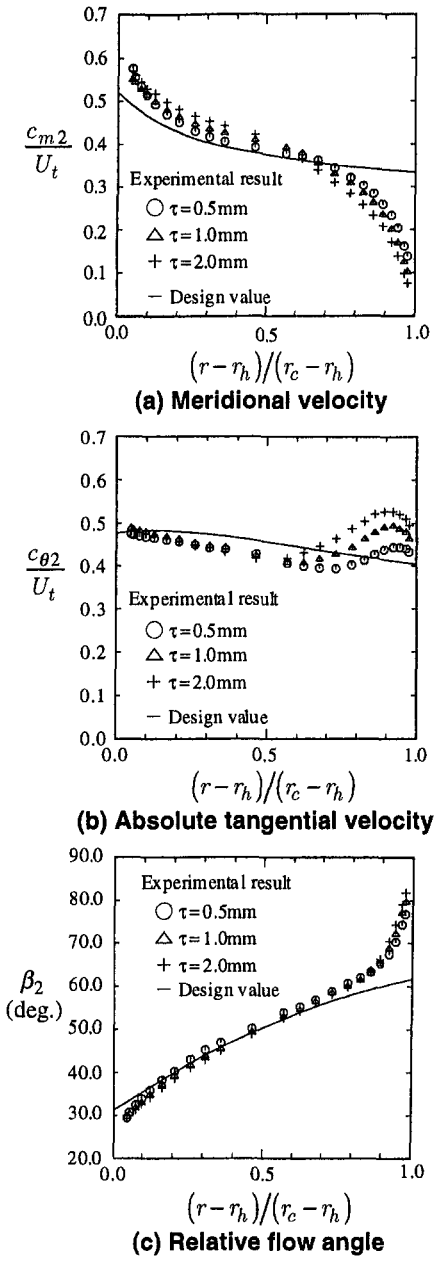

Fig. 5 Tangentially averaged flow distributions downstream of diagonal flow rotor

It should be noted that the outflow boundary conditions implemented in the present scheme allowed the pressure to vary on the boundary according to effects of streamline curvature and swirl. Details of the boundary conditions are described in the previous paper (Furukawa et al., 1995b).

In order to simulate the flow fields on the same flow conditions as the experiments, the inlet boundary conditions were given by experimental results measured upstream of the rotors using a five-hole cobra probe. The numerical simulations were carried out at the design flow rate for both the diagonal and axial flow rotors with the blade tip clearance of $\tau = 2.0$ mm.

Results and Discussion

Tangentially Averaged Flows Downstream of Rotor. Spanwise distributions of the tangentially averaged flow properties downstream of the diagonal flow rotor are shown in Fig. 5. The tangentially averaged flow distributions are obtained by averaging the phase-locked flow data measured with the hot-wire anemometer. In the figure the abscissa represents a nondimensional distance from the hub wall, and symbols and solid lines denote the experimental results and the design values, respectively. The velocity is normalized by the blade tip speed at the rotor exit, U_t. According to the meridional velocity distributions, the growth of the boundary layer is suppressed on the hub wall. On the other hand, the boundary layer on the casing wall is so thick that its thickness reaches about 50 percent of span height in the case of $\tau = 2.0$ mm. As compared with tangentially averaged flow distributions downstream of the axial flow rotor, which are shown in Fig. 6, it is readily seen that the casing wall boundary layer in the diagonal flow rotor is much thicker than that in the axial flow rotor with the larger tip clearances. This implies that the tip leakage flow in the diagonal flow rotor causes the much larger growth of the casing wall boundary layer. And furthermore, in contrast to the axial flow rotor, the absolute tangential velocity downstream of the diagonal flow rotor increases considerably in the casing wall boundary layer as seen in Fig. 5(*b*).

Phase-Locked Flow Fields Downstream of Rotor. The phase-locked velocity fields measured just downstream of the diagonal flow rotor are compared with those for the axial flow rotor. Figures 7 and 8 show secondary flow vectors and relative kinetic energy defect distributions for the diagonal flow rotor. The secondary flow vector is defined by a velocity component perpendicular to the design relative flow direction, and the relative kinetic energy defect, ζ_d, is defined as

$$\zeta_d = (w^{*2} - w^2)/w^{*2} \tag{3}$$

where w and w^* denote the measured and design values of the relative flow velocity, respectively. The phase-locked velocity fields downstream of the axial flow rotor are also presented in

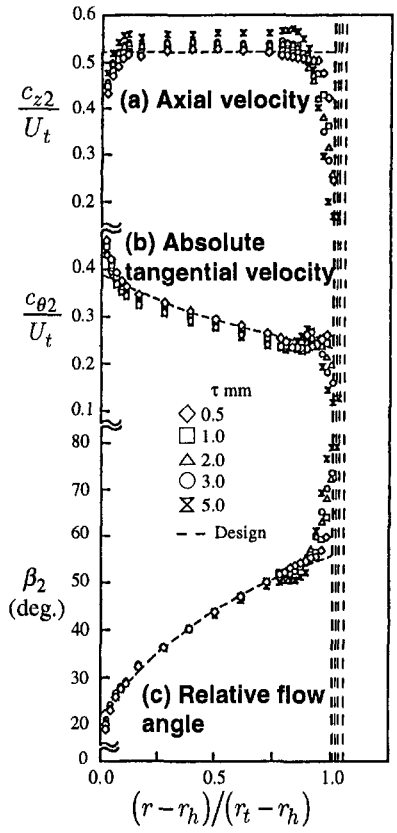

Fig. 6 Tangentially averaged flow distributions downstream of axial flow rotor, from Inoue et al. (1986)

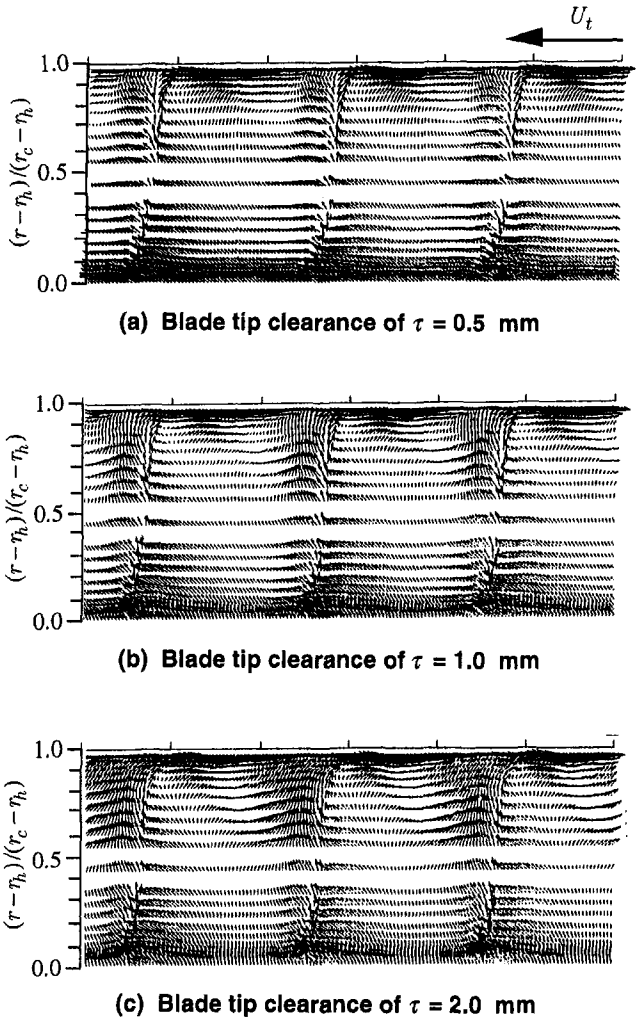

Fig. 7 Secondary flow vectors downstream of diagonal flow rotor

Figs. 9 and 10 where only the flow field from 60 percent span to the casing is shown. It should be noted that the contours of ζ_d shown by the broken line correspond to ζ_d of 0, and that the increments of ζ_d in the contours shown in Figs. 8 and 10 are 0.1 and 0.05, respectively.

In the secondary flow fields downstream of the axial flow rotor, the small rolling-up of the leakage vortex is visible even in the case of τ = 1.0 mm (0.8 percent of tip chord) shown in Fig. 9(b), and the distinct rolling-up is observed in the case of $\tau > 1.0$ mm.

In contrast to the axial flow rotor, no rolling-up of the tip leakage vortex is observed in the secondary flow fields downstream of the diagonal flow rotor shown in Fig. 7. In addition, Fig. 8 indicates that spread of the low-energy fluid accumulating on the casing is extremely large, compared with that for the axial flow rotor (Fig. 10). The spread in the spanwise direction even for the smallest tip clearance is more extensive than that for the axial flow rotor with the largest clearance. The spread reaches about a half of span in the case of τ = 2.0 mm. This corresponds well to the large growth of the casing wall boundary layer shown in Fig. 5(a). The above implies that the behavior of the tip leakage flow in the diagonal flow rotor is substantially different from that in the axial flow rotor.

Phase-Locked Pressure Fields on Casing Wall. The phase-locked distributions of the ensemble-averaged pressure on the casing wall in the diagonal and axial flow rotors are shown in Fig. 11. The distributions are presented by the static pressure coefficient, C_p, defined as

$$C_p = (p_w - P_1)/(\rho U_t^2/2) \quad (4)$$

where p_w and P_1 are the ensemble-averaged wall pressure and the inlet stagnation pressure, respectively.

In the case of $\tau > 0.5$ mm (0.4 percent of tip chord) for the axial flow rotor, as seen in Fig. 11(b), a pressure trough extends from the minimum pressure region near the blade suction side to the rotor exit. It should be noted that the pressure trough following the minimum pressure region corresponds to a locus of the tip leakage vortex core (Inoue and Kuroumaru, 1989).

On the other hand, the pressure trough in the diagonal flow rotor with the tip clearance of $\tau > 0.5$ mm (0.3 percent of tip chord) appears clearly at the fore part of the rotor passage and decays at the aft part of the passage, as seen in Fig. 11(a). This implies that the tip leakage vortex formed near the leading edge disappears at the aft part of the rotor passage. This behavior of the tip leakage vortex corresponds well to the fact that no rolling-up of the vortex is observed in the secondary flow fields downstream of the diagonal flow rotor (Fig. 7).

Leakage Flow Fields Inside Rotor. As mentioned above, the behavior of the tip leakage flow in the diagonal flow rotor has been found to be substantially different from that in the axial flow rotor. It is very difficult to investigate experimentally what causes the behavior. In the following, comparisons of the computational results between the diagonal and axial flow rotors with the tip clearance of 2.0 mm are presented to look deep into the cause of the behavior.

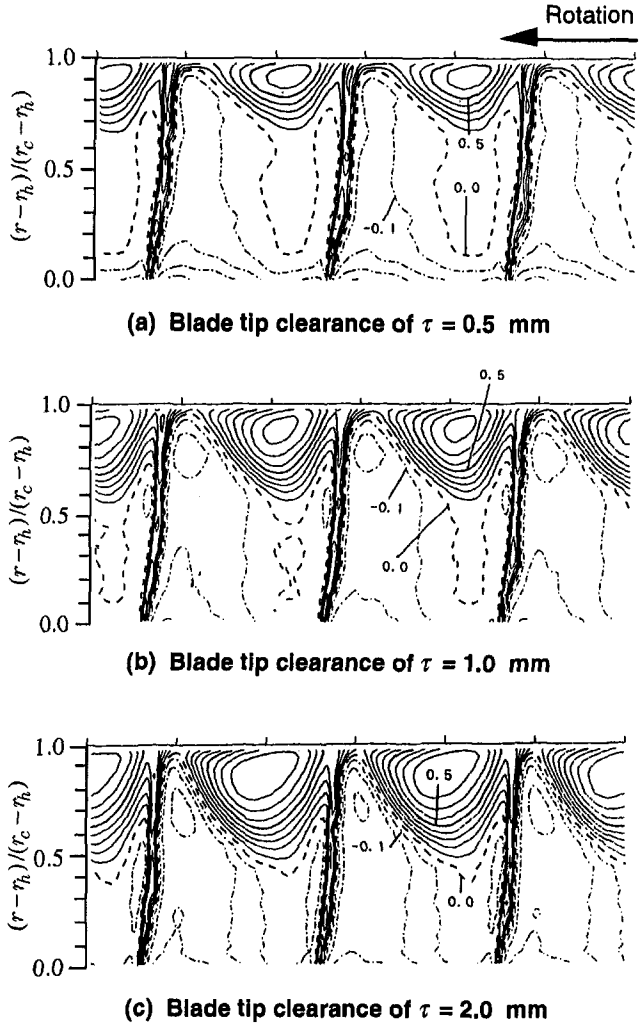

Fig. 8 Relative kinetic energy defect distributions downstream of diagonal flow rotor

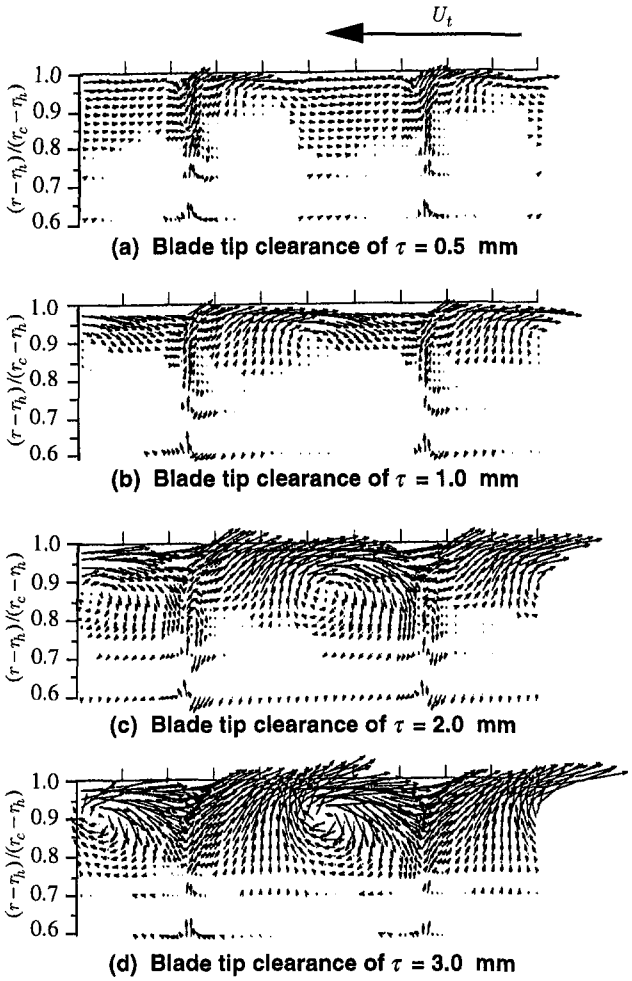

Fig. 9 Secondary flow vectors downstream of axial flow rotor, from Inoue et al. (1986)

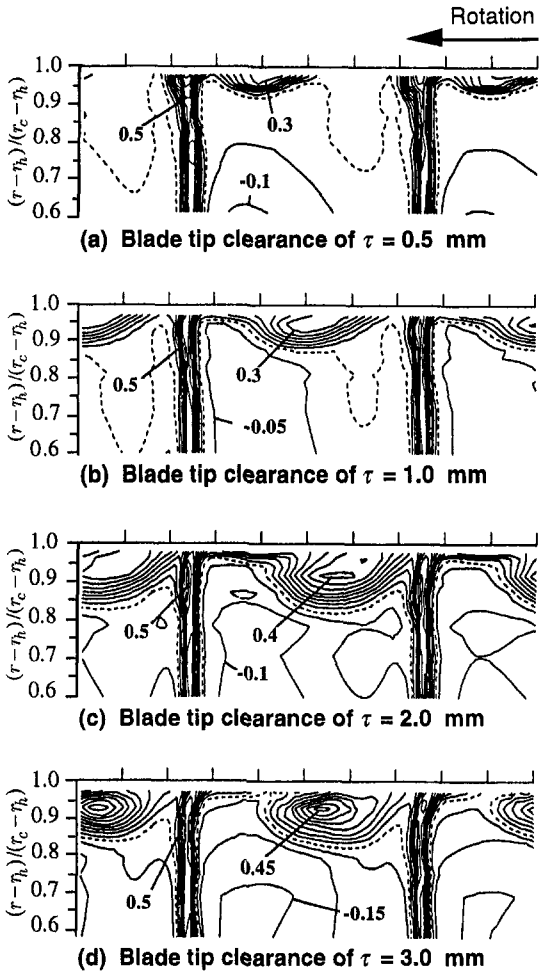

Fig. 10 Relative kinetic energy defect distributions downstream of axial flow rotor, from Inoue et al. (1986)

Figure 12 shows contours of the static pressure coefficient on the casing wall and distributions of the absolute streamwise vorticity along a tip leakage vortex core. The static pressure coefficient is defined by Eq. (4), and its increment in the contours is the same as that for the experimental results shown in Fig. 11. The absolute streamwise vorticity is defined and normalized as

$$\xi_s = \frac{\vec{\xi} \cdot \vec{w}}{2\omega|\vec{w}|} \tag{5}$$

where $\vec{\xi}$ and $\vec{w}$ are vectors of the absolute vorticity and the relative flow velocity, respectively, and ω is the angular velocity magnitude of the rotor. In Fig. 12 the streamwise vorticity distribution is shown by colors only along the leakage vortex core, and a few leakage streamlines surrounding the vortex core are indicated by violet lines. The trajectory of the leakage vortex core is approximately defined by the streamline that has the minimum curvature and emanates from the tip clearance near the leading edge. In the computational results for both the diagonal and axial flow rotors, the pressure trough on the casing wall is captured, and its behavior corresponds well to the experimental results shown in Fig. 11.

The well-known behavior of the tip leakage flow in the axial flow rotor is obtained in the computational result shown in Fig. 12(b). The rolling-up of the tip leakage vortex, which can be observed as the coiling of the leakage streamlines around the vortex core, is clearly seen both in the rotor passage and downstream of the rotor. The leakage vortex core traces the casing pressure trough well. The streamwise vorticity decays gradually along the vortex core.

The behavior of the leakage vortex different from that in the axial flow rotor is captured in the diagonal one shown in Fig. 12(a). The rolling-up of the leakage vortex is observed at the fore part of the rotor passage where the vortex core traces

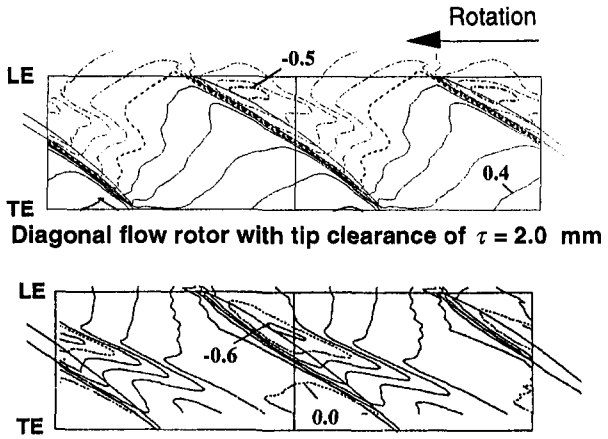

Fig. 11 Casing wall pressure distributions

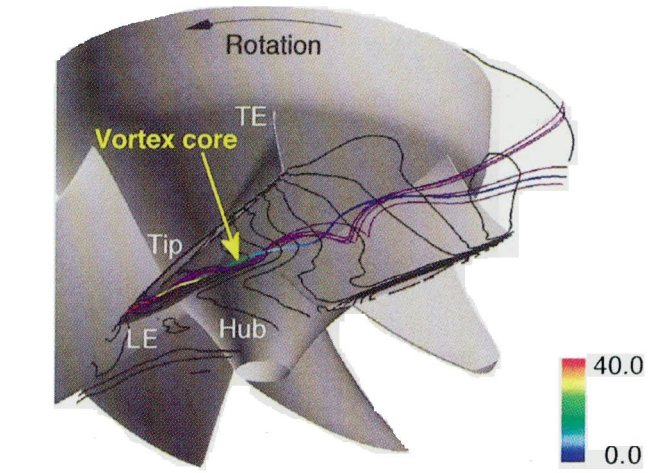

(a) Diagonal flow rotor with tip clearance of 2.0 mm

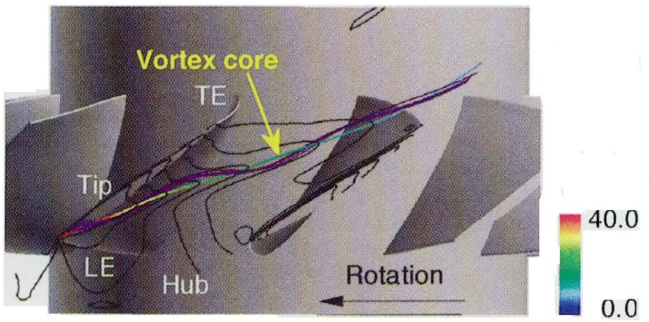

(b) Axial flow rotor with tip clearance of 2.0 mm

Fig. 12 Tip leakage vortex core with absolute streamwise vorticity distribution, leakage streamlines surrounding vortex core, and casing wall pressure distribution

the pressure trough. As the pressure trough becomes smaller, however, the leakage vortex core curves abruptly, and the streamwise vorticity along it decreases to about zero. Then, the rolling-up of the vortex seems to disappear at the aft part of the passage.

In order to investigate the rolling-up of the leakage vortex quantitatively, we introduce a normalized helicity similar to that used by Levy et al. (1990). The normalized helicity used in the present paper is defined as

$$H_n = \frac{\vec{\xi} \cdot \vec{w}}{|\vec{\xi}|\,|\vec{w}|} \tag{6}$$

where $\vec{\xi}$ and $\vec{w}$ denote the vectors of the "absolute" vorticity and the "relative" flow velocity, respectively, in the same way as Eq. (5). Note that the normalized helicity is not defined by the "relative vorticity," but by the "absolute vorticity," considering that secondary flow fields in the rotors are dominated by the component of "absolute vorticity" along the "relative flow" direction. The normalized helicity is the cosine of the angle between the absolute vorticity and relative velocity vectors. This means that the magnitude of the normalized helicity tends to unity in the vortex core, and its sign indicates the direction of swirl of the vortex relative to the streamwise velocity component. In contrast to the streamwise vorticity defined by Eq. (5), the normalized helicity allows us to examine quantitatively the strength of the vortex rolling-up regardless of the decay of vorticity in the streamwise direction.

Figure 13 shows distributions of the normalized helicity along the tip leakage flow together with the casing wall pressure contours. In the figure, red denotes the normalized helicity of unity, and green denotes that of zero. For the axial flow rotor the normalized helicity is about unity along the leakage flow to the downstream of the rotor, which means that the leakage vortex is tightly rolled up to the downstream of the rotor. This corresponds well to the experimental results downstream of the rotor shown in Fig. 9(*c*).

On the other hand, in the diagonal flow rotor shown in Fig. 13(*a*), the nature of the leakage vortex is substantially different from that in the axial flow rotor. The strong rolling-up of the leakage vortex with the normalized helicity of about unity is formed from just downstream of the leading edge to about 35 percent of the meridional chord, thus causing the steep pressure trough on the casing wall. Near 50 percent of the meridional chord, however, a gradual decrease in the normalized helicity occurs and corresponds to the decay of the pressure trough. Then, the nature of the leakage vortex changes drastically at the aft part of the passage: The leakage vortex is expanded remarkably, and the vortex core is occupied by the flows with negative normalized helicity, thus being destroyed. This change corresponds well to the disappearance of the casing pressure trough. It seems that the significant change in the nature of the leakage vortex indicates the occurrence of "vortex breakdown."

In order to confirm the occurrence of vortex breakdown in the diagonal flow rotor, the detailed flow structure in the leakage vortex is investigated on crossflow planes. The planes are located in four positions nearly perpendicular to the leakage vortex core, as shown by planes I, II, III, and IV in Figs. 14, 15,

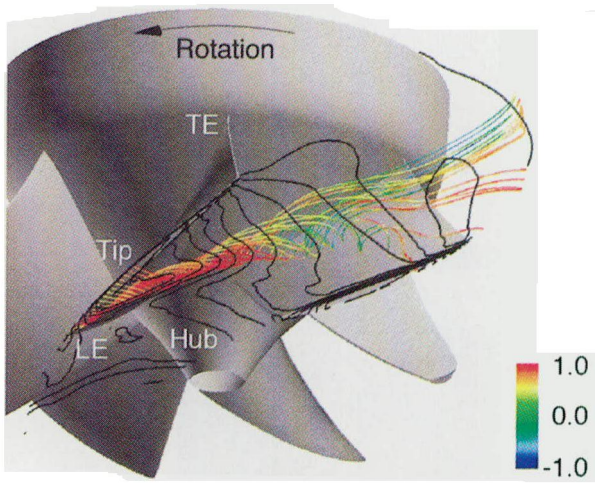

(a) Diagonal flow rotor with tip clearance of 2.0 mm

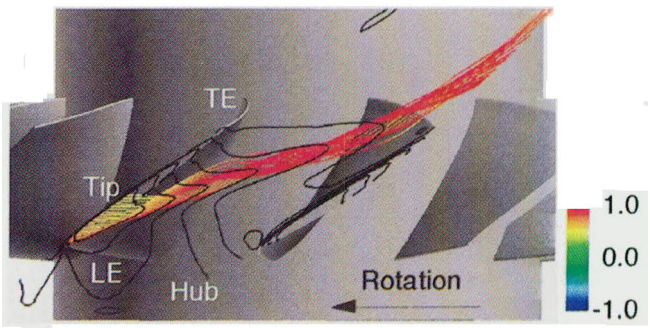

(b) Axial flow rotor with tip clearance of 2.0 mm

Fig. 13 Normalized helicity distribution along tip leakage flow and casing wall pressure distribution

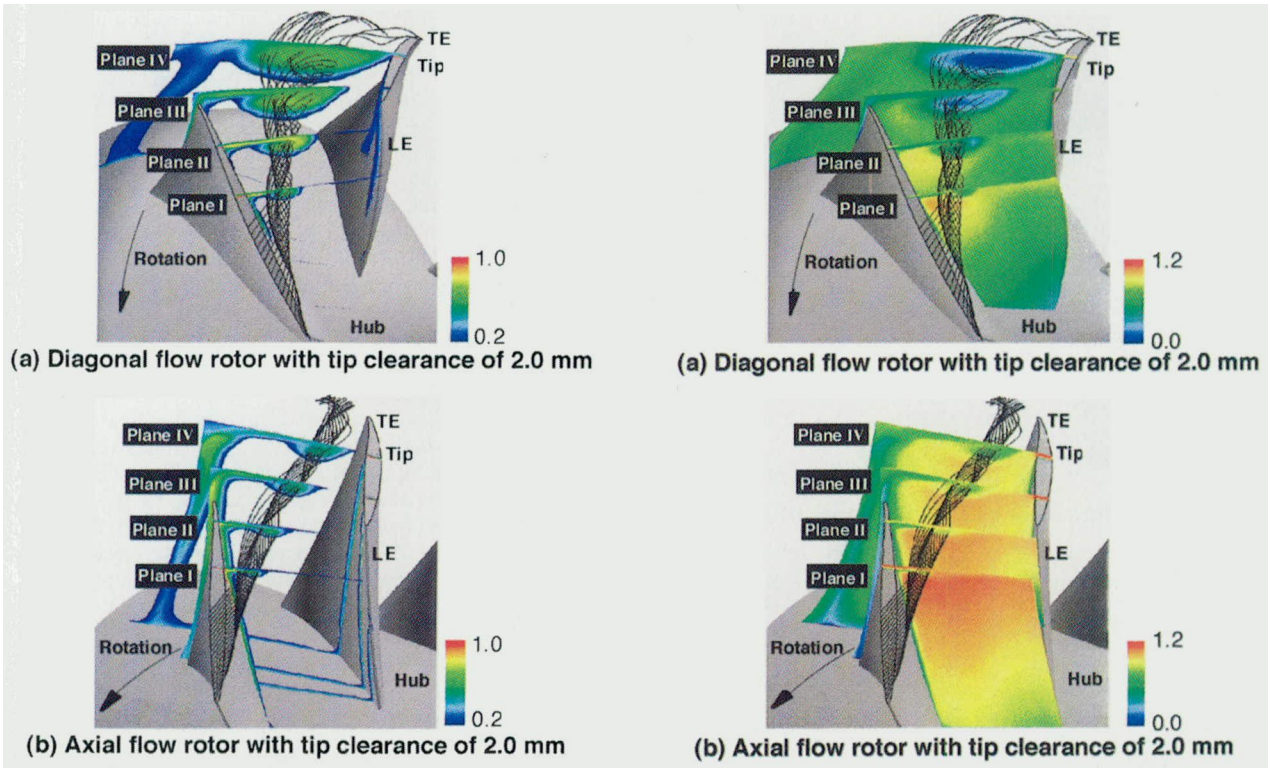

Fig. 14 Total pressure loss coefficient distributions on crossflow planes perpendicular to tip leakage vortex

Fig. 16 Relative velocity distributions on crossflow planes perpendicular to tip leakage vortex

and 16. In these figures the same leakage streamlines as Fig. 13 are shown by black lines. For the diagonal flow rotor, planes III and IV are located in the region where the "vortex breakdown" seems to occur.

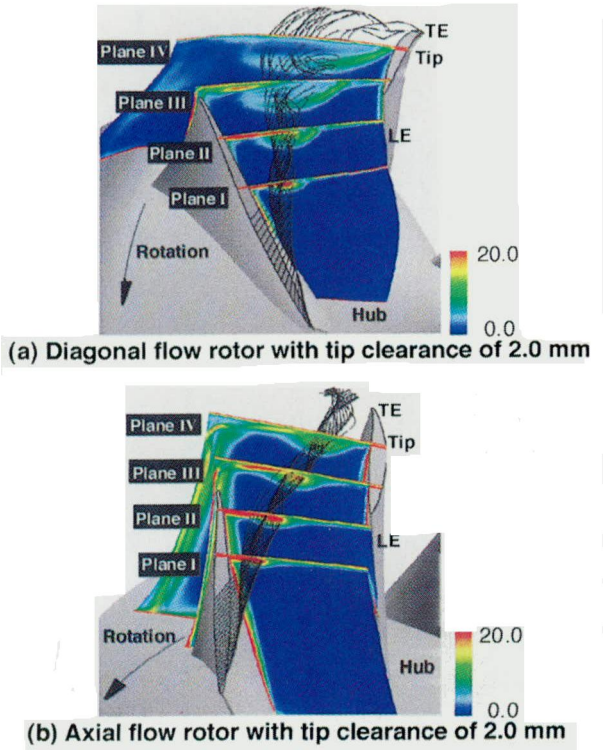

Fig. 15 Absolute vorticity distributions on crossflow planes perpendicular to tip leakage vortex

Figure 14 shows distributions of a total pressure loss coefficient on the crossflow planes. The total pressure loss coefficient is defined as

$$\zeta_p = \frac{\omega(rc_\theta - r_1 c_{\theta 1}) - (P - P_1)/\rho}{U_t^2/2} \tag{7}$$

where r is the radius from the axis of rotation, c_θ is the absolute tangential velocity component, P is the total pressure, and subscript of 1 denotes the rotor inlet. Only the region with the total pressure loss coefficient above 0.2 is shown in Fig. 14. For both the diagonal and axial flow rotors, it is clearly seen that the high loss fluid accumulates in the tip leakage vortex. This means that the size of the high loss region accumulating on the casing corresponds to the leakage vortex size. In contrast to the axial flow rotor in which the high loss region in the leakage vortex grows gradually in the streamwise direction, the extremely large spread of the high loss region is observed on planes III and IV in the diagonal flow rotor. It should be realized that in the diagonal flow rotor the large expansion of the leakage vortex occurs at the aft part of the rotor passage. This expansion of the vortex size corresponds well to the experimental results: the large growth of the casing wall boundary layer (Fig. 5(*a*)), and the large spread of the low-energy fluid (Fig. 8) downstream of the rotor.

Distributions of the absolute vorticity on the crossflow planes are shown in Fig. 15. The vorticity is normalized by twice the angular velocity of the rotor, 2ω. For the axial flow rotor, the absolute vorticity in the leakage vortex decays in the streamwise direction, but the vortex core can be observed as the region with the concentrated vorticity. On the other hand, in the diagonal flow rotor the drastic change in the leakage vortex structure is observed on crossflow planes III and IV: The high vorticity region due to the leakage flow is spread out, and the vortex core with the concentrated vorticity is not observed in the leakage flow field. It is found that the core of the leakage vortex disappears at the aft part of the passage in the diagonal flow

rotor. The disappearance of the vortex core corresponds to the experimental results, namely no rolling-up of the leakage vortex downstream of the rotor (Fig. 7), and the disappearance of the casing pressure trough (Fig. 11(*a*)). It should be noted that the normalized helicity distribution along the leakage flow, shown in Fig. 13(*a*), indicates the disappearance of the leakage vortex core, also.

Figure 16 shows distributions of the relative velocity, w/U_t, normalized by the blade tip speed at the rotor exit. For the diagonal flow rotor, as compared with the axial one, the region with lower relative velocity is observed in the leakage flow on crossflow planes III and IV. At plane IV the velocity in this region is so low as to decrease almost to zero, and the region is spread out remarkably. It should be realized that the low-velocity region appears in the leakage flow away from the casing wall. In Fig. 17 the low-velocity region is shown by a blue isosurface of the relative velocity of $w/U_t = 0.1$, and the leakage streamlines with the normalized helicity distributions are also presented. Figure 17 indicates that the low-velocity region appears along the leakage vortex in the aft part of the rotor passage and causes the expansion of the vortex. It should be noted that the region contains reverse flows (not shown in Figs. 16 and 17). The low-velocity region apparently results in the large growth of the casing wall boundary layer. Figure 18 shows the streamwise distributions of the meridional displacement thickness of the casing wall boundary layer in the diagonal and axial flow rotors. In the figure the abscissa denotes the meridional distance from the leading edge. The displacement thickness is evaluated by averaging the computational results in the tangential direction. In Fig. 18 it is observed that the growth of the boundary layer in the diagonal flow rotor is much larger than that in the axial one, and its thickness distribution has a maximum in the aft part of the passage where the low-velocity region appears. Moreover, it is obvious that the fluid in the low relative velocity region has a large tangential component of the absolute velocity, like the wake of the blade. This fact corresponds well to the experimental result that the absolute tangential velocity downstream of the diagonal flow rotor increases considerably in the casing wall boundary layer as seen in Fig. 5(*b*).

From the significant changes in the nature of the tip leakage vortex, namely the large expansion of the vortex, the disappearance of the vortex core and the appearance of the low relative velocity region in the vortex, it is hard to escape the conclusion that the "breakdown" of the tip leakage vortex occurs in the diagonal flow rotor. The appearance of the low-velocity region with reverse flow is evidence of the fact that the large expansion

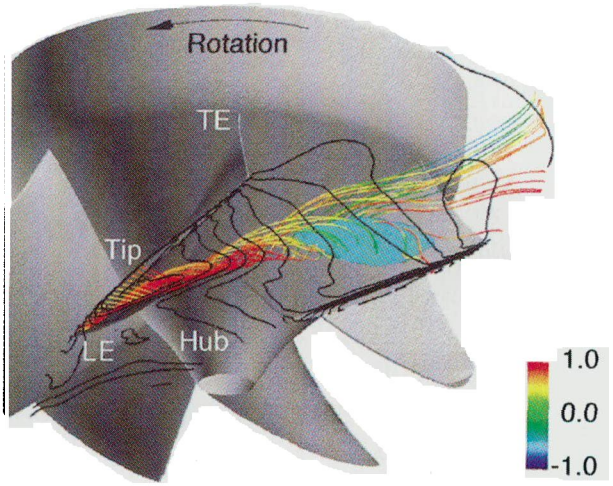

Fig. 17 Isosurface of relative velocity of w/Ut = 0.1 (shown by blue surface) and normalized helicity distributions along tip leakage flow for diagonal flow rotor with tip clearance of 2.0 mm

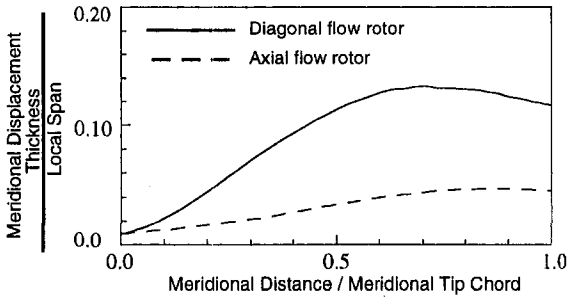

Fig. 18 Meridional displacement thickness distributions of casing wall boundary layer in diagonal and axial rotors with tip clearance of 2.0 mm

of the vortex and the disappearance of the vortex core do not result from the diffusion. The "breakdown" of the tip leakage vortex can be regarded as a phenomenon similar to the breakdown of the leading edge vortices on a delta type wing. The vortex breakdown on a delta type wing is a well-known phenomenon and has been investigated by many experimental and numerical works (Rom, 1992). It is evident that not only does the "vortex breakdown" result in the behavior of the tip leakage flow substantially different from that in the axial flow rotor, but also it influences the overall performance of the rotor. The large growth of the casing wall boundary layer due to the vortex breakdown causes the large reduction of efficiency with the tip clearance: for the present diagonal flow rotor, an increase in the clearance/chord ratio from 0.3 percent to 1.3 percent brings about 6 percent reduction of efficiency at the design flow rate, as seen in Fig. 2, which is about three times as large as that of the axial flow rotor. On the other hand, the disappearance of the leakage vortex core due to the breakdown gives the diagonal flow rotor a superiority to the axial one: The noise level of the diagonal flow rotor is considerably lower, compared with the axial one (Inoue et al., 1984). The low level of noise appears to result from the fact that the vortex breakdown leads to the loss of the pressure gradient around the vortex core, which can be observed in the casing wall pressure distribution (Fig. 12(*a*)), and so pressure fluctuations induced by the leakage vortex decrease on solid walls.

In order to simulate the tip leakage flow fields accurately, special attention must be paid to grid resolution. Not only the wall boundary layers but the main flow region away from the wall requires the high grid resolution, because the tip leakage vortex consisting of the concentrated vorticity is formed outside the boundary layer. In the present simulations the tip leakage vortices, including the vortex breakdown, are captured relatively well. However, the computational grids used for the present simulations are not sufficient to capture the more detailed flow structure, such as the detailed structure in the vortex breakdown region. In addition to the calculations presented in this paper, other calculations were performed using a coarse grid system in which the main and embedded grids consisted of $59(I) \times 43(J) \times 37(K)$ cells and $31(I) \times 11(J) \times 15(K)$ cells, respectively. The simulation with the coarse grid system captured no breakdown of the tip leakage vortex in the diagonal flow rotor. It should be noted that the high grid resolution is indispensable to the tip leakage flow simulation, including the vortex breakdown.

Conclusions

Experimental and computational results of the tip leakage flow in a diagonal flow rotor have been compared with those in an axial flow rotor. It was found out that "breakdown" of the tip leakage vortex occurs at the aft part of the passage in the diagonal flow rotor. The "vortex breakdown" causes significant changes in the nature of the tip leakage vortex: disap-

pearance of the vortex core, large expansion of the vortex, and appearance of low relative velocity region in the vortex. These changes result in the following behavior of the tip leakage flow, which is substantially different from that in the axial flow rotor:

1 Because of the disappearance of the vortex core with the concentrated vorticity, the rolling-up of the tip leakage vortex is not observed downstream of the diagonal flow rotor.

2 The disappearance of the vortex core leads to the loss of the pressure gradient induced by the concentrated vorticity, so that the pressure trough vanishes from the casing wall at the aft part of the rotor passage.

3 The disappearance of the vortex core seems to result in the fact that the noise level of the diagonal flow rotor is considerably low, compared with the axial one.

4 Because of the large expansion of the leakage vortex caused by the low relative velocity region with reverse flow, the low-energy fluid due to the leakage flow is spread out from the casing to about a half of span. As a result, much larger growth of the casing wall boundary layer occurs, compared with the axial flow rotor.

5 Downstream of the diagonal flow rotor, the absolute tangential velocity increases considerably in the casing wall boundary layer, because the fluid in the low relative velocity region has a large tangential component of the absolute velocity, like the wake.

6 The large growth of the casing wall boundary layer causes large reduction of efficiency with the tip clearance: The reducing rate of efficiency is about three times as large as that of the axial flow rotor.

In order to examine the rolling-up of the tip leakage vortex quantitatively, we have introduced the normalized helicity defined by the vectors of the absolute vorticity and the relative velocity. It should be noted that the normalized helicity is useful in investigating the nature of the tip leakage vortex.

In the present study the occurrence of "breakdown" of the tip leakage vortex in the diagonal flow rotor has been found out. However, its mechanism has been unresolved. Many attempts must be made to investigate the "vortex breakdown" in the tip leakage flows.

Acknowledgments

The present research was supported by the Ministry of Education through the Grant-in-Aid for Scientific Research (C). The authors gratefully acknowledge the research fund from Harada Memorial Foundation.

References

Adamczyk, J. J., Celestina, M. L., and Greitzer, E. M., 1993, "The Role of Tip Clearance in High-Speed Fan Stall," ASME JOURNAL OF TURBOMACHINERY, Vol. 115, pp. 28–38.

Anderson, W. K., Thomas, J. L., and van Leer, B., 1986, "Comparison of Finite Volume Flux Vector Splittings for the Euler Equations," *AIAA Journal,* Vol. 24, pp. 1453–1460.

Baldwin, B. S., and Lomax, H., 1978, "Thin Layer Approximation and Algebraic Model for Separated Turbulent Flow," AIAA Paper No. 78-257.

Chakravarthy, S. R., 1986, "The Versatility and Reliability of Euler Solvers Based on High-Accuracy TVD Formulations," AIAA Paper No. 86-0243.

Chen, G. T., Greitzer, E. M., Tan, C. S., and Marble, F. E., 1991, "Similarity Analysis of Compressor Tip Clearance Flow Structure," ASME JOURNAL OF TURBOMACHINERY, Vol. 113, pp. 260–271.

Dawes, W. N., 1987, "A Numerical Analysis of the Three-Dimensional Viscous Flow in a Transonic Compressor Rotor and Comparison With Experiment," ASME JOURNAL OF TURBOMACHINERY, Vol. 109, pp. 83–90.

Foley, A. C., and Ivey, P. C., 1996, "Measurement of Tip-Clearance Flow in a Multistage, Axial Flow Compressor," ASME JOURNAL OF TURBOMACHINERY, Vol. 118, pp. 211–217.

Furukawa, M., Yamasaki, M., and Inoue, M., 1991, "A Zonal Approach for Navier-Stokes Computations of Compressible Cascade Flow Fields Using a TVD Finite Volume Method," ASME JOURNAL OF TURBOMACHINERY, Vol. 113, pp. 573–582.

Furukawa, M., Nakano, T., and Inoue, M., 1992, "Unsteady Navier–Stokes Simulation of Transonic Cascade Flow Using an Unfactored Implicit Upwind Relaxation Scheme With Inner Iterations," ASME JOURNAL OF TURBOMACHINERY, Vol. 114, pp. 599–606.

Furukawa, M., Inoue, M., Kuroumaru, M., and Saiki, K., 1995a, "Behavior of Tip Leakage Flow in a Diagonal Flow Impeller With High Specific Speed," *Proc. 1995 Yokohama International Gas Turbine Congress,* Vol. 1, pp. 109–114.

Furukawa, M., Saiki, K., and Inoue, M., 1995b, "Numerical Simulation of Three-Dimensional Viscous Flow in Diagonal Flow Impeller," in: *Numerical Simulations in Turbomachinery,* ASME FED-Vol. 227, pp. 29–36.

Goto, A., 1992a, "Study of Internal Flows in a Mixed-Flow Pump Impeller at Various Tip Clearances Using Three-Dimensional Viscous Flow Computations," ASME JOURNAL OF TURBOMACHINERY, Vol. 114, pp. 373–382.

Goto, A., 1992b, "The Effect of Tip Leakage Flow on Part-Load Performance of a Mixed-Flow Pump Impeller," ASME JOURNAL OF TURBOMACHINERY, Vol. 114, pp. 383–391.

Hah, C., 1986, "A Numerical Modeling of Endwall and Tip-Clearance Flow of an Isolated Compressor Rotor," ASME *Journal of Engineering for Gas Turbines and Power,* Vol. 108, pp. 15–21.

Inoue, M., Ikui, T., Kamada, Y., and Tashiro, M., 1980, "A Quasi-Three-Dimensional Design of Diagonal Flow Impellers by Use of Cascade Data," *Proc. 10th Symposium, The International Association for Hydraulic Research,* Vol. 1, pp. 403–414.

Inoue, M., Wu, K.-C., Kuroumaru, M., Furukawa, M., Fukuhara, M., and Ikui, T., 1984, "A Design of Diagonal Impeller by Means of SCM and Cascade Data," *Proc. China–Japan Joint Conference on Hydraulic Machinery and Equipment,* Vol. 1, pp. 21–30.

Inoue, M., Kuroumaru, M., and Fukuhara, M., 1986, "Behavior of Tip Leakage Flow Behind an Axial Compressor Rotor," ASME *Journal of Engineering for Gas Turbines and Power,* Vol. 108, pp. 7–14.

Inoue, M., and Kuroumaru, M., 1989, "Structure of Tip Clearance Flow in an Isolated Axial Compressor Rotor," ASME JOURNAL OF TURBOMACHINERY, Vol. 111, pp. 250–256.

Inoue, M., and Furukawa, M., 1994, "Artificial Dissipative and Upwind Schemes for Turbomachinery Blade Flow Calculations," VKI, Lecture Series, No. 1994-06.

Kang, S., and Hirsch, C., 1996, "Numerical Simulation of Three-Dimensional Viscous Flow in a Linear Compressor Cascade With Tip Clearance," ASME JOURNAL OF TURBOMACHINERY, Vol. 118, pp. 492–505.

Klapproth, J. F., 1959, Discussion in: Lieblein, S., "Loss and Stall Analysis of Compressor Cascades," ASME *Journal of Basic Engineering,* Vol. 81, pp. 387–400.

Kuroumaru, M., Inoue, M., Higaki, T., Abd-Elkhalek, F. A., and Ikui, T., 1982, "Measurements of Three-Dimensional Flow Field Behind an Impeller by Means of Periodic Multi-sampling of a Slanted Hot Wire," *Bulletin of the JSME,* Vol. 25, No. 209, pp. 1674–1681.

Lakshminarayana, B., Zaccaria, M., and Marathe, B., 1995, "The Structure of Tip Clearance Flow in Axial Flow Compressors," ASME JOURNAL OF TURBOMACHINERY, Vol. 117, pp. 336–347.

Levy, Y., Degani, D., and Seginer, A., 1990, "Graphical Visualization of Vortical Flows by Means of Helicity," *AIAA Journal,* Vol. 28, pp. 1347–1352.

Moyle, I. N., Walker, G. J., and Shreeve, R. P., 1992, "Stator Averaged Rotor Blade to Blade Near Wall Flow in a Multistage Axial Compressor With Tip Clearance Variation," ASME JOURNAL OF TURBOMACHINERY, Vol. 114, pp. 668–674.

Murthy, K. N. S., and Lakshminarayana, B., 1986, "Laser Doppler Velocimeter Measurement in the Tip Region of a Compressor Rotor," *AIAA Journal,* Vol. 24, pp. 807–814.

Osher, S., and Chakravarthy, S. R., 1983, "Upwind Schemes and Boundary Conditions With Applications to Euler Equations in General Coordinates," *Journal of Computational Physics,* Vol. 50, pp. 447–481.

Rains, D. A., 1954, "Tip Clearance Flows in Axial Flow Compressors and Pumps," California Institute of Technology, Hydrodynamics and Mechanical Engineering Laboratories, Report No. 5.

Roe, P. L., 1981, "Approximate Riemann Solvers, Parameter Vectors, and Difference Schemes," *Journal of Computational Physics,* Vol. 43, pp. 357–372.

Rom, J., 1992, *High Angle of Attack Aerodynamics: Subsonic, Transonic, and Supersonic Flows,* Springer-Verlag, New York.

Smith, L. H., Jr., 1970, "Casing Boundary Layers in Multistage Axial-Flow Compressors," in: *Flow Research on Blading,* Dzung, L. S., ed., Elsevier, New York, pp. 275–304.

Stauter, R. C., 1993, "Measurement of the Three-Dimensional Tip Region Flow Field in an Axial Compressor," ASME JOURNAL OF TURBOMACHINERY, Vol. 115, pp. 468–476.

Storer, J. A., and Cumpsty, N. A., 1991, "Tip Leakage Flow in Axial Compressors," ASME JOURNAL OF TURBOMACHINERY, Vol. 113, pp. 252–259.

Suder, K. L., and Celestina, M. L., 1996, "Experimental and Computational Investigation of the Tip Clearance Flow in a Transonic Axial Compressor Rotor," ASME JOURNAL OF TURBOMACHINERY, Vol. 118, pp. 218–229.

Swanson, R. C., and Turkel, E., 1993, "Aspects of a High-Resolution Scheme for the Navier-Stokes Equations," AIAA Paper No. 93-3372-CP.

Van Leer, B., Thomas, J. L., Roe, P. L., and Newsome, R. W., 1987, "A Comparison of Numerical Flux Formulas for the Euler and Navier–Stokes Equations," AIAA Paper No. 87-1104.

Zierke, W. C., Farrell, K. J., and Straka, W. A., 1995, "Measurement of the Tip Clearance Flow for a High-Reynolds-Number Axial Flow Rotor," ASME JOURNAL OF TURBOMACHINERY, Vol. 117, pp. 522–532.

N. A. Cumpsty[1]

This is an interesting and informative paper that raises important issues about the way clearance flows behave in rotors. The different behavior of the clearance flow in the mixed-flow rotor gives us another example on which to test our ideas.

I have come to believe that what matters to the flow is not so much the circulation of the vortex but the deficit in stagnation pressure at its center. The deficit in stagnation pressure gives a lower streamwise velocity (i.e., the component of velocity parallel to the vortex) at the core of the vortex than the streamwise velocity outside the core. The low streamwise velocity at the core becomes significant when the streamwise velocity of the whole flow is reduced. In a way analogous to a wake (or the low velocity in a boundary layer) the reduction in the free-stream streamwise velocity produces a proportionately bigger effect where the velocity is initially low, in this case in the vortex core. What is referred to as the bursting of the vortex is therefore likely to be the flow reversal in the core brought about by a reduction in the streamwise velocity of the whole flow.

In the case of the axial rotor, when the streamlines remain at an approximately constant radius, there is a simple relation between the reduction in free-stream streamwise velocity and the rise in static pressure. In the mixed flow rotor, however, the increase in streamline radius produces a rise in static pressure in addition to that produced by any reduction in streamwise velocity. In other words the static pressure change across a mixed flow rotor does not provide a clear indication of the flow deceleration. Static pressure does not therefore provide a good means of comparing the behavior of vortices in different types of rotor.

In comparing the behavior of the vortices in the two rotors, I think that it would be helpful to look at the streamwise velocity. Compared with the axial rotor, does the mixed flow rotor have a markedly greater reduction in streamwise velocity between the inlet near the tip and the exit? If it does it would help to explain the very different behavior for the vortex in the two rotors. Could the authors therefore show results of their calculations to demonstrate whether this is the case?

Authors' Closure

The authors would like to thank Professor Cumpsty for his discussion regarding the bursting or breakdown of the tip leakage vortex in compressor rotors.

Based on Professor Cumpsty's question, we have evaluated the reduction in streamwise velocity across the diagonal (mixed) and axial flow rotors. Spanwise distributions of tangentially averaged relative velocity, w, at the inlet and outlet of the rotors are shown in Fig. 19 where design distributions, as well as computational results obtained by Navier–Stokes flow simulations, are presented. The computational results indicate that the relative velocity decreases considerably near the casing at the outlet of the diagonal flow rotor as compared with the axial one. In the design, however, the reduction in relative velocity of $(w_1 - w_2)/U_t = 0.208$ near the casing across the diagonal flow rotor is almost equal to 0.202 across the axial flow rotor. Although the greater reduction in streamwise velocity is observed near the casing across the diagonal flow rotor, it is found to result from the flow reversal caused by the breakdown of the tip leakage vortex.

Vortex breakdown or vortex bursting is a phenomenon widely observed in streamwise slender vortices. For the last four decades, it has been investigated by experimental, theoretical, and numerical research efforts, which have been reviewed by Hall (1972), Leibovich (1978, 1984), Escudier (1988), and Delery (1994). These efforts show that a distinctive feature of the vortex breakdown is the existence of a stagnation point in the vortex core. Various criteria for the onset of vortex breakdown have been proposed. Based on the previous experimental, theoretical, and numerical studies, Spall et al. (1987) gave a breakdown criterion by defining a local Rossby number whose inverse corresponded to the inverse tangent of a local helix angle at the point where the swirl velocity is a maximum. In spite of the extensive research, however, the mechanism of the vortex breakdown still remains one of unresolved and intriguing problems in fluid mechanics. Needless to say, no generally accepted criterion for the breakdown has been found even for isolated slender vortices. The structure of the tip leakage vortex is more complicated than that of the isolated vortices, because the leakage vortex interacts with the nonuniform main flow and the boundary layer on the casing wall having a motion relative to the rotor. It is evident that further study

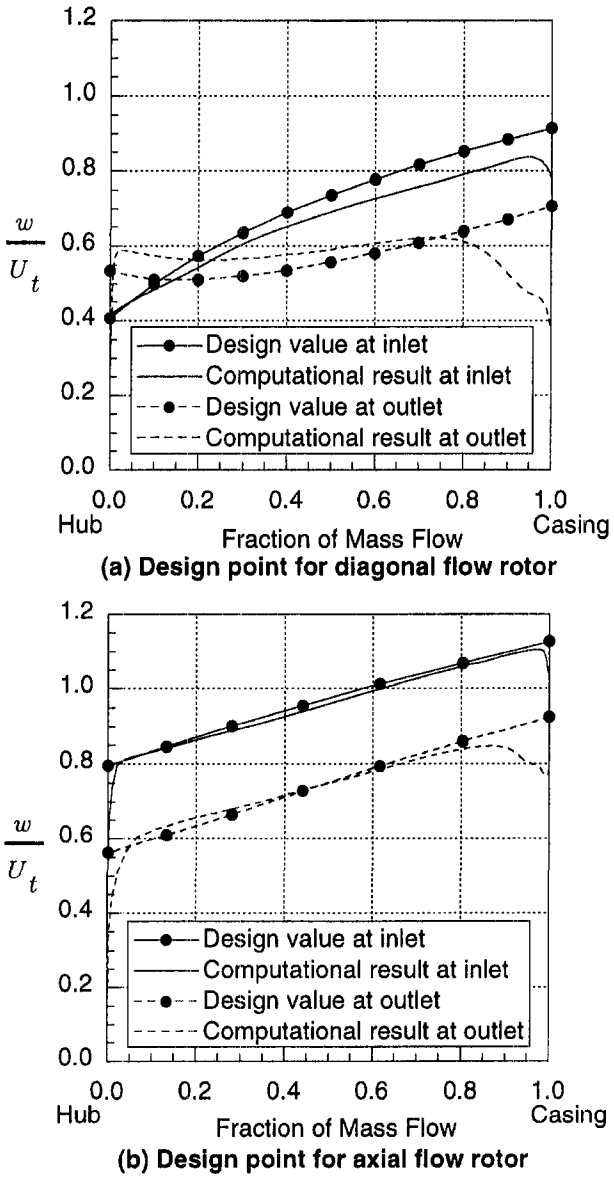

Fig. 19 Spanwise distributions of tangentially averaged relative velocity at inlet and outlet of rotors: (*a*) design point for diagonal flow rotor; (*b*) design point for axial flow rotor.

[1] Whittle Laboratory, University of Cambridge, Madingley Road, Cambridge CB3 0DY, United Kingdom.

G. J. Walker

J. D. Hughes

Department of Civil & Mechanical Engineering, University of Tasmania, Hobart, Australia

I. Köhler

Fachgebiet Gasturbinen und Flugantriebe, Technische Hochschule, Darmstadt, Germany

W. J. Solomon

Department of Civil & Mechanical Engineering, University of Tasmania, Hobart, Australia

The Influence of Wake–Wake Interactions on Loss Fluctuations of a Downstream Axial Compressor Blade Row

The interaction between wakes of an adjacent rotor–stator or stator–rotor blade row pair in an axial turbomachine is known to produce regular spatial variations in both the time-mean and unsteady flow fields in a frame relative to the upstream member of the pair. This paper examines the influence of such changes in the free-stream disturbance field on the viscous losses of a following blade row. Hot-wire measurements are carried out downstream of the outlet stator in a 1.5-stage axial compressor having equal blade numbers in the inlet guide vane (IGV) and stator rows. Clocking of the IGV row is used to vary the disturbance field experienced by the stator blades; the influence on stator wake properties is evaluated. The magnitude of periodic fluctuations in ensemble-averaged stator wake thickness is significantly influenced by IGV wake-rotor wake interaction effects. The changes in time-mean stator losses appear marginal.

Introduction

It has long been appreciated from studies such as those of Smith (1966), Kerrebrock and Mikolajczak (1970), Lockhart and Walker (1974), and Zierke and Okiishi (1982) that wake dispersion and mixing effects in an axial turbomachine with multiple blade rows may cause uneven energy addition and redistributions of losses and high-temperature fluid, with resultant periodic circumferential variations in both the time-mean and unsteady flow fields. The early investigation by Walker (1974) also showed that the periodic disturbances associated with passing wakes may produce periodic unsteady transition phenomena on the surfaces of axial turbomachine blades. However, the complexity of the problem has largely precluded any significant consideration of these effects in axial turbomachine design.

Improvements in computing power and high-speed data acquisition capability have brought a renewed interest in this field in recent years. Further analytical and numerical studies of the influence of rotor–stator axial gap on axial compressor performance have been reported by Deregel and Tan (1996) and Adamczyk (1996). They examine the potential for performance improvement by passing a wake through a blade row prior to being mixed out by viscous diffusion, and indicate potential increases in efficiency and pressure rise of 1 or 2 percent. These analyses do not, however, account for variations in blade losses, which may accompany a change in the free-stream disturbance field.

Suryavamshi et al. (1998) reported total temperature and pressure measurements downstream of an embedded stator in a multistage axial compressor, which clearly show periodic circumferential variations associated with interactions between upstream rotor and stator wakes. Variations in efficiency of 2.5 percent between the best and worst rotor blades were observed at the stator midpitch location. Similar clocking effects in a multistage turbine were investigated numerically by Eulitz et al. (1996). They predicted an efficiency improvement of 0.4 percent when the dispersed wake street of an upstream stator was incident on the downstream vane, but the model assumed a fully turbulent flow and ignored unsteady wake-induced transition effects on the downstream vanes.

The recent experiments of Halstead et al. (1997), Solomon and Walker (1995a, b), and Solomon (1996) have indicated that transitional flow may cover as much as 70 percent of compressor airfoil suction surfaces and 50 percent of turbine airfoil suction surfaces in the presence of periodic wake disturbances. The periodic transitional or turbulent flow strips generated by wake disturbances are followed by regions of relaxing laminar flow with a shear stress higher than steady laminar flow levels. Independent studies of the latter phenomena in a compressor rotor (Cumpsty et al., 1995), turbine cascade (Schulte and Hodson, 1998) and triggered turbulent spot and compressor experiments (Gostelow et al., 1997) have shown these "calmed" regions to be more stable and resistant to separation than a steady laminar boundary layer flow. More extensive surveys of periodic transition effects and their importance in relation to blading design for axial turbomachines can be found in discussions by Hourmouziadis (1989), Mayle (1991, 1992), and Walker (1993).

The present paper investigates the influence on blade losses of free-stream disturbance field variations associated with wake dispersion and interaction effects in a 1.5-stage axial compressor. This is achieved by examining the influence of inlet guide vane (IGV) clocking on the viscous losses of the outlet stator blades. The work is partly motivated by an interest in wake-induced transition phenomena and a resulting desire to identify cases of interest for more detailed unsteady boundary layer measurements on the stator blades. We also wish to know how variations in free-stream unsteadiness produced by changing rotor–stator axial gaps might affect the performance characteristics of an axial turbomachine blade row. Will potential efficiency gains from reduced mixing losses in upstream blade wakes be enhanced or diminished by associated changes in downstream blade row losses as the axial gap is altered? And might such efficiency gains be accompanied by some other penalty such as reduced stall margin? The optimization of axial gap is outside the scope of this paper. However, the ultimate resolution of this problem requires a proper appreciation of the influence of wake mixing and interaction effects on blade losses.

Contributed by the International Gas Turbine Institute and presented at the 42nd International Gas Turbine and Aeroengine Congress and Exhibition, Orlando, Florida, June 2–5, 1997. Manuscript received at ASME Headquarters February 1997. Paper No. 97-GT-469. Associate Technical Editor: H. A. Kidd.

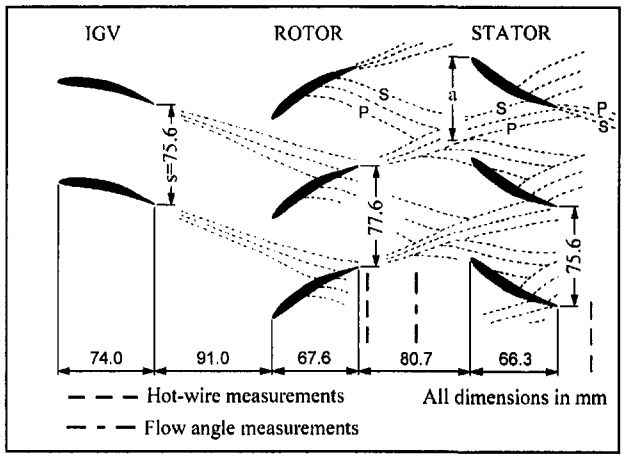

Fig. 1 Cross section of compressor blading at midpassage, showing typical instantaneous wake dispersion: *S* = suction side; *P* = pressure side

Experimental Detail

Research Compressor. Air enters the compressor radially through a cylindrical screened inlet 2.13 m diameter by 0.61 m wide. A flared bend with a 6.25 to 1 contraction ratio then turns the flow through 90 deg into a concentric cylindrical duct with 1.14 m outside diameter and 0.69 m inside diameter, which contains the compressor blade rows. Downstream of the compressor there is an annular diffuser, and a cylindrical sliding throttle at the outlet is used to control the throughflow.

The compressor is a 1.5-stage axial flow machine with three blade rows: inlet guide vanes (IGV), rotor, and stator. Figure 1 shows a cross section of the compressor blading at midpassage. There are 38 blades in each of the stationary rows and 37 blades in the rotor, giving space/chord ratios at midblade height of 0.99 and 1.02, respectively. The blades all have a constant chord of 76.2 mm and an aspect ratio of 3.0. The blade sections were designed for free vortex flow with 50 percent reaction at midblade height at a flow coefficient ($\phi = V_a/U_{mb}$) of 0.76. The design values of inlet and outlet blade angles from axial at midblade height are, respectively: IGV 0.0, 27.8 deg; rotor and stator 45.0, 14.0 deg. However, for these tests the rotor was restaggered by 2.0 deg to give blade angles of 43.0 and 12.0 deg with a resultant increase in stalling flow coefficient.

Instrument slots in the outer casing of the compressor allow radial and axial traversing of measuring probes at a fixed circumferential position. The IGV and stator rows are each mounted on rotatable supporting rings to permit circumferential traversing of these blades relative to a stationary probe or clocking of one row relative to the other.

Further details of the research compressor can be found in Oliver (1961), Walker (1972), and Solomon (1996).

Range of Investigation. All measurements were conducted at midspan, where radial flows are small. Data were obtained for flow coefficients ($\phi = V_a/U_{mb}$) of 0.600, 0.675, and 0.840. These correspond, respectively, to incidence values of 4.1, 1.2, and −6.1 deg, and will be referred to as high, medium, and low loading cases. The medium loading case is close to the Howell (1945) nominal incidence value of 0.6 deg.

A constant reference Reynolds number of $Re_{ref} = 120{,}000$ was used for all tests. This gives stator inlet Reynolds numbers of $Re_1 = 107{,}000$, 112,000, and 123,000 for the high, medium, and low loading cases. These values are low compared with those typical of aircraft gas turbine engine operation, as reported by Hourmouziadis (1989) and Mayle (1991); they are also generally lower than those in the experimental studies of Halstead et al. (1997). The test compressor was nevertheless operating above the critical Reynolds number range where laminar separation starts to cause a significant increase in blade losses (see Walker, 1975). As discussed by Solomon (1996), the critical Reynolds number for the test machine is lower than that for modern compressors because of the generally milder pressure gradients on the suction surface of C4 blading. Surface hot film observations on the stator blading reported by Solomon and Walker (1995a, b) show essentially similar behavior to that in the higher Reynolds number multistage compressor experiments of Halstead et al. (1997).

The influence of IGV clocking on the stator losses was investigated through hot-wire measurements acquired at an axial distance of 13.3 percent chord downstream of the stator for values of $a/s = 0.00$, 0.25, 0.50, and 0.75. The coordinate a is the circumferential distance of the stator leading edge from the center of the avenue of dispersed IGV wake segments, as shown in Fig. 1. Hot-wire observations were also obtained at an axial distance of 5.5 percent chord downstream of the rotor to indicate the stator inflow disturbance field. Measurements at this near-wake position indicate the IGV wake dispersion process without the complications of subsequent IGV wake–rotor wake interactions. They also give a clearer indication of unsteady rotor blade surface phenomena.

Measurement Techniques. The compressor and measurement systems were controlled by two IBM-compatible 486 personal computers. One computer was used to control the compressor and acquire data from slow response instrumentation. The other was used for high-speed data acquisition from the hot-wire anemometer. Operating speeds at $Re_{ref} = 120{,}000$ were typically 500 rpm, and the compressor speed was continuously adjusted with a speed setting accuracy of ±0.1 rpm to maintain constant Reynolds number. The throttle setting was left unchanged for an individual flow traverse, after setting the desired flow coefficient prior to the start of measurement.

Nomenclature

a = circumferential offset of stator blade leading edge from center of IGV wake avenue
c = blade chord
i = blade incidence
s = blade pitch
$s^* = y/s$ = dimensionless circumferential position
t = time
$t^* = t/T$ = dimensionless time
u = streamwise velocity
$\bar{u}_s$ = pitchwise average velocity
w_1 = relative inlet velocity
y = circumferential distance
$H = \delta^*/\theta$ = shape factor
$Re_1 = w_1 c/\nu$ = chord Reynolds number
$Re_{ref} = U_{mb} c/\nu$ = reference Reynolds number
T = rotor blade passing period
Tu = random disturbance level (turbulence)
Tu_D = total disturbance level
$\tilde{T}u$ = periodic disturbance level (unsteadiness)
U = local free-stream velocity
U_{inv} = hypothetical inviscid velocity
U_{mb} = rotor midspan velocity
V_a = mean axial velocity
α = flow angle from axial
δ^* = displacement thickness
$\phi = V_a/U_{mb}$ = flow coefficient
θ = momentum thickness
ν = kinematic viscosity

Superscripts

$\langle\ \rangle$ = ensemble (phase-lock) average value
$-$ = time-mean value
$'$ = instantaneous fluctuation from time mean
$''$ = instantaneous fluctuation from ensemble mean

Hot-wire measurements were obtained with a TSI IFA-100 system containing TSI Model 150 anemometer bridges and TSI Model 157 signal conditioners. A Dantec 55P03 probe with sensor and support both oriented radially was used for the measurements downstream of the rotor. Measurements behind the stator were obtained with a Dantec 55P01 probe oriented with the sensor parallel to the stator trailing edge. The latter probe was supported from downstream by a mounting tube aligned approximately with the local flow direction. The frequency response of the probes was better than 70 kHz. This is much higher than the rotor blade passing frequency of around 300 Hz in these tests.

The anemometer output was backed with a DC offset voltage and low-pass filtered at 20 kHz before sampling and digitizing at 50 kHz and data storage. The DC offset and signal amplification were adjusted automatically by the data acquisition computer for each spatial measurement point to optimize the signal to noise ratio. Ensemble-averaged values of measured quantities were obtained from 512 records, with sampling triggered at the same point on each rotor revolution from an optical encoder on the motor end of the drive shaft so that the wakes of the same rotor blades were observed in each record. Each record consisted of 1024 samples, and covered about six rotor blade passing periods. Circumferential traverses used 32 points per blade spacing, with a greater concentration of measurement points in wake regions. Time-mean flow data were determined from separate sets of observations with continuous sampling at random phase relative to the rotor motion and an averaging time of about 30 seconds.

The hot-wire probes were calibrated in situ in the compressor against velocity data obtained from prior measurements with slow response pressure probes. Calibration drift was monitored during each traverse and corrected by assuming a linear variation in the calibration with time. Velocity values were evaluated digitally for each sample point from the full dimensionless heat transfer relation for the probe, as discussed by Solomon (1996).

Preliminary hot-wire measurements downstream of the stator with different relative circumferential settings of the inlet guide vanes were conducted at $\phi = 0.675$ to determine the datum position ($a/s = 0$) corresponding to alignment of the stator leading edge with the center of the IGV wake avenue. The circumferential streamline shift with flow coefficient was then computed to estimate the corresponding datum stator positions for the other two loading cases. Subsequent detailed measurements indicate an accuracy of about 0.05 in the values of a/s. Circumferential traverses downstream of the stator were conducted by jointly indexing the IGV and stator rows relative to the fixed probe for each chosen IGV/stator index configuration a/s.

Slow response pressure measurements with a United Sensor CA-120 three-hole cobra probe were used to obtain pitch-averaged flow angle data at 54 percent chord axial distance upstream of the stator. Local pressure probe measurements over a range of compressor speeds were obtained at convenient stations in the hot-wire traverse planes to provide data for in-situ anemometer calibrations. No significant differences were observed between the calibration curves for different axial stations, even though some variable influence of flow unsteadiness on the slow response probe might have been expected.

Disturbance and Turbulence Level Analysis. The reduction of turbulence and unsteadiness data from the hot-wire measurements follows the procedure of Evans (1975) with some changes in notation. The instantaneous velocity may be expressed as

$$u = \bar{u} + u' = \langle u \rangle + u'' \tag{1}$$

where $\bar{u}$ is the long-term time-mean of a continuous record, and $\langle u \rangle(t_i)$ is the ensemble average of N samples at time t_i relative to the rotor phase reference, defined by

$$\langle u \rangle(t_i) = \frac{1}{N} \sum_{k=1}^{N} \{ u(t_i) \}_k \tag{2}$$

The ensemble-averaged velocity only exhibits blade-to-blade periodicity in the test machine, due to the equal blade counts in the IGV and stator rows.

The periodic disturbance level or "unsteadiness" is defined by

$$\tilde{T}u = (\langle u \rangle - \bar{u})_{\text{rms}}/U \tag{3}$$

Values of $\tilde{T}u$ must be evaluated from averages over an integral number of blade-passing periods.

The random disturbance level or "turbulence" associated with fluctuations about the ensemble average value is given by

$$Tu = u''_{\text{rms}}/U \tag{4}$$

and the total disturbance level associated with fluctuations about the long-term mean is given by

$$Tu_D = u'_{\text{rms}}/U \tag{5}$$

Assuming $(\langle u \rangle(t) - \bar{u})$ and u'' to be statistically independent, the three disturbance levels are related by

$$Tu_D^2 = \tilde{T}u^2 + Tu^2 \tag{6}$$

Observations and Discussion

IGV Wake Dispersion by Rotor. The variation of IGV wake dispersion with flow coefficient, obtained from a circumferential hot-wire traverse immediately downstream of the rotor, is shown in Fig. 2. These data were acquired by moving the IGV and stator rows together at a fixed circumferential offset ($a/s = 0.0$). This was done as a precaution even though previous measurements for the medium loading case had shown no measurable influence of the stator circumferential position on the unsteady flow field at this station. The data were obtained over one IGV pitch only, but have been plotted over two blade pitches by assuming pitchwise periodicity. Ensemble average velocity (nondimensionalized by pitchwise average time-mean velocity) is indicated by shading. The line contours indicate ensemble-averaged values of random velocity fluctuations about the ensemble mean (or "turbulence").

This figure represents the instantaneous spatial distribution that would be observed on a cylindrical surface if the flow disturbances were convected unaltered downstream of the measuring station with zero whirl. The variable s^* on the axis represents dimensionless circumferential position relative to the inlet guide vanes. Dimensionless time t^* on the abscissa has been plotted in the reverse direction so that the earliest observed points appear at the right, corresponding to the farthest downstream axial position. The data have been time-shifted to make the rotor–IGV relative circumferential position constant for each probe relative position s^*. This is necessary because the IGV was clocked relative to the trigger point, which was fixed relative to the machine and the probe.

The rotor wakes can be identified as the parallel bands of high turbulence running diagonally from bottom left to top right as in Fig. 1. The avenue of dispersed IGV wake segments runs horizontally from left to right. This differs from the picture in Fig. 1 because whirl velocity has been ignored. The suction and pressure surface sides of both IGV and rotor wakes (indicated by symbols S and P) are at the top and bottom of the wake regions, respectively.

The rotation of the IGV wake segments relative to the local flow direction increases with rotor blade loading as the flow coefficient is decreased from 0.840 to 0.600. The curvature of the IGV wake segments near the suction side of the rotor wake indicates a retardation of flow by the rotor suction surface boundary layer, which can be seen to thicken as loading is

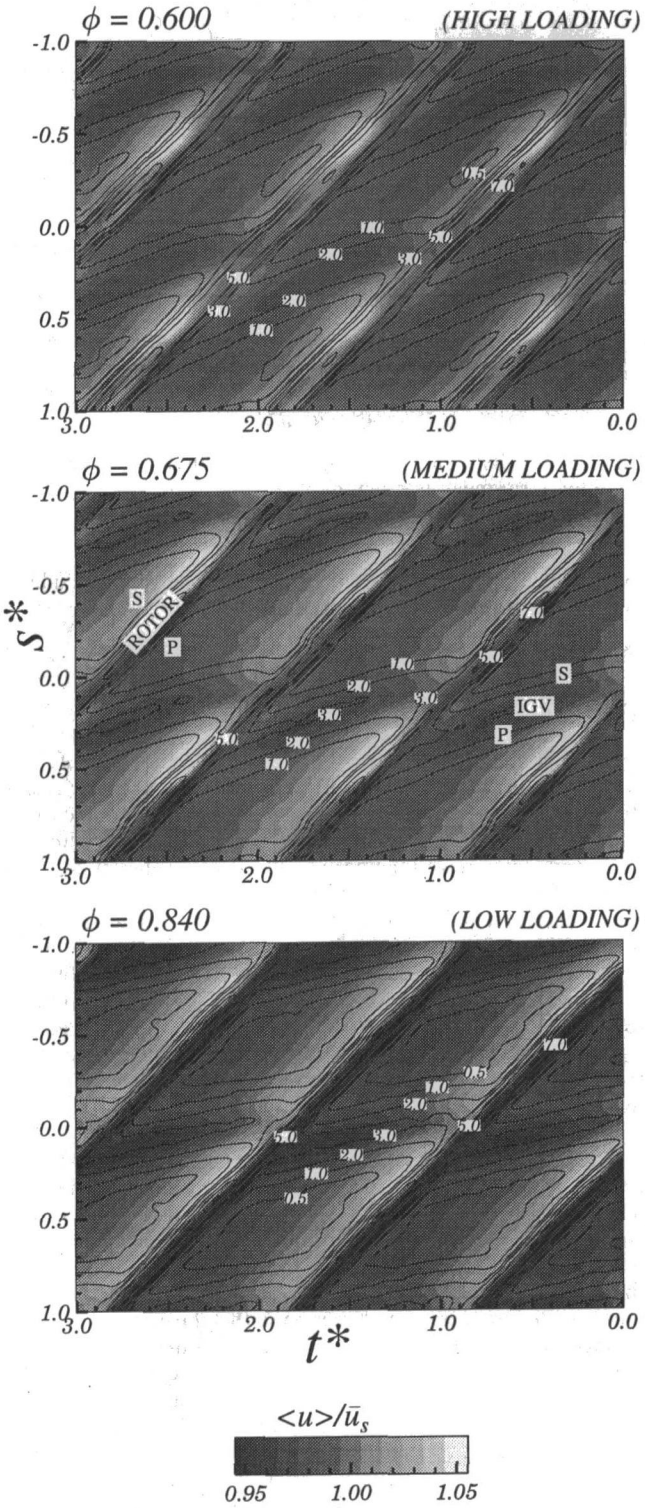

Fig. 2 Variation of IGV wake dispersion with flow coefficient. Hot-wire measurements 5.5 percent chord axially downstream of rotor trailing edge at midpassage. Line contours indicate ensemble average turbulence level, $\langle Tu \rangle$ (percent). Re_{ref} = 120,000. S = suction side; P = pressure side.

increased. This feature is very similar to the numerical predictions of Deregel and Tan (1996). The peak turbulence level in the IGV wakes is about 3 percent, while the minimum turbulence level in the free stream (corresponding to inflow regions uncontaminated by wakes) is about 0.5 percent.

The rotor wakes exhibit periodic variations in thickness indicative of blade loss fluctuations, and gradually thicken as loading is increased (as indicated by separation of the 1 percent turbulence contours). There is a strong gradient in ensemble-averaged velocity across the rotor blade passage at $\phi = 0.840$. This decreases as loading is increased, and is evidently a potential flow effect. A common feature observed at all loadings is a region of higher velocity in the corner between the suction side of the rotor wake and the pressure side of the IGV wake segment. This may be partly due to the negative jet effect of the relative flow in the IGV wake. The higher rotor wake turbulence level at low loading (which may appear anomalous) is thought to result from the proximity of the suction surface transition zone to the rotor blade trailing edge.

Stator Outlet Flow Field. Similar plots of the flow field downstream of the stator are presented in Fig. 4 for the medium loading case, $\phi = 0.675$. The stator wakes appear as horizontal bands of high turbulence. The suction and pressure sides of the various wake segments are again denoted by S and P. These figures have been complemented by the distributions of dimensionless time-mean velocity $\bar{u}/\bar{u}_s$ and total disturbance level Tu_D plotted at left. $\bar{u}_s$ is the pitchwise-averaged time-mean velocity.

Separate figures are shown for values of a/s = 0.00, 0.25, 0.50, and 0.75 to indicate the effect of clocking the stator relative to the IGV wake street. The case a/s = 0.00 nominally corresponds to the stator leading edge lying in the center of the IGV wake street, but the accuracy of positioning is at best 0.05. The IGV wake regions are again identified from the bands of higher turbulence level reaching values of over 2 percent. They are now more diffuse than at the rotor exit, and the minimum background turbulence level has risen to 1 percent. The minimum total disturbance level Tu_D is much higher at about 3 percent, indicating the effect of unsteadiness from passing rotor wakes. The clocking effect is clearly evident from the movement of the higher turbulence bands and associated concentrations of low-energy rotor wake fluid, which appear as darker regions of low ensemble average velocity. The peak turbulence level outside the stator wakes, which occurs near these low-velocity regions, reaches values of over 7 percent—a surprisingly high value for a compressor. There is a noticeably greater fluctuation in stator wake thickness for a/s = 0.25 and 0.50, which is most clearly evident on the suction side.

The circumferential variations of time-mean velocity and total disturbance level for different a/s values at the high loading case of $\phi = 0.600$ have been superimposed in Fig. 3 to indicate more clearly the effects of IGV clocking. Variations of up to 10 percent in $\bar{u}/\bar{u}_s$ and 3 percent in Tu_D outside the stator wake region can be seen to move in phase with the IGV wake street. The amplitude of these periodic circumferential variations in the mean flow is strongly loading dependent, and evidently associated with the strength of the rotor wakes. The variation in $\bar{u}/\bar{u}_s$ reduces to about 5 percent for $\phi = 0.675$ (see Fig. 4) and 2 percent for $\phi = 0.840$. The minimum values of Tu_D are again much higher than those of Tu, indicating a significant level of periodic fluctuation $\tilde{T}u$ in the free-stream region. Note that the local peak values of Tu_D outside the stator wakes correspond to circumferential positions where there is a lower time-mean velocity due to local accumulation of low-energy fluid within the rotor wakes. A similar feature, with lower amplitude, is evident in Fig. 4.

Evaluation of Stator Wake Properties. It is of interest to evaluate the stator wake properties to provide some quantitative indication of the influence of IGV clocking on stator losses. This is not a trivial problem, however, because of the nonuniform free stream outside the stator wake region. Figure 5 shows typical circumferential distributions of ensemble-averaged velocity and turbulence obtained downstream of the stator at several different values of dimensionless time t^*. The free-stream flow is not uniform at any stage, and there is a differential in free-stream velocity across the stator wake that changes sign with the phase of the rotor wake passage. These variations

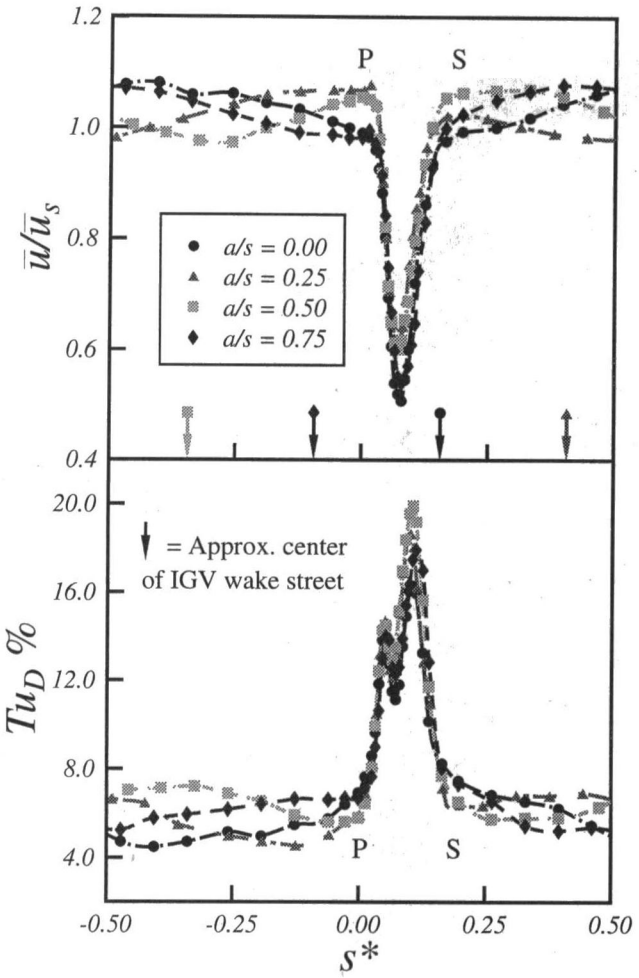

Fig. 3 Influence of IGV clocking on circumferential variation of time mean velocity and total disturbance level. Hot-wire measurements 13.3 percent chord axially downstream of stator trailing edge at midpassage. ϕ = 0.600, Re_{ref} = 120,000. *S* = suction side; *P* = pressure side.

may result from nonuniform energy addition, vortex shedding phenomena, redistribution of low-energy fluid associated with intrawake relative flows, or a combination of all three effects.

An algorithm for identifying the stator wake region was developed by examining changes in curvature of the ensemble-averaged velocity profile. It was considered that a local peak in curvature would generally occur just inside the wake boundary. This provided an adequate means of identification in the majority of cases, but there were still some situations where no distinct peak in curvature occurred. Such ambiguities were resolved by further considering changes in slope of the turbulence distributions, thus making possible a completely automatic processing of the wake data. A typical example of an ensemble-averaged velocity profile with the identified wake edge points is shown in Fig. 6.

Having decided on the wake boundaries, it is next necessary to prescribe an appropriate inviscid velocity distribution $U_{inv}(s^*)$ so that the wake properties can be evaluated. Two alternative models were considered:

(a) a constant value equal to the local velocity at the wake edge point; and

(b) a third-power polynomial of best fit to several points outside the wake edge.

The polynomial fit would be the more appropriate model if the free-stream region were a steady inviscid flow. However, that is not true in the present case where free-stream velocity variations may result from variable energy addition and loss redistribution phenomena.

For each of these models, the hypothetical inviscid distribution was extrapolated to the circumferential position corresponding to the minimum velocity within the wake. A discontinuity in the inviscid distribution was allowed to occur at this location, and momentum thickness values for the pressure and suction side shear layers were calculated separately from

$$\langle\theta\rangle/s = \int_0^1 \frac{\overline{u}/\overline{u}_s}{U_{inv}/\overline{u}_s}\left[1 - \frac{\overline{u}/\overline{u}_s}{U_{inv}/\overline{u}_s}\right]\cos\alpha ds^*\Big|_{t^*=\text{const}} \quad (7)$$

where α is the mean flow angle from axial. The separate thicknesses for the two shear layers were finally added to give the momentum thickness value for the whole wake.

It should be noted that purely inviscid flow modeling requires a velocity discontinuity within the wake region to represent the pressure differential that exists across a curved shear layer.

Influence of IGV Clocking on Stator Losses. A detailed discussion of compressor blade losses and their evaluation has been given by Cumpsty (1989). For steady two-dimensional cascade flow the wake momentum thickness at the normal outlet measuring station (around one chord length downstream of the blades) can be related to the total pressure loss coefficient for the cascade using the expression developed by Lieblein and Roudebush (1956).

It is assumed here that the values of wake momentum thickness evaluated by this procedure from the measurements 13.3 percent chord axial distance downstream of the stator trailing edge will be reasonably representative of the stator blade viscous losses. A significant proportion of the wake mixing losses will have occurred by this stage, where the maximum observed value of wake velocity profile shape factor H was about 1.4. All of the momentum thickness data presented here have been evaluated using the third-power polynomial fit for the hypothetical inviscid flow model. Momentum thickness values obtained from the constant inviscid velocity model are about 10 percent greater on average, and this indicates the order of accuracy that can be expected in the absolute values of momentum thickness. There are no detectable differences in behavior between these momentum thickness values and the total pressure loss coefficient values calculated from Lieblein and Roudebush's (1956) analysis.

Both the time-mean and ensemble-averaged values of wake momentum thickness are of interest. The time-mean value is relevant to blade row efficiency, while temporal variations in ensemble-averaged values provide information on periodic fluctuations in shear layer thickness associated with wake-induced transition on the stator blade surfaces. Studies by Cumpsty et al. (1995), Halstead et al. (1997), and Solomon and Walker (1995b) all provide evidence of a greater susceptibility to turbulent separation of the thicker boundary layer regions within wake-induced turbulent strips. It is therefore conceivable that an increased level of unsteadiness in wake properties could indicate reduced stall margins.

Figure 7 shows the influence of IGV clocking on the temporal variation of ensemble average stator wake momentum thickness for the medium loading case of ϕ = 0.675. Values of $\langle\theta\rangle/s$ have been evaluated at intervals of t^* = 0.03 and smoothed with a fourth-power best fit polynomial to five adjacent points on each side of the point under consideration. The variation of $\langle\theta\rangle/s$ with t^* is broadly sinusoidal, with phase differences of $\pm$0.1 in t^* according to the dimensionless IGV wake street location a/s.

The periodic variation in $\langle\theta\rangle/s$ noted previously from Fig. 4 is more clearly evident in Fig. 7. Its amplitude is greatest for a/s = 0.25 and 0.50, when the IGV wake street passes through the center of the blade passage and the stator blades are subjected to higher levels of periodic unsteadiness from the passing

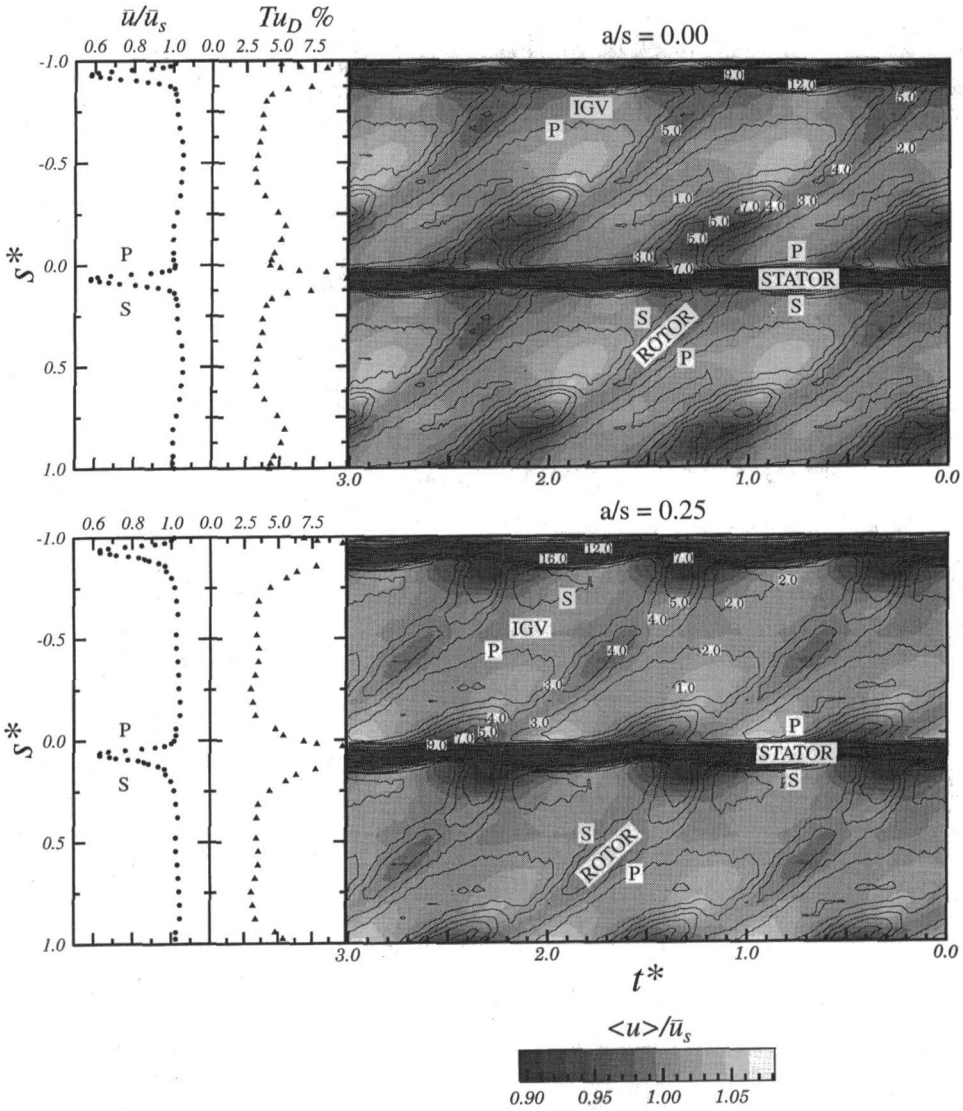

Fig. 4 Influence of IGV clocking on unsteady flow field downstream of stator. Hot-wire measurements 13.3 percent chord axially downstream of stator trailing edge at midpassage. *a/s* indicates circumferential position of stator blades relative to center of IGV wake street. Line contours indicate ensemble average turbulence level, $\langle Tu \rangle$ (percent). $\phi = 0.675$, $Re_{ref} = 120{,}000$. *S* = suction side; *P* = pressure side.

rotor wake disturbances. Here the maximum value of $\langle\theta\rangle/s$ is nearly four times the minimum.

The lowest level of unsteadiness in the stator wake thickness occurs for $a/s = 0.00$, when the IGV wake street is incident on the stator blade leading edge. Here the ratio of maximum to minimum $\langle\theta\rangle/s$ has fallen to around 2. This reduction is mostly due to an increase in the minimum value of $\langle\theta\rangle/s$, but the maximum value is nevertheless about 10 percent lower than that for $a/s = 0.50$.

The results for all three loading cases have been summarized in Table 1. The time-mean values of dimensionless wake momentum thickness $\overline{\theta}/s$ have been evaluated from an average of the ensemble means over three rotor blade passing periods. The degree of unsteadiness in the stator wake is indicated by the standard deviation in values of $\langle\theta\rangle/s$ over the same interval.

There is a consistent trend in the data for significantly higher values of wake unsteadiness, S.D. $(\langle\theta\rangle/s)$, at $a/s = 0.25$ and 0.50. The minimum value of S.D. $(\langle\theta\rangle/s)$ always occurs for $a/s = 0.00$, when the stator blades are immersed in the IGV wake street, although the unsteadiness for $a/s = 0.75$ is closely comparable.

It is difficult to draw firm conclusions on the values of time-mean wake thickness $\overline{\theta}/s$, as these show no clear trend. The fluctuation in $\overline{\theta}/s$ with a/s is similar in magnitude to the uncertainty in evaluating $\overline{\theta}/s$ from different models for $U_{inv}(s^*)$ for all three loading cases. Values of $\overline{\theta}/s$ for the minimum unsteadiness configuration of $a/s = 0.00$ are slightly less than the average for all a/s values with polynomial $U_{inv}(s^*)$ model; but with the constant $U_{inv}(s^*)$ model they tend to be about the average of $\overline{\theta}/s$ over all a/s values. In summary, the evidence favors a slight reduction in loss for the minimum unsteadiness configuration. At least, there is no suggestion of a serious performance decrement in this case. There is certainly no evidence here that would negate the conclusions of Eulitz et al.'s (1996) numerical study of the influence of IGV clocking on axial turbine performance.

It is stressed that only a single blade element has been considered here. The blade elements at different radii will lie at different values of a/s due to skewing of the IGV wake street associated with the radial flow distribution in the compressor. The integrated effect on performance for the whole stator blade will therefore be less than that for an isolated element. No significant

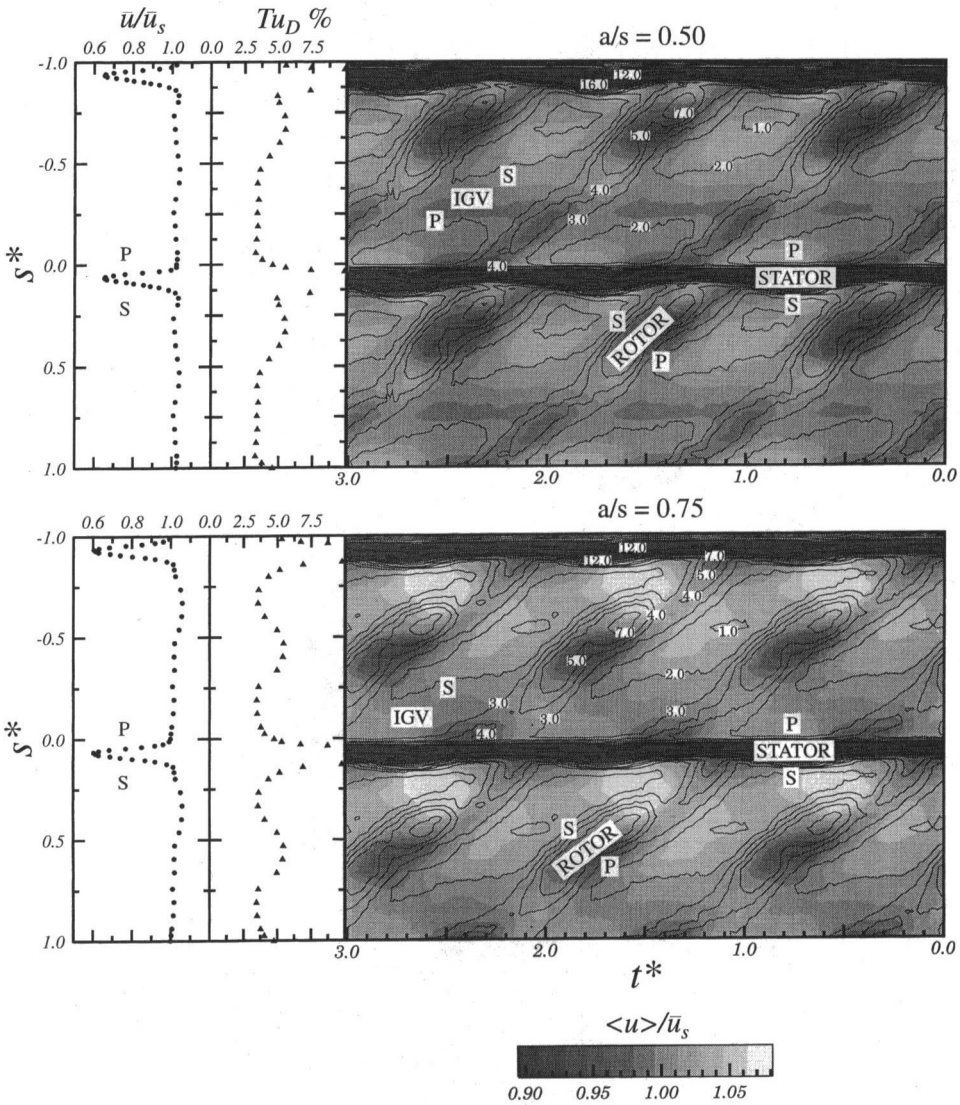

Fig. 4 (continued)

variation in flow coefficient could be detected with IGV clocking at constant throttle.

The fluctuations in ensemble-averaged stator wake thickness $\langle\theta\rangle/s$ for the minimum and maximum unsteadiness configurations of $a/s = 0.00$ and $a/s = 0.50$ are shown in Fig. 8 for all three loading cases. The suction and pressure side contributions to the total wake thickness are shown separately. While there may have been some decay in wake asymmetry in the 13.3 percent chord axial distance downstream of the trailing edge, these curves should give a useful indication of the loss fluctuations on the individual blade surfaces. Additional data obtained at 1.5 percent chord axial distance downstream of the stator for a more limited range of conditions are presented by Solomon (1996).

For $a/s = 0.00$ and $\phi = 0.840$ the pressure and suction side fluctuations are almost identical, with the exception of an asymmetric feature around $t^* = 0, 1, 2$, which is suggestive of potential flow interaction effects as the rotor wakes pass over the stator leading edge. This asymmetry develops with increases in loading to $\phi = 0.675$ and 0.600. There is a simultaneous increase in the relative thickness of the suction side layer, and a phase lead develops in the suction side perturbation due to the effects of blade circulation. The oscillations in individual shear layer thicknesses are clearly indicative of periodic wake-induced transition in the blade boundary layers. They closely resemble the measured boundary layer thickness fluctuations in the unsteady compressor cascade tests of Cumpsty et al. (1995) and the multistage compressor tests of Halstead et al. (1997). The fluctuations in total wake momentum thickness have developed harmonic content due to the combination of these two out-of-phase components.

The general behavior is quite similar for the maximum stator wake unsteadiness configuration of $a/s = 0.50$. However, there is much greater periodicity and the ratio of maximum to minimum momentum thickness is significantly greater for both shear layer components in all three loading cases. It is particularly interesting to note that the peak values of $\langle\theta\rangle/s$ for $a/s = 0.50$ are typically 10 percent higher than the corresponding values for $a/s = 0.00$. This suggests that the stator blades should be more resistant to intermittent separation and stall in the latter case, when the stator blades are immersed in the IGV wake street.

Physical Model for Stator Wake Unsteadiness. The amplitude of the stator wake unsteadiness can be explained in terms of transition phenomena on the blade surface. The peak momentum thickness corresponds to the boundary layer thickening caused by wake-induced transition initiated by the rotor wakes. This is slightly lower for the case $a/s = 0.0$, where the IGV wake street is incident on the stator blade and the amplitude

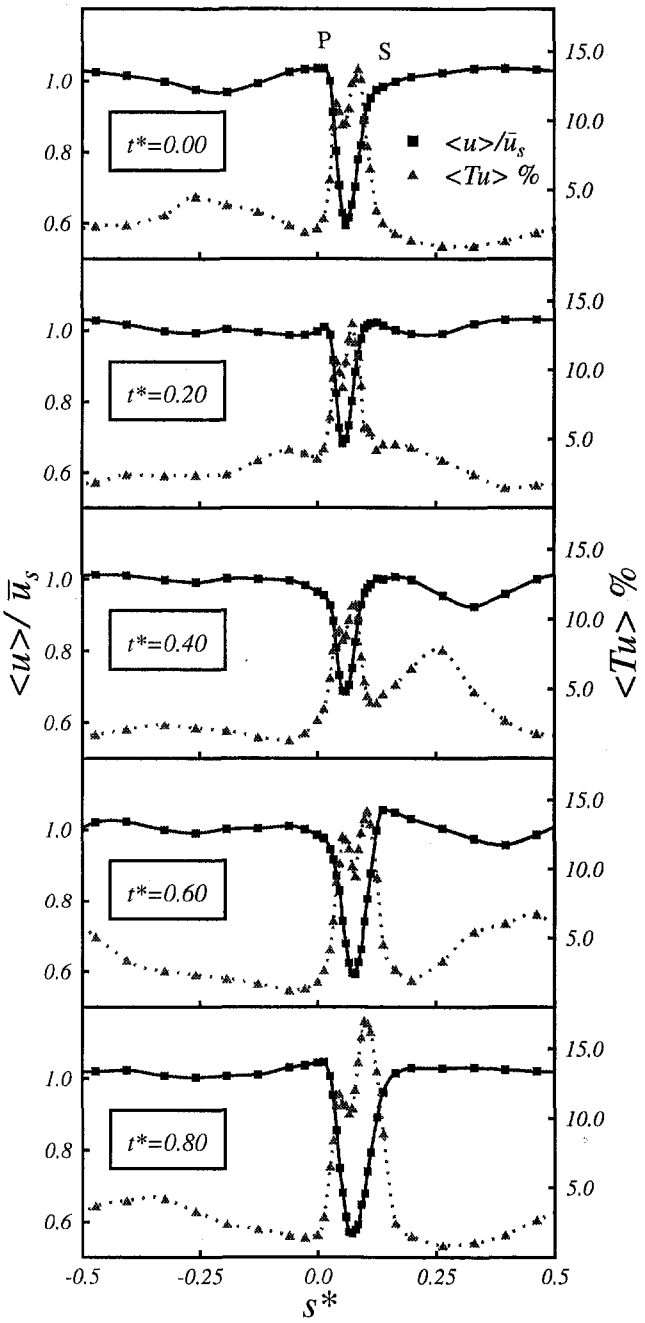

Fig. 5 Typical variation in circumferential distributions of ensemble mean velocity and turbulence with phase of rotor wake passage. Hot-wire measurements 13.3 percent chord axially downstream of stator trailing edge at midpassage. ϕ = 0.675, Re_{ref} = 120,000. *S* = suction side; *P* = pressure side.

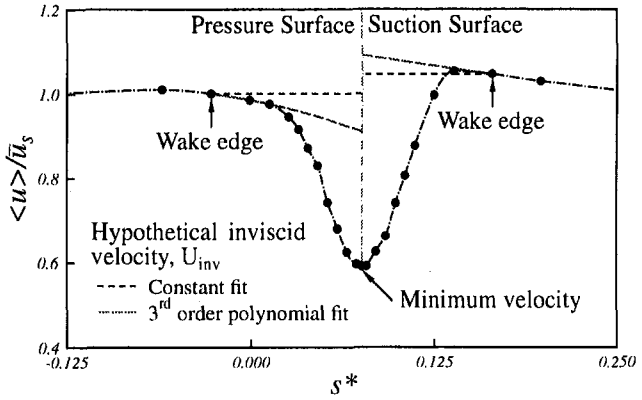

Fig. 6 Alternative models for inviscid velocity distribution used for computing stator wake properties

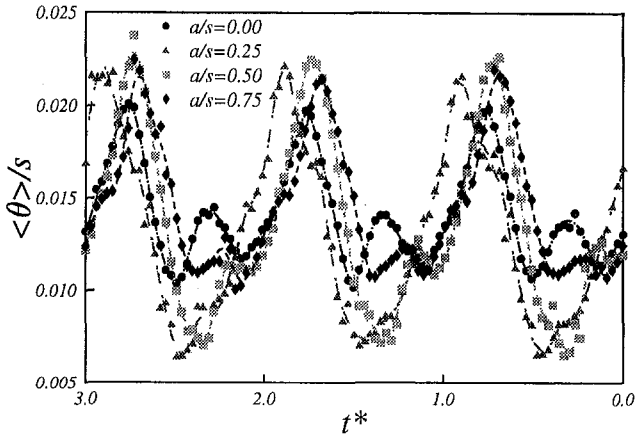

Fig. 7 Influence of IGV clocking on temporal variation of ensemble average stator wake momentum thickness. Hot-wire measurements 13.3 percent chord axially downstream of stator trailing edge at midpassage. ϕ = 0.675, Re_{ref} = 120,000.

of rotor wake disturbances is somewhat lower because of IGV wake–rotor wake interactions.

The minimum momentum thickness in the stator wake corresponds to later transition within the stator blade boundary layers in the region between the rotor wakes. This is controlled by other modes, principally bypass transition and separated flow transition. Bypass transition depends on the level of free-stream turbulence, which varies from the background inlet turbulence level of about 0.5 percent to around 3 percent within the IGV wake street.

While the peak turbulence in the IGV wakes varies little with loading, the average turbulence over the region between rotor wakes steadily increases with loading. This follows from the increased dispersion of IGV wakes associated with higher rotor circulation. It is interesting to note that the ratio of maximum to minimum stator wake thickness also decreases steadily as loading is increased. This is suggestive of stronger bypass transition between the rotor wakes causing a more uniform stator wake. Similar effects could be expected to occur with changes in rotor–stator axial gaps.

Table 1 Influence of IGV clocking and flow coefficient on time-mean stator wake thickness and stator wake unsteadiness

ϕ	a/s	$\bar{\theta}/s$	S.D. $(\langle\theta\rangle/s)$ (%)
0.600	0.00	0.0175	32
	0.25	0.0187	46
	0.50	0.0185	49
	0.75	0.0190	32
0.675	0.00	0.0153	29
	0.25	0.0143	51
	0.50	0.0146	51
	0.75	0.0157	37
0.840	0.00	0.0111	14
	0.25	0.0121	35
	0.50	0.0113	33
	0.75	0.0123	14

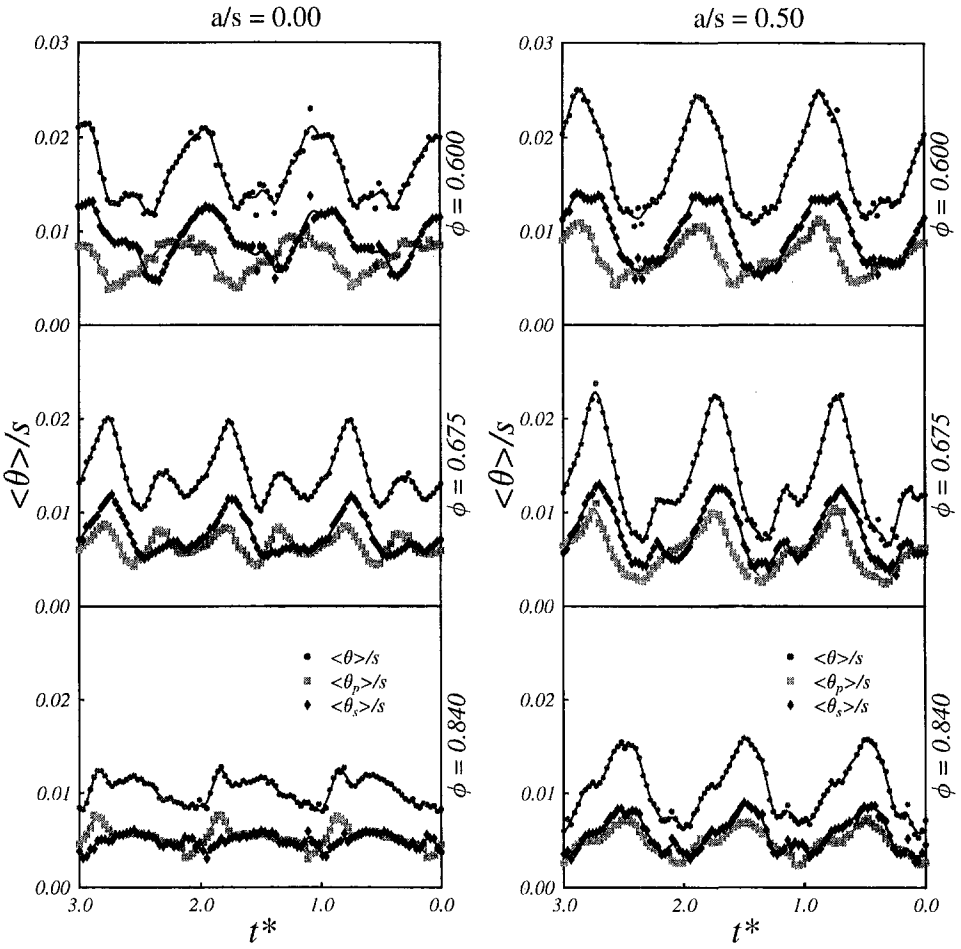

Fig. 8 Temporal variation of stator wake momentum thickness 13.3 percent chord axially downstream of stator trailing edge at midpassage, showing division into pressure and suction side components and influence of IGV clocking. Re_{ref} = 120,000

Conclusions

The dispersion of inlet guide vane wakes by the rotor, and subsequent interactions between the IGV and rotor blade wakes, produced regular circumferential variations in both the time-mean and unsteady flow downstream of the rotor in the test compressor. The influence of these variations on stator losses was examined through ensemble-averaged measurements of the stator wake properties.

Separate evaluation of the suction and pressure side momentum thickness components for the stator wake proved very useful. The individual components showed a lower harmonic content than the composite wake thickness, which was influenced by phase lags between periodic wake-induced phenomena on the stator blade suction and pressure surfaces.

Significantly lower amplitudes of periodic fluctuations in the stator wake were observed when the stator blades were immersed in the avenue of dispersed IGV wake segments. The peak values of shear layer thickness were always lower in this configuration.

It is considered that this should make the stator blades less susceptible to intermittent separation and stall. No firm conclusions could be drawn about the time-mean stator loss values in this case, as the observed variation in losses was comparable in magnitude with the uncertainty in the data. However, there was certainly no serious performance deterioration.

The unsteady variations of flow behavior on blade surfaces and in the wakes are strong and should be taken into account when determining blade clocking effects and rotor–stator axial gaps for axial turbomachines.

Acknowledgments

The authors wish to acknowledge the support of the Australian Research Council and Rolls-Royce plc.

They are also indebted to reviewers for their thorough consideration of the manuscript and helpful comments.

Mr. Jason Roberts provided valuable advice on typesetting of the manuscript.

References

Adamczyk, J. J., 1996, "Wake Mixing in Axial Flow Compressors," ASME Paper No. 96-GT-29.

Cumpsty, N. A., 1989, *Compressor Aerodynamics,* 1st ed., Longman Scientific & Technical.

Cumpsty, N. A., Dong, Y., and Li, Y. S., 1995, "Compressor Blade Boundary Layers in the Presence of Wakes," ASME Paper No. 95-GT-443.

Deregel, P., and Tan, C. S., 1996, "Impact of Rotor Wakes on Steady-State Axial Compressor Performance," ASME Paper No. 96-GT-253.

Eulitz, F., Engel, K., and Gebing, H., 1996, "Numerical Investigation of Clocking Effects in a Multistage Turbine," ASME Paper No. 96-GT-26.

Evans, R. L., 1975, "Turbulence and Unsteadiness Measurements Downstream of a Moving Blade Row," ASME *Journal of Engineering for Power,* Vol. 97, pp. 131–139.

Gostelow, J. P., Walker, G. J., Solomon, W. J., Hong, G., and Melwani, N., 1997, "Investigation of the Calmed Region Behind a Turbulent Spot," ASME JOURNAL OF TURBOMACHINERY, Vol. 119, pp. 802–809.

Halstead, D. E., Wisler, D. C., Okiishi, T. H., Walker, G. J., Hodson, H. P., and Shin, H.-W., 1997, "Boundary Layer Development in Axial Compressors and Turbines: Parts 1–4," ASME JOURNAL OF TURBOMACHINERY, Vol. 119, Part 1: pp. 114–127; Part 2: pp. 426–444; Part 3: pp. 225–237; Part 4: pp. 128–139.

Hourmouziadis, J., 1989, "Aerodynamic Design of Low Pressure Turbines," pp. 8-1–8-40, Fottner, L., ed., *AGARD Lecture Series No. 167, Blading Design for Axial Turbomachines,* AGARD.

Howell, A. R., 1945, "Fluid Dynamics of Axial Compressors," *Proc. Inst. Mech. Eng. E,* Vol. 153, pp. 441–452.

Kerrebrock, J. L., and Mikolajczak, A. A., 1970, "Intra-Stator Transport of Rotor Wakes and Its Effect on Compressor Performance," ASME *Journal of Engineering for Power,* Vol. 92, pp. 359–368.

Lieblein, S., and Roudebush, W., 1956, "Theoretical Loss Relations for Low-Speed Two-Dimensional Cascade Flow," NACA TN 3662.

Lockhart, R. C., and Walker, G. J., 1974, "The Influence of Viscous Interactions on the Flow Downstream of an Axial Compressor Stage," presented at the 2nd International Symposium on Air Breathing Engines.

Mayle, R. E., 1991, "The Role of Laminar–Turbulent Transition in Gas Turbine Engines," ASME JOURNAL OF TURBOMACHINERY, Vol. 113, pp. 509–537, The 1991 IGTI Scholar Lecture.

Mayle, R. E., 1992, "Unsteady Multimode Transition in Gas Turbine Engines," AGARD PEP 80.

Oliver, A. R., 1961, "Comparison Between Sand Cast and Machined Blades in the Vortex Wind Tunnel," Report ME 103, Aeronautical Research Laboratories, Melbourne, Australia.

Schulte, V., and Hodson, H. P., 1998, "Unsteady Wake-Induced Boundary Layer Transition in High Lift LP Turbines," ASME JOURNAL OF TURBOMACHINERY, Vol. 120, pp. 28–35.

Smith, L. H., Jr., 1966, "Wake Dispersion in Turbomachines," ASME *Journal of Basic Engineering,* Vol. 88, pp. 688–690.

Solomon, W. J., and Walker, G. J., 1995a, "Incidence Effects on Wake-Induced Transition on an Axial Compressor Blade," *Proc. 12th Int. Symp. on Air Breathing Engines,* Vol. 2, pp. 954–964, ISABE 95-7088, Melbourne.

Solomon, W. J., and Walker, G. J., 1995b, "Observations of Wake-Induced Transition on an Axial Compressor Blade," ASME Paper No. 95-GT-381.

Solomon, W. J., 1996, "Unsteady Boundary Layer Transition on Axial Compressor Blades," Ph.D. Thesis, University of Tasmania.

Suryavamshi, N., Lakshminarayana, B., and Prato, J., 1998, "Aspirating Probe Measurements of the Unsteady Total Temperature Field Downstream of an Embedded Stator in a Multistage Axial Flow Compressor," ASME JOURNAL OF TURBOMACHINERY, Vol. 120, pp. 156–169.

Walker, G. J., 1972, "An Investigation of the Boundary Layer Behaviour on the Blading of a Single-Stage Axial-Flow Compressor," Ph.D. Thesis, University of Tasmania.

Walker, G. J., 1974, "The Unsteady Nature of Boundary Layer Transition on an Axial Compressor Blade," ASME Paper No. 74-GT-135.

Walker, G. J., 1975, "Observations of Separated Laminar Flow on Axial Compressor Blading," ASME Paper No. 75-GT-63.

Walker, G. J., 1993, "The Role of Laminar–Turbulent Transition in Gas Turbine Engines—A Discussion," ASME JOURNAL OF TURBOMACHINERY, Vol. 117, pp. 207–217.

Zierke, W. C., and Okiishi, T. H., 1982, "Measurement and Analysis of Total-Pressure Unsteadiness Data From an Axial Compressor Stage," ASME *Journal of Engineering for Power,* Vol. 104, pp. 479–488.

Reduction of Unsteady Blade Loading by Beneficial Use of Vortical and Potential Disturbances in an Axial Compressor With Rotor Clocking

S. T. Hsu
Doctoral student.

A. M. Wo
Associate Professor.
andrew@spring.iam.ntu.edu.tw

Institute of Applied Mechanics,
National Taiwan University,
Taipei 106, Taiwan

This paper demonstrates reduction of stator unsteady loading due to forced response in a large-scale, low-speed, rotor/stator/rotor axial compressor rig by clocking the downstream rotor. Data from the rotor/stator configuration showed that the stator response due to the upstream vortical disturbance reaches a maximum when the wake impinges against the suction surface immediately downstream of the leading edge. Results from the stator/rotor configuration revealed that the stator response due to the downstream potential disturbance reaches a minimum with a slight time delay after the rotor sweeps pass the stator trailing edge. For the rotor/stator/rotor configuration, with Gap1 = 10 percent chord and Gap2 = 30 percent chord, results showed a 60 percent reduction in the stator force amplitude by clocking the downstream rotor so that the time occurrence of the maximum force due to the upstream vortical disturbance coincides with that of the minimum force due to the downstream potential disturbance. This is the first time, the authors believe, that beneficial use of flow unsteadiness is definitively demonstrated to reduce the blade unsteady loading.

1.0 Introduction

Multistage turbomachinery blades experience fluid-induced, unsteady force either due to self-excited instability or forced response. The first situation arises when a blade is able to extract energy from the upstream *steady* flow in order to sustain its own unsteady motion. The latter case involves flow disturbances, or gust, which usually arise due to the passing of upstream wakes, potential effect from upstream and downstream blade rows, and other time-varying local flows. In both situations, disastrous blade failure can occur when the excitation force is beyond the structural limit of the blade.

Forced response had been studied by many researchers. Theoretical work on unsteady disturbances includes Goldstein and Atassi (1976) and Goldstein (1978). Excellent series of experiments (Henderson and Fleeter, 1993a, b; Feiereisen et al., 1994; Weaver and Fleeter, 1994) were conducted by Professor Fleeter and his students on illuminating the physics of vortical and potential disturbances. Gallus et al. (1982) also studied potential and wake interactions experimentally. The work by Manwaring and Wisler (1993) provided extensive comparison between the state-of-the-art analysis methods and data. Chung and Wo (1997) used both Navier–Stokes and panel codes to split the gust between blade rows into vortical and potential contributions, and Wo et al. (1997) provided details on decomposition of gust response. Although the researchers aforementioned differ somewhat in their approach to decomposing disturbances into vortical and potential contributions, all agree that both need to be considered for loaded compressors and turbines, especially at small axial gap.

Clocking, or indexing, of blade rows had been conducted in a few studies. Capece and Fleeter (1987) circumferentially clocked the first and second stator rows independently to study their effects on aerodynamic forcing function input to the downstream stator row, and its gust response. This form of clocking mostly affected the chordwise gust of the aerodynamic function, with a small effect on the overall blade unsteady loading, since the clocked stators upstream were in the same reference frame as the downstream stator of interest. Manwaring and Wisler (1993) clocked both the IGV of the GE compressor and the inlet nozzle of the turbine in order to average the effect of their wakes on the instrumented stationary blades downstream. The authors believe that the present study is the first that documented concrete reduction of unsteady blade loading using clocking.

2.0 Objective and Approach

This paper attempts to test a straightforward hypothesis: Distinct physical sources of disturbance will cause a unique "footprint" on the unsteady blade response, and these "footprints" may partially cancel each other if, somehow, their phase relationship can be altered. This hypothesis will be tested experimentally for a rotor/stator/rotor compressor with the focus on the stator unsteady response. Sources of unsteadiness experience by the stator include[1]

1 vortical disturbance from the *upstream* rotor ($R1$),
2 potential disturbance from the *upstream* rotor and
3 potential disturbance from the *downstream* rotor ($R2$).

These are shown in Fig. 1, calculated using a Navier–Stokes code (Chung and Wo, 1997).

To test the hypothesis and to provide physical insight, the following approach is taken: First, a *rotor/stator* configuration

Contributed by the International Gas Turbine Institute and presented at the 42nd International Gas Turbine and Aeroengine Congress and Exhibition, Orlando, Florida, June 2–5, 1997. Manuscript received at ASME Headquarters February 1997. Paper No. 97-GT-86. Associate Technical Editor: H. A. Kidd.

[1] To address the issue of the importance of entropic disturbance raised by a reviewer, consider the linearized disturbance $Ds'/Dt = (Cv/P_0)Dp'/Dt - (Cp/\rho_0)D\rho'/Dt$ (Kerrebrock, 1992), where the subscript 0 denotes the mean state and the superscript $'$ denotes disturbed state. In the present experiment the change in the particle density term can be ignored since the stator inlet Mach number is 0.113. An order of magnitude calculation shows the entropic disturbance is less than 1 percent of the pressure disturbance.

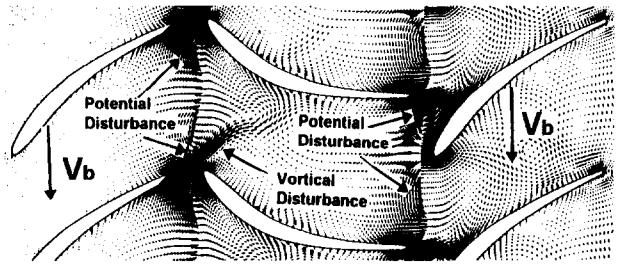

Fig. 1 Sources of disturbance acting on the stator: vortical and potential disturbances from upstream and potential disturbance from downstream (Navier–Stokes calculation)

Table 1 General compressor and blade parameters at design condition

	IGV	Rotor (R1 or R2)	Stator
Blade Number	60	58	60
Chord (cm), C	6.00 (2.36in.)	6.00 (2.36in.)	6.00 (2.36in.)
Span (cm), S	8.88 (3.50in.)	8.88 (3.50in.)	8.88 (3.50in.)
Solidity	1.415	1.368	1.415
Tip Clearance (cm)	0.12 (2.0%C)	0.12 (2.0%C)	0.12 (2.0%C)
Aspect Ratio (S/C)	1.48	1.48	1.48
Trailing Edge Radius	1.0 %C	1.0 %C	1.0 %C
Stagger (deg.)	6.58 °	-39.50 °	20.67 °
Camber (deg.)	3.2 °	35.0 °	48.0 °
Inlet Angle, β 1 (deg.)*	0.0 °	56.21 °	46.80 °
Exit Angle, β 2 (deg.)*	9.78 °	31.03 °	4.76 °
Diffusion Factor	-	0.407	0.485
Axial Gap (% chord)	175%		variable; see text
Casing Diameter (cm)			90.0 (35.43 in.)
Hub/Tip Ratio			0.8
Mass Flow Coefficient			0.53 to 0.70
Shaft Speed (RPM)			1050 (max. 1500)
Reduced Frequency ($\omega C/2C_x$)			7.161
Mach number (C_x/a)			0.0776
Reynold's Number at 1050RPM (rotor relative)			1.92×10^5

* from hot-wire at mid-gap, mid-pitch, for axial gap of 30% chord.

is tested to study the first two sources of unsteadiness. The axial gap between the rotor and stator is varied since the gap can affect the stator response due to the potential contribution. Second, a *stator/rotor* configuration is studied to focus on the third source of unsteadiness considered. Third, a *rotor/stator/rotor* configuration is tested to account for all three sources. The circumferential relative positions between the two rotor rows are adjusted, or *clocked,* to vary the phase relationship among the unsteady sources, with the ultimate goal of minimizing the stator unsteady response. This goal is justified since a small percentage reduction in the blade force amplitude can lead to a substantial increase in blade life, as suggested by the blade stress-cycle, or Goodmann, diagram.

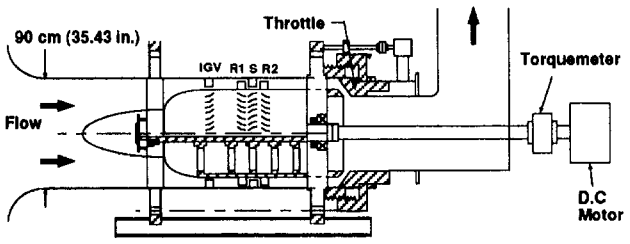

Fig. 2 Experimental compressor in the rotor/stator/rotor configuration

3.0 Experimental Setup

The experimental compressor is a low-speed, large-scale, one-to-three stage rig, designed after modern compressors; see Table 1 and Fig. 2. Flow enters the compressor through a bell-mouth contraction and into the constant blade height annulus. The IGV trailing edge is located 1.75 chord upstream of the rotor leading edge to allow for wake dissipation. The blades were designed using the controlled diffusion concept of Hobbs and Weingold (1984), with the coordinates provided in the appendix. Two special features are designed in the rig; axial gaps between blade rows are variable, from 10 to 60 percent chord, and the clocking position between rotor rows can be adjusted.

The measured static-to-static pressure rise characteristic is shown in Fig. 3. The pressure rise obtained is believed to be representative of highly loaded blade of modern design. In this work, tests were conducted at near-design loading ($\Phi = 0.60$) and high loading ($\Phi = 0.53$). The compressor achieves an

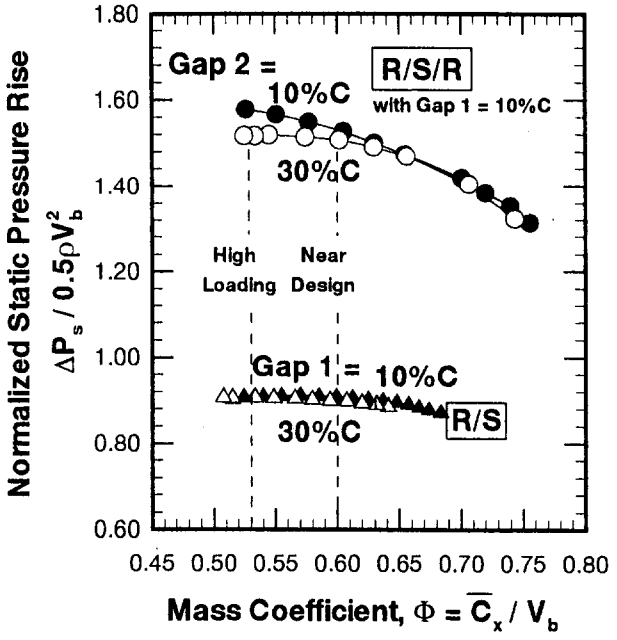

Fig. 3 Measured static-to-static pressure rise characteristic for rotor/stator and rotor/stator/rotor configurations with varying axial gaps

Nomenclature

C = chord
F_n = force on the stator, normal to chord
P = static pressure
S = blade pitch
t, T = time, blade-to-blade period
$\mathbf{V}_b$ = rotor blade wheel velocity vector
v^+ = transverse component of unsteady velocity
ρ = density of fluid
Φ = flow coefficient
C_x = axial velocity
ΔP_s = static pressure rise
$\overline{\ }$ = time mean
$\sim$ = unsteady part, instantaneous minus time mean

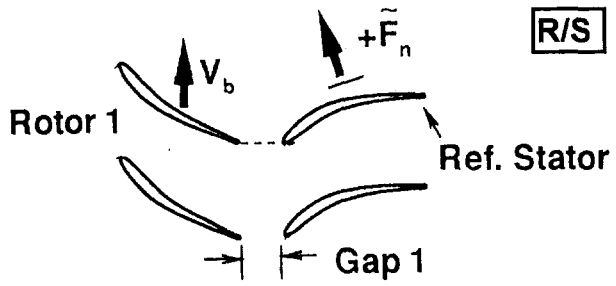

Fig. 4 Rotor/stator configuration at time $t/T = 0.0$; rotor trailing edge is axially upstream of the stator leading edge. Direction of *positive* stator force, normal to chord, is also shown.

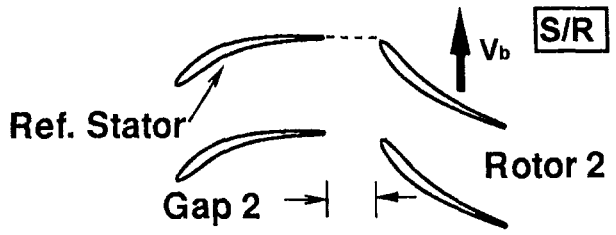

Fig. 5 Stator/rotor configuration at time $t/T = 0.0$; rotor leading edge is axially downstream of the stator trailing edge

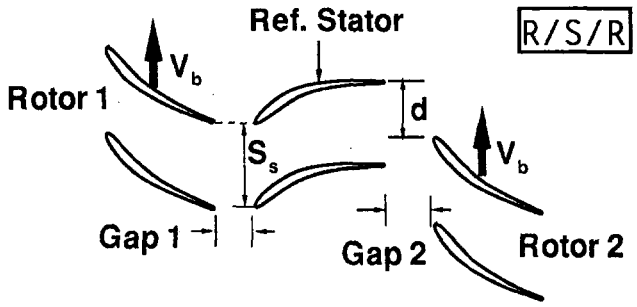

(a)Rotor/Stator/Rotor configuration at clocking = d/S_s

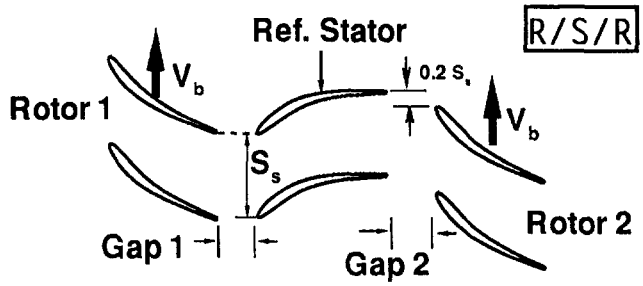

(b)Rotor/Stator/Rotor configuration at clocking = 0.2

Fig. 6 Rotor/stator/rotor configuration at time $t/T = 0.0$ with downstream rotor clocked by d/Ss. Figure (*a*) shows clocking = 0.7 and (*b*) clocking = 0.2.

efficiency, based on static-to-static pressure rise, of slightly over 90 percent for rotor/stator configuration at both 10 and 30 percent chord axial gaps.

In this work, three compressor configurations were tested: rotor/stator, stator/rotor and rotor/stator/rotor, as sketched in Figs. 4, 5, and 6, respectively. In all these figures, the dash lines defined the blade relative position at time $t/T = 0.0$ in an unsteady period. Figure 4 shows the definition of *positive* stator unsteady force normal to the chord, which is used throughout this work for all configurations. In the stator/rotor configuration, a row of upstream rotors, with its trailing edge located two chord-lengths upstream of the stator leading edge, provided correct flow angles entering the stators. To establish the baseline for this arrangement, tests were conducted with the upstream rotors and the stators but without the downstream rotors. The gust at the stator leading edge plane was measured to be less than 2 percent of the time mean flow, and the stator response was also measured, which was subtracted from all stator/rotor data reported herein. For the rotor/stator/rotor configuration, Fig. 6 serves to define the *clocking* between Rotor 1 and Rotor 2, which is the distance that the leading edge of Rotor 2 is offset circumferentially from the stator trailing edge when the Rotor 1 trailing edge is axially upstream of the stator leading edge. In the compressor rig, the hub was designed in three cylindrical pieces, each can mount a row of rotor blades (thus the rig can be tested as a three-stage compressor), with the two downstream pieces movable circumferentially up to one blade pitch with respect to the adjacent piece.

The unsteady pressure on the stator suction and pressure surfaces were measured using fast-response pressure transducers (Kulite LQ-125), which were embedded within two adjacent blades (10 transducers per surface). The system response, calculated from Doebelin (1990), was found to be determined by the isolated transducer alone. Transducer signals of 128 data points in a rotor blade-to-blade period were acquired per shaft revolution, thus data from the *same* rotor wake were recorded. The pressure transducer output, as a differential signal, was connected to a low-noise amplifier (Stanford Research SR560), then digitized with a 12-bit analog-to-digital resolution. The accuracy of the surface pressure measurement is ±3 percent determined from calibration.

To provide timing information, a photo-sensitive diode was used to sense the passing of a metal protrusion rotating with the shaft, with a timing accuracy of 0.1 percent of a blade-to-blade period. To preserve the time series, an analog filter was not used prior to digitization, but the signal was monitored using a spectrum analyzer (HP 3561A); no high-frequency content exists that could alias the blade-to-blade frequency and next few higher modes. Moreover, phase-locked averaging technique was also used to filter non-blade-to-blade periodic signals (240 typical ensembles were used).

Hsu et al. (1996) provides details on gust measurement using the slanted hot-wire technique, with an accuracy from calibration of ±1 percent in magnitude and ±1.5 deg in flow angles.

4.0 Rotor/Stator Results: Vortical and Potential Disturbances From Upstream of Stator

The rotor/stator configuration includes the effect of (*a*) rotor wake impinging upon the stator and subsequent wake convection along the stator passage, and (*b*) the potential field of the

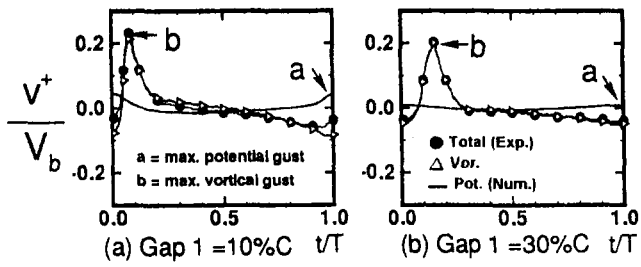

Fig. 7 Vortical and potential transverse guests at the midgap point axially upstream of the stator leading edge (*R/S*)

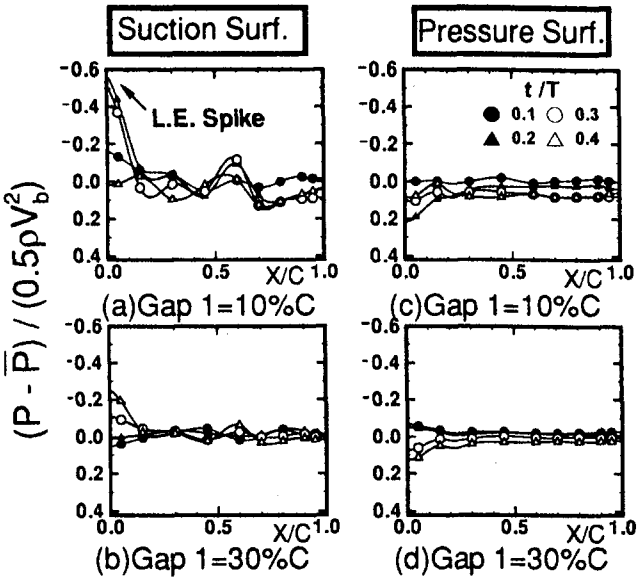

Fig. 8 Unsteady pressure on the stator surfaces with varying axial gap (*R/S*)

rotor on the stator. Results due to these two phenomena follow for two axial gaps, Gap1 = 10 and 30 percent chord.

4.1 Vortical and Potential Disturbances. Figure 7 presents the transverse vortical and potential gusts decomposed from slanted hot-wire data using the procedure described in Hsu et al. (1996) (also see Chung and Wo (1997), which used Navier–Stokes results where Hsu et al. used experimental data). The hot-wire was located axially upstream of the stator leading edge at the midgap position for both 10 and 30 percent chord gap cases.

The vortical gust signature shows an abrupt increase as the wake passes, which is the dominant feature for both gap cases. The vortical contribution essentially represents the total (prior to decomposition) transverse gust, since the potential contribution is small even at 10 percent chord gap between blade rows. Figure 7 thus provides further justification for using wake/blade calculation to model the unsteady effect from the upstream blade on the downstream blade (e.g., Giles, 1988, and Hall and Crawley, 1989). Moreover, the distinct difference in time scale between the vortical and potential gusts—the vortical gust on the order of passing of the wake width and the potential gust being blade-to-blade period—can be clearly seen.

In this work, it is important to note the time when the gust reaches a maximum since phase information is vital to test the hypothesis stated in Section 2.0. Location *a* represents the maximum value of the potential gust, which occurs at t/T =

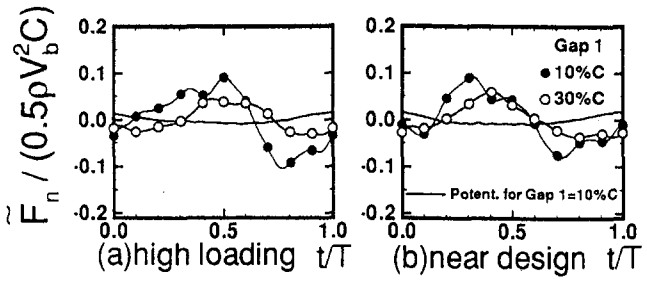

Fig. 9 Unsteady force on stator due to total and potential contributions with varying axial gap (*R/S*)

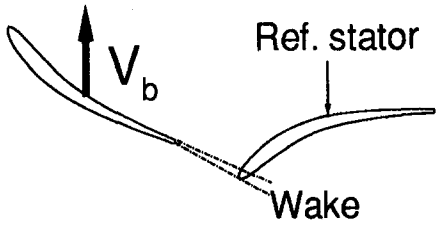

Fig. 10 Sketch of the time instant when the stator force reaches maximum (*R/S*)

1.0, or 0.0; this coincides with the time instant when the rotor trailing edge is axially forward of the stator leading edge, as shown in Fig. 4. The location marked *b* represents the instant when the vortical gust is largest, which occurs at the time when the wake passes the hot-wire. Thus, the maximum vortical gust occurs when the rotor wake passes and the maximum potential gust occurs when the rotor blade itself passes. The time occurrence of location *a* precedes that of *b* due to the rotor exit flow angle.

4.2 Stator Unsteady Loading. Figure 8 shows the near-design stator unsteady pressure on the suction and pressure surfaces for several time instants of interest. As can be seen spatial pressure variation is generally greater on the suction than that on the pressure surface, with a strong spike near the leading edge on the suction surface. This is due to the rotor wake impinging near the stator leading edge region, as confirmed by the time occurrence of maximum vortical gust (Fig. 7) essentially coinciding with that of the pressure spike. The pressure spike occurs near t/T = 0.2 for 10 percent chord gap and t/T = 0.4 for 30 percent chord gap, which agree well with the wake impinging near the leading edge at t/T = 0.16* for 10 percent chord gap and t/T = 0.32[2] for 30 percent chord gap. The slight time delay between the pressure spike and the wake impingement suggests the response reaches a maximum when the wake arrives on the suction surface just downstream of the leading edge.

Secondary in importance is the pressure variation along the surface, as seen most prominently in Fig. 8(*a*). Navier–Stokes calculation, which provides greater flow details within the stator passage, suggests that this is related to the wake requiring two blade-to-blade periods to convect through the stator passage on the suction surface. Numerics show that at time t/T = 0.3 the wakes are located near the leading edge and at x/C = 0.6 on the suction surface. Vorticity contour results suggest there is a region of concentrated vorticity adjacent to the suction surface at x/C = 0.6, which corresponds to the pressure variation near x/C = 0.6 in Fig. 8(*a*). This is likely related to the work of Valkov and Tan (1995) which provides insight into the convection of so-called "B-vortices" on the suction surface. These vortices are formed upon wake impingement on the leading edge and move along the suction surface, which resulted in local pressure variation.

Figure 9 shows the stator unsteady force, in the direction normal to the chord, obtained by integrating the unsteady pressure of Fig. 8. Results are shown for the total force, from surface Kulite output, and the potential contribution. The near-design loading result shows that the maximum unsteady force occurs at t/T = 0.3 for 10 percent chord gap and t/T = 0.4 at 30 percent chord gap. These times are in reasonable agreement with that of the pressure spike (t/T = 0.2 for 10 percent chord gap and t/T = 0.4 for 30 percent chord gap) of Fig. 8. Thus

[2] This value is twice that corresponding to the maximum vortical gust in Fig. 7 since the data of Fig. 7 were obtained with the hot-wire located at the midgap position.

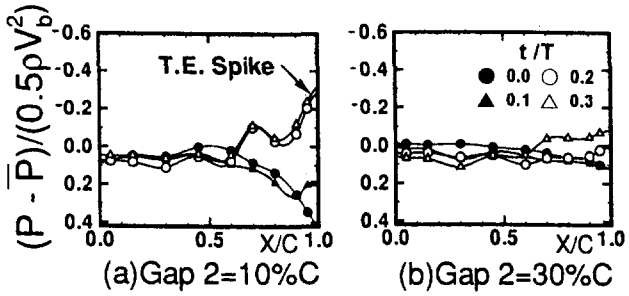

Fig. 11 Unsteady pressure on stator suction surface when the downstream rotor passes (*S/R*)

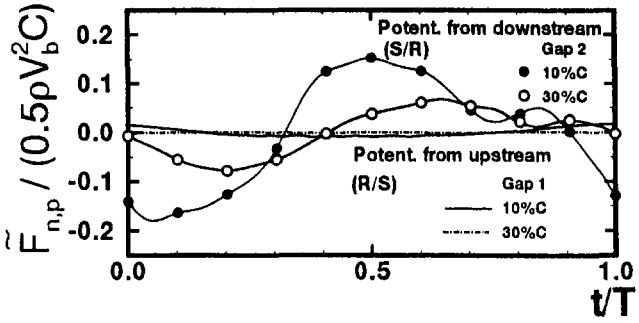

Fig. 13 Potential contributed stator force from upstream (*R/S*) and downstream (*S/R*)

the maximum stator force occurs when the upstream wake impinges on the stator suction surface immediately downstream of the leading edge, as illustrated in Fig. 10.

The potential contribution in Fig. 8 is shown to be small even for 10 percent chord gap between blade rows. Thus the total force in Fig. 9 is almost entirely due to vortical contribution. This fact greatly simplifies testing of the hypothesis for rotor/stator/rotor configuration since the balance between unsteady forces on the stator is then between the vortical contribution from the upstream rotor wake and the potential contribution from the downstream rotor.

5.0 Stator/Rotor Results: Potential Disturbance From Stator Downstream

For the stator/rotor configuration, the stator experiences a gust response originating from the moving pressure field of the downstream rotor, if the axial gap between blade rows is not too large. Thus, this response is purely potential in nature; other sources of disturbance, e.g., the rotor wake, are small in comparison.

5.1 Stator Unsteady Loading. Figure 11 presents the stator suction surface unsteady pressure distribution at four consecutive time instants when the rotor leading edge sweeps pass the stator trailing edge. For Gap2 = 10 percent chord, the time variation near the trailing edge suggests the stator begins to respond to the rotor passage near $t/T = 0.0$ to 0.1. (Recall that $t/T = 0.0$ is when the rotor leading edge is axially downstream of the stator trailing edge, see Fig. 5.) At $t/T = 0.2$ and 0.3, large suction spikes can be clearly seen. This feature is also present for Gap2 = 30 percent chord but to a lesser degree. Data show that the time variation near the leading edge is much smaller than that at the trailing edge, which agrees with the understanding that potential disturbance decays exponentially, as shown by Chung and Wo (1997) and others. The unsteady pressure distribution on the stator pressure surface exhibits similar overall trend with approximately half the pressure amplitude of that on the suction surface.

Figure 12 shows the stator unsteady force normal to the chord. Data show a clear maximum and minimum in the signature, with the amplitude decreasing with increased axial gap. This is certainly expected since the only unsteady source, the rotor downstream, is further separated from the stator. As before, the time instant when the force signature reaches an extremum is of primary interest. In the case of stator/rotor, the *minimum* in the force excursion is of concern since this is needed to offset the maximum in the rotor/stator configuration to reduce the unsteady loading for the rotor/stator/rotor configuration. At Gap2 = 10 percent chord and near-design condition, Fig. 12(*b*) shows the unsteady force reaches a minimum near $t/T = 0.05$, which is *prior to* the occurrence of large pressure spike near the stator trailing edge as the rotor passes (see Fig. 11(*a*)). In other words, minimum force on the stator (defined in Fig. 4) is reached shortly after the rotor leading edge passes the stator trailing edge. This time lag increases with increasing axial gap, as shown by the path of minimum force in Fig. 12. Figure 12(*b*) shows the force minimum is delayed to $t/T = 0.2$ for an axial gap of 30 percent chord, along with a decrease in the amplitude.

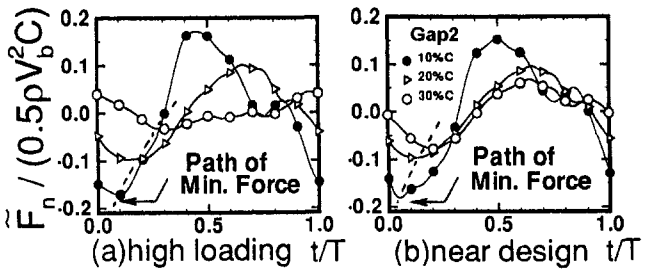

Fig. 12 Unsteady force on stator due to downstream potential disturbance with varying axial gap (*S/R*)

5.2 Potential Disturbances From Upstream and Downstream. Results thus far show a curious fact that the extent of the effect of potential disturbance differ greatly between rotor/stator and stator/rotor configurations. Figure 13 presents the potential induced unsteady force on the stator for the two configurations, with axial gaps of 10 and 30 percent chord for both cases. (The rotor/stator results are taken from Fig. 9 and the stator/rotor from Fig. 12.) Results suggest that the unsteady force response contributed by downstream potential disturbance is substantially larger than that contributed by upstream potential disturbance for the same axial gap. At 30 percent chord gap, the effect of upstream disturbance is essentially zero while the downstream effect is clearly shown. The implication of this result for multistage compressors, where the rotor response is of primary interest, is that the axial gap between a stator and the downstream rotor can be smaller than that between the rotor and the successive stator, from the standpoint of potential disturbance alone.

6.0 Rotor/Stator/Rotor Results: With All Three Sources of Disturbance

One of the main goals of this work is to reduce the unsteady loading on the stator, which arises from the three sources of disturbance as shown in Fig. 1. Results from the *rotor/stator* configuration suggest that the stator response due to vortical disturbance from upstream is much larger than that due to upstream potential disturbance, even for as small an axial gap as 10 percent chord, and thus can be ignored to first order

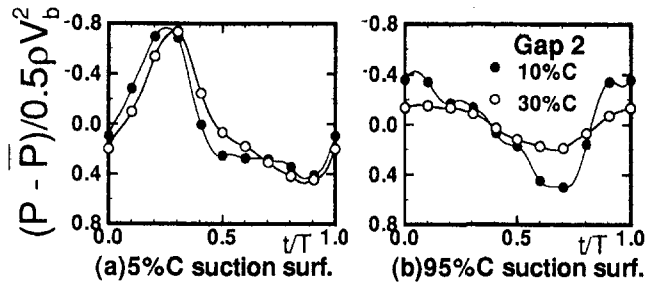

Fig. 14 Unsteady pressure on stator suction surface at 5 and 95 percent chord, for Gap1 = 10 percent chord and varying Gap2 (clocking = 0.7, *R/S/R*)

approximation (Fig. 9). We now proceed to the case of rotor/stator/rotor, using results from rotor/stator and stator/rotor to help interpret the data.

6.1 Effect of Downstream Gap. Figure 14 presents the excursion of the stator suction surface unsteady pressure measured at the 5 percent chord (Fig. 14(a)) and 95 percent chord position (Fig. 14(b)), for Gap1 = 10 percent chord and Gap2 = 10 and 30 percent chord, at near-design loading. Near the leading edge, Fig. 14(a) suggests the unsteady pressure is dominated by the upstream rotor, as shown by similarity in the two signatures. Near the trailing edge, Fig. 14(b) suggests that the unsteady pressure is strongly dependent on the downstream gap spacing, with closer gap produces greater time variation as expected. Note that this variation does not affect the pressure near the leading edge; the exponential decay characteristic of potential disturbance has reached a negligible level at approximately one chord-length upstream.

Figure 15 presents the unsteady force excursion. The force signature shows a large amplitude with the blade-to-blade frequency dominating. Interpretation of this must consider both the effect of upstream vortical and downstream potential disturbances. At this clocking position, 0.7 as shown in Fig. 6(a), the force amplitude is twice that of Fig. 9 with only upstream vortical disturbance, and the time occurrence of maximum force, at $t/T = 0.3$, in Fig. 15(b) coincides with that of Fig. 9(b). These facts suggest that effect of the downstream potential disturbance might be adding to that due to the upstream vortical, thus causing the large amplitude. This proves to be the case based on the force signature from stator/rotor (Fig. 12) and consideration of rotor clocking. For the rotor/stator/rotor configuration, the instantaneous position of the downstream rotor for clocking = 0.7 at $t/T = 0.0$ is the same as that at $t/T = -0.7$, or $t/T = 0.3$, for stator/rotor (Fig. 6(a)). At nondimensional time 0.3 later, the rotor/stator/rotor configuration is at $t/T = 0.3$, when the maximum force occurs, which corresponds to $t/T = 0.6$ for stator/rotor. At this time, Figs. 12(a) and 12(b) show the force is near maximum. Thus contributions due to the upstream vortical and downstream potential disturbances add for clocking = 0.7.

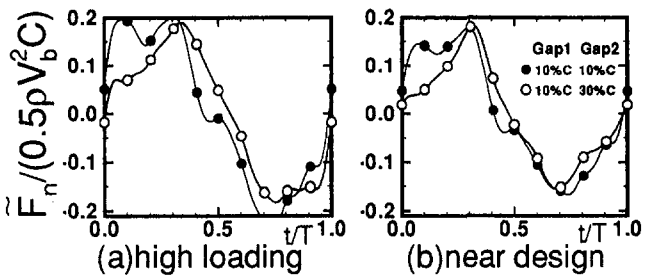

Fig. 15 Unsteady force on stator for Gap1 = 10 percent chord and varying Gap2 (clocking = 0.7, *R/S/R*)

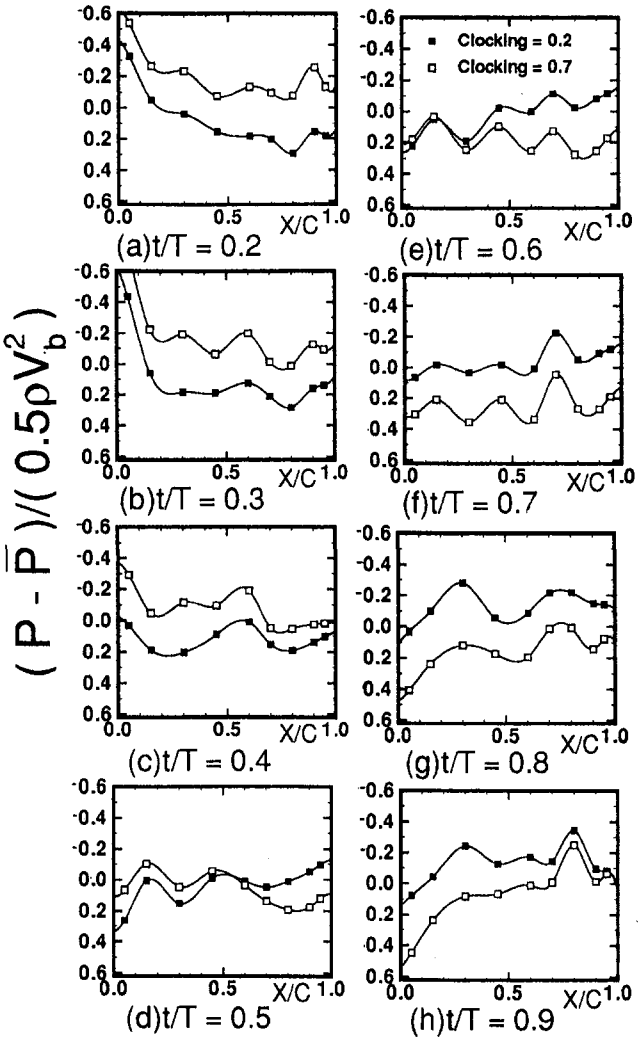

Fig. 16 Unsteady pressure on stator suction surface for clocking = 0.2 and 0.7 (Gap1 = 10 percent C, Gap2 = 30 percent C, *R/S/R*)

6.2 Effect of Rotor Clocking. We now discuss the effect of clocking the downstream rotor, with respect to the upstream rotor, for rotor/stator/rotor/configuration for Gap1 = 10 percent chord and Gap2 = 30 percent chord. Two clocking positions, 0.2 and 0.7, will be presented, since they contain major flow phenomena of interest.

Figure 16 compares the near-design stator suction surface unsteady pressure for both clockings at several time instants. Overall, the chordwise pressure variation of the two curves are similar over the unsteady period, with the major difference in the spatial mean component. Figure 16(b) shows that both clocking positions have a leading edge suction spike near $t/T = 0.3$, which is the occurrence of maximum force for rotor/stator configuration (Fig. 9(b)). The reason for this is that clocking is adjusted for the downstream rotor only; the relative position between the upstream rotor and the stator remains the same for both clocking positions.

Near the trailing edge the unsteady pressure is dominated by the effect of the downstream rotor. Knowing that minimum stator force for stator/rotor configuration occurs at $t/T = 0.2$, for Gap2 = 30 percent chord (Fig. 12(b)), this suggests that the trailing edge should have a large positive pressure near $t/$

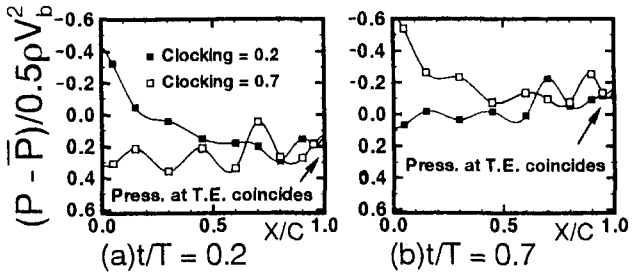

Fig. 17 Unsteady pressure on stator suction surface with clocking = 0.7 data time-shifted by t/T = 0.5 (Gap1 = 10 percent C, Gap2 = 30 percent C, *R/S/R*)

T = clocking + 0.2, or t/T = 0.4 for clocking = 0.2 and t/T = 0.9 for clocking = 0.7. Figure 16(*c*) (t/T = 0.4) for clocking = 0.2 indeed shows that the trailing edge pressure on the suction surface is near maximum before abruptly decreasing at t/T = 0.5. Similar trend for clocking = 0.7 is also shown in Fig. 16(*h*) (t/T = 0.9), which shows the pressure at the trailing edge already beginning to decrease.

Further data interrogation allows one to conclude that the trailing edge pressure is essentially unaffected by the vortical disturbance from upstream. Figure 17 presents results of Fig. 16 at two time instants but with data from clocking = 0.7 case phase-shifted by t/T = 0.5. Physically, the comparison of the two cases—clocking = 0.2 and clocking = 0.7 phase-shifted—implies clocking the *upstream* rotor, with the downstream rotor at the same location for both cases. Figures 17(*a*) and 17(*b*), which are representative of all time instants, show that the pressure at the trailing edge is equal for both clocking positions, with a large variation in the pressure near the leading edge.

Figure 18 compares the unsteady force, integrated from Fig. 16, for both clocking positions near design loading. Data show a reduction of 60 percent in the force amplitude is achieved by clocking the downstream rotor from 0.7 to 0.2 position. Physical reason for the drastic reduction is as follows. Recall that the stator response due to upstream vortical disturbance alone reaches a maximum when the wake impinges against the stator suction surface immediately downstream of the leading edge (Fig. 10), which is near t/T = 0.3 for Gap1 = 10 percent chord (Fig. 9(*b*)). Also the stator response due to downstream potential disturbance alone reaches a minimum with a slight time delay after the rotor sweeps pass the stator trailing edge, which is near t/T = 0.2 for Gap3 = 30 percent chord (Fig. 12(*b*)). Reduction of the overall stator response is achieved by clocking the downstream rotor so that the time instant when the contribution

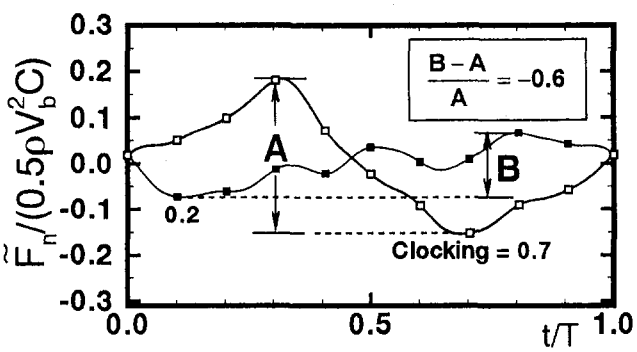

Fig. 18 Unsteady force on stator for clocking = 0.2 and 0.7 (Gap1 = 10 percent C, Gap2 = 30 percent C, *R/S/R*)

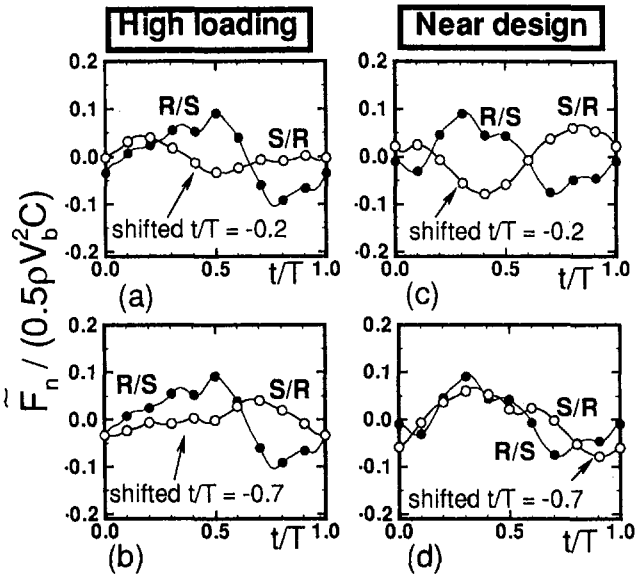

Fig. 19 Unsteady force on stator for rotor/stator and stator/rotor configurations with data from stator/rotor time-shifted (Gap1 = 10 percent C, Gap2 = 30 percent C, *R/S*, *S/R*)

due to upstream vortical disturbance reaches a maximum coincides with the minimum of that due to downstream potential disturbance. Clocking of 0.2 (see Fig. 6) means the downstream rotor will require t/T = clocking + 0.2 = 0.4 to arrive at the same circumferential location, relative to the stator, that will result in minimum stator force for stator/rotor configuration. This t/T = 0.4 is close to the time at which maximum force occurs, t/T = 0.3, for stator/rotor configuration, thus contributions to the unsteady force partially cancels. Fine tuning of clocking and axial gap can probably produce further force amplitude decrease, but it is of second order. At high loading, reduction of 56 percent is achieved with a similar force signature as that at near-design.

6.3 Superposition of Stator Unsteady Loading. With the results for the three configurations it is worthwhile to compare the unsteady response from superposing rotor/stator and stator/rotor configurations with that of rotor/stator/rotor configuration. This is a more strenuous check of the linearity relationship between gust and gust response than that by Giles, in Manwaring and Wisler (1993), using a Navier–Stokes code (UNSFLO). With the inlet boundary condition of a wake/stator calculation based on purely first harmonic (blade-to-blade) gust, measured in the midgap of the GE large-scale compressor rig, Giles found that the calculated stator response of the second harmonic was less than 2 percent of that of the first harmonic. This suggests that nonlinearity can be neglected; the gust *response,* even though scales with velocity squared, can indeed be linearized, about a nonlinear time-mean (Hall and Crawley, 1989). In the present study, response to gust from upstream *and* downstream of the stator are considered.

The results are presented in Figs. 19 and 20 for clocking = 0.2 and 0.7. Figure 19 shows the stator unsteady force for rotor/stator (Gap1 = 10 percent chord) and stator/rotor (Gap2 = 30 percent chord) configurations with the result of stator/rotor time shifted by t/T = −0.2 and −0.7. The sum of the two curves in each subfigure can thus be used to compare with that of the rotor/stator/rotor configuration for clocking = 0.2 and 0.7, which is shown in Fig. 20. At near-design loading, good agreement in the *amplitude* is obtained for both clockings (Figs. 20(*c*) and 20(*d*)). Close examination reveals, however, that for clocking = 0.2 (Fig. 20(*c*)) the phase is better matched

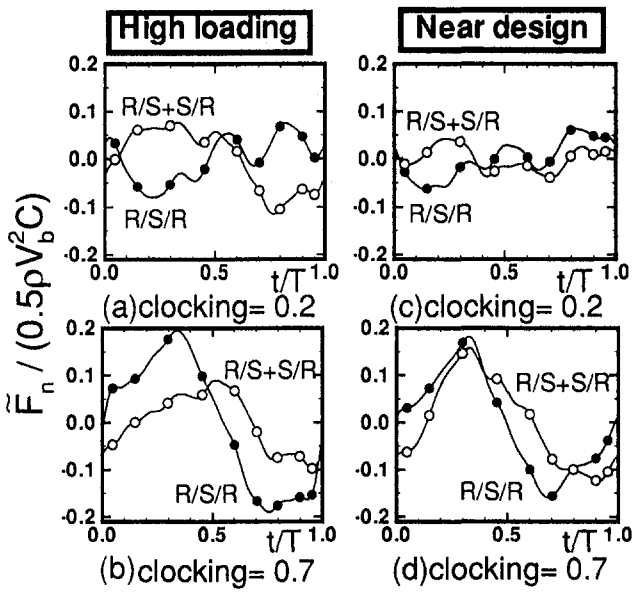

Fig. 20 Comparison of stator unsteady force between the sum of rotor/stator and stator/rotor (time-shifted as in Fig. 19) and that directly from rotor/stator/rotor configuration (Gap1 = 10 percent C, Gap2 = 30 percent C, *R/S*, *S/R*, *R/S/R*)

near the end of the blade-to-blade period than the beginning. This is also seen in Fig. 20(d) where the phase is slightly off between $t/T = 0.7$ and 0.9. At high loading, although the agreement in the phase is rather poor for clocking = 0.2 (Fig. 20(a)) linearity certainly applies for the amplitude. For clocking = 0.7 (Fig. 20(b)), matching of the amplitude is not as desirable. Overall, data show that linearity is valid with both upstream and downstream gusts, but the agreement for the phase is not as desirable as that for the amplitude.

7.0 Further Discussions

7.1 Effect of Clocking on Moment About Midchord. Data show clocking of the downstream rotor also reduces the moment about the midchord, which is of importance for blade torsional mode. For rotor/stator/rotor configuration with Gap1 = 10 percent chord and Gap2 = 30 percent chord, moment amplitude reduction of 13 percent is achieved at near-design and 20 percent at high loading, when the downstream rotor clocking is changed from 0.7 to 0.2 position. The flow physics is essentially identical to that which resulted in force amplitude reduction.

7.2 Different Blade Counts. Results presented herein are for equal counts of upstream and downstream rotor blades. If the blade counts between successive rotor rows differ, then, in a shaft revolution, a stator would experience variation of unsteady amplitude ranging from a minimum, if the rotor rows are optimally clocked at some circumferential location, to a maximum, if the rotor rows are arranged so that the worst clocked position occurs at another circumferential position. The difference between the rotor and stator blade count, however, does not alter the results presented, since the disturbances that give rise to stator unsteady load reduction originate from the upstream and downstream rotors. Hence, the kinematic consideration of interaction tone noise (Tyler and Sofrin, 1962), which is based on the rotor and stator count, is not affected.

8.0 Conclusions

Experimental study is conducted on rotor/stator, stator/rotor, and rotor/stator/rotor configurations to test a hypothesis: unsteady stator response due to distinct sources of disturbance may partially cancel if their resulting phase relationship can be altered. Sources of disturbances considered are vortical disturbance from the *upstream* rotor, potential disturbance from the *upstream* rotor, and potential disturbance from the *downstream* rotor. Alteration in the phase relationship of the unsteady sources is achieved by clocking the downstream rotor with respect to the upstream rotor. Major findings are summarized as follows:

- A 60 percent reduction in the stator unsteady force is found when the clocking of the downstream rotor is changed from 0.7 to 0.2, for rotor/stator/rotor configuration with Gap1 = 10 percent chord and Gap2 = 30 percent chord (Fig. 18).
- In this case, dominant sources of disturbance are vortical disturbance from the upstream rotor and potential disturbance from the downstream rotor, with the upstream potential disturbance negligible (Figs. 9 and 12).
- Stator response due to upstream vortical disturbance reaches a maximum when the wake impinges against the stator suction surface immediately downstream of the leading edge (Fig. 10). This causes a pressure spike near the leading edge region, which is the dominant feature of the unsteady force signature (Fig. 8).
- Stator response due to downstream potential disturbance reaches a minimum with a slight time delay after the rotor sweeps pass the stator trailing edge. The time delay is shown to increase with downstream gap (Fig. 12).
- Physically, reduction of the stator response is achieved by clocking the downstream rotor so that the time instant when the contribution due to upstream vortical disturbance reaches a maximum (Fig. 10) coincides with the minimum of that due to downstream potential disturbance (Fig. 12) (as sketched in Fig. 6(b)).
- The unsteady force response contributed by downstream potential disturbance is much larger than that contributed by upstream potential disturbance for the same Gap1 and Gap2. For Gap1 = 30 percent chord, the stator response due to upstream disturbance is essentially zero while that due to downstream disturbance is still substantial (Fig. 13).
- Superposing the unsteady response of rotor/stator and stator/rotor configurations and comparing with that of rotor/stator/rotor configuration provide a check for the linearity relationship between gust and gust response. Data show that linearity is valid with both upstream and downstream gusts, but the agreement for the phase is not as desirable as that for the amplitude (Fig. 20).

Acknowledgments

The authors are grateful for the financial support of the National Science Council, Republic of China (Grant No. NSC 85-2212-E-002-040). The help of Christ throughout the course of this work is also acknowledged.

References

Capece, V. R., and Fleeter, S., 1987, "Unsteady Aerodynamic Interactions in a Multistage Compressor," ASME JOURNAL OF TURBOMACHINERY, Vol. 109, pp. 420–428.

Chung, M. H., and Wo, A. M., 1997, "Navier–Stokes and Potential Calculations of Axial Spacing Effect on Vortical and Potential Disturbances and Gust Response in an Axial Compressor," ASME JOURNAL OF TURBOMACHINERY, Vol. 119, pp. 472–481.

Doebelin, E. O., 1990, *Measurement Systems: Application and Design*, 4th ed., McGraw-Hill, p. 482.

Feiereisen, J. M., Montgomery, M. D., and Fleeter, S., 1994, "Unsteady aerodynamic forcing functions: a comparison between linear theory and experiment," ASME JOURNAL OF TURBOMACHINERY, Vol. 116, pp. 676–685.

Gallus, H. E., Groillus, H., and Lambertz, J., 1982, "The Influence of Blade

Number Ratio and Blade Row Spacing on Axial-Flow Compressor Stator Blade Dynamic Load and Stage Sound Pressure Level," ASME *Journal of Engineering for Power,* Vol. 104, pp. 633–644.

Giles, M. B., 1988, "Calculation of unsteady wake/rotor interaction," *J. of Propulsion and Power,* Vol. 4, pp. 356–362.

Goldstein, M. E., and Atassi, H., 1976, "A complete second-order theory for the unsteady flow about an airfoil due to periodic gust," *Journal of Fluid Mechanics,* Vol. 74, Part 4, pp. 741–765.

Goldstein, M. E., 1978, "Unsteady vortical and entropic distortions of potential flows round arbitrary obstacles," *Journal of Fluid Mechanics,* Vol. 89, Part 3, pp. 433–468.

Hall, K., and Crawley, E., 1989, "Calculation of unsteady flows in turbomachinery using the linearized Euler equations," *AIAA J.,* Vol. 27, No. 6, pp. 777–787.

Henderson, G., and Fleeter, S., 1993a, "Forcing function effects on unsteady aerodynamic gust response: part 1—forcing functions," ASME JOURNAL OF TURBOMACHINERY, Vol. 115, pp. 741–750.

Henderson, G., and Fleeter, S., 1993b, "Forcing function effects on unsteady aerodynamic gust response: part 2—low solidity airfoil row response," ASME JOURNAL OF TURBOMACHINERY, Vol. 115, pp. 751–761.

Hobbs, D. E., and Weingold, H. D., 1984, "Development of controlled diffusion aerofoils for multistage compressor applications," ASME *Journal of Engineering for Gas Turbines and Power,* Vol. 106, pp. 271–278.

Hsu, S. T., Wo, A. M., and Wu, C. K., 1996, "Experimental and Numerical Study of Gust and Gust Response in a Rotor/Stator Axial Compressor," presented in the ASME Turbo Asia '96, Jakarta, ASME Paper No. 96-TA-043.

Kerrebrock, J. L., 1992, *Aircraft Engines and Gas Turbines,* 2nd ed., M.I.T. Press, p. 371.

Manwaring, S. R., and Wisler, D. C., 1993, "Unsteady aerodynamics and gust response in compressors and turbines," ASME JOURNAL OF TURBOMACHINERY, Vol. 115, pp. 724–740.

Tyler, J. M., and Sofrin, T. G., 1962, "Axial Compressor Noise Studies," *SAE Trans.,* Vol. 70, pp. 309–332.

Valkov, T., and Tan, C. S., 1995, "Control of the Unsteady Flow in a Stator Blade Row Interacting With Upstream Moving Wakes," ASME JOURNAL OF TURBOMACHINERY, Vol. 117, pp. 97–105.

Weaver, M. M., and Fleeter, S., 1994, "Turbine Rotor Generated Forcing Functions for Flow Induced Vibrations," ASME Paper No. 94-GT-328.

Wo, A. M., Chung, M. H., and Hsu, S. T., 1997, "Gust Response Decomposition in a Stator/Rotor Axial Compressor With Varying Axial Gap," *J. of Prop. and Power,* Vol. 13, No. 1.

APPENDIX

Rotor and the stator coordinates[3]

ROTOR				STATOR			
RESSURE SUR.		SUCTION SUR.		PRESSURE SUR.		SUCTION SUR.	
X	Y	X	Y	X	Y	X	Y
0.771625	-0.636078	0.000002	0.000001	0.935629	0.352985	0.000000	0.000000
0.772617	-0.632417	0.002822	0.002713	0.934957	0.349194	0.002279	-0.003324
0.767948	-0.62279	-0.005387	-0.0139	0.926439	0.342487	-0.002352	0.01515
0.752036	-0.614321	-0.003911	-0.032516	0.908164	0.341587	0.003056	0.033618
0.730906	-0.603092	0.002765	-0.05642	0.883908	0.340367	0.014603	0.05643
0.705539	-0.589495	0.014023	-0.084083	0.85474	0.338756	0.031501	0.082143
0.676918	-0.57396	0.029048	-0.114357	0.821749	0.336703	0.052784	0.109699
0.645953	-0.556872	0.047388	-0.146153	0.785944	0.334135	0.077857	0.138006
0.613433	-0.538549	0.068511	-0.178633	0.74819	0.330969	0.106066	0.166241
0.580003	-0.519215	0.091902	-0.211182	0.709185	0.327094	0.136772	0.193848
0.546167	-0.499024	0.117224	-0.243297	0.66947	0.322385	0.169637	0.22021
0.512256	-0.478136	0.144291	-0.274543	0.629428	0.316823	0.20434	0.244892
0.478498	-0.456642	0.173162	-0.304405	0.589321	0.310393	0.24088	0.267152
0.445124	-0.434469	0.203577	-0.332769	0.549362	0.302834	0.278937	0.286824
0.412295	-0.411533	0.235407	-0.359501	0.509695	0.293957	0.318323	0.303619
0.380116	-0.387758	0.268475	-0.384624	0.470439	0.283565	0.358783	0.317513
0.348665	-0.363072	0.302523	-0.408353	0.43169	0.271514	0.399984	0.328921
0.318023	-0.33739	0.337289	-0.43102	0.393562	0.257627	0.441692	0.338324
0.288336	-0.31057	0.372648	-0.452803	0.356272	0.24156	0.483764	0.346092
0.259666	-0.282609	0.408578	-0.473713	0.320002	0.223223	0.526143	0.352267
0.232251	-0.253391	0.444944	-0.493898	0.285078	0.202392	0.568714	0.357129
0.2058	-0.223361	0.481672	-0.513305	0.251265	0.179889	0.611358	0.360711
0.180127	-0.192912	0.518541	-0.532014	0.218534	0.156165	0.653873	0.363265
0.155353	-0.162272	0.555252	-0.550044	0.186988	0.131585	0.695974	0.364997
0.131616	-0.131811	0.59147	-0.567225	0.156781	0.106608	0.737261	0.365897
0.108639	-0.102392	0.626661	-0.583439	0.127727	0.082291	0.777177	0.366135
0.086626	-0.074713	0.660135	-0.59851	0.100222	0.059224	0.814997	0.365898
0.065858	-0.04963	0.691052	-0.612182	0.07466	0.038268	0.849818	0.365352
0.046692	-0.028162	0.718436	-0.624127	0.051545	0.020409	0.880588	0.364654
0.029294	-0.011755	0.741235	-0.633982	0.031249	0.007093	0.906167	0.363954
0.014248	-0.001884	0.758432	-0.641359	0.014556	-0.000331	0.925437	0.363372
0.003611	0.001112	0.769291	-0.639247	0.003425	-0.001711	0.93481	0.356954
0.000002	0.000001	0.771625	-0.636078	0.000000	0.000000	0.935629	0.352985

[3] For code validation contact the second author (E-mail address on the first page) if you need the coordinates in a file or other additional information.

The Influence of Downstream Passage on the Flow Within an Annular S-Shaped Duct

T. Sonoda

T. Arima

M. Oana

Honda R&D Co., Ltd.,
Saitama, Japan

Experimental and numerical investigations were carried out to gain a better understanding of the flow characteristics within an annular S-shaped duct, including the influence of the shape of the downstream passage located at the exit of the duct on the flow. A duct with six struts and the same geometry as that used to connect the compressor spools on our new experimental small two-spool turbofan engine was investigated. Two types of downstream passage were used. One type had a straight annular passage and the other a curved annular passage with a meridional flow path geometry similar to that of the centrifugal compressor. Results showed that the total pressure loss near the hub is large due to instability of the flow, as compared with that near the casing. Also, a vortex related to the horseshoe vortex was observed near the casing. In the case of the curved annular passage, the total pressure loss near the hub was greatly increased compared with the case of the straight annular passage, and the spatial position of this vortex depends on the passage core pressure gradient. Furthermore, results of calculation using an in-house-developed three-dimensional Navier–Stokes code with a low-Reynolds-number $k-\epsilon$ turbulence model were in good qualitative agreement with experimental results. According to the simulation results, a region of very high pressure loss is observed near the hub at the duct exit with the increase of inlet boundary layer thickness. Such regions of high pressure loss may act on the downstream compressor as a large inlet distortion, and strongly affect downstream compressor performance.

Introduction

A swan-neck duct is used to connect the low- and high-pressure compressors of aircraft gas turbine engines. In a small gas turbine, a centrifugal high-pressure compressor is often used. In this case, the swan-neck duct is S-shaped due to the aerodynamic design restriction of the centrifugal compressor. Within this duct, flow separation must be avoided to minimize the total pressure loss within the duct. In addition, a uniform flow field at the duct exit must also be achieved. However, it is very difficult to satisfy these various requirements in practice, because the S-shaped duct has struts supporting loads and passages for engine accessories and support systems, resulting in a highly complex flow field due to interaction of the duct passage with the struts. Furthermore, the requirements must be fulfilled for a short axial length.

Recently, some studies have been reported on S-shaped ducts (Britchford et al., 1994; Bailey et al., 1997; Bailey and Carrotte, 1996). Their long-term objective is to apply CFD methods to enable the optimum design of S-shaped ducts. Therefore, comprehensive measurements were done using an LDV system under ideal and typical actual engine inlet conditions. However, the S-shaped duct inlet velocity was relatively low and the duct itself was of constant-flow area. Only one radial strut was used in order to assess the effect on performance of placing radial struts within the duct. In this stage of progress in research, it would be worthwhile to investigate the flow within a duct with a more practical configuration and under realistic test conditions. According to the performance test of our centrifugal compressor with an S-shaped duct, the decrease in efficiency was much greater than expected. The S-shaped duct pressure loss seemed to be much larger than that in isolated S-duct performance. Therefore, we have begun research on the flow within an S-shaped duct.

The objectives of this investigation are: (1) to study the flow resulting from the interaction of the S-shaped passage with the struts, (2) to investigate the effect on the flow of a downstream passage located at the exit of an S-shaped duct, and (3) to evaluate the reliability of an in-house-developed three-dimensional Navier–Stokes code.

Experimental Methods

Experimental Facility. A schematic of the S-shaped duct test rig is shown in Fig. 1. Air is supplied by laboratory compressors into a plenum chamber prior to passing through the S-shaped duct, and is exhausted to atmospheric pressure via an exhaust diffuser system set up in the test cell. The detailed configuration of the S-shaped duct is shown in Fig. 2 and Table 1. This duct has a geometry similar to that used to connect the compressor spools on our new experimental small two-spool turbofan engine. The inlet passage upstream of the S-shaped duct has the same geometry as that of the LPC OGV. In Fig. 2, station 1 corresponds to the trailing edge position of the LPC OGV. The inlet Mach number used in this rig is 0.386 ± 0.03, based on the inlet total pressure (station 0) and the mean value of the hub and casing static pressures at station 1.

In order to investigate the effect of the downstream passage on the flow within the S-shaped duct, two different downstream passages were fitted alternatively at the S-shaped duct exit. One has a straight annular passage and the other a curved annular passage with a similar meridional flow path geometry to that of the centrifugal compressor. Static pressure taps are located at various streamwise positions on the hub and the casing, which allow for the estimation of the flow characteristic and the effect of the downstream passage. The circumferential position of these taps corresponds to the midpoint between the struts. Also, on the strut surface, static pressure taps are located at 11, 44,

Contributed by the International Gas Turbine Institute and presented at the 42nd International Gas Turbine and Aeroengine Congress and Exhibition, Orlando, Florida, June 2–5, 1997. Manuscript received at ASME Headquarters February 1997. Paper No. 97-GT-83. Associate Technical Editor: H. A. Kidd.

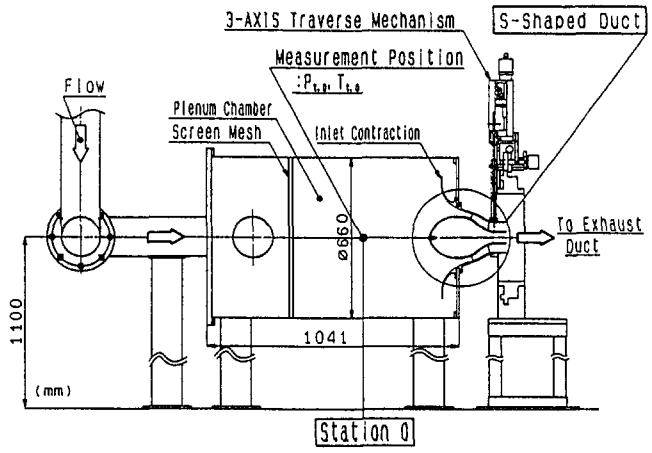

Fig. 1 Schematic test rig

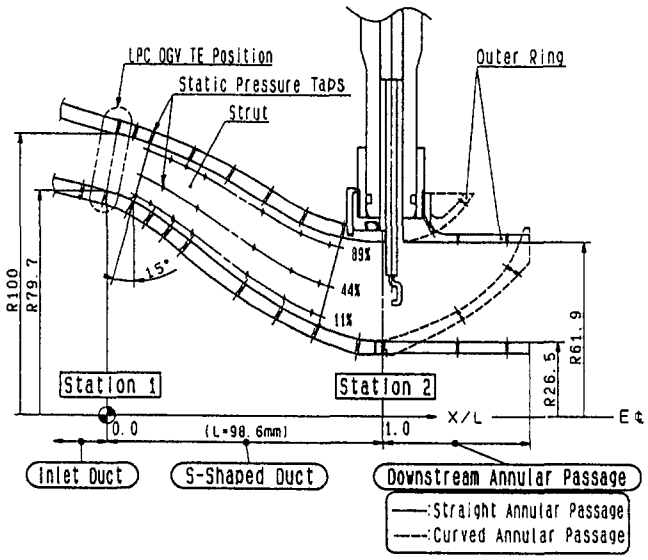

Fig. 2 S-shaped duct geometry and downstream annular passage

and 89 percent of the strut span. The area ratio (A1/A2) of the S-shaped duct is about 1.2. The S-shaped duct has six struts with NACA 0021 profile geometry, which are canted by 15 deg to match the S-shaped duct passage. The flows on the strut and the hub/casing surfaces have been visualized using a mixture of titanium dioxide and oleic acid.

Instrumentation. Inlet total pressure and temperature are measured at the center of the plenum chamber (Fig. 1). At the outlet, using the three-axis traverse mechanism, traverse measurements of pressure were made using a miniature five-hole pressure probe with an overall diameter of 1.5 mm, which was calibrated in advance. The axial positions of these measurements ($X/L = 1.03$) correspond nearly to the centrifugal impeller leading edge (station 2). The outer ring of both straight and curved annular passages moves in the circumferential direction by the three-axis traverse mechanism. The data are mainly obtained at eight radial positions traversed along 20 circumferential points. The area traversed corresponds to half of the strut pitch.

Data Reduction. Static pressures along the hub, the casing, and the strut surface are given in terms of the pressure recovery coefficient (C_p), while the total pressure loss coefficient between the S-shaped duct inlet (station 1: $X/L = 0.0$) and the duct exit ($X/L = 1.03$: near station 2) is defined as λ.

$$C_p \equiv \frac{P_{s,w} - \overline{P_{s,1}}}{P_{t,1} - \overline{P_{s,1}}}; \quad \lambda \equiv \frac{P_{t,1} - P_{t,2}}{P_{t,1} - \overline{P_{s,1}}}$$

$$\overline{P_{s,1}} \equiv \frac{1}{2}(P_{s,1,\text{casing}} + P_{s,1,\text{hub}})$$

Here, the total pressure at station 1 is the same as the pressure at station 0 in the plenum chamber.

The five-hole pressure probe provides information on total and static pressure as well as flow direction (pitch and yaw angles) and velocity is calculated from these data.

Estimate of Experimental Error. The inlet total pressure probe, static taps, and five-hole pressure probe discussed above were connected to a precalibrated differential pressure transducer, which had a range of ±98 kPa. The output was read automatically from an integrating digital voltmeter. Total and static pressure measurements were reproducible to within ±10 mm of water. Based on these values, it was estimated that the static pressure recovery and the total pressure loss coefficient were reproducible to within ±0.02 and ±0.01, respectively.

Computational Methods

A three-dimensional compressible Navier–Stokes code with a low-Reynolds-number $k-\epsilon$ turbulent model (Arima et al., 1997) has been applied to the flow within the S-shaped duct. The computational body-fitted grid, for example, used for the S-shaped duct with a curved annular passage, is shown in Fig. 3. Part of the casing grid is omitted to allow a better view of the S-shaped duct with struts. The grid consists of 61 nodes in the strut-to-strut direction, 41 nodes in the spanwise direction, and 156 nodes in the streamwise direction. Calculations have been done under various inlet boundary layer thickness conditions (1.0, 2.0, 5, and 10 percent of the inlet passage height) for the two configurations (the straight annular passage and the curved annular passage). As inlet boundary conditions, standard pressure and temperature were used, and inlet flow direction was along the hub and the casing without swirling. As a Euler solver, Denton's code was also used. Downstream back pressure was adjusted to coincide with the corrected mass flow.

Results and Discussion

Inlet Boundary Layer. The inlet boundary layer thickness was estimated by the assumption of laminar flow (i.e., Blasius

Nomenclature

A = local cross-sectional area, mm^2
C_p = static pressure recovery coefficient
L = representative axial length of S-shaped duct-98.6 mm (see Fig. 2)
P_t = total pressure, kPa
P_s = static pressure, kPa
R = radius, mm
Tt = total temperature, K
X = axial distance, mm
λ = total pressure loss coefficient

Superscripts and subscripts

$-$ = time average
hub = inner casing wall
casing = outer casing wall
w = wall
0, 1, 2 = streamwise position (see Figs. 1 and 2)

Table 1 Flow path dimension of S-shaped duct

X(mm)	R(mm)			
	Hub		Casing	
	Straight	Curved	Straight	Curved
-8.60	81.89	←	103.01	←
0.00 (Stn 1)	79.66	←	100.77	←
3.44	78.51	←	99.98	←
9.40	75.70	←	98.39	←
15.02	72.37	←	96.53	←
22.59	67.05	←	93.60	←
29.19	61.92	←	90.72	←
36.07	56.43	←	87.36	←
42.81	51.22	←	83.71	←
48.97	46.71	←	80.02	←
55.91	42.07	←	75.76	←
62.17	38.33	←	72.19	←
69.36	34.60	←	68.44	←
75.23	31.98	←	65.93	←
83.77	28.88	←	63.33	←
90.06	27.23	←	62.26	←
93.49	26.66	←	61.97	←
95.98	26.51	←	61.87	←
98.59 (Stn 2)	↑	26.87	↑	61.87
100.97	↑	27.53	↑	61.87
108.98	↑	30.04	↑	62.64
116.61	↑	33.01	↑	65.20
125.36	↑	37.39	↑	71.56
131.42	↑	41.35	↑	79.50
137.78	↑	46.82	–	–
143.08	↑	53.31	–	–
149.24	↑	67.23	–	–

flow). The calculated boundary layer thickness is about 0.2 mm at the inlet of the S-shaped duct (Station 1), and it corresponds to about 1 percent of passage height.

Flow Visualization. Flow has been visualized experimentally and numerically to gain a qualitative understanding of the flow pattern within the S-shaped duct. The representative results for the straight annular duct are shown in Fig. 4. The inlet boundary layer thickness used in calculations corresponds to 1 percent of passage height. Figure 4(*a*) shows the flow pattern on the casing. The strut has been removed. The resulting flow pattern on the casing shows a typical horseshoe vortex that forms ahead of the blunt strut leading edge with a stagnation point (saddle point). From this stagnation point, two streamlines emerge and wrap around the strut, while at the trailing edge, two new limiting streamlines form. This pattern is very similar to that observed by Karim Abdulla-Altaii and Raj (1994). They investigated the flow downstream of the corner formed by a blade and a flat plate and called the two limiting streamlines at the trailing edge "wake limiting streamlines." This "wake limiting streamline" in Fig. 4(*a*) corresponds to the high-loss region shown later (Fig. 8) and it shows that there is a very high concentration of vortices adjacent to the casing. The wake pattern on the hub is shown in Fig. 4(*b*). The "wake limiting streamline" observed in the casing is not detected on the hub, experimentally or numerically. This is due to the differences of a streamwise pressure gradient between the casing and the hub field shown later (Fig. 5). There is a slight discrepancy between the experiments and calculations in Fig. 4(*b*). The calculated results show the existence of a week vortex on the hub, while the oil flow results do not.

The horseshoe vortex observed on the casing can also be seen on the hub as shown in Fig. 4(*c*). As the limiting streamline is traced downstream, it is seen to move toward the strut surface and to be migrating in the spanwise direction on the strut surface. This is due to a streamwise positive pressure gradient on the hub and a spanwise pressure gradient on the strut surface, respectively (see Figs. 5 and 6). The horseshoe vortex on the hub is away from the hub endwall due to the streamwise positive pressure gradient.

There is no separation region on the hub or the casing. However, a small separation region is observed at the trailing edge on the strut surface (Fig. 4(*c*)), experimentally and numerically.

On the whole, the calculated results are in good agreement with the experimental results, qualitatively.

Hub and Casing Static Pressure. The hub and casing wall pressure coefficient, C_p is presented in Fig. 5 for different exit annular passages (i.e., straight or curved annular passage). As the flow follows a curved path within the S-shaped duct, a modification to the static pressure field occurs due to the balance between centrifugal force and radial pressure gradient. Across the first bend, the pressure close to the casing is higher than that adjacent to the hub. However, this situation is reversed at the second bend since the flow returns to the axial direction, as already described by Britchford et al. (1994). The flow experiences a significant positive streamwise pressure gradient in the latter half of the duct on the hub surface as indicated by C_p, which rises from −0.33 to +0.12. This positive gradient is lower than Britchford et al.'s results (−0.33 to +0.24). Design effort was done to minimize the streamwise positive pressure gradient along the hub in the latter half of the S-shaped duct.

In contrast, the pressure gradient is almost negative adjacent to the casing where C_p decreases from +0.2 to −1.05 along approximately 80 percent of the duct length. This negative gradient is very large compared to Britchford et al.'s result (+0.2 to −0.26). This is due to the difference in the area ratio and the blockage effect caused by the presence of the six struts.

With the curved downstream annular passage, the static pressure is significantly modified near the exit of the S-shaped duct. The positive pressure gradient is enhanced at the hub, while the positive pressure gradient is suppressed at the casing.

As shown in Fig. 5, the results calculated using the Euler code (Denton) and the three-dimensional Navier–Stokes code are in good agreement with experimental results. In particular, the results obtained using our code show excellent agreement. However, it is worthwhile to note that the Denton code is very attractive to aerodynamic designers because of the good agreement within very short times (about 3 minutes of CPU time). In contrast, our code requires about 4 hours on the Honda Fujitsu VX2.

Strut Static Pressure. The strut wall static pressure coefficient, C_p, is presented in Fig. 6 at 11, 44, and 89 percent of the strut span. There are no effects of the downstream passage curvature on the strut surface static pressure from 11 to 89 percent of the strut span. Although the strut has a two-dimensional profile, there are significant differences in the pressure

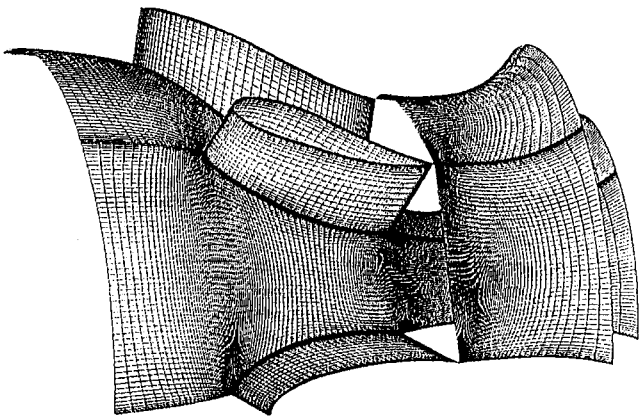

Fig. 3 Computational grid for S-shaped duct

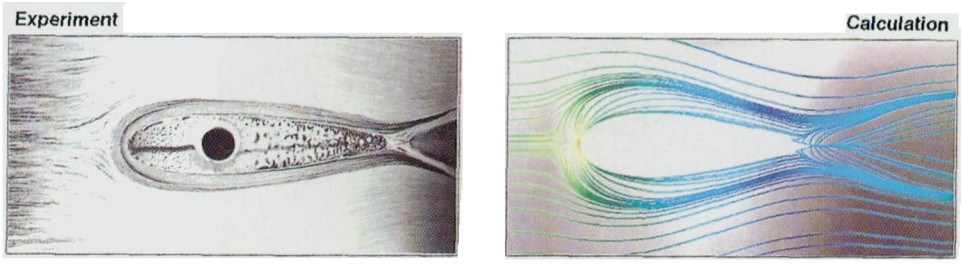

Fig. 4(*a*) Flow pattern along casing

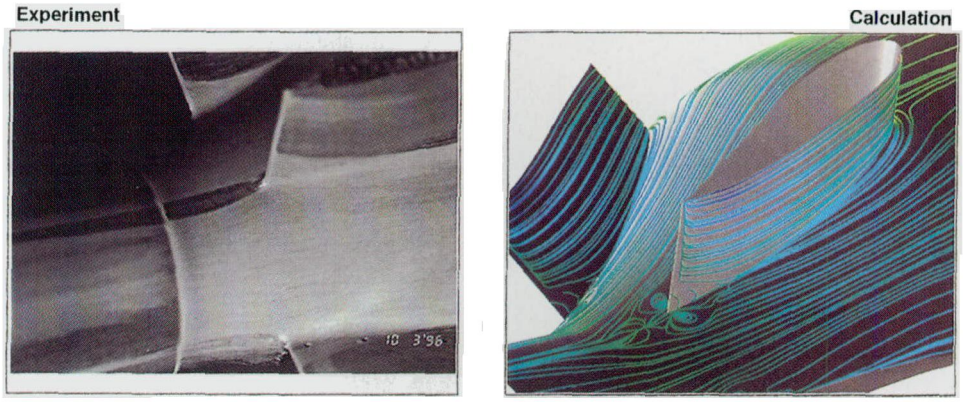

Fig. 4(*b*) Flow pattern along hub

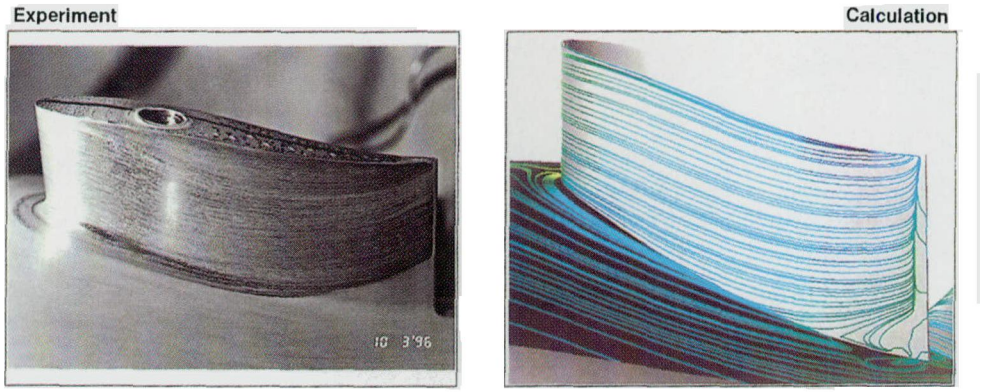

Fig. 4(*c*) Flow pattern along strut surface

distribution across the strut span. These differences are mostly due to the differences in the streamwise pressure gradients between the hub and the casing within the S-shaped duct presented earlier, as already described by Bailey et al. (1997). Again, the results calculated using the three-dimensional Navier–Stokes code are in good quantitative agreement with experimental results, except at one point at about 10 percent of the axial chord at 11 percent of the strut span.

Total Pressure Loss Coefficient. Experimental and calculated contours of the total pressure loss coefficient obtained at the S-shaped duct exit ($X/L = 1.03$) are shown in Fig. 7 for (a) the straight annular passage and (b) the curved annular duct. In the calculated contours of the total pressure loss coefficient, each contour value is in order of 5, 10, 15, 20, 30, 40, 50, and 70 percent. According to the experimental results in the case of the straight annular duct (Fig. 7(a) left), the boundary layer near the hub at the midpoint between the struts is thicker than that near the casing. This is due to the streamwise positive pressure gradient along the hub in the latter half of the duct, as already shown in Fig. 5. It is very interesting that circumferential variation of the total pressure loss is observed adjacent to the casing. The total pressure loss coefficient estimated in the circumferential direction by traverse measurement over a constant-radius surface first increases, then decreases and again increases as the probe moves toward the strut wake. The total pressure loss coefficient shows two maxima in the outer region. This first maximum (about 5 deg in circumferential position) corresponds to the "wake limiting streamline," as already shown in Fig. 4(a). This deformation of the total pressure loss is due to the horseshoe vortex. The contours of the total pressure loss coefficient for the curved annular downstream passage are shown in Fig. 7(b). The boundary layer thickness near the hub region is greatly increased, as compared with the case of the straight annular downstream passage. This is due to the enhancement of the streamwise positive pressure gradient (see Fig. 5). In contrast, the boundary layer thickness near the casing is slightly decreased due to the suppression of streamwise positive pressure gradient. The remaining regions seem to have only minor differences.

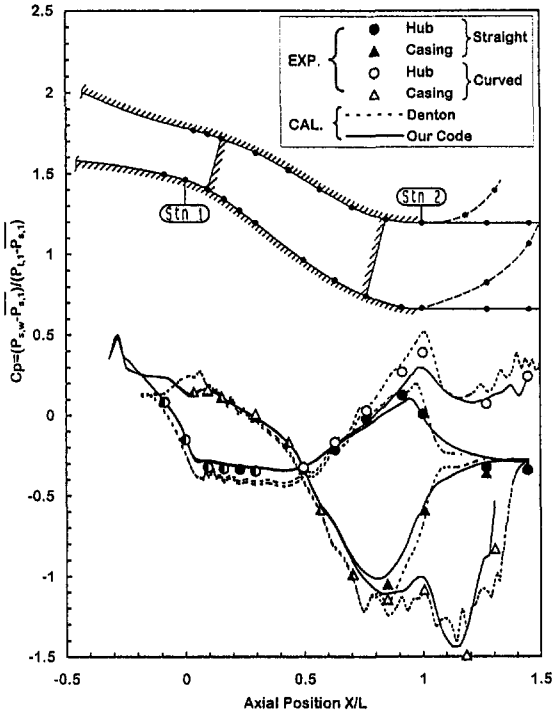

Fig. 5 Static pressure distribution on hub and casing

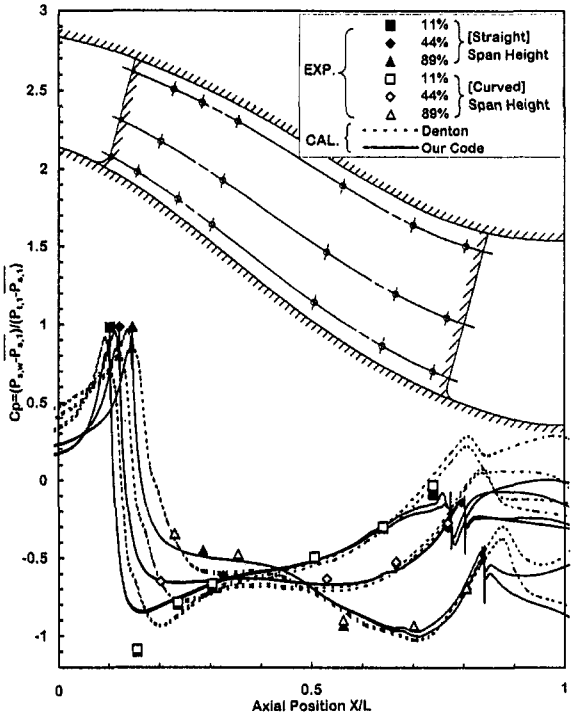

Fig. 6 Static pressure distribution on strut surface

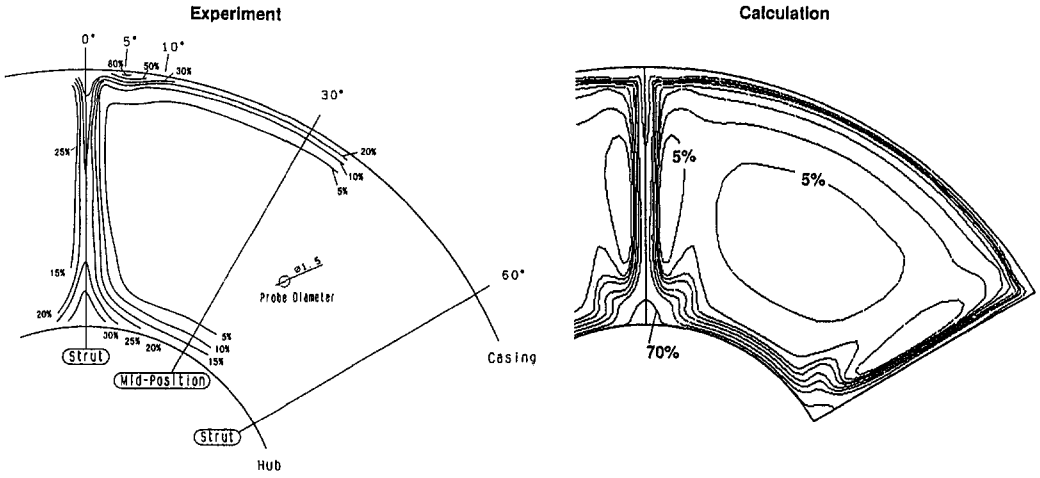

Fig. 7(a) Total pressure loss coefficient contours for the case of the straight annular passage

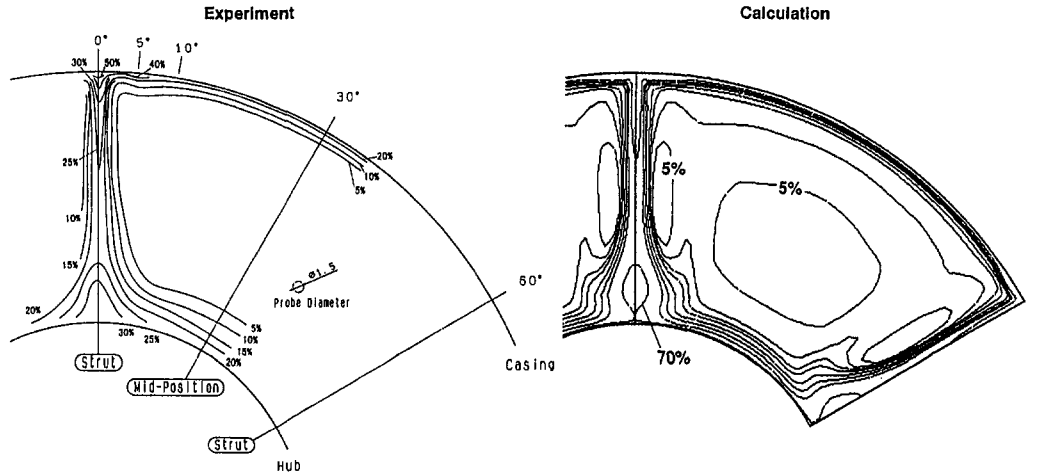

Fig. 7(b) Total pressure loss coefficient contours for the case of the curved annular passage

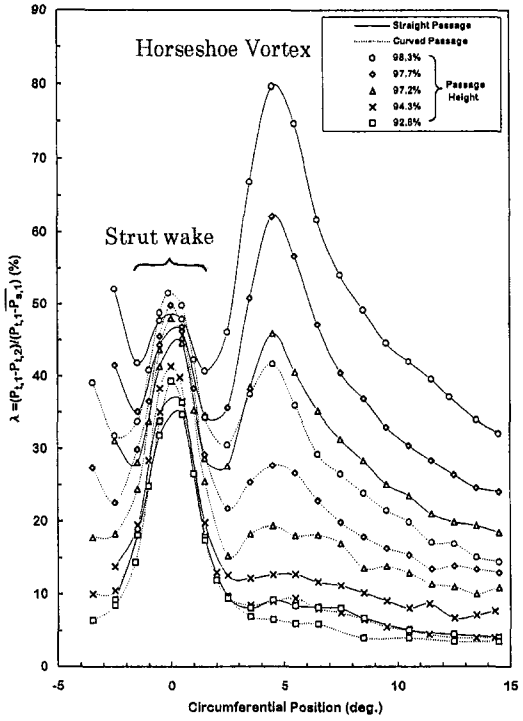

Fig. 8 Total pressure loss distribution at various heights near casing

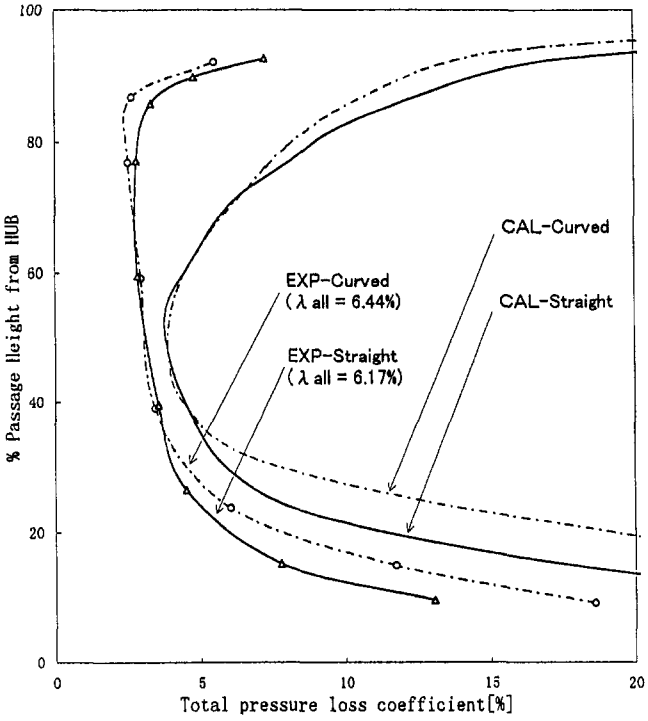

Fig. 9 Spanwise distribution of mass-averaged total pressure loss coefficient

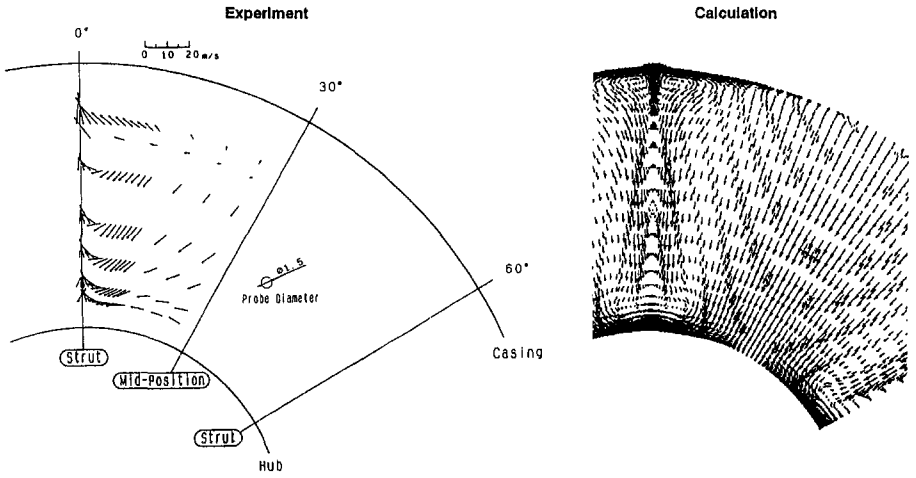

Fig. 10(*a*) Secondary flow vectors for the case of the straight annular passage

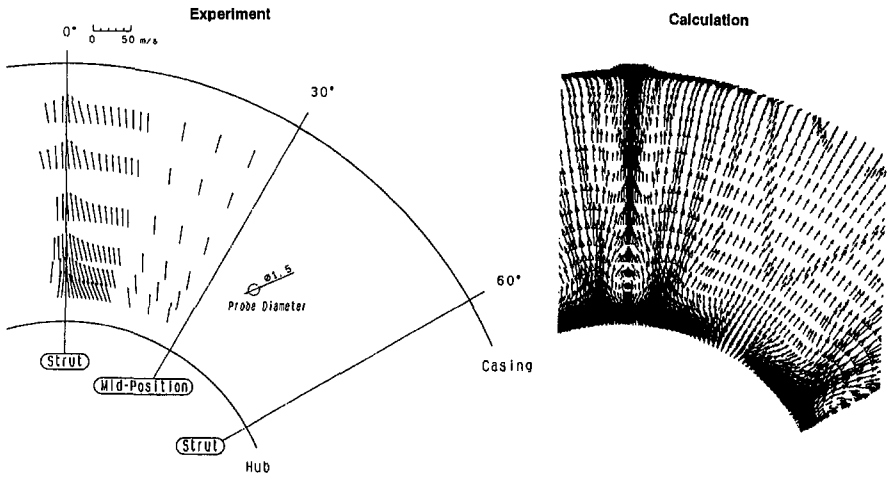

Fig. 10(*b*) Secondary flow vectors for the case of the curved annular passage

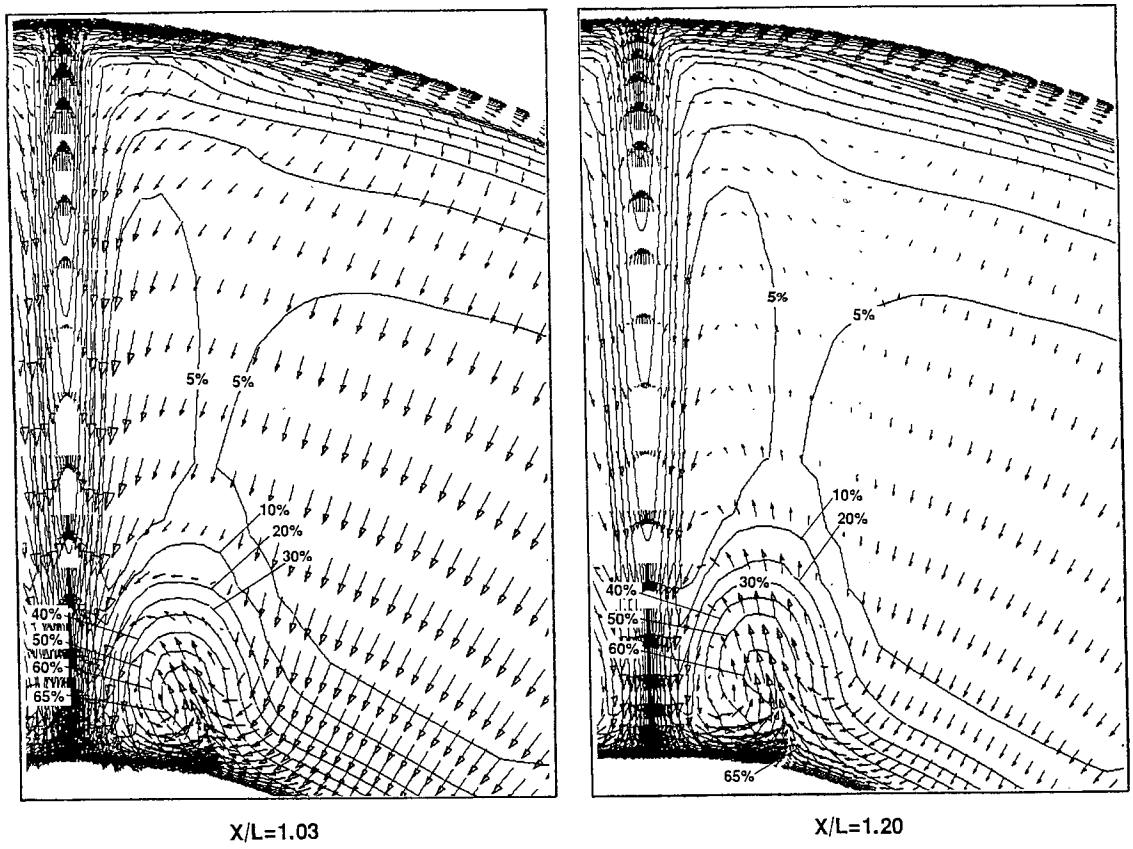

Fig. 11 Formation of vortical motion for the case of straight annular passage (inlet boundary layer thickness = 10 percent of passage height)

Figure 8 shows the total pressure loss coefficient distribution at various heights near the casing. Although these experimental data are not sufficiently reliable due to the wall effect, qualitative analysis is possible. Two peaks of the pressure loss coefficient (one is due to the strut wake and the other is due to the horseshoe vortex) are clearly revealed in the experiment, and the magnitude of the deformation of the total pressure loss coefficient is larger in the case of the straight annular passage than that in the case of the curved annular passage. This is due to the differences in the passage core streamwise pressure gradient along the casing near the S-shaped duct exit region (see Fig. 5). That is, in the case of the straight passage, the horseshoe vortex moves away from the casing, due to the positive pressure gradient, than that in the case of the curved annular duct (see Fig. 7). A very high concentration of vortices related to the horseshoe vortex is thought to exist adjacent to the casing. This small concentrated vortex may have an adverse effect on the downstream centrifugal compressor performance, such as a large inlet distortion, since, in a real engine, a positive pressure gradient generated on the shroud of an impeller may influence the pressure gradient on the casing of the duct and displace the vortex.

Figure 9 shows the spanwise distribution of mass-averaged total pressure loss coefficient. The total pressure loss near the hub in the case of the curved annular downstream passage is greatly increased due to the enhancement of the streamwise positive pressure gradient, as compared with the case of the straight annular passage. On the other hand, the total pressure loss near the casing in the case of the curved annular downstream passage is reduced due to the suppression of the streamwise positive pressure gradient, as compared with the case of the straight annular passage. Therefore, the difference of the overall mass flow averaged total pressure loss (λ all) for each configuration is not so large.

The calculated results do not clearly show the concentrated vortex near the casing as a vortex core in the form of total pressure loss coefficient. In comparing the experimental and calculated results, there are discrepancies in the levels of loss in the wake. Both results, however, indicate the same overall behavior.

Secondary Flow Vectors. Experimental and calculated secondary flow vectors obtained for the S-shaped duct exit ($X/L = 1.03$) are shown in Fig. 10 for (a) the straight annular passage and (b) the curved annular duct. Experimental results of velocity vectors near the hub and the casing have been omitted from these figures due to the high radial gradient of the total pressure. In the case of the straight annular passage (Fig. 10(a)), the experimental and calculated results of the secondary vectors indicate radially inward flow. In contrast, in the case of the curved annular passage, the vectors indicate radially outward flow due to the hub passage curvature (Fig. 10(b)). On the whole, the experimental and calculated results show good qualitative agreement. It is very interesting that the vortical motion (clockwise) of the horseshoe vortex is clearly revealed near the casing by the calculations (Fig. 10(a)). However, in the case of the curved annular passage (Fig. 10(b)), it is very difficult to reveal this vortical motion due to the reduction of the streamwise positive pressure gradient along the casing in the S-shaped duct exit (see Fig. 5) and due to the hub passage curvature (the magnitude of the radially outward flow vectors). In this calculation, the inlet boundary layer is very thin (i.e., 1 percent of passage height). If the inlet boundary layer is thicker, a vortical motion of the horseshoe vortex near the hub will be more distinct. The features of secondary flow vectors downstream of $X/L = 1.03$ are shown in Fig. 11. The inlet boundary layer thickness is 10 percent of the passage height. The formation of vortical motion (counterclockwise) related to the horse-

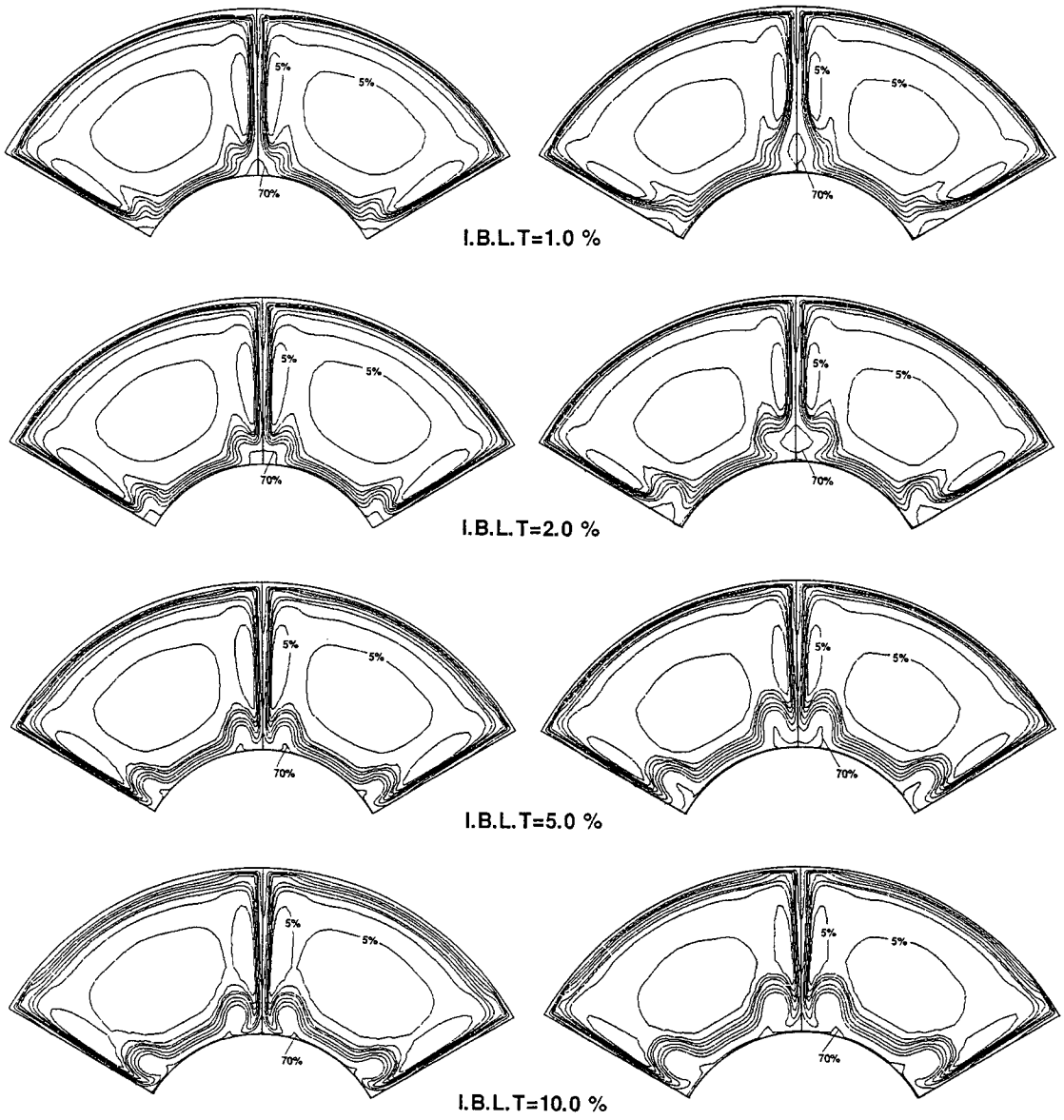

Fig. 12 Effect of inlet boundary layer thickness on total pressure loss contours

shoe vortex is more clearly captured at $X/L = 1.03$. Furthermore, the vortices grow with increasing distance from the strut and that, at $X/L = 1.20$, a large vertical vortex appears at midpassage.

Effect of Inlet Boundary Layer Thickness. As already described, the inlet boundary layer of our **S**-shaped duct is estimated to be only about 1 percent of the passage height due to the high acceleration rate. This value is very different from that for real engines. Therefore, it is worthwhile to calculate the effect of the inlet boundary layer thickness on the flow field within the **S**-shaped duct. Figure 12 shows the variation of the total pressure at $X/L = 1.03$ for (a) the straight annular passage and (b) the curved annular passage. As the inlet boundary layer becomes thicker, the total pressure loss near the hub and the casing at the midpoint between the struts increases, and at the same time, the higher loss regions related to the horseshoe vortex are observed on either side of the strut wake near the hub. These regions of high pressure loss on either side of the strut wake near the hub may act on a downstream compressor as a large inlet distortion, and strongly affect the downstream compressor performance.

Flow Development Within S-Shaped Duct. A bird's-eye view of the flow development within the duct with inlet boundary layer thickness of 10 percent of the passage height is shown in Fig. 13. The contours of the total pressure are shown for the case of the curved annular passage. A low total pressure region near the hub has already started on either side of strut surface at the latter half of the **S**-shaped duct due to the positive pressure gradient. In contrast, the development of the boundary layer along the casing is suppressed by the negative pressure gradient (see Fig. 5).

Concluding Remarks

Experimental and numerical investigations were carried out to gain a better understanding of the flow characteristics within

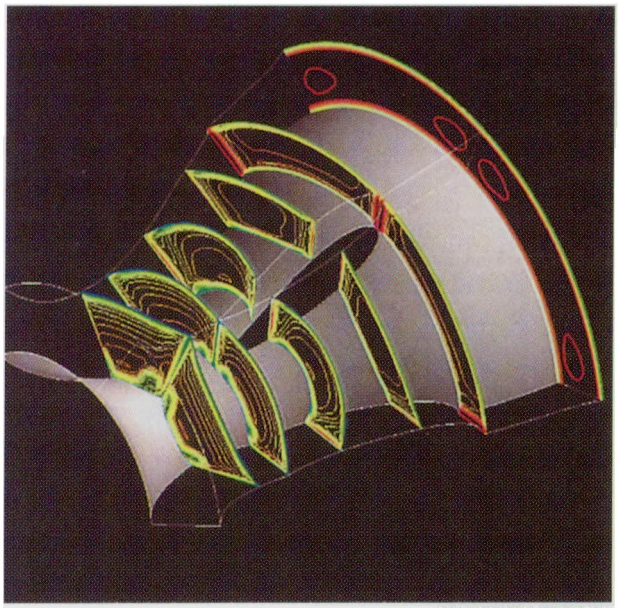

Fig. 13 Bird's-eye view of flow development within an annular S-shaped duct (inlet boundary layer thickness = 10 percent of passage height)

an annular S-shaped duct, including the influence of the shape of the downstream passage located at the exit of the duct on the flow. The following conclusions were drawn.

- The total pressure loss near the hub is large due to instability of the flow, as compared with that near the casing. Furthermore, a vortex related to the horseshoe vortex is observed in the form of high loss region near the casing, experimentally.
- In the case of the curved annular downstream passage, the total pressure loss near the hub is greatly increased compared with the case of the straight annular passage, and the spatial position of this vortex near the casing depends on the passage core streamwise pressure gradient.
- Results of calculations using the three-dimensional Navier–Stokes code with a low-Reynolds-number $k-\epsilon$ turbulent model are in good agreement with experimental results. However, quantitative discrepancies are observed in the wake region; this is a subject for future study.
- According to the simulation results showing the effect of inlet boundary layer thickness, a region of very high pressure loss is generated near the hub. This is due to the formation of the horseshoe vortex related to the inlet boundary layer thickness. Such regions of high pressure loss may act on the downstream compressor as a large inlet distortion, and strongly affect the downstream compressor performance.

The phenomena observed in this investigation may be different when the downstream flow field is controlled by an impeller. Therefore, we are planning to investigate the flow of S-shaped duct with a downstream impeller, in the near future.

Acknowledgments

The authors thank Honda R&D Co., Ltd., for permission to carry out this study and to publish this work.

References

Arima, T., Sonoda, T., Shirotori, M., Tamura, A., and Kikuti, K., 1997, "A Numerical Investigation of Transonic Axial Compressor Rotor Flow Using a Low Reynolds Number $k-\epsilon$ Turbulence Model," ASME JOURNAL OF TURBOMACHINERY, in press.

Bailey, D. W., and Carrotte, J. F., 1996, "The Influence of Inlet Swirl on the Flow Within an Annular S-Shaped Duct," ASME Paper No. 96-GT-60.

Bailey, D. W., Britchford, J. F., Carrotte, J. F., and Stevens, S. J., 1997, "Performance Assessment of an Annular S-Shaped Duct," ASME JOURNAL OF TURBOMACHINERY, Vol. 119, pp. 149–156.

Britchford, K. M., Carrotte, J. F., Stevens, S. J., and McGuirk, J. J., 1994, "The Development of the Mean Flow and Turbulence Structure in an Annular S-Shaped Duct," ASME Paper No. 94-GT-457.

Denton, J. D., 1985, "The Calculation of Fully 3D Flow Through Any Type of Turbomachine Blade Row," AGARD Lecture Series—3D Computational Techniques Applied to Internal Flows in Propulsion Systems, AGARD LS 140.

Karim Abdulla-Altaii, A., and Raj, R. S., 1994, "Secondary Flow Development Downstream of a Blade Endwall Corner," ASME Paper No. 94-GT-459.

On the Design Criteria for Suppression of Secondary Flows in Centrifugal and Mixed Flow Impellers

M. Zangeneh
Department of Mechanical Engineering,
University College London,
London, United Kingdom

A. Goto

H. Harada

Ebara Research Co., Ltd.,
Fujisawa-shi, Japan

In this paper, for the first time, a set of guidelines is presented for the systematic design of mixed flow and centrifugal compressors and pumps with suppressed secondary flows and a uniform exit flow field. The paper describes the shape of the optimum pressure distribution for the suppression of secondary flows in the impeller with reference to classical secondary flow theory. The feasibility of achieving this pressure distribution is then demonstrated by deriving guidelines for the design specifications of a three-dimensional inverse design method, in which the blades are designed subject to a specified circulation distribution or $2\pi r\bar{V}_\theta$. The guidelines will define the optimum choice of the blade loading or $\partial r\bar{V}_\theta/\partial m$ and the stacking condition for the blades. These guidelines are then used in the design of three different low specific speed centrifugal pump impellers and a high specific speed industrial centrifugal compressor impeller. The flows through all the designed impellers are computed numerically by a three-dimensional viscous code and the resulting flow field is compared to that obtained in the corresponding conventional impeller. The results show consistent suppression of secondary flows in all cases. The design guidelines are validated experimentally by comparing the performance of the inverse designed centrifugal compressor impeller with the corresponding conventional impeller. The overall performance of the stage with the inverse designed impeller with suppressed secondary flows was found to be 5 percent higher than the conventional impeller at the peak efficiency point. Exit flow traverse results at the impeller exit indicate a more uniform exit flow than that measured at the exit from the conventional impeller.

Introduction

In 1971, Dean wrote that "The future of centrifugal compressor appears to be bright, provided that its complicated fluid dynamics can be unscrambled and mastered for design optimisation." Since then, as a result of developments in experimental and computational techniques, considerable progress has been made in our understanding of the complicated flow effects in centrifugal compressors.

In the case of the impeller, one of the most important problems at the time, which still remains unresolved, was the impeller exit flow nonuniformity in which a low-velocity wake region was found near the suction surface and a jet region near the pressure surface. Dean and Senoo (1961) called this flow pattern the "jet-wake" flow. The mixing of this "jet-wake" flow was known to be a source of significant loss generation. In the case of a 10:1 pressure ratio stage, Dean (1971) attributed 9 percent of total stage efficiency loss to the mixing of the "jet-wake."

The most significant development in this area was the LDV measurements of Eckardt (1976, 1980) for relatively low pressure ratio impellers. Similar measurements were made by Krain (1988) on a higher pressure ratio compressor with backsweep and more recently, by Hathaway et al. (1993) on a low-speed large-diameter impeller with backsweep. Generally all these experimental results confirm the basic structure of the jet-wake flow as proposed by Dean and Senoo (1961), with the difference that the exit flow field shows both pitchwise and spanwise variations. The work of Dean and Senoo (1961) and Inoue and Cumpsty (1984) shows that circumferential variations in the exit flow mix up very rapidly, while the axial variations in the flow seem to persist well into the diffuser. This axial flow variation has an adverse effect on the pressure recovery of the diffuser (vaned or vaneless) and has been shown to be one of the main causes of inception of stage instability in compressors, see Senoo and Kinoshita (1977); while Goto (1992b) has shown that the instability is caused by impeller stall. Therefore, the minimization or possible suppression of the formation of the exit flow nonuniformity should not only lead to substantial improvement in stage performance but also result in increases in the stable operating range of the machine.

In order to design impellers with a more uniform exit flow field, it is important to understand the basic mechanisms behind the generation of the exit flow nonuniformity and then produce appropriate design guidelines to minimize their effects by changes to the impeller geometry. From the experimental results it is possible to hypothesize three main mechanisms behind the generation of the exit flow nonuniformity: first, the secondary flows that have been known to have a significant effect on the movement of low-momentum fluids on the blade surface and endwall boundary layers; second, the interaction of the low-momentum fluid in the boundary layer with the tip leakage flows, which is only important in unshrouded impellers; finally, the presence of boundary layer separation especially on the suction surface at the shroud. There is no doubt that boundary layer separation when present can have a significant effect on the generation and intensification of the exit flow nonuniformity. However, it is the action of the secondary flows and the way they move the low-momentum fluids in the impeller that is the main cause of the generation of the jet-wake flow. Recent

Contributed by the International Gas Turbine Institute and presented at the 42nd International Gas Turbine and Aeroengine Congress and Exhibition, Orlando, Florida, June 2–5, 1997. Manuscript received at ASME Headquarters February 1997. Paper No. 97-GT-393. Associate Technical Editor: H. A. Kidd.

application of three-dimensional viscous methods to analysis of flow through radial and mixed flow impellers [see Goto (1992a), Casey et al. (1992) and more recently Hirsch et al. (1996), among many others] have shown that it is possible to predict the extent and location of the exit wake without the presence of any significant flow separation in the prediction.

The dominating influence of secondary flows on the generation of the "jet-wake" flow has been known since early seventies; see Dean (1971), as well as Johnson (1978) and Johnson and Moore (1983). However, there have been very few successful attempts in controlling the secondary flows in the impeller. Some attempts to control secondary flows in the impeller by the use of blade lean have been reported by Cox (1990) and Howard and Ashrafizaadeh (1994). The authors in their earlier papers (see Zangeneh et al., 1996, and Goto et al., 1996) provided some guidelines on how blade lean or spanwise stacking can be used to minimize secondary flows in the impeller and to obtain a more uniform exit flow field. The use of excessive amounts of blade lean, however, can result in structural problems or manufacturing difficulties. The main purpose of this paper is to use our current understanding of the flow field in the impeller to "unscramble" the mechanism of secondary flow generation and then to derive general guidelines for the design of impellers with minimized secondary flow and uniform exit flow field. These guidelines are then verified both numerically and experimentally by their applications to an industrial centrifugal compressor impeller and a centrifugal pump impeller.

Secondary Flows in Mixed Flow and Radial Impellers

In the Classical Secondary Flow theory as developed by Hawthorne (1967), the effect of viscosity is ignored and the secondary flow development is considered in an inviscid fluid. Hawthorne's work has confirmed the validity of such an approach in providing an excellent qualitative picture of the secondary flow development. In Hawthorne (1974), a number of expressions are derived based on such an approach for the development of secondary flow in a stationary or rotating system. However, for a qualitative discussion, it is more useful to consider the following simple kinematic equation derived by Zangeneh et al. (1988), for the development of secondary flows in incompressible flow in rotating systems:

$$\mathbf{W}\cdot\nabla(\mathbf{W}\cdot\Omega) = 2\Omega\cdot(\mathbf{W}\cdot\nabla)\mathbf{W} + \Omega(2\omega\times\mathbf{W}) \qquad (1)$$

In this equation, $(\mathbf{W}\cdot\Omega)$ represents the streamwise component of absolute vorticity. According to Eq. (1) streamwise components of vorticity (and therefore secondary flows) are generated when there is a component of acceleration (streamline curvature or Coriolis) in the direction of absolute vorticity. Furthermore, the secondary flows tend to move low-momentum fluids toward a stable location, which can be shown to be the location of minimum reduced static pressure Pr (or relative Mach number); see the discusion of Johnson (1978). Using this relationship and assuming that the only vorticity in the flow is the vorticity on the blade surface and endwall boundary layers, one can divide the secondary flows in the impeller into three different regions.

1 *Inducer:* In the inducer region, the radial component of Corriolis acceleration ($2\omega W\theta$) is in the direction of vorticity in the blade surface boundary layers. This can potentially result in a hub to shroud secondary flow on both blade surfaces. At the same time the acceleration due to the curvature of the inducer is in the direction of vorticity in the endwall boundary layer. This in turn can result in a blade–blade secondary flow, which will move low-momentum fluids from the pressure surface to the suction surface. In practice, however, very little secondary flow can be observed in the inducer region as the boundary layer is relatively thin.

2 *Axial–Radial Bend:* In this region, the secondary flow is again due to a combination of rotational (Coriolis) and curvature effects. The meridional curvature due to axial to radial bend is in the direction of vorticity in the blade surface boundary layers. As a result of the rapid growth of the boundary layer thickness in this region, usually quite significant meridional secondary flow moving low-momentum fluids from hub to shroud can be observed on both surfaces. However, the secondary flow will be stronger on the suction surface due to the more rapid growth of the boundary layer. At the same time the tangential component of Coriolis acceleration ($2\omega Wr$) will be in the direction of endwall boundary layers, resulting in pressure to suction surface secondary flows.

3 *Radial Part:* In the purely radial part of the impeller, the tangential component of Coriolis acceleration is in the direction of endwall boundary layers, which can result in strong blade–blade secondary flows.

Although the magnitude of streamline curvature or Coriolis acceleration can be found easily in different parts of the impeller (say from an inviscid or viscous computation), it is perhaps more useful from a designer's point of view to relate the secondary flow generation to an easily calculated variable such as pressure, Mach number, etc. This can be done quite easily by considering the momentum equation in inviscid flow, which can be written as:

$$W\cdot\nabla W + 2(\omega\times W) = -\frac{1}{\rho}\nabla p - \omega\times(\omega\times r)$$

Now it can be shown that

$$\omega\times(\omega\times r) = -\nabla(\omega^2 r^2/2)$$

So the momentum equation in incompressible flow can be written as:

$$W\cdot\nabla W + 2(\omega\times W) = -\frac{1}{\rho}\nabla\left(p - \frac{\rho\omega^2 r^2}{2}\right) \qquad (2)$$

where the term in brackets on the right side is the well-known "reduced static pressure" usually denoted by Pr. Equation (2)

Nomenclature

B = number of blades
$D_{cp} = \Delta Cp(\min) - \Delta Cp(m_{\min} - 0.4)$
f = blade wrap angle (θ value at the blade)
h = static enthalpy
M = relative Mach number
M_{u2} = Mach number based on inlet stagnation temperature and U_{2m}
m = percentage meridional distance
r = radius
$r\bar{V}_\theta$ = pitchwise-averaged swirl velocity
$\mathbf{V}$ = velocity
$\mathbf{W}$ = relative velocity
ΔCp = difference between Cp at shroud and hub on suction surface
ΔCp_{BB} = blade pressure loading
ρ = density
ϕ = compressor flow coefficient = $4Q/\pi U_{2m} D_{2m}^2$
ω = rotational speed
Ω = vorticity

Subscripts

bl = at the blade
m = meridional direction
min = location of minimum ΔCp
$2m$ = impeller mean exit radius

Superscripts

$\bar{A}$ = pitchwise mean value
$+$ = relative to upper blade surface
$-$ = relative to lower blade surface

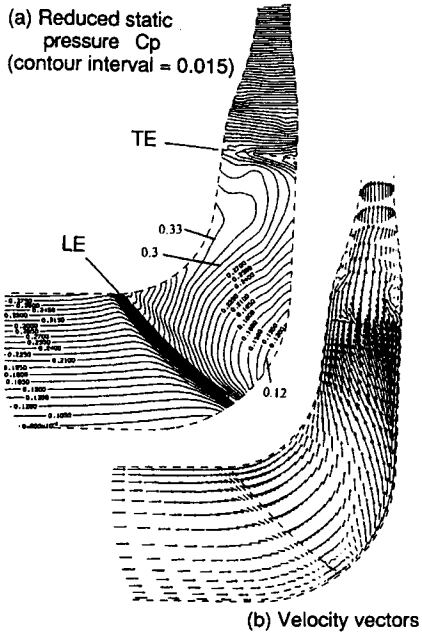

Fig. 1 Secondary flows on blade suction surface (conventional NS280 impeller)

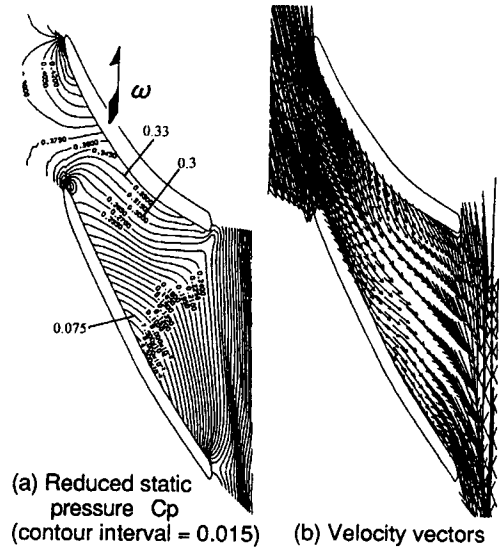

Fig. 2 Secondary flows on shroud surface (conventional NS280 impeller)

clearly shows that in a rotating system the gradients of reduced static pressure are produced as a result of streamline curvature and Coriolis accelerations. Using Eq. (2) we can conclude that *secondary flow is generated whenever there is a gradient of reduced static pressure in the direction of vorticity in the flow field.* In compressible flow, regions of low reduced static pressure correspond to regions of high relative Mach number and vice versa. By monitoring gradients of reduced static pressure (or relative Mach number in compressible flow) it should then be possible to obtain a qualitative understanding of the intensity of secondary flows in different parts of the impeller. Furthermore, by controlling the gradients of reduced static pressure at certain locations in the impeller, it should be possible to minimize secondary flows and reduce the exit flow nonuniformity.

To illustrate the direct relationship between gradients of reduced static pressure and secondary flows, the results of numerical predictions for a conventionally designed low specific speed shrouded centrifugal pump impeller are presented in Figs. 1–3. The pump specific speed Ns is 0.7 (or 285 using units rpm, m^3/min and m) with the design flow rate of 3.26 m^3/min, rotational speed of 800 rpm, and pump head of 8.77 m. The flow through the seven-bladed pump impeller was computed by using the incompressible version of Dawes' three-dimensional Navier–Stokes code (Walker and Dawes, 1990) using a computational mesh consisting of 115 points in the streamwise direction (with 30 points upstream of the impeller and 60 points inside the impeller region), 29 points in the spanwise direction and 29 points in the pitchwise direction. To resolve the blade surface and endwall boundary layers, grid clustering was used in the spanwise and pitchwise directions. Since the impeller is shrouded, no tip leakage was modeled and the shroud surface was made to rotate with the blade speed. In order to avoid convergence instability caused by flow reversal near the exit boundary, the downstream passage was contracted as shown in Fig. 1. The Dawes incompressible program has been validated extensively for pump impeller computations (see Goto, 1992a).

In Fig. 1, the distribution of the predicted reduced static pressure coefficient on the suction surface of the impeller defined by Cp = (Rotary stagnation pressure $- P_r$)/$(1/2\rho U_{2m}^2)$ is presented. Also shown in Fig. 1 is the predicted velocity vectors near the suction surface. The velocity vectors show clearly that meridional secondary flows start at about 10–15 percent of meridional chord (or m = 0.1 to 0.15) from the impeller leading edge. There is a good correlation between the intensity of secondary flows and the gradients of Cp. For example, there is a stronger secondary flow in the region around m = 0.3 to m = 0.5 where there are higher gradient of Cp as compared to the region m = 0.7 to m = 1 (or the trailing edge). In Fig. 2, the corresponding predictions near the shroud surface are presented. It is interesting to note that despite the strong gradients of Cp on the shroud surface, only limited secondary flow from pressure to the suction surface can be seen. However, there are some secondary flows from the suction surface toward the midpitch location. This is due to the action of the low-momentum fluids that have accumulated on the shroud suction corner and that continue to move around the corner region under the action of their remaining momentum. The collision of this low-momentum fluid with the blade–blade secondary flows leads to the formation of the exit flow field shown in Fig. 3, where a distinct wake region can be observed on the shroud about 35 percent of pitch from the suction surface.

Optimum CP (M) Distribution for Uniform Exit Flow

The results given above indicate clearly that due to the thicker boundary layers, the meridional secondary flows on the suction surface have the most important effect on the formation of the jet-wake flow. This fact has already been demonstrated in the earlier work of the authors, Zangeneh et al. (1996) and Goto et al. (1996), in which by suppressing the secondary flows on the suction surface a uniform exit flow from a mixed flow pump impeller was obtained. So our aim here is to optimize the Cp

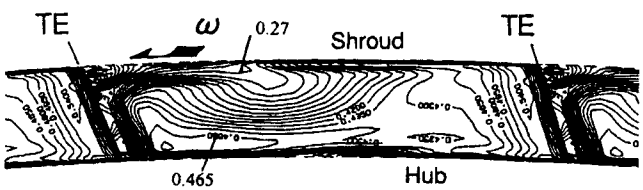

Fig. 3 Predicted exit flow field for conventional pump

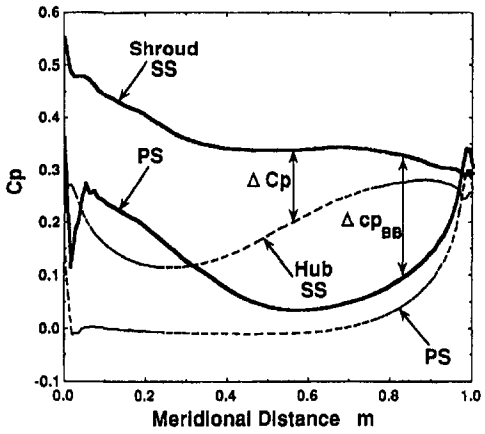

Fig. 4 Predicted C_p distribution for conventional pump impeller

(or M) distribution in such a way as to minimize secondary flows on the suction surface of the impeller.

The Cp distribution on the hub and shroud of this conventional centrifugal pump impeller, as predicted by the Dawes code, is presented in Fig. 4. The Cp distribution on the hub and shroud has been plotted on the same figure in order to highlight the spanwise gradients in Cp (or ΔCp). Although ΔCp is quite high in the first 30 percent of meridional chord (i.e., from the leading edge to $m = 0.3$) very little secondary flow can be observed on the suction surface (see Fig. 1) due to the thin blade surface boundary layers. However, the large value of ΔCp in the region from $m = 0.3$ to $m = 0.8$ has led to strong meridional secondary flows, as shown in Fig. 1. In order to suppress these secondary flows, it is important to minimize ΔCp in this region. This can be achieved in the following three different ways:

(i) First by decreasing the value of Cp on the shroud suction surface, which can be achieved by decreasing the blade pressure loading (or ΔCp_{BB}) on the shroud in the aft part of the impeller. Of course to ensure the same overall turning and work, it is then essential to increase the blade loading in the fore part of the impeller. Reducing ΔCp_{BB} in the aft part of the impeller will also reduce the blade to blade secondary flows whose strength is directly related to the pitchwise gradients of Cp in the aft part of the impeller.

(ii) Increasing the value of Cp on the hub suction surface also helps to reduce ΔCp. This can be achieved by increasing the blade pressure loading (or ΔCp_{BB}) near the trailing edge region. Again in order to ensure a similar turning, the blade pressure loading at the hub near the leading edge region should be reduced by a corresponding amount.

(iii) In many circumstances, the degree that the shroud suction surface Cp can be reduced, as described above, is limited by the diffusion ratio or other design criteria such as caviation or shockwave control. So in practice it is important to use a combination of (i) and (ii) in which the shroud suction surface Cp is reduced in the aft part of the impeller, while at the same time the hub suction surface Cp is increased there. An example of such a Cp distribution is shown in Fig. 6(b), where as a result of using a combination of (i) and (ii) it has been possible to minimise ΔCp.

One important aspect of the application of this optimum distribution of Cp for suppression of meridional secondary flows is to establish the limit that the ΔCp needs to be minimized in order to suppress secondary flows. Since the reduction in ΔCp is only important from about meridional distance of 40 percent (or $m = 0.4$), it is quite useful to define a parameter $D_{cp} = (\Delta Cp(\min) - \Delta Cp(m_{\min} - 0.4))$, where $\Delta Cp(\min)$ is the minimum value of ΔCp and $m_{\min}$ is the nondimensional meridional distance location of this minimum. $\Delta Cp(m_{\min} - 0.4)$ is the value of ΔCp at the meridional location given by $(m_{\min} - 0.4)$. The limiting value of D_{Cp} (i.e., the minimum amount that ΔCp should be reduced in order to suppress meridional secondary flows) can vary from impeller to impeller and *can be shown to be dependent on the specific speed of the machine.*

Design of Blades With Optimum C_P (or M) Distribution

Currently most centrifugal compressor impeller and some pump impellers are designed with straight (or in some cases even radial) blade filaments. As a result the designer can only control the ΔCp_{BB} on one streamline, which is usually taken as the shroud streamline. Dallenbach (1961) has provided a discussion of some of the basic features of Mach number distributions that can be achieved for radial-bladed centrifugal compressor impellers. For example, he shows that with radial blade filaments, when the shroud is fore-loaded then the hub also becomes fore-loaded, which will in fact result in an increase in ΔCp in the aft part of the impeller.

In order to design impeller blades with the type (iii) Cp distribution, it is important to be able to control the loading distribution or ΔCp_{BB} on the hub and shroud independently. To design such blades it is then essential to remove the restriction of straight-blade filaments. Using conventional techniques, based on the use of geometry representation tools such as Bezier curves together with the iterative application of analysis methods, to achieve the type (iii) Cp distribution will be a very inefficient process. The most efficient means of designing blades with controlled Cp distribution as described above is to use a three-dimensional inverse design method in which the loading distribution can be specified. So for this purpose the three-dimensional inverse design method of Zangeneh (1991) can be used. In this method the $r\bar{V}_\theta$ distribution, defined by:

$$r\bar{V}_\theta = \frac{B}{2\pi}\int_0^{2\pi/B} rV_\theta d\theta \tag{3}$$

is specified as the design input. As has been shown before (see Hawthorne et al., 1984, and Zangeneh, 1991) the meridional derivative of $r\bar{V}_\theta$ is related to the blade loading through the following expression in incompressible flow:

$$p^+ - p^- = \frac{2\pi}{B}\rho W_{mbl}\frac{\partial r\bar{V}_\theta}{\partial m} \tag{4}$$

and the corresponding relation in compressible flow:

$$h^+ - h^- = \frac{2\pi}{B}W_{mbl}\frac{\partial r\bar{V}_\theta}{\partial m} \tag{5}$$

where superscripts + and − correspond to values on either side of the blades, B is the blade number, W_{mbl} is the meridional velocity on the blades, and m is in the direction of streamlines in the meridional plane. According to Eqs. (4) and (5) by making changes to the meridional derivative of $r\bar{V}_\theta$ or $\partial r\bar{V}_\theta/\partial m$ it should then be possible to control the blade pressure loading.

The other important input specification for the inverse design method, which affects the Cp (or M) distribution on the blades, is the stacking condition. As discussed in Zangeneh (1991), this condition is required in order to compute the wrap angle throughout the blade region by integrating the first-order hyperbolic equation, which is obtained as a result of the application of the inviscid slip (or flow tangenency) condition. For this condition, the distribution of wrap angle f should be specified along a quasi-orthogonal (called the stacking quasi-orthogonal) from hub to shroud. If the values of f are set to be the same along the stacking quasi-orthogonal, then straight blade filament on that quasi-orthogonal is obtained. By specifying a higher

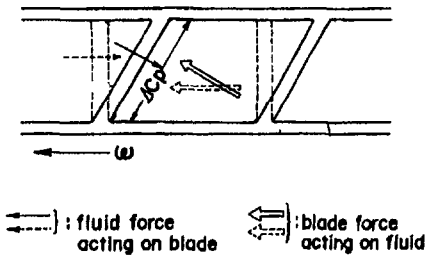

Fig. 5 Effect of blade lean

value of f at the shroud and a lower value of f at the hub and a linear (or other) distribution in between, it is possible to obtain a leaned blade filament on the stacking quasi-orthogonal.

In the following section the optimum choice of loading distribution and stacking condition for obtaining type (*iii*) Cp (or M) distributions will be described.

Optimum Loading Distribution. Equations (4) and (5) show the direct relationship between $\partial r\bar{V}_\theta/\partial m$ and the difference between pressure (or enthalpy) on the upper and lower surfaces of the blade or ΔCp_{BB}. In order to reduce the Cp (or Mach number) on the suction surface of the shroud in the aft part of the impeller one should specify a $\partial r\bar{V}_\theta/\partial m$ distribution as shown by the solid line in Fig. 6(*a*). This distribution reduces the blade loading in the aft part of the impeller, thereby helping to reduce the Cp (or M) on the suction surface of the shroud. Similarly to increasing the Cp (or Mach number) at the hub in the aft part of the impeller, it is possible to specify a $\partial r\bar{V}_\theta/\partial m$ distribution as shown by the dashed line in Fig. 8(*a*). To achieve a type (*iii*) Cp distribution, it is then essential to specify a $\partial r\bar{V}_\theta/\partial m$ as shown in Fig. 8(*a*) with the maximum value of $\partial r\bar{V}_\theta/\partial m$ at the shroud in the fore part of the impeller and the maximum value of $\partial r\bar{V}_\theta/\partial m$ at the hub in the aft part of the impeller. The optimum location of maximum value of $\partial r\bar{V}_\theta/\partial m$ on the hub and shroud will vary from impeller to impeller, depending on the specific speed and other design criteria such as pressure ratio in compressors and cavitation control in pumps. Once the optimum distribution of $\partial r\bar{V}_\theta/\partial m$ at the hub and shroud are obtained, they can be integrated to find the $r\bar{V}_\theta$ distribution on the hub and shroud. The overall $r\bar{V}_\theta$ distribution on the meridional plane can then be obtained by using linear interpolation between hub and shroud; see Zangeneh et al. (1996) for more details.

Optimum Stacking. Leaned blades have been used extensively in the design of low pressure ratio, high aspect ratio axial turbines to affect spanwise stage reaction (see Grant and Borthwick, 1987) and high-pressure, low aspect ratio turbines to control spanwise secondary flows (Harrison, 1992, and Han et al., 1994). However, there are some subtle but important differences between the use of stacking in the inverse design method and its application in conventional design. In order to bring out these differences, it is important to discuss how stacking affects the loading distribution on the blade surfaces.

The main effect of blade lean is to introduce a spanwise (or radial in the case of axial turbines) blade force as shown in Fig. 5. If the blades are leaned against the direction of rotation (i.e., the blades at the hub leading the blades at the shroud) the result is a blade force, which will increase the pressure at the shroud and reduce the pressure at the hub. The application of blade lean to axial turbine stators has shown that this type of linear lean can increase the blade loading at the low-pressure wall and reduce the blade loading at the high-pressure end as compared to the corresponding straight blade (see Harrison, 1992). The main reason behind the increase or reduction in loading can be explained with reference to Eq. (4). At the high-pressure end the velocity at the blade W_{bl} is reduced and so from Eq. (4), this will result in a reduction in blade loading, while at the low pressure end the W_{bl} rises and as a result the blade loading is increased. The main difference between conventional stacking and stacking used in the inverse method is that in the inverse method $\partial r\bar{V}_\theta/\partial m$ will remain fixed and the computed blade angles will change to give the correct Euler head. While in the conventional method, as used in axial turbines (see Harrison, 1992, and Han et al., 1994) and also used by Howard and Ashrafizaadeh (1994), the blade angle is fixed and therefore the changes in blade lean will change the $r\bar{V}_\theta$ distribution and thereby the Euler work.

The ideal type of stacking condition for suppression of secondary flows in radial and mixed flow turbomachines is to lean the blades linearly against the direction of rotation, as shown in Fig. 5, in the aft part of the impeller. Using this type of lean, as discussed above, will lead to a reduction in loading at the shroud and a corresponding increase in loading at the hub in the aft part of impeller. In this way the ΔCp is reduced in the aft part of impeller resulting in the minimization (or suppression) of meridional component of secondary flow on the suction surface.

Verification of Design Criteria

In order to demonstrate the validity of the design criteria described above, a number of computational and experimental studies were undertaken. In this paper, the application of the design criteria to the design of a low specific speed pump impeller and a high specific speed industrial centrifugal compressor impeller will be described.

Application to Pumps. The basis of this study was the conventional pump impeller mentioned earlier in the paper. For the purpose of this study three different impellers were designed in order to suppress the meridional secondary flows on the suction surface of the conventional impeller as shown in Fig. 1 and to improve the impeller exit flow field. To test the validity of design criteria described above impellers A and B were designed by using the optimum stacking and optimum loading conditions, respectively. In the case of impeller C, however, the design was based on a combination of optimum loading and stacking. This was mainly because in practice the use of too much lean may cause structural and/or manufacturing difficulties. While in many cases the choice of loading distribution may be governed by other criteria such as cavitation control in pumps, etc.

Impeller A. Impeller A was designed by using the optimum stacking condition at the trailing edge. For this purpose the blades were stacked with a linear variation in blade wrap angle from hub to shroud of 0.15 radians. The $\partial r\bar{V}_\theta/\partial m$ distribution used for this design is presented in Fig. 6(*a*). In order to show the effectiveness of optimum stacking to suppress secondary flows, in this design a nonoptimum type $\partial r\bar{V}_\theta/\partial m$ was specified, in which the maximum value of $\partial r\bar{V}_\theta/\partial m$ was placed in the forepart of the impeller at both hub and shroud. The procedure used to generate $\partial r\bar{V}_\theta/\partial m$ is described in detail in Zangeneh et al. (1996).

Using the design specification given above, the seven-bladed impeller was designed using the three-dimensional inverse design method. For the inverse design a (89 × 25) meridional computational mesh was used together with 10 Fourier harmonics to represent the flow variations in the tangential direction. The inverse design program not only computes the blade shape, it also determines the three-dimensional flow field in the designed impeller. So for normal design applications the predicted Cp distribution by the inverse design method is used. However, in order to make a proper comparison between the Cp distribution for the inverse designed impeller A and the conventional impeller, the Cp distribution predicted by the Dawes code will be used.

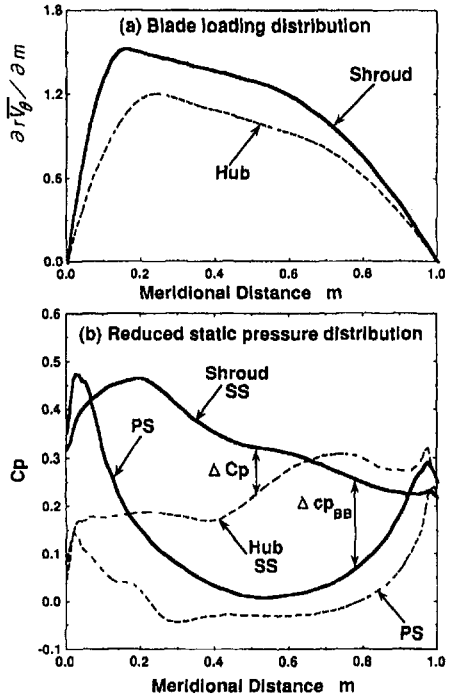

Fig. 6 Specified blade loading and *Cp* distribution obtained for NS280A impeller

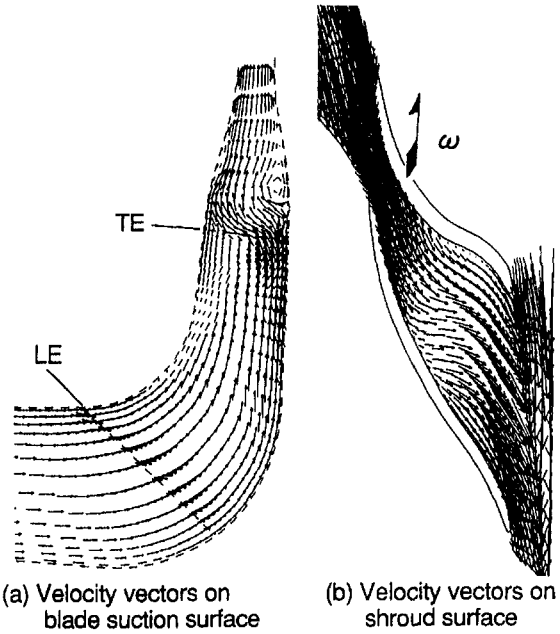

Fig. 7 Predicted flow field in NS280A impeller

The flow through the designed impeller was computed by the Dawes Navier–Stokes solver using the same mesh size as employed in the conventional impeller calculation (i.e., $29 \times 115 \times 29$). The predicted *Cp* distribution is shown in Fig. 6(b). The predicted negative incidence at the leading edge of the shroud is mainly due to the poor H-grid resolution for the low inlet blade angle at the shroud. Comparing this *Cp* distribution with that of the conventional impeller, shown in Fig. 4, it is possible to see clearly that as a result of using the stacking condition the ΔCp_{BB} on the shroud has been reduced in the aft part of impeller while the ΔCp_{BB} on the hub has been increased. As a result, the spanwise gradient in *Cp* (or ΔCp) has been reduced considerably from 40 percent of meridional chord. In fact ΔCp becomes negative from about 60 percent meridional chord to the trailing edge. The value of D_{cp}, which measures the rate of reduction in ΔCp between the minimum location and a point about 40 percent of meridional chord upstream of it, is 0.23 as opposed to only 0.12 in the case of the conventional impeller. The predicted velocity vectors near the suction surface of the impeller, presented in Fig. 7(a), confirm that as a result of the reduction in ΔCp secondary flows are well suppessed on the suction surface. In the absence of meridional secondary flows on the suction surface, very little low-momentum fluid is accumulated at the shroud suction corner and therefore no blade–blade secondary flow can be observed from suction to pressure surface (see Fig. 7(b)), as was predicted in the case of the conventional impeller. However, blade–blade secondary flows can be observed from pressure to suction surface at about 50 percent of meridional chord.

Impeller B. Impeller B was designed by using the $\partial r\bar{V}_\theta/\partial m$ distribution shown in Fig. 8(a), in which the maximum value of $\partial r\bar{V}_\theta/\partial m$ is set in the forepart of the impeller at the shroud and in the aft part of the impeller at the hub. In order to show the effectiveness of the optimum loading distribution in minimizing the secondary flows, in this case the blades were stacked axially at the trailing edge. Again the flow through the designed impeller was computed by the Dawes Navier–Stokes code, using the same computational grid as employed in impeller A and the conventional impeller computations. The *Cp* distribution predicted by the viscous code is presented in Fig. 8(b), where it can be clearly seen that the use of loading distribution shown in Fig. 8(a) has resulted in a reduction in ΔCp from 40 percent of meridional chord to the trailing edge. In this case, however, ΔCp does not become negative in the aft part of impeller and so the rate of reduction in ΔCp (or D_{Cp}) is only 0.14. As a result the predicted velocity vectors near the suction surface of impeller B, presented in Fig. 9(a), show some meridional secondary flows, although the extent of the secondary flows has been reduced substantially as compared to the conventional impeller. Furthermore, the predicted velocity vectors on the shroud surface, presented in Fig. 9(b), show some blade-blade

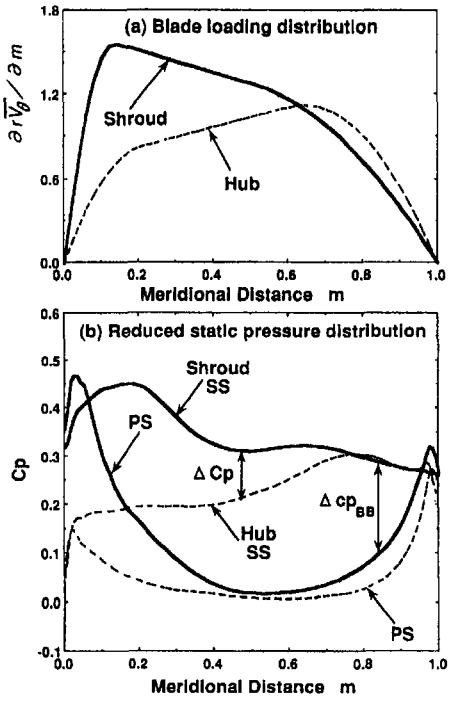

Fig. 8 Specified blade loading and obtained *Cp* distribution for NS280B impeller

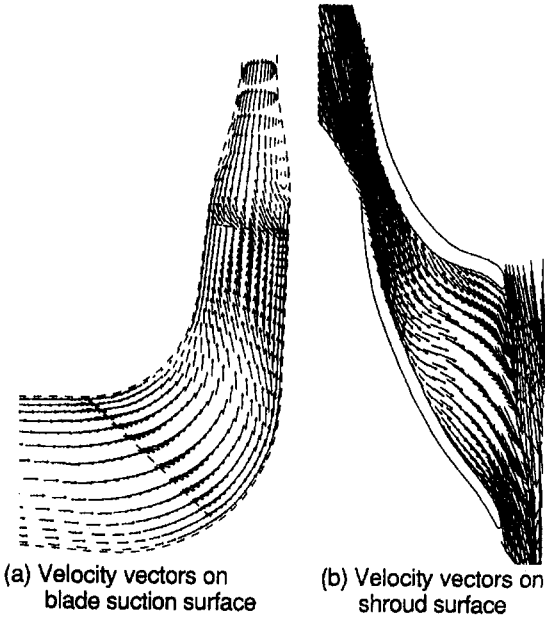

Fig. 9 Predicted flow field in NS280B impeller

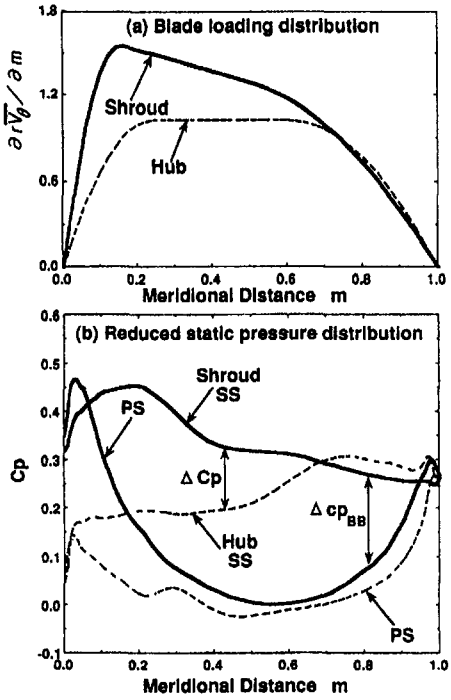

Fig. 10 Specified blade loading and *Cp* distribution obtained for NS280C impeller

secondary flows from suction surface toward the midpitch location as a result of the slight accumulation of low-momentum fluids on the shroud/suction surface corner by the meridional secondary flows. However, the magnitude of these secondary flows are not as high as that observed for the conventional impeller, see Fig. 2.

Impeller C. The application of excessive amounts of blade lean can result in manufacturing and structural problems, while in many cases the use of optimum $\partial r\bar{V}_\theta/\partial m$ distribution may not be adequate for complete suppression of secondary flows in the impeller. So in many applications it is important to use a combination of optimum stacking condition (or blade lean) and the $\partial r\bar{V}_\theta/\partial m$ distribution. To demonstrate the feasibility of such an approach for suppression of meridional secondary flows, impeller C was designed by using the $\partial r\bar{V}_\theta/\partial m$ distribution shown in Fig. 10(a) and a linear stacking at the trailing edge plane with a hub to shroud variation of 0.1 rad. The flow through this impeller was also computed by using Dawes code by employing the same mesh size as employed in the computation of the other impellers. The predicted *Cp* distribution is presented in Fig. 10(b). In this case the rate of reduction in ΔCp or D_{Cp} is found to be 0.16, which is slightly higher than that for impeller B. The resulting velocity vectors near the suction surface in Fig. 11(a) confirm that by using a combination of optimum loading and stacking condition, it is possible to suppress secondary flows effectively.

Concluding Comments on the Pump Impellers. The predicted relative velocity distributions at the exit of the impellers A, B, and C are presented in Fig. 12. Comparing these velocity distributions with the predicted conventional impeller exit flow, shown in Fig. 3, it is possible to see that as a result of the suppression of the meridional secondary flows, there is little accumulation of low-momentum fluids on the shroud/suction surface corner as compared to that predicted in the conventional impeller and therefore there is no jet-wake exit flow in the conventional sense. The variation of predicted area-averaged meridional velocity at the exit of the impellers A, B, and C is compared with the conventional impeller in Fig. 13(a). The results show clearly that as a result of the suppression of the secondary flows, the meridional velocity near the shroud has increased appreciably in the case of the inverse designed impellers. To compare the degree of pitchwise nonuniformity in the exit flow field, the difference between the predicted area-averaged and mass-averaged *Vm* is presented in Fig. 13(b) for all four impellers. The results indicate an appreciable improvement in the pitchwise flow nonuniformity at the exit of all three inverse design impellers, especially near the shroud.

Comparing the results presented in Fig. 12, it is possible to see some slight differences between the predicted exit flow field between impellers A, B, and C. This difference is mainly due to the degree of suppression of meridional secondary flows, which in turn depends on the *Cp* distribution. In Table 1 the different D_{Cp} parameters, which as explained above quantify the rate of reduction in ΔCp_m, are compared.

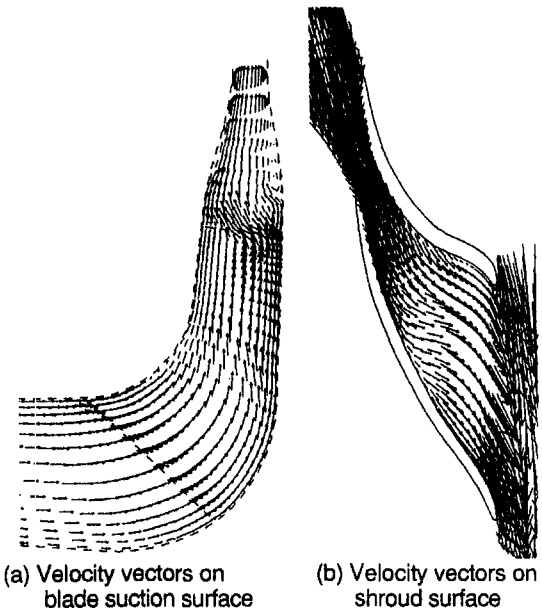

Fig. 11 Predicted flow field in NS280B impeller

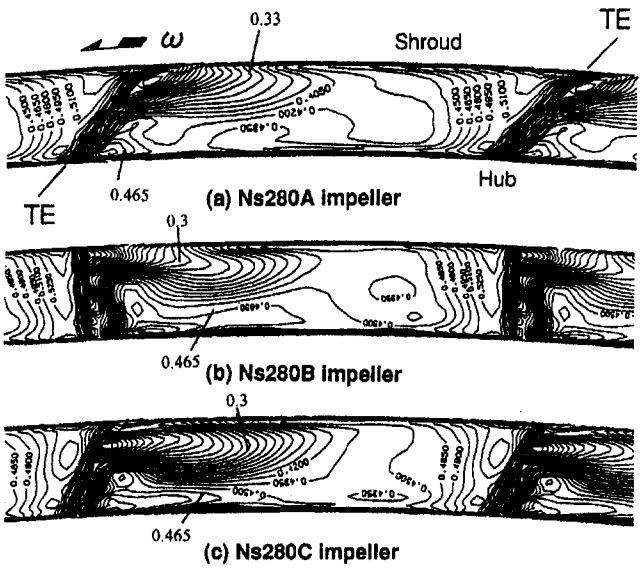

Fig. 12 Relative velocity contours at trailing edge (contour interval = 0.015, normalized by U_{2m})

By comparing the degree of exit flow nonuniformity, as shown in Fig. 13(*b*), with the values of D_{Cp} for each impeller, it is possible to conclude that the value of D_{Cp} is a good measure of the degree of suppression of secondary flows in the impeller. These results demonstrate clearly that by specifying the optimum loading and stacking conditions and using the three-dimensional inverse design method, it is possible to suppress the meridional secondary flows on the suction surface of the impeller and thereby obtain a more uniform exit flow field. Theoretically, it is possible to arrive at the optimum *Cp* distribution with the required D_{cp} value by using conventional methods in which the blade geometry (or blade angle distribution) is changed iteratively until the optimum D_{cp} value is obtained. In practice, however, such a process can be quite inefficient. In Fig. 14, the blade angle distributions for impellers A, B, C, and Conventional are compared at the hub and shroud. Clearly, there is a large difference between the blade angle distribution for the conventional impeller and that obtained for the inverse designed impellers. It is difficult to envisage how a designer can arrive at the blade geometry of impellers A (or B or C) using the conventional approach.

Table 1 Predicted D_{cp} parameter for pumps

Impeller Type	D_{Cp}
Conventional	0.12
A	0.23
B	0.14
C	0.16

Application to Compressors and Experimental Validation. To demonstrate the applicability of the above-mentioned optimum design criteria for suppression of secondary flows to compressors and to investigate its effect experimentally, the method was applied to the design of a high specific speed industrial centrifugal compressor. The compressor's design conditions are presented in Table 2, and its meridional geometry is shown in Fig. 15. For the purpose of this design a combination of optimum loading and stacking condition was used. The $\partial r\bar{V}_\theta/\partial m$ distribution specified on the hub and shroud is presented in Fig. 16. The blades were stacked at the trailing edge with the optimum stacking condition and a linear variation in blade wrap

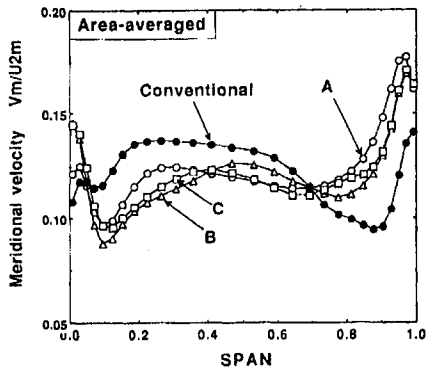

(a) Predicted Area-averaged Meridional Velocity V_m

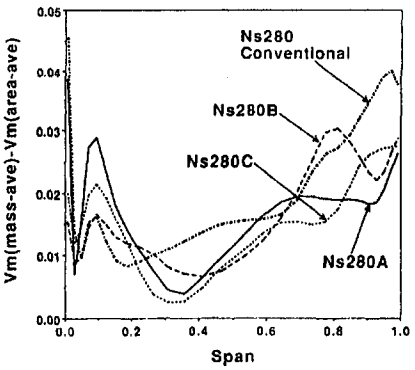

(b) Difference Between Mass-Averagred and Area-Averaged V_m

Fig. 13 Comparison of flow at exit from pump impellers

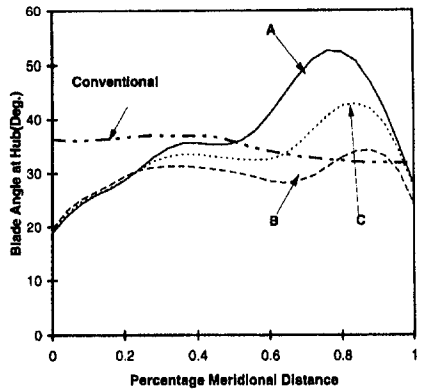

(a) Blade Angle Distribution at Hub

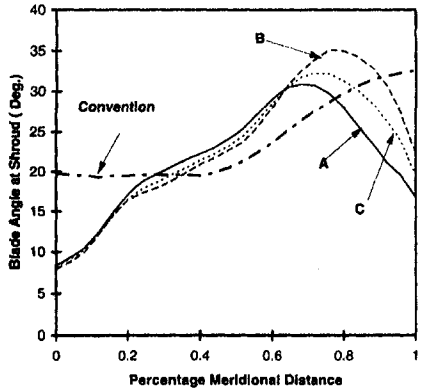

(b) Blade Angle Distribution at Shroud

Fig. 14 Comparison of blade angle distribution

Table 2 Compressor design specification

Specific Speed NS	0.98
Flow coefficient ϕ	0.16
Mu2	0.72
Tip Diameter	0.25m
Exit axial width	0.0212 m
Number of blades	17

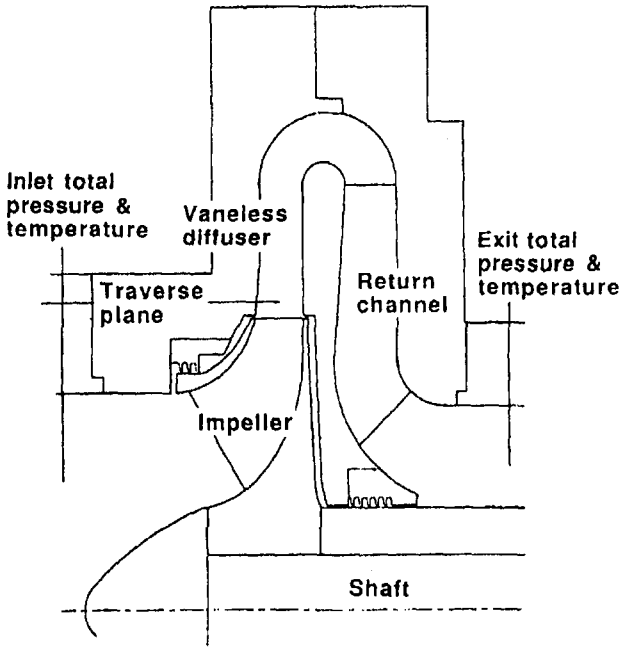

Fig. 15 Sectional view of the compressor stage and test rig

angle of 0.15 rad between the hub and shroud. The specified data were then used in the inverse design method, using a (73 × 25) mesh with 51 points inside the blade and 15 Fourier harmonics to represent the blade–blade variations. The plan view of the resulting blade shape is compared with that of the conventional impeller in Fig. 17. There is a substantial difference between the two blade profiles, which is further confirmed by the blade angle distributions at the hub and shroud, presented in Fig. 18. In Fig. 18, the blade angles have been normalized by the conventional impeller blade angle at the leading edge.

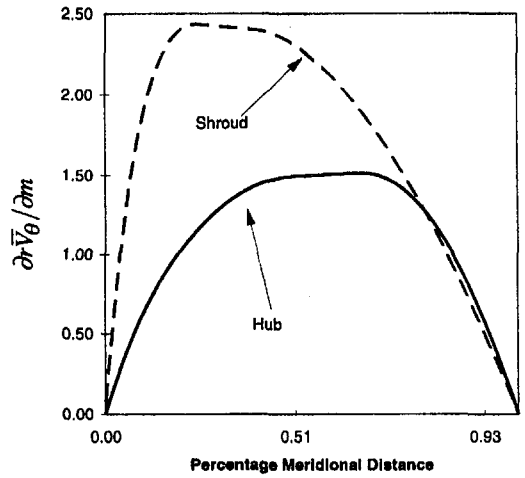

Fig. 16 Specified loading distribution: compressor impeller

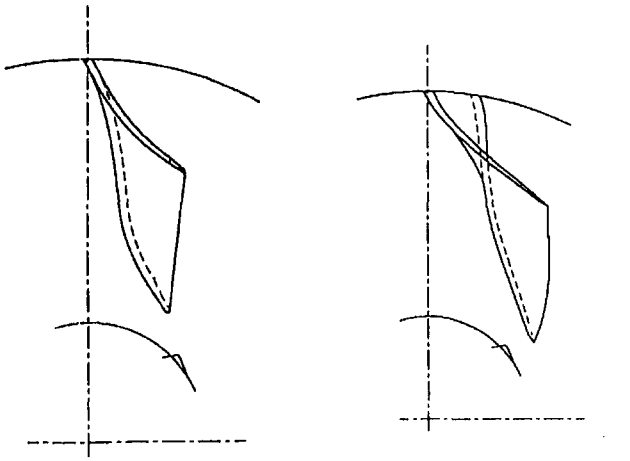

Fig. 17 Plan view of the centrifugal compressor impellers

Numerical Verification. To compare the resulting Mach number on the surfaces of the inverse designed impeller with the conventional impeller, the flows through both impellers were computed by using Denton's (1983) inviscid three-dimensional Euler solver. A (13 × 73 × 13) computational mesh was used for both calculations, with 51 points inside the blade region and uniform pitchwise and spanwise mesh spacing. The predicted Mach number distributions for the conventional and inverse designed impellers are presented in Figs. 19(*a*) and 19(*b*), respectively. It is clear from these figures that in the case of the inverse designed impeller the spanwise gradients of Mach number (or ΔM) has been reduced substantially from 30 percent of meridional chord (or $m = 0.3$) to the trailing edge. The value of D_M that measures the rate of drop in ΔM (which is defined in the same way as D_{Cp}) is 0.25 for the conventional impeller and 0.28 for the inverse-designed impeller.

To confirm the effect of the sharp reduction in ΔM on the secondary flows on the suction surface, the flow through both

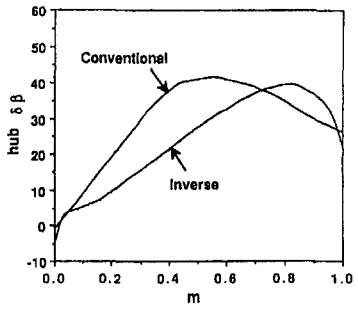

(a) Blade Angle at Hub

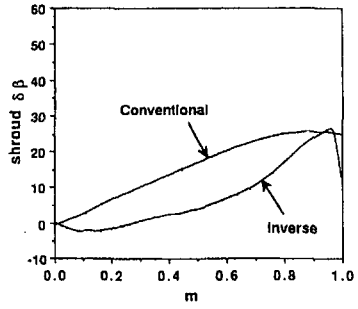

(b) Blade Angle at Shroud

Fig. 18 Blade angle distribution compressor impeller

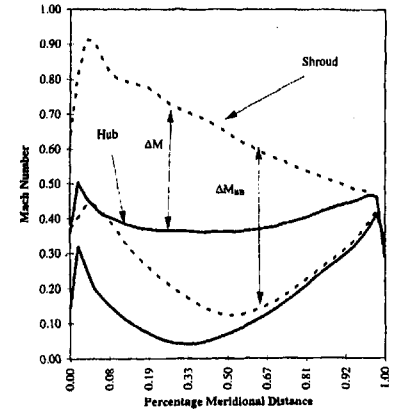

(a) Conventional Impeller

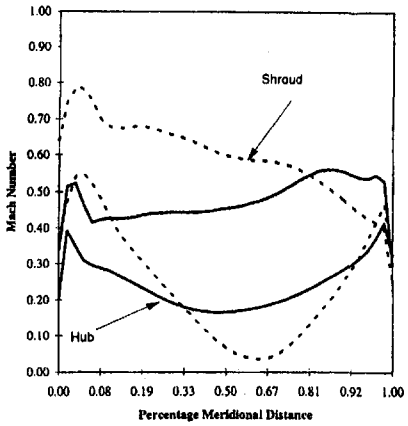

(b) Inverse Designed Impeller

Fig. 19 Predicted Mach number distribution: Denton's code

impellers were computed by using Dawes (1988) three-dimensional viscous method. For both calculations a ($19 \times 75 \times 19$) computational mesh was used. To resolve the boundary layers, grid clustering was used in the pitchwise and spanwise directions. As in the case of pump impeller calculations, the mesh downstream of the blade region was contracted to avoid convergence difficulties caused by the presence of a recirculation region near the exit boundary. This compressor impeller is also shrouded and therefore in the computation the shroud surface was made to rotate with the blade speed. The predicted velocity vectors for both conventional and inverse designed impellers, near the suction surface, are presented in Fig. 20. The results

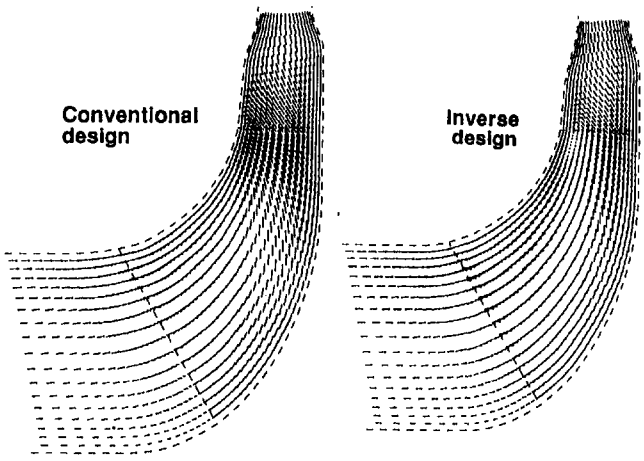

Fig. 20 Comparison of predicted relative velocity vector suction surface

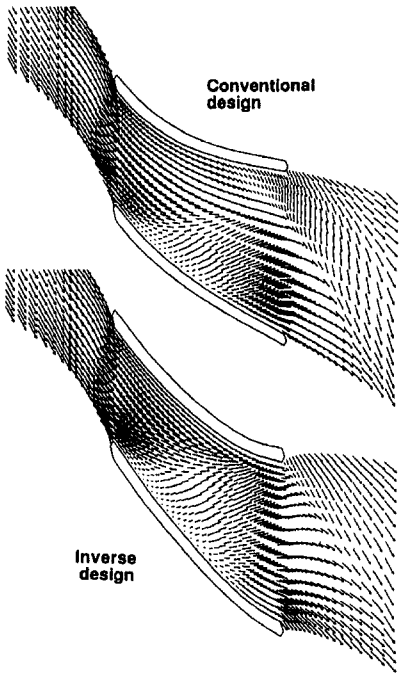

Fig. 21 Comparison of relative velocity vector: shroud

confirm that the secondary flows on the suction surface have been well suppressed in the inverse designed impeller. The predicted velocity vectors on the shroud of the conventional impeller, presented in Fig. 21, show the presence of a blade-blade secondary flow from the suction surface toward the mid-pitch, due to the accumulation of low-momentum fluids at the shroud suction corner.

This is very similar to the flow in the conventional pump impeller (see Fig. 2). This type of blade–blade secondary flow is not present on the shroud of the inverse designed impeller. The predicted exit velocity distribution for the conventional impeller, presented in Fig. 22(a), is very similar to that pre-

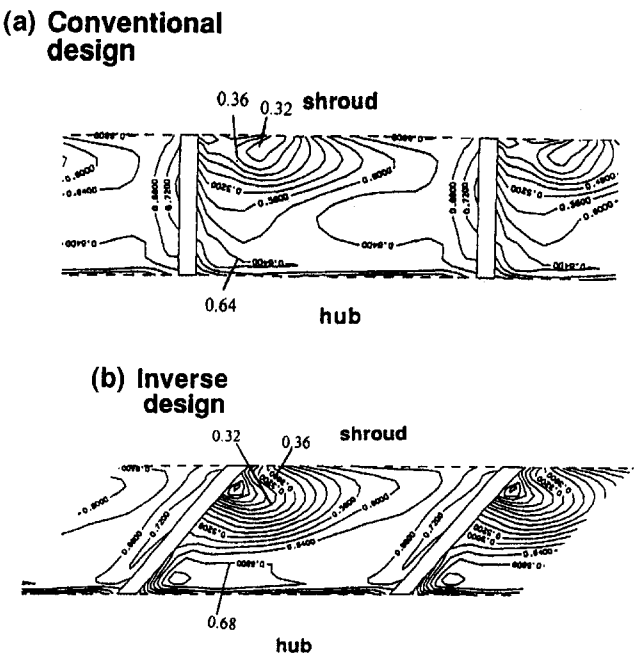

Fig. 22 Comparison of predicted exit relative velocity (contour interval = 0.04, normalized by U_2)

dicted for the conventional pump impeller (see Fig. 3), with a distinct jet/wake type flow near the shroud/suction surface corner. In the case of the inverse designed impeller, see Fig. 22(*b*), no distinct jet-wake flow can be observed.

Experimental Validation. The numerical studies detailed above demonstrated the possibility of designing pump or compressor impellers with suppressed secondary flows and uniform exit flow field by using the three-dimensional inverse design method and the optimum design specification described above. In order to be able to use these design guidelines with confidence, in the design of a new generation of mixed and radial flow impellers, it is essential to validate the results experimentally. For this purpose the inverse-designed centrifugal impeller was manufactured. The impeller was then tested in a closed-loop test stand, in which refrigerant R-134a was used as the working fluid. A direct current motor was used to drive the compressor through a gearbox to enable the compressor speed to be changed continuously. Pressures were measured by using semiconductor pressure transducers and temperatures by quartz thermometers and CC thermocouples. Flow rate was measured by an orifice meter and the torque and rotational speed were measured by a torque meter. Overall performance was determined from the inlet of the compressor to the exit of the return channel, see Fig. 15. Velocity and total pressure distributions were measured by using a five-hole probe, which was traversed automatically in the spanwise direction. The same conventional vaneless diffuser and deswirl vanes were used for testing both the conventional and inverse-designed impellers.

The overall performance of the inverse designed impeller is compared with the conventional impeller in Fig. 23. The peak measured stage efficiency of the inverse designed impeller together with conventional diffuser is found to be 5 percent higher than the conventional impeller, with appreciable efficiency improvements at off-design conditions. The main reason for the substantial improvement in stage efficiency can be attributed to the suppression of secondary flows in the impeller which, as was shown in the predictions, results in less pitchwise as well as spanwise variation in the exit flow field. As was mentioned in the introduction, the rapid mixing of the pitchwise variation in exit flow field, which occurs in the immediate vicinity of impeller exit [see Inoue and Cumpsty (1984)] can result in substantial losses. Furthermore, the spanwise variations in radial velocity can have an adverse effect on the diffuser performance. The measured distributions of radial and tangential velocity for the conventional and inverse designed impellers are compared in Fig. 24. The results indicate clearly that as a result of suppression of secondary flows, the axial variation in radial velocity has been reduced considerably in the inverse-designed impeller, which has a beneficial effect on the diffuser pressure recovery and stage efficiency.

One puzzling results now under investigation is the pressure rise characteristic for the stage with the inverse-designed impeller, which shows a positive slope at about 85 percent of design flow rate. This phonomenon may be attributed to the mismatch between the inverse-designed impeller and the conventional diffuser and deswirl vane. Further investigation into the cause of this is now in progress.

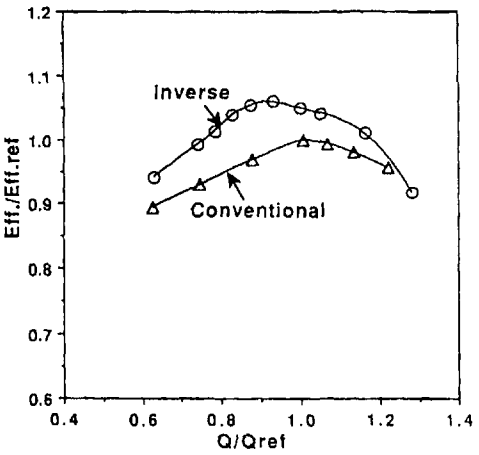

(a) Comparison of Measured Stage Efficiency

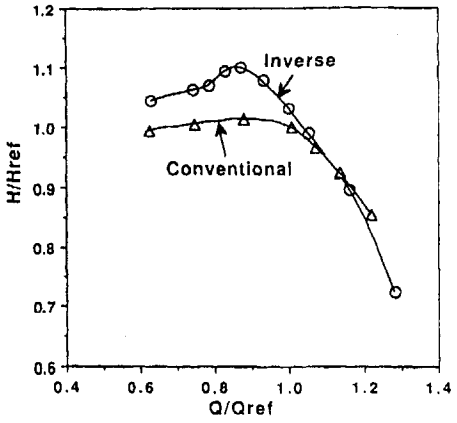

(b) Comparison of Measured Head Rise

Fig. 23 Comparison of overall performance: compressor

Conclusions

In this paper a set of guidelines was developed for the suppression of secondary flows on radial and mixed flow impeller blades in order to achieve a uniform impeller exit flow field. The main conclusions of this study are as follows:

- In order to suppress secondary flows in the impeller, it is essential to control the Cp (or M) distribution in such a way that the difference in Cp on the suction surface between the hub and shroud (or ΔCp) is minimized in the aft part of the impeller.
- Impeller blades with this type of Cp (or M) distribution can be designed efficiently and systematically by using the three-dimensional inverse design method in which the the blades are designed for a specified circulation distribution, or $2\pi r \bar{V}_\theta$. Using this inverse method, this Cp (or M) distribution can be achieved by using a loading (or $\partial r \bar{V}_\theta / \partial m$) distribution in which the maximum loading is set at the forepart of the impeller at the shroud and the aft part of the impeller at the hub. In addition it is possible to further control the Cp (or M) distribution by specifying a stacking (or lean) condition toward the trailing edge in which the blades are leaned linearly from hub to shroud against the direction of rotation.
- Using these guidelines, three different pump impellers were designed for a low specific speed centrifugal pump. The results of numerical computations confirmed that the secondary flows are well suppressed in all cases as compared to the corresponding conventional impeller flow field. The design guidelines were further validated numerically and experimentally for a high specific speed centrifugal compressor impeller. The performance of the inverse design impeller designed using these guidelines was found to be 5 percent higher at the peak efficiency point as compared to the corresponding conventional impeller.

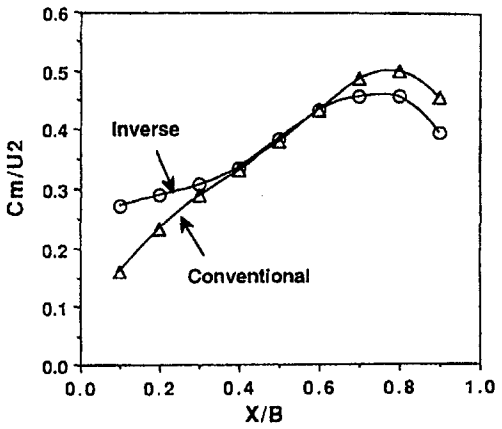

(a) Measured Impeller Exit Radial Velocity

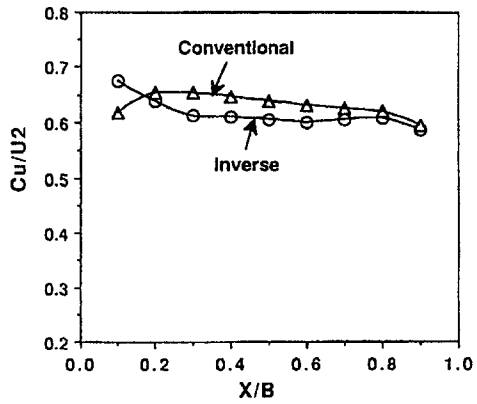

(b) Measured Impeller Exit Tangentiall Velocity

Fig. 24 Measured impeller exit velocity distribution

- The degree of suppression of secondary flows in the impeller was found to be dependent on the rate of reduction of ΔCp (or ΔM) from about 40 percent of meridional chord to the trailing edge. To assess the degree of suppression of secondary flows quantitatively, a number D_{cp} (or D_M) was defined that measures the reduction in ΔCp (or ΔM) between the minimum location of ΔCp (or ΔM) and a point 40 percent of meridional chord upstream. The results of numerical studies presented confirm a direct correlation between D_{cp} (or D_M) and the degree of suppression of secondary flows and the uniformity of the impeller exit flow field. It is also shown that for suppression of secondary flows there is a limiting (or minimum) value of D_{cp}.

Extensive parametric studies are currently under way to establish the limiting value of D_{cp} for different impellers with a range of specific speeds. The results so far obtained indicate a direct correlation between the limiting value of D_{cp} and specific speed.

These design guidelines should enable turbomachinery designers to design a new generation of mixed flow and radial turbomachines with suppressed secondary flows and a uniform exit flow field, which, as was shown in this paper, should lead to substantial performance improvements. To achieve this objective it is essential to remove the radial-blade filament restriction. No doubt the removal of such a restriction will have some implications for structural integrity and manufacturability of the impeller. But with improvements in material technology and the widespread application of structural analysis programs, as well as the rapid development of new manufacturing technologies it is now possible to manufacture impellers with nonradial filaments at reasonable costs. There is already considerable evidence that many major turbomachinery manufacturers are interested in the feasibility of this type of impeller (Baldwin, 1996).

The future of mixed flow and centrifugal pumps and compressors appears to be bright.

Acknowledgments

The authors are most grateful to Ebara Research Co. Ltd. for supporting this work and for their permission to publish this paper.

References

Baldwin, P., 1996, Northern Research and Engineering Corporation, private communication.

Casey, M. V., Dalbert, P., and Roth, P., 1992, "The use of 3D Viscous Flow Calculations in the Design and Analysis of Industrial Centrifugal Compressors," ASME JOURNAL OF TURBOMACHINERY, Vol. 114, pp. 27–37.

Cox, J. C., 1990, "Radial or Mixed Flow Rotor," UK patent No. GB2224083A.

Dallenbach, F., 1961, "The Aerodynamic Design and Performance of Centrifugal and Mixed Flow Compressors," *SAE Tech. Progress Series,* Vol. 3, pp. 2–30.

Dawes, W. N., 1988, "The development of a 3D Navier–Stokes Solver for Application to All Types of Turbomachinery," ASME paper 88-GT-70.

Dean, R., and Senoo, Y., 1961, "Rotating Wakes in Vaneless Diffusers," ASME *Journal of Basic Engineering,* Vol. 82, pp. 563–574.

Dean, R., 1971, "On the unresolved fluid dynamics of the centrifugal compressor," *Advanced Centrifugal Compressors,* ASME, New York.

Denton, J. D., 1983, "An improved time marching method for turbomachinery flow calculations," ASME *Journal of Engineering for Power,* Vol. 105, p. 514.

Eckardt, D., 1976, "Detailed flow investigation within a high speed centrifugal compressor impeller," ASME *Journal of Fluids Engineering,* Vol. 98, pp. 390–402.

Eckardt, D., 1980, "Flow Field Analysis of Radial and Backswept Centrifugal Compressor Impellers—Part I. Flow measurements using a laser velocimeter," *Performance Prediction of Centrifugal Pumps and Compressors,* Gopalakrishnan, ed., ASME, pp. 77–86.

Goto, A., 1992a, "Study of Internal Flow in a Mixed Flow Pump Impeller at Various Tip Clearances Using 3D Viscous Flow Calculations," ASME JOURNAL OF TURBOMACHINERY, Vol. 114, pp. 373–382.

Goto, A., 1992b, "The Effect of Tip Leakage Flow on Part-Load Performance of a Mixed-Flow Pump Impeller," ASME JOURNAL OF TURBOMACHINERY, Vol. 114, pp. 383–391.

Goto, A., Takemura, T., and Zangeneh, M., 1996, "Suppression of secondary flows in a mixed flow pump impeller by application of 3D inverse design method: Part 2—Experimental validation," ASME JOURNAL OF TURBOMACHINERY, Vol. 118, pp. 544–551.

Grant, J., and Borthwick, D., 1987, "Fully 3D Inviscid Flow Calculations for the Final Stage of a Large Low Pressure Steam Turbine," *Turbomachinery-Efficiency Prediction and Improvement,* IMEChE Conference No. 1987-6, Paper No. C281/87.

Han, W, Wang, Z, Tan, C, Shi, H., and Zhou, M., 1994, "Effects of Leaning and Curving of Blades With High Turning Angles on the Aerodynamic Characteristic of Turbine Rectangular Cascades," ASME JOURNAL OF TURBOMACHINERY, Vol. 116, pp. 417–424.

Hathaway, M. D., Chriss, R. M., Wood, J. R., and Strazisar, A. J., 1993, "Experimental and computational investigation of the NASA low-speed centrifugal compressor flow field," ASME JOURNAL OF TURBOMACHINERY, Vol. 115, pp. 527–542.

Hawthorne, W. R., Tan, C. S., Wang, C., and McCune, J., 1984, "Theory of Blade Design for Large Deflections: Part 1—Two Dimensional Cascades," ASME *Journal of Engineering for Gas Turbines and Power,* Vol. 106, pp. 346–353.

Hawthorne, W. R., 1967, "The Applicability of Secondary Flow Analysis to the Solution of Internal Flow Problems," *Fluid Mechanics of Internal Flow,* Elsevier.

Hawthorne, W. R., 1974, "Secondary vorticity in stratified compressible fluids in rotating systems," Cambridge University Eng. Department Report No. CUED/A-Turbo/TR63.

Hirsch, Ch., Kang, S., and Pointel, G., 1996, "A Numerically Supported Investigation of the 3D Flow in Centrifugal Impellers. Part II: Secondary Flow Structure," ASME Paper No. 96-GT-152.

Howard, J. H. G., and Ashrafizaadeh, M., 1994, "A numerical investigation of blade lean angle effects on flow in a centrifugal impeller," ASME Paper No. 94-GT-149.

Inoue, M., and Cumpsty, N. A., 1984, "Experimental Study of Centrifugal Compressor Impeller Discharge Flow in Vaneless and Vaned Diffusers," ASME *Journal of Engineering for Gas Turbines and Power,* Vol. 106, pp. 455–467.

Johnson, M. W., 1978, "Secondary Flows in Rotating Bends," ASME *Journal of Engineering for Power,* Vol. 100, pp. 553–560.

Johnson, M. W., and Moore, J., 1983, "Influence of Flow Rate on the Wake in a Centrifugal Impeller," ASME *Journal of Engineering for Gas Turbines and Power,* Vol. 105, pp. 33–39.

Krain, H., 1988, "Swirling Impeller Flow," ASME JOURNAL OF TURBOMACHINERY, Vol. 110, pp. 122–128.

Senoo, Y., and Kinoshita, Y., 1977, "Influence of inlet flow conditions and geometries of centrifugal vaneless diffusers on critical flow angles for reverse flow," ASME *Journal of Fluids Engineering,* Vol. 99, pp. 98–107.

Walker, P. J., and Dawes, W. N., 1990, "The extension and application of three-dimensional time-marching analysis to incompressible turbomachinery flows," ASME JOURNAL OF TURBOMACHINERY, Vol. 112, pp. 385–390.

Zangeneh, M., Dawes, W. N., and Hawthorne, W. R., 1988, "Three-dimensional flow in radial-inflow turbines," ASME Paper No. 88-GT-103.

Zangeneh, M., 1991, "A compressible three dimensional blade design method for radial and mixed flow turbomachinery blades," *Int. J. Numerical Methods in Fluids,* Vol. 13, pp. 599–624.

Zangeneh, M., 1993, "Inviscid/viscous interaction method for 3D inverse design of centrifugal impellers," ASME JOURNAL OF TURBOMACHINERY, Vol. 118, pp. 385–393.

Zangeneh, M., Goto, A., and Takemura, T., 1996, "Suppression of secondary flows in a mixed flow pump impeller by application of 3D inverse design method: Part 1—Design and Numerical validation," ASME JOURNAL OF TURBOMACHINERY, Vol. 118, pp. 536–543.

Sound Generation by a Centrifugal Pump at Blade Passing Frequency

M. Morgenroth
Acres International Ltd.,
4342 Queen Street,
Niagara Falls, Ont., Canada
L2E 6W1

D. S. Weaver
weaverds@mcmaster.ca
Dept. of Mechanical Engineering,
McMaster University,
Hamilton, Ont., Canada
L8S 4L7

This paper reports the results of an experimental study of the pressure pulsations produced by a centrifugal volute pump at its blade passing frequency and their amplification by acoustic resonance in a connected piping system. Detailed measurements were made of the pressure fluctuations in the piping as a function of pump speed and flow rate. A semi-empirical model was used to separate acoustic standing waves from hydraulic pressure fluctuations. The effects of modifying the cut-water geometry were also studied, including the use of flow visualization to observe the flow behavior at the cut-water. The results suggest that the pump may act as an acoustic pressure or velocity source, depending on the flow rate and the cut-water geometry. At conditions of acoustic resonance, the pump acted as an open termination of the piping, i.e., as a node in the acoustic pressure standing waves. Rounding the cut-water had the effect of reducing the amplitude of acoustic resonance, apparently because of the ability of the stagnation point to move and thereby reduce the vorticity generated.

Introduction

A centrifugal pump produces pressure pulsations in its associated piping system at the Blade Pass Frequency (BPF). These pressure pulsations can be classified as acoustic or hydraulic, according to the mechanism of their generation and propagation in the fluid. In particular, the speed of propagation and the wave nature of the acoustic pulsations that result in standing wave patterns can be utilized to distinguish acoustic from hydraulic pressure pulsations.

Generally speaking, pressure pulsations in a piping system will be unacceptable if they excite mechanical components in the system to oscillate at unacceptable levels. If the pressure pulsations produce acoustic resonance in the piping system, then the potentially damaging effects of the oscillations may be felt throughout the system. A notable example of such an acoustic resonance was observed in the Primary Heat Transport (PHT) system at Ontario Hydro's Darlington nuclear power station. The resonance at the PHT pump blade passing frequency caused fatigue failure in the fuel bundle end plates, and ultimately the breakup, of some nuclear fuel bundles (Hartlen et al., 1993).

Literature on the subject of aero-acoustics dates back to the 1950s, but these early works focused on sound generation by turbulence. The theory of vortex sound by Powell (1964) related the vorticity in an incompressible flow field, the acoustic near field, to the sound produced. An important implication of this work is that, in order to generate sound, the vortices must have a component of their propagation velocity normal to the mean flow field. The subject of self-excitation in flow tones was reviewed by Rockwell and Naudascher (1979). Florjancic et al. (1980) reported trials of pump modifications to the impeller and casing for acoustic performance improvement. Neise (1975, 1982) studied the noise generated by centrifugal fans and presented a list of design options to improve the acoustic performance of centrifugal blowers, both from the broad band and the blade pass frequency perspectives. Bolleter (1988) provided the first publication that dealt systematically with blade pass tones of centrifugal pumps. Hartlen et al. (1993) described the dynamic interaction between pump and pipeline in a full-scale model of a primary heat transport pump. Dong et al. (1992) employed the methodology of particle image velocimetry (PIV) to investigate the detailed flow structures of the flow field around a pump cut-water. More recently, these authors have extended this work to examine noise generation through blade-tongue interaction and the effects of modifying the tongue and impeller geometries (Chu et al., 1993; Dong et al., 1997). These studies are very close to the present one, but there are some important differences. Those authors placed emphasis on the flow structure in the region of the tongue, or cut-water, using quantitative analysis of PIV measurements, and concluded that unsteady separated flow at the cut-water was a primary source of noise. Their noise measurements were obtained from hydrophones located about 1 m upstream and downstream of the pump. No results were reported for acoustic standing waves in the piping system as have been studied in the present work. Another significant difference is that Dong et al. (1997) modified both cut-water geometry and impeller-casing gap simultaneously so that their independent effects could not be determined. In the present study, the cut-water radius was modified without changing the impeller gap.

The primary objective of the research reported in this paper was to improve our understanding of the sound generation behavior of a centrifugal pump, and to investigate how it might be modified by a change to the cut-water geometry. A second objective was to investigate the possibility of an acoustic pump pipeline interaction, which might amplify the sound generation characteristics of the pump. A method to distinguish between acoustic and hydraulic pressure pulsations, where both types are measured close to the source, is presented. Dynamic pressure measurements were taken at flow rates below, equal to, and above the nominal rate for the pump. The results are explained using flow visualization observations of the flow region around the cut-water. Also presented are the effects of rounding the tip of the cut-water on the acoustic pressure and flow behavior at the cut-water.

Experimental Apparatus

The experimental loop shown in Fig. 1 was designed and built for this study (Morgenroth, 1996). The overhead tank has

Contributed by the Turbomachinery Division for publication in the JOURNAL OF TURBOMACHINERY. Manuscript received by the Turbomachinery Division February 5, 1997; revised manuscript received October 21, 1997. Associate Technical Editor: R. A. Delaney.

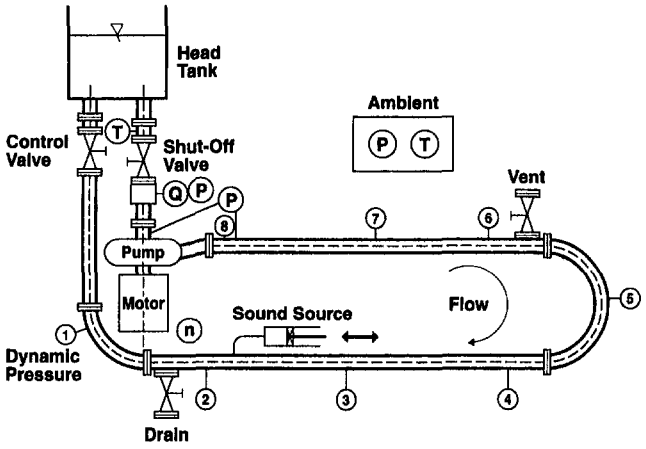

Fig. 1 Experimental test loop

a capacity of 7 m^3 and the loop is 13.1 m long from tank outlet to inlet. The centrifugal volute pump is mounted with its impeller in a horizontal plane and outlet flange 1.75 m below the water surface in the tank. Details of the pump are given in Table 1. The manufacturer's nominal (best efficiency) flow rate is 17.4 l/s. The stainless steel schedule 40 pipe upstream and downstream of the pump had diameters of 102 mm and 76 mm, respectively, to match the pump suction and discharge flanges.

The water temperature in the loop was measured using a thermocouple just upstream of the pump, the temperature being in the range 13–16°C. The pump head was determined using a differential pressure transducer with measurements corrected for elevation and velocity differences across the pump. Discharge was measured using a magnetic inductive flow meter upstream of the pump. Analogue signals from the flow meter and differential pressure transducer were sampled 100 times over a 10-second period over the entire flow range of interest and found to vary less than 1.5 percent from the average signal.

Pressure fluctuation amplitude was measured at 8 approximately equally spaced intervals around the loop using piezoelectric pressure transducers, as shown in Fig. 1. As relative pressure fluctuation amplitudes were of particular interest for identification of acoustic standing waves, 7 of these transducers were calibrated against the 8th, including the transducer cables, preamplifiers, and amplifiers. The calibration was conducted at 50 Hz, approximately the fundamental acoustic frequency of the loop, and about 100 mbar pressure fluctuation amplitude. Thus, relative pressure calibration for the 8 transducers was achieved within 1 percent of each other.

Flow visualization was made possible by cutting windows into the bronze pump casing at the cut-water, one for a light sheet parallel to the plane of the impeller and one for observation perpendicular to the plane of the impeller. Figure 2 shows a schematic cross section of the pump including the window for flow visualization and flow tracer injection system. The acrylic windows were faired into the internal shape of the casing so as not to disturb the flow. Preliminary observations with the original V-shaped cut-water indicated that the flow was rather three-dimensional and clear flow visualization images could not be obtained. Therefore, the original cut-water was replaced with a two-dimensional one, also with a sharp leading edge. This replacement also made substitution of rounded leading edge cut-waters quite straightforward without changing the impeller-to-cut-water gap (5.8 percent). This is particularly important

Table 1 Pump data

Manufacturer's Best Efficiency Point Data	
Flow rate	17.4 l/s (275 USGPM)
Head	19.2 m (63 ft.)
Speed	1150 rpm
Specific Speed	
SI	16.5 rpm $(m^3/s)^{1/2}/(m\ water)^{3/4}$
US System	853 rpm $gpm^{1/2}/(ft\ water)^{3/4}$
Impeller - 5 blades	
Inlet	
Diameter, D_1	89 mm
Blade Angle, β_2	35°
Passage Width, b_2	20 mm
Outlet	
Diameter, D_2	343 mm
Blade Angle, β_2	21°
Passage Width, b_2	9 mm
Casing	
Spiral Casing with Diameter,	
D_3 at tongue	363 mm
Tongue Radius:	
Original Casing	1.6 mm
2 D Wedges	0 mm
Impeller Tip Clearance	
$(D_3-D_2)/D_2$	5.8%

Nomenclature

b = impeller exit passage width
c = speed of sound
D_2 = impeller outlet diameter
f = blade passing frequency = $5f_s$
f_n = natural frequency of first acoustic pipe mode
f_r = frequency ratio = f/f_n
f_s = pump shaft speed
$G(x/x_p, f_r, L/x_p)$ = Green's function solution of one-dimensional wave equation
He = Helmholtz number = $L/\lambda = Lf/c$
k = empirical hydraulic decay parameter
L = overall pipe length
p_a = peak amplitude of acoustic pressure fluctuation
p_c = computed total pressure amplitude fluctuation
p_h = peak amplitude of hydraulic pressure fluctuation
p_m = measured amplitude of total pressure fluctuation
Q = pump flow rate
u_T = impeller tip speed
x = distance along pipe from entrance reservoir
x_p = location of pump in pipe; x_p/L = 0.10
Δp = pump head
λ = acoustic wavelength
τ = period of blade passing = $1/f$
ϕ = pump flow rate coefficient = $Q/f_s D_2^3 b$
ψ = pump head coefficient = $\Delta p/(\frac{1}{2}\rho u_T^2)$

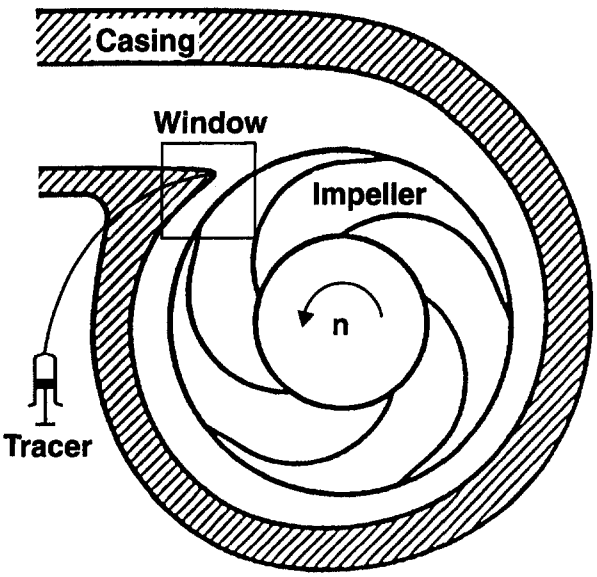

Fig. 2 Schematic cross section of pump showing flow visualization window

since this gap by itself can have a profound influence on pressure fluctuations and pump performance.

A solution of fluorescein in water was found to produce a reasonable flow tracer with acceptable contrast and minimum diffusion in the highly turbulent flow. This was fed through a 0.46 mm hole at the cut-water tip using a motorized injector, which produced a constant feed rate (see Fig. 2). The optimum feed rate was selected to minimize disturbance to the flow and was adjustable with pump flow rate. A light sheet was produced using two 300 W projector lamps and observations were made with a high-speed digital video camera with speeds up to 1000 frames per second.

Separation of Hydraulic and Acoustic Pressures

The pressure pulsations in a pipeline produced by a pump at the blade passing frequency, f, will be comprised of acoustic and hydraulic components. The hydraulic component is vorticity, which will decay as it is convected downstream, while the acoustic component is a sound wave, which may be amplified by pipeline acoustics. Clearly, the magnitude of the pressure pulsations will be strongly dependent on where they are measured along the pipe. Separation of the hydraulic and acoustic components will provide useful information regarding their relative magnitudes as well as insights into the pump-piping acoustic interaction. It will also permit determination of the magnitude and location of the maximum acoustic pressures.

The computed total pressure fluctuation at some location in the pipe, p_c, can be expressed in terms of acoustic and hydraulic components as:

$$p_c = p_a G(x/x_p, f_r, L/x_p) + p_h e^{-k(x-x_p)/L} \qquad (1)$$

where p_a is the peak acoustic pressure amplitude, p_h is the peak hydraulic pressure amplitude, and k is a hydraulic decay parameter. These parameters are independent of the location of pressure measurement and represent the behavior of the pump-piping system. The hydraulic pressure is assumed to decay exponentially from the pump. $G(x/x_p, f_r, L/x_p)$ is the acoustic wave form along the pipe given by the Green's function solution of the one-dimensional wave equation with open boundary conditions at the ends of the pipe ($x = O, L$) and with a harmonic pressure disturbance at frequency, f, located at the pump ($x = x_p$). The Green's function is normalized to unity at its peak value and its relative magnitude will clearly depend on the location along the pipe, x. First mode resonance occurs when the excitation frequency, f, is equal to the lowest pipeline acoustic natural frequency, f_n, i.e., when $f_r = f/f_n = 1$. The corresponding wavelength, λ, will be twice the overall pipe length ($\lambda = 2L$) for the open-ended system considered here. Figure 3 shows the normalized Green's function solution for a range of frequency ratios from 0.5 to 2.0. The solution is analogous to a taut string being shaken harmonically at the "source" point (pump location). The wave form is discontinuous at the source except at resonance, i.e., when the frequency ratio is 1 or 2.

To effect the separation of acoustic and hydraulic pressure components, a least-squares residual method is used. The residual is given by:

$$R = \sum_{i=1}^{8} (p_{ci} - p_{mi})^2 \qquad (2)$$

where p_{ci} is the pressure computed from Eq. (1) at location i, p_{mi} is the pressure at the blade pass frequency measured at location i, and the summation is taken over the 8 pressure transducer locations. A minimum residual is sought by varying the four parameters, p_a, p_h, f_r, and k. Thus, peak values of the acoustic and hydraulic pressure fluctuation amplitudes are found that, in general, will not occur at a measurement location.

Some examples of this separation process are shown in Fig. 4 for the original pump V-shaped cut-water. The measured pressures at each transducer location are the peak values at the blade passing frequency taken from the Fast Fourier Transform spectra of 60 sample averages. The pressures have been normalized by the pump dynamic head where the blade tip velocity, u_T, has been used as an appropriate velocity scale. The solid line in each figure is the total pressure computed using Eq. (1) with optimum parameters determined as described above, while the dashed lines and dotted lines are the separate acoustic and hydraulic components, respectively. Results are given for four different frequency ratios from well below first acoustic resonance mode to a value approaching the second acoustic resonance mode. Clearly, the empirical curve fit to the data is very good with the average root mean square residual being less than 1.5 percent of the peak measured pressure in all cases. Figure 4(a) suggests acoustic standing wave resonance ($\frac{1}{4}$ wave) with a pressure antinode at the pump. However, this is simply the forced response of the system at a frequency well below resonance as seen in Fig. 3. Figures 4(b) and (c) show standing waves below and above the first mode resonance, respectively, with

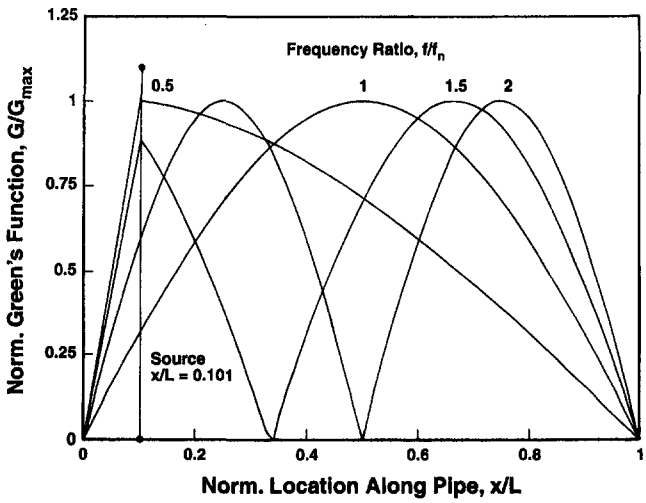

Fig. 3 Normalized Green's function solution of one-dimensional wave equation (open ends at x/L = 0, 1, pressure source at x/L = 0.10)

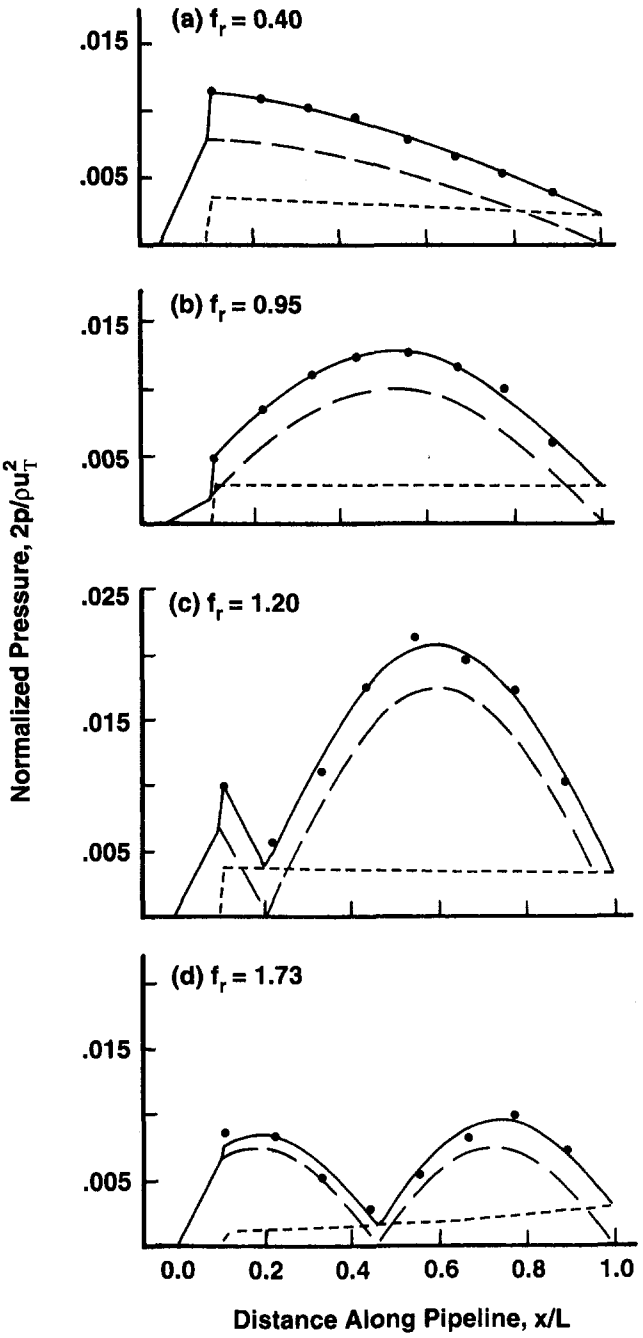

Fig. 4 Separation of acoustic and hydraulic pressure components (— = total pressure p_c; --- = acoustic pressure p_a; · · · · = hydraulic pressure p_h; ● ● ● = experimental data)

wavelengths nearly double the pipe length, i.e., half sine waves over the pipe length. Figure 4(*d*) shows a standing wave approaching the second resonance mode with wavelength, λ, approaching the pipe length L. It is interesting to note the growth in the hydraulic pressure component along the length of the pipe in Fig. 4(*d*). This apparent anomaly can be explained by the occurrence of cavitation at the downstream control valve at very high flow rates. It is noteworthy that the hydraulic and acoustic pressure components under these operating conditions could still be reliably separated and that the peak acoustic pressure, p_a, occurring anywhere along the pipe could be determined. It is this peak acoustic pressure, computed from the pressure transducer data for every test condition, that is used in subsequent sections of this paper.

Effects of Flow Rate and Pump Speed on Acoustic Pressure

Experiments were conducted with the two-dimensional sharp tipped cut-water in the pump to determine the maximum acoustic pressure, p_a, as a function of pump speed and flow rate. For a given pump speed, flow rate was controlled using the downstream globe valve. For each test condition, the maximum acoustic pressure, p_a, was determined as described in the previous section. These data are plotted against the blade passing frequency, f, in the form of Helmholtz number, He, in Fig. 5. Helmholtz number is defined as:

$$\mathrm{He} = \frac{L}{\lambda} = \frac{Lf}{c} \tag{3}$$

where L is the total pipe length, λ is the acoustic wave length, f is the blade passing frequency, and c is the speed of sound. The latter parameter was determined experimentally for each test series by measuring the time taken for an acoustic pulse to travel between pressure transducers (Morgenroth, 1996). The

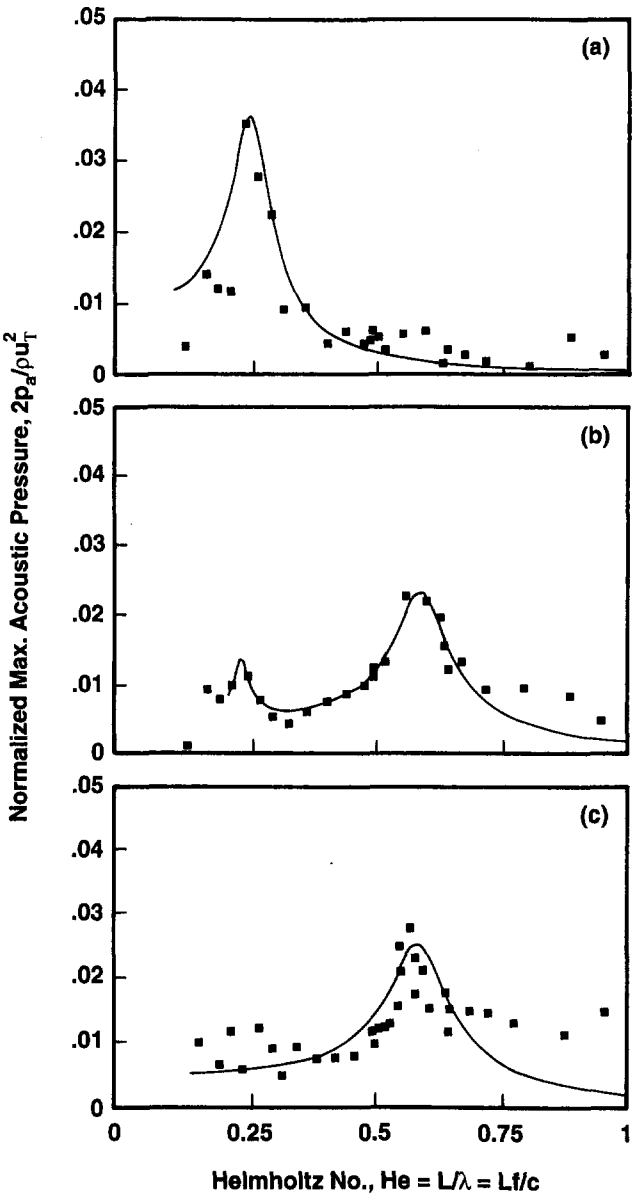

Fig. 5 Normalized maximum acoustic pressure versus Helmholtz number: (*a*) 40 percent nominal flow rate, (*b*) 100 percent, (*c*) 120 percent

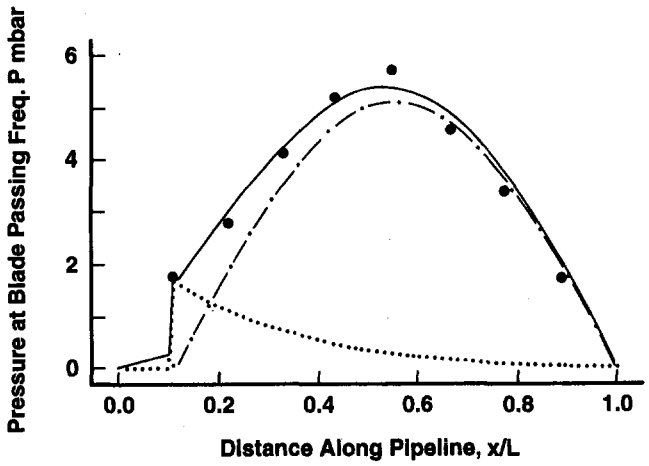

Fig. 6 Pressure versus location for two-dimensional sharp-tipped cut-water at 40 percent flow rate, He ≃ 0.25 (— = total pressure p_c; – · – = acoustic pressure p_a; · · · · = hydraulic pressure p_h; ● ● ● = experimental data)

sound speed so determined varied between 1355 and 1390 m/s. This agrees reasonably well with the theoretical value of 1339 m/s, computed for water, including the effect of pipe elasticity. The variation in measured sound speed is likely due to differences in temperature and a small degree of aeration of the water between test series.

The results for nominal flow rate and 120 percent nominal flow rate, Figs. 5(*b*) and (*c*), respectively, show a clear resonance peak at a Helmholtz number of about 0.57. The expected resonance for the entire pipe between tank openings (13.1 m) would have a natural frequency of about 52 Hz and a corresponding Helmholtz number of 0.50. On the other hand, a resonance between the pump and the downstream tank (11.8 m) would have a natural frequency of about 66 Hz, corresponding to a Helmholtz number of 0.57. Thus, it appears that the pump acts as a volume expansion in the pipeline and the first acoustic natural frequency is a half-sine wave between the downstream tank and the pump, not between upstream and downstream tanks as originally assumed. It follows that, if the pipe length between the pump and the downstream tank were used to compute Helmholtz number, its value for first mode resonance would be 0.50. Calculations for Figs. 5(*b*) and (*c*) confirm this within experimental error.

The apparent resonance peak at 40 percent nominal flow rate, Fig. 5(*a*), and to a lesser extent at 100 percent nominal flow rate occurs at a Helmholtz number of about 0.25. This suggests a quarter-wave resonance with a pressure node at one end of the pipe. However, this is not supported by any of the tests conducted. The possibility of wave reflection from the downstream control valve was examined carefully using pressure pulses under no-inflow conditions. As soon as the valve was opened a small amount, it became transparent to the pressure pulses. At every valve opening used during the flow tests, there was no evidence of acoustic wave reflection from the valve.

In order to examine this unexpected resonance further, the pressure data for Helmholtz number of 0.25 and 40 percent flow rate, determined from the separation process described above, are shown in Fig. 6. A clear half-sine wave between the pump and the downstream tank opening is seen to fit the experimental data well. In particular, there is no evidence of $\frac{1}{4}$ wave resonance produced by reflection from the downstream valve (near $x/L = 1$). However, the Green's function frequency ratio, f_r, a free parameter found in the optimization process, was twice the experimental blade passing frequency. This rather curious result could possibly be explained if the pump were acting at a velocity source, forcing a half wave in the pipe with pressure nodes at the pump and tank. An attempt was made to confirm the nature of the acoustic source at the pump by examining the phase relationship of the pressures across the pump. However, the upstream pipe length is very short, and since the pump appeared as a pressure node, the pressure fluctuation amplitudes were small and the phase measurements were too noisy to be of any value. This behavior is peculiar to the two-dimensional sharp-edged cut-water and was not observed for the original cut-water design. It should also be noted that, for the resonance peak at He = 0.57, the computed Green's function frequency always agreed with the measured blade passing frequency.

Effect of Rounding the Cut-Water

Similar tests to those described above were conducted with cut-water leading edges rounded to a radius of 2.5 mm and 5 mm. The clearance gap between the impeller and cut-water was kept the same for all tests, 10 mm or 5.8 percent. Results for nominal flow rate are presented in Fig. 7. The most obvious effect observed is that the resonance peak acoustic pressure at He ≃ 0.57 is reduced with increasing cut-water radius. It should be noted that the original V-shaped three-dimensional cut-water was noisier (produced

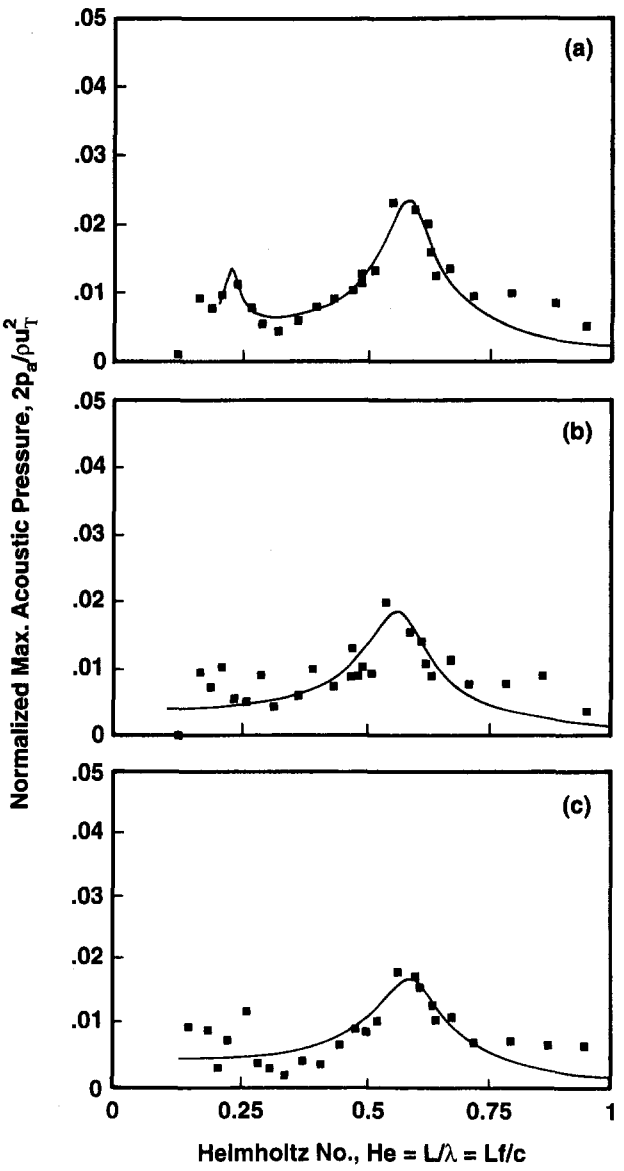

Fig. 7 Normalized maximum acoustic pressure versus Helmholtz number for nominal flow rate: (*a*) sharp-tipped cut-water, (*b*) 2.5 mm radius, (*c*) 5 mm radius

higher acoustic pressures) than the sharp two-dimensional cut water used here as the standard for comparison.

These tests results are summarized in Fig. 8, which shows that the effect of rounding the cut-water is similar for the three flow rates examined. Furthermore, the spread in the peak acoustic pressures for the different flow rates seems to be reduced with rounding the cut-water. Thus, not only is the peak acoustic pressure reduced by rounding the cut-water, but it becomes less sensitive to relative flow rate.

It is also useful to know how rounding the cut-water affects pump performance. Figure 9 shows the head-discharge curves of the pump for the original, the two-dimensional sharp edged, and the 2.5 mm and 5 mm radius cut-waters. The head and discharge coefficients are defined as follows:

$$\text{Head coefficient} \quad \psi = \frac{\Delta p}{1/2\rho u_T^2} \tag{4}$$

$$\text{Flow coefficient} \quad \phi = \frac{Q}{f_s D_2^2 b} \tag{5}$$

The pump head, Δp, has been corrected for elevation and velocity differences between inlet and outlet, and is normalized by the same dynamic head used to normalize acoustic pressure (velocity scale is the impeller tip speed). For the flow coefficient, Q is the discharge, f_s is the shaft speed, D_2 is the impeller diameter, and b is the width of the impeller discharge passage.

The upper graph of Fig. 9 shows that all three two-dimensional cut-waters have essentially identical curves, which coincide with the original V-shaped cut-water curve above a flow coefficient of about 0.10. The nominal flow rate corresponding to the manufacturer's "best efficiency point" occurs for a flow coefficient of 0.154. It is noted that at low flow rate, below a flow coefficient of about 0.10, the two-dimensional cut-water curves all fall slightly below that for the original cut-water. This effect is emphasized in the lower graph of Fig. 9, produced by expanding the scales of the upper graph.

The general observation of the present study, that rounding the cut-water reduces the noise generated, is supported by the work of Dong et al. (1997). These authors examined five different cut-water radii but their impeller tip-to-cut-water gap increased with increasing cut-water radius. They found that increasing the cut-water radius up to a point significantly reduced noise levels at the pump. However, since the impeller gap was also increasing, the head-flow coefficient curves were also affected and the effects of cut-water radius and impeller gap could not be separated.

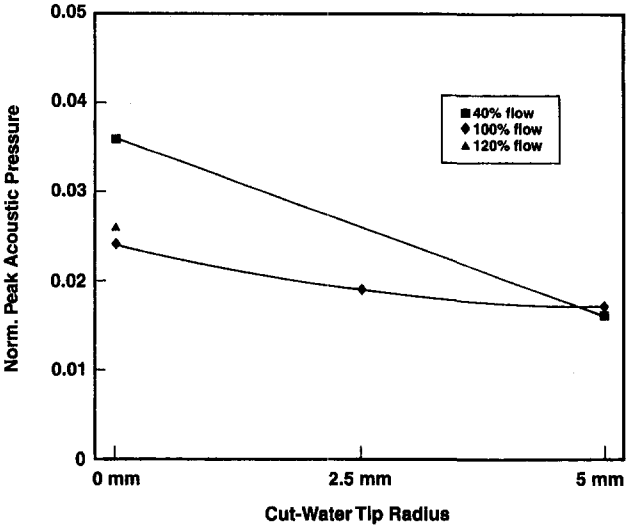

Fig. 8 Normalized peak acoustic pressure as a function of cut-water tip radius

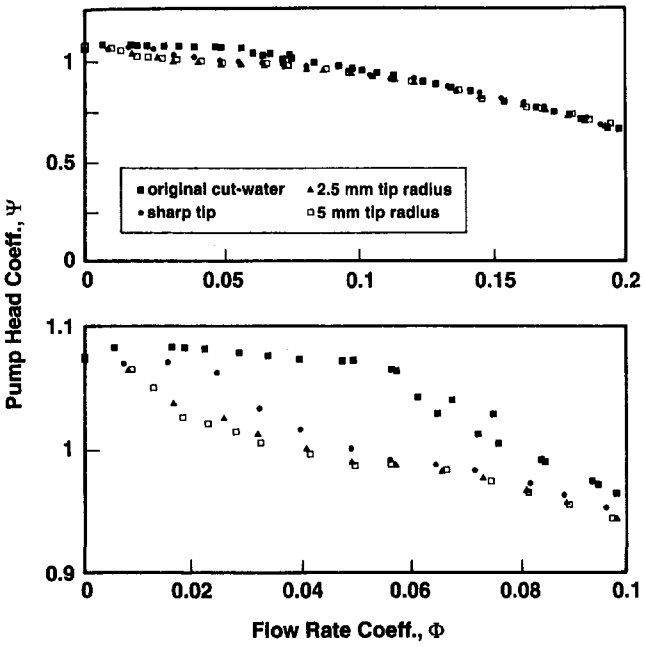

Fig. 9 Head-discharge coefficient curves (lower graph is expanded scale portion of upper graph)

Flow Visualization

Flow visualization studies were conducted in an effort to observe how the flow structure in the region of the cut-water was related to sound generation. High turbulence levels and inadequacies of the lighting system made it difficult to identify fine details of the flow, but some significant observations could be made. To make the flow structure more visible, the video images were digitally processed and the contrast was thereby enhanced. Figure 2 gives a schematic view of a cross section through the midplane of the impeller and shows the window through which flow visualization pictures were taken.

Figure 10 shows a series of pictures for the two-dimensional sharp tipped cut-water operating at 40 percent nominal flow rate and a Helmholtz number of 0.4 (500 rpm). The video framing rate was 500 fps which, for a period of blade passing, τ, of 0.024 s, gives about 12 frames per blade passing cycle. The beginning of a cycle, $t = 0$, is arbitrarily taken as the time when the impeller blade passes the cut-water. Flow separation produces a concentration of the flow tracer in the recirculating vortex and is therefore evident in the pictures as a brighter region. The impeller blade tip, which is moving at about 9 m/s at 500 rpm, appears as a bright smear in those pictures where it is passing the window. In Fig. 10, a vortex becomes clear on the recirculation side of the cut-water tip at about $t = -0.25\tau$ ($\frac{1}{4}$ of a blade passing cycle period before the blade passes the cut-water). It reaches a maximum size, filling about 80 percent of the gap, just as the blade is passing the cut-water, $t = 0.083\tau$. By $t = 0.417\tau$, the vortex has been swept away in the recirculating flow.

Figure 11 shows a series of images for 120 percent nominal flow rate, with other experimental parameters the same as for Fig. 10 (500 rpm, $\tau = 24$ ms, framing rate 500 fps). In this series, the vortex forms on the discharge side of the cut-water, is much smaller in size and is apparent for a shorter portion of the blade passing cycle. At nominal flow rate, the flow structure details were much less obvious than for either 40 or 120 percent nominal flow rate as should be expected for the optimum design conditions. These overall visual observations for flows from

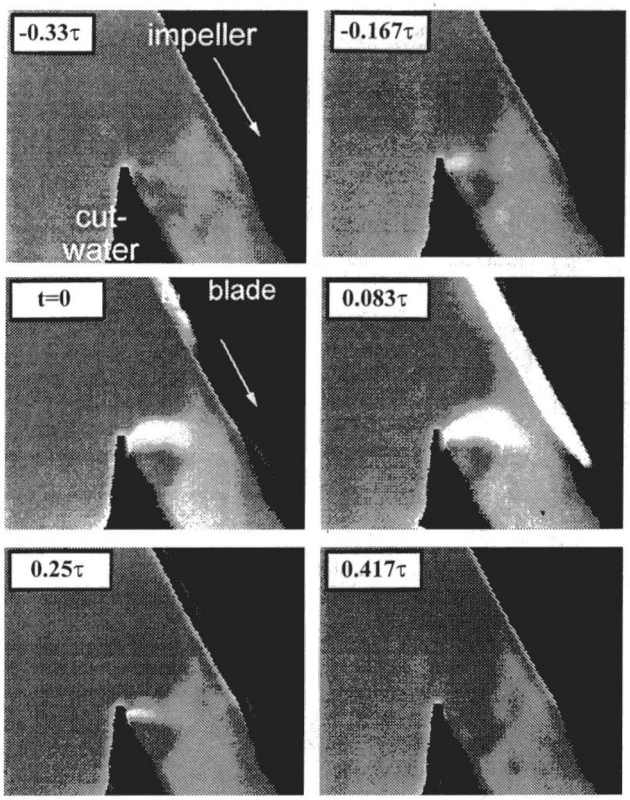

Fig. 10 Flow visualization sequence, two-dimensional sharp tip 40 percent nominal flow rate, Helmholtz number = 0.4 (500 rpm), blade passing period τ = 24 ms

Figs. 10 and 11 agree well with similar observations made by Brownell et al. (1985). These authors reported that the stagnation point of the flow on the cut-water tongue moved from the discharge side to the recirculation side of the tongue as the flow increased from 30 to 140 percent nominal flow rate with the 100 percent stagnation point at the tip. Significantly, they also observed that the streamlines, stagnation points, and separation zones for a given flow rate were not affected by a change in rotor speed from 570 to 1750 rpm.

The apparent length scale of the vorticity seen in Figs. 10 and 11 seems to be directly related to the magnitude of the resonance peak observed in Fig. 5. The significant difference in the location of the stagnation point and flow separation vortex between flow rates below and above the nominal may also help explain the peculiar difference in acoustic excitation discussed above. The difficulty in seeing clear flow separation at nominal flow rates is then consistent with the lower acoustic pressures observed under these conditions. Ideally, little flow separation should occur at the nominal design flow conditions.

The effect of rounding the cut-water is illustrated in Fig. 12. All conditions are the same as for Fig. 10 (40 percent nominal flow rate, 500 rpm, 500 fps) except that the cut-water tip has a 5 mm radius (half the radial impeller-to-cut-water gap). Qualitatively, a comparison of Figs. 12 and 10 shows significant differences. The curved tip of the cut-water permits movement of the stagnation point. The flow separation vortex first appears on the discharge side of the cut-water as the blade passes, t = 0, and then rolls around the end of the cut-water to be convected downstream in the recirculating flow. The vortex appears to be smaller and to remain near the cut water tip for a shorter period of time than observed for the sharp-tipped cut-water. These observations support the argument that rounding the cut-water reduces the sound generation at the cut-water by permitting movement of the stagnation point and thereby reducing the vorticity generated.

Conclusions

An experimental study has been conducted to improve our understanding of the acoustic behavior of a pump-piping system that is excited by a centrifugal pump at its blade passing frequency. A method was developed to separate the hydraulic pressure fluctuations from the acoustic pressure fluctuations. Tests were conducted at various flow rates, pump speeds, and with different cut-water geometries, and flow visualization was used to study the unsteady flow behavior in the region of the cut water. The effects of rounding the tip of the cut-water were examined. The principal conclusions drawn from this research are as follows:

1 The acoustic and hydraulic pressure fluctuations were successfully separated using assumed general forms for each and a least-squares residual optimization process with pressure spectra data from a number of measurement locations along the pipe. This process permits determination of the acoustic standing wave forms and the location and magnitude of the maximum acoustic pressure in the pipe.

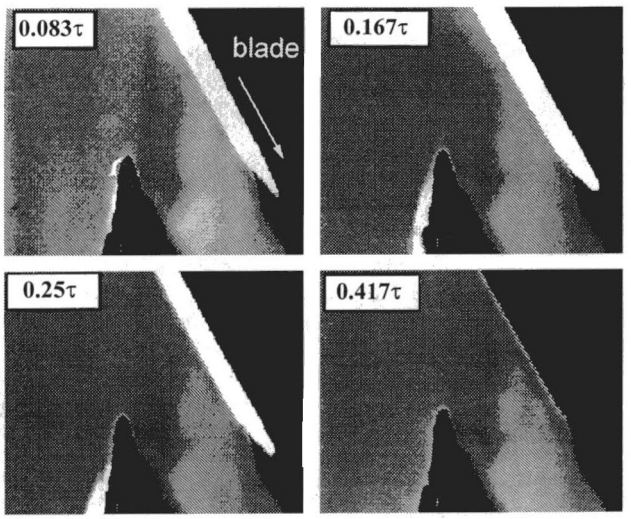

Fig. 11 Flow visualization sequence, two-dimensional sharp tip 120 percent flow rate, Helmholtz number = 0.4 (500 rpm), blade passing period τ = 24 ms

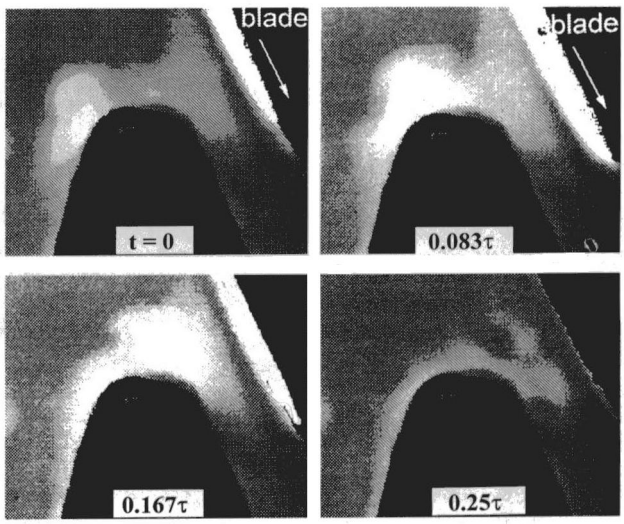

Fig. 12 Flow visualization sequence, 5 mm rounded tip, 40 percent flow rate, He = 0.4 (500 rpm), blade passing period τ = 24 ms

2 From the limited data obtained, it appears that the peak acoustic pressure at resonance is a minimum in the region of the nominal rated flow of the pump. In this region, the flow separation and attendant vorticity generated at the cut-water are substantially less than at the other flow rates studied (40 and 120 percent nominal). Flow visualization suggests that unsteady flow separation at the cut-water is directly related to the sound generation. Significant flow separation occurs at flow rates away from the nominal rating and the amplitude of the acoustic pressure fluctuations is commensurately greater.

3 Rounding the tip of the cut-water without changing the blade tip clearance was found to significantly reduce the amplitude of the acoustic pressure fluctuations without having any obvious negative effect on pump performance. A sharp cut-water tends to fix the point of flow separation. Flow visualization suggests that rounding the cut-water permits movement of the stagnation point around the cut-water tip during a blade passing cycle, thereby reducing the unsteady vorticity generated.

Acknowledgments

The authors gratefully acknowledge the financial support of NSERC and Ontario Hydro Technologies. They particularly appreciate the technical support and encouragement of Drs. R. T. Hartlen and G. Rzentkowski.

References

Bolleter, U., 1988, "Blade Passage Tones in Centrifugal Pumps," *Vibrations,* Vol. 4, No. 3.

Brownell, R. B., Flack, R. D., and Kostzewsky, G. J., 1985, "Flow Visualization in the Tongue Region of a Centrifugal Pump," *Journal of Thermal Engineering,* Vol. 4(2), pp. 35–45.

Chu, S., Dong, R., and Katz, J., 1993, "Unsteady Flow, Pressure Fluctuation and Noise Associated With the Blade Tongue Interaction in a Centrifugal Pump," ASME *Symp. Flow Noise Modelling, Measurement and Control,* ASME WAM, New Orleans, 1993.

Dong, R., Chu, S., and Katz, J., 1992, "Quantitative Visualization of the Flow Within the Volute of a Centrifugal Pump, Part B: Results and Analysis," ASME *Journal of Fluids Engineering,* Vol. 114, pp. 396–403.

Dong, R., Chu, S., and Katz, J., 1997, "Effect of Modification to Tongue and Impeller Geometry on Unsteady Flow, Pressure Fluctuations and Noise in a Centrifugal Pump," ASME JOURNAL OF TURBOMACHINERY, Vol. 119, pp. 506–515.

Florjancic, D., Schoeffler, W., and Zogg, H., 1980, "Primaere Geraeuschminderung an Kreiselpumpen," *Technische Rundschau Sulzer,* No. 1, pp. 24–26.

Hartlen, R. T., Urbanowicz, J. T., and Barecca, S. L., 1993, "Dynamic Interaction Between Pump and Piping System," CETIM—*1st Int. Symposium on Pump Noise and Vibrations,* Clamard, France, July 7–9, pp. 485–492.

Morgenroth, M., 1996, "Sound Generation by a Centrifugal Volute Pump at Blade Pass Frequency," Ph.D. Thesis, McMaster University, Hamilton, Ontario, Canada.

Neise, W., 1975, "Application of Similarity Laws on the Blade Passage Sound of Centrifugal Fans," *Journal of Sound and Vibration,* Vol. 43(1), pp. 61–75.

Neise, W., 1982, "Review of Noise Reduction Methods for Centrifugal Fans," ASME *Journal of Engineering for Industry,* Vol. 104, No. 2, pp. 151–161.

Powell, A., 1964, "Theory of Vortex Sound," *The Journal of the Acoustical Society of America,* Vol. 36, No. 1, pp. 177–195.

Rockwell, D., and Naudascher, E., 1979, "Self-Sustaining Oscillations of Impinging Free Shear Layers," *Annual Review of Fluid Mechanics,* Vol. 11, pp. 67–94.

An Analysis Method for Multistage Transonic Turbines With Coolant Mass Flow Addition

F. Mildner

H. E. Gallus

Institut für Strahlantriebe und Turboarbeitsmaschinen, Rheinisch-Westfälische Technische Hochschule Aachen, Aachen, Germany

The subject of this paper is a numerical method for the calculation of the transonic flow field of multistage turbines, taking high coolant flow into account. To reduce the processing time, a throughflow method based on the principels of Wu is used for the hub-to-tip calculation. The flow field is obtained by an iterative solution between a three-dimensional inviscid hyperbolic time-dependent algorithm with an implicit finite volume method for the blade-to-blade calculations using C-meshes and a single representative meridional S_{2m}-streamsurface. Along the S_{2m}-plane with respect to nonorthogonal curvilinear coordinates, the stream function equation governing fluid flow is established. The cooling air inflow inside the blade passage forbids the assumption of a constant mass flow along the main stream direction. To consider the change of the aerodynamic and thermodynamic behavior, a cooling air model was developed and implemented in the algorithm, which allows the mixing of radially arbitrarily distributed cooling air in the trailing edge section of each blade row. The viscous effects and the influence of cooling air mixing are considered by the use of selected loss correlations for profile, tip leakage, secondary flow and mixing losses in the S_{2m}-plane in terms of entropy. The method is applied to the four-stage high-temperature gas turbine Siemens KWU V84.3. The numerical results obtained are in good agreement with the experimental data.

Introduction

Continuous improvements in gas turbine development and thermodynamic cycle process are needed to conserve energy resources, cut back emissions, and lower costs. To reach these goals, current development tends toward an increase of the turbine inlet temperature with a concurrent rise in the mass flow to increase the power/weight ratio of the machines. For this, the maximum power output and the overall thermal efficiency play major roles in the development of modern heavy-duty high-temperature gas turbines. The rise of the aerodynamic load of the blades in combination with the influence of modern cooling air configurations due to the high turbine inlet temperature hinder the aerodynamic design. Under these preconditions further improvement of the efficiency requires not only the investigation of single blade rows, but also the analysis of the flow field of complete transonic cooled turbomachine components.

In the early 1990s, several methods to calculate multistage turbomachinery components were developed based on solving the three-dimensional Navier–Stokes equations (Ni and Bogoian, 1989; Dawes, 1992; Denton, 1992; Adamczyk et al., 1990; Chima, 1991; Gallus, et al., 1995; Arnone et al., 1994, 1996; Fan and Lakshminarayana, 1996). Even taking into account the rapidly rising computer capacities, this is a very extensive and computer-time consuming method and still requires a long calculation time.

To reduce the processing time, throughflow methods are still in use, especially when, during the design process of a turbomachine, several calculations become necessary. The described numerical code is based on the publication of Wu (1951), in which he reduced the three-dimensional flow problem into several two-dimensional problems. In case of a pure subsonic flow pattern, the stream function equation can be solved with the finite difference method iteratively on S_1 (blade-to-blade) and one representative S_{2m}-plane (hub-to-tip) using nonorthogonal body-fitted H-grids. In the case of transonic flow, especially when the flow is choked on several blade-to-blade planes, this procedure fails due to the non-uniqueness of the density in the stream function formulation. Therefore Wu's approach in the described code for S_1-planes is replaced by an inviscid hyperbolic algorithm with an implicit finite volume method using body fitted C-meshes (Benetschik et al., 1996). The interactive coupling of the three-dimensional calculation of the single blade rows is performed on the S_{2m}-stream filament, which covers all blade rows of the turbomachine component. The S_{2m}-streamsurface contains circumferentially averaged flow variables requiring that the S_1-planes be surfaces of revolution. The geometry of the S_{2m}-streamsurface shape and the thickness are to be updated from the last cycle calculation on S_1-stream surface family.

Using the Artificial Compressibility Method (Hafez et al., 1978) on the S_{2m}-stream surface the discretization of the partial differential equation is carried out by use of the standard central difference formula and hence the procedure is greatly simplified. In order to overcome the non-uniqueness of density in transonic flow on S_{2m}-planes by use of the stream function equation, Hafez and Lowell (1981) proposed a technique. According to this method the velocities in the flow field are first obtained by integrating the momentum equation and then the density is determined by the energy equation.

Due to the results of a comparison of different loss correlations with a single-stage Navier–Stokes calculation applied to the Siemens V84.3 (Mildner and Gallus, 1993), the correlation of Craig and Cox (1970) shows the best coincidence with the experimental data and is therefore integrated in the numerical code.

Effective turbine blade cooling is necessary to enhance the efficiency of gas turbines. Usually the coolant is mainly ejected through the trailing edge of the blades. In addition to the desired temperature reduction at the trailing edge, there is a three-dimensional aerodynamic interaction between hot gas and the coolant. The complex mechanism of the mixture is a main prob-

Contributed by the International Gas Turbine Institute and presented at the 42nd International Gas Turbine and Aeroengine Congress and Exhibition, Orlando, Florida, June 2–5, 1997. Manuscript received at ASME Headquarters February 1997. Paper No. 97-GT-183. Associate Technical Editor: H. A. Kidd.

lem in the numerical prediction of the flow field of cooled turbomachine components. The cooling air inflow inside the blade passage forbids the assumption of a constant mass flow and constant rothalpy along the main stream direction. While such phenomena are predictable with new Navier–Stokes solvers (Bohn et al., 1995; Michelassi et al., 1994) there is still a lack of methods when cooling air effects should be considered in Q3D-algorithms. Therefore, a cooling air mixing model will be presented within this paper that allows the mixing of radially distributed cooling air in the trailing edge section of each blade row.

Hub-to-Tip Calculation

S_{2m}-Stream Function Equation. Newton's second Law of motion is initially cast into a cylindrical coordinate system rotating about the x axis at an angular speed Ω. For a steady, adiabatic, inviscid flow the equation of motion reads as follows:

radial direction:

$$-\frac{w_u}{r}\left(\frac{\partial r w_u}{\partial r}-\frac{\partial w_r}{\partial \varphi}\right)+w_x\left(\frac{\partial w_r}{\partial x}-\frac{\partial w_x}{\partial r}\right)-2\Omega w_u = T\frac{\partial \hat{s}}{\partial r}-\frac{\partial h_{rot}}{\partial r} \quad (1)$$

circumferential direction:

$$-\frac{w_r}{r}\left(\frac{\partial r w_u}{\partial r}-\frac{\partial w_r}{\partial \varphi}\right)-w_x\left(\frac{\partial w_x}{r\partial \varphi}-\frac{\partial w_u}{\partial x}\right)+2\Omega w_r = \frac{T\partial \hat{s}}{r\partial \varphi}-\frac{\partial h_{rot}}{r\partial \varphi} \quad (2)$$

axial direction:

$$-w_r\left(\frac{\partial w_r}{\partial x}-\frac{\partial w_x}{\partial r}\right)+w_u\left(\frac{1}{r}\frac{\partial w_x}{\partial \varphi}-\frac{\partial w_u}{\partial x}\right)=T\frac{\partial \hat{s}}{\partial x}-\frac{\partial h_{rot}}{\partial x} \quad (3)$$

The streamsurface shape can be described by $\varphi = \varphi(\bar{r}, \bar{x})$. The barred signs are used to denote a quantity q following the motion along S_{2m}-streamsurface with respect to $\bar{x}$ and $\bar{r}$ lines on the meridional plane. The relations between these partial derivatives and ordinary spatial partial derivatives are given by:

$$\frac{\partial q}{\partial r}=\frac{\partial q}{\partial \bar{r}}+\frac{\mu_1}{r}\frac{\partial q}{\partial \varphi} \quad (4)$$

$$\frac{\partial q}{\partial x}=\frac{\partial q}{\partial \bar{x}}+\frac{\mu_2}{r}\frac{\partial q}{\partial \varphi} \quad (5)$$

where the streamsurface gradients μ_1 and μ_2 are:

$$\mu_1=-r\frac{\partial \varphi}{\partial \bar{r}} \quad (6)$$

$$\mu_2=-r\frac{\partial \varphi}{\partial \bar{x}} \quad (7)$$

A stream function equation can be introduced, obtained from the continuity equation for flow along a S_{2m}-streamsurface

$$\frac{\partial \psi}{\partial \bar{x}}=-rb\rho w_r \quad (8)$$

$$\frac{\partial \psi}{\partial \bar{r}}=-rb\rho w_x \quad (9)$$

where b is the thickness of the stream filament. Using the condition that the circumferential velocity component has to follow the S_{2m}-streamsurface

$$w_u=-\mu_1 w_r-\mu_2 w_x \quad (10)$$

the principal streamsurface equation can then be obtained from Eqs. (1)–(10). By taking into account that the formulation is transformed into a nonorthogonal curvilinear s, n-coordinate system, the formulation reads:

$$\bar{A}_2\frac{\partial^2\psi}{\partial \bar{s}^2}+\bar{B}_2\frac{\partial^2\psi}{\partial \bar{n}^2}+\bar{C}_2\frac{\partial^2\psi}{\partial \bar{n}\partial \bar{s}}+\bar{D}_2\frac{\partial \psi}{\partial \bar{s}}+\bar{E}_2\frac{\partial \psi}{\partial \bar{n}}=\bar{F}_2 \quad (11)$$

with the coefficients:

$$A_2=\frac{1+\mu_1^2}{r} \quad (12)$$

$$B_2=\frac{1+\mu_2^2}{r} \quad (13)$$

$$C_2=-\frac{2\mu_1\mu_2}{r} \quad (14)$$

Nomenclature

$A_2 \ldots E_2$, $\bar{A}_2 \ldots \bar{F}_2$ = coefficients of the stream function equation
A = area
$\hat{A}, \hat{B}, \hat{C}$ = flux Jacobian matrices
b = stream sheet thickness
c = dissipation constant
e = energy per unit volume
$\hat{E}, \hat{F}, \hat{G}$ = flux vectors
f_k = radial coolant distribution
h = enthalpy
$\hat{H}$ = source vector
J = Jacobian
L, R = left- and right-sided Eigenvector matrices
Ma = Mach number
$\dot{m}$ = mass flow rate
p = static pressure
Q = vector of dependent conservative variables
R = gas constant
$\hat{s}$ = entropy
s, n = curvilinear coordinates
t = time
T = temperature
u = circumferential velocity
u, v, w = absolute Cartesian velocities
w = velocity
x, y, z = Cartesian coordinates
x, r, φ = cylindrical coordinates
β = relative flow angle
κ = ratio of specific heat
Λ = matrix of Eigenvalues
μ_1, μ_2 = streamsurface gradients
μ = numerical dissipation
ξ, η, ζ = curvilinear coordinates
$\rho, \tilde{\rho}$ = density, artificial density
ψ = stream function
Ω = angular velocity

Subscripts

g = gas
i = inlet
k = coolant
m = meridional
rot = rothalpy
t = total
x, y, z = partial derivative
x, r, u = direction of velocity
1 = mixed-out state

Superscripts

$\hat{}$ = vector or matrix in transformed plane
l, r = left- and right sided values, respectively
ξ, η, ζ = direction of velocity

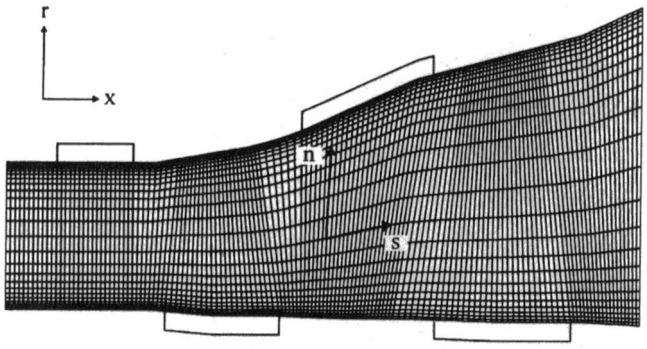

Fig. 1 Nonorthogonal coordinates and computational grid

$$D_2 = \frac{1}{r}\left(\mu_1 \frac{\partial \mu_1}{\partial \bar{x}} - \mu_2 \frac{\partial \mu_1}{\partial \bar{r}}\right) \tag{15}$$

$$E_2 = \frac{1}{r}\left(\mu_2 \frac{\partial \mu_2}{\partial \bar{r}} - \mu_1 \frac{\partial \mu_2}{\partial \bar{x}} - \frac{1}{r}\right) \tag{16}$$

$$\bar{A}_2 = A_2\left(\frac{\partial s}{\partial \bar{x}}\right)^2 + B_2\left(\frac{\partial s}{\partial \bar{r}}\right)^2 + C_2 \frac{\partial s}{\partial \bar{x}} \frac{\partial s}{\partial \bar{r}} \tag{17}$$

$$\bar{B}_2 = A_2\left(\frac{\partial n}{\partial \bar{x}}\right)^2 + B_2\left(\frac{\partial n}{\partial \bar{r}}\right)^2 + C_2 \frac{\partial n}{\partial \bar{x}} \frac{\partial n}{\partial \bar{r}} \tag{18}$$

$$\bar{C}_2 = 2A_2 \frac{\partial s}{\partial \bar{x}} \frac{\partial n}{\partial \bar{x}} + 2B_2 \frac{\partial s}{\partial \bar{r}} \frac{\partial n}{\partial \bar{r}} + C_2\left(\frac{\partial n}{\partial \bar{x}} \frac{\partial s}{\partial \bar{r}} + \frac{\partial n}{\partial \bar{r}} \frac{\partial s}{\partial \bar{x}}\right) \tag{19}$$

$$\bar{D}_2 = A_2 \frac{\partial^2 s}{\partial \bar{x}^2} + B_2 \frac{\partial^2 s}{\partial \bar{r}^2} + C_2 \frac{\partial^2 s}{\partial \bar{x} \partial \bar{r}} + D_2 \frac{\partial s}{\partial \bar{x}} + E_2 \frac{\partial s}{\partial \bar{r}} \tag{20}$$

$$\bar{E}_2 = A_2 \frac{\partial^2 n}{\partial \bar{x}^2} + B_2 \frac{\partial^2 n}{\partial \bar{r}^2} + C_2 \frac{\partial^2 n}{\partial \bar{x} \partial \bar{r}} + D_2 \frac{\partial n}{\partial \bar{x}} + E_2 \frac{\partial n}{\partial \bar{r}} \tag{21}$$

$$\bar{F}_2 = \left[\frac{\partial s}{\partial \bar{r}} r\left(w_x B_2 - w_r \frac{C_2}{2}\right) - \frac{\partial s}{\partial \bar{x}} r\left(w_r A_2 - w_x \frac{C_2}{2}\right)\right] \frac{\partial b\rho}{\partial s} + \left[\frac{\partial n}{\partial \bar{r}} r\left(w_x B_2 - w_r \frac{C_2}{2}\right) - \frac{\partial n}{\partial \bar{x}} r\left(w_r A_2 - w_x \frac{C_2}{2}\right)\right] \times \frac{\partial b\rho}{\partial n} - \left[\frac{1}{w_x}\left(T\left(\frac{\partial s}{\partial \bar{r}} \frac{\partial \hat{s}}{\partial s} + \frac{\partial n}{\partial \bar{r}} \frac{\partial \hat{s}}{\partial n}\right) - \left(\frac{\partial s}{\partial \bar{r}} \frac{\partial h_{rot}}{\partial s} + \frac{\partial n}{\partial \bar{r}} \frac{\partial h_{rot}}{\partial n}\right)\right) + 2\mu_2 \Omega\right] b\rho \tag{22}$$

Mesh Generation. As the equation to be solved is expressed with respect to a nonorthogonal curvilinear coordinate system, the discretization can be done directly on a arbitrary type mesh. In the present calculation a body-fitted H-type mesh was used. Figure 1 shows an example for a two-stage gas turbine with 143 × 25 grid nodes. To consider strong flow variable gradients due to the implemented loss and cooling air mixing model, mesh refining near hub and shroud is utilized.

Determination of Density. In the stream function formulation the density is not a unique function of the mass flux, and for subsonic flow the density is updated by using the following iteration procedure, where the entropy is taken into account in the density calculation:

$$\rho_{NEW} = \rho_i \left[\frac{h_{rot} + \frac{1}{2}\Omega^2 r^2 - \frac{\frac{1}{2}(\rho w)^2}{\rho_{OLD}^2}}{h_i}\right]^{1/(\kappa-1)} e^{(\hat{s}_i - \hat{s})} \tag{23}$$

To calculate the density in mixed flow domains, Eq. (1) is rewritten as a velocity gradient equation:

$$w_{x_{i,j+1}}^{NEW} = w_{x_{i,j}}^{NEW} + \int_{r_{i,j}}^{r_{i,j+1}} \left[\frac{\partial w_r}{\partial \bar{x}} + \mu_2\left(\frac{w_u}{r} + \frac{\partial w_u}{\partial \bar{r}} + 2\Omega\right) - \mu_1 \frac{\partial w_u}{\partial \bar{x}} - \frac{1}{w_x^{OLD}}\left(T \frac{\partial \hat{s}}{\partial \bar{r}} - \frac{\partial h_{rot}}{\partial \bar{r}}\right)\right] dr \tag{24}$$

The terms on the right-hand side are updated consistently with the main calculation of ψ. The distribution of w_x from hub to shroud may be determined by integrating Eq. (24) along the radial direction after transformation into the s, n-coordinate system. The integration procedure proceeds from an assumed value of w_x on an initial data curve. Since the supersonic flow regions of the circumferential averaged S_{2m}-flow normally do not extend to the hub for rotors and to the casing for stators in case of transonic turbines, the integration direction can be selected as shown in Fig. 2. Along an initial data curve near hub or shroud, where the flow is subsonic, the distribution of ρ and w_x along the corresponding curve may be obtained by use of Eq. (23) as in subsonic flow.

After integration, w_r is updated from

$$w_r = w_x \frac{\partial \psi / \partial \bar{x}}{\partial \psi / \partial \bar{r}} \tag{25}$$

Knowing w_x and w_r, the density ρ can then obtained from Eq. (23).

Since Eq. (11) is of mixed type in the transonic regime, the artificial density is introduced to ensure the stability of the computation in the supersonic regions. This method consists of modifying the density so as to introduce numerical dissipation. The modified density $\tilde{\rho}$ is obtained as follows:

$$\tilde{\rho} = \rho - \mu \frac{\partial \rho}{\partial s} \Delta s \quad \mu = \max\left[0, c\left(1 - \frac{1}{\mathrm{Ma}^2}\right)\right] \tag{26}$$

where c ranges from 1.5 to 2. The discretization scheme for the density at grid point (i, j) takes the form:

$$\tilde{\rho}_{i,j} = \rho_{i,j} - \mu_{i,j}\left(\frac{w_x}{w_m}(\rho_{i,j} - \rho_{i-1,j}) + \frac{w_r}{w_m}(\rho_{i,j} - \rho_{i,j-1})\right) \quad \text{for } [w_r > 0] \tag{27}$$

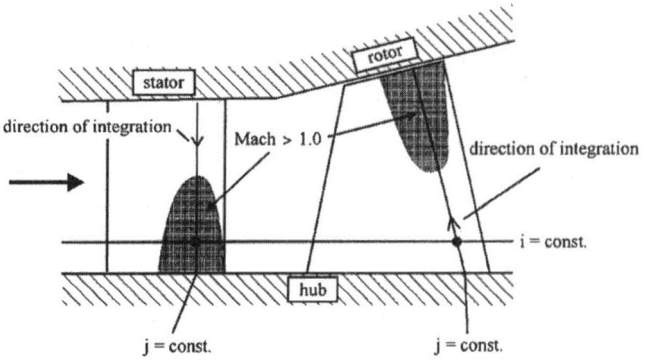

Fig. 2 Location of transonic regions

$$\tilde{\rho}_{i,j} = \rho_{i,j} - \mu_{i,j}\left(\frac{w_x}{w_m}(\rho_{i,j} - \rho_{i-1,j}) + \frac{w_r}{w_m}(\rho_{i,j+1} - \rho_{i,j})\right)$$

$$\text{for } [w_r < 0] \quad (28)$$

Boundary Conditions and Solution Method. The boundary conditions of flow along the S_{2m}-streamsurface should be specified. At the inlet boundary the stagnation pressure, stagnation temperature, and the mass flow rate are given. At the solid walls, the stream function value should be equal to zero (at hub), or $\dot{m}$ (at shroud). At the outlet boundary, the relative flow angle is given.

Standard finite discretizing of Eq. (11) leads to a large system of nonlinear algebraic equations in the unknown stream function values at the grid points in the form:

$$|A|\vec{\psi} = \vec{B} \quad (29)$$

The coefficient matrix A contains only metric quantities and remains unchanged, while the right-hand side contains the density $\tilde{\rho}$, the independent thermodynamic properties entropy $\hat{s}$, and the stagnation rothalpy h_{rot}, and must be updated during the iteration process. Together with the discretized boundary conditions, the formulation of the discrete problem is complete, and a direct matrix method is utilized to solve the nonlinear algebraic equation.

Blade-to-Blade Calculation

Governing Equations. The three-dimensional, compressible, inviscid, and unsteady flow is described by the Euler equations. For the correct computation of the propagation speed and the intensity of discontinuities, a conservative formulation in a rotating cartesian frame of reference is used. Transformed into a general curvilinear system the Euler equations are defined as follows:

$$J\frac{\partial Q}{\partial t} + \frac{\partial \hat{E}}{\partial \xi} + \frac{\partial \hat{F}}{\partial \eta} + \frac{\partial \hat{G}}{\partial \zeta} = \hat{H} \quad (30)$$

where the state vector Q comprising the conserved quantities $\hat{E}$, $\hat{F}$, $\hat{G}$, are the Euler fluxes and $\hat{H}$ describes the source term:

$$Q = \begin{pmatrix} \rho \\ \rho u \\ \rho v \\ \rho w \\ e_{rot} \end{pmatrix} \qquad \hat{E} = J\begin{pmatrix} \rho w^{\xi} \\ \rho u w^{\xi} + p\xi_x \\ \rho v w^{\xi} + p\xi_y \\ \rho w w^{\xi} + p\xi_z \\ w^{\xi}(e_{rot} + p) \end{pmatrix}$$

$$\hat{F} = J\begin{pmatrix} \rho w^{\eta} \\ \rho u w^{\eta} + p\eta_x \\ \rho v w^{\eta} + p\eta_y \\ \rho w w^{\eta} + p\eta_z \\ w^{\eta}(e_{rot} + p) \end{pmatrix}$$

$$\hat{G} = J\begin{pmatrix} \rho w^{\zeta} \\ \rho u w^{\zeta} + p\zeta_x \\ \rho v w^{\zeta} + p\zeta_y \\ \rho w w^{\zeta} + p\zeta_z \\ w^{\zeta}(e_{rot} + p) \end{pmatrix} \qquad \hat{H} = J\begin{pmatrix} 0 \\ 0 \\ \rho w \Omega \\ -\rho v \Omega \\ 0 \\ 0 \end{pmatrix} \quad (31)$$

This set is closed by the assumption of a perfect gas:

$$e_{rot} = \frac{p}{\kappa - 1} + \frac{\rho}{2}(u^2 + v^2 + w^2) - \rho\Omega(yw - zv) \quad (32)$$

The Jacobian J represents the volume of the discretization element. In these equations u, v, w denote the absolute Cartesian velocities. The contravariant relative transport velocities are given by:

$$w^{\xi} = u\xi_x + (v + \Omega z)\xi_y + (w - \Omega y)\xi_z$$
$$w^{\eta} = u\eta_x + (v + \Omega z)\eta_y + (w - \Omega y)\eta_z$$
$$w^{\zeta} = u\zeta_x + (v + \Omega z)\zeta_y + (w - \Omega y)\zeta_z \quad (33)$$

To solve the Euler equations, a quasi-conservative formulation is used. This formulation results from the Euler equations by exchanging the fluxes by products of the flux-Jacobian-matrices and the spatial derivatives of the vector of dependent variables:

$$\frac{\partial \hat{Q}}{\partial t} + \hat{A}\frac{\partial \hat{Q}}{\partial \xi} + \hat{B}\frac{\partial \hat{Q}}{\partial \eta} + \hat{C}\frac{\partial \hat{Q}}{\partial \zeta} = \hat{H} \quad (34)$$

with the flux-Jacobian-matrices following from:

$$\hat{A} = \frac{\partial \hat{E}}{\partial \hat{Q}}, \quad \hat{B} = \frac{\partial \hat{F}}{\partial \hat{Q}}, \quad \hat{C} = \frac{\partial \hat{G}}{\partial \hat{Q}} \quad (35)$$

Numerical Algorithm. The numerical solution follows a Godunov-type upwind scheme, formulated in node centered finite volume technique using body fitted C-meshes. Assuming initial states Q^r to the right and Q^l to the left of each finite volume cell face being defined, fluxes are computed using Roe's approximate Riemann solver (Roe, 1981). Across a cell face $\xi_{i+1/2,j,k}$ the numerical flux function reads:

$$\hat{E}_{i+1/2,j,k} = \tfrac{1}{2}[\hat{E}(Q^l_{i+1/2,j,k}) + \hat{E}(Q^r_{i+1/2,j,k}) - \hat{R}^{\xi}|\hat{\Lambda}^{\xi}|\hat{L}^{\xi}(Q^r_{i+1/2,j,k} - Q^l_{i+1/2,j,k}] \quad (36)$$

where $\hat{R}^{\xi}$, $\hat{L}^{\xi}$, and Λ^{ξ} are the matrices of right and left eigenvectors and the diagonal eigenvalue matrix with respect to the Jacobian matrix of the inviscid flux vector.

The described scheme is only first-order accurate. To reduce the diffusive character of first-order schemes and to obtain a high-resolution result an extension to higher order has to be made. This is possible by replacing the piecewise constant data in the discretization cells by linear varying initial data (van Leer, 1979) and leads to the MUSCL technique (Monotonic Upstream Schemes for Conservation Laws). A third-order accuracy can be achieved with this technique. The flux functions are still evaluated using only right and left states, but these states are second or third-order accurate in space.

The disadvantage of a higher order scheme is its liability to oscillations in case of a discontinuous solution. To prevent this, a switch is needed, which reduces the extrapolation to first order in such regions. The scheme mostly used is the TVD-scheme (Total Variation Diminishing; Harten, 1983). It contains a limiter function based on sensors for strong changes in the flow values and reduces the order of extrapolation in these regions. A differentiable flux-limiter function following van Albada was chosen here, which is a compromise between the claim on stability and the claim on smooth extrema.

The solution is advanced implicitly in time using the delta form:

$$\left(\frac{JE}{\Delta t} + \frac{\Delta_{\xi}\hat{A}^{-} + \nabla_{\xi}\hat{A}^{+}}{\Delta \xi} + \frac{\Delta_{\eta}\hat{B}^{-} + \nabla_{\eta}\hat{B}^{+}}{\Delta \eta} + \frac{\Delta_{\zeta}\hat{C}^{-} + \nabla_{\zeta}\hat{C}^{+}}{\Delta \zeta} - \frac{\partial \hat{H}_{i,j,k}}{\partial Q}\right)^{n}\Delta Q$$
$$= -\left(\frac{\hat{E}_{i+1/2,j,k} - \hat{E}_{i-1/2,j,k}}{\Delta \xi} + \frac{\hat{F}_{i,j+1/2,k} - \hat{F}_{i,j-1/2,k}}{\Delta \eta} + \frac{\hat{G}_{i,j,k+1/2} - \hat{G}_{i,j,k-1/2}}{\Delta \zeta} - \hat{H}_{i,j,k}\right)^{n} \quad (37)$$

where $\hat{A}^{\pm}$, $\hat{B}^{\pm}$, and $\hat{C}^{\pm}$ are the 5×5 Jacobians of the inviscid

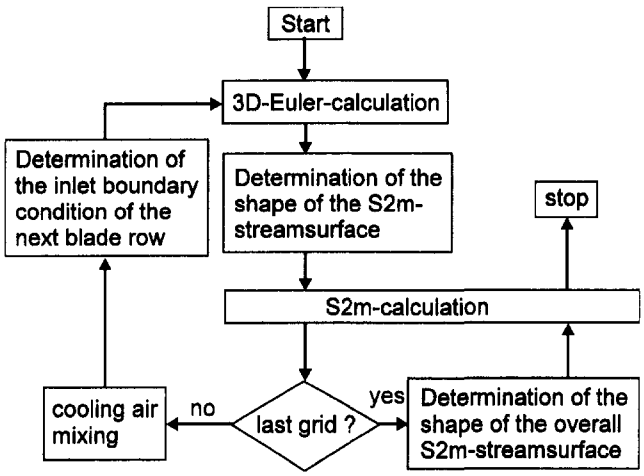

Fig. 3 Flowchart of the Q3DM algorithm

fluxes, which are computed from Roe's scheme first order of accuracy. To avoid excessive computational complexity, the Roe matrices, e.g., with respect to a cell face ξ = const $\hat{R}^{\xi}|\hat{\Lambda}^{\xi}|\hat{L}^{\xi}$, are not linearized in time.

Boundary Treatment. For a correct physical formulation of the boundary conditions, the method of characteristics is used. If the eigenvectors of the characteristic equations run out of the computational domain, they have to be replaced by explicit boundary conditions. The added conditions are upstream total temperature, total pressure, inflow angle, and downstream static pressure. Due to the fact that the Euler algorithm is embedded into the multistage calculation procedure, the downstream boundary condition has to satisfy the conservation of mass of the turbomachine component. For that, the static pressure in combination with the radial equilibrium between the radial stream sheets in the axial gap is updated during the iteration procedure. For supersonic upstream or downstream conditions, the influence of the corresponding prescribed values is modified. On the profile the slip condition for inviscid flow is utilized, which means that the flow is tangent to the blade and the component of the flow velocities normal to the blade is equal to zero.

Coupling of the Flow Solvers

The coupling of the stream function solver on S_{2m}-streamsurface and the Euler algorithm is shown in Fig. 3. In a first step, each blade row is calculated with the Euler algorithm to provide the thickness b and the streamsurface gradients μ_1 and μ_2 of the stream surface of the individual blade row. The circumferential coordinate φ of the S_{2m}-streamsurface results from the circumferentially mass-averaged primitive variables of the Euler solution:

$$\tan\varphi = \frac{\int_{\text{pitch}} \left(\frac{1}{\sqrt{y^2+z^2}} (vz - wy) + \Omega\sqrt{y^2+z^2} \right) d\dot{m}}{\int_{\text{pitch}} u d\dot{m}} \quad (38)$$

After knowing the circumferential coordinate φ, the S_{2m}-streamsurface gradients μ_1 and μ_2 are determined by finite differences. The S_{2m}-stream sheet thickness b results from the blockage of the blade profils and reads:

$$b = \frac{\text{pitch} - \text{blade thickness}}{\text{pitch}} \quad (39)$$

Subsequently the S_{2m}-stream solver is utilized. Considering the mixing of the cooling air and the losses described by the implemented loss model, the solution provides a realistic inflow boundary condition to the next blade row. In this manner each blade row is handled until the last one is reached. In a final step the interaction between the single blade rows takes place by calculating the whole turbomachine component with an overlapping S_{2m}-solution of all blade rows.

Cooling Air Mixing

Mathematical Model. The mixing of cooling air with the main flow can be described by the conservation of mass, momentum, and energy of a perfect gas:

$$\frac{w_{x,1}\rho_1 A_1}{\dot{m}_1} - 1 = 0 \quad (40)$$

$$\dot{m}_1 w_{x,1} - w_{x,g}(\dot{m}_g + C_2\dot{m}_k) + p_1 A_1 - p_g(A_g + C_1 C_3 A_1) = 0 \quad (41)$$

$$\frac{T_1}{T_{t,1}} + \frac{(\kappa-1)(w_{x,1}^2 + w_{r,1}^2 + (w_{x,1}\tan(\beta_1) + u_1)^2)}{2\kappa R T_{t,1}} - 1 = 0 \quad (42)$$

$$\frac{p_1}{\rho_1} - RT_1 = 0 \quad (43)$$

In these equations it is assumed that the coolant is mainly ejected through the trailing edge of the blades and the mixing takes place at a constant static pressure. Moreover, it is assumed that the coolant is ejected in the direction of the main gas flow, and does not influence the deviation. The index 1 denotes the totally mixed-out state downstream of the mixing area, whose axial extension is supposed to be small. The index g stands for the main gas flow quantities, while the index k describes the coolant.

The set of equations is triple undetermined and can be closed by the definition of the constants C_1 to C_3:

$$C_1 = \frac{A_k}{A_1} \quad C_2 = \frac{w_{x,k}}{w_{x,g}} \quad C_3 = \frac{p_k}{p_g} \quad (44)$$

While C_1 depends only on geometry, C_2 and C_3 are assumptions based on empirical data and have to be updated during the design process. The solution of this set of equations is found by applying a Newton–Raphson iteration where the given variable combination $(\dot{m}_1, T_{t,1}, w_{x,1}/w_{u,1}, w_{x,1}/w_{r,1})$ is transformed into the state vector of the mixed out quantities $(w_{x,1}, \rho_1, T_1, p_1)^T$.

Numerical Algorithm. Due to the assumption, that the axial extension of the mixing area is small, numerically, the mixing takes place in a mixing plane *IK* downstream of the trailing edge shown in Fig. 4. This yields to a jump in terms

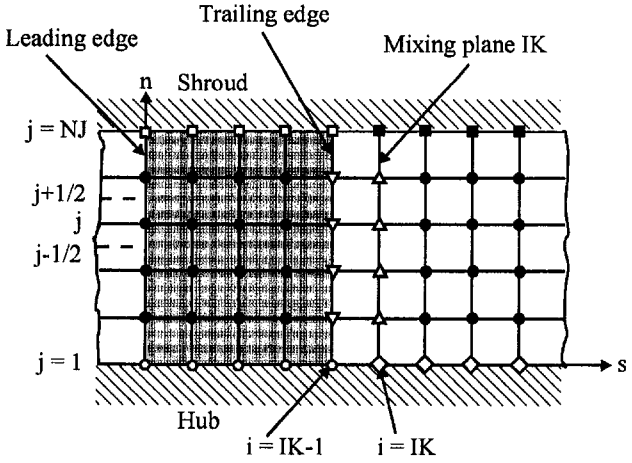

Fig. 4 Schematic section of the computational grid of the S_{2m}-streamsurface

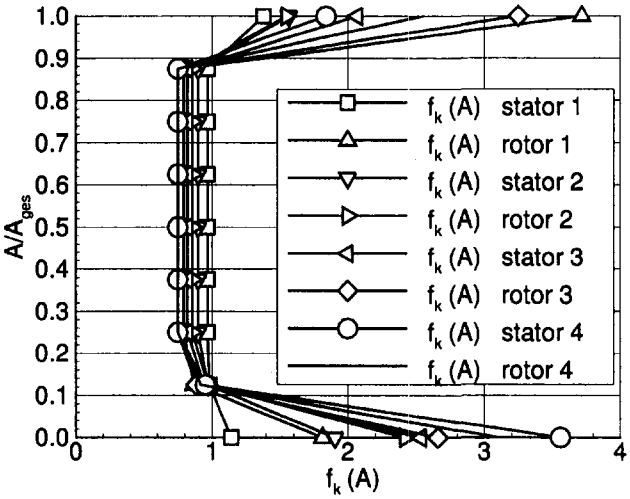

Fig. 5 Radial distribution of the cooling air of the V84.3

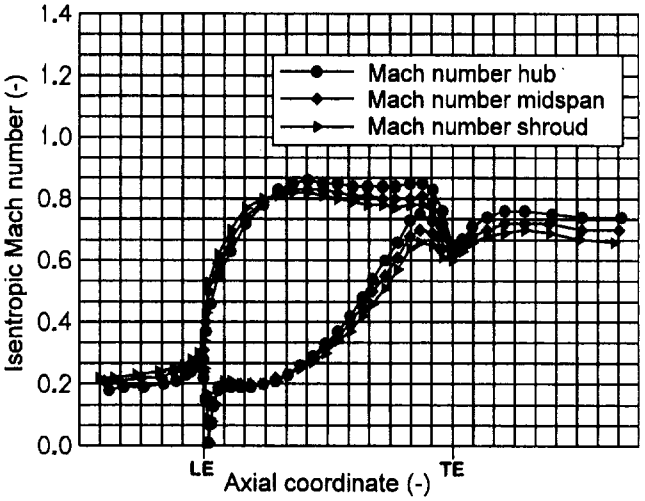

Fig. 7 Isentropic Mach number distribution, blade row 1

of mass, momentum, and energy and influences the dependent variable ψ. For this, additional jump conditions have to be introduced. The different signs at the grid nodes in Fig. 4 represent the varying boundary and mixing conditions in the computational domain described as follows. Upstream the mixing plane ψ is given by:

$$\bigcirc \quad \psi_{i,1} = \text{const}$$

$$\square \quad \psi_{i,NJ} = \psi_{i,1} + \dot{m}_g/2\pi$$

Downstream of the mixing plane, the boundary conditions define the grown mass flux:

$$\diamond \quad \psi_{IK,1} = \psi_{IK-1,1} - \dot{m}_k/4\pi$$

$$\blacksquare \quad \psi_{IK,NJ} = \psi_{IK-1,NJ} + \dot{m}_k/4\pi$$

To consider the convective transport mechanisms across the mixing plane, the calculation of the stream function at the Δ nodes takes place by integration of the continuity equation in the radial direction:

$$\psi_{IK,j} = \psi_{IK,j-1} + \psi_{IK-1,j} - \psi_{IK-1,j-1} + \dot{m}_k \int_{(A/A_{ges})_{j-1/2}}^{(A/A_{ges})_{j+1/2}} f_k(A)\, d\left(\frac{A}{A_{ges}}\right) \quad (45)$$

where the function f_k describes the radial distribution of the cooling air. Figure 5 shows the implemented distribution for the calculated Siemens gas turbine. Due to the jump of the density in the mixing plane, Eq. (11) is not steadily differentiable across the mixing plane. Therefore all ∇ nodes were discretized in upstream direction with first order in space, while the Δ nodes were discretized in downstream direction with first order in space. All $\bullet$ nodes are approximated with a central differential scheme.

Results

For validation of the developed code, called Q3DM, the Siemens gas turbine V84.3 has been investigated. At design conditions, the mass flow is 417 kg/s at a rotation rate of 3600 rpm. Due to the high turbine inlet temperature, the first seven of the eight blade rows in the four-stage turbine are cooled, whereby an intercooler is provided for more effective blade cooling in the first turbine stage. Figure 6 illustrates a cross section of the described turbine. Referring to Fig. 6, it can be seen that the rotating blades in the first stage are shrouded in order to reduce the tip losses. The proven combination of convection and impingement was selected as the cooling method.

Figures 7–9 show the results of the three-dimensional Euler calculation. As expected, the Mach number level increases from turbine inlet to turbine outlet. While the Mach number distribution remains below the critical value in the first blade row (Fig. 7), choked flow can be found at the turbine exit (Fig. 8). The contour plot of the Mach number at midspan in Fig. 9 gives a

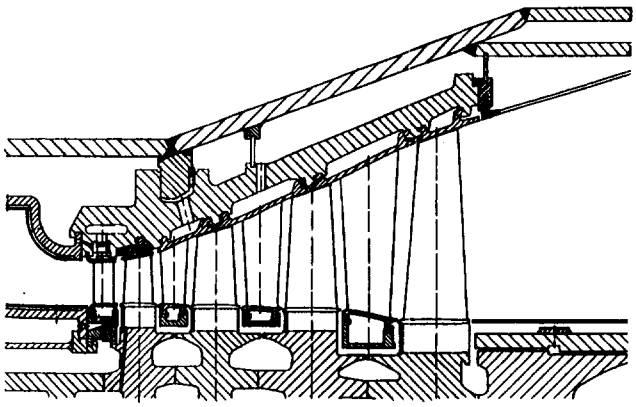

Fig. 6 Cross section of gas turbine V84.3

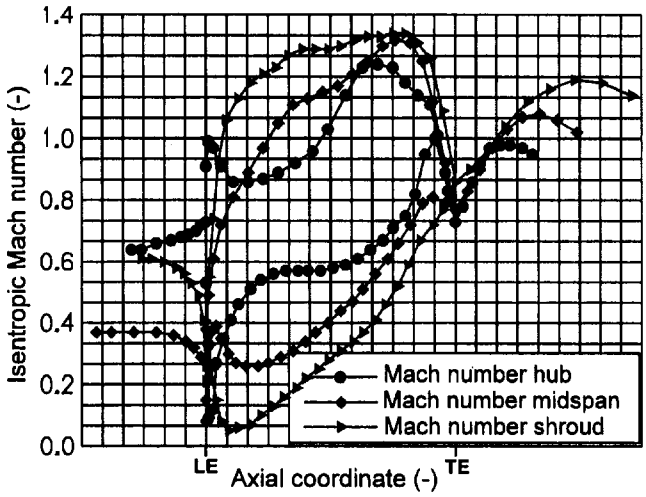

Fig. 8 Isentropic Mach number distribution, blade row 8

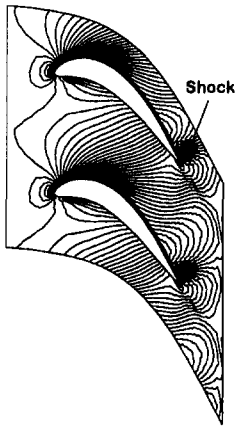

Fig. 9 Mach contour 8, blade row (midspan)

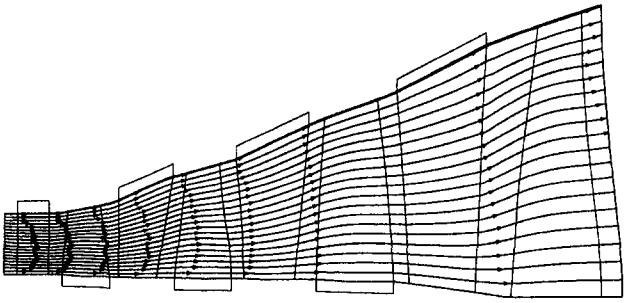

Fig. 10 Computed streamlines on S_{2m}-streamsurface

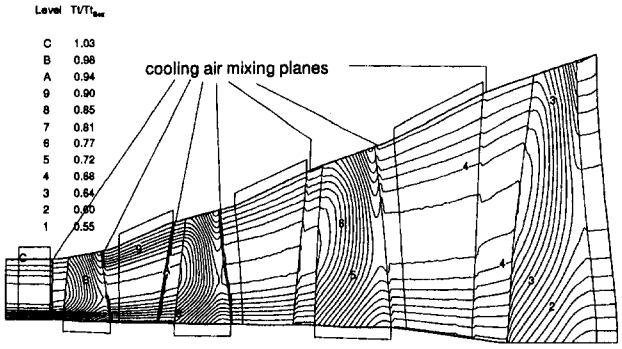

Fig. 11 Computed total temperature contour

survey of the location of the shock. In order to reduce the overall CPU time, a coarse computational mesh ($9 \times 65 \times 9$ grid nodes) was selected, which causes a nonsharp resolution of the shock. Since the result of the Euler calculation is circumferentially averaged to generate the thickness and the shape of the S_{2m}-streamsurface, it has been shown that the resolution of the computational domain is sufficient. For brevity, a more detailed documentation of the inviscid solution is omitted here.

Figure 10 illustrates the streamline pattern through the turbine, obtained from the solution of the stream function equation. As demanded in the cooling air mixing model, the coolant does not influence the direction of the main flow. Contrary to this, the contour plot of the total temperature (Fig. 11) shows the strong influence of the coolant, in terms of total temperature drops in the mixing planes. The tip leakage of the coolant and the cooling air flow through the sealings at hub produce an inhomogeneous distribution of the coolant over the span. This leads to strong temperature gradients in the radial direction.

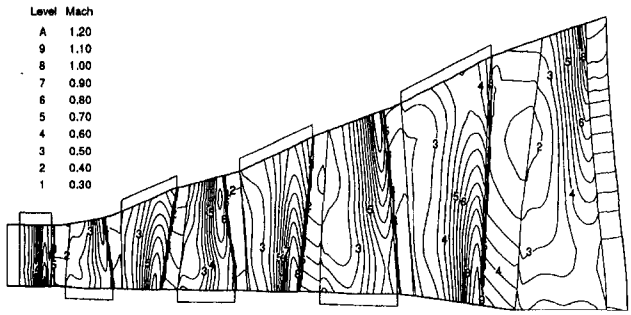

Fig. 12 Computed Mach number distribution

Figure 12 shows the contour plot of the relative Mach number. The change of the reference frame coincides with the location of the mixing plane. The highest Mach numbers up to Ma = 1.22 are located near the hub in the stators due to the blockage of the blades, whereas the peak Mach numbers appear near tip in the rotors due to the high circumferential velocity.

Figure 13 shows the comparison between calculated and designed mass flux. Due to an agreement with Siemens, Fig. 13 shows only the qualitative development of the mass flux along the flow passage. The highest mass flow rates are ejected in the first four blade rows, while the last ones are less influenced. The numerical results obtained are in good agreement with the design as long as the circumferential averaged peak Mach numbers in the S_{2m} calculation do not exceed a value of about 1.15. Up to this Mach number the artificial density $\tilde{\rho}$ represents the real density in the transonic region in a good manner. Higher peak Mach numbers lead to an increasing numerical dissipation μ and therefore to an increasing difference between the real density and the artificial density $\tilde{\rho}$. This effect causes a small difference between the calculated and the designed mass flux in the end stage of the calculated gas turbine.

Finally, the computed pressure and total temperature distribution are compared with experimental data according to Figs. 14–17. The overall agreement is best for the static pressure distribution, whereas for the total temperature plots some small discrepancies between measurement and computational data are found. A reason for this seems to be the simplicity of the mixing air model. This question still needs to be examined.

Concluding Remarks

A new analysis method for multistage transonic turbines with coolant mass flow addition has been developed. This procedure

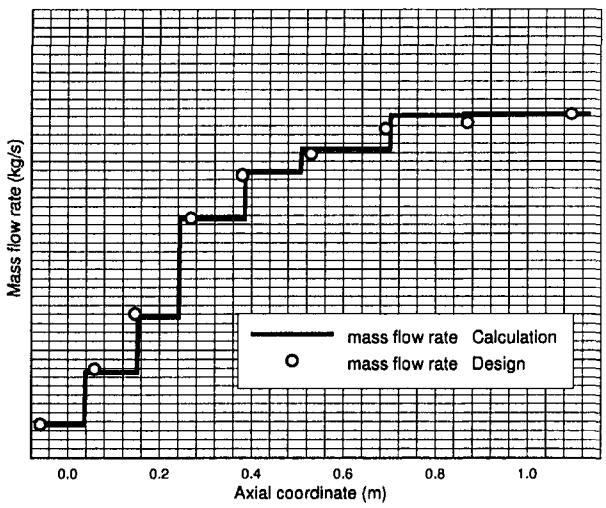

Fig. 13 Computed mass flow rate

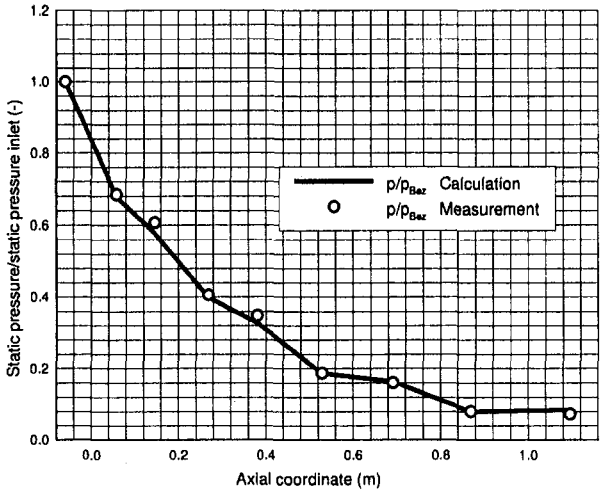

Fig. 14 Static pressure at hub

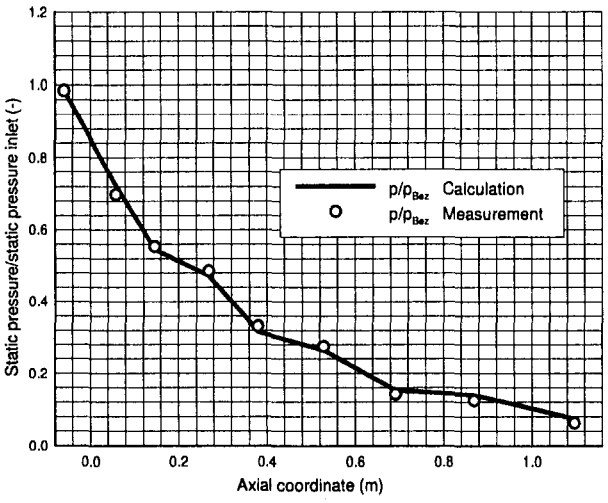

Fig. 15 Static pressure at tip

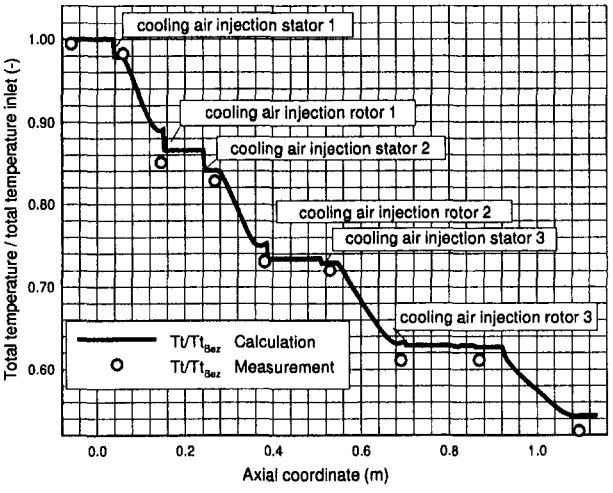

Fig. 16 Total temperature at hub

combines the advantages of a throughflow method with the advantages of a three dimensional calculation. By replacing the calculation on S_1 planes by a three-dimensional inviscid hyperbolic time-dependent algorithm, the iterative coupling of

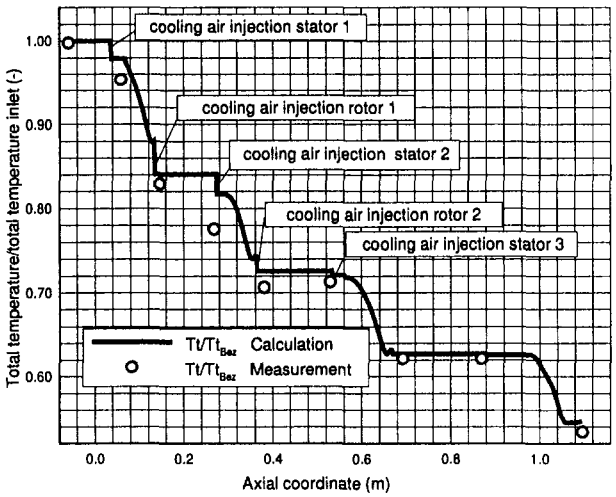

Fig. 17 Total temperature at tip

Wu's approach between blade-to-blade planes and hub-to-tip planes can be dropped. Due to the character of the hyperbolic algorithm, transonic flow can be calculated on the S_1 planes without an artificial density model, which can become instable, when choked flow with high Mach numbers occurs. To avoid expensive Navier–Stokes calculations, as in the mixing plane approaches, and to achieve short computation time, the three-dimensional algorithm calculates only the inviscid flow field, while the viscous effects and the influence of the cooling air mixing can be considered in the fast stream function algorithm. The circumferential averaging of the flow variables in the S_{2m} plane leads to smaller peak Mach numbers in the S_{2m} plane than in the blade-to-blade planes. Therefore the artificial density approach can be used, even when choked flow occurs in the S_1 planes. This method can be applied to machines whose circumferential averaged peak Mach numbers do not exceed Ma = 1.15.

This method needed for the calculation of the four stages of the Siemens gas turbine about 20 minutes CPU time on a Siemens/Fujitsu S600 machine.

Acknowledgments

The development of this computer code was part of the AG TURBO research program, a cooperational effort between industry, universities, and national German research centers. It was financially supported by the German Ministry of Education, Science, Research, and Technology (BMBF) under contract No. 0326821.

References

Adamczyk, J. J., Celestina, M. L., and Beach, T. A., 1990, "Simulation of Viscous Flow Within a Multistage Turbine," ASME JOURNAL OF TURBOMACHINERY, Vol. 112, pp. 370–376.

Arnone, A., and Benvenuti, E., 1994, "Three-Dimensional Navier–Stokes Analysis of a Two-Stage Gas Turbine," ASME Paper No. 94-GT-88.

Arnone, A., and Pacciani, R., 1996, "Rotor–Stator Interaction Analysis Using the Navier–Stokes Equations and a Multigrid Method," ASME JOURNAL OF TURBOMACHINERY, Vol. 118, pp. 679–689.

Benetschik, H., Lohman, A., Lücke, J. R., and Gallus, H. E., 1996, "Inviscid and Viscous Analysis of Three-Dimensional Turbomachinery Flows Using an Implicit Upwind Algorithm," AIAA Paper No. 96-2556.

Bohn, D. E., Becker, V. J., Behnke, K. D., and Bonhoff, B. F., 1995, "Experimental and Numerical Investigations of the Aerodynamic Effects of Coolant Injection Through the Trailing Edge of a Guide Vane," ASME Paper No. 95-GT-26.

Chima, R., 1991, "Viscous Three-Dimensional Calculations of Transonic Fan Performance," *Proc. 77th Symposium of the Propulsion and Energetics Panel*, AGARD.

Craig, H. R. M., and Cox, H. J. A., 1970, "Performance Estimation of Axial Flow Turbines," *Proc. Institutions of Mechanical Engineers*, Vol. 185, 1970/1991.

Dawes, W. N., 1992, "Toward Improved Throughflow Capability: The Use of Three-Dimensional Viscous Flow Solvers in a Multistage Environment," ASME JOURNAL OF TURBOMACHINERY, Vol. 114, pp. 8–17.

Denton, J. D., 1992, "The Calculation of Three-Dimensional Viscous Flow Through Multistage Turbines," ASME JOURNAL OF TURBOMACHINERY, Vol. 114, pp. 18–26.

Fan, S., and Lakshminarayana, B., 1996, "Time Accurate Euler Simulation of Interaction of Nozzle Wake and Secondary Flow With Rotor Blade in an Axial Turbine Stage Using Nonreflecting Boundary Conditions," ASME JOURNAL OF TURBOMACHINERY, Vol. 118, pp. 663–678.

Gallus, H. E., Zeschky, J., and Hah, C., 1995, "Endwall and Unsteady Flow Phenomena in an Axial Turbine Stage," ASME JOURNAL OF TURBOMACHINERY, Vol. 117, pp. 562–570.

Hafez, M., and Lovell, D., 1981, "Numerical Solution of Transonic Stream Function Equation," *AIAA Journal*, Vol. 21, No. 3.

Hafez, M., South, J., Murmann, E., 1978, "Artificial Compressibility Methods for Numerical Solutions of Transonic Full Potential Equation," *AIAA Journal*, Vol. 17, No. 8.

Harten, A., 1983, "High Resolution Schemes for Hyperbolic Systems of Conservation Laws," *J. Comp. Physics*, Vol. 49.

Michelassi, V., Martelli, F., and Amecke, J., 1994, "Aerodynamic Performance of a Transonic Turbine Guide Vane With Trailing Edge Coolant Ejection, Part II: Numerical Approach," ASME Paper No. 94-GT-248.

Mildner, F., and Gallus, H. E., 1993, "Calculation of Viscous Flow in Turbine Cascades With a Partially-Parabolic Algorithm and Linkage With a Quasi-Three-Dimensional Throughflow Method," AG TURBO Report No. 1.1.2.7.

Ni, R. H., and Bogoian, J. C., 1989, "Prediction of 3D Multi-Stage Turbine Flow Field Using a Multi-Grid Euler Solver," AIAA Paper No. 89-0203.

Roe, P. L., 1981, "Approximate Riemann Solvers, Parameter Vectors and Difference Schemes," *J. Comp. Phys.*, Vol. 34, pp. 357–372.

van Leer, B., 1979, "Towards the Ultimate Conservative Difference Scheme V. A Second-Order Sequel to Godunov's Method," *J. Comp. Phys.*, Vol. 32, pp. 101–136.

Wu, Chung-Hua, 1951, "A General Through-Flow-Theory of Fluid Flow With Subsonic or Supersonic Velocity in Turbomachines of Arbitrary Hub and Casing Shapes," NACA TN 2302.

A. A. Ameri
AYT Corporation,
Brook Park, OH 44135

E. Steinthorsson
Institute for Computational Mechanics in Propulsion (ICOMP),
NASA Lewis Research Center,
Brook Park, OH 44142

D. L. Rigby
NYMA, Inc.,
NASA Lewis Group,
Brook Park, OH 44142

Effect of Squealer Tip on Rotor Heat Transfer and Efficiency

Calculations were performed to simulate the tip flow and heat transfer on the GE-E^3 first-stage turbine, which represents a modern gas turbine blade geometry. Cases considered were a smooth tip, 2 percent recess, and 3 percent recess. In addition, a two-dimensional cavity problem was calculated. Good agreement with experimental results was obtained for the cavity calculations, demonstrating that the $k-\omega$ turbulence model used is capable of representing flows of the present type. In the rotor calculations, two dominant flow structures were shown to exist within the recess. Also areas of large heat transfer rate were identified on the blade tip and the mechanisms of heat transfer enhancement were discussed. No significant difference in adiabatic efficiency was observed for the three tip treatments investigated.

Introduction

The tips of turbine blades in gas turbines experience large thermal loads, which can lead to tip burnout. The large thermal load on blade tips is due to hot gases flowing through the gap between the blade tip and the shroud. The flow accelerates due to pressure difference between the pressure and suction sides, causing thin boundary layers and high heat transfer rates. The flow across the tip is also undesirable from the perspective of efficiency since it increases the losses in the flow.

A common strategy to reduce the flow on the tip is to use a recessed tip, also known as a squealer tip. By using a squealer tip, the tip gap can be made smaller without the unacceptable risk of catastrophic failure should the tip rub against the shroud in the course of turbine operation. The smaller gap reduces the flow rate through the tip clearance, which leads to smaller losses and lower heat transfer. It is believed that the tip recess also acts to increase the resistance to the flow (Metzger et al., 1989).

In order to study the effects of a squealer tip geometry on heat transfer and losses, Metzger et al. (1989) and Chyu et al. (1989) performed experiments using cavities of varying depth to width and gap to width ratios. As a result of these experiments, Metzger et al. drew a number of important conclusions. In particular, they concluded that for a given pressure difference across the gap, there is an optimum value of depth to width ratio beyond which no further flow reduction will occur. They also concluded that although the rate of heat transfer on the cavity floor is lower than that on a flat tip, the reduction in heat transfer is offset by the high heat transfer in the redeveloping flow on the downstream gap and by the additional heat transfer area created on the side walls. Thus, they recommended that shallow cavities are preferred if overall heat transfer reduction on the cavity wall is the goal.

The experimental studies cited above provide insight into the nature of the flow field around the squealer tip. However, actual turbine blades differ greatly from the idealized experimental setup. The flow in the blade tip and gap are highly three dimensional. The relevant parameters, namely, depth to width and clearance gap to width ratios of the recess, vary widely along the gap. The pressure difference across the tip also varies widely along the blade. Thus it is unlikely that a simple model will provide the designer of a turbine blade with the information needed to understand the flow in the tip region. At the present time neither experimental data nor numerical simulations are available in open literature that shed light on the details of the flow and heat transfer on a squealer tip flow. Also, with the exception of the heat transfer data of Yang and Diller (1995), which were taken at a single point on the cavity floor of a rotor blade, there are no data available on heat transfer on squealer tips. In this paper we conduct a numerical study of heat transfer on a squealer tip of a generic modern gas turbine blade. This numerical simulation also allows insight into the nature of the flow within the cavity and its effects on efficiency. The blade chosen for this study is the General Electric E^3 design detailed in two NASA reports (Halila et al., 1982; Timko, 1982). The numerical simulations of the heat transfer within the simplified squealer tip model used by Metzger et al. (1989) are first performed with a view to demonstrate the ability of the numerical model to predict the flow and heat transfer accurately as well as to forewarn us as to the possible limitations of the analysis.

In the section to follow we will give a brief description of the numerical method used in the simulations, the turbulence model, and the numerical boundary conditions. Afterward we will present the results of heat transfer predictions and comparison with experimental data on the walls and rim of transverse grooves used in the experiments cited above to simulate the squealer tip. We will subsequently show the heat transfer results obtained for the GE-E^3 turbine blade for a flat tip and two recessed tip cases and discuss the results. Finally we will present the calculation of efficiency and close by presenting a summary and the conclusions.

Computational Method

The simulations performed in this study were done using a multiblock computer code called TRAF3D.MB (Steinthorsson et al., 1993). This code is a general purpose flow solver designed for simulations of flows in complicated geometries. The code is based on TRAF3D, an efficient computer code designed for simulations of steady flows in turbine cascades (Arnone et al., 1994). The TRAF3D.MB code solves the full compressible Navier–Stokes equations. It uses the finite volume method to discretize the equations. The code uses central differencing together with artificial dissipation to discretize the convective terms. The overall accuracy of the code is second order. The TRAF3D.MB code was described in detail by Steinthorsson et al. (1993). The present version of the code, which employs a two-equation model, has been used in connection with an internal flow calculation of heat transfer as described by Rigby et al. (1996).

Turbulence and Transition Models. The algebraic model of Baldwin and Lomax (1978) has been quite successful in predicting the rate of heat transfer to turbine blades. Combining

Contributed by the International Gas Turbine Institute and presented at the 42nd International Gas Turbine and Aeroengine Congress and Exhibition, Orlando, Florida, June 2–5, 1997. Manuscript received International Gas Turbine Institute February 1997. Paper No. 97-GT-128. Associate Technical Editor: H. A. Kidd.

this turbulence model with other models simulating laminar–turbulent transition and models simulating leading edge heat transfer enhancement have been shown to produce accurate results (Ameri and Arnone, 1996; Boyle, 1991). When using a multiblock approach in connection with complex geometries involving many no-slip surfaces, it is advantageous to use a turbulence model that does not require the computation of the dimensionless distance to the wall (y^+) as is done in the Baldwin–Lomax zero-equation model and many two-equation models. Therefore, for the present computations, it was decided to use the $k-\omega$ turbulence model developed by Wilcox (1994a, 1994b) with subsequent modifications by Menter (1993). The model integrates to the walls. Chima (1996) incorporated the latter model in a Navier–Stokes solver and presented results of its application to turbomachinery flows and heat transfer. Below we present the equations describing the turbulence in tensor notation:

$$(\rho s_i)_{,t} + (\rho s_i u_j + q_{ij})_{,j} = (P - D) \tag{1}$$

$$q_{i,j} = -\left(\mu + \frac{\mu_t}{\sigma}\right) s_{i,j} \quad j = 1, 3 \tag{2}$$

where $s_1 = k$ and $s_2 = \omega$ also $\mu_t = \alpha^*(\rho k/\omega)$. The production source terms, P, of Eq. (1) are defined as:

$$\frac{P}{\rho} = \begin{bmatrix} \dfrac{4\mathrm{Re}^{-1}}{\rho}\mu_t\Omega^2 - \dfrac{2k}{3}u_{i,i} \\ \alpha[\alpha^*\Omega^2 - \frac{2}{3}\omega u_{i,i}] \end{bmatrix} \tag{3}$$

where Ω is the magnitude of vorticity. The destruction terms, D, are given by

$$\frac{D}{\rho} = \begin{bmatrix} \beta^*\omega k \\ \beta\omega^2 \end{bmatrix} \tag{4}$$

The coefficients appearing in the model are as follows:
$\sigma = 2.0$, $\beta = 3/40$, $\beta^* = 0.09F_\beta$, $\alpha = (5/9)(F_\alpha/F_\mu)$, and $\alpha^* = F_\mu$, where

$$F_\beta = \frac{5/18 + (\mathrm{Re}_T/R_\beta)^4}{1 + (\mathrm{Re}_T/R_\beta)^4} \tag{5}$$

$$F_\alpha = \frac{\alpha_0 + (\mathrm{Re}_T/R_\omega)}{1 + (\mathrm{Re}_T/R_\omega)} \tag{6}$$

$$F_\mu = \frac{\alpha_0^* + (\mathrm{Re}_T/R_\beta)}{1 + (\mathrm{Re}_T/R_\beta)} \tag{7}$$

$$\mathrm{Re}_T = \frac{\rho k}{\mu\omega} \tag{8}$$

$\alpha_0 = 0.1$, $\alpha_0^* = 0.025$, $R_\beta = 8$, $R_\omega = 2.7$ and $R_k = 6$.
The turbulent thermal diffusivity is computed from:

$$\alpha_t = \frac{\mu_t}{\rho\,\mathrm{Pr}_t} \tag{9}$$

where ρ is density. A constant value of 0.9 is used for turbulent Prandtl number Pr_t.

Boundary Conditions. The types of boundary conditions encountered are as follows:

1 Inlet: The inlet boundary condition for axially subsonic flows is treated by specifying the inlet total temperature and inlet total pressure as well as the inlet angle profiles. The outgoing Riemann invariant is extrapolated to the inlet from within. The total temperature and total pressure profiles are determined to match the law of the wall for the specified hydrodynamic and thermal boundary layer thicknesses on the hub and/or the shroud. For the turbulence quantities for the blade row, an inlet turbulence intensity of 8 percent and a length scale of 10 percent of axial chord is used. These values are estimated and believed to be representative of the conditions existing at the inlet of the blade row.

2 Exit: At the exit boundary, for the subsonic axial flow, the pressure is specified and all the other conditions (including the turbulence quantities) are extrapolated from within. The pressure at the exit plane for the turbine blade considered here is computed by integration of the radial equilibrium equation with specified hub endwall pressure at the exit.

3 Walls: At the walls, the normal pressure gradient is set to zero, the temperature is specified, and the no-slip condition is enforced. The density and total energy are computed from the pressure and the temperature. Also the kinetic energy of turbulence (k) is set to zero while the specific dissipation (ω) is calculated using the following boundary conditions:

$$\omega = S_R \left.\frac{\partial u}{\partial y}\right|_{\text{wall}} \tag{10}$$

where

$$S_R = \begin{bmatrix} \left(\dfrac{50}{K_R}\right)^2, & K_R < 25 \\ \dfrac{100}{K_R}, & K_R \geq 25 \end{bmatrix} \tag{11}$$

K_R is the equivalent sand roughness height. Here $K_R = 5$ corresponding to an hydraulic smooth surface is used.

4 *Periodic boundaries:* These are computed as interior points.

Results and Discussion

We first compute the rate of heat transfer on the surfaces of a cavity and determine the pressure losses due to such a flow. This is done in order to verify the ability of the numerical procedure and in particular the turbulence model, to handle the similar problem of predicting the heat transfer on the rim and within the cavity on the blade tip for which no measured data are available.

Cavity. The geometry and the data chosen for this test were taken from Metzger et al. (1989). The sketch of the geometry used in the experiment and some of the nomenclature are shown in Fig. 1. Two cases with different cavity depth to width ratios (D/W) of 0.2 and 0.5 were considered. For both cases, heat transfer data for the rim as well as the bottom of the cavity are available. For the deeper cavity, the heat transfer data on the side walls were also taken. For both cases considered, the gap to width ratio (C/W) is 0.1 and the Reynolds number based

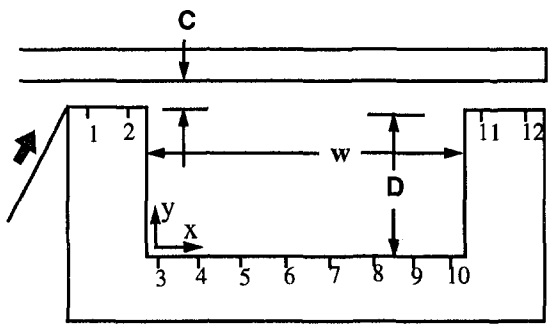

Fig. 1 Diagram and nomenclature of the cavity used in the experiments of Metzger et al. (1989)

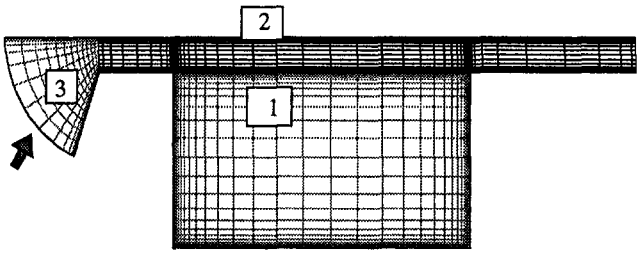

Fig. 2 Three-block grid used for the discretization of the flow

on gap height and average inlet velocity is 15,000. Figure 2 shows a three-block grid used to discretize the flow (the grid is coarsened for clarity). The blocks contain 81 × 65 (81 × 41 for the shallower case), 129 × 41, and 25 × 41 grid points, respectively. A coarser grid was also used to calculate the flow and the results presented herein are spatially converged. Note that in the computations, the grid in the exit region was extended to allow complete flow attachment very near the rim before exiting the computational domain.

Figure 3 presents the rate of heat transfer as computed and measured for the deeper cavity. The abscissa is the string distance measured along the rim and walls of the cavity, starting from $x = 0$, $y = 4$. The ordinate is the Nusselt number defined as:

$$\mathrm{Nu} = \frac{hc}{k} \tag{12}$$

In Eq. (11), h is the heat transfer coefficient based on the inlet temperature, c is the inlet gap height, and k is thermal conductivity of the bulk inlet flow. The figure shows generally good agreement between the experimental results and the analysis. However, a large rise in heat transfer is predicted on the upper portion of the downstream side wall. A rise in the rate of heat transfer in that region is expected to exist due to flow stagnation. The data however do not indicate as large a rise as predicted by the analysis.

In Fig. 4, the comparison between analysis and experimental data for the shallow cavity is presented. The experimental data were taken on the rim and the bottom of the cavity but not on the side walls. Again it is observed that the agreement in general is good.

Finally, in Fig. 5 the measured pressure loss coefficients, defined as:

$$f = (\Delta pC)/(2L\rho V^2), \tag{13}$$

are plotted as a function of cavity depth ratio for three families of gap clearance ratios. In this definition, L is the gap length in flow direction, ρ and V are the bulk density and velocity of the

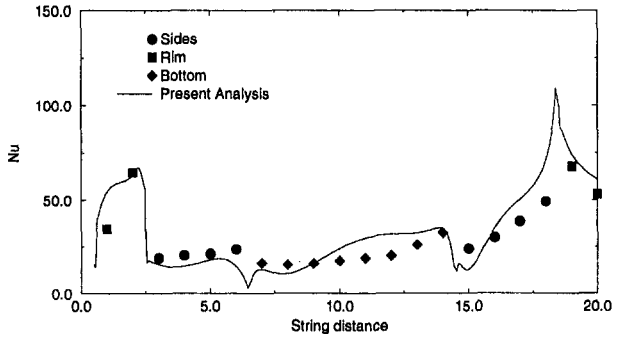

Fig. 3 Nusselt number distribution along the rim, side walls and the bottom of the cavity from Metzger et al. (1989). $D/W = 0.5$, $C/W = 0.1$, Re = 15,000.

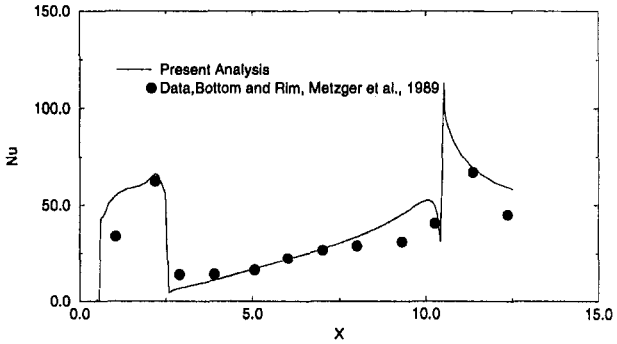

Fig. 4 Nusselt number distribution along the rim, and the bottom of the cavity from Metzger et al. (1989). $D/W = 0.2$, $C/W = 0.1$, Re = 15,000.

inlet flow, and Δp is the pressure difference across the gap. The calculated values of the pressure loss coefficient for the two cases considered here are superimposed on this plot using open symbols. The agreement is very good.

The two computed cases of flow in a cavity demonstrate the capability of the present turbulence model to produce results of reasonable accuracy for this particular type of flow. Although this flow is essentially two dimensional while the flow on a blade tip is three dimensional, these results lend credence to the predictions presented in the following section. The turbulence model has been shown to perform quite well for flow and heat transfer predictions on turbine blades, as was demonstrated by Chima (1996).

Blade Tip

Geometry and the Grid. The geometry of the GE-E^3 blade with the simulated squealer tip is shown in Fig. 6(a). The blades have a constant chord length of 2.87 cm and an aspect ratio of 1.39. A squealer tip thickness of 0.030 in. (0.77 mm) was chosen for this study. Three geometric cases were considered, a flat tip, and two typical tip recesses of 2 and 3 percent. The tip gap clearance was 1 percent for all three cases. Figures 6(b) and 6(c) show the grid on the blade, the hub, and the tip surfaces. Note that every other grid line has been eliminated for clarity. The grid topology is essentially the same as given in Ameri and Steinthorsson (1996) with the exception of the grid in the tip. For the present geometry, the tip grid is constructed using two blocks. One block covers the entire tip clearance, excluding the cavity, while the second block covers the space within the cavity. Grid is refined close to all no-slip surfaces such that the distance of the cell centers adjacent to solid walls, measured in wall units (y^+), is close to unity. This aspect of the grid construction is crucial to both the solution accuracy and to convergence. The dimension of the C grid covering the blade from hub to shroud is 193 × 49 × 99. In the tip clearance the grid dimension is 129 × 57 × 33. In the cavity there are 129 × 33 × 41 grid points for both the 2 and the 3 percent cases. The flat tip case was run with the same grid in the tip as the recessed cases (129 × 57 × 33) to allow

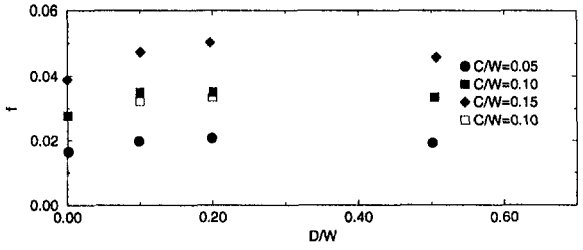

Fig. 5 Measured pressure coefficient (closed symbols) of Metzger et al. (1989) and present computations (open symbols)

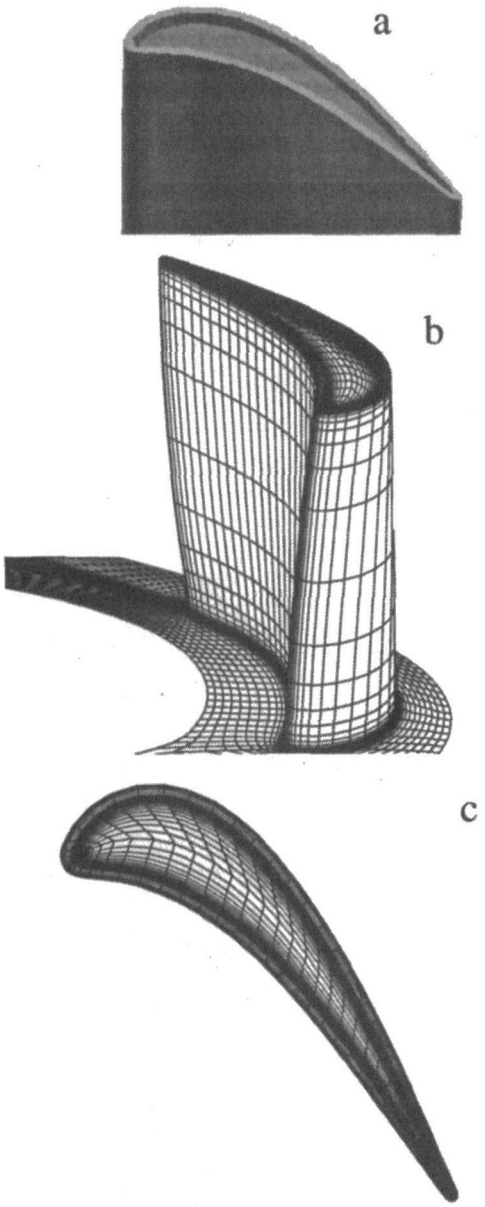

Fig. 6 Geometry and grid distribution for the E^3 blade. Alternate grid lines are eliminated for clarity.

direct comparison of heat transfer devoid of resolution differences. A single block of 9 × 9 × 99 grid points covers the entire inlet upstream of the blade.

Flowfield. The conditions used for the numerical simulations are the same as experimental conditions of the warm rig used by Timko (1982) for the GE-E^3 turbine and are as listed in Table 1. The inlet angle variation is taken from measurements but the wall to total temperature ratio was set at a typical value.

In Fig. 7 plots of computed velocity vectors in the tip region projected on planes normal to the machine axis for various axial locations are shown. The flow is shown in the rotating blade frame of reference, hence the nonzero velocity on the shroud. The tip flow is highly three dimensional. The variation in flow patterns in the tip clearance is apparent from examining the vector plots. For the 20 to 60 percent axial distance the plots show a complex system of vortices in the tip clearance. Figure 8 shows the streamline patterns in the tip. In that figure at least two distinct vortices can be discerned to exist within the cavity. One vortex is a separation vortex, generated as the incoming

Table 1 Run conditions

Absolute pressure Ratio across the Blade Row	0.44
Absolute inlet angle	69° Hub 74.5° Mid Span 78.5° Shroud
Rotation Rate	8450 RPM
T_w/T_t	0.7

flow separates off the inner edge of the pressure side rim. This vortex hugs the pressure side, sidewall and "spills" out of the cavity near the trailing edge of the blade. The second vortex, which is apparently also a separation vortex, runs from the stagnation region to the suction side of the blade. These vortices are generated in addition to the separation vortex along the pressure side rim, suction side rim, and the blade suction side tip flow vortex.

This vortex system apparently offers additional blockage to the flow through the gap. The flow rate through the tip gap for the flat tip case was calculated to be 3.96 percent of the mass flow through the blade row. The 2 and 3 percent recessed blades had leakage mass flow rates of 1.8 and 1.7 percent of the total mass flow rate equivalent to 90 and 86 percent of that of the flat tip case.

Heat Transfer. The rate of heat transfer is presented in terms of Stanton number, defined as:

$$\mathrm{St} = \frac{h}{\rho_{\mathrm{ref}} V_{\mathrm{ref}} C_p} \tag{14}$$

where h is the heat transfer coefficient based on the absolute inlet total temperature. The reference velocity is the inlet mass flow rate divided by the area at a location 20 percent of the axial chord upstream of the blade. The reference temperature is the average absolute total temperature and the reference density is the average density at that location. (The inlet relative total temperature at the midspan is 0.879 times the absolute inlet total temperature.)

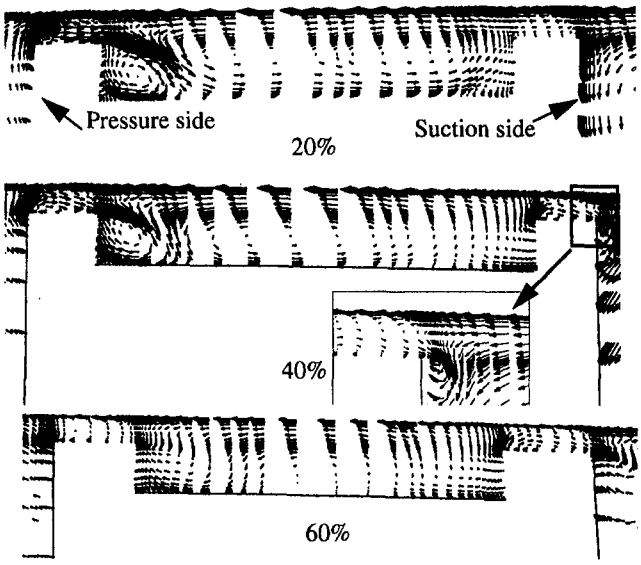

Fig. 7 View of the velocity vectors in and around the tip at various axial locations for the case of 3 percent recess

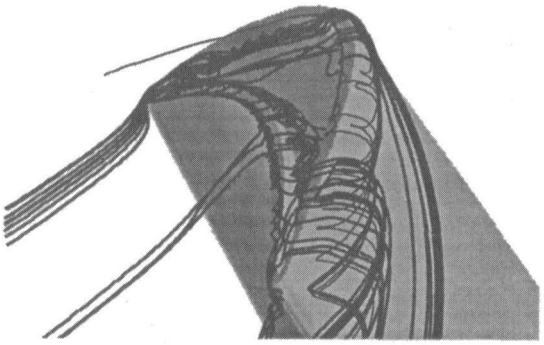

Fig. 8 Streamlines showing the blade tip flow patterns

Heat transfer rates on the blade surface at three spanwise locations are given in Fig. 9. This figure serves as a guide as to the magnitude of the tip heat transfer as compared to the blade surface heat transfer.

The heat transfer results on the tip of the blade are given in Fig. 10(a–c). Figure 10(a) shows the Stanton number distribution on the flat tip surface. The patterns of heat transfer contours on the blade tip are as expected and have been seen before in connection with our previous studies (Ameri and Steinthorsson, 1995, 1996). Those patterns include sharp entrance effect on the pressure side of the tip surface where the rate of heat transfer reaches a maximum due to flow reattachment; the ensuing drop in heat transfer downstream of that location; a large rate of heat transfer around the corner from the blade stagnation point, and the large increase in heat transfer on the suction side of the blade (near the crown). The average level of heat transfer on the flat tip is similar in magnitude to the heat transfer rate on the blade leading edge. For the two recessed cases, the heat transfer distribution is shown using one figure, which shows the heat transfer on the bottom of the cavity and the rim surface of the squealer tip, and a separate Fig. 11 to show the heat transfer on the side wall of the recess. Figure 10(b, c) shows the heat transfer on the surfaces of the 2 and 3 percent cavity, respectively. It is observed that the rate of heat transfer on the bottom of the cavity reaches higher values than is seen on the flat tip. On the rim, the rate of heat transfer on the pressure side is comparable to the flat case but is somewhat higher on the suction side. The large rate of heat transfer on the bottom of the cavity is due to flow impingement containing hot gas. This impingement can best be seen in Fig. 7 for the 20 percent axial distance.

It is worth mentioning that in both the experimental investigations cited above, the rate of heat transfer on the bottom of the cavity was always observed to be less than that on the rim. However, in their numerical calculations, Chyu et al. (1987) do show instances where the bottom of the cavity has substantially higher heat transfer coefficient compared to the rims.

Squealer side wall heat transfer is presented in Fig. 11. The inside wall surface is unwrapped around the minimum axial

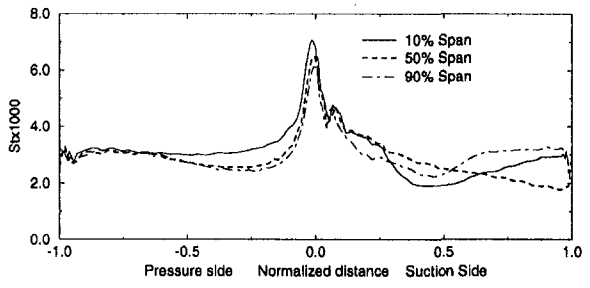

Fig. 9 Surface heat transfer at 10, 50, and 90 percent span on the flat-tipped blade

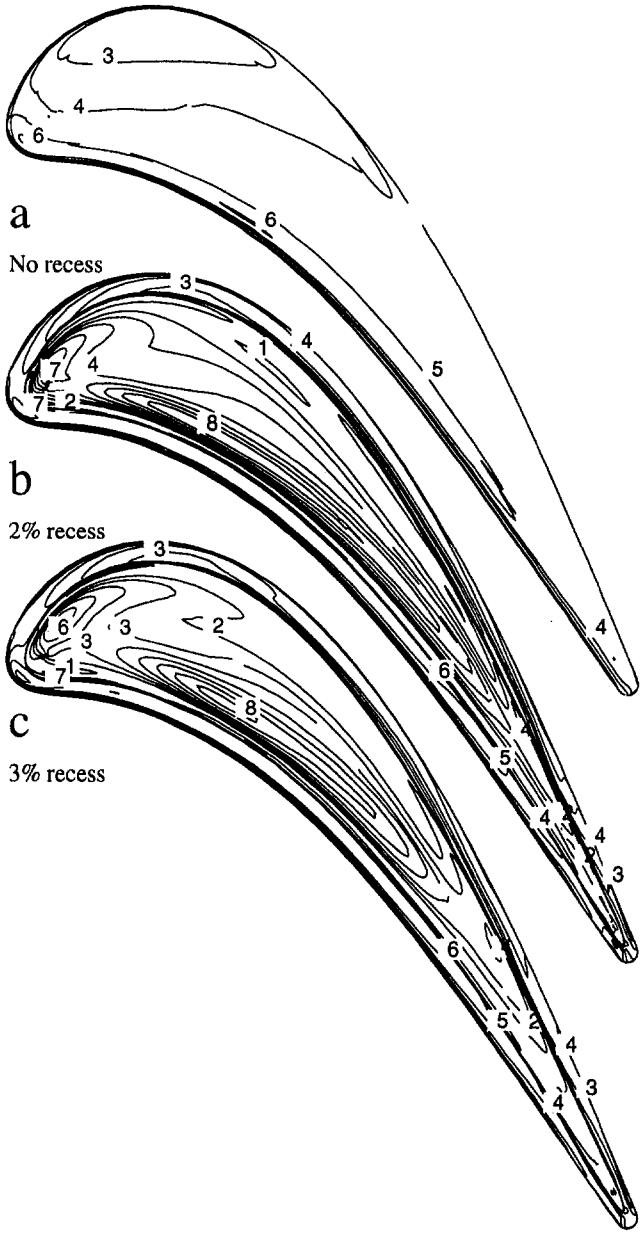

Fig. 10 Heat transfer distribution (1000x Stanton number) on the cavity floor and rim for no recess as well as 2 and 3 percent tip recess

location. The ordinate is exaggerated for clarity. The abscissa is the axial chord distance. Areas of large heat transfer rates are generated as a result of the vortical action inside the cavity. The vortical action increases due to flow acceleration and stretching of these vortices. The highest rate of heat transfer is observed to exist near the trailing edge of the blade on the suction side wall. The cause of this increase was found to be the impact of the vortex spillage with the side wall. As such this rise in heat transfer, although present, may be exaggerated as was discussed in connection with the two-dimensional cavity.

The shroud heat transfer is presented in Fig. 12. As can be seen from this figure, the rate of heat transfer on the shroud is higher for the flat tip case as compared to the two recessed cases.

Finally, the total tip heat transfer for the three cases was compared. It was found that the 2 and 3 percent recess cases had an increase of 80 and 90 percent respectively in total heat addition to the tip compared to the flat tip case of the same tip clearance.

Efficiency. As a byproduct of our heat transfer computations, it is possible to compute the efficiency and the possible effect of recess on efficiency. The expression for the adiabatic efficiency is

$$\eta = \frac{T'_{in} - T'_{ex}}{T'_{in}\left[1 - \left(\frac{p'_{ex}}{p'_{in}}\right)^{(\gamma-1)/\gamma}\right]} \tag{15}$$

In Eq. (14) the primes signify relative total values, subscript in and ex signify inlet and exit mass-averaged values, and γ is the specific heat ratio. The calculated efficiency is based on the assumption of an ideal stator upstream and the average inlet values are computed at 20 percent axial chord upstream of the rotor. The exit values are computed at 50 percent axial chord downstream of the rotor. Because the blade surface temperature was set at a constant temperature of $0.7x$ the inlet total temperature, in order to recover adiabatic conditions, the gas total temperature at the exit was modified to reflect the loss of energy through heat transfer. Failure to do so leads to an error of 5 points in the efficiency for the present computations. The change in mass-averaged normalized total temperature at the exit of the blade row can be computed as follows:

$$\Delta T'_{ex} = \frac{\Sigma \int_A (\mu \partial T/\partial n|_w) dA}{\dot{m}\ \mathrm{Re}\ \mathrm{Pr}} \tag{16}$$

In this equation, μ is dimensionless viscosity and n is the normalized distance to the wall; $\dot{m}$ is the normalized mass flow rate through the blade passage and A is the surface area. The integration is performed over all of the heat transfer surfaces. The mass-averaged value of the exit total temperature is thus computed as:

$$T'_{ex} = T'_{\text{unmodified}} + \Delta T'_{ex} \tag{17}$$

The efficiency for the row of blades was computed to be 91.3, 91.4, and 91.4 percent for the 0, 2, and 3 percent recess cases, in spite of the fact that there was a 10 to 14 percent reduction in gap flow.

Summary and Conclusions

In this paper, results are presented from three-dimensional simulations of flow and heat transfer over a turbine blade with a squealer tip. The simulations were carried out using a second-order-accurate finite volume scheme on a multiblock grid system containing 1.2 million grid points. Effects of turbulence on the flow field were modeled using a $k-\omega$ two-equation turbulence model. The ability of the turbulence model to predict the heat transfer in flows of the type considered here was verified by simulating the flow in a two-dimensional model of squealer tips for which experimental data is available. For the three-dimensional case an actual modern gas turbine geometry, namely the GE-E^3 first-stage turbine blade, was used. Two dominant vortical structures were identified in the recess region. The heat transfer rate on the recess surfaces were found to be strongly affected by these flow structures. Especially high heat transfer rates were observed where the vortices exit the recess region. No significant effect due to the recessed tip on efficiency was detected, although the mass flow rate through the tip gap was found to be smaller by as much as 14 percent for the squealer tip as compared to flat tip of the same clearance height.

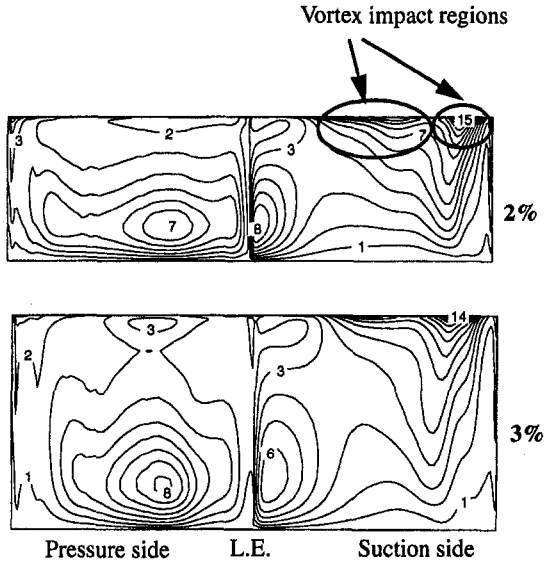

Fig. 11 Heat transfer distribution on the side wall of the cavity as unwrapped about the minimum x location in terms of 1000x St

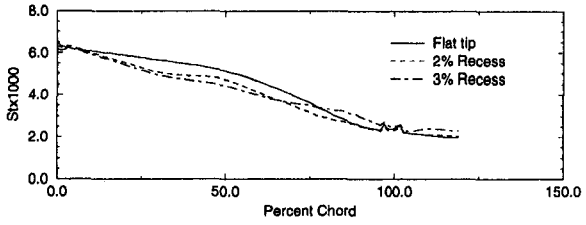

Fig. 12 Tangentially averaged shroud heat transfer

Acknowledgments

The authors wish to express their gratitude to Dr. Raymond Gaugler, Chief of the Turbine Branch, as well as to Dr. Louis Povinelli, Chief of the Turbomachinery and Propulsion Systems Division of NASA Lewis Research Center and Director of ICOMP for their support and encouragement of this work. Thanks are also due to Mr. Robert Boyle for his suggestions and his guidance. The computations were performed on the CRAY-C90 of NAS at NASA Ames Research Center.

References

Ameri, A. A., and Steinthorrson, E., 1995, "Prediction of Unshrouded Rotor Blade Tip Heat Transfer," ASME Paper No. 95-GT-142.

Ameri, A. A., and Arnone, A., 1996, "Transition Modeling Effects on Turbine Rotor Blade Heat Transfer Predictions," ASME JOURNAL OF TURBOMACHINERY, Vol. 118, pp. 307–313.

Ameri, A. A., and Steinthorrson, E., 1996, "Analysis of Gas Turbine Rotor Blade Tip and Shroud Heat Transfer," ASME Paper No. 96-GT-189.

Arnone, A., Liou, M. S., and Povinelli, L. A., 1994, "Viscous Analysis of Three-Dimensional Rotor Flow Using a Multigrid Method," ASME JOURNAL OF TURBOMACHINERY, Vol. 116, pp. 435–445.

Baldwin, B. S., and Lomax, H., 1978, "Thin Layer Approximation and Algebraic Model for Separated Turbulent Flows," AIAA Paper No. 78-0257.

Boyle, R. J., 1991, "Navier–Stokes Analysis of Turbine Blade Heat Transfer," ASME JOURNAL OF TURBOMACHINERY, Vol. 113, pp. 392–403.

Chima, R. V., 1996, "A $k-\omega$ Turbulence Model for Quasi-Three-Dimensional Turbomachinery Flows," AIAA Paper No. 96-0248.

Chyu, M. K., Moon, H. K., and Metzger, D. E., 1989, "Heat Transfer in the Tip Region of Grooved Turbine Blades," ASME JOURNAL OF TURBOMACHINERY, Vol. 111, pp. 131–138.

Chyu, M. K., Metzger, D. E., and Hwan, C. L., 1987, "Heat Transfer in Shrouded Rectangular Cavities," *J. of Thermophysics*, Vol. 1, No. 3, pp. 247–252.

Halila, E. E., Lenahan, D. T., and Thomas, L. L., 1982, "Energy Efficient Engine, High Pressure Turbine Test Hardware Detailed Design Report," NASA CR-167955.

Menter, F. R., 1993, "Zonal Two-Equation $k-\omega$ Turbulence Models for Aerodynamic Flows," Paper No. AIAA-93-2906.

Metzger, D. E., Bunker, R. S., and Chyu, M. K., 1989, "Cavity Heat Transfer on a Transverse Grooved Wall in a Narrow Channel," ASME *Journal of Heat Transfer*, Vol. 111, pp. 73–79.

Rigby, D. L., Ameri, A. A., and Steinthorsson, E., 1996, "Internal Passage

Heat Transfer Prediction Using Multiblock Grids and $k-\omega$ Turbulence Model," ASME Paper No. 96-GT-188.

Steinthorsson, E., Liou, M. S., and Povinelli, L. A., 1993, "Development of an Explicit Multiblock/Multigrid Flow Solver for Viscous Flows in Complex Geometries," Paper No. AIAA-93-2380.

Timko, L. P., 1982, "Energy Efficient Engine High Pressure Turbine Component Test Performance Report," NASA CR-168289.

Wilcox, D. C., 1994a, Turbulence Modeling for CFD, DCW Industries, Inc., La Canda, CA.

Wilcox, D. C., 1994b, "Simulation of Transition With a Two-Equation Turbulence Model," *AIAA Journal,* Vol. 32, No. 2, pp. 247–255.

Yang, T. T., and Diller, T. E., 1995, "Heat Transfer and Flow for a Grooved Turbine Blade Tip in a Transonic Cascade," ASME Paper No. 95-WA/HT-29.

Unsteady Total Temperature Measurements Downstream of a High-Pressure Turbine

D. R. Buttsworth

T. V. Jones

Department of Engineering Science,
University of Oxford,
Parks Road,
Oxford, United Kingdom

K. S. Chana
DRA Pyestock,
Farnborough, United Kingdom

An experimental technique for the measurement of flow total temperature in a turbine facility is demonstrated. Two thin film heat transfer gages located at the stagnation point of fused quartz substrates are operated at different temperatures in order to determine the flow total temperature. With this technique, no assumptions regarding the magnitude of the convective heat transfer coefficient are made. Thus, the probe can operate successfully in unsteady compressible flows of arbitrary composition and high free-stream turbulence levels without a heat transfer law calibration. The operation of the total temperature probe is first demonstrated using a small wind tunnel facility. Based on results from the small wind tunnel tests, it appears that the probe total temperature measurements are accurate to within ±1 K. Experiments using the probe downstream of a high-pressure turbine stage are then described. Both high and low-frequency components of the flow total temperature can be accurately resolved with the present technique. The probe measures a time-averaged flow total temperature that is in good agreement with thermocouple measurements made downstream of the rotor. Frequencies as high as 182 kHz have been detected in the spectral analysis of the heat flux signals from the total temperature probe. Through comparison with fast-response aerodynamic probe measurements, it is demonstrated that at the current measurement location, the total temperature fluctuations arise mainly due to the isentropic extraction of work by the turbine. The present total temperature probe is demonstrated to be an accurate, robust, fast-response device that is suitable for operation in a turbomachinery environment.

Introduction

Despite the development of advanced nonintrusive techniques, probes continue to play a key role in turbomachinery research and development due to their low cost and relative ease of operation in many situations. Relatively slow response total pressure and temperature probes, which indicate time-averaged values, have been used for many years (Smout and Cook, 1996). However, as turbomachinery flows are inherently unsteady, performance augmentation is better served through a detailed understanding of the unsteady physics of the flow. Computational techniques that capture aspects of the unsteady flow processes have been developed (Giles, 1988). However, such codes must be validated using experimental measurements of unsteady flow parameters such as the pressure and temperature before they can be used reliably in the design and development process.

Aerodynamic probes based on high frequency response semiconductor technology have been developed to measure the total pressure, and other parameters such as the flow direction and Mach number (Ainsworth et al., 1995). Fast-response total temperature measurements are also possible, and the aspirating probe first developed by Ng and Epstein (1983) has achieved considerable popularity (e.g., Alday et al., 1993; Van Zante et al., 1995; Suryavamshi et al., 1996). Nevertheless, the aspirating probe has a number of limitations (e.g., Van Zante et al.) including a restricted frequency response (the claimed bandwidths are generally lower than 40 kHz), which may not be sufficient in many applications.

This paper describes a new fast-response total temperature probe that has a bandwidth significantly higher than that of the aspirating probe. Furthermore, it offers a number of other advantages including ease of operation and robustness. It is not necessary to calibrate the present probe to determine its heat transfer law (in contrast to devices based on hot-wire anemometry). The new probe is a versatile device that offers a measurement of the total temperature that is independent of the gas composition and other flow parameters. An earlier version of the probe has already been successfully operated in a number of high-speed flow situations (Buttsworth and Jones, 1996). The present work represents the first application of the new fast-response total temperature probe in a turbomachinery environment.

Probe Operation

Theoretical Background. The operating principles of this probe have been discussed previously (Buttsworth and Jones, 1996) so only a brief description will now be given. Fast-response total temperature measurements are obtained by operating two thin film transient heat transfer gages at two different temperatures. In the present investigation, platinum thin films were painted onto fused quartz substrates as shown in Fig. 1. The thin films are located close to the stagnation point of nominally identical hemispherical probes. Therefore, the convective heat transfer between the flow and the probes is proportional to the temperature difference between the flow *total temperature* and the probe surface temperature. That is,

$$q = h(T_t - T_w) \tag{1}$$

The surface temperatures are measured by monitoring the voltage across each of the thin films (which are powered with a constant current supply). The convective heat fluxes are obtained from the film temperature history using either electrical analogues of the transient one-dimensional heat diffusion process (Oldfield et al., 1982), or numerical methods (Buttsworth,

Contributed by the International Gas Turbine Institute and presented at the 42nd International Gas Turbine and Aeroengine Congress and Exhibition, Orlando, Florida, June 2–5, 1997. Manuscript received at ASME Headquarters February 1997. Paper No. 97-GT-407. Associate Technical Editor: H. A. Kidd.

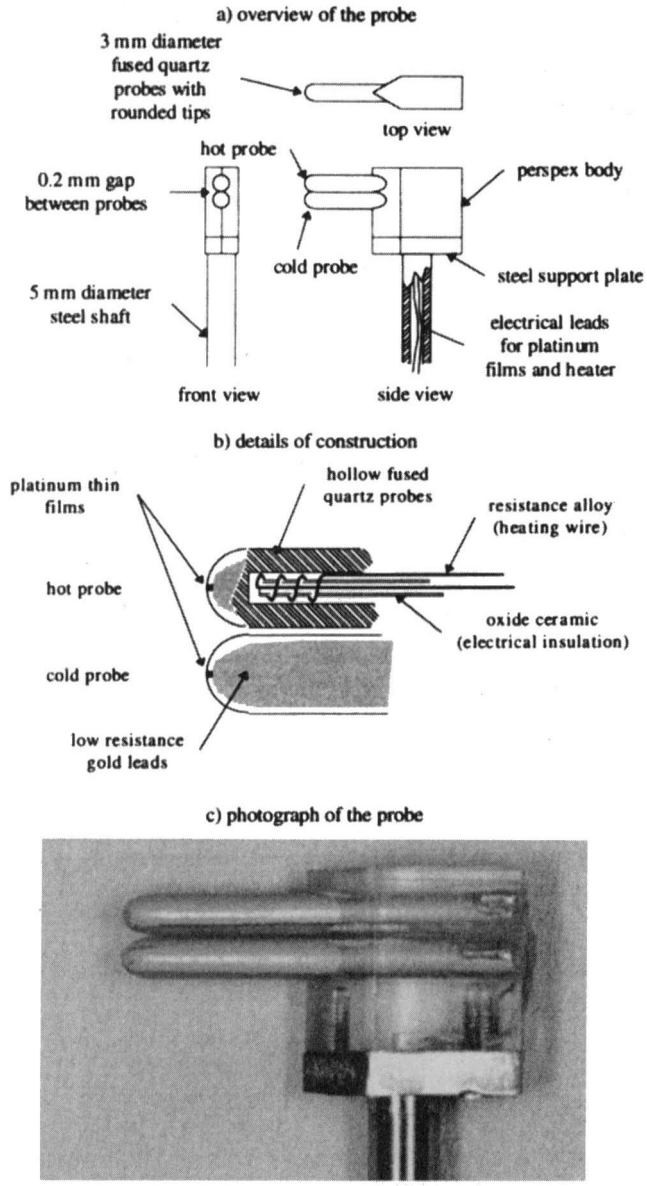

Fig. 1 Total temperature probe

1997), which similarly model the transient heat diffusion within the quartz substrate of the probes. Since it is assumed that the two nominally identical probes are exposed to the same flow, the values of h for each probe will be virtually the same. Thus, it is possible to write two equations in two unknowns,

$$q_1 = h(T_t - T_{w1}) \tag{2}$$

$$q_2 = h(T_t - T_{w2}) \tag{3}$$

which can be solved to obtain the flow total temperature,

$$T_t = T_{w1} + q_1(T_{w2} - T_{w1})/(q_1 - q_2) \tag{4}$$

and the convective heat transfer coefficient,

$$h = (q_1 - q_2)/(T_{w2} - T_{w1}) \tag{5}$$

The probe measures the flow *total temperature* irrespective of the flow Mach number because stagnation enthalpy is conserved as the flow decelerates to the stagnation point and there is virtually no viscous dissipation in the stagnation point boundary layer. Thus, even in flows where an immersed body would eventually reach a recovery (or adiabatic wall) temperature somewhat lower than the flow total temperature, the probe accurately detects the flow total temperature. This is because the thin films measure the transient heat flux close to the stagnation point, which is driven by the flow total temperature as described in Eq. (1).

Total temperature measurements are made without reference to other flow parameters such as the Mach number, pitot pressure, and the flow composition. Thus, the probe offers a measurement of total temperature without needing to know the probe heat transfer law, and therefore many of the calibration issues associated with hot-wire devices are avoided. Because the probe operates through the measurement of transient heat flux, the device can in principle be injected into high-temperature environments such as combustors (temperatures around 1800 K), provided it is retracted again before the probe surface temperature exceeds the quartz softening point (around 850 K).

Design and Practical Operation. Details of the present implementation of the total temperature probe concept are given in Fig. 1. Both fused quartz probes were hollow, and a small heating element was inserted into the hot probe. The heating element had a resistance of around 12 Ω, and, during the turbine experiments, the heater was driven with approximately 4.6 V (from a battery supply). A temperature increase was experienced at the cold probe due to the heating of the hot probe. To maximize the temperature difference between the hot and cold probes, the heater power supply was only switched on approximately 10 seconds before the run commenced. This gave an initial temperature difference between the two films of approximately 50°C at the start of the flow. Immediately prior to the start of the flow, the temperature of the hot and cold probes was still increasing slightly (however, the rate of change was very small relative to the temperature changes experienced dur-

Nomenclature

c = specific heat of the substrate, $J \cdot kg^{-1} \cdot K^{-1}$
C = nondimensional constant in the lateral conduction correction
h = convective heat transfer coefficient, $W \cdot m^{-2} \cdot K^{-1}$
k = conductivity of the substrate, $W \cdot m^{-1} \cdot K^{-1}$
N = rotational speed, rpm
p = pressure, Pa, bar
q = surface heat transfer rate, $W \cdot m^{-2}$
q_l = heat flux due to lateral conduction
q_n = heat flux in the direction normal to the probe surface
R = radius of the probe, radius of curvature
R = specific gas constant, $J \cdot kg^{-1} \cdot K^{-1}$
s = entropy, $J \cdot kg^{-1} \cdot K^{-1}$
t = time
T = temperature of the flow or substrate surface, K
α = thermal diffusivity of substrate material, $m^2 \cdot s^{-1}$
γ = ratio of specific heats = 1.4
ρ = density of the flow or substrate material
ω = frequency, $rad \cdot s^{-1}$

Subscripts

mean = value averaged over the steady flow run time
t = total or stagnation condition
w = value at probe surface (stagnation point)
1 = NGV inlet; first probe
2 = NGV exit, turbine inlet; second probe
3 = turbine exit

Superscript

′ = fluctuating quantity

ing a run). Such pre-run variations can easily be accounted for when determining the convective heat flux during the run (Buttsworth and Jones, 1996). The heater remained on during the run so that additional transient temperature changes (which would accompany switching the heating power off) did not complicate the interpretation of the temperature changes associated with the convective heating.

Suction Tunnel Experiment. A usual condition for the accurate operation of transient thin film heat transfer gages is that the heat penetration depth must be small relative to the width or depth of the substrate. For the present geometry, this condition could be written $\alpha t/R^2 \ll 1$ (where t is measured relative to the start of the heat transfer process). However, in order to maximize the number of rotor blade passing events (maximizing the run time, t) while maintaining a reasonable level of spatial resolution (minimizing the probe size, R), it is possible, with the appropriate thermal modeling, to relax this requirement. In the present section, the thermal modeling required to successfully operate the gages for relatively long periods is demonstrated with specific reference to a preliminary experiment that was performed to verify the probe operation.

Measurements were obtained using the total temperature probe within the suction tunnel illustrated in Fig. 2. Initially, the duct was evacuated to around 1 kPa and the hot probe was heated to approximately 140°C. Atmospheric air was drawn into the duct after the mylar diaphragm at the entrance to the duct was ruptured. The Mach number of the flow approaching the probe was approximately 0.38 (Fig. 2(b)). The air flow was terminated after approximately 0.5 s by releasing the shutter, which sealed the duct from the atmosphere. Figure 3(a) shows the static pressure measured on the wall of the duct at a location 10 mm upstream of the probe (in the row 1 pressure tappings,

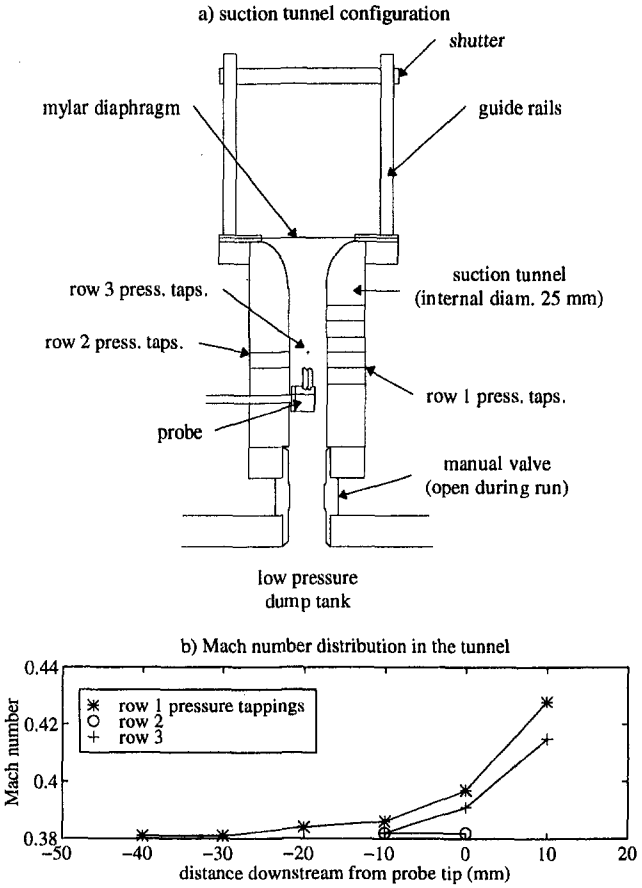

Fig. 2 Illustration of the suction tunnel experiment

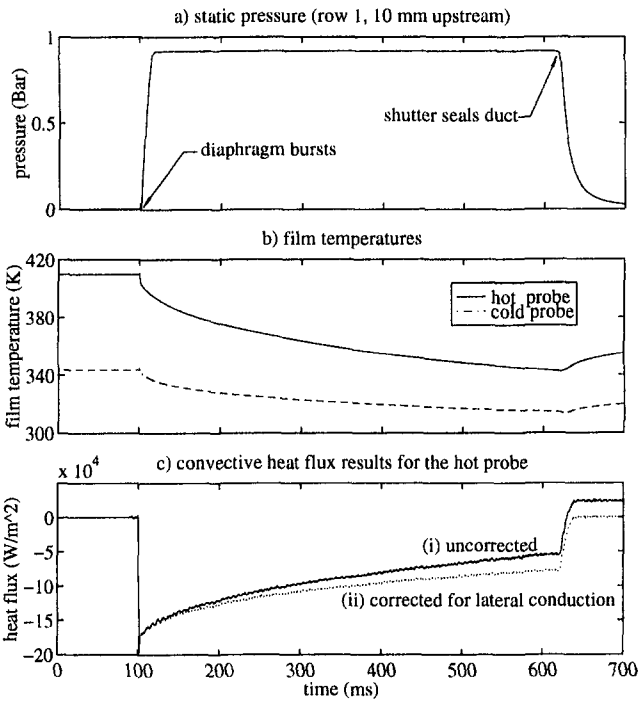

Fig. 3 Results from the suction tunnel experiment

Fig. 2(a)), and Fig. 3(b) gives the surface temperature histories for the hot and cold probes. After the shutter isolated the duct from the air flow, the actual heat transfer from the probe would have quickly returned to the pre-run level (which was close to zero on the scale in Fig. 3(c)) due to the rapid flow breakdown (see Fig. 3(a)).

Heat transfer data (e.g., Fig. 3(c), curve i) were obtained by analyzing the temperature histories (Fig. 3(b)) using a finite difference routine (Buttsworth, 1997), which incorporates radius of curvature and variable thermal property effects. Although the quartz probes have a nominal radius of 1.5 mm, the actual radius of curvature close to the probe tip can vary significantly due to the glass blowing technique that was used to construct the rounded quartz probes. For example, from the measurements in Fig. 4, it can be seen that the rounded tip of the hot probe closely follows that of a hemisphere with $R \approx 1.3$ mm over the majority of the curved profile. In contrast, the cold probe initially has a very tight radius of curvature near the stagnation point ($R \approx 1.1$ mm), but the overall shape of the

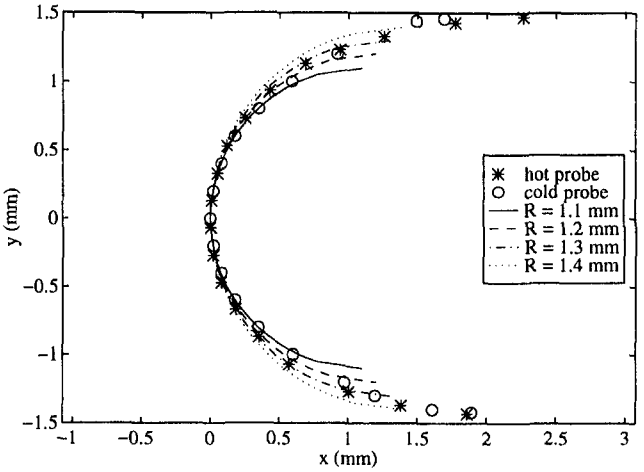

Fig. 4 Profiles of the hot and cold heat transfer probes

probe tip more closely resembles that of a hemisphere-cone than a perfect hemisphere. Since the surface curvature at points well away from the stagnation point can influence the heat diffusion process if the condition $\alpha t/R^2 \ll 1$ no longer applies, it is *not* immediately clear (from the profile measurements alone) what radius of curvature should be used in the transient heat conduction analysis, particularly in the case of the cold probe.

To determine the radius of curvature that should be used in the heat diffusion analysis, an empirical approach was adopted. An effective radius of curvature of each probe was selected so that the apparent post-run heat flux (determined using the finite difference routine) remained constant (see curve i, Fig. 3(c)). The actual post-run heat flux was essentially zero, but a constant (nonzero) apparent post-run heat flux is the appropriate condition at this stage because a finite amount of lateral heat diffusion has taken place. In the case of the hot probe, where the probe tip was reasonably hemispherical, the empirical approach indicated a value of $R = 1.37$ mm, which is within approximately 5 percent of the measured physical radius of curvature (which was around 1.3 mm, Fig. 4).

A first-order lateral diffusion analysis gives the correction,

$$q_l = 4C \frac{\alpha}{R^2} \int_0^t q_n d\tau \tag{6}$$

for a hemispherical probe (Buttsworth, 1997). The constant C depends on the gradients of the convective heat flux around the probe tip. Again, adopting an empirical approach, the value of C was selected so that the post-run heat flux ($q_n + q_l$) was brought to zero (see curve ii, Fig. 3(c)). (Note that q_n is the heat flux inferred from the finite difference routine prior to lateral conduction correction, e.g., curve i, Fig. 3(c).) For further details of the lateral diffusion correction, see Buttsworth (1997). The fact that the apparent post-run heat flux level remains at zero after the correction is applied suggests that the heat diffusion modeling is accurate.

Further justification for this heat diffusion modeling is obtained from the values of the convective heat transfer coefficient and the flow total temperature indicated by the individual hot and cold probes. The convective heat transfer coefficients of the hot and cold probes and the flow total temperature remained essentially constant during the run. Thus, the indicated flow total temperature and the convective heat transfer coefficients can be obtained from the individual hot and cold probes by fitting Eq. (1) to the experimental heat flux data using the measured surface temperatures. Results from this line-fitting exercise are shown in Fig. 5. For the hot probe, the line fit gave $T_t = 293.5$ K, and $h = 1.55$ kW $\cdot$ m^{-2} $\cdot$ K^{-1}; for the cold probe,

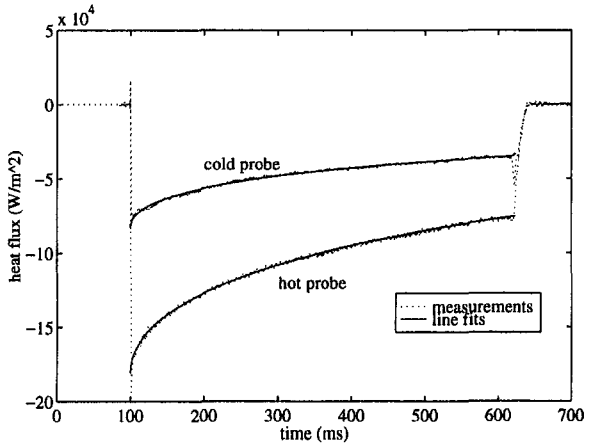

Fig. 5 Heat flux results from the suction tunnel with line fits based on the film temperature measurements

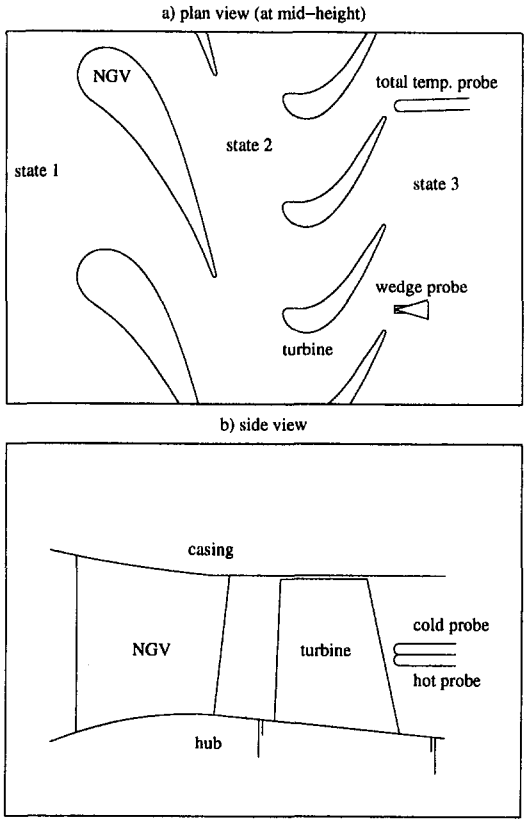

Fig. 6 Illustration detailing the instrumentation and its relative location in the turbine experiments (not to scale)

$T_t = 292.0$ K, and $h = 1.57$ kW $\cdot$ m^{-2} $\cdot$ K^{-1}. The ambient temperature (which is the flow total temperature in this suction tunnel experiment) was measured at 293.0 K (using a mercury-filled glass thermometer, with an estimated accuracy of ± 0.2°C). Thus, it is concluded that in the present configuration, total temperature measurements to an accuracy of within ± 1 K are certainly possible.

Considering the excellent agreement between the curve fits and the experimental data (Fig. 5), the accuracy of the individual probe total temperature measurements, and the consistency of the values of h for the hot and cold probes (these were within ± 1 percent of the mean value), it is concluded that the current thermal modeling is indeed valid. It is of interest to note that for the current flow conditions, the slightly different shape of the hot and cold probe tips appears to have had little influence

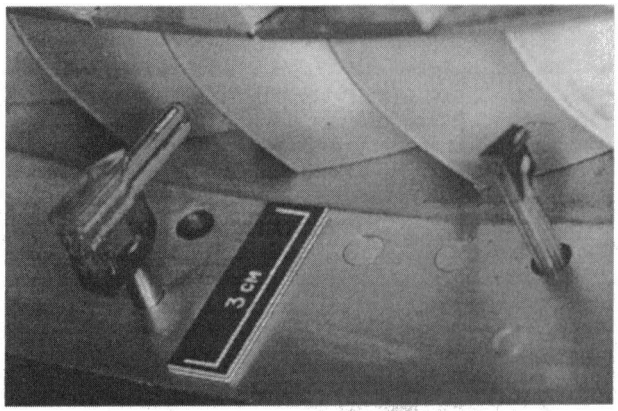

Fig. 7 Photograph of the total temperature probe (left) and wedge probe (right) downstream of the turbine blades

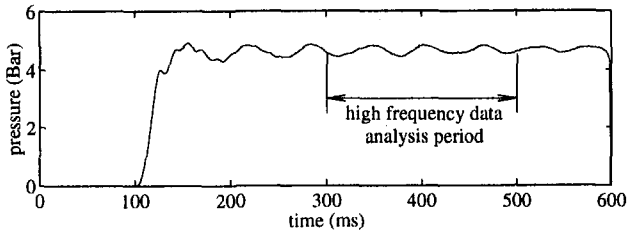

Fig. 8 Example of the NGV inlet total pressure

on the values of h for the hot and the cold probes. Thus, the key assumption in the operation of the present total temperature probe, which is that both probes have the same value of h, is certainly valid in this steady uniform flow.

Turbine Experiments

Facility and Instrumentation. Total temperature measurements were made in the Isentropic Light Piston Facility (ILPF) at DRA Pyestock. Currently, the ILPF has a high-pressure turbine stage with film cooling on both the nozzle guide vanes (NGVs) and the rotor. However, for the runs presented in the current paper, no film cooling was utilized. Details of the facility are give elsewhere (Hilditch et al., 1994) and various measurements including high-frequency pressure and heat flux measurements on the NGV and turbine blades have already been obtained (e.g., Hilditch et al., 1995).

For the present work, the total temperature probe (Fig. 1) was located approximately 2.5 mm behind the rotor at midheight of the flow annulus as shown in Fig. 6. A photograph of the probe located behind the turbine blades is given in Fig. 7. A fast-response wedge probe was also located at the midheight and at the same distance downstream of the rotor, but was offset in the circumferential direction (relative to the total temperature probe) a distance of one NGV pitch in the direction of rotation (Figs. 6 and 7). Thus, both the total temperature probe and the wedge probe should experience a similar flow; however, the phase of the wedge probe signal will lead that of the total temperature signal because the number of rotor blades was not a whole number multiple of the number of NGV blades.

An example of the total pressure measured at the NGV inlet (using a relatively slow response pitot tube) is given in Fig. 8 for a typical ILPF run. The high-frequency results presented in this paper were obtained during the period shown in Fig. 8. The relevant flow parameters given in Table 1 are based on the average conditions measured during the period shown in Fig. 8. The variations given in Table 1 correspond to the maximum and minimum values measured during the current series of experiments. Piston oscillations within the pump tube are responsible for the observed temporal variations in the pressure measurements (Jones et al., 1993). The oscillations amount to a variation in NGV inlet total pressure of approximately ±4 percent over the period indicated in Fig. 8. During this period, the turbine speed was typically held constant (to within ±0.06 percent) by a turbo-brake located downstream of the rotor (Goodisman et al., 1992).

Data Analysis. For each run, the film temperatures were amplified and low-pass filtered (−3 dB point around 200 Hz) and then recorded at 500 Hz (referred to as the low sample rate). Heat transfer data from the analogues were low-pass filtered (−3 dB point around 200 kHz) and recorded at 1 MHz (referred to as the high sample rate). Total pressure fluctuations from the wedge probe were also recorded at the high sample rate and later were processed with a digital low-pass filter having a −3 dB point at 80 kHz to reduce the noise associated with the natural frequency of the transducer. A once-per-revolution signal was also recorded at the high sample rate to allow the high-frequency total temperature measurements to be averaged over a number of revolutions (typically 30).

Table 1 ILPF operating conditions

p_{tl} (Bar)	4.60 (± 1 %)
T_{tl} (K)	445 (± 1 %)
N (rpm)	9564 (± 0.08 %)

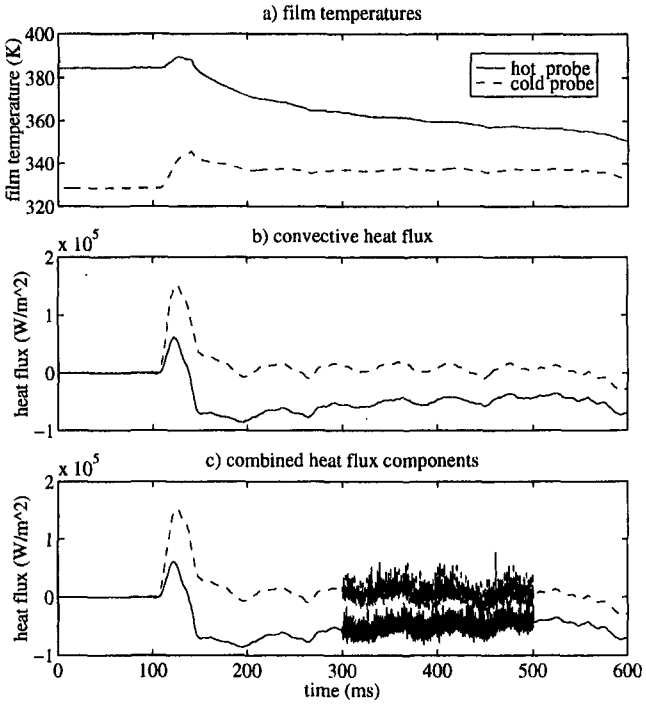

Fig. 9 Example of the film temperature and heat flux measurements from the total temperature probe

Using the low sample rate film temperature history (Fig. 9(*a*)), the time-averaged heat flux level was determined from the finite difference routine (which modeled the spherical probe geometry and variable thermal property effects) and the lateral conduction correction technique, which was described previously. Time-averaged heat fluxes corresponding to the temperatures in Fig. 9(*a*) are shown in Fig. 9(*b*). Time-averaged total temperature results (as given in Fig. 10) were then obtained using the time-averaged film temperature and heat flux results (Figs. 9(*a*) and 9(*b*)) using Eq. (4).

The analogue heat transfer signals (recorded at 1 MHz) were later conditioned using a digital high-pass filter (having a −3 dB point at 1 kHz and virtually no attenuation at 10 kHz) and a variable sensitivity that was dependent on the thermal product ($\sqrt{\rho ck}$) at the surface of the substrate (which was a function of the measured surface temperature). An example of the high-

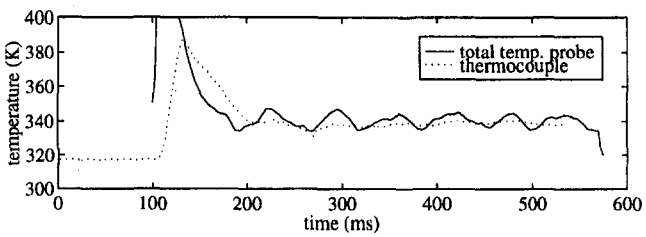

Fig. 10 Comparison of the total temperature probe and thermocouple probe measurements

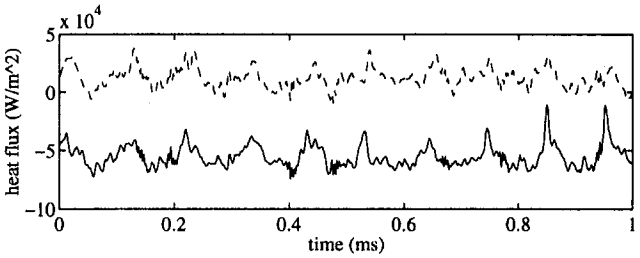

Fig. 11 Example of the high-frequency heat flux data (solid line: hot probe; broken line: cold probe)

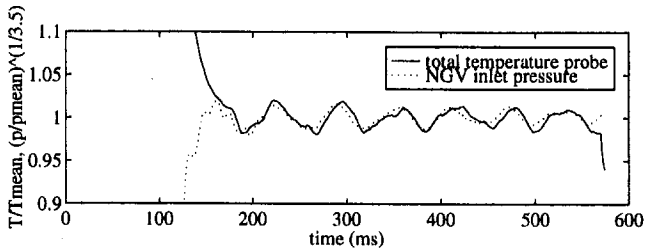

Fig. 13 Comparison of total temperature probe results and the scaled total pressure measurements

frequency component of the heat flux processed in this manner is given in Fig. 11. (The spherical geometry and lateral conduction effects do not have a significant influence on the heat transfer fluctuations at such frequencies.) The total heat flux levels were determined from the sum of the heat fluxes obtained using the low and high sample rate data (as illustrated in Fig. 9(c)). Total temperature fluctuations (as given in Fig. 12) were then determined from the time-averaged film temperature (Fig. 9(a)) and the total convective heat flux results (Fig. 9(c)) using Eq. (4).

It is valid to use time-averaged film temperature data to derive the fluctuating components of flow total temperature because the changes in the substrate surface temperature associated with the high-frequency fluctuations are not significant. For example, at 10 kHz (which is approximately the blade passing frequency) the magnitude of the fluctuations in the convective heat flux at the hot and the cold probes was around 40 kW · m^{-2} peak-to-peak (Fig. 11), corresponding to surface temperature fluctuations of around 0.1 K (since $|q| = \sqrt{\rho c k}\sqrt{\omega}|T|$), which is negligible in comparison with the measured flow total temperature variations of approximately 15 K (Fig. 12).

Results and Discussion. Time-averaged temperature results from the fast-response total temperature probe are given in Fig. 10 where a comparison is made with thermocouple measurements obtained using a shrouded thermocouple probe downstream of the rotor. The thermocouple probe consisted of a 0.0005″ K-type bead junction located inside a 1.5-mm-dia hypodermic tube (at approximately 1 mm from the open tip of the tube). The hypodermic tube had two diametrically opposed vent holes (approximately 0.25 mm in diameter). In the present application, the accuracy of the thermocouple measurements is estimated at around ±5 K.

There is good agreement between the overall level of the fast-response total temperature probe and the thermocouple probe measurements (Fig. 10). That is, both measurement techniques indicate a time-averaged flow total temperature during the facility run time of around 340 K. However, it may be noted (see Fig. 10) that the poor frequency response of the thermocouple has a significant influence on the temperature measurements even at the relatively low piston oscillation frequency (which is around 15 Hz).

In Fig. 13, the magnitudes of the temperature variations associated with the piston oscillations are compared with isentropic predictions based on the measured NGV inlet total pressure variations. Both the temperature (from the fast response total temperature probe) and the pressure signals have been normalized using their respective mean values over the run time, and the pressure signal has been conditioned using the isentropic exponent, $(\gamma - 1)/\gamma$. After the tunnel starting process is complete (i.e., for times >200 ms on the scale in Fig. 13) there is good agreement between the measured total temperature variations and the isentropic predictions based on the measured pressure. This result indicates that while there may be temperature losses associated with the initial compression stroke, the subsequent piston oscillations give rise to variations in the flow conditions that are virtually isentropic. Furthermore, since the oscillations in the temperature measurement downstream of the rotor compare so favorably with the isentropic prediction based on pressure measurement upstream of the NGV, it is concluded that the piston oscillations do not have a significant influence on the stage performance.

Prior to examining the high-frequency total temperature results in some detail, the frequency response of the probe is briefly discussed with reference to the power density spectrum results given in Fig. 14. These results were obtained using the high sample rate heat flux signal from the cold probe over the period shown in Fig. 8. The fundamental harmonic corresponding to the blade passing frequency is easily identified at approximately 9.5 kHz. Significant peaks in the spectrum right up to the 19th harmonic of the rotor blade passing frequency (corresponding to approximately 182 kHz) can also be identified. The significance of these results is that the potential bandwidth of the present fast-response total temperature probe is well beyond the capability of other techniques. For example, the highest claimed frequency response of the aspirating probe currently stands at around 40 kHz (Suryavamshi et al., 1996), which arises mainly due to the time required to establish a steady flow in the duct upstream of the choked orifice. However, it should be noted that the actual bandwidth of the present total temperature measurements is restricted to around 85 kHz, which is the −3 dB of the heat transfer analogues. Nevertheless, with the appropriate signal conditioning, it may be possible in future applications to extend the bandwidth to well beyond 100 kHz.

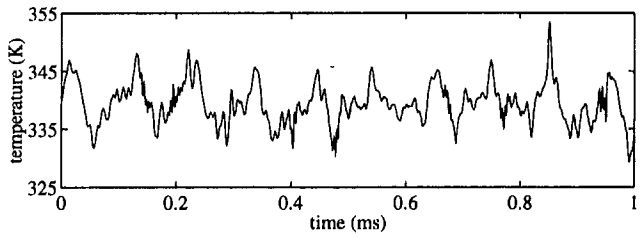

Fig. 12 Example of the high-frequency total temperature measurements (prior to averaging)

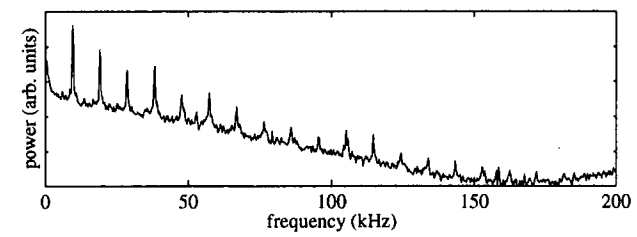

Fig. 14 Power spectrum from the total temperature probe (using the cold probe heat flux signal)

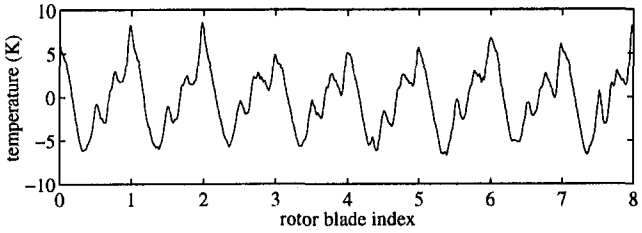

Fig. 15 Example of the high-frequency (rotor-averaged) total temperature results

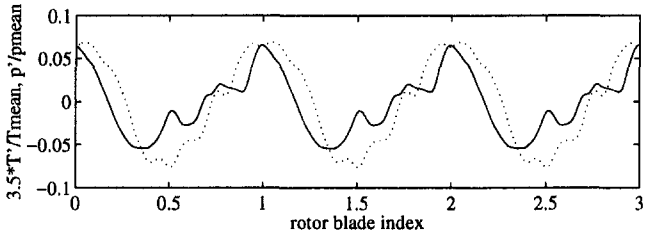

Fig. 17 Scaled high-frequency total temperature (solid line) and total pressure (broken line) (pitch-averaged)

By averaging the raw total temperature measurements (e.g., Fig. 12) over 30 rotor revolutions, rotor-averaged total temperature results were obtained for each rotor blade passing event, eight of which are shown in Fig. 15. The corresponding ensemble-averaged total pressure measurements from the wedge probe are given in Fig. 16. The location of the instrumentation relative to the rotor blades at the point given by a "rotor blade index" of 0 (in Figs. 15–18) is shown in Fig. 6(*a*).

The rotor-averaged temperature and pressure results (e.g., Figs. 15 and 16) were averaged over the total number of blade passing events to yield the pitch-averaged results as shown in Fig. 17. In this figure, the total temperature and total pressure fluctuations have been normalized using the time-averaged values during the run, and, in the case of the temperature results, the scaling factor $\gamma/(\gamma - 1)$ has also been employed. This scaling factor arises in the context of the Second Law of Thermodynamics, which gives the expression,

$$s'/R \approx \gamma/(\gamma - 1)T'/T_{\text{mean}} - p'/p_{\text{mean}} \qquad (7)$$

where R is the specific gas constant. Three blade passing events are shown in Fig. 17 to provide a clear picture of the periodic nature of the flow, even though the second and third events are identical to the first (since results from all of the rotor blade passing events have been used in the averaging process). The total temperature and wedge probes were located 1 NGV pitch apart (Fig. 6(*a*)). As this distance does not correspond exactly with a whole number of rotor pitches, it was necessary to adjust the rotor blade index of pressure measurements relative to the temperature results so that both the temperature and pressure measurements given in Fig. 17 are in phase.

There exists good agreement between the scaled temperature and pressure results in Fig. 17 in terms of the magnitude and phase of the *large-scale* fluctuations. Such agreement suggests that the fluctuations occurring at this location arise mainly because of isentropic processes associated with the work extracted by the rotor. This appears to be a reasonable result since these measurements were obtained at the annulus midheight where it is anticipated that viscous and heat transfer effects are smallest.

Conclusions

In excess of 15 runs were performed using the total temperature probe in the present turbine facility without any noticeable change in the ambient resistance of the films, or degradation of the frequency response. It is concluded that the present total temperature probe is a robust device that is well suited to operation in the turbine facility. The expected life of the present total temperature probe far exceeds the life of hot-wire probes (i.e., the time prior to recalibration) when operated in a similar environment. The present total temperature probe does not require calibration to ascertain its convective heat transfer coefficient, and thus it has further advantages over hot-wire devices. Total temperature measurements are obtained without reference to other flow parameters such as the Reynolds number, the Mach number, or the flow composition, and thus it offers ease-of-use without compromising its considerable versatility. The probe is relatively cheap to construct and easy to implement as it is driven with a constant current supply.

The current results indicate that the bandwidth of the probe is more than adequate for resolving the unsteady flow field associated with rotor passing events and it far exceeds the quoted bandwidth of the aspirating probe. Frequencies as high as 182 kHz have been detected in the spectral analysis of the heat flux signals from the total temperature probe. The accuracy of the present total temperature probe appears comparable with that of the aspirating probe. An accuracy of around ±1 K was indicated by a calibration experiment performed in a small wind tunnel facility. The probe is essentially a transient device, which means that it cannot be operated in a continuous flow facility unless it is injected into the stream. With the appropriate modeling of the substrate heat diffusion, the probe can certainly operate for at least 0.5 s. At present, the spatial resolution of the total temperature probe is approximately 3 mm (which corresponds to the distance between the two films). Ideally, this resolution should be improved, although as it stands, the probe resolution is comparable with that of other probes commonly employed in turbomachinery research.

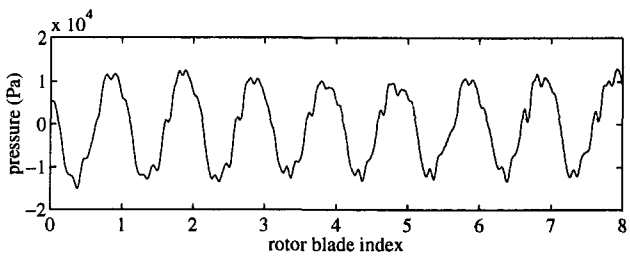

Fig. 16 Example of the high-frequency (rotor-averaged) total pressure results (from the wedge probe)

Acknowledgments

The authors wish to thank Mr. T. Godfrey for building the total temperature probe, and Mr. S. J. Anderson for his assistance during the experiments. This work was funded by DERA Farnborough. The fast response temperature probe is the subject of Patent Application No. GB9612096.9.

References

Ainsworth, R. W., Allen, J. L., and Batt, J. J. M., 1995, "The Development of Fast Response Aerodynamic Probes for Flow Measurements in Turbomachinery," ASME JOURNAL OF TURBOMACHINERY, Vol. 117, pp. 625–634.

Alday, J., Osborne, D. J., Morris, M. B., Ng, W., and Gertz, J., 1993, "Flow Randomness and Tip Losses in Transonic Rotors," ASME Paper No. 93-GT-189.

Buttsworth, D. R., 1997, "A Finite Difference Routine for the Solution of Transient One Dimensional Heat Conduction Problems With Varying Thermal Property and Curvature Effects," Department of Engineering Science, University of Oxford, Report.

Buttsworth, D. R., and Jones, T. V., 1996, "A Fast-Response Total Temperature Probe for Unsteady Compressible Flows," ASME Paper No. 96-GT-350; ASME *Journal of Engineering for Gas Turbines and Power*, in press.

Goodisman, M. I., Oldfield, M. L. G., Kingcombe, R. C., Jones, T. V., Ainsworth, R. W., and Brooks, A. J., 1992, "An Axial Turbobrake," ASME JOURNAL OF TURBOMACHINERY, Vol. 114, pp. 419–425.

Giles, M. B., 1988, "Calculation of Unsteady Wake/Rotor Interaction," *J. Prop. and Power,* Vol. 4, No. 4, pp. 356–362.

Hilditch, M. A., Fowler, A., Jones, T. V., Chana, K. S., Oldfield, M. L. G., Ainsworth, R. W., Hogg, S. I., Anderson, S. J., and Smith, G. C., 1994, "Installation of a Turbine Stage in the Pyestock Isentropic Light Piston Facility," ASME Paper No. 94-GT-277.

Hilditch, M. A., Smith, G. C., Anderson, S. J., Chana, K. S., Jones, T. V., Ainsworth, R. W., and Oldfield, M. L. G., 1995, "Unsteady Measurements in an Axial Flow Turbine," AGARD PEP 85th Symposium, May 1995, Derby, U.K.

Jones, T. V., Oldfield, M. L. G., Ainsworth, R. W., and Arts, T., 1993, "Transient Cascade Testing," *Advanced Methods for Cascade Testing,* C. Hirsch, ed., AGARDograph 328.

Ng, W. F., and Epstein, A. H., 1983, "High-Frequency Temperature and Pressure Probe for Unsteady Compressible Flows," *Rev. Sci. Instrum.,* Vol. 54, No. 12, pp. 1678–1683.

Oldfield, M. L. G., Burd, H. J., and Doe, N. G., 1982, "Design of Wide-Bandwidth Analogue Circuits for Heat Transfer Instrumentation in Transient Wind Tunnels," *Proc. 16th Symp. of International Centre for Heat and Mass Transfer,* Hemisphere Publishing, pp. 233–257.

Smout, P. D., and Cook, S. C., 1996, "Simple Instrumentation Rake Designs for Gas Turbine Engine Testing," ASME Paper No. 96-GT-32.

Suryavamshi, N., Lakshminarayana, B., and Prato, J., 1998, "Aspirating Probe Measurements of the Unsteady Total Temperature Field Downstream of an Embedded Stator in a Multistage Axial Flow Compressor," ASME JOURNAL OF TURBOMACHINERY, Vol. 120, pp. 156–169.

Van Zante, D. E., Suder, K. L., Strazisar, A. J., and Okiishi, T. H., 1995, "An Improved Aspirating Probe for Total-Temperature and Total-Pressure Measurements in Compressor Flows," ASME JOURNAL OF TURBOMACHINERY, Vol. 117, pp. 642–649.

Aspects of Vane Film Cooling With High Turbulence: Part I—Heat Transfer

F. E. Ames
forrest_ames@mail.und.nodak.edu,
University of North Dakota,
Grand Forks, ND 58202

A four-vane subsonic cascade was used to investigate the influence of film injection on vane heat transfer distributions in the presence of high turbulence. The influence of high turbulence on vane film cooling effectiveness and boundary layer development was also examined in part II of this paper. A high-level, large-scale inlet turbulence was generated for this study with a mock combustor (12 percent) and was used to contrast results with a low level (1 percent) of inlet turbulence. The three geometries chosen to study in this investigation were one row and two staggered rows of downstream cooling on both the suction and pressure surfaces in addition to a showerhead array. Film cooling was found to have only a moderate influence on the heat transfer coefficients downstream from arrays on the suction surface where the boundary layer was turbulent. However, film cooling was found to have a substantial influence on heat transfer downstream from arrays in laminar regions of the vane such as the pressure surface, the stagnation region, and the near-suction surface. Generally, heat transfer augmentation was found to scale on velocity ratio. In relative terms, the augmentation in the laminar regions for the low turbulence case was found to be higher than the augmentation for the high-turbulence case. The absolute levels of heat transfer were always found to be the highest for the high turbulence case.

Introduction

Performance, durability, and cost drive the gas turbine market and subsequently drive the design of engines. The resulting increases in rotor inlet temperature (RIT) and pressure ratio to enhance performance have been accompanied by the need to maintain or lower metal temperatures to preserve durability. As temperatures rise, more compressed air is diverted from the cycle to cool gas path components and some form of film cooling is needed to reduce heat loads, to cool locally with film holes, or even to dump spent air somewhere other than the trailing edge. The discrete injection of film cooling complicates the already uncertain evaluation of surface heat load. This research examines the effect of discrete film cooling on vane surface heat transfer with high turbulence and the dissipating effect of turbulence on vane film cooling coverage. In part I of this paper the heat transfer downstream of suction surface, pressure surface, and showerhead film cooling with high and low inlet turbulence levels is investigated.

The heat transfer designer needs to know how the surface heat load is distributed over the component surface and how the application of film cooling will alter this distribution. The most conventional approach in estimating the heat load of a film-cooled surface is to determine the adiabatic wall temperature (T_{aw}) using an effectiveness $\{\eta_{ad} = (T_{aw} - T_r)/(T_{co} - T_r)\}$ distribution combined with a gas side heat transfer coefficient, which accounts for the influence of the discrete injection. For streamwise film cooling with shallow holes at low velocity ratios on a flat plate with a turbulent boundary layer, the augmentation of the gas side heat transfer coefficient (h_g) has typically been found to be small, as shown by Hartnett (1985) in chapter one of the *Handbook of Heat Transfer Applications*. However, whenever the boundary layer is not turbulent, the injection is not streamwise or shallow, or the velocity ratio is not low; the downstream heat transfer coefficient can be augmented substantially. Mayle (1991) suggests film cooling will cause an immediate transition but that high favorable acceleration can relaminarize boundary layers downstream of injection. Mehendale and Han (1992) have shown that leading edge (or showerhead) film cooling can produce substantial levels of heat transfer augmentation, with increasing blowing ratio, even when high levels of inlet turbulence are present. Additionally, Gartshore et al. (1993) in an experiment and Garg and Gaugler (1995) in a calculation have shown the heat flux in the showerhead region may not be uniform in either the spanwise or streamwise directions due to the joining of coolant jets from different rows leaving regions of good and poor coverage. In addition to showerhead configurations, which typically have spanwise inclined holes, studies with spanwise and compound angle holes on flat plates such as those of Ligrani and Ramsey (1997), Sen et al. (1996), and Ekkad et al. (1997) have also documented high levels of augmentation for turbulent boundary layers. Substantial levels of heat transfer augmentation have also been found in studies using vane and blade geometries. Nirmalan and Hylton (1990) who studied heat transfer to a C3X vane at warm compressible conditions ($T_g \geq 800$ F, $0.60 \leq M_{ex} \leq 1.05$) found low to negative values of Stanton number reduction $\{SNR = 1 - (St_{fc}/St_{nfc})\}$ for two staggered rows of 20 deg holes at moderate to high pressure ratios at their maximum T_c/T_g condition. Ou et al. (1994) studied the combined effects of wakes and film cooling on heat transfer to a blade in a linear cascade and found substantial increases in heat transfer in the leading edge region and downstream from the pressure side film cooling holes and also documented early transition on the suction surface downstream from both rows of film cooling. Based on the leading edge and the airfoil film cooling studies, the largest levels of heat transfer augmentation due to film cooling will occur in and around the leading edge, on the near suction surface, and on the pressure surface where the boundary layer is laminar or in the early stages of transition.

The gas path in a modern gas turbine engine has flow with high levels of turbulence, which augments heat transfer substantially. The increase in heat transfer due to film injection above

Contributed by the International Gas Turbine Institute and presented at the 42nd International Gas Turbine and Aeroengine Congress and Exhibition, Orlando, Florida, June 2–5, 1997. Manuscript received International Gas Turbine Institute February 1997. Paper No. 97-GT-239. Associate Technical Editor: H. A. Kidd.

this already aggressive state has the most usefulness to heat transfer designers. Combustor exit turbulence is the inlet turbulent boundary condition for the first-stage vane and as noted by Ames (1996) turbulence levels can range widely (from 7 to 20 percent or more) with combustor geometry. Combustor and wake turbulence has a substantial effect on vane and blade heat transfer. Heat transfer increases ranging up to 60 percent were found on the pressure surface of a vane by Ames (1997) due to turbulence generated in a mock combustor. Han et al. (1993) found heat transfer increases ranging up to 100 percent on the pressure surface of their blade due to turbulence generated by a spoked wheel wake generator.

Film cooling data are typically characterized in any one or all of three ways. Blowing ratio ($M = \rho_c U_c / \rho_\infty U_\infty$) is probably the most useful measure in quantifying film effectiveness since blowing ratio essentially gives the ratio of the coolant to free-stream thermal capacitance. The momentum flux ratio ($I = \rho_c U_c^2 / \rho_\infty U_\infty^2$) is also critical since the penetration of a jet is proportional to the square root of the momentum flux ratio times the sine of the injection angle according to Norster (see Lefebvre, 1983). The velocity ratio ($VR = U_c / U_\infty$) is another important variable since the coolant to free-stream velocity gradients generate turbulence, which both mixes away cooling coverage and enhances downstream heat transfer. L'Ecuyer and Soechting (1985) surveyed discrete hole film cooling data with 35 deg holes and a pitch-to-diameter ratio (P/D) of three over a four to one range in density ratio and found three general regimes that could best be characterized by velocity ratio. The mass addition regime has velocity ratios of 0.25 and below and effectiveness levels increase with blowing ratio due to the increased thermal capacitance of the coolant. The mixing regime is characterized by velocity ratios from 0.25 to 0.8 because the effectiveness distribution depends on the opposing influences of increased thermal capacitance with increasing blowing ratio and increased coolant penetration with increased momentum flux ratio. L'Ecuyer and Soechting call the velocity ratios above 0.8 the penetration regime because the effectiveness distribution is dominated by excessive coolant penetration and the augmented diffusivity due to the jet/free stream interaction. While L'Ecuyer and Soechting describe their three film cooling regimes in terms of velocity ratio, they point out that the momentum flux ratio is an implicit part of their correlation.

In this study, the data are taken at density ratios close to one and the conditions are varied over a range of relevant velocity ratios after L'Ecuyer and Soechting. Velocity ratios are varied from 0.31 to 0.57 on the suction surface encompassing a reasonable range. For example, the suction surface of a turbine vane in an engine with a gas-to-coolant temperature ratio of two, a hole discharge coefficient of around 0.7, and a coolant static to inlet total pressure ratio of one, will have a velocity ratio of about 0.5. Velocity ratios were varied from 0.5 to 1.5 on the pressure surface where the low free-stream Mach numbers can result in values in this range. Since showerhead arrays are typically fed from a common plenum, the leading edge array in this study was varied over a relevant range of coolant-to-inlet total pressure ratios. The data in this study were taken at low Mach numbers so the pressure was varied over equivalent pressure ratios $\{(P_c - P_t)/(P_t - P_{s,\mathrm{ex}})\}$ of 0.0175, 0.07, and 0.35.

The objective of this study has been to document the enhancement of heat transfer due to film cooling on a vane surface subjected to high levels of flow field turbulence and to demonstrate the corresponding dissipation of film cooling coverage. Heat transfer and adiabatic effectiveness measurements were taken in an ambient four-vane cascade. Both a high turbulence ($Tu = 12$ percent) condition and a low turbulence ($Tu = 1$ percent) condition were developed for this study. In part I of this paper, the influence of velocity ratio on heat transfer is examined for one and two rows of holes for a laminar boundary layer developing on the pressure surface and for a turbulent boundary layer developing on the suction surface of the vane at both levels of turbulence. Additionally, the heat transfer downstream from showerhead injection is investigated for the pressure and suction surfaces over the range of equivalent pressure ratios for the two levels of turbulence. In part II of this paper the corresponding adiabatic effectiveness measurements are examined with specific emphasis on the influence high inlet turbulence has on mixing away the film cooling coverage. Selected velocity profiles taken downstream from the film cooling

Nomenclature

C = airfoil chord length (true chord)
Cp = specific heat at constant pressure
D = coolant hole diameter
DR = density ratio = ρ_c / ρ_∞
h = heat transfer coefficient = $q''_{\mathrm{net}} / (T_w - T_r)$
I = momentum flux ratio = $\rho_c U_c^2 / \rho_\infty U_\infty^2$
K = free-stream acceleration parameter = $\mu / (\rho_\infty U_\infty^2) dU_\infty / dx$
Lu = energy scale = $1.5\ |u'|^3 / \epsilon$
Lx = longitudinal integral scale
M = blowing ratio = $\rho_c U_c / \rho_\infty U_\infty$
$\mathrm{M_{ex}}$ = Mach number based on exit conditions
P = pressure
P = pitch, hole-to-hole spanwise spacing
PR_{equ} = equivalent pressure ratio $(P_c - P_t)/(P_t - P_{s,\mathrm{ex}})$
P_s = static pressure
P_t = total pressure
q'' = heat flux
Re = Reynolds number
$\mathrm{Re_{ex}}$ = exit Reynolds number = $\rho_{\mathrm{ex}} U_{\mathrm{ex}} C / \mu$
SNR = Stanton number reduction = $(1 - \mathrm{St_{fc}}/\mathrm{St_{nfc}})$
St = Stanton number = $h / (\rho U_{\mathrm{ex}} Cp)$, based on exit conditions
$\mathrm{St_0}$ = base vane Stanton number for low or high turbulence, with film cooling
T = temperature
T_t = stagnation temperature
Tu = turbulence intensity = u'/U_∞
U = streamwise velocity
u' = rms streamwise fluctuation velocity
VR = velocity ratio = U_c/U_∞, area-averaged coolant velocity divided by local free-stream velocity
X = streamwise distance along airfoil, except in Fig. 4
X/D = streamwise distance from trailing edge exit of last film hole normalized by D
Y = normal distance from the vane surface, except in Fig. 4
ϵ = turbulent dissipation
η_{ad} = adiabatic wall effectiveness, also η; $\eta_{\mathrm{ad}} = (T_{aw} - T_r)/(T_{co} - T_r)$
μ = dynamic viscosity coefficient, Pa · s

Subscripts

∞ = references to free-stream conditions
aw = adiabatic wall
c = coolant (static pressure, recovery temperature)
co = coolant outlet
ex = references to vane exit static pressure tap plane location
fc = refers to value with film cooling
loss = net loss due to outflow from conduction and radiation
net = net due to inflow from conduction, resistance heating, and radiation
nfc = refers to value without film cooling
g = refers to gas or free-stream total conditions
in = references to inlet static pressure tap plane location
r = recovery
w = surface or wall

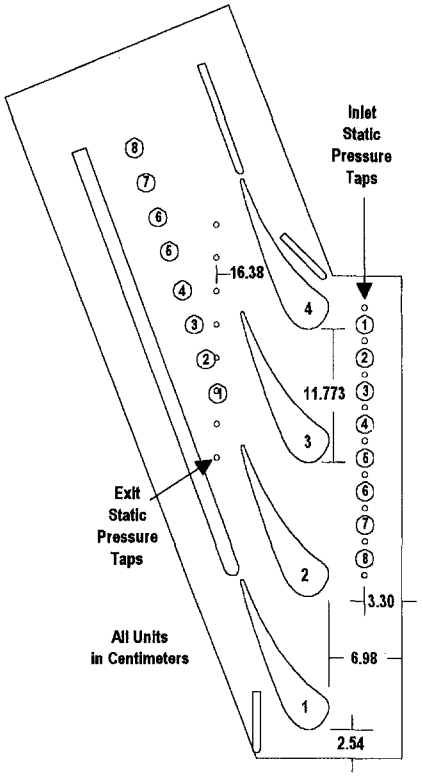

Fig. 1 Schematic of four vane cascade

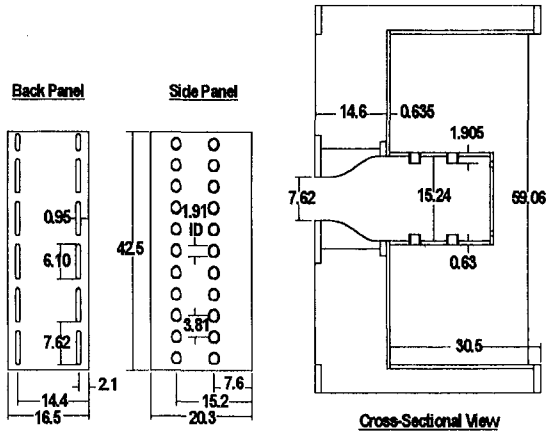

Fig. 2 Schematic of combustor turbulence generator

are also presented to provide additional evidence of the substantial mixing process that is occurring. A comprehensive documentation of this research including detailed figures and tabulations of the heat transfer, film cooling, velocity, and turbulence profile data is given by Ames (1996).

Experimental Approach

The four vane cascade used in this study, shown schematically in Fig. 1, is connected to an in-draft blower. The 4.5 times scale C3X vanes used in the cascade are a two-dimensional slice from a first-stage nozzle for a helicopter engine. The row of inlet static pressure taps along with adjustment plates shown on the schematic control bleed around the top and bottom vanes accommodating control of inlet flow uniformity. The row of exit static pressure taps along with the tailboards at the trailing edge of vanes 1 and 4 allow setting exit flow periodicity. Inlet and exit ports labeled 1 through 8 provide access for various thermocouple, pressure, and hot wire probes. Further details of this facility can be found in either Ames (1996) or Ames (1997).

The true chord length of the vane is 14.493 cm and the axial chord is 7.816 cm. The vane spacing is 11.773 cm and the passage has a throat of 3.292 cm. The diameter of the leading edge is 2.337 cm and the diameter of the trailing edge is 0.340 cm. The stagger angle of the vane is 55.47 deg and the calculated air exit angle is 72.4 deg. The height of the vane is 7.62 cm.

The cascade was run at exit Reynolds numbers based on chord length of about 800,000 and 500,000 corresponding to exit Mach numbers of about 0.27 and 0.17. This range of Reynolds numbers is comparable to a first vane of a small helicopter gas turbine engine at sea level takeoff. Vanes for medium sized turboprops, turbofans, or industrial engines typically run at Reynolds numbers between one and two million at sea level and values for large turbofans and industrial engines can range to several million. Exit Reynolds numbers at altitude cruise could be a factor of three to four smaller than this. Hence, the range of Reynolds numbers investigated in this study fall in a relevant range of values for small to medium-sized gas turbines.

Turbulence Conditions. A low turbulence level (1.1 percent) base case and a high-level (12 percent) large-scale turbulence condition were chosen for this study. The low turbulence level is representative of the condition used to develop many of the film cooling data that exist in the open literature while the high level condition is closely representative of turbulence conditions that are believed to be typical at the inlet to first-stage vanes. The inlet geometry for the low turbulence condition consisted of an inlet filter to remove dust, two nylon screens to reduce the inlet velocity fluctuations, an eight-to-one two-dimensional contraction nozzle that uniformly increases the velocity relative to the turbulent kinetic energy, and a rectangular section connecting the nozzle with the cascade.

The mock combustor used to generate the high-intensity large scale turbulence is shown schematically in Fig. 2. The air is directed from a large inlet area through the liner of the mock combustor. The liner measures 15.24 cm in width by 20.32 cm long prior to directing the air into a smooth 2 to 1 contraction, which accommodates the span of the cascade. The back plate of the liner has a series of slots that direct the air along the wall of the liner. The side plates have two rows of plunged 1.9 cm inside diameter holes spaced at 3.81 cm, which are placed 7.62 and 15.24 cm downstream from the back plate. The flow produced by the rectangular mock combustor is similar to a two-dimensional representation of flow in a typical annular combustor and the turbulence level and scales are representative of current technology combustors. Recently, Moss and Oldfield (1991) measured spectra downstream from several combustors and concluded that the normalized spectra of the combustor was not significantly changed with combustion. Essentially, they found the same turbulence level and scale with and without combustion. This finding by Moss and Oldfield supports the contention that this mock combustor produces turbulence representative of a modern combustor.

The inlet-averaged values of velocity (U_∞), integral scale (Lx), energy scale (Lu), and dissipation (ϵ) are given in Table 1 for the two turbulence conditions and the two exit Mach

Table 1 Inlet turbulence characteristics

Condition	Tu	U (m/s)	Lx (cm)	Lu (cm)	ε (m^3/s^2)
Low Turb.	.011	29.6	5.11	6.64	0.74
Low Turb.	.009	19.3	8.50	18.7	0.045
Comb(1)	.129	29.5	1.70	3.36	2460
Comb(1)	.134	19.5	1.56	3.16	840

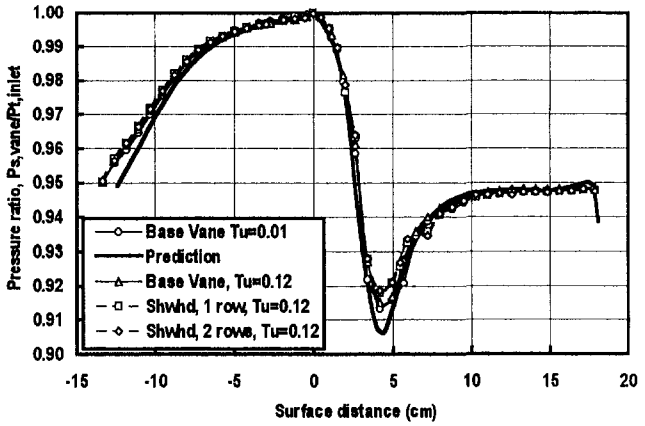

Fig. 3 C3X vane surface pressure with geometry, M_{ex} = 0.27

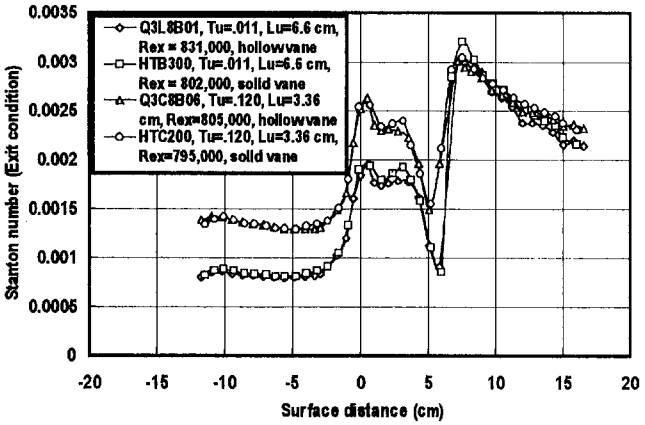

Fig. 5 Hollow and solid vane Stanton number distributions, Re_{2ex} = 800,000

numbers (0.27 and 0.17). The high turbulence {comb(1)} configuration allowed for 3.68 cm of decay from the measuring location to the vane leading edge plane. This decay was accounted for in the figure legends. The turbulence kinetic energy and dissipation in the turbine passage were found to stay reasonably constant. Estimates for the local turbulence levels along the vane can be made using the local velocity determined from the pressure distribution. For more details, see Ames (1994) and Ames (1996).

Vane Pressure Distribution. The base vane pressure distributions for the low and high turbulence cases are given in Fig. 3 along with distributions with showerhead injection with both one and two rows of downstream holes. The two cases with injection were measured with an equivalent pressure ratio of 0.07. The measured pressure distributions, shown with symbols, are compared to a numerical prediction based on a compressible stream function formulation. The analysis assumes the air exit angle is 72 deg. In general, the measured and predicted distributions compare well. The injection cases show a small but noticeable change on the suction surface. The strong adverse pressure gradient essentially sets the location of transition on the suction surface of this vane. Producing transition upstream of the suction surface film holes allows a comparison between turbulent boundary layer heat transfer with and without film cooling. Since film cooling is known to cause transition (Mayle, 1991), this turbulent to turbulent comparison is more useful in assessing heat transfer augmentation than a laminar to turbulent comparison.

Film Cooled Heat Transfer Vane Description. A schematic of the epoxy vane used for heat transfer and film cooling measurements is shown in Fig. 4. The vane had fine gage chromel-alumel thermocouples cast into the outer surface of the epoxy at a depth of 0.038 cm as well as the inner surface of the plenum. In the plenum or hollow region of the vane, the thermocouples were placed on a surface normal plane to reduce

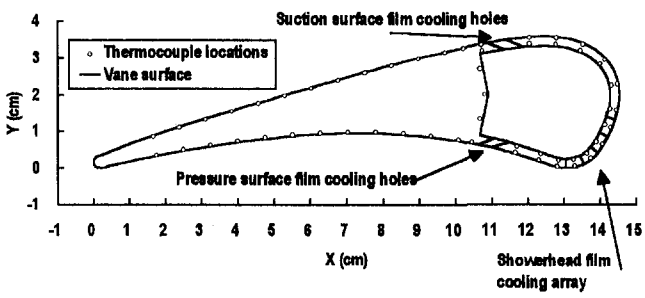

Fig. 4 C3X film cooled vane thermocouple locations

the uncertainty of estimating the surface normal conduction. The vane was covered with a 0.025-mm-thick Inconel foil used to generate a constant surface heat flux. The Inconel foil was adhered to a 0.127 mm Kapton film, which in turn was placed on the vane using a 0.05-mm-thick acrylic adhesive. The heating ended at 1 cm from the trailing edge on both the suction and pressure surfaces. The ends of the foils were soldered to a 0.254-mm-thick, 6.35-mm-wide copper bus bar. A shallow indentation was milled in the airfoil surface to accept the bus bar. The resulting vane surface was aerodynamically smooth and visually attractive.

A two-dimensional finite element analysis was made of the epoxy vane along the plane of the thermocouples to reduce the uncertainty in the surface heat flux and temperature due to conduction through the vane. The resulting surface normal heat flux was added to the flux dissipated in the foil. The calculated surface normal heat flux due to conduction was also used to extrapolate the thermocouple temperatures to the outer surface. A spanwise finite element analysis of the surface was also made. The analysis demonstrated that spanwise conduction in the foil and epoxy substrate produced about an 18 to one attenuation of hole spacing produced periodic variations in adiabatic wall temperature or heat transfer coefficient. Therefore, both the heat transfer data and adiabatic effectiveness data should be interpreted as span averaged.

Heat transfer baselining tests were conducted at both low and high turbulence levels prior to drilling any cooling holes in the vane or the foil and were compared to data taken previously using a solid vane by Ames (1997). The procedure included running the vane without heating to obtain recovery temperatures along the surface prior to obtaining temperatures with power to the heater foil. The thermocouple temperatures from the heated case provided boundary conditions for the finite element analysis. The heat transfer coefficient was determined from the net surface heat flux divided by the surface to recovery temperature difference. The net heat flux accounted for heat loss due to radiation assuming the foil had an emissivity of 0.2 and was radiating to a black body at the inlet temperature. The maximum heat loss due to radiation amounted to about 1.8 percent of the local heat flux. Figure 5 compares hollow vane Stanton number distributions at high and low turbulence levels with the solid vane data of Ames (1997) at an exit Reynolds number of 800,000. The comparisons are generally excellent with a root mean square deviation of ±2 percent between both the low and high turbulence data sets. Hollow vane Stanton number distributions for an exit Reynolds number of 500,000 at low and high turbulence levels also compared well with the solid vane data of Ames (1997). The excellent replication between these two vanes at two turbulence conditions and Reynolds numbers gives confidence in the experimental method. The

estimated uncertainty for the heat transfer coefficient is ±5 percent based on the root mean square deviation (see Moffat, 1988).

Three separate tests were made to determine heat transfer with film cooling and adiabatic effectiveness. First, recovery wall temperatures were determined for the given condition without any heating or coolant injection. Second, a test was made for surface heat transfer with injection at a particular velocity ratio using the heated foil technique. Finally, a test for effectiveness was made with the foil heater off by heating the coolant and recording the vane and plenum temperatures. Initially, the procedure described for determining the base vane heat transfer was used to estimate the heat transfer distribution. Next, the wall temperatures measured during the adiabatic effectiveness test for a particular condition were input into the finite element analysis to determine the surface normal conduction. The temperature drop in the coolant due to conduction in the coolant holes was also determined at this time. The temperatures recorded during the adiabatic effectiveness test were corrected for conduction and radiation effects by dividing the net loss from the surface by the local heat transfer coefficient:

$$T_{aw} = T_w + q''_{\text{loss}}/h \tag{1}$$

where q''_{loss} is the sum of the net radiative loss from the surface and the conduction loss into the vane from the surface. The adiabatic effectiveness was determined using the corrected coolant outlet temperature. In the heat transfer test the coolant temperature, which is nominally set at the free-stream temperature, increases in the plenum and hole due to convection. This coolant outlet to free-stream total temperature difference was typically on the order of 1–2°C. Because of this temperature difference, the adiabatic wall temperature needed to determine surface heat transfer will vary slightly from the local recovery temperature. This adiabatic wall temperature for heat transfer can be estimated using the local recovery temperature, the adiabatic effectiveness distribution, and the estimated coolant outlet temperature:

$$T_{aw} = T_r + \eta(T_{co} - T_r) \tag{2}$$

The two tests for heat transfer and adiabatic effectiveness produce two independent equations for the determination of the local h and η. Outside of the near-hole region ($X/D < 5$), the corrections for Eqs. (1) and (2) are typically small. The uncertainty in the surface heat transfer coefficient increases to ±6 percent in this region due to the coolant air heat up. During the tests, only the holes in the configuration of interest were open to ensure the highest accuracy in the flow rates. A more detailed account of the experimental method is given by Ames (1996).

Data Acquisition and Uncertainties. A PC-based data acquisition system was used in this experiment. Pressure measurements were made using a Scanivalve and three 6.9 kPa (1 psid) pressure transducers calibrated against an AMETEK dead weight tester. Steady-state voltage signals were integrated over 1 power line cycle ($\frac{1}{60}$ second) using an HP digital multimeter with 100 nV sensitivity and 2.5 μV accuracy and were averaged over 10 independent readings. Signals were multiplexed using an HP scanner. Flow rates to a particular film cooling array were determined using an ASME sharp-edged orifice tube. The hot wire was powered with a DISA 55M system and collected using an Analog Devices RTI-860 board with 200 kHz throughput. The hot wire was biased and amplified to enhance resolution and was calibrated against a low free-stream turbulence jet and fitted to a fourth-order polynomial.

The data uncertainties were estimated based on the root mean square method (see Moffat, 1988). The uncertainty in determining total pressure was about 1 percent at the cascade inlet and about 0.25 percent at the exit. The uncertainty in velocity estimated from the total to static pressure ratios at the inlet and exit was about two percent due to the uncertainty in the local static pressure. The uncertainty in the velocity determined from the single wire was also estimated to be two percent. The absolute uncertainty of the heat transfer coefficient was estimated to be ±5 percent except in the near hole region were the uncertainty was estimated to be ±6 percent. The relative uncertainty of the experimental data was estimated to be ±2.4 percent for run to run comparisons. The estimated uncertainty in determining the energy (Lu) and integral (Lx) scales was ±13 percent.

Heat Transfer Results

This section examines the influence of film cooling velocity ratio, geometry, and inlet turbulence level on vane heat transfer. The results from one and two rows of film cooling for both the suction and pressure surfaces are compared in terms of both Stanton number and Stanton number ratio for low and high turbulence levels. The suction surface configuration consisted of holes 0.159 cm in diameter with a spanwise spacing of 0.478 cm, and a 30 deg streamwise incline with the surface. The single row of holes was located at an arc of 6.93 cm from the stagnation line while the configuration for two rows had an additional row staggered at 6.45 cm from the stagnation line. The pressure surface configuration consisted of holes 0.132 cm in diameter with a spanwise spacing of 0.396 cm, and a 30 deg streamwise incline with the surface. The single row of holes was located at an arc of −2.72 cm from the stagnation line while the configuration for two rows had an additional row staggered at −2.33 cm from the stagnation line. The heat transfer downstream of the showerhead cooling array is also examined in terms of Stanton number for three equivalent pressure ratios and for the two turbulence levels. The showerhead configuration consisted of five staggered rows of 0.132 cm diameter 20 deg spanwise inclined holes with a spanwise spacing of 0.847 cm. The rows were located at surface arcs with respect to the stagnation line of −0.254, 0.254, 0.762, 1.270, and 1.778 cm. The hollow plenum wall thickness was 0.292 cm.

Suction Surface Heat Transfer Results. The *Handbook of Heat Transfer Applications* (1985) suggests that for 35 deg air injection with a spanwise spacing of 3.0 diameters at velocity ratios at or below 1.0, St/St_0 should be close to 1.0. Liess (1975) found augmentation levels of up to 15 percent in the near-hole region for a velocity ratio around 0.4 on a flat plate with a newly transitioned boundary layer. In the present experiment the suction surface boundary layer completes transition at a surface arc ranging from 6.0 to 7.0 cm from the stagnation line depending on turbulence level in the absence of film cooling holes. This position is very close to the position of the downstream row of holes. At the position of the holes ($X = 6.93$ cm) the pressure gradient is adverse with an acceleration constant K equal to −0.97E-06, which decreases to zero at a surface arc of around 12 cm. According to Teekaram et al. (1991) adverse pressure gradients are known to enhance jet penetration.

Stanton number distributions for the single row of holes with high inlet turbulence for velocity ratios ranging from 0.42 to 0.56 are shown in Fig. 6. The heat transfer data with film cooling clearly show a significant increase in Stanton number over the base vane case, which is also shown. The heat transfer peaks immediately downstream from the holes and decays slowly in the streamwise direction. The film cooling data have an average increase in Stanton number of about 11 percent in the near hole region. The data are presented in terms of the ratio of the film cooled Stanton number divided by the base vane Stanton number in Fig. 7 for the high turbulence case. The Stanton number ratios collected over the three velocity ratios and the second Reynolds number show little significant difference. Based on velocity profiles taken downstream from the film cooling at an X/D of 12 compared to one taken at the same location on the

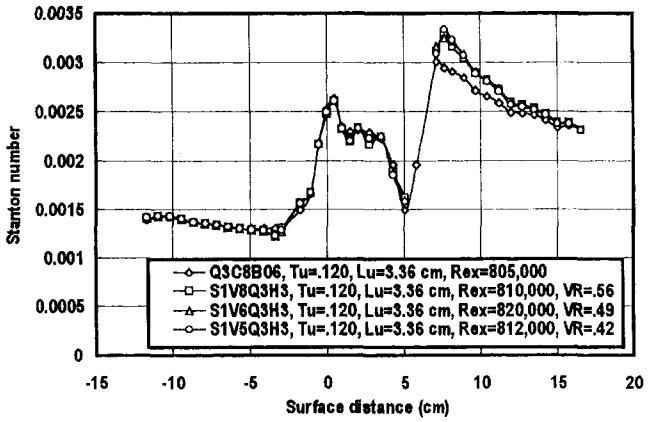

Fig. 6 Suction surface Stanton number distribution, 1 row 30 deg holes, Comb(1)

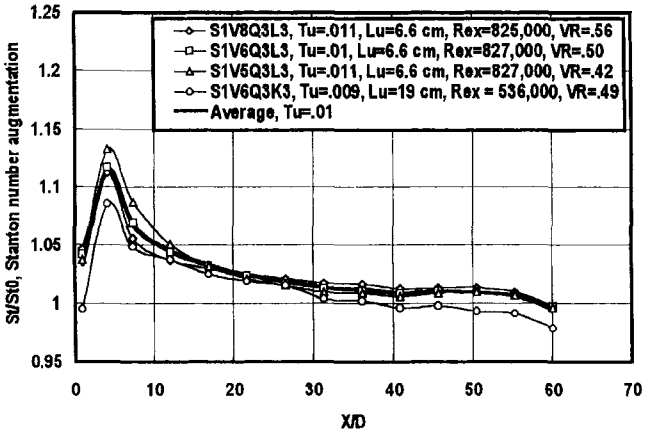

Fig. 8 Stanton number ratio, low turbulence, 1 row 30 deg holes, suction surface, P/D = 3

base vane [both documented in Ames (1996)] the span-averaged skin friction coefficient is slightly reduced by the film injection for the high turbulence case. The lack of enhancement of the skin friction coefficient by the film injection suggests that the increase in Stanton number is due to the disruption of the thermal boundary layer. Evidently, the coolant jet, which is injected at a temperature close to the free-stream temperature for the heat transfer tests, restarts the thermal boundary layer. Stanton number ratios for the low turbulence case collected over the three velocities and two Reynolds numbers are shown in Fig. 8. Both the near hole level of increase and the downstream distribution of Stanton number ratio are quite similar for the two turbulence levels. Span-averaged skin friction coefficients inferred from velocity profiles taken 12 diameters downstream from the holes for the low turbulence case showed no significant change from the base case.

Stanton number ratios taken for two staggered rows of film cooling are shown in Fig. 9 for the high turbulence case. Similar to the single row data, the double row distributions exhibit a near-hole peak in Stanton number, which decays in the downstream direction. The decay of Stanton number to the base vane value is more rapid for the double row than the single row. However, the peak Stanton number ratio is about 1.18 compared with 1.11 for the single row. Similar to the single row data, double row Stanton number ratios taken for the low turbulence case over the same conditions and shown in Fig. 10 compare closely with the high turbulence data. Span-averaged skin friction coefficients inferred from downstream velocity profiles [see Ames (1996)] indicate a significant reduction over the base vane case. The inferred reduction in skin friction again suggests that disruption of the thermal boundary layer due to the jets causes the enhancement to heat transfer for this turbulent boundary layer flow.

Pressure Surface Heat Transfer Results. Ou et al. (1994) found a substantial level of pressure surface heat transfer augmentation due to film cooling from two rows of compound angle holes on a blade, with and without wakes from a spoked wheel generator. The near-hole heat transfer augmentation in-

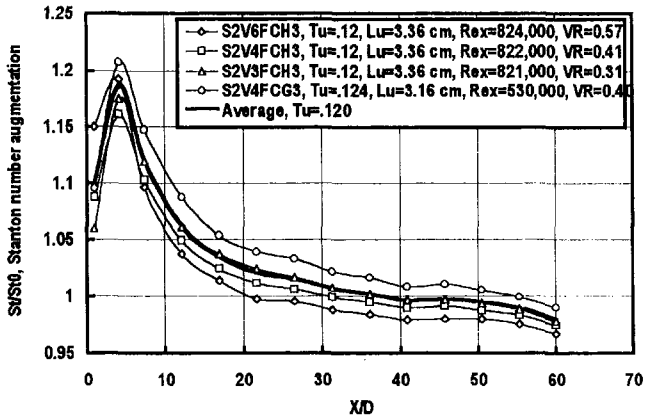

Fig. 9 Stanton number ratio, Comb(1), 2 rows 30 deg holes, suction surface, P/D = 3

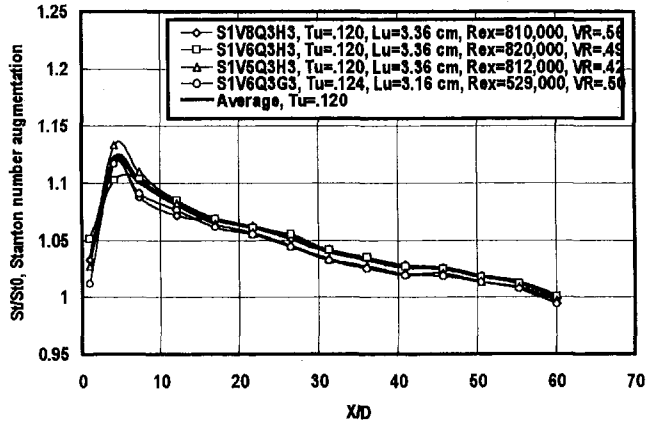

Fig. 7 Stanton number ratio, Comb(1), 1 row 30 deg holes, suction surface, P/D = 3

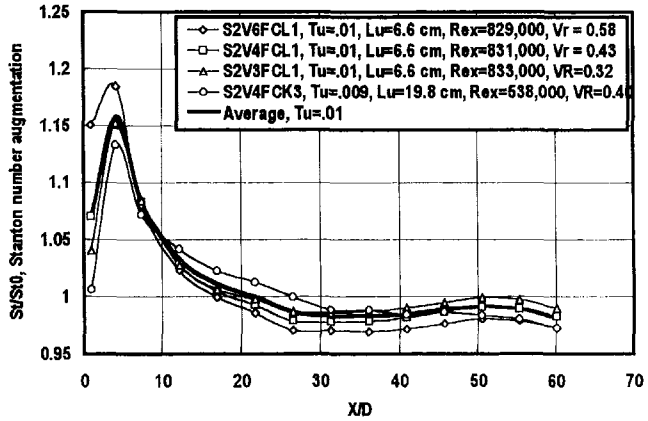

Fig. 10 Stanton number ratio, low turbulence, 2 rows 30 deg holes, suction surface, P/D = 3

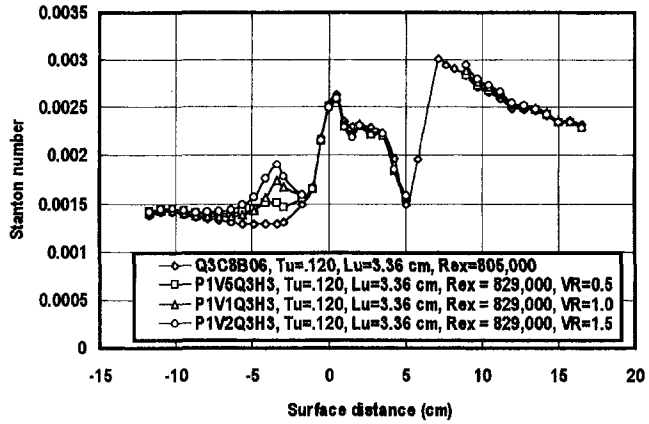

Fig. 11 Pressure surface Stanton number distribution, 1 row 30 deg holes, Comb(1)

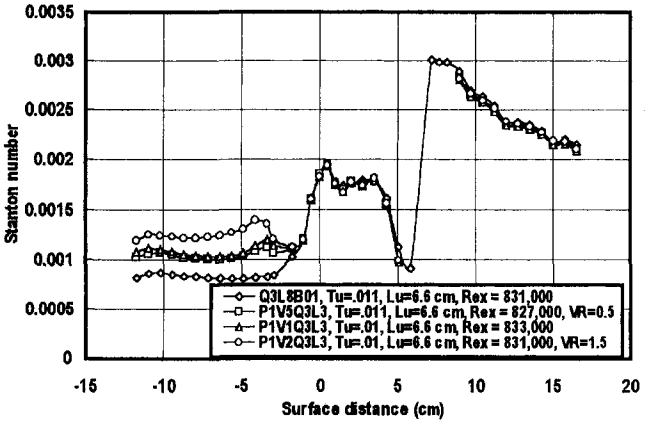

Fig. 13 Pressure surface Stanton number distribution, 1 row 30 deg holes, low turbulence

creased with increasing blowing ratio and injection of air produced higher levels of augmentation than CO_2 with a density ratio of 1.52. The wakes produced an incremental increase in Nusselt number across the entire pressure surface, indicating transition had not occurred.

Stanton number distributions for velocity ratios ranging from 0.5 to 1.5 for a single row of holes and the high turbulence condition are presented in Fig. 11. The Stanton number is substantially enhanced due to the coolant injection and the near-hole peak in heat transfer increases with increasing velocity ratio. Downstream, the level of heat transfer decays to the base vane value with high turbulence. Velocity spectra taken nine diameters downstream from the coolant injection show a substantial increase in the dissipation, based on the inertial subrange, compared to the base vane level. Figure 12 compares the pressure surface heat transfer with high turbulence in terms of the ratio of Stanton number with film injection. The ratios show high near-hole peaks, which decay quickly in the downstream direction. The peak Stanton number ratio scales reasonably well on velocity ratio and the curves for velocity ratios of 1.5 and 1.0 look very similar. The Stanton ratio data for the 0.5 velocity ratio shows a delayed peak and decay. This difference is likely due to reduced jet penetration, which weakens the boundary layer interaction, and the formation of a shear layer due to the injection of low momentum fluid. Single wire measurements show an increased turbulence level and dissipation level due to this shear layer.

Stanton number distributions for a single row of holes and the low turbulence condition are plotted in Fig. 13 for velocity ratios ranging from 0.5 to 1.5. Similar to the high turbulence case, the Stanton number is substantially enhanced due to coolant injection in near-hole region but unlike the high turbulence data, the heat transfer increase never decays back down to the base vane value. This sustained level of augmentation may be due to the formation of some type of boundary layer structure, which is generated by the jets and stabilized by the free-stream acceleration. Although this feature is interesting, it has little relevance to the high turbulence environment of first-stage turbine nozzles.

Stanton number distributions for a double row of holes taken at the high turbulence condition are shown over velocity ratios ranging from 0.5 to 1.5 in Fig. 14. Similar to data for the single row of holes, the double row data show peaks that scale on velocity ratio but are much higher. Although the near-hole peaks are very high, the heat transfer augmentation decays back down to the base vane value. The heat transfer data for two rows is plotted in terms of Stanton number ratio in Fig. 15. In comparison with the peaks in augmentation shown in Fig. 12, the double row peaks show values that are to a good approximation twice as high above one as the single row peaks. Again, the curves for velocity ratios of 1.0 and 1.5 are very similar while the curve for a velocity ratio of 0.5 shows a somewhat later peak and delayed decay. In comparison with the single row data, the decay of Stanton number ratio for the double row in terms of X/D is roughly 30 percent faster. This increased decay rate could be due to the interaction of the adjacent jets.

Stanton number distributions for a double row of holes and the low turbulence condition are plotted in Fig. 16 for velocity

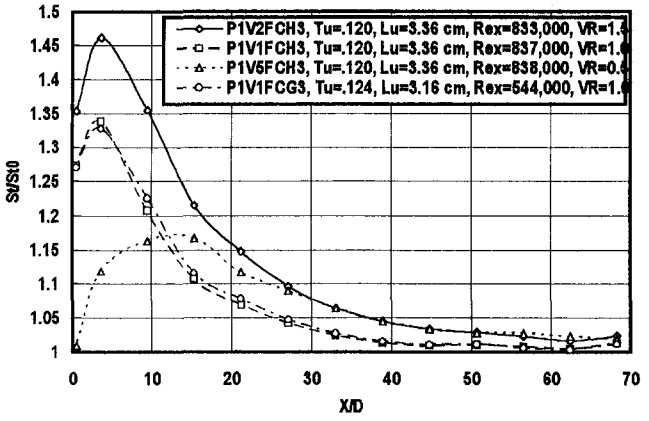

Fig. 12 Stanton number ratio, Comb(1), 1 row 30 deg holes, pressure surface, P/D = 3

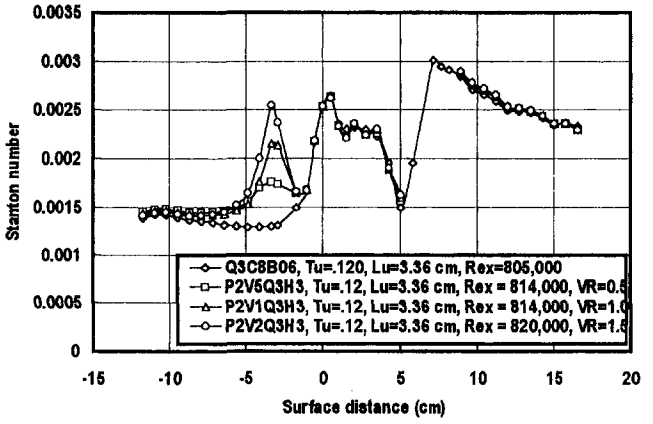

Fig. 14 Pressure surface Stanton number distribution, 2 rows 30 deg holes, Comb(1)

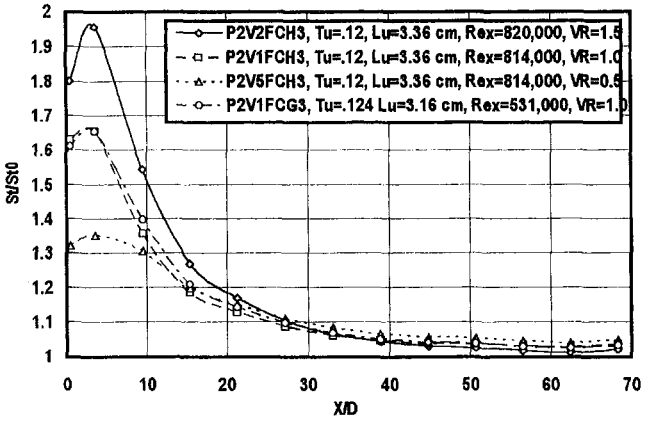

Fig. 15 Stanton number ratio, Comb(1), 2 rows 30 deg holes, pressure surface, P/D = 3

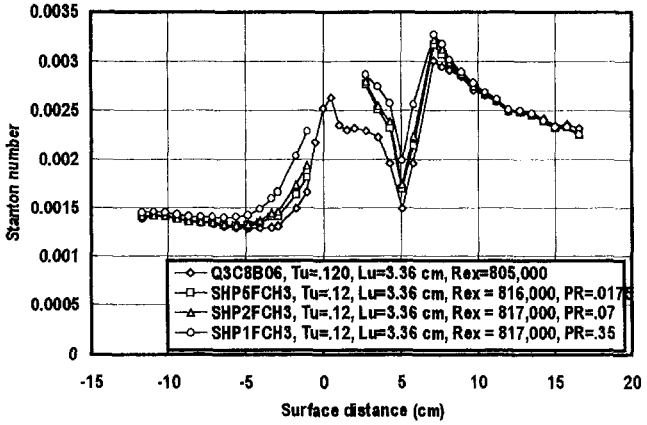

Fig. 17 Stanton number distribution for showerhead cooling, Comb(1)

ratios ranging from 0.5 to 1.5. Similar to the high turbulence case, the Stanton number is substantially enhanced due to coolant injection in near-hole region but like the single row low turbulence data, the heat transfer increase never decays back down to the base vane value. Again, though this feature is interesting, it has little relevance to the high turbulence environment of first stage turbine nozzles.

Showerhead Heat Transfer Results. Showerhead film ejection can substantially increase heat transfer due to the relatively high velocity ratios, spanwise injection, and pretransitional state of the boundary layer. Previously, Mehendale and Han (1992) investigated the combined influence of high turbulence and showerhead injection on cylindrical stagnation region and downstream flat plate heat transfer and found heat transfer augmentation levels of two or more between and directly downstream of the injection rows. Augmentation was generally found to increase with increased rates of blowing. The augmentation level in the cylindrical region was found to be much higher than in the flat plate region where flow was transitional or turbulent.

Stanton number distributions downstream from showerhead injection in the presence of high inlet turbulence are shown in Fig. 17. The showerhead data were taken at equivalent pressure ratios [$PR_{eqv} = (P_c - P_t)/(P_t - P_{s,ex})$] of 0.0175, 0.07, and 0.035. On the pressure surface, the peak level of augmentation scales on the square root of equivalent pressure ratio. Due to the low velocity at this location, the square root of PR_{eqv} is roughly proportional to velocity ratio for this single row of holes on the pressure side of the stagnation line. Four rows of spanwise inclined holes are present on the suction side of the stagnation line. Again, the jet velocity from the row of holes nearest the stagnation region scales on the square root of PR_{eqv}. However, the last two downstream rows are relatively insensitive to the pressure ratio due to much higher local velocities. Generally, the augmentation found on the suction surface increases with pressure ratio but augmentation does not scale with it. Additionally, downstream of transition, the levels of augmentation are much lower.

Stanton number distributions downstream from showerhead injection for the low turbulence condition are shown in Fig. 18. Downstream of injection on the pressure side, augmentation levels are high and generally decay slowly in the streamwise direction. However, similar to the pressure side film injection, the level of augmentation due to showerhead injection stays significant over the entire surface. On the suction surface, augmentation levels in the near-hole area are again high and the showerhead injection is also responsible for an earlier transition. In the turbulent region, little augmentation is found. Again, this low turbulence case offers little relevance to the highly turbulent gas path of a gas turbine first vane.

Conclusions

The present data documented the influence of discrete coolant injection on the gas side heat transfer coefficient of a vane subjected to high levels of inlet turbulence. Stanton number augmentation ratios were found to be higher in the laminar regions than in the turbulent regions of the flow. On the pressure surface, the peak in Stanton number ratio scaled on velocity

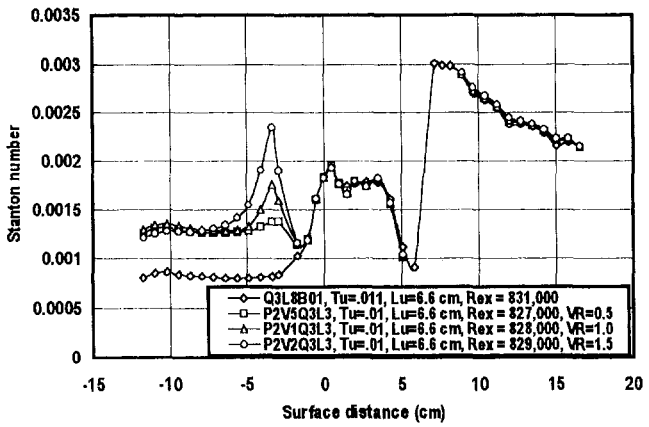

Fig. 16 Pressure surface Stanton number distribution, 2 rows 30 deg holes, low turbulence

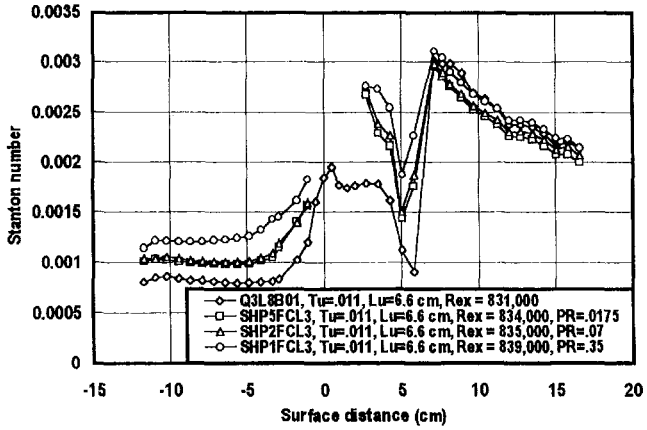

Fig. 18 Stanton number distribution for showerhead cooling, low turbulence

ratio and the number of rows and decayed quickly in the downstream direction. Heat transfer augmentation due to film injection on the suction surface was insensitive to the narrow range of velocity ratios examined but increased with a second row of injection. Showerhead injection was found to produce substantial levels of augmentation in the laminar regions of flow and augmentation increased with increasing pressure ratio.

Acknowledgments

This research was conducted under the support of NASA Lewis Research Center at Allison Engine Company Research Laboratories where the author was previously employed. Additionally, Amy Porter, a co-op student from Virginia Polytechnic Institute, made substantial contributions in the fabrication of the test vanes used in this study. The author is also grateful to Dr. Steven Gegg for reading this document and offering many helpful suggestions.

References

Ames, F. E., 1994, "Experimental study of vane heat transfer and aerodynamics at elevated levels of turbulence," NASA CR 4633.

Ames, F. E., 1996, "Experimental study of vane heat transfer and film cooling at elevated levels of turbulence," NASA CR 198525.

Ames, F. E., 1997, "The influence of large scale high intensity turbulence on vane heat transfer," ASME JOURNAL OF TURBOMACHINERY, Vol. 119, pp. 23–30.

Ekkad, S. V., Zapata, D., and Han, J. C., 1997, "Heat transfer coefficients over a flat surface with air and CO_2 injection through compound angle holes using a transient liquid crystal image method," ASME JOURNAL OF TURBOMACHINERY, Vol. 119, pp. 580–586.

Garg, V. K., and Gaugler, R. E., 1995, "Leading edge film cooling effects on turbine blade heat transfer," ASME Paper No. 95-GT-275.

Gartshore, I. S., Salcudean, M., Barnea, Y., Zhang, K., and Aghadsi, F., 1993, "Some effects of coolant density on film cooling effectiveness," ASME Paper No. 93-GT-76.

Han, J. C., Zhang, L., and Ou, S., 1993, "Influence of unsteady wake on heat transfer coefficient from a gas turbine blade," ASME JOURNAL OF TURBOMACHINERY, Vol. 115, p. 904.

L'Ecuyer, M. R., and Soechting, F. O., 1985, "A model for correlating flat plate film cooling effectiveness for rows of round holes," *Heat Transfer and Cooling in Gas Turbines: AGARD Conference Proceedings No. 390.*

Lefebvre, A. W., 1983, *Gas Turbine Combustion,* McGraw-Hill, New York.

Liess, C., 1975, "Experimental investigation of film cooling with ejection from a row of holes for the application to gas turbine blades," ASME *Journal of Engineering for Power,* Vol. 97, p. 21.

Ligrani, P., and Ramsey, 1997, "Film cooling from spanwise oriented holes in two staggered rows," ASME JOURNAL OF TURBOMACHINERY, Vol. 119, pp. 562–567.

Mayle, R. E., 1991, "The role of laminar-turbulent transition in gas turbine engines, 1991 ASME International Gas Turbine Institute Scholar Award Paper," ASME JOURNAL OF TURBOMACHINERY, Vol. 113, pp. 509–537.

Mehendale, A. B., and Han, J. C., 1992, "Influence of high mainstream turbulence on leading edge film cooling heat transfer," ASME JOURNAL OF TURBOMACHINERY, Vol. 114, p. 707.

Moss, R. W., and Oldfield, L. G., 1991, "Measurements of hot combustor turbulence spectra," ASME Paper No. 91-GT-351.

Moffat, R. J., 1988, "Describing the uncertainties in experimental results," *Experimental Thermal and Fluid Science,* Vol. 1, p. 3.

Nirmalan, N. V., and Hylton, L. D., 1990, "An experimental study of turbine vane heat transfer with leading edge and downstream film cooling," ASME JOURNAL OF TURBOMACHINERY, Vol. 112, p. 477.

Ou, S., Han, J. C., Mehendale, A. B., and Lee, C. P., 1994, "Unsteady wake over a linear turbine blade cascade with air and CO_2 film injection: Part I—Effect on heat transfer coefficients," ASME JOURNAL OF TURBOMACHINERY, Vol. 116, p. 721.

Rohsenow, Hartnett, and Ganic, 1985, *Handbook of Heat Transfer Applications,* 2nd ed., McGraw-Hill, New York.

Sen, B., Schmidt, D. L., and Bogard, D. G., 1996, "Film cooling with compound angle holes: heat transfer," ASME JOURNAL OF TURBOMACHINERY, Vol. 118, pp. 800–806.

Teekaram, A. J. H., Forth, C. J. P., and Jones, T. V., 1991, "Film cooling in the presence of mainstream pressure gradients," ASME JOURNAL OF TURBOMACHINERY, Vol. 113, p. 484.

Aspects of Vane Film Cooling With High Turbulence: Part II—Adiabatic Effectiveness

F. E. Ames
forrest_ames@mail.und.nodak.edu,
University of North Dakota,
Grand Forks, ND 58202-8359

A four-vane subsonic cascade was used to investigate the influence of turbulence on vane film cooling distributions. The influence of film injection on vane heat transfer distributions in the presence of high turbulence was examined in part I of this paper. Vane effectiveness distributions were documented in the presence of a low level of turbulence (1 percent) and were used to contrast results taken at a high level (12 percent) of large-scale turbulence. All data were taken at a density ratio of about 1. The three geometries chosen to study included one row and two staggered rows of downstream film cooling on both the suction and pressure surfaces as well as a showerhead array. Turbulence was found to have a moderate influence on one and two rows of suction surface film cooling but had a dramatic influence on pressure surface film cooling, particularly at the lower velocity ratios. The strong pressure gradients on the pressure surface of the vane were also found to alter film cooling distributions substantially. At lower velocity ratios, effectiveness distributions for two staggered rows of holes could be predicted well using data from one row superposed. At higher velocity ratios the two staggered rows produced significantly higher levels of effectiveness than values estimated from single row data superposed. Turbulence was also found to reduce effectiveness levels produced by showerhead film cooling substantially.

Introduction

The influence of film cooling on vane heat transfer was examined for one and two rows of suction and pressure surface film injection and for showerhead injection in part I of this paper. Here, in the second part of this paper, effects of high inlet turbulence on vane film cooling effectiveness distributions are examined. In examining the influence of turbulence on vane film cooling, the results need to be presented in the context of the many variables present on a turbine vane that can influence the distribution of effectiveness.

The *Handbook of Heat Transfer Applications* (2nd ed., 1985) reviews many of the variables that can influence discrete hole film cooling. Velocity ratio, density ratio, turbulence level and scale, displacement thickness to hole diameter (δ_1/D), pressure gradient, curvature, injection angle, and pitch-to-diameter ratio have all been found to have a measurable if not a substantial influence on effectiveness distributions. The primary variable investigated in this study has been the influence of high-level turbulence. In addition, velocity ratios have been varied over a range consistent for a first-stage vane. Other variables, including the strong pressure gradients that are present along the vane surface and strongly influence the results, could not be varied independently but are reported in some manner in this paper. In part I of this paper, a rationale for reporting these results in terms of velocity ratio was made as was the reasoning behind the selection of the particular velocity ratios studied. In part II of this paper, literature is reviewed on both the influence of turbulence on effectiveness distributions as well the influence of pressure gradients. Additionally, some results from studies on turbine airfoil and showerhead film cooling are summarized.

The greatest influence of turbulence can be expected on the near pressure surface and the stagnation region of a vane due to relatively low local convective velocities combined with combustor turbulence which result in high levels of turbulence. Recently, Bons et al. (1996) determined the effect of a range of turbulence levels on flat plate film cooling from a single row of 35 deg holes with a pitch to diameter ratio of 3. Generally, they found that turbulence substantially reduced centerline effectiveness at moderate velocity ratios having an increased effect with increasing turbulence levels and downstream distance. The influence of turbulence was considerably less substantial at higher velocity ratios. Additionally, they found that external turbulence quickly mixed out effectiveness distributions in the spanwise direction. For their 17 percent turbulence case, a level consistent with the pressure surface of a vane, spanwise uniformity in effectiveness was achieved within an X/D of 10.

The pressure surface of a first vane is known to produce highly favorable pressure gradients. Teekaram (1991) investigated the influence of a favorable pressure gradient on film cooling effectiveness and found a substantial increase in the near hole region over their zero pressure gradient data. For a velocity ratio of 0.5 (for a density ratio of 1.5), they found respective increases of about 50, 30, and 24 percent at X/D's of 2, 8, and 14. Their acceleration ranged from a K of 2.62E-06 at the injection point to 1.05E-06 at an X/d of 14. More recently, Schmidt and Bogard (1995) found substantial increases of laterally averaged effectiveness in the near-hole region due to a favorable pressure gradient. Their data indicated that the pressure gradient caused an increased spreading of the coolant jet near the hole for low velocity ratios. They did not report span-averaged effectiveness levels past an X/D of 15.

Film cooling studies on airfoil surfaces generally indicate that turbulence reduces effectiveness distributions and that effectiveness levels on the suction surface are higher than levels on the pressure surface. Mehendale et al. (1994) studied the influence of a wake from a spoke-wheeled generator on blade film cooling in a linear cascade. Generally, film cooling effectiveness levels dropped on both suction and pressure surfaces with passing wakes. Dring et al. (1980) investigated film cooling on a turbine rotor blade and found reasonable correlation

Contributed by the International Gas Turbine Institute and presented at the 42nd International Gas Turbine and Aeroengine Congress and Exhibition, Orlando, Florida, June 2–5, 1997. Manuscript received International Gas Turbine Institute February 1997. Paper No. 97-GT-240. Associate Technical Editor: H. A. Kidd.

with flat plate results on the suction surface. However, on the pressure surface they found a comparatively lower level and a much faster decay of effectiveness as well as a significant radial component in the film trajectory. Takeishi, et al. (1992) conducted a similar study and reached conclusions similar to Dring in terms of the level of effectiveness and the decay rate. Abhari and Epstein (1994) took transient heat transfer data on a film cooled rotor blade and found a significant reduction of time-averaged heat transfer on the suction surface but found little effect on the pressure surface. Nirmalan and Hylton (1990) studied two staggered rows of film cooling on the suction surface and pressure surface of a vane in a warm linear cascade and generally found much higher levels of heat load reduction on the suction side compared to the pressure side at engine typical coolant to inlet total pressure ratios.

Showerhead film cooling studies with cylindrical leading edges show a similar lowering of effectiveness with elevated free-stream turbulence levels but with the added feature of effectiveness distributions, which can show poor spanwise distributions depending on blowing ratio. Gartshore et al. (1993) show that depending on geometry and velocity ratio, spanwise-oriented leading edge cooling jets may pair, leaving portions of the downstream surface unprotected by leading edge injection. Mehendale and Han (1992) have shown that free-stream turbulence can substantially reduce effectiveness levels, particularly at lower blowing ratios.

The objective of this paper has been to document the influence of high inlet turbulence in mixing away vane film cooling coverage. Adiabatic effectiveness distributions for one and two rows of film cooling on the suction and pressure surface and for five rows of showerhead cooling are investigated at low (1 percent) and high (12 percent) inlet turbulence levels. The effectiveness levels are studied over a range of engine relevant velocity ratios at a density ratio of around one. Selected velocity profiles taken downstream from the film cooling are also presented to provide supporting evidence of the substantial mixing which is occurring. Part I of this paper presents results showing the influence of velocity ratio on heat transfer downstream from film injection at the two turbulence levels. Additionally, a reasonably complete account of the experimental approach of this research is given in part I. Comprehensive documentation of the heat transfer, film cooling, velocity profile, turbulence, and length scale data are given by Ames (1996).

Experimental Uncertainties

The largest sources of uncertainty in the adiabatic effectiveness data were due to uncertainty in correcting for the influence of conduction and unsteadiness in the room air temperature. Uncertainties in correcting for conduction were due to uncertainties in the epoxy conductivity and in the effective location of the thermocouple junction with respect to the surface. These effects were much more pronounced in the region close to the holes due to high levels of conduction. The estimated absolute level of uncertainty in the effectiveness data based on the root mean square method (see Moffat, 1988) was ±5 percent. However, in the near-hole region ($X/D < 5$) uncertainties on the pressure side were substantially higher (±20 percent) due to the relatively high levels of conduction to the surface near the coolant holes. This near-hole correction for conduction was much smaller (±7 percent at $X/D = 2$) on the suction surface. These data were taken using thermocouples placed along a single span on the hollow epoxy airfoil downstream from a hole centerline. The vane used in this study is described in part I of this paper. A finite element model of the surface with a sinusoidally varying temperature boundary condition indicated the vane surface was effective in averaging the spanwise variations in temperature. The peak-to-peak variation in spanwise temperature distribution at the thermocouple depth was less than 6 percent of the peak-to-peak variation imposed on the surface.

The skin friction coefficients for the turbulent boundary layers on the suction surface were estimated from the velocity profiles. Ludwieg and Tillmann's correlation as modified by White (1974) $\{Cf/2 = 0.144 \exp(-1.37\ \delta_1/\delta_2)/(\log \mathrm{Re}_{\delta 2})^{1.753+0.283\delta 1/\delta 2}$, ±3 percent$\}$ was used as the primary method and was checked for consistency with a log law analysis. The estimated accuracy of this method in the region downstream from film cooling injection is about ±10 percent.

Adiabatic Effectiveness Results

This section examines the influence of film cooling velocity ratio, geometry, and inlet turbulence level on adiabatic effectiveness along a vane. The results from one and two rows of 30 deg streamwise inclined holes with a pitch to diameter ratio of 3 for both the suction and pressure surfaces are presented. Additionally, effectiveness distributions for five rows of 20 deg spanwise inclined showerhead injection are shown and contrasted for a range of coolant to total pressure ratios. The data were all taken at a density ratio of about 0.94. Further details about the vane and film cooling geometry are given in part I of this paper.

Suction Surface Film Cooling Results. Suction surface film cooling results are typically expected to be comparable to the results from flat plate film cooling studies. L'Ecuyer and

Nomenclature

C = airfoil chord length (true chord)
$Cf/2$ = skin friction coefficient
D = coolant hole diameter
DR = density ratio = ρ_c/ρ_∞
K = free-stream acceleration parameter = $\mu/(\rho_\infty U_\infty^2) dU_\infty/dx$
Lu = energy scale = $1.5|u'|^3/\epsilon$
M = blowing ratio = $\rho_c U_c/\rho_\infty U_\infty$
P = pressure
P = pitch, hole to hole spanwise spacing
PR_{eqv} = equivalent pressure ratio = $(P_c - P_t)/(P_t - T_{x,ex})$
P_s = static pressure
P_t = total pressure
Re = Reynolds number
Re_{ex} = exit Reynolds number = $\rho_{ex} U_{ex} C/\mu$
$\mathrm{Re}_{\delta 2}$ = momentum thickness Reynolds number = $\rho_\infty U_\infty \delta_2/\mu$
T = temperature
T_t = stagnation temperature
Tu = turbulence intensity = u'/U_∞
U = streamwise velocity
u' = rms streamwise fluctuation velocity
VR = velocity ratio = U_c/U_∞, area average coolant velocity divided by local free-stream velocity
X = streamwise distance along airfoil
X/D = streamwise distance from trailing edge exit of last film hole normalized by D
Y = normal distance from the vane surface
Z = spanwise distance from a coolant hole centerline
δ_1 = displacement thickness = $\int_0^\infty (1 - \rho U/\rho_\infty U_\infty) dy$
δ_2 = momentum thickness = $\int_0^\infty \rho U/\rho_\infty U_\infty (1 - \rho U/\rho_\infty U_\infty) dy$
ϵ = turbulent dissipation
η_{ad} = adiabatic wall effectiveness, also η; $\eta_{ad} = (T_{aw} - T_r)/(T_\infty - T_r)$
μ = dynamic viscosity

Subscripts

∞ = references to free-stream conditions
aw = adiabatic wall
c = coolant (static pressure, recovery temperature)
co = coolant outlet
ex = references to vane exit static pressure tap plane location
in = references to inlet static pressure tap plane location
r = recovery

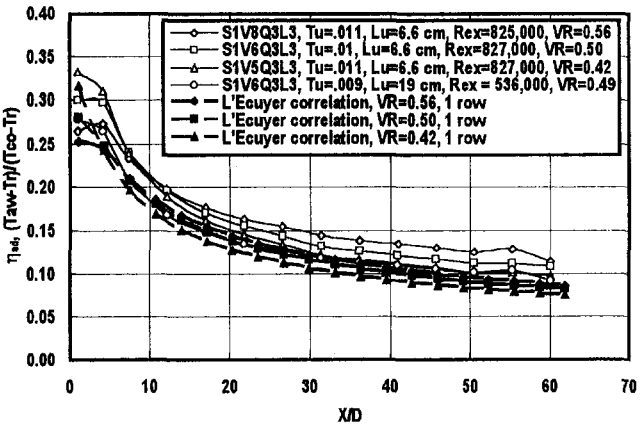

Fig. 1 Comparison suction surface film cooling with correlation varying *VR* and Re_{ox} number, 1 row, 30 deg holes, low turbulence, *DR* = 0.94

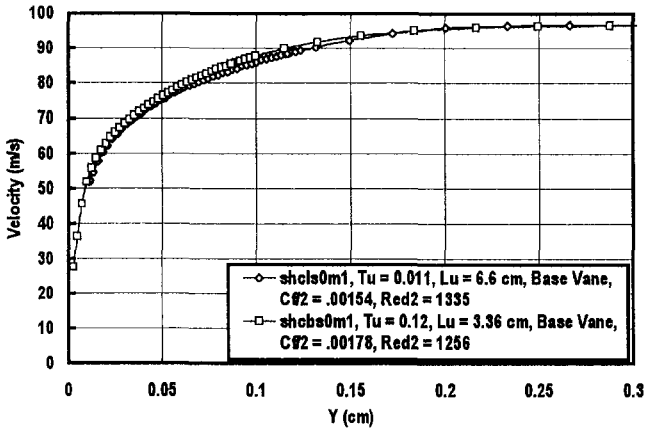

Fig. 3 Baseline suction surface velocity profiles, high and low turbulence, *X* = 8.82 cm

Soechting (1985) developed a correlation based primarily on the flat plate data of Pedersen et al. (1977) for a low-turbulence free stream. Figure 1 shows a comparison between suction surface effectiveness distributions for a single row of holes over a range of velocity ratios with L'Ecuyer and Soechting's correlation plotted as a function of distance from the hole trailing edge (X) divided by the hole diameter (D). The comparison shows excellent trendwise agreement and good agreement with level indicating the span-averaged nature of the data. The level of the data is about 0.02 and 0.03 above the correlation, which is roughly the quoted uncertainty level of the correlation. In the near-hole region, both the data and correlation show higher effectiveness levels with lower velocity ratios due to reduced penetration of the jets. Downstream a crossover occurs and effectiveness levels of both the data and correlation are seen to increase with an increasing thermal capacitance of the film layer. The comparison for the high-turbulence case is given in Fig. 2, showing similar trends to the low-turbulence data. However, in the near-hole region, the data are higher in effectiveness than the low-turbulence data. Also, the ratio of minimum to maximum effectiveness for the high-turbulence data is 75 percent of the low-turbulence data ratio indicating a more rapid decay rate presumably due to the turbulence. Figure 3 gives a comparison between the measured velocity profiles on the suction surface taken at 8.82 cm from the stagnation region on the base vane for both the high and low-turbulence data. At the measurement point, the boundary layers are developing under a moderately adverse pressure gradient. The boundary layer developing under high turbulence is fuller, with a skin friction about 16 percent higher than the low-turbulence case. The ratio of displacement thickness to diameter is about 0.19 for the high-turbulence case and 0.21 for the low-turbulence case. One plausible explanation is that the high-turbulence boundary layer with its fuller profile reduces the penetration of the film cooling jet, enhancing the near-hole effectiveness level. Also, the turbulence might improve near-hole effectiveness by diffusing the coolant toward the plate.

Film cooling data were also taken for two staggered rows of holes on the suction surface for both the high and low-turbulence cases. Two staggered rows of holes are typically considered to enhance film cooling effectiveness levels above the level estimated from one row superposed $\{\eta_{2\text{rows}} \cong \eta\ (2 - \eta)$, see *Handbook of Heat Transfer Applications,* (1985)$\}$ due to a reduced level of penetration caused by the blockage of the jets. However, at lower velocity ratios, the penetration is probably not sufficient to produce a noticeable influence on effectiveness level. Figure 4 shows a comparison between the effectiveness distribution downstream from a double row of holes compared to values from single row data superposed at the same velocity ratio (0.42) for the high and low-turbulence cases. A prediction from L'Ecuyer's correlation for one row superposed is shown in comparison agreeing reasonably well with the results. The comparison also shows that the high-turbulence data for the double row are noticeably higher than the low-turbulence data in the near hole region. This difference is also present in the single row data and could be due to the fuller upstream velocity profile or the enhanced mixing caused by the elevated turbulence level. Generally, the double row data and the values from

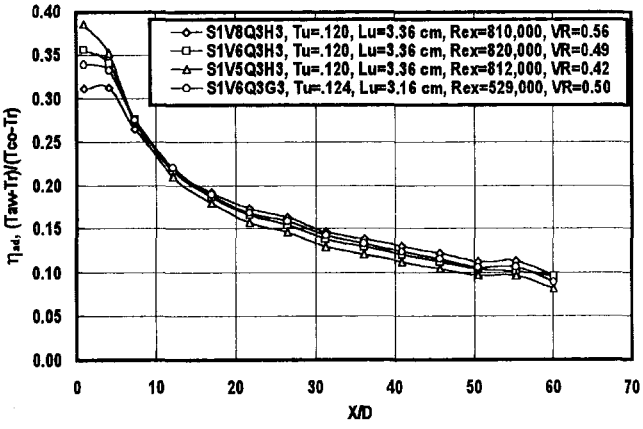

Fig. 2 Comparison of *VR* and Re_{ox} effects on η_{ad}, 1 row, 30 deg holes, suction surface, high turbulence, *DR* = 0.94

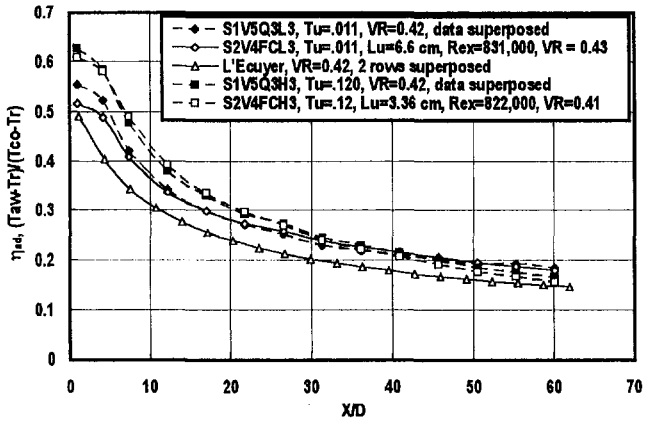

Fig. 4 Superposed single row and double row data compared with correlation, suction surface, low and high turbulence, *DR* = 0.94

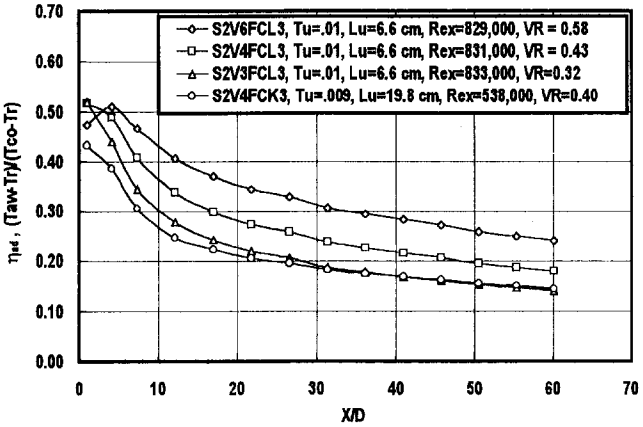

Fig. 5 Comparison of *VR* and Re_{ex} effects on adiabatic effectiveness, 2 rows, 30 deg suction surface holes, low turbulence, *DR* = 0.94

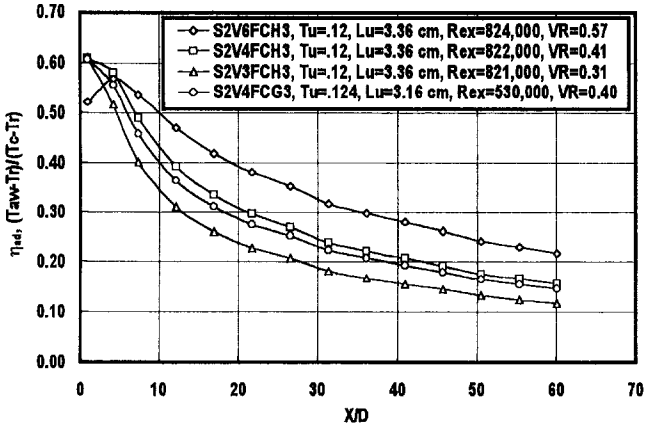

Fig. 6 Comparison of *VR* and Re_{ex} effects on adiabatic effectiveness, 2 rows, 30 deg suction surface holes, high turbulence, *DR* = 0.94

a single row superposed compare very well indicating that at this velocity ratio the double staggered row does not benefit significantly from the increased blockage of the second row. The comparison also indicates the single row data are reasonably well averaged laterally. Since local effectiveness distributions are known to be strongly periodic with the peak occurring directly downstream from the hole, an additional periodic distribution staggered and superposed would not be expected to increase effectiveness significantly in the near-hole region directly downstream from the original coolant hole. However, the addition of a second span-averaged effectiveness distribution would produce a significant increase in effectiveness, independent of the relative spanwise placement of the second row of holes. A similar comparison made (but not shown) at a velocity ratio of 0.56 indicated that two staggered rows of holes performed significantly better than a single row of holes superposed.

Data taken at three velocity ratios (0.58, 0.42, and 0.31) are compared in Fig. 5 for the low-turbulence case. Similar to the single row data, the double row data show higher values of effectiveness in the downstream region with increasing velocity ratio. The relative increase with velocity ratio is much larger for the staggered rows than for the single rows, suggesting the staggered rows do reduce penetration with more noticeable effects occurring at higher velocity ratios. For the high-Reynolds-number case, the level of protection in the far field scales approximately with the velocity ratio. This increasing protection with increasing mass addition demonstrates the importance of thermal capacitance in enhancing film cooling protection when increased thermal capacitance is not tied to increased penetration. The lower Reynolds number case shows a substantial reduction in effectiveness below the level of the higher Reynolds number case for the same velocity ratio (0.42). Although some influence of Reynolds number might be expected, the level of reduction is more substantial than expected. This large difference is likely due to the state of the boundary layer developing upstream in the low-Reynolds-number case, which would be expected to be thicker relative to the hole diameter. The *Handbook of Heat Transfer Applications* suggests that film cooling performance for low blowing rates can deteriorate above a δ_1/D of about 0.25. As noted previously, the δ_1/D for the high-Reynolds-number case was found to be about 0.21 and the δ_1/D for the low-Reynolds-number case would be expected to be higher.

Data taken at three velocity ratios (0.58, 0.42, and 0.31) are compared in Fig. 6 for the high turbulence case. Similar to the single row data, the staggered row data show higher near-hole peaks in effectiveness and lower levels downstream than the low turbulence data. These data do show larger relative variations in effectiveness level with blowing than the single row data, indicating again that for the higher velocity ratios shown here, the staggered row configuration increases jet blockage, causing a reduced penetration and enhancing the level of effectiveness. Unlike the low turbulence level case, the lower Reynolds number shows only a small reduction below the comparable higher Reynolds number case. This smaller difference in effectiveness suggests a smaller difference between the developing boundary layers for the two Reynolds numbers with the high turbulence.

Pressure Surface Film Cooling Results. The pressure surface of a typical first vane is subjected to a high level of favorable acceleration. Due to the high inlet turbulence levels generated by the combustor and the low convective velocities along the pressure surface, film cooling is typically subjected to very high levels of turbulence. The C3X vane used in this study has an acceleration parameter, K, of 11.0 E-06 at the point of injection diminishing to a K of 2.6E-06 at an X/D of 60. The low convective velocities along the C3X produce a free-stream turbulence level of over 16 percent at the point of injection for the high turbulence case.

The influence of acceleration on film cooling effectiveness can be examined by comparing the effectiveness distribution along the pressure surface with the distribution from the suction surface at the same velocity ratio. Figure 7 presents adiabatic effectiveness distributions for three velocity ratios and two Reynolds numbers for a single row of holes on the pressure side at the low turbulence condition along with a suction surface distribution for comparison. Comparing the effectiveness distributions for the pressure and suction surface for a velocity ratio of 0.5 shows a substantial contrast. In the near-hole region, the

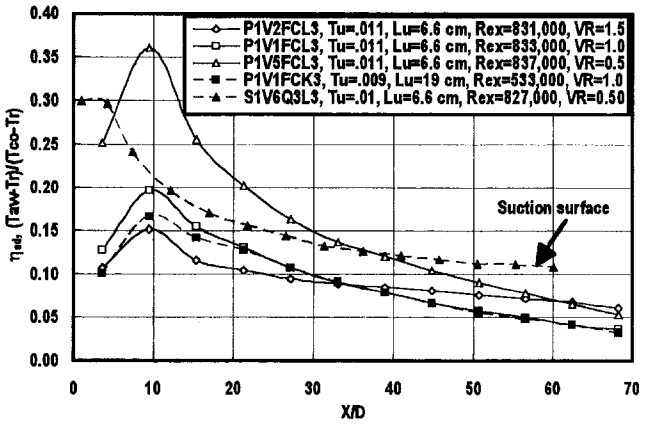

Fig. 7 Comparison of *VR* and Re_{ex} effects on adiabatic effectiveness, 1 row, 30 deg pressure surface holes, low turbulence, *DR* = 0.94

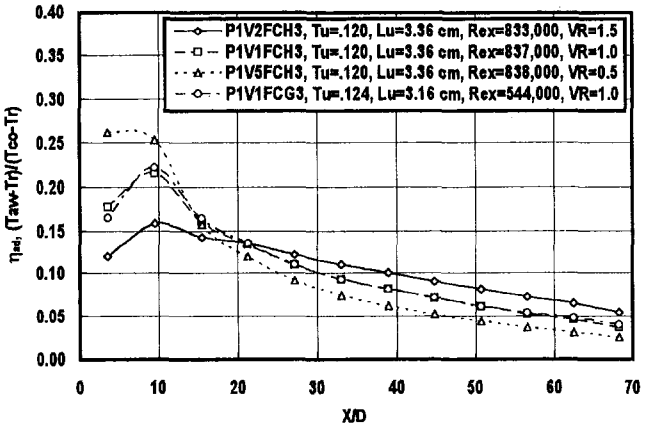

Fig. 8 Comparison of VR and Re_{ex} effects on adiabatic effectiveness, 1 row, 30 deg pressure surface holes, high turbulence, DR = 0.94

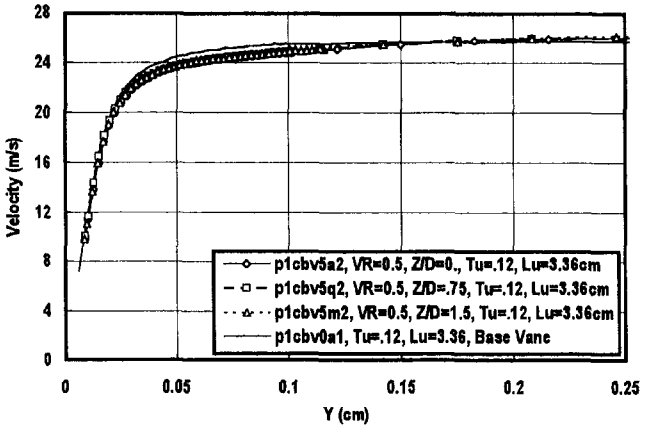

Fig. 10 Spanwise comparison of pressure surface velocity profiles with 1 row of 30 deg holes, high turbulence, X/D = 9, VR = 0.5, P/D = 3

pressure surface data displays a peak substantially above the suction surface data. However, downstream, the suction surface maintains a much better level of effectiveness. As noted previously, Teekaram et al. (1991) found respective increases of about 50, 30, and 24 percent at X/D's of 2, 8, and 14 for accelerations ranging from a K of 2.62E-06 at the injection point to 1.05E-06 at an X/d of 14. Similarly, Schmidt and Bogard (1995) found substantial increases in near hole in laterally averaged effectiveness with favorable pressure gradient due to an increased spreading of the coolant jet near the hole for low velocity ratios. The low effectiveness level of the first point at an X/D of 3.7 could be caused by increased uncertainties associated with high rates of conduction in the close proximity of the holes which are not present over the remainder of the surface. The data for the velocity ratios of 1.0 and 1.5 show how the increased jet penetration with higher velocity ratios reduces the effectiveness level.

Pressure surface effectiveness data for the single-row high-turbulence case are shown in Fig. 8. Effectiveness levels for a velocity ratio of 0.5 are substantially reduced below those for the low-turbulence case. The high turbulence apparently promotes rapid reduction in film cooling coverage. As previously noted, Bons et al. (1996) found that high-level turbulence substantially reduced effectiveness at moderate velocity ratios, having an increased effect with increasing turbulence levels and downstream distance. These data suggest that the reduced level of film cooling coverage on a blade pressure surface reported by Dring et al. (1980) and Takeishi et al. (1992) is due to a combination of the turbulence and the streamwise acceleration. The effectiveness levels produced at the higher velocity ratios show surprising similarity between the low and high-turbulence cases suggesting that the jet penetration associated with the higher velocity ratios is the dominate influence. Interestingly, the near-hole level of effectiveness for the high-turbulence case is slightly higher than for the low-turbulence case indicating the turbulence actually enhances coverage of separating jets by mixing coolant down to the surface.

The dramatic influence of turbulence on mixing can be clearly shown by a comparison between velocity profiles taken at an X/D of 9 for the high and low inlet turbulence conditions. Figure 9 shows three velocity profiles taken with the low inlet turbulence at spanwise locations directly downstream from a coolant jet (Z/D = 0.), in between two coolant jets (Z/D = 1.5), and in between these two locations (Z/D = 0.75). The profile downstream from the jet clearly shows the velocity deficit caused by the injection of jet fluid at a velocity ratio of 0.5. The two other profiles, which are outside the jet, are comparable to the base vane profile. The high turbulence case shows a marked contrast to Fig. 9. Figure 10 shows profiles at the same three spanwise positions compared to the base vane profile for the high turbulence case. The spanwise uniformity in velocity is quite good but perhaps should not be surprising in light of the findings of Bons et al. (1996), who demonstrated spanwise uniformity in effectiveness by an X/D of 10 for their 17 percent turbulence case.

Effectiveness data for two rows of holes on the pressure surface at the low and high-turbulence condition are compared with data from one row superposed in Fig. 11 for a velocity ratio of 0.5. For the high-turbulence condition, the superposed

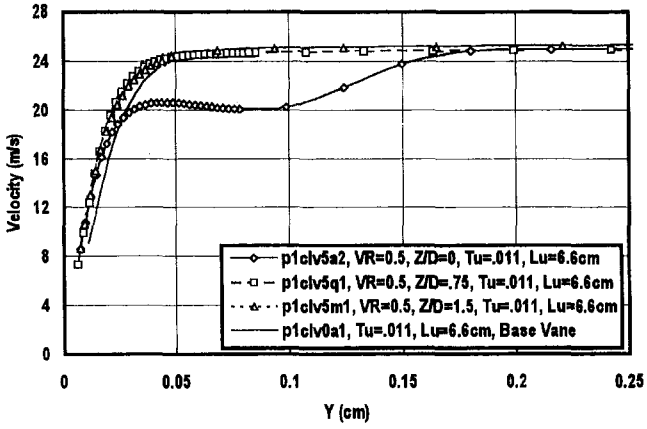

Fig. 9 Spanwise comparison of pressure surface velocity profiles with 1 row of 30 deg holes, low turbulence, X/D = 9, VR = 0.5, P/D = 3

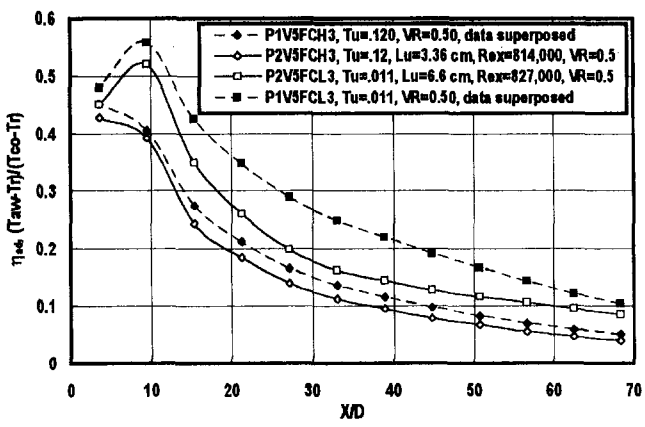

Fig. 11 Superposed single row and double row data, pressure surface, low and high turbulence, DR = 0.94, VR = 0.5

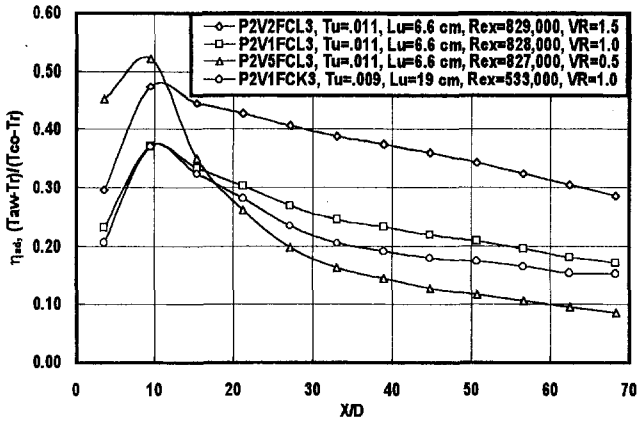

Fig. 12 Comparison of *VR* and Re_{ex} effects on adiabatic effectiveness, 2 rows, 30 deg pressure surface holes, low turbulence, *DR* = 0.94

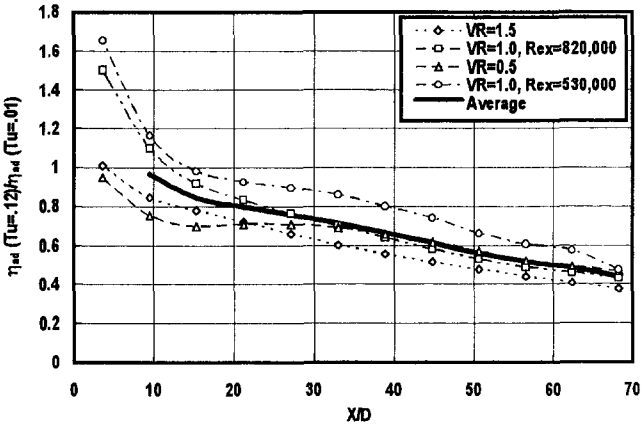

Fig. 14 Influence of turbulence on relative level of pressure surface adiabatic effectiveness, 2 rows, 30 deg holes, *DR* = 0.94, *P/D* = 3.0

data compare reasonably well with the double row data, falling an average of 0.02 above the double row data. However, the comparison between double row data and superposed single row data does not agree as well for the low-turbulence data. Turbulence profiles for the double row data (reported by Ames, 1996) show a substantial increase in the level above the single row data due to the development of shear layers around the low-momentum injected fluid. Speculation would be that this enhanced level of turbulence results in a more rapid mixing with the accompanying more rapid decay rate in effectiveness. In the near-hole region, the comparison between the double row and the superposed data is much better.

A double row of staggered holes causes a much higher blockage than a single row of holes. For moderate velocity ratios (VR = 1.0 and 1.5), this blockage effect reduces penetration enough to produce good levels of film cooling protection for the low-turbulence case as shown in Fig. 12. For the higher velocity ratios the effectiveness levels for a double row are substantially higher than values superposed from the single row data of Fig. 7 (not shown). Double row data for the high-turbulence case are compared over the three velocity ratios in Fig. 13. For the higher velocity ratio data, the double row arrangement enhances film cooling coverage in the near hole region above levels estimated from Fig. 8 data superposed (not shown). However, the turbulence quickly mixes away this advantage. Overall, the effectiveness levels produced by the high-turbulence condition are substantially lower than the low turbulence data. Figure 14 plots the ratio of film cooling effectiveness for the high-turbulence condition divided by the comparable value from the respective low-turbulence case as a function of X/D. Except for the first data point, the ratios show a steady monotonic decay graphically demonstrating the influence of turbulence in steadily mixing away film cooling protection. The ratios average 0.45 at the furthest downstream station quantifying, in an average sense, the aggressive nature of turbulent mixing.

Showerhead Film Cooling Results. The showerhead array consists of five staggered rows of 20 deg spanwise slanted holes, four of which are on the suction side of the calculated stagnation point. The pitch-to-diameter of the holes is 6.4 and the streamwise spacing is 3.85 diameters. The first row of 0.132-cm-dia holes is 0.254 cm from the predicted stagnation point and the resulting velocity ratio is quite sensitive to the equivalent pressure ratio $(P_c - P_{t,in})/(P_{t,in} - P_{s,ex})$. The free-stream velocity at the first row of holes is about 11 percent of the exit velocity while the velocity at the last row is 60 percent of the exit value. Effectiveness distributions taken downstream from the showerhead array on the suction surface are shown for the three equivalent pressure ratios and extra Reynolds number in Fig. 15 for the low turbulence condition. The four rows of holes produce a good level of cooling effectiveness, even for this relatively low (0.94) density ratio. The 20 deg holes of the showerhead array reduce the penetration of the jets and the spanwise orientation presents a broader cross section to the flow enhancing blockage and further reducing jet penetration. The levels of all four distributions are closely comparable due to the insensitivity of the later rows to changes in pressure ratio due to the relatively high free-stream velocity. Only the highest pressure ratio produces a noticeable reduction in the near-hole

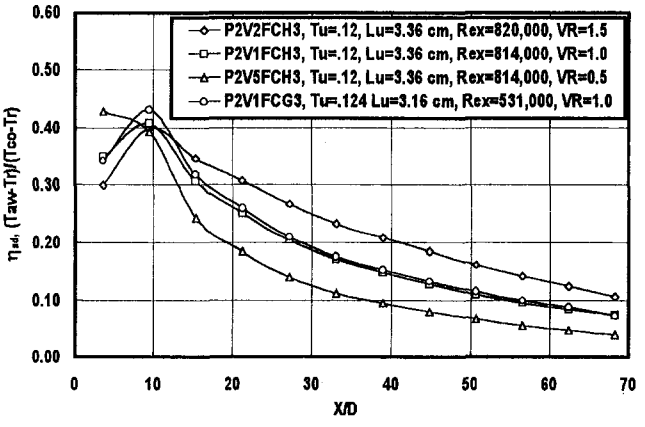

Fig. 13 Comparison of *VR* and Re_{ex} effects on adiabatic effectiveness, 2 rows, 30 deg pressure surface holes, high turbulence, *DR* = 0.94

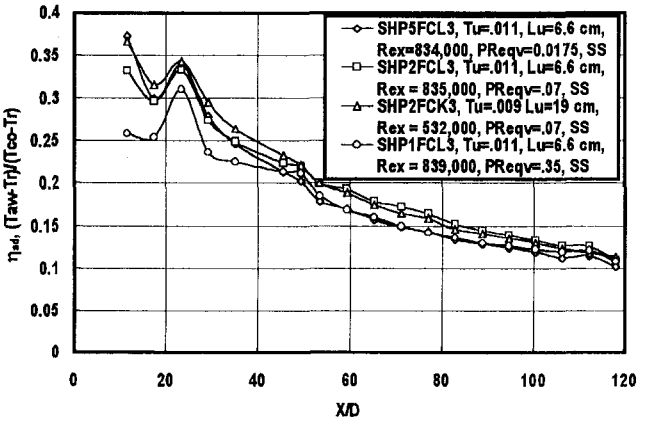

Fig. 15 Comparison of PR_{eqv} and Re_{ex} effects on showerhead adiabatic effectiveness, suction surface, low turbulence, *DR* = 0.94

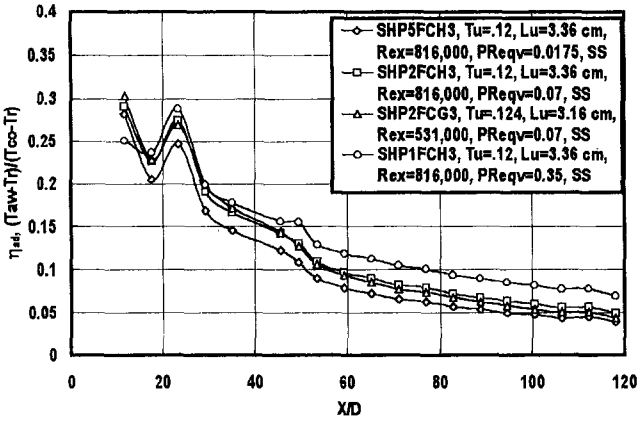

Fig. 16 Comparison of PR_{eqv} and Re_{ex} effects on showerhead adiabatic effectiveness, suction surface, high turbulence, DR = 0.94

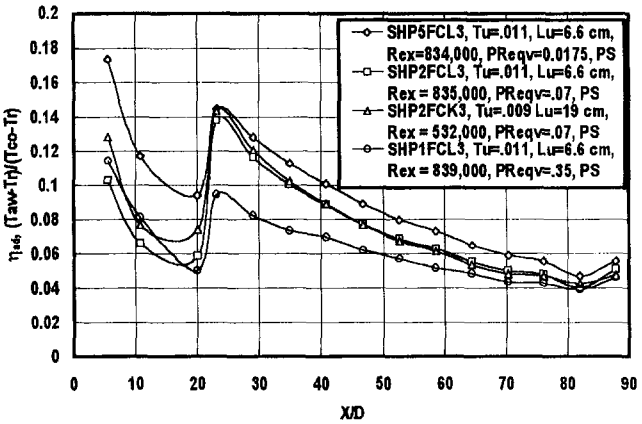

Fig. 18 Comparison of PR_{ev} and Re_{ex} effects on showerhead adiabatic effectiveness, pressure surface, low turbulence, DR = 0.94

effectiveness, presumably due to more penetration of the coolant jet. One interesting feature of the distributions is the abrupt variation in the level of effectiveness. These streamwise variations may be due to the pairing of jets similar to the observations of Gartshore et al. (1993).

The level of effectiveness produced by the showerhead array on the suction surface for the high-turbulence condition is substantially reduced compared to the low turbulence case. Figure 16 compares the high turbulence effectiveness distributions for the three equivalent pressure ratios and the extra Reynolds number. The relatively high local level of turbulence in the region of the array apparently is responsible for a significant reduction of effectiveness due to enhanced mixing. For the high-turbulence case the downstream level of effectiveness scales noticeably with equivalent pressure ratio, indicating the flow rate of coolant sets downstream effectiveness levels when relatively high levels of mixing are present. Figure 17 plots the ratio of film cooling effectiveness for the high-turbulence condition divided by the comparable value from the respective low-turbulence case as a function of X/D. All data sets generally show a monotonic decrease with surface distance, indicating that the turbulence actively mixes away cooling protection as the flow develops downstream. The decay rate is noticeably higher in the near-hole region due to the higher local level of turbulence. The data for the highest equivalent pressure ratio are noticeably less sensitive to the turbulence than the lower pressure ratios. This insensitivity to turbulence is similar to the results of the higher velocity ratio data for one row of holes on the pressure surface.

Only one of the showerhead rows is downstream of the predicted stagnation point on the pressure surface and provides little in the way of cooling protection. Figure 18 compares the low-turbulence effectiveness distributions for the three equivalent pressure ratios and the extra Reynolds number on the pressure surface. The relative level of effectiveness is quite sensitive to the equivalent pressure ratio due to the low convective velocity and generally decreases with increasing pressure ratio. Streamwise variations in effectiveness due to the sparse array and spanwise injection are also clearly present. Figure 19 gives similar comparisons for the high-turbulence case. Similar to the suction surface, the high-turbulence effectiveness distributions are much lower than their low-turbulence counterparts. The structural effect of the jets passing the measurement plane is also present in the data. The trend of higher effectiveness levels with lower pressure ratios is reversed with the presence of the high turbulence level. This result is similar to the suction surface showerhead data for the high turbulence level. Apparently in the stagnation region, the turbulent mixing is so active that the dilution effect of increased coolant flow rate is more important than the increased coolant penetration with higher velocity ratios.

Conclusions

The present study demonstrated the important influences of turbulence level, pressure gradients, velocity ratio, and one row versus two staggered rows on vane cooling effectiveness distributions. The level of inlet turbulence was found to have a substantial influence on pressure surface and showerhead effectiveness distributions where the local level of turbulence can be

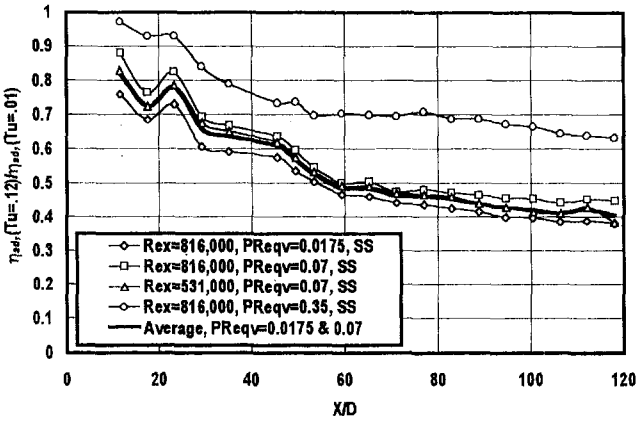

Fig. 17 Influence of turbulence on relative level of suction surface adiabatic effectiveness for showerhead array, DR = 0.94

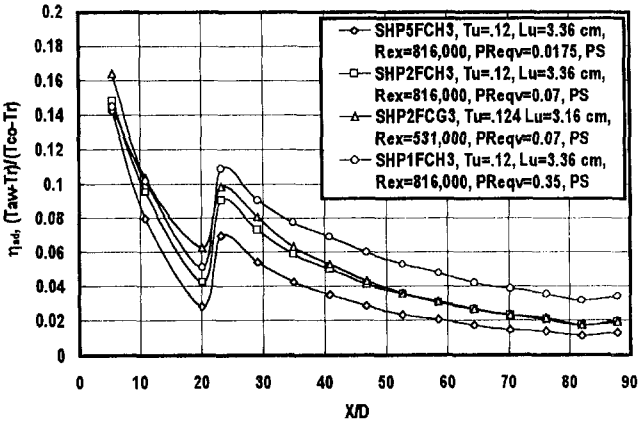

Fig. 19 Comparison of PR_{eqv} and Re_{ex} effects on showerhead adiabatic effectiveness, pressure surface, high turbulence, DR = 0.94

quite high. Turbulence had a noticeable but less pronounced influence on the suction surface where local levels of turbulence were lower due to higher velocities. For low velocity ratios, the strong favorable pressure gradients on the pressure surface generally enhanced the near-hole effectiveness levels well above the suction surface levels for the low-turbulence case, but as convective velocities rose the level of effectiveness decreased sharply. On the suction surface where typical velocity ratios are below 0.6, effectiveness levels were generally high and increased with increasing velocity ratio in the downstream region. At the lower velocity ratios with limited penetration, superposed data from one row of holes accurately predicted the level of effectiveness for two staggered rows. At the higher velocity ratios, the benefit to effectiveness of the reduced penetration due to the increased blockage of staggered rows was clearly evident. Staggered rows were very beneficial to effectiveness distributions on the pressure surface for the higher velocity ratios and the low-turbulence condition. However, at the high turbulence level, two staggered rows only produced a moderate increase in effectiveness over levels of effectiveness estimated from one row of data superposed.

Acknowledgments

This research was conducted under the support of NASA Lewis Research Center at Allison Engine Company Research Laboratories, where the author was previously employed. The author is grateful for the contributions of Steve LePera and Frank "Scott" Carter who aided in the acquisition of these data and were supported under the AGTSR Summer Fellowship Program. The author is also grateful to Dr. John Weaver for reading this document and offering many helpful suggestions.

References

Abhari, R. S., and Epstein, A. H., 1994, "An experimental study of film cooling in a rotating transonic turbine," ASME JOURNAL OF TURBOMACHINERY, Vol. 116, p. 63.

Ames, F. E., 1996, "Experimental study of vane heat transfer and film cooling at elevated levels of turbulence," NASA CR 198525.

Bons, J. P., MacArthur, C. D., and Rivir, R. B., 1996, "The effect of high freestream turbulence on film cooling effectiveness," ASME JOURNAL OF TURBOMACHINERY, Vol. 118, pp. 814–825.

Dring, R. P., Blair, M. F., and Joslyn, H. D., 1980, "An experimental investigation of film cooling on a turbine rotor blade," ASME *Journal of Engineering for Power,* Vol. 102, No. 1, p. 88.

Gartshore, I. S., Salcudean, M., Barnea, Y., Zhang, K., and Aghadsi, F., 1993, "Some effects of coolant density on film cooling effectiveness," ASME Paper No. 93-GT-76.

L'Ecuyer, M. R., and Soechting, F. O., 1985, "A model for correlating flat plate film cooling effectiveness for rows of round holes," *Heat Transfer and Cooling in Gas Turbines: AGARD Conference Proceedings No. 390.*

Liess, C., 1975, "Experimental investigation of film cooling with ejection from a row of holes for the application to gas turbine blades," ASME *Journal of Engineering for Power,* Vol. 97., p. 21.

Mehendale, A. B., Han, J. C., Ou, S., and Lee, C. P., 1994, "Unsteady wake over a linear turbine blade cascade with air and CO_2 film injection: Part II—Effect on film effectiveness and heat transfer distributions," ASME JOURNAL OF TURBOMACHINERY, Vol. 116, p. 730.

Mehendale, A. B., and Han, J. C., 1992, "Influence of high mainstream turbulence on leading edge film cooling heat transfer," ASME JOURNAL OF TURBOMACHINERY, Vol. 114, p. 707.

Moffat, R. J., 1988, "Describing the uncertainties in experimental results," *Experimental Thermal and Fluid Science,* Vol. 1, p. 3.

Nirmalan, N. V., and Hylton, L. D., 1990, "An experimental study of turbine vane heat transfer with leading edge and downstream film cooling," ASME JOURNAL OF TURBOMACHINERY, Vol. 112, p. 477.

Pedersen, D. R., Eckert, E. R. G., and Goldstein, R. J., 1977, "Film cooling with large density differences between the mainstream and the secondary fluid measured by the heat-mass transfer analogy," ASME *Journal of Heat Transfer,* Vol. 99, p. 620.

Rohsenow, Hartnett, and Ganic, 1985, *Handbook of Heat Transfer Applications,* 2nd ed., McGraw-Hill, New York.

Schmidt, D. L., and Bogard, D. G., 1995, "Pressure gradient effects on film cooling," ASME Paper No. 95-GT-18.

Takeishi, K., Aoki, S., Sato, T., and Tsukagoshi, K., 1992, "Film cooling on a gas turbine rotor blade," ASME JOURNAL OF TURBOMACHINERY, Vol. 114, pp. 828–834.

Teekaram, A. J. H., Forth, C. J. P., and Jones, T. V., 1991, "Film cooling in the presence of mainstream pressure gradients," ASME JOURNAL OF TURBOMACHINERY, Vol. 113, p. 484.

White, F. M., 1974, *Viscous Fluid Flow,* McGraw-Hill, New York.

Effects of Very High Free-Stream Turbulence on the Jet–Mainstream Interaction in a Film Cooling Flow

A. Kohli[1]

D. G. Bogard

Department of Mechanical Engineering,
The University of Texas at Austin,
Austin, TX 78712

Dispersion of coolant jets in a film cooling flow field is the result of a highly complex interaction between the film cooling jets and the mainstream. Understanding this complex interaction, particularly near the injection location, is critical for improving the predictive capabilities of existing film cooling models, especially when very high free-stream turbulence levels exist. This study uses a high-frequency-response temperature sensor to investigate the mean and fluctuating thermal field of a film cooling flow for two vastly different free-stream turbulence levels (0.5 and 20 percent). The high-frequency-response temperature sensor provides new information about the film cooling flow in terms of actual rms levels (Θ'), probability density functions (pdf's), and frequency spectra of the thermal field. Results are presented for both free-stream conditions using round holes inclined at 35 deg, at a momentum flux ratio of I = 0.156 and density ratio of DR = 1.05. The mean thermal field results show severe degradation of the film cooling jet occurs with very high free-stream turbulence levels. Temperature rms results indicate levels as high as Θ' = 0.25 exist at the jet–mainstream interface. More information is provided by the temperature pdf's, which are able to identify differences in the jet–mainstream interaction for the two free-stream conditions. With small free-stream turbulence, strong intermittent flow structures generated at the jet–mainstream interface disperse the jet by moving hot mainstream fluid into the coolant core, and ejecting coolant fluid into the mainstream. When the free stream has large scales and very high turbulence levels, the jet–mainstream interface is obliterated by large-scale turbulent structures originating from the free stream, which completely penetrate the coolant jet, causing very rapid dispersion of the film cooling jet.

Introduction

Film cooling of gas turbine airfoils is achieved by injecting relatively cold air through discrete holes angled to the surface such that the coolant remains attached to the surface and acts as a barrier to the hot mainstream gases. The most effective cooling is achieved when the coolant jet remains coherent and mixing with the mainstream is minimized. However, the interaction of the coolant jet with the mainstream causes a strong turbulent mixing and dispersion of the coolant jet immediately downstream of the hole. The nature of this mixing process is particularly apparent from measurements of the high-frequency temperature fluctuations as described in the earlier study in our laboratory (Kohli and Bogard, 1998). In this study, the mixing and dispersion process was found to be dominated by large-scale turbulent structures generated at the shear region between the coolant jet and the mainstream. These turbulent structures were found to promote mixing by causing penetration of free-stream fluid into the coolant, and by causing ejection of coolant fluid into the free stream. Domination of the turbulent mixing process by these large-scale structures was speculated to account for the lack of success of conventional turbulence modeling techniques in predicting the rapid dispersion of coolant jets near the hole.

Although valuable insight into the coolant jet dispersion process was gained from the Kohli and Bogard (1998) study, these experiments were done with low free-stream turbulence levels, as has predominantly been done in laboratory simulations of film cooling. Actual turbine airfoils, however, are subjected to very high free-stream turbulence levels, which can be in excess of Tu = 20 percent. Very few studies have investigated the effect of realistic free-stream turbulence levels on adiabatic effectiveness. A recent study on the effect of high free-stream turbulence on film cooling with four different turbulence levels ranging from Tu = 0.9 up to 17.4 percent was done by Bons et al. (1994). Grids were used to generate the lower turbulence levels and jets in crossflow for the higher turbulence levels. Experiments were conducted on round holes inclined at 35 deg, with a lateral spacing of P/D = 3, at a density ratio of DR = 0.95. This study found that, for low blowing ratios ($0.55 < M < 0.95$), the centerline effectiveness decreased as the free-stream turbulence level increased, by as much as 70 percent for Tu = 17 percent. While the increased mixing caused by free-stream turbulence reduced the centerline effectiveness, midpitch effectiveness was increased, which could be attributed to an increase in the lateral spread of the jets. Similar conclusions were reached in our laboratory as described by Schmidt and Bogard (1996), who studied the effect of free-stream turbulence (Tu = 0.3, 10, and 17 percent) on cooling effectiveness for round holes inclined at 30 deg to the surface and with a hole spacing of P/D = 6.5. This study concluded that for attached jets, even though the lateral spreading improved, the laterally averaged effectiveness decreased substantially with high free-stream turbulence levels. It is clear that the presence of high

[1] Present address: Pratt & Whitney, 400 Main St., M/S 169-02, East Hartford, CT 06108.

Contributed by the International Gas Turbine Institute and presented at the 42nd International Gas Turbine and Aeroengine Congress and Exhibition, Orlando, Florida, June 2–5, 1997. Manuscript received International Gas Turbine Institute February 1997. Paper No. 97-GT-121. Associate Technical Editor: H. A. Kidd.

free-stream turbulence affects the jets significantly; therefore, the jet–mainstream interaction in this case should be completely different compared to that with low free-stream turbulence.

The goal of this study was to explore details of the interaction between the coolant jet and mainstream flow with very high free-stream turbulence levels, and to determine the mechanisms causing greatly increased dispersion of the coolant jet near the hole. These details were obtained using temperature measurements with a high-frequency-response temperature sensor. Besides mean and rms temperature statistics, pdf's (probability density function) and frequency spectra of the fluctuating temperature field are presented to provide insight into the mechanisms of turbulent mixing and dispersion. Understanding this complex interaction, especially for the case of very high free-stream turbulence levels, is essential for improving the predictive capabilities of existing film cooling models. This is especially true near the injection location, where the current models are unable to make good predictions. Results from this study will also serve as benchmarks for large eddy simulations of film cooling flowfields.

Experimental Facilities and Techniques

The facilities and instrumentation used in this study have been described by Kohli and Bogard (1998), and only a brief description is given here. This study was performed in a recirculating boundary layer wind tunnel with a test section that was 0.13 m high, 0.6 m wide, and 1.8 m long. The wind tunnel was equipped with a unique turbulence generator, which used two opposing rows of jets in crossflow with the free stream to generate turbulence levels of about 20 percent near the injection location. Such high levels cannot be attained using traditional grid-generated turbulence. Development of the turbulence generator and characterization of the free-stream turbulence has been described in detail by Thole (1992) and Thole et al. (1994). The streamwise integral length scale was $\Lambda_x/D = 3$ for a free-stream turbulence level of about 20 percent, as reported in the study by Thole et al. (1994) using the same facility.

The free-stream velocity was fixed at $U_\infty = 10$ m/s for all the measurements. The approach boundary layer was tripped to ensure that it was turbulent, and for the low-turbulence case ($Tu = 0.5$ percent) had boundary layer parameters of $\mathrm{Re}_\theta = 420$, $\delta^*/D = 0.1$, and $H = 1.66$. The film cooling geometry used in this study consisted a single row of nine round holes inclined at 35 deg to the streamwise direction as shown in Fig. 1. The holes had a diameter of $D = 11.11$ mm spaced $P/D = 3$ apart and had a short development length of $L/D = 4$, similar to that found in actual gas turbines. To minimize conduction losses, the film cooling hole plate was constructed out of polystyrene foam (Styrofoam), which had a thickness of 25.4 mm.

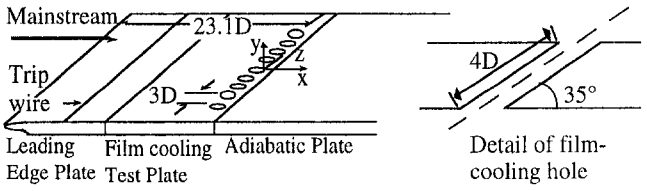

Fig. 1 Schematic of test section geometry

The downstream adiabatic plate comprised 12.7-mm-thick polystyrene foam glued on to a 12.7 mm fiberglass composite (Extren) sheet for structural rigidity. The operating condition for these holes was fixed at $I = 0.16$ based on the results of Schmidt et al. (1996) who showed that maximum effectiveness is expected at this momentum flux ratio for these holes.

A density ratio of $DR = 1.05$ was used for the current study. Although this density ratio is not representative of that in the actual turbine environment, Thole et al. (1992) showed that, for film cooling flows, similar thermal fields occur for a wide range of density ratios when the jet-to-mainstream momentum flux ratio (I) is matched. This was verified by Kohli and Bogard (1998) by comparing with results at $DR = 1.6$. Assuming that a similar scaling with momentum flux ratio holds with high-free-stream turbulence conditions, all measurements were made using a momentum flux ratio of $I = 0.16$ for the film cooling jets, with corresponding mass flux ratio of $M = 0.40$ and velocity ratio of $VR = 0.38$.

The high-frequency cold wire used for the mean and fluctuating temperature measurements in this study has been characterized in detail and the validation results presented by Kohli and Bogard (1998). As outlined in this study, an etched Wollaston wire of length $l = 0.6$ mm and diameter $d = 1.5$ μm was used for the temperature measurements. End effects were avoided by using a wire with $l/d = 400$, which is twice as large as the requirement recommended by Ligrani and Bradshaw (1987). In addition, a very low operating current of $i = 0.25$ mA was used to ensure negligible sensitivity to velocity. The frequency response of the cold wire was measured at 2.6 kHz using an electronic test outlined by Thole and Bogard (1994).

Thermal field measurements were made on the jet centerline at $x/D = -1.75$, -1, -0.5, 0, 1, 3, 6, and 10. The vertical measurement locations were typically, $y/D = 0.1$, 0.2, 0.3, 0.4, 0.5, 0.7, 1, 1.5, 2, 2.5, and 3. In addition to the profiles on the jet centerline, measurements in the span were made at $z/D = 0.2$, 0.4, 0.7, 1, and 1.5 at streamwise locations of $x/D = -0.5$, 0, 1, and 3. The wall temperatures for the mean temperature results presented in this study were extrapolated from measurements close to the wall. Typically the extrapolated wall tempera-

Nomenclature

d = diameter of cold wire
D = diameter of film cooling hole
DR = density ratio of jet to mainstream $= \rho_j/\rho_\infty$
E_T = one-dimensional temperature spectrum
f = frequency, Hz
H = shape factor $= \delta^*/\theta$
I = momentum flux ratio of jet to mainstream $= \rho_j U_j^2/\rho_\infty U_\infty^2$
l = active sensing length of cold wire
L = hole length
M = mass flux (blowing) ratio of jet to mainstream $= \rho_j U_j/\rho_\infty U_\infty$
P = hole spacing
pdf = probability density function, see Eq. (1)
rms = root mean square
Re_θ = Reynolds number $= U_\infty\theta/\nu$
T = temperature
T^2_{rms} = variance of temperature record
Tu = free-stream turbulence level defined as $(u^2_{\mathrm{rms}} + v^2_{\mathrm{rms}})^{1/2}/U_\infty$
U = mainstream velocity
x = streamwise distance from the downstream edge of holes
y = wall normal distance
z = spanwise distance measured from the centerline of holes
δ^* = displacement thickness
ρ = density
θ = momentum thickness
Θ = normalized temperature $= (T - T_\infty)/(T_j - T_\infty)$
Θ' = normalized rms temperature $= T'/(T_j - T_\infty)$
Λ_x = streamwise integral length scale of free-stream turbulence

Subscripts

j = jet
∞ = mainstream

Superscripts

$'$ = root mean square
$\bar{}$ = mean

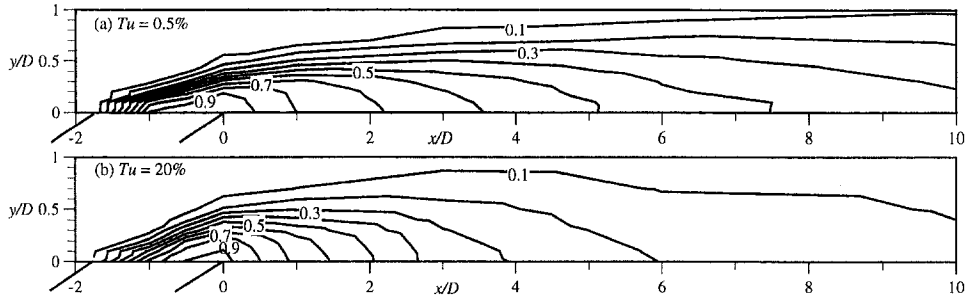

Fig. 2 Mean temperature contours ($\bar{\Theta}$) on the jet centerline for (*a*) *Tu* = 0.5 percent and (*b*) *Tu* = 20 percent. *M* = 0.4, *DR* = 1.05, *I* = 0.156.

tures were less than 0.3°C ($\Theta = 0.02$) different from the temperature measured at $y/D = 0.1$, and previous measurements in our laboratory comparing similar extrapolations with direct surface temperature measurements have verified the accuracy of this extrapolation. At each measurement location 81,920 data points were acquired over a duration of 16.4 s, which gave a mean temperature within ±0.1°C.

The temperature spectrum was calculated using fast Fourier transforms to operate on a data window consisting of 1024 points. This data window was advanced by half its size (512 points), resulting in 158 records that were averaged to obtain each spectrum. In order to avoid spectral leakage, a Hann windowing function was applied to the first and last 10 percent of each record. For the experiments done in this study, the mainstream and jet temperatures were maintained within ±0.1°C of their nominal values, which were $T_\infty = 30$°C and $T_j = 15$°C, respectively. Flow through the turbulence generator was cooled using liquid nitrogen and its temperature was maintained within ±0.1°C of the free-stream temperature. The mass flux ratio for the injection flow loop was held constant within $\delta M = \pm 1.8$ percent. The uncertainty in the thermal field results at a nominal value of $\Theta = 0.5$ due to variation in the mainstream and jet temperatures, and the uncertainty in the temperature measurement was $\delta\Theta = \pm 1.6$ percent.

Results and Discussion

As stated earlier, the motivation behind this study was to understand the changes introduced in the jet–mainstream interaction with the addition of very high free-stream turbulence levels, for a momentum flux ratio that was known to give optimum performance for the low free-stream turbulence case. The focus of this study was to identify the mechanisms causing reduction of effectiveness in each case. As the results for the low free-stream case have been presented and discussed at length by Kohli and Bogard (1998), they will mainly be used to provide a comparison for the results with very high free-stream turbulence.

Figures 2(*a*) and 2(*b*) show the normalized mean temperature contours, $\bar{\Theta}$, with low and very high free-stream turbulence levels, respectively. These contours clearly show that for $I = 0.156$, the coolant jets remain attached to the wall for both the low and high free-stream turbulence cases. The rapid decrease in $\bar{\Theta}$ levels for the high-intensity free-stream turbulence case indicates a much more rapid dispersion of the coolant, consistent with the rapid decrease in adiabatic effectiveness found in the earlier study by Schmidt and Bogard (1996). Over the hole, between $x/D = -1.75$ and 0, increased dispersion of the coolant by the high free-stream turbulence has already occurred so that the extent of the region with $\bar{\Theta} \geq 0.9$ is considerably smaller. With low free-stream turbulence the jet loses 50 percent of its effectiveness, i.e., $\bar{\Theta} \leq 0.5$, by $x/D = 5$. With the addition of high free-stream turbulence the dispersion rate is much larger, resulting in no levels greater than $\bar{\Theta} = 0.5$ beyond $x/D = 2$. Downstream of $x/D = 6$, there are no levels greater than $\bar{\Theta} = 0.2$ for the high free-stream turbulence case, suggesting that the dispersion of the jet is almost complete. Therefore, very high free-stream turbulence levels causes significant dispersion of the jet after it comes out of the hole leading to severe degradation in performance.

Comparison of lateral mean temperature contours for low and high free-stream are shown in Fig. 3 for streamwise positions of $x/D = 0$ and 3. At the downstream edge of the hole, $x/D = 0$, the mean temperature distributions are somewhat similar, although the region in which $\bar{\Theta} \geq 0.9$ is much smaller for the high-turbulence case. This latter results suggests that the highly turbulent free stream has significantly affected the core of the coolant jet over the hole. By $x/D = 3$ downstream, the core of the coolant jet for the low-turbulence case has a mean temperature of $\bar{\Theta} = 0.6$, but for the high-turbulence case it has reduced to $\bar{\Theta} = 0.3$ indicating a much greater dispersion of the coolant jet. However, the lateral and vertical extent of coolant with $\bar{\Theta} \geq 0.1$ is nominally the same for the two cases. Note that this result is not necessarily expected since the increased dispersion of the coolant might be expected to result in a larger area of coolant distribution for the high turbulence case. Evidently much of the dispersed coolant has been reduced to $\bar{\Theta} \leq 0.1$.

Contours of the normalized rms temperature, Θ', along the jet centerline for the low and high-turbulence cases are shown in Fig. 4. Note that the free stream is isothermal so that even for the high-turbulence case, the fluctuating temperature levels in the free stream are negligible. The Θ' contours are quite similar for the high and low free-stream turbulence cases with maximum levels of $\Theta' \geq 0.25$ occurring at the leading edge of the coolant jet. The two key differences between the high and low-turbulence cases are (1) a more extensive region where $\Theta' \geq 0.25$ and (2) a tendency for high Θ' to extend toward the

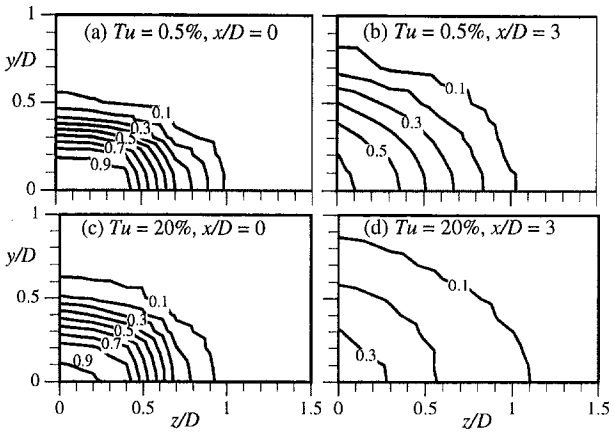

Fig. 3 Lateral mean temperature ($\bar{\Theta}$) contours at *x*/*D* = 0 and 3 for *Tu* = 0.5 percent (*a* and *b*), and *Tu* = 20 percent (*c* and *d*)

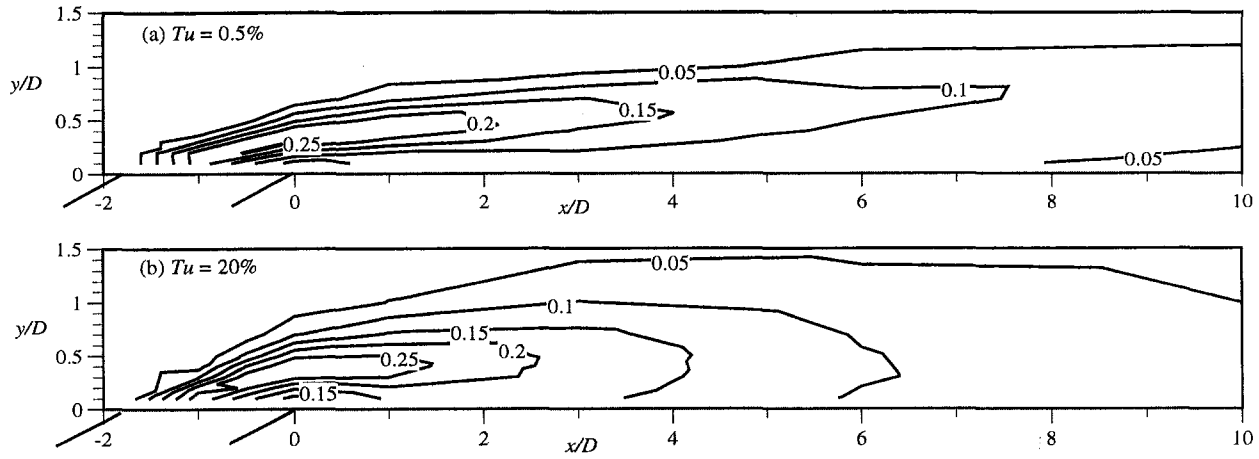

Fig. 4 The rms temperature contours (Θ') on the jet centerline for (*a*) *Tu* = 0.5 percent and (*b*) *Tu* = 20 percent. *M* = 0.4, *DR* = 1.05, *I* = 0.156.

wall. For the low-turbulence case there is a relatively narrow peak in Θ' away from the wall, which roughly corresponds to the region of maximum $\bar{\Theta}$ gradient at the outer edge of the coolant jet. A similar correspondence of peak Θ' levels with regions of maximum $\bar{\Theta}$ gradient does not occur for the high-turbulence case. Lateral cross sections of Θ' contours for the low and high-turbulence cases at $x/D = 0$ and 3 are shown in Fig. 5. Again at $x/D = 0$, contours of Θ' for the low and high-turbulence cases are similar, with the high-turbulence case having broader regions of high Θ' levels. Downstream at $x/D = 3$ there is a distinct difference between the low and high-turbulence cases with the high-turbulence cases having much broader regions of high Θ' levels with maximum levels extending toward the wall, while the low-turbulence case has a distinct maximum away from the wall. Reasons for these differences become evident from an examination of the probability density functions for Θ, which is discussed next.

In order to determine the mechanisms responsible for these large rms levels, probability density functions (pdf) were constructed for the fluctuating temperature data. The pdf of Θ at a point was obtained from the following equation:

$$\text{pdf}(\Theta_i) = N_i/(N\Delta\Theta) \quad i = 1, 2, \ldots \tag{1}$$

where N_i = number of occurrences of a Θ value in the interval $\Theta_i + \Delta\Theta$, and N = total number of Θ data points. The pdf gives more insight into the nature of the turbulent transport process by indicating the fraction of time that fluid of a certain temperature is passing through a point in the flow.

The jet dispersion and dilution process at the exit of the hole is evident from the series of pdf distributions taken across the jet at $z/D = 0$ and $x/D = 0$ as shown in Fig. 6. Both low and high-turbulence cases are presented to allow a direct comparison between the two, and $\bar{\Theta}$ at each height is listed in the accompanying table. The highest position shown is essentially the mainstream with $\Theta \approx 0$. Here the sharp peak in the pdf distribution indicates a very narrow range for Θ, which is merely an indication of the steady temperature of the mainstream. Close to the wall sharp peaks in the pdf 's indicate a steady stream of coolant fluid without incursion of higher temperature free-stream fluid. At increasing heights ($y/D = 0.2$ and 0.3), the presence of free-stream fluid can be seen from the tail extending toward warmer temperatures. Physically this may be interpreted as a

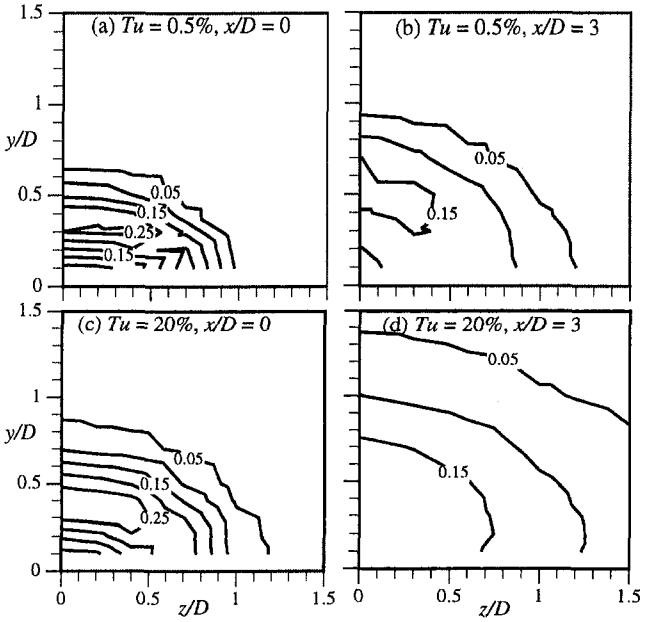

Fig. 5 Lateral rms temperature (Θ') contours at $x/D = 0$ and 3 for *Tu* = 0.5 percent (*a* and *b*), and *Tu* = 20 percent (*c* and *d*)

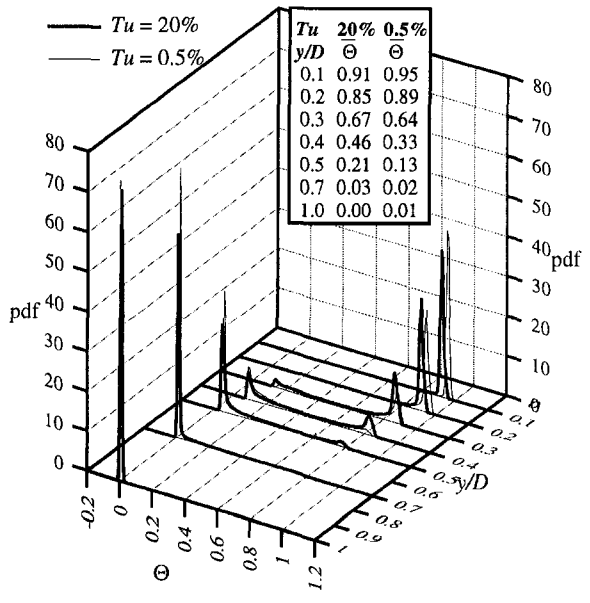

Fig. 6 Variation of the pdf 's with height on the jet centerline at x/D = 0, for *Tu* = 0.5 percent and *Tu* = 20 percent. Table indicates value of $\bar{\Theta}$ at each height.

region generally occupied by coolant flow, but intermittently elements of free-stream fluid are thrust into the coolant jet. For the high free-stream turbulence case there are double peaks for the pdf's at $y/D = 0.3$, 0.4, and 0.5. This double peak characteristic is more clearly evident in Fig. 7 in which the pdf's for low and high-turbulence cases at $y/D = 0.4$, $x/D = 0$, and $z/D = 0$ are shown. Large peaks at low and high temperatures in the Θ pdf for the high-turbulence case indicates an intermingling of distinct elements of fluid from the free stream and from the coolant jet. For the low-turbulence case, there is only a weak peak in the Θ pdf at low temperature, indicating that at this height the flow primarily consists of free-stream fluid with occasional ejections of coolant fluid into the free stream. Also note that the $\bar{\Theta}$ values indicate colder temperatures away from the wall for the case with very high free-stream turbulence. This is a direct result of the high free-stream turbulence ejecting coolant fluid far away from the wall.

By $x/D = 3$, there are distinct differences between the Θ pdf distributions for the low and high free-stream turbulence cases as shown in Fig. 8. Near the wall, i.e., $y/D = 0.1$ to 0.2, the Θ pdf's for the low-turbulence case have a single peak with almost Gaussian distribution indicating a somewhat homogeneous turbulent flow. At the same position for the high-turbulence case there is a very broad Θ pdf distribution with peaks at the low and high-temperature ends. Again, the double peak Θ pdf indicates that there is an intermingling of distinct elements of fluid from the free stream and from the coolant jet. For the high-turbulence case, distinct peaks at the high temperature end of the Θ pdf are present at all heights, even at $y/D = 0.1$, indicating distinct elements of free-stream fluid penetrating to the wall. Penetration of distinct elements of free-stream fluid is limited to a height of $y/D = 0.5$ for the low turbulence case.

Changes in the near-wall Θ pdf's with streamwise position, from $x/D = 0$ to 10, are shown in Fig. 9. These Θ pdf results are for a height of $y/D = 0.1$ on the jet centerline. Again there is a distinct difference between the Θ pdf's for low and high free-stream turbulence. For the high-turbulence case the pdf distribution is broader due to the continued presence of the distinct elements of free-stream fluid (evident from the sharp peak in the Θ pdf's at the high-temperature side) intermingled with the coolant fluid. In contrast, the low-turbulence case shows single peak, somewhat Gaussian pdf distributions indicating no incursions of elements of free-stream fluid for this case, even as far downstream as $x/D = 10$. Recall that the Θ' levels were significantly higher near the wall for the high free-stream turbulence case; these results show that the increased Θ' levels are due to penetration of free-stream eddies into the near-wall region.

Further insight into the nature of the coolant mixing and dispersion can be gained from an examination of the power spectral distribution of the temperature fluctuations. Normalized temperature spectra for a height near the wall and for varying streamwise positions are presented in Figs. 10(*a*) and 10(*b*) for low and high free-stream turbulence cases, respectively.

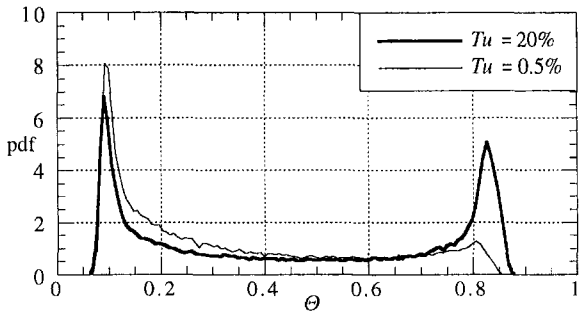

Fig. 7 The pdf's at a height of $y/D = 0.4$, on the jet centerline at $x/D = 0$ for $Tu = 0.5$ percent and $Tu = 20$ percent

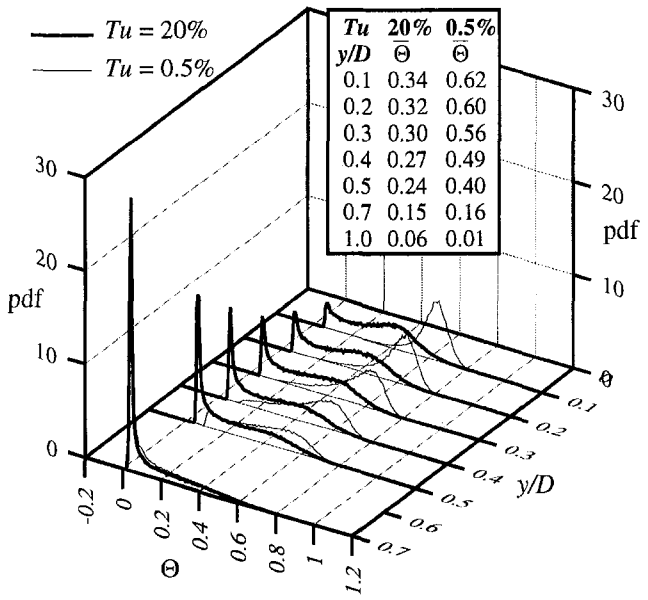

Fig. 8 Variation of the pdf's with height on the jet centerline at $x/D = 3$, for $Tu = 0.5$ percent and $Tu = 20$ percent. Table shows value of $\bar{\Theta}$ at each height.

Note that the energy density of the temperature fluctuations, E_T, is multiplied by frequency f to provide an amplitude proportional to the magnitude of the temperature fluctuations at each frequency. This amplitude is normalized with the total energy of the temperature fluctuations, i.e., T^2_{rms}. Also, the frequency scale has been normalized with a time scale based on the free-stream velocity and hole diameter, i.e., D/U_∞. At $x/D = -0.5$ and $x/D = 0$ the temperature spectra for the low and high-turbulence cases are similar with the peak in temperature fluctuations occurring at a normalized frequency a little less than $fD/U_\infty = 1$. Note that this normalized frequency corresponds to a length scale for the temperature fluctuations nominally equal to the hole diameter. Farther downstream there is a distinct difference between the temperature spectra for the low and high-turbulence cases. Temperature spectra for the low-turbulence

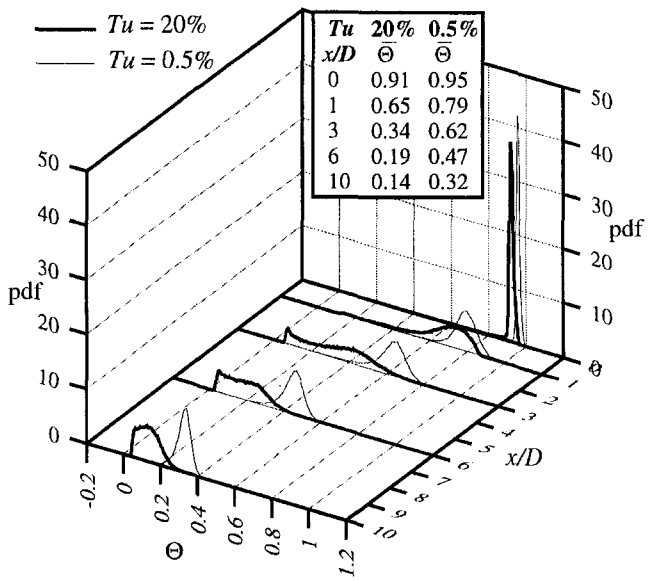

Fig. 9 Variation of pdf's downstream of the hole exit on the jet centerline at $y/D = 0.1$, for $Tu = 0.5$ percent and $Tu = 20$ percent. Table shows value of $\bar{\Theta}$ at each streamwise location.

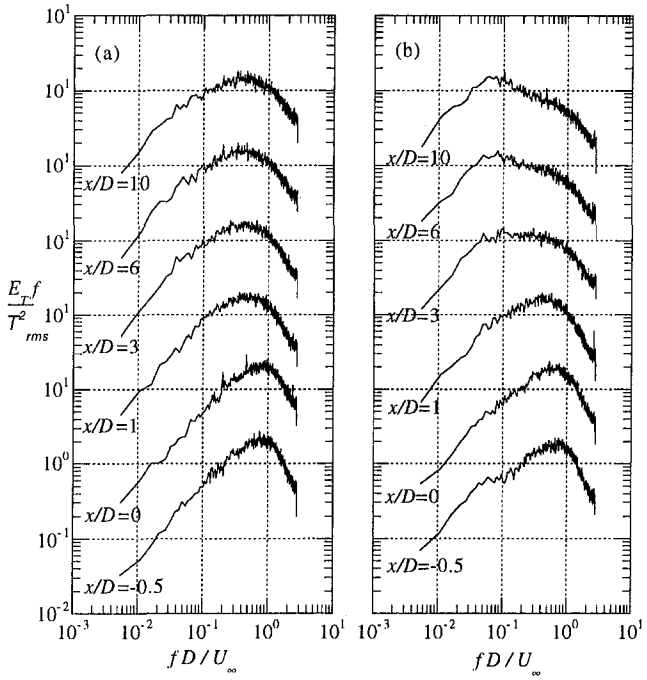

Fig. 10 Variation of normalized temperature spectra on the jet centerline with streamwise distance, at a height of y/D = 0.1 for (*a*) Tu = 0.5 percent and (*b*) Tu = 20 percent

case maintain peaks at a normalized frequency of fD/U_∞ = 0.5; whereas, for the high-turbulence case the peak in the temperature spectrum moves to a much lower frequency of fD/U_∞ = 0.08 by x/D = 10. This shift in the peak for the temperature spectra can be attributed to the dominance of free-stream fluctuation by x/D = 10 for the high-turbulence case. Recall that the integral length scale for the high free-stream turbulence was significantly larger than the hole diameter, Λ_x/D = 3, and this would lead to a decrease in the frequency of the temperature fluctuations.

Conceptual Model of Coolant Dispersion Process and Conclusions

The goal of this study was to obtain a better understanding of the physical mechanisms responsible for the rapid dispersion of film cooling jets at, and immediately downstream of the hole exit, particularly with regard to differences caused by low and high free-stream turbulence. Measurements were made at the same momentum flux ratio for low and high free-stream turbulence. This momentum flux ratio corresponded to that which gave the best adiabatic effectiveness near the injection location for low free-stream turbulence. Results from this study showed that the process of coolant dispersion is distinctly different for the low and high free-stream turbulence flows. For low free-stream turbulence, turbulent mixing and dispersion of the coolant are primarily due to large-scale turbulent structures generated by the large shear layer between the mainstream and the coolant jet. For high free-stream turbulence, the shear layer generated turbulence is quickly superseded by large-scale turbulent structures from the free stream, and free-stream fluid is thrust through the core of the coolant jet all the way to the wall. Consequently the turbulent mixing and dispersion process is more complicated with high free-stream turbulence, with an intermingling of distinct elements of free-stream and coolant fluid causing highly non-Gaussian temperature pdf distributions. This intermingling of free-stream and shear layer generated turbulent structures was also evident in the temperature spectra, which showed initial dominance of higher frequency turbulence associated with the shear layer, followed farther downstream by a dominance of low-frequency turbulent structures associated with the free-stream turbulence. These results have important implications with regard to modeling of the turbulent mixing and dispersion of the coolant jets. Turbulence dominated by large-scale turbulent structures, and involving intermingling of distinct turbulence regimes is very different from the homogeneous turbulence fields for which most current turbulence models have been developed, and will probably require development of specialized turbulence models to obtain reasonable predictions. Details of the turbulence statistics found in this study will also provide a valuable validation of large eddy simulations of the film cooling process.

Acknowledgments

The authors gratefully acknowledge AlliedSignal Aerospace Company for partial support of this research.

References

Bons, J. P., MacArthur, C. D., and Rivir, R. B., 1994, "The Effect of High Free-Stream Turbulence on Film Cooling Effectiveness," ASME JOURNAL OF TURBOMACHINERY, Vol. 118, pp. 814–825.

Kohli, A., and Bogard, D. G., 1998, "Fluctuating Thermal Field in the Near Hole Region for Film Cooling Flows," ASME JOURNAL OF TURBOMACHINERY, Vol. 120, pp. 86–91.

Ligrani, P. M., and Bradshaw, P., 1987, "Spatial Resolution and Measurements of Turbulence in the Viscous Sublayer Using Subminiature Hot-Wire Probes," *Experiments in Fluids,* Vol. 5, pp. 407–417.

Schmidt, D. L., and Bogard, D. G., 1996, "Effects of Freestream Turbulence and Surface Roughness on Film Cooling," ASME Paper No. 96-GT-462.

Schmidt, D. L., Sen, B., and Bogard, D. G., 1996, "Film Cooling With Compound Angle Holes: Adiabatic Effectiveness," ASME JOURNAL OF TURBOMACHINERY, Vol. 118, pp. 807–813.

Thole, K. A., 1992, "High Freestream Turbulence Effects on the Transport of Heat and Momentum," Ph.D. Dissertation, The University of Texas at Austin.

Thole, K. A., Sinha, A. K., Bogard, D. G., and Crawford, M. E., 1992, "Mean Temperature Measurements of Jets With a Crossflow for Gas Turbine Film Cooling Application," *Rotating Machinery Transport Phenomena,* J. H. Kim and W. J. Yang, eds., Hemisphere Pub. Corp., New York.

Thole, K. A., and Bogard, D. G., 1994, "Simultaneous Temperature and Velocity Measurements," *Meas. Sci. Technol.,* Vol. 5, pp. 435–439.

Thole, K. A., Bogard, D. G., and Whan-Tong, J. L., 1994, "Generating High Freestream Turbulence Levels," *Experiments in Fluids,* Vol. 17, pp. 375–380.

Measurements in Film Cooling Flows: Hole *L/D* and Turbulence Intensity Effects

S. W. Burd

R. W. Kaszeta

T. W. Simon

Heat Transfer Laboratory,
University of Minnesota,
Minneapolis, MN 55455

Hot-wire anemometry measurements of simulated film cooling are presented to document the influence of the free-stream turbulence intensity and film cooling hole length-to-diameter ratio on mean velocity and on turbulence intensity. Measurements are taken in the zone where the coolant and free-stream flows mix. Flow from one row of film cooling holes with a streamwise injection of 35 deg and no lateral injection and with a coolant-to-free-stream flow velocity ratio of 1.0 is investigated under free-stream turbulence levels of 0.5 and 12 percent. The coolant-to-free-stream density ratio is unity. Two length-to-diameter ratios for the film cooling holes, 2.3 and 7.0, are tested. The measurements document that under low free-stream turbulence conditions pronounced differences exist in the flowfield between L/D = 7.0 and 2.3. The differences between L/D cases are less prominent at high free-stream turbulence intensities. Generally, short-L/D injection results in "jetting" of the coolant farther into the free-stream flow and enhanced mixing. Other changes in the flowfield attributable to a rise in free-stream turbulence intensity to engine-representative conditions are documented.

Introduction

Film cooling is commonly used to avert distress and failure of turbine blades in gas turbine engines resulting from excessive operating temperatures. In film cooling, cool air is bled from the compressor stage, ducted to the internal chambers of the turbine blades, and discharged through small holes in the blade walls. This air provides a thin, cool, insulating blanket along the external surface of the turbine blade. The cooling effectiveness is dependent upon the approach flow turbulence; the film cooling flow temperature, velocity distribution, and turbulence; and the blade and film cooling hole geometries.

Film cooling literature is extensive. It concentrates primarily on surface and flowfield measurements. Surface measurements include film cooling effectiveness and heat transfer coefficient measurements, whereas flowfield measurements include mean velocity and turbulence intensity distributions and turbulent shear stress. Computational studies have shown advancements in algorithms, grid flexibility, and turbulence modeling. Continued modeling success, though, relies on experimental support.

Surface and flowfield measurements may be found in the literature for slot, transpiration, and single- or multiple-row injection configurations. Surface measurements are presented by Goldstein et al. (1968), Pedersen et al. (1977), Foster and Lampard (1980), and Forth and Jones (1988). Flowfield measurements include pitot probe mapping by Le Brocq et al. (1973) and Foster and Lampard (1980). Crabb et al. (1981) studied the hydrodynamics of a normal jet of $L/D = 30$ in crossflow using hot wires in the far field and laser-Doppler velocimetry in the near field. Andreopoulos and Rodi (1984) investigated the turbulence field for a normal jet in crossflow with $L/D = 12$, $DR = 1.0$, and $VR = 0.5$. They documented (1) skewing of the velocity toward the downstream edge of the hole exit and (2) flow disturbances created by the jet–crossflow interaction upstream of the hole exit and within the jet supply. Inclined jets were studied by Launder and York (1974), Kadotani and Goldstein (1979), Yoshida and Goldstein (1984), and Jubran and Brown (1985). Lee et al. (1994) presented three-dimensional mean velocity and vorticity distributions, accompanied by flow visualization, for 35 deg-inclined streamwise injection with $L/D = 50$ and free-stream turbulence intensity (FSTI) of 0.2 percent. They showed that a pair of bound vortices accompanied with a complex three-dimensional flow exists downstream of the jet exit, as with normal injection. All these studies were with large length-to-diameter ratios (ranging from 10 to 62), atypical of gas turbines. The benefit of a long L/D was that a fully developed, turbulent velocity exit profile was achieved. Goldstein et al. (1974) found no appreciable difference in effectiveness between an $L/D = 5.2$ and long injection lengths. Thus, the investigations of Jumper et al. (1991) ($L/D = 6$) and Ligrani et al. (1994) ($L/D = 8$) are in the long-L/D category.

Other researchers have elected to use shorter length-to-diameter ratios, which are more representative of turbines. Sinha et al. (1991) used a length-to-diameter ratio of 1.75 while Sen et al. (1996) and Schmidt et al. (1996) used $L/D = 4$. Similarly, $L/D = 3.5$ was used by Bons et al. (1996) and Pietrzyk et al. (1989, 1990) for studies of 35 deg streamwise injection.

The majority of these cases were conducted with FSTI <1 percent. Launder and York (1974) found no influence of 4 percent FSTI. Brown and Saluja (1979) and Brown and Minty (1975) found losses in cooling effectiveness for FSTI ranging from 2 to 8 percent. Bons et al. (1996) documented film cooling effectiveness with FSTI = 0.9, 6.5, 12, and 17.5 percent, several velocity ratios, and $L/D = 3.5$. High FSTI enhanced mixing, reduced film cooling effectiveness (by up to 70 percent) in the region directly downstream of the injection hole, and increased film cooling effectiveness 50–100 percent in the near-hole regions between holes. Flowfield measurements were presented by MacMullin et al. (1989) for FSTI in the range of 7 to 18 percent. Gogineni et al. (1996) used two-color particle image velocimetry to investigate velocity and vorticity fields in 35 deg, single-row injection with FSTI values from 1 to 17 percent. Wang et al. (1996) used three-wire anemometry to document the flowfield just downstream of injection for FSTI = 0.5 and 12 percent. Computed from the data were eddy viscosity in the lateral and wall-normal directions and the ratio of the two. This ratio documents the anisotropy of turbulent transport.

These studies demonstrate that film cooling is strongly dependent upon the FSTI. Measurements of combustor exit flows by Goebel et al. (1993) document levels of 8–12 percent.

Contributed by the Heat Transfer Division for publication in the JOURNAL OF TURBOMACHINERY. Manuscript received at ASME Headquarters September 1997. Associate Technical Editor: M. G. Dunn.

Computation includes a two-dimensional, parabolic model with low-Reynolds-number, $k-\epsilon$ turbulence by Tafti and Yavuzkurt (1988) and three-dimensional computations by Patankar and Spalding (1972) and Patankar et al. (1973). Bergeles et al. (1976, 1978) used the partially parabolic, three-dimensional procedure of Pratap and Spalding (1976) to predict discrete-hole cooling performance. Demuren and Rodi (1983) applied the locally elliptic procedure of Rodi and Srivatsa (1980) to allow computation at high blowing rates and later extended the study (Demuren et al., 1986). Leylek and Zerkle (1994) performed three-dimensional, Navier–Stokes computation and compared their results to the experiments of Pietrzyk et al. (1989, 1990) and Sinha et al. (1991). They found that film cooling exit flow includes counterrotating vortices and local jetting effects. They suggested that film cooling experiments with long L/D may be misleading. These computational works were performed using the $k-\epsilon$, two-equation turbulence model to estimate the Reynolds stress terms in the time-averaged momentum equations. Most computations assumed isotropy in that lateral eddy diffusivity was set equal to wall-normal eddy diffusivity. This was found to be unsatisfactory by Sathyamurthy and Patankar (1990). They showed improvements with a modification proposed by Bergeles et al. (1978). Wang et al. (1996) measured larger anisotropy than given by the Bergeles et al. modification. Recent computations at the University of Minnesota show further improvement with the Wang et al. values.

Over the years, researchers have restricted their test cases to a limited number of film cooling parameters. Although each has contributed to general understanding, differences in test and flow configurations make comparing results of one with another difficult. Specifically, no direct comparisons of the roles of L/D and turbulence intensity can be clearly made for they were often conducted in separate facilities and under different conditions. In this paper, the results of an experimental study of the effects of both the film cooling hole length-to-diameter ratio and FSTI on the flowfield zone where the coolant and free-stream flows mix are presented, all from a common facility. Mean velocity and local turbulence intensity distributions are presented for planes that are normal to the flow at $x/D = 2.5$ downstream of injection and measurements at $x/D = 5.0$ are discussed. Two L/D values (7.0 and 2.3) and two FSTI levels (0.5 and 12 percent), with $VR = 1.0$, are presented. The focus of the current program is on the differences between long and short L/D delivery and between low and high FSTI.

Experimental Test Facility

High-Turbulence Free-Stream Facility. The high-turbulence free-stream facility is a small, blown-type wind tunnel that simulates the flow of a gas turbine combustor. The facility is described by Wang et al. (1996). The measured free-stream turbulence is nearly isotropic at the 68.6 cm × 12.7 cm nozzle exit (Fig. 1) with an intensity, FSTI, of 12 percent. With decay, the FSTI in the regions where measurements are taken is in the range of 11–11.5 percent. The FSTI level is characteristic of flow exiting the combustor stage in actual gas turbine engines (Goebel et al., 1993). The exit-plane turbulence intensity and mean velocity are uniform to within 2 percent of their mean values. The integral length scale calculated from a u' power spectrum is 7.7 cm (Hinze, 1975).

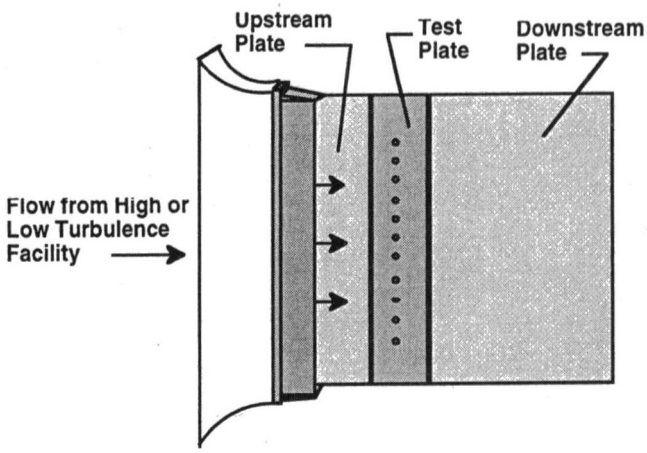

Fig. 1 Test section

Low-Turbulence Free-Stream Facility. The low-turbulence free-stream facility is also a blown-type wind tunnel. This is a standard configuration with a fan, screens, a setting chamber, and a 6.4:1 area-reduction nozzle of exit area 68.6 cm × 12.7 cm (Fig. 1). Measured turbulence intensity is 0.5 percent, reaching closer to 1.0 percent in the region downstream of injection due to some unsteadiness driven by the external shear layer. Mean velocity is uniform within 2 percent over the core of the nozzle exit.

Test Section. The test section (Fig. 1) consists of an upstream plate (25.4 cm × 68.6 cm), the test plate (15.2 cm × 68.6 cm), a downstream plate (91 cm × 68.6 cm), and the film coolant supply system. There is a single row of eleven film cooling holes distributed uniformly across the test plate. Film cooling flow is injected at an angle of 35 deg in the streamwise direction with the film cooling holes machined to a diameter of

Nomenclature

D = diameter of the film cooling holes
DR = coolant-to-free-stream density ratio
FSTI = free-stream turbulence intensity
L = length of the film cooling delivery tube
Re_D = Reynolds number based on bulk mean film cooling hole velocity and hole diameter
Re_θ = Reynolds number based on mean streamwise velocity and momentum thickness
TI = local turbulence intensity normalized with local mean streamwise velocity = u_{rms}/U
U = time-averaged local streamwise velocity
U_{eff} = mean effective velocity as seen by a hot-wire parallel to film-cooled surface and normal to free-stream flow
U_{hole} = bulk mean velocity of coolant flow through film cooling hole
U_o = time-averaged free-stream velocity
u' = instantaneous values of streamwise velocity fluctuations
u_{rms} = rms fluctuation of streamwise velocity = $\sqrt{\overline{u'^2}}$
VR = ratio of film coolant mean velocity to free-stream velocity
x = streamwise distance from center of the hole
y = distance normal to the test wall
z = lateral/spanwise distance from center of the middle hole
θ = momentum thickness
δ = boundary layer thickness 99 percent
δ^* = displacement thickness

Subscripts

A-H = test case designation

Superscripts

$\bar{}$ = time-averaged

Table 1 Approach flow

	x/D=-4.0 [x/D=0.0#]					
	U_o (m/s)	FSTI	δ/D	θ/D	δ*/D	Re_θ
Low FSTI	10.8	0.5	0.52 [0.62]	0.05 [0.060]	0.073 [0.084]	655 [780]
High FSTI	10.8	12	1.01 [1.13]	0.073 [0.082]	0.094 [0.105]	960 [1070]

Projected with turbulent boundary layer growth rate

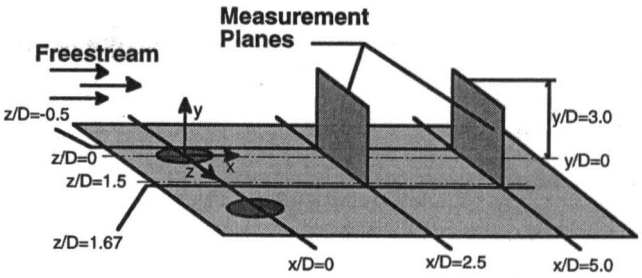

Fig. 3 Streamwise-normal measurement planes

1.9 cm and positioned three diameters apart, center-to-center. The film cooling delivery tubes have length-to-diameter ratios of 7 and 2.3. An $L/D = 7.0$ is achieved with tubes attached to the back of the test plate to provide an additional 4.7D of length. At entrance, these tubes are cut normal to the tube axis, not inclined like the entrance to the $L/D = 2.3$ holes. With the tubes in place, the advertised length is the minimum distance inside the tubes from entrance to exit ($L/D = 7.7$ along centerline). This long length establishes fully developed flow within the delivery tube (Goldstein et al., 1974). The smaller represents film cooling designs in modern airfoils. A square-edged, rectangular polycarbonate strip (1.6 mm thick × 13 mm wide × 68.6 cm long) is attached to the upstream plate as a boundary layer trip. Its upstream edge is 21.2 cm upstream of the hole centers. Film cooling flow is supplied by a fan through a metering section and a large, unrestricted supply plenum. The supply system is designed for uniform distribution of flow to the holes. The metering section is fabricated with two laminar flow meters.

Table 1 and Fig. 2 document the approach flows. The coolant has $Re_D = 13{,}000$ to achieve a velocity ratio of 1.0. The coolant-to-free-stream density ratio is unity.

Instrumentation. Single-sensor (TSI model 1218-T1.5) hot-wire probes are used to obtain the velocity and turbulence data. They are driven by a TSI IFA-100 bridge unit. A total of 4096 data points was recorded for each measurement location over a sampling time of 40 seconds. Hot-wire measurements are suitable for they are made in regions where there is no recirculating flow and local turbulence intensities are sufficiently low.

An automated, two-axis traversing system allowed high-spatial-resolution (0.025 mm capability) measurements in the wall-normal and spanwise directions. Movement in the streamwise direction was accomplished manually.

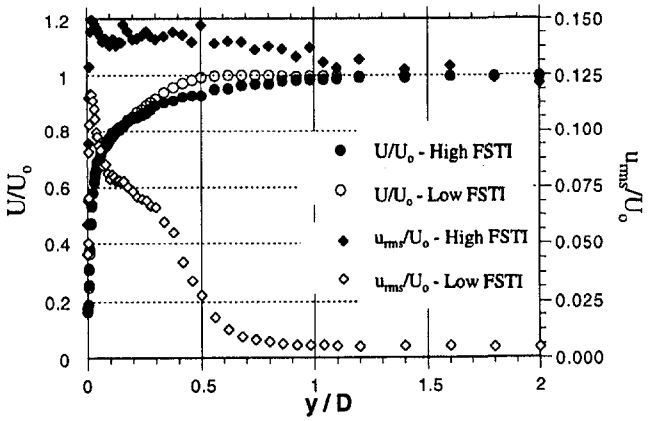

Fig. 2 Velocity and turbulence intensity profiles of the approach flow (measurement location: $x/D = -4.0$)

Experimental Uncertainty. Hot-wire uncertainty comes from precision and bias error. Such uncertainties, which arise during calibration and measurement, are larger at smaller velocities. They result from items such as changes in fluid properties between calibration and measurement, near-wall effects, and sensor drift. A standard propagation, as detailed by Kline and McClintock (1953), of uncertainty contributions assigned for these various effects yields a combined uncertainty of 7 percent (~3 m/s) to 5 percent (~10 m/s). Due to the large sample sizes and long sampling time associated with the hot-wire calibration and measurement, stochastic errors associated with sampling size and time fall well below the deterministic errors and are negligible in comparison. The rms velocity fluctuation and the mean velocity have the same uncertainty.

Comparisons of mean velocity and turbulence intensity to data by Laufer (1953) in a fully developed pipe are used to corroborate these uncertainty values. Per these data, bias error contributions on the order of 5 percent of mean values are reasonable under the conditions of the bulk of the present data, so long as velocity fluctuation rms levels remain below 25 percent of the mean streamwise velocity. These uncertainties are consistent with previous experience with such measurements and with Yavuzkurt (1984). Uncertainty in the total coolant mass flow rate is 2.3 percent. All uncertainties are expressed with 95 percent confidence.

Cases Studied. Surveys were taken at the two planes shown in Fig. 3. Data are taken in the lateral direction at 14 evenly spaced locations. The extrema of these locations are $z/D = -0.5$ and $z/D = 1.67$. Data are distributed in the wall-normal direction with high-resolution ($y/D = 0.0025$) in the near-wall region and with a gradual transition to coarser resolution ($y/D = 0.3$) in the free stream. All measurements were taken about the middle hole of the eleven film cooling holes. Cases with different hole length-to-diameter ratios, FSTI values, and streamwise positions are documented in Table 2.

Experimental Results

To separate effects, results are presented in three sections. The first highlights the influence of the hole length-to-diameter ratio with FSTI = 0.5 percent. The second documents the effects

Table 2 Cases in this study

CASE	L/D	FSTI	VR	x/D
A	7.0	0.5%	1.0	2.5
B	2.3	0.5%	1.0	2.5
C	7.0	0.5%	1.0	5.0
D	2.3	0.5%	1.0	5.0
E	7.0	12%	1.0	2.5
F	2.3	12%	1.0	2.5
G	7.0	12%	1.0	5.0
H	2.3	12%	1.0	5.0

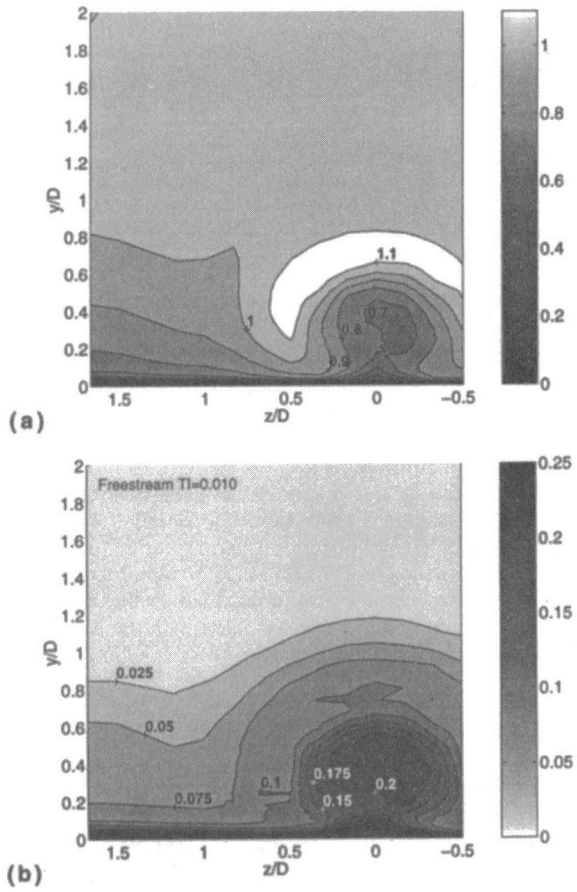

Fig. 4 Case *A: L/D* = 7.0, *VR* = 1.0, *x/D* = 2.5, and FSTI = 0.5 percent; (*a*) U/U_o; (*b*) *TI*

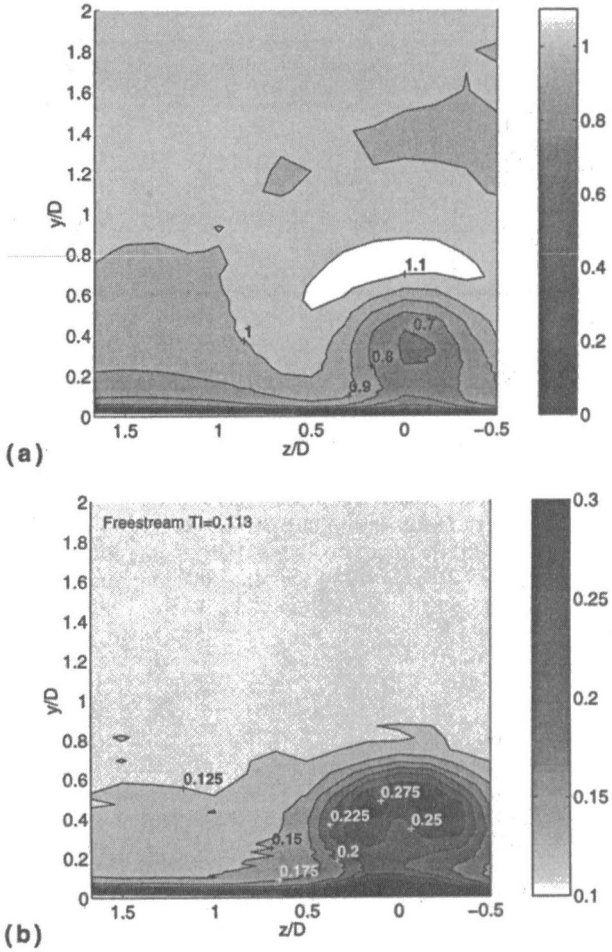

Fig. 5 Case *E: L/D* = 7.0, *VR* = 1.0, *x/D* = 2.5, and FSTI = 12.0 percent; (*a*) U/U_o; (*b*) *TI*

of the hole length-to-diameter ratio with FSTI = 12 percent. The third explores the effects of FSTI with a fixed geometry. It will be shown that both the hole length-to-diameter ratio and FSTI play influential roles. The reader is cautioned to interpret the figures presented carefully and refer to the legends and labels provided as grayscales may vary in magnitude from figure to figure.

Figures 4(*a*) and 4(*b*) show contour plots of the normalized mean velocity (U/U_o) and local turbulence intensity (*TI*), respectively, for Case A (L/D = 7.0, 0.5 percent FSTI) and Figs. 5(*a*) and 5(*b*) are for Case E (L/D = 7.0, 12 percent FSTI). These cases will serve as base cases for comparison. Looking at these figures, it is observed, with VR = 1.0, that the coolant forms a blockage for the free stream as noted by low velocities directly downstream from the hole. In response, the free-stream flow accelerates around this blockage, leading to velocities in excess of free-stream magnitudes. TI levels are observed to be greatest in the blocked region. In the following sections, the term "core" refers to the center of the region influenced by the coolant flow in which velocity gradients are small, primarily corresponding to the blockage. The "mixing region" refers to the coolant jet periphery in which velocity gradients are large.

***L/D* Influence at Low FSTI.** This section documents the hole L/D effect by comparing Case A to Case B. Pietrzyk et al. (1989, 1990) and Leylek and Zerkle (1994) recorded a strong effect of L/D, noting that short-hole injection is subject to "jetting" effects. With jetting, the jet velocity profile is not uniformly distributed across the majority of the plane at which it exits, but is skewed with substantially higher velocities upstream (Fig. 6). Although the data presented in Fig. 6 are for high FSTI, Leylek and Zerkle describe similar profiles for low FSTI. More detail on the film cooling hole-exit profiles under high-FSTI conditions are presented by Burd and Simon (1997).

Figure 7(*a*) shows, at x/D = 2.5, the percent increase in mean velocity (U/U_o) and Fig. 7(*b*) shows the increase in *TI* for L/D = 2.3 (Case B) relative to L/D = 7.0 (Case A). Higher normalized velocities are observed over the majority of the region defined by $0.2 < y/D < 0.4$ and $-0.4 < z/D < 0.4$ for the short delivery length case relative to those of the long delivery length case. The flow emerging from the shorter hole is able to exert its influence farther into the free-stream flow in both the wall-normal and spanwise directions, accelerating the

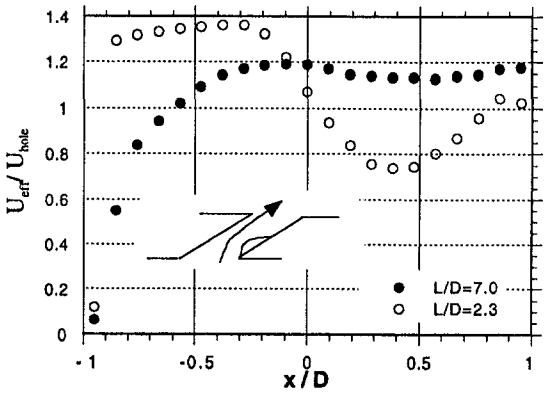

Fig. 6 Centerline mean effective velocity profiles at the hole-exit plane: FSTI = 12 percent (Cases *E* and *F*)

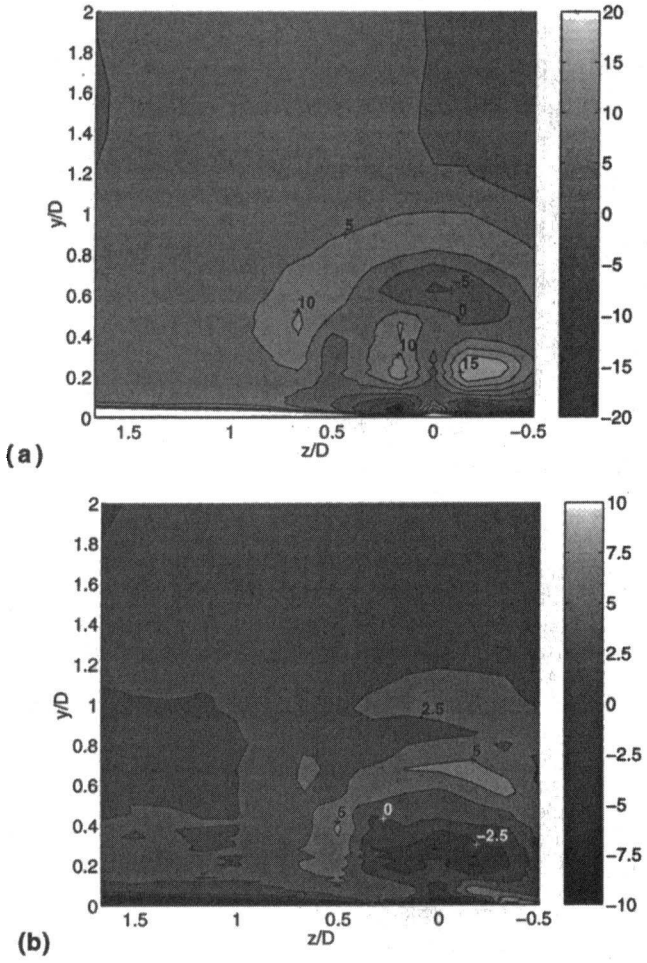

Fig. 7 Case *A* (L/D = 7.0) versus Case *B* (L/D = 2.3); (*a*) percent change in mean velocity ratio $[((U/U_o)_B/(U/U_o)_A) - 1] \times 100$; (*b*) percent differences in local turbulence $(TI_B - TI_A) \times 100$

free stream over the jet. Spreading in the spanwise direction, for instance, is visible in the larger values of U/U_o and TI at $y/D \sim 0.5$ and $z/D = \pm 0.6$. Enhanced mixing by this type of "jetting" was discussed by Leylek and Zerkle (1994). Negative velocity difference values (Fig. 7(*a*)) in the zone $y/D = 0.05$ and $z/D = \pm 0.3$ indicate weaker downward convection by secondary flow in the short L/D case. This convection by secondary flows is believed to have an important influence on film cooling effectiveness as shown by Burd and Simon (1997). The effects on the local turbulence intensity differences (Fig. 7(*b*)) are also pronounced, showing that mixing occurs further into the free-stream with short-hole injection: Note 5 percent higher values for the short-hole case directly downstream of the film cooling holes ($z/D = 0$) at $y/D \sim 0.7$. In addition, higher turbulence levels extend into the region between the holes, to as far as $z/D = 0.7$, emphasizing the jet lateral spreading. The region of negative TI differences ($y/D \sim 0.3$, $z/D \sim 0$) in Fig. 7(*b*) indicate that the influence of free-stream/injectant shear and associated turbulence penetrates less into the higher-momentum core of the short-L/D jet.

Under low-FSTI, measurements (not shown) were also taken at the downstream location $x/D = 5.0$ (Cases C and D). Here, differences between the short-hole and long-hole injection have been reduced substantially. Velocity differences do not exceed ±10.0 percent and differences in TI do not exceed ±2.5 percent.

***L/D* Influence at High FSTI.** This section documents the role of L/D when the FSTI is elevated to combustor exit levels (~12 percent). Contour plots showing the normalized mean velocity ratio (U/U_o) and local turbulence intensity (TI) distributions are given for Case F (high FSTI, short-L/D case) in Figs. 8(*a*) and 8(*b*). This case is most representative of the engine. The role of L/D, with high FSTI, is shown by comparing Cases E and F, as done in Fig. 9. Centerline hole-exit profiles are given for these cases in Fig. 6. There remains a region downstream of the hole centerline ($0.2 < y/D < 0.5$ and $-0.3 < z/D < 0.3$) where the mean velocities of the short L/D case are higher, indicative of the higher momentum associated with the short-hole jet. This is similar to the low-FSTI case comparison (Fig. 7(*a*)). Also, consistent with the low-FSTI comparison, negative velocity differences in the zone $y/D = 0.05$ and about $z/D = \pm 0.3$ of Fig. 9(*a*) show a weaker convection by secondary flow of the high-momentum external flow to this near-wall region with short-hole injection. This reduced secondary flow may be due to a reduced blockage of the main flow in the short-L/D case where the influence of the jet has been diminished more extensively by the highly turbulent free-stream than with the long-hole case (note higher U/U_o values in Fig. 9(*a*) at $z = 0$, $y/D = 0.3$ for the $L/D = 7.0$ case). Negative values of turbulence intensity difference (Fig. 9(*b*)) in the zone given by $y/D < 0.4$ along the jet centerline are attributable to the higher momentum of the short-hole jet and the associated reduction of shear with the mainstream flow in this region.

At $x/D = 5.0$ under high FSTI (Cases G and H), differences between L/D cases are reduced in magnitude, similar to those described for $x/D = 5.0$ (Cases C and D) under low FSTI.

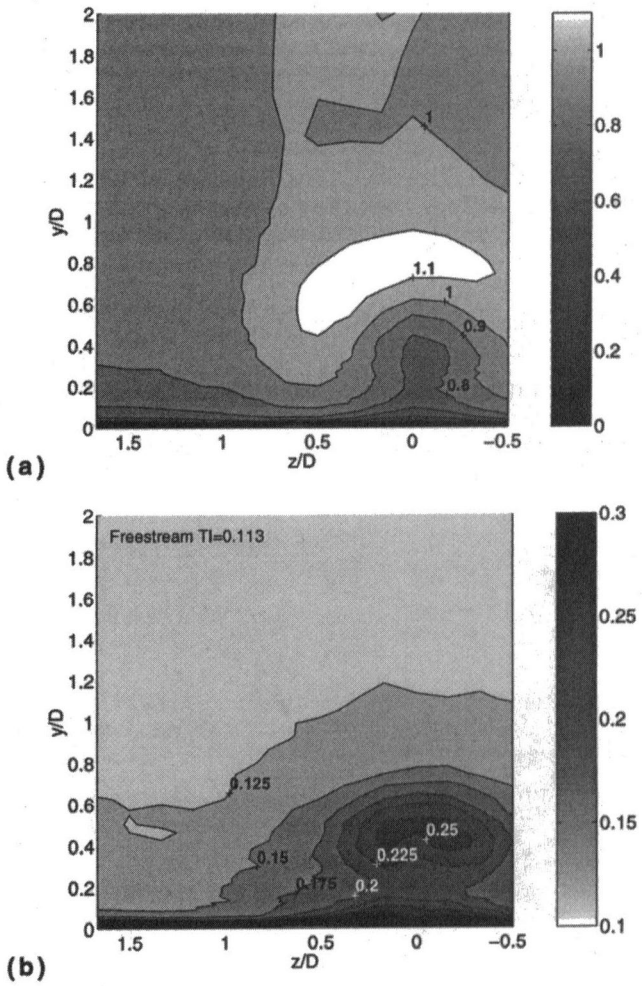

Fig. 8 Case *F*: L/D = 2.3, *VR* = 1.0, x/D = 2.5, and FSTI = 12.0 percent; (*a*) U/U_o; (*b*) *TI*

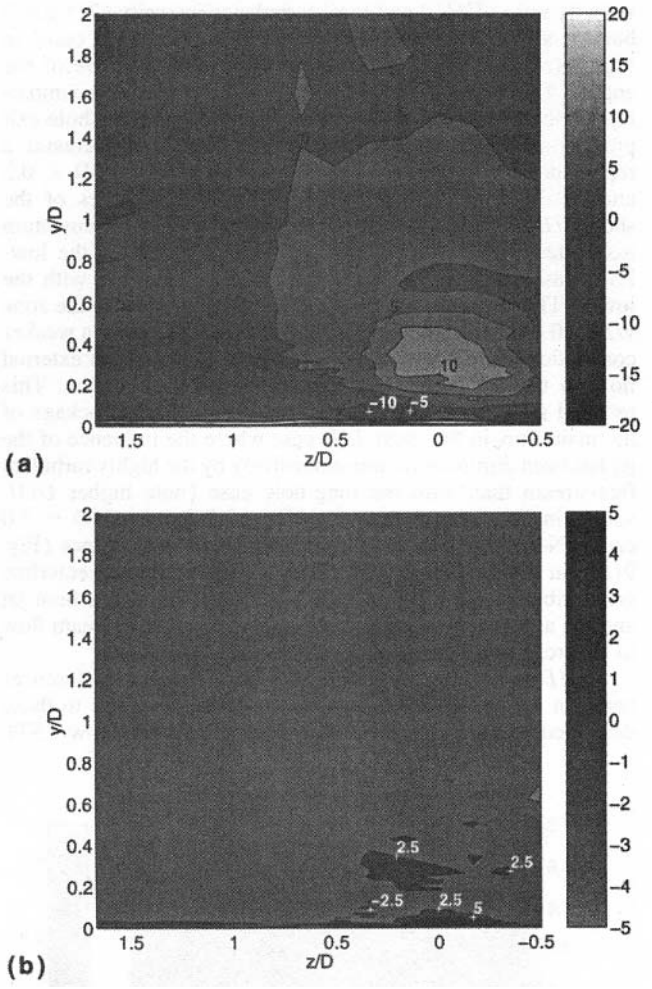

Fig. 9 Case E (L/D = 7.0) versus Case F (L/D = 2.3); (a) percent change in mean velocity ratio $[(U/U_o)_F/(U/U_o)_E) - 1] \times 100$; ($b$) percent differences in local turbulence $(TI_F - TI_E) \times 100$

Velocity and TI differences do not exceed ±5 and ±2.5 percent, respectively (not shown).

FSTI Effects. With elevated FSTI, film coolant rapidly mixes with the free-stream flow. With this, the film cooling jets diffuse more rapidly, resulting in a dispersed film cooling jet

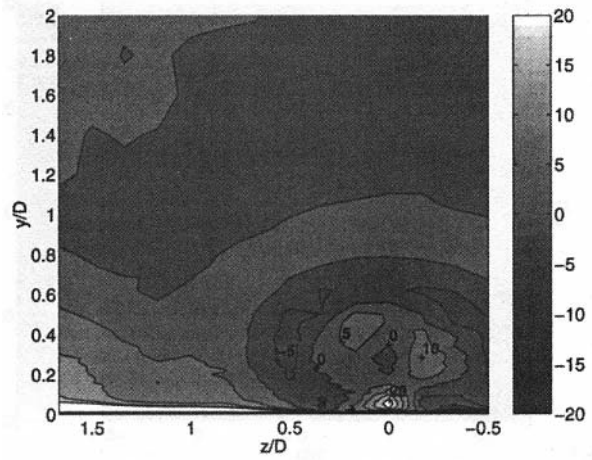

Fig. 10 Percent change in mean velocity ratio with L/D = 7.0: Case E (FSTI = 12 percent) versus Case A (FSTI = 0.5 percent) $[(U/U_o)_E/(U/U_o)_A) - 1] \times 100$

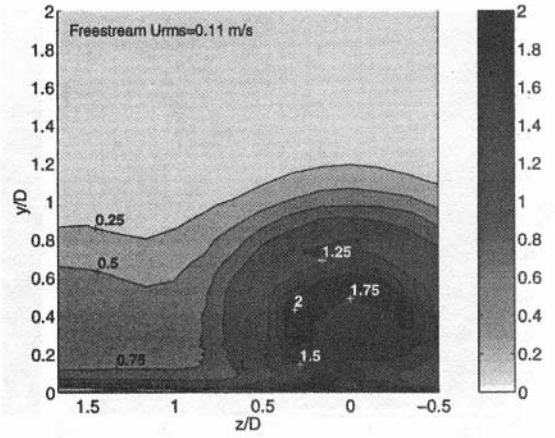

Fig. 11 u_{rms} (m/s) distribution for Case A (FSTI = 0.5 percent, L/D = 7.0)

with less influence on the flowfield. Enhanced mixing decreases the extent of acceleration (reduction of U/U_o) over the jet and reduces the blockage caused by the jet. In the following section, comparisons at two FSTI levels for the long-hole injection cases (Cases A and E) and the short-hole cases (Cases B and F), at x/D = 2.5, are given. These cases are of the same L/D so that the effects of FSTI alone are isolated.

With long L/D, the normalized mean velocity distributions have significant differences. Figure 10 shows an increase in mean velocity ratios for the high-FSTI case relative to the low-FSTI case in the core. About the jet periphery ($0.3 < y/D < 0.5$ and $z/D = \pm 0.5$), the high-FSTI case has lower mean velocities. This observation indicates more mixing in this region with elevated FSTI. Figure 11 shows u_{rms} contours for the low-FSTI case and Fig. 12 shows u_{rms} contours for the high-FSTI case. Their turbulence structures are similar, with distinct regions detailing the core and mixing regions of the jets. The low-FSTI case shows the influence of coolant injection penetrating further from the wall (to $y/D \sim 1.0$ along the centerline but to only $y/D \sim 0.8$ for the high-FSTI case).

The same comparison of different FSTI cases is made for short-L/D injection. Higher mean streamwise velocity for case F relative to the mean velocity distribution of Case B is noted in Fig. 13.

Although generally the regions of difference are similar to those of the long-L/D comparison case in Fig. 10, the magnitudes are changed. The low-FSTI case maintains higher mean velocities downstream from the edges of the hole (negative

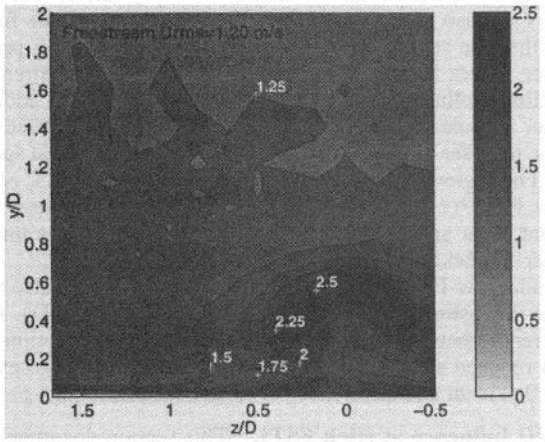

Fig. 12 u_{rms} (m/s) distribution for Case E (FSTI = 12 percent, L/D = 7.0)

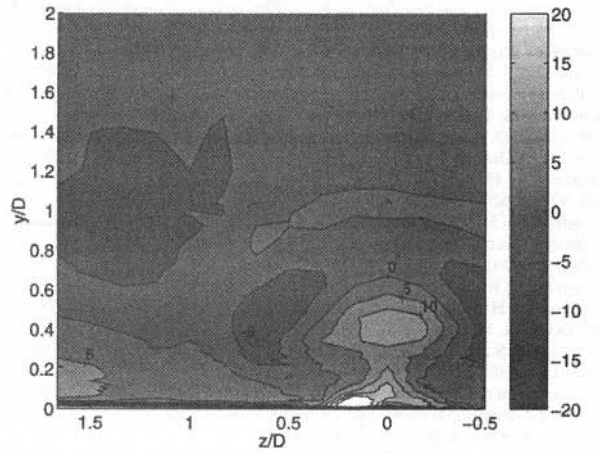

Fig. 13 Percent change in mean velocity ratio with L/D = 2.3: Case F (FSTI = 12 percent) versus Case B (FSTI = 0.5 percent) $[((U/U_o)_F/(U/U_o)_B) - 1] \times 100$

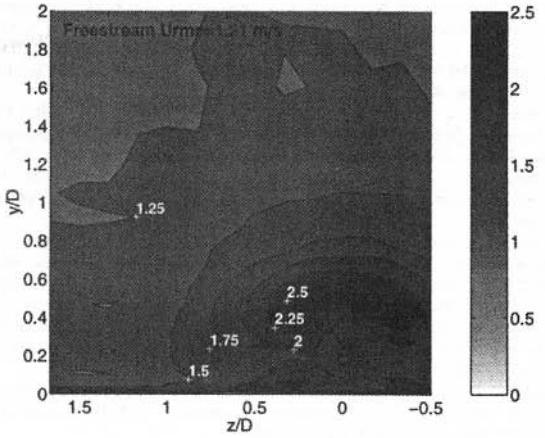

Fig. 15 u_{rms} (m/s) distribution for Case F (FSTI = 12 percent, L/D = 2.3)

values in the range $y/D \sim 0.3$–0.7 and $z/D = \pm 0.6$). This is again indicative of the enhanced mixing with elevated FSTI in this region. About the hole centerline ($-0.4 < z/D < 0.4$ and $y/D < 0.6$), mean velocities are higher for the high-FSTI case than for the low-FSTI case. This again shows that the high-FSTI case has a reduced blockage due to the jet. A comparison of u_{rms} distributions (Figs. 14, for the low-FSTI case, and 15, for high-FSTI) shows an influence of the jets in both cases to extend beyond $y/D \sim 1$.

Concluding Remarks

The results presented, although primarily fluid dynamics in focus, provide a great deal of insight into the flowfield interaction mechanisms found with film cooling flows. The comparisons emphasize that L/D and FSTI play influential roles in film cooling. They also note a dependence of one effect on the other, which makes interpretation of one in isolation of the other incomplete. In general, short- and long-hole injection have fundamentally different velocity profiles at the hole exit. As a result, the ejected coolant interacts differently with the free-stream. Thus, one cannot draw conclusions about the FSTI effect on short-hole operation from experiences gained regarding the FSTI effect on long-hole operation.

Under low-FSTI conditions, short-hole injection ejects farther from the wall and spreads more in the spanwise direction than with long-hole injection. In the core region, the jetting associated with short-hole injection is observed to produce higher streamwise velocities and a reduced blockage as seen by the free-stream flow. Short-hole injection is also noted to have weaker convection of secondary in the near-wall region. With high FSTI, differences between the L/D = 2.3 and L/D = 7.0 cases are diminished.

In comparing cases of like geometry but under differing FSTI conditions, one notes that high-FSTI cases are more dominated by the free-stream, giving a reduced effect of the hole L/D.

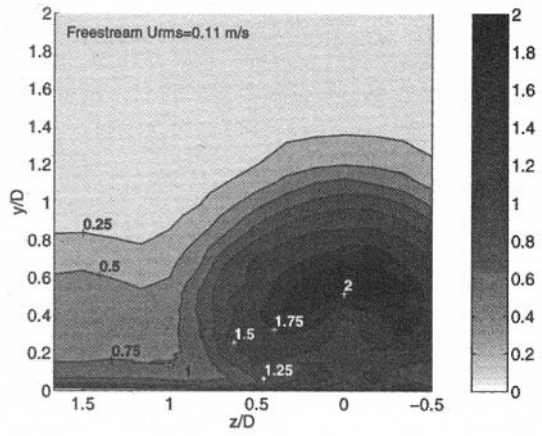

Fig. 14 u_{rms} (m/s) distribution for Case B (FSTI = 0.5 percent, L/D = 2.3)

Acknowledgments

This work is part of a combined study of film cooling with short-hole delivery holes and with lateral injection sponsored by NASA-Lewis Research Center and DOE, respectively. The DOE project is managed by Dr. Daniel Fant of the South Carolina Energy R&D Center and the NASA study Project Monitor is Douglas Thurman. The authors would also like to acknowledge Dr. E. R. G. Eckert for his invaluable contributions to this work.

References

Andreopoulos, J., and Rodi, W., 1984, "Experimental Investigation of Jets in a Crossflow," *J. Fluid Mechanics,* Vol. 138, pp. 93–127.

Bergeles, G., Gosman, A. D., and Launder, B. E., 1976, "The Prediction of Three-Dimensional Discrete-Hole Cooling Processes: Part 1—Laminar Flow," ASME *Journal of Heat Transfer,* Vol. 98, No. 3, p. 379.

Bergeles, G., Gosman, A. D., and Launder, B. E., 1978, "The Turbulent Jet in a Cross Stream at Low Injection Rates: A Three-Dimensional Numerical Treatment," *Num. Heat Transfer, Part A: Applications,* Vol. 1, pp. 217–242.

Bons, J. P., MacArthur, C. D., and Rivir, R. B., 1996, "The Effect of High Freestream Turbulence of Film Cooling Effectiveness," ASME JOURNAL OF TURBOMACHINERY, Vol. 118, pp. 814–825.

Brown, A., and Minty, A. G., 1975, "The Effects of Mainstream Turbulence Intensity and Pressure Gradient on Film Cooling Effectiveness for Cold Air Injection Slits of Various Ratios," ASME Paper No. 75-WA/HT-17.

Brown, A., and Saluja, C. A., 1979, "Film Cooling From Three Rows of Holes on an Adiabatic Constant Heat Flux and Isothermal Surfaces in the Presence of Variable Free-Stream Velocity Gradients and Turbulence Intensity," ASME Paper No. 79-GT-24.

Burd, S. W., and Simon, T. W., 1997, "The Influence of Coolant Supply Plenum Geometry on Coolant Exit Flow and Surface Adiabatic Effectiveness," ASME Paper No. 97-GT-25.

Crabb, D., Durao, D. F. G., and Whitelaw, J. H., 1981, "A Round Jet Normal to a Crossflow," ASME *Journal of Fluids Engineering,* Vol. 103, pp. 1006–1012.

Demuren, A. O., and Rodi, W., 1983, "Three-Dimensional Calculation of Film Cooling by a Row of Jets," *Notes Num. Fluid Mech.,* Vol. 7, pp. 49–56.

Demuren, A. O., Rodi, W., and Schonung, B., 1986, "Systematic Study of Film Cooling With a Three-Dimensional Calculation Procedure," ASME JOURNAL OF TURBOMACHINERY, Vol. 108, pp. 124–130.

Forth, C. J. P., and Jones, T. V., 1988, "Scaling Parameters in Film Cooling," *Proc. 8th Int. Heat Transfer Conference,* Vol. 3, pp. 1271–1276.

Foster, N. W., and Lampard, D., 1980, "The Flow and Film Cooling Effectiveness Following Injection Through a Row of Holes," ASME *Journal of Engineering for Power,* Vol. 102, pp. 584–588.

Goebel, S. G., Abuaf, N., Lovett, J. A., and Lee, C.-P., 1993, "Measurements of Combustor Velocity and Turbulence Profiles," ASME Paper No. 93-GT-228.

Gogineni, S. P., Rivir, R. B., Pestian, D. J., and Goss, L. P., 1996, "PIV Measurements of Flat Plate Film Cooling Flow With High Free Stream Turbulence," AIAA Paper No. 96-0617.

Goldstein, R. J., Eckert, E. R. G., and Ramsey, J. W., 1968, "Film Cooling with Injection Through Holes: Adiabatic Wall Temperatures Downstream of a Circular Hole," ASME *Journal of Engineering for Power,* pp. 384–395.

Goldstein, R. J., Eckert, E. R. G., and Burggraf, F., 1974, "Effects of Hole Geometry and Density on Three-Dimensional Film Cooling," *Int. J. Heat Mass Transfer,* Vol. 17, pp. 595–607.

Hinze, J. O., 1975, *Turbulence,* 2nd ed., McGraw-Hill, New York.

Jubran, B., and Brown, A., 1985, "Film Cooling From Two Rows of Holes Inclined in the Streamwise and Spanwise Directions," ASME *Journal of Engineering for Gas Turbines and Power,* Vol. 107, pp. 84–91.

Jumper, G. W., Elrod, W. C., and Rivir, R. B., 1991, "Film Cooling Effectiveness in High-Turbulence Flow," ASME JOURNAL OF TURBOMACHINERY, Vol. 113, pp. 479–483.

Kadotani, K., and Goldstein, R. J., 1979, "On the Nature of Jets Entering a Turbulent Flow, Part A: Jet–Mainstream Interaction," ASME *Journal of Engineering for Power,* Vol. 101, pp. 459–465.

Kline, S. J., and McClintock, F. A., 1953, "Describing Uncertainties in Single-Sample Experiments," *Mechanical Eng.,* Jan., pp. 3–8.

Laufer, J., 1953, "The Structure of Turbulence in Fully-Developed Pipe Flow," NACA Report 1174.

Launder, B. E., and York, J., 1974, "Discrete-Hole Cooling in the Presence of Free Stream Turbulence and Strong Favorable Pressure Gradients," *Int. J. Heat Mass Transfer,* Vol. 17, pp. 1403–1409.

Le Brocq, P. V., Launder, B. E., and Priddin, C. H., 1973, "Discrete Hole Injection as a Means of Transpiration Cooling: An Experimental Study," *Proc. Inst. Mech. Eng.,* Vol. 187, pp. 149–157.

Lee, S. W., Lee, J. S., and Ro, S. T., 1994, "Experimental Study of the Flow Characteristics of Streamwise Inclined Jets in Crossflow on Flat Plate," ASME JOURNAL OF TURBOMACHINERY, Vol. 116, pp. 97–105.

Leylek, J. H., and Zerkle, R. D., 1994, "Discrete-Jet Film Cooling: A Comparison of Computational Results With Experiments," ASME JOURNAL OF TURBOMACHINERY, Vol. 116, pp. 358–368.

Ligrani, P. M., Wigle, J. M., Ciriello, S., and Jackson, S. M., 1994, "Film Cooling From Holes With Compound Angle Orientations: Part 1—Results Downstream of Two Staggered Rows of Holes With 3d Spanwise Spacing," ASME *Journal of Heat Transfer,* Vol. 116, pp. 341–352.

MacMullin, R., Elrod, W. C., and Rivir, R. B., 1989, "Free Stream Turbulence From a Circular Wall Jet on Flat Plate Heat Transfer and Boundary Layer Flow," ASME JOURNAL OF TURBOMACHINERY, Vol. 111, pp. 78–86.

Patankar, S. V., and Spalding, D. B., 1972, "A Calculation Procedure for Heat, Mass and Momentum Transfer in Three-Dimensional Parabolic Flows," *Int. J. Heat Mass Transfer,* Vol. 15, p. 1787.

Patankar, S. V., Rastogi, A. K., and Whitelaw, J. H., 1973, "The Effectiveness of Three-Dimensional Film-Cooling Slots—II. Predictions," *Int. J. Heat Mass Transfer,* Vol. 16, pp. 1665–1681.

Pedersen, D. B., Eckert, E. R. G., and Goldstein, R. J., 1977, "Film Cooling With Large Density Differences Between the Mainstream and Secondary Fluid Measured by Heat-Mass Transfer Analogy," ASME *Journal of Heat Transfer,* Vol. 99, pp. 620–627.

Pietrzyk, J. R., Bogard, D. G., and Crawford, M. E., 1989, "Hydrodynamic Measurements of Jets in a Crossflow for Gas Turbine Film Cooling Applications," ASME JOURNAL OF TURBOMACHINERY, Vol. 111, pp. 139–145.

Pietrzyk, J. R., Bogard, D. G., and Crawford, M. E., 1990, "Effects of Density Ratio on the Hydrodynamics of Film Cooling," ASME JOURNAL OF TURBOMACHINERY, Vol. 112, pp. 437–443.

Pratap, V. S., and Spalding, D. B., 1976, "Fluid Flow and Heat Transfer in Three-Dimensional Duct Flows," *Int. J. Heat Mass Transfer,* Vol. 19, p. 1183.

Rodi, W., and Srivatsa, S. K., 1980, "A Locally Elliptic Calculation Procedure for Three-Dimensional Flows and Its Application to a Jet in Cross-Flow," *Comp. Mech. App. Mech. Eng.,* Vol. 23, pp. 67–83.

Sathyamurthy, P., and Patankar, S. V., 1990, "Prediction of Film-Cooling With Lateral Injection," *Heat Transfer in Turbulent Flows,* ASME-HTD, Vol. 138, pp. 61–70.

Schmidt, D. L., Sen, B., and Bogard, D. G., 1996, "Film Cooling With Compound Angle Holes: Adiabatic Effectiveness," ASME JOURNAL OF TURBOMACHINERY, Vol. 118, pp. 807–813.

Sen, B., Schmidt, D. L., and Bogard, D. G., 1996, "Film Cooling With Compound Angle Holes: Heat Transfer," ASME JOURNAL OF TURBOMACHINERY, Vol. 118, pp. 800–806.

Sinha, A. K., Bogard, D. G., and Crawford, M. E., 1991, "Film Cooling Effectiveness of a Single Row of Holes With Variable Density Ratio," ASME JOURNAL OF TURBOMACHINERY, Vol. 113, pp. 442–449.

Tafti, D. K., and Yavuzkurt, S., 1988, "Prediction of Heat Transfer Characteristics of Discrete Hole Film Cooling—One Row of Injection Into a Turbulent Boundary Layer," ASME HTD-Vol. 103, pp. 45–52.

Wang, L., Tsang, H., Simon, T. W., and Eckert, E. R. G., 1996, "Measurements of Mean Flow and Eddy Transport over a Film Cooled Surface," ASME HTD-Vol. 327, pp. 71–79.

Yavuzkurt, S., 1984, "A Guide to Uncertainty Analysis of Hot-Wire Data," ASME *Journal of Fluids Engineering,* Vol. 106, pp. 181–186.

Yoshida, T., and Goldstein, R. J., 1984, "On the Nature of Jets Issuing From a Row of Holes into a Low Reynolds Number Mainstream Flow," ASME *Journal of Engineering for Gas Turbines and Power,* Vol. 106, pp. 612–618.

Detailed Film Cooling Measurements on a Cylindrical Leading Edge Model: Effect of Free-Stream Turbulence and Coolant Density

S. V. Ekkad[1]

J. C. Han

H. Du[2]

Turbine Heat Transfer Laboratory,
Department of Mechanical Engineering,
Texas A&M University, MS 3123,
College Station, TX 77843

Detailed heat transfer coefficient and film effectiveness distributions are presented on a cylindrical leading edge model using a transient liquid crystal technique. Tests were done in a low-speed wind tunnel on a cylindrical model in a crossflow with two rows of injection holes. Mainstream Reynolds number based on the cylinder diameter was 100,900. The two rows of injection holes were located at ±15 deg from stagnation. The film holes were spaced four hole diameters apart and were angled 30 and 90 deg to the surface in the spanwise and streamwise directions, respectively. Heat transfer coefficient and film effectiveness distributions are presented on only one side of the front half of the cylinder. The cylinder surface is coated with a thin layer of thermochromic liquid crystals and a transient test is run to obtain the heat transfer coefficients and film effectiveness. Air and CO_2 were used as coolant to simulate coolant-to-mainstream density ratio effect. The effect of coolant blowing ratio was studied for blowing ratios of 0.4, 0.8, and 1.2. Results show that Nusselt numbers downstream of injection increase with an increase in blowing ratio for both coolants. Air provides highest effectiveness at blowing ratio of 0.4 and CO_2 provides highest effectiveness at a blowing ratio of 0.8. Higher density coolant (CO_2) provides lower Nusselt numbers at all blowing ratios compared to lower density coolant (air). An increase in free-stream turbulence has very small effect on Nusselt numbers for both coolants. However, an increase in free-stream turbulence reduces film effectiveness significantly at low blowing ratios for both coolants.

Introduction

Gas turbine blades need to be cooled to protect them from high-temperature gases. Cooler air is injected through discrete holes along the blade surface to provide protection. This type of cooling is called film cooling. The leading edge of the turbine blade is the most critical heat transfer region as some of the highest heat transfer occurs in that region. So, film cooling near the turbine blade leading edge is essential to protect the blade from the hot gases and prevent failure. The inlet high-temperature gases from the combustor to the turbine inlet are highly turbulent. Also, since the coolant is cooler than the mainstream, the coolant is at a higher density than the mainstream. The present study focuses on the influence of free-stream turbulence and coolant density on the turbine blade leading edge film effectiveness and heat transfer coefficients.

The leading edge region of the turbine blade has been a focus for many film cooling studies. Luckey and L'Ecuyer (1976) and Bonnice and L'Ecuyer (1983) studied a circular cylinder with several rows of spanwise injection holes to model the leading edge region. They reported that the surface heat flux was very much dependent on the injection geometry and coolant blowing ratio. Mick and Mayle (1988) studied film cooling on a blunt body with a semi-circular leading edge and flat afterbody. They concluded that leading edge injection reduces the surface heat load for lower blowing ratios. They also determined that the regions of high effectiveness do not necessarily correspond to the regions having a high heat transfer coefficient. Karni and Goldstein (1990) used the naphthalene sublimation technique to study the effects of surface injection on local mass transfer from a circular cylinder in crossflow with one row of inclined holes. Mehendale and Han (1992) studied the effect of free-stream turbulence on leading edge film effectiveness and heat transfer coefficient. They used a blunt body similar to that of Mick and Mayle (1988). They reported that high free-stream turbulence reduced film effectiveness and enhanced heat transfer coefficient. Ou et al. (1992) studied the effect of film hole row location on the same test model as that of Mehendale and Han (1992). They reported that film cooling effectiveness was higher for injection farther downstream from the true leading edge. Ou and Han (1992) studied the effect of slot injection and free-stream turbulence on the blunt body model. Salcudean et al. (1994) studied the effect of coolant density on film effectiveness on a semi-circular leading edge with a flat afterbody. They reported that higher density fluid (CO_2) provides highest effectiveness at a higher blowing ratio compared to a lower density fluid (air), particularly farther downstream of injection. Lee et al. (1994) studied the effect of free-stream turbulence and horseshoe vortices on mass transfer on a film cooled cylinder. They reported that an increase in free-stream turbulence reduces the effects of horseshoe vortex structure. Funazaki et al. (1997) studied the effects of periodic wake passing on film effectiveness around the leading edge of a blunt body. They reported a decrease in film effectiveness with an increase in

[1] Present address: Asst. Professor, Louisiana State University, Baton Rouge, LA.

[2] Present address: Schlumberger SPT Center, Rosharon, TX.

Contributed by the International Gas Turbine Institute and presented at the 42nd International Gas Turbine and Aeroengine Congress and Exhibition, Orlando, Florida, June 2–5, 1997. Manuscript received International Gas Turbine Institute February 1997. Paper No. 97-GT-181. Associate Technical Editor: H. A. Kidd.

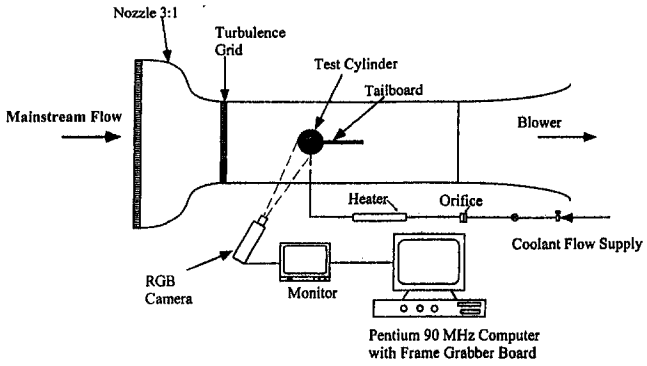

Fig. 1 Experimental setup

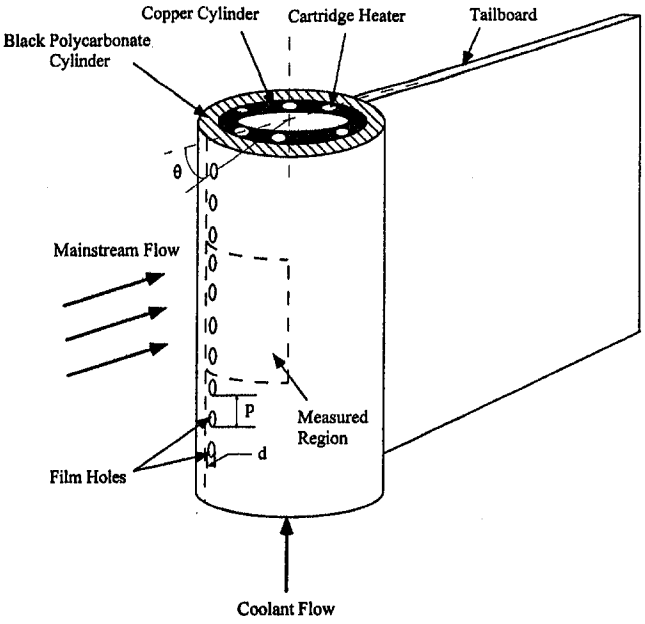

Fig. 2 Cylindrical test model

wake strength. The present study uses a transient liquid crystal technique to measure detailed heat transfer coefficient and film effectiveness distributions on a film cooled cylindrical leading edge model. Results are presented in the near film hole region. The effects of coolant density and free-stream turbulence are also presented. Although the coolant-to-mainstream density ratios in the real engine are closer to 2.0, studies with density ratios higher than 1.0 will provide a trend toward predicting film cooling behavior for real engine conditions. This study provides results for density ratios of 1.0 and 1.5.

Ekkad et al. (1997a, b) used a transient liquid crystal technique to study film cooling over a flat surface with compound angle hole injection with air and CO_2 as coolants. The present study uses a transient liquid crystal technique similar to the one presented by Ekkad et al. (1997a, b). The detailed heat transfer coefficient and film effectiveness distributions will provide a better understanding of the film cooling process on the blade leading edge, particularly in the near hole region, where it is difficult to obtain data using the thin foil-thermocouple method.

Test Apparatus and Instrumentation

Figure 1 presents the experimental setup. The setup consists of a suction-type blower, which has a straight section with the test cylinder and an upstream nozzle. The flow enters through the nozzle into the test tunnel. The test tunnel is 25.4 cm × 76.2 cm in cross section and is 183 cm long with the test cylinder placed 77.5 cm downstream of the nozzle exit. A tailboard is placed at the rear of the cylinder to reduce wake effects on the upstream heat transfer. The image processing system used for measuring the detailed heat transfer coefficient and film effectiveness distributions consists of a RGB camera, monitor, and a PC with a color frame grabber board. A turbulence grid is placed between the nozzle and the test tunnel to generate higher levels of free-stream turbulence intensity. Two different size grids were used to generate the turbulence levels of 4.1 and 7.1 percent. The coolant flow loop is also shown in the figure. Compressed air or CO_2 is routed through an orifice meter for the coolant flow. The coolant is initially directed away from the test cylinder using a three-way ball diverter valve. The valve is switched as the transient test is initiated. A heater heats the coolant flow for the film effectiveness test.

Figure 2 shows the test cylinder. The cylinder is 7.62 cm in diameter and 25.4 cm long. The cylinder is hollow with a polycarbonate exterior and copper interior. The copper interior has six heaters embedded along the circumference to heat the cylinder uniformly. The six cartridge heaters are 25.4 cm long and 0.32 cm in diameter. There is no air space between the copper interior and the polycarbonate exterior. The polycarbonate layer is 0.64 cm thick and has low thermal conductivity and diffusivity. Film holes are drilled through the copper and polycarbonate layers. Coolant is sent into the hollow of the cylinder from the bottom of the cylinder and ejected out of the film holes. The front half of the polycarbonate exterior can be replaced as a smooth or film holed surface. Film holes, placed ±15 deg from the leading edge of the cylinder, are 0.475 cm

Nomenclature

b = bar grid width
d = film hole diameter
D = cylinder model diameter
DR = coolant-to-mainstream density ratio = ρ_c/ρ_∞
h = local heat transfer coefficient with film injection
k = thermal conductivity of test surface material
k_{air} = thermal conductivity of inlet mainstream air
I = coolant-to-mainstream momentum flux ratio = $(\rho U^2)_c/(\rho U^2)_\infty$
L = length of film hole
M = coolant-to-mainstream blowing ratio = $(\rho U)_c/(\rho U)_\infty$
Nu = Nusselt number based on cylinder diameter = hD/k_{air}
$\overline{\text{Nu}}$ = span-averaged Nusselt number
P = film hole pitch
Re = mainstream Reynolds number = $U_\infty D/\nu$
t = time of color change of liquid crystals
T = temperature
Tu = streamwise turbulence intensity = $((\overline{u'}^2)^{1/2}/U_\infty)$
U = flow velocity
u' = local streamwise fluctuating velocity
X = axial distance measured from grid location
Z = spanwise distance
α = thermal diffusivity of test surface material
η = local film effectiveness
$\overline{\eta}$ = span-averaged film effectiveness
ν = kinematic viscosity of inlet mainstream air
ρ = fluid density

Subscripts

c = coolant
i = initial
f = film
w = wall
∞ = mainstream

in diameter and are inclined 30 and 90 deg in the spanwise and streamwise directions, respectively. Ten holes in each row are spaced four hole diameters apart ($P/d = 4$). The film hole-to-cylinder diameter ratio (d/D) was 0.063 and the film hole length-to-diameter ratio (L/d) was 3.1. The measurement region is also indicated in Fig. 2. The measured region is limited to one side of the front half of the cylinder from stagnation (0 deg) to about 70 deg from stagnation. A total of 7000 points were measured on the test surface.

The test surface is heated uniformly using the cartridge heaters. Cartridge heater power inputs are controlled using a variac for each heater, and surface temperature is monitored by placing several thermocouples on the surface. Uniformity of the surface temperature is within ±0.6°C when the test surface is heated to a temperature above the liquid crystal range. Thermochromic liquid crystals are sprayed uniformly on the surface using an air gun. Liquid crystal (Hallcrest: BM/R32C5W/C17-10) color change temperatures for appearance of red, green, and blue were 31.6°C, 32.7°C, and 37.2°C, respectively. In the present experiment, the surface is heated to a temperature above the blue color. The test surface is suddenly cooled by inducing the mainstream flow by the fast starting blower. The blower takes less than three seconds from initiation for full flow rate. The liquid crystal color changes from blue to green to red, and then becomes colorless during the transient test. The coolant flow is initiated by the solenoid controlled three-way diverter valve. The earliest color changes during the transient test occur around 15–20 seconds from initiation. The frame grabber board is programmed to capture data 10 frames per second in real time. The time of color change at every pixel location is analyzed and stored in a file on the computer. The heat transfer coefficient and film effectiveness are calculated using the theory described below.

Theory and Procedure

A one-dimensional conduction into a semi-infinite surface with a convective boundary condition at the surface is assumed. The surface temperature response is described by the solution:

$$\frac{T_r - T_i}{T_\infty - T_i} = 1 - \exp\left(\frac{h^2\alpha t}{k^2}\right) \operatorname{erfc}\left(\frac{h\sqrt{\alpha t}}{k}\right) \qquad (1)$$

where T_r is the color change temperature from green to red (32.7°C) during the transient cooling, T_i is the initial temperature of the heated test surface, and the oncoming mainstream temperature is T_∞. The time (t) for the actual appearance of red at any location on the surface is measured during the transient test. The thermal conductivity (k) and diffusivity (α) of the test surface material are known. The local heat transfer coefficient at any location on the test surface can be obtained from Eq. (1). For a film cooling test, the mainstream temperature (T_∞) in Eq. (1) is replaced by the local film temperature (T_f) that is a mixture of the coolant (T_c) and mainstream temperature. To find the unknown T_f with known quantities, T_∞ and T_c, a nondimensional temperature is the film cooling effectiveness (η):

$$\eta = \frac{T_f - T_\infty}{T_c - T_\infty};$$

$$\text{or} \quad T_f = \eta(T_c - T_\infty) + T_\infty = \eta T_c + (1 - \eta)T_\infty \qquad (2)$$

Replacing T_∞ in Eq. (1) by T_f from Eq. (2), we get the following equation with two unknowns, h and η:

$$T_r - T_i = \left[1 - \exp\left(\frac{h^2\alpha t}{k^2}\right) \operatorname{erfc}\left(\frac{h\sqrt{\alpha t}}{k}\right)\right] \times [\eta T_c + (1 - \eta)T_\infty - T_i] \qquad (3)$$

Running two similar transients is necessary to both obtain the heat transfer coefficient (h) and film effectiveness (η). The two tests will be run with two different coolant temperatures. In the first test, the coolant and the mainstream temperatures

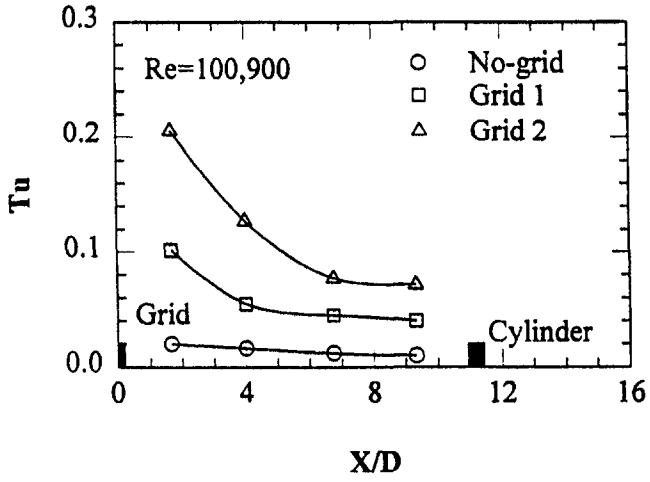

Fig. 3 Streamwise turbulence distributions inside the test tunnel

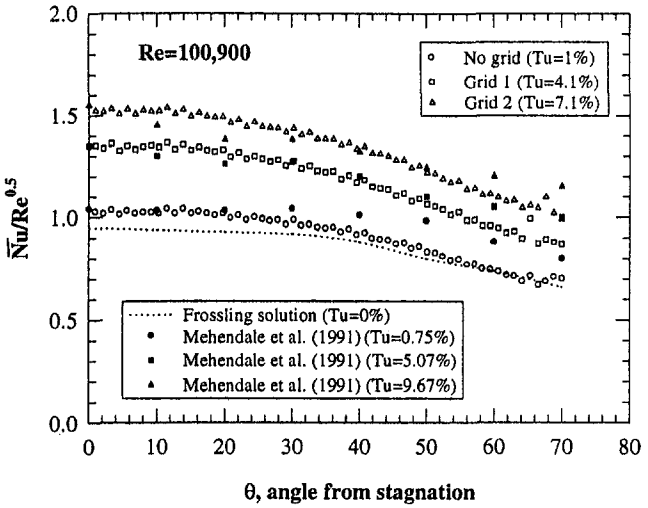

Fig. 4(a) Free-stream turbulence effects on span-averaged $Nu/Re^{0.5}$ distributions for a smooth surface

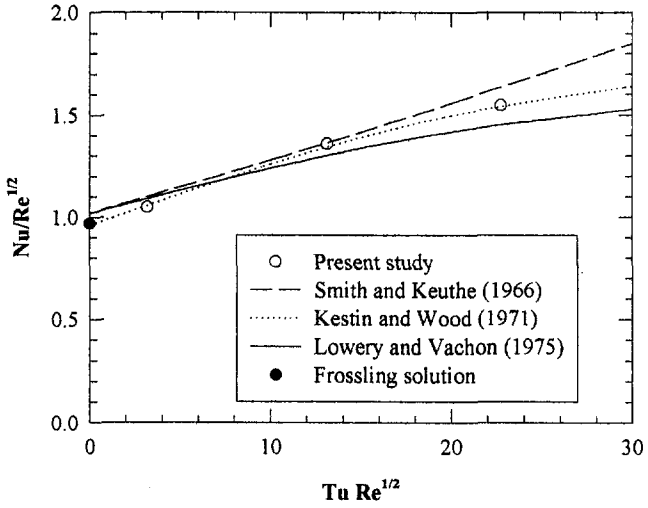

Fig. 4(b) Comparison of stagnation point heat transfer results with published correlations

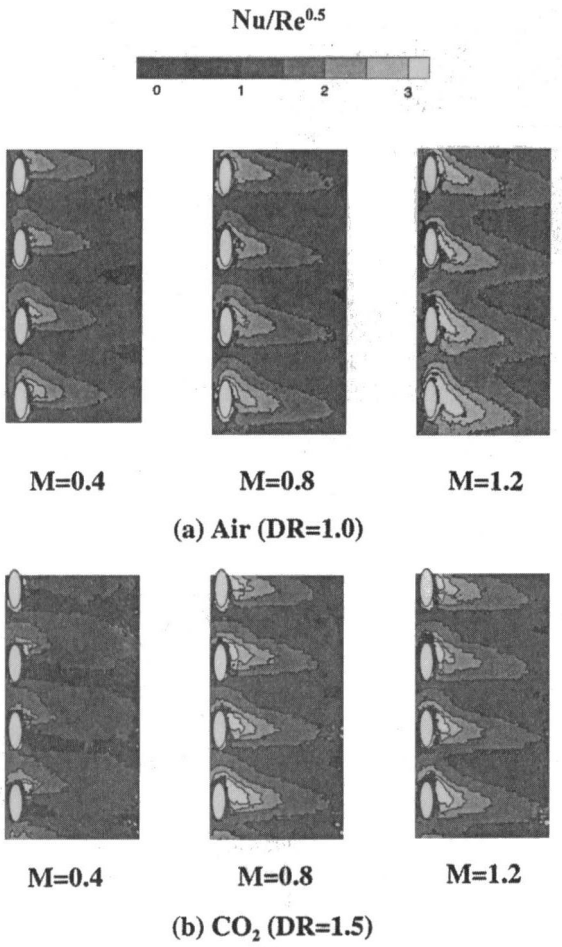

Fig. 5 Effect of blowing ratio on detailed $Nu/Re^{0.5}$ distributions for air and CO_2 injection

are nearly the same. Since the film temperature (T_f) is replaced by the known mainstream temperature (T_∞), the heat transfer coefficient is calculated from Eq. (1). For the second test, the coolant flow is heated to a temperature close to the initial heated surface temperature. Film effectiveness is obtained by rearranging Eq. (3) as

$$\eta = \frac{T_r - T_{i_2}}{T_{c_2} - T_{\infty_2}} \frac{1}{F(h)} + \frac{T_{i_2} - T_{\infty_2}}{T_{c_2} - T_{\infty_2}}$$

where

$$F(h) = 1 - \exp\left(\frac{h^2 \alpha t_2}{k^2}\right) \operatorname{erfc}\left(\frac{h\sqrt{\alpha t_2}}{k}\right) \qquad (4)$$

The subscript (2) indicates the second test. The heat transfer coefficient (h) is obtained from the first test for the same experimental conditions. The duration for each test is a maximum of 60 seconds, which helps maintain the semi-infinite solid assumption on the test surface.

Experimental uncertainty in heat transfer coefficient and film effectiveness measurement is estimated to be about ±4.5 and ±6.8 percent, respectively. The individual uncertainties in color change time (t) is ±0.5 s; mainstream temperature (T_∞) is ±0.2°C; surface initial temperature (T_i) is ±0.5°C; coolant temperature (T_c) is ±0.2°C; and material physical properties ($\sqrt{\alpha/k}$) is ±3 percent. It should be noted that the uncertainty in the immediate vicinity of the film hole could be as high as ±17 percent. These estimated levels could be due to the invalidation of the semi-infinite model assumption.

Results and Discussion

Tests were conducted in a low-speed wind tunnel for a Reynolds number of 100,900 based on cylinder diameter. Air is used as coolant to simulate a coolant-to-mainstream density ratio (DR) of 1.0 and CO_2 is used to simulate a density ratio of 1.5. The coolant-to-mainstream momentum flux ratio (I) is a function of the blowing ratio and the density ratio, $I = M^2/DR$. The mainstream inlet velocity and density is used for evaluating the blowing and density ratios. Heat transfer coefficient results are presented on a smooth surface for three turbulence levels of 1, 4.1, and 7.1 percent. Film effectiveness and heat transfer coefficient distributions are presented for three blowing ratios of 0.4, 0.8, and 1.2 and two coolant density ratios of 1.0 (air) and 1.5 (CO_2) at a low free-stream turbulence intensity of 1 percent. Film effectiveness and heat transfer coefficient distributions are also presented at $M = 0.4$ and 1.2 for both coolants at $Tu = 4.1$ and 7.1 percent.

The coolant-to-mainstream density ratio for the heat transfer coefficient and film effectiveness tests are almost equal. The heat transfer coefficient test is run with both mainstream and coolant at room temperature whereas in the film effectiveness test, the coolant is slightly hotter ($T_c - T_\infty \sim 6$°C) than the mainstream. Such a small difference in temperatures does not produce significant variation in the density ratios between the two tests.

Velocity and turbulence measurements were measured along the wind tunnel. Incident mainstream velocity (U_∞) was obtained to be 21 m/s at $X/D = 9.5$ from the grid location. Figure 3 presents the centerline streamwise turbulence intensity distributions for the three turbulence levels. As the distance from the

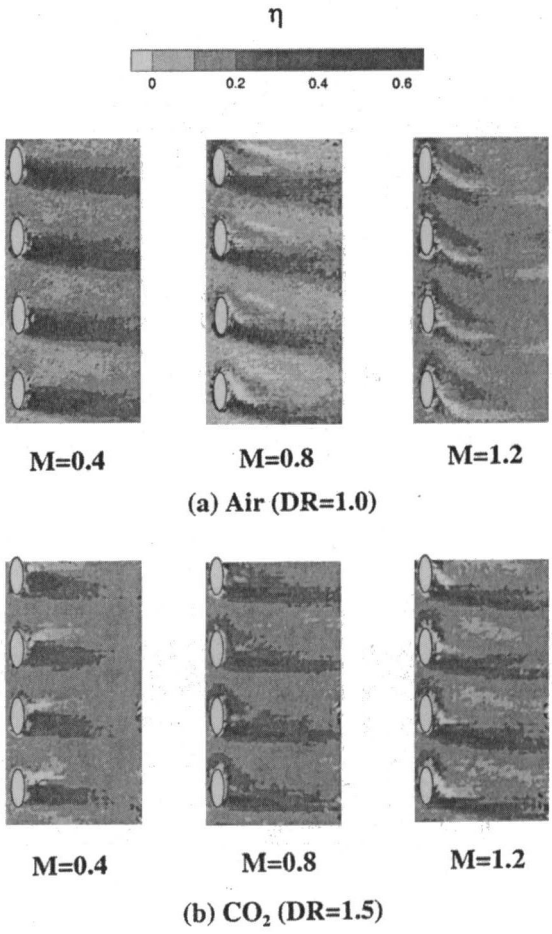

Fig. 6 Effect of blowing ratio on detailed film effectiveness distributions for air and CO_2 injection

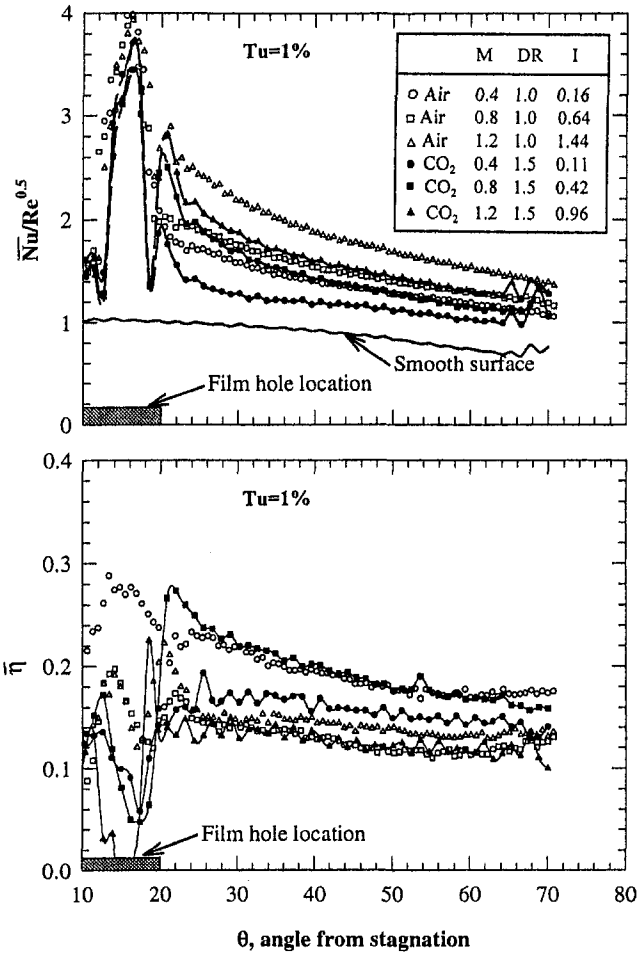

Fig. 7 Effect of coolant blowing ratio and density ratio on span-averaged $Nu/Re^{0.5}$ and film effectiveness distributions

nozzle increases, the streamwise turbulence decays and reaches a low just upstream of the cylinder. This low value is defined as the oncoming free-stream turbulence intensity and is obtained to be 1 percent for no-grid case, 4.1 percent for grid 1, and 7.1 percent for grid 2. Corresponding streamwise dissipation length scales at the same location were estimated to be about 1.3 cm for grid 1 and 1.5 cm for grid 2.

Smooth Surface Heat Transfer. Heat transfer coefficients were measured on a smooth surface with no film holes under the three free-stream turbulence levels. The local Nusselt number is normalized by the mainstream Reynolds number and presented as $Nu/Re^{1/2}$. The viscosity and the conductivity used to evaluate the $Nu/Re^{1/2}$ values are based on the oncoming mainstream inlet flow. Figure 4(*a*) presents the span-averaged $Nu/Re^{0.5}$ distributions under free-stream turbulence effects. Results are presented on one side of the front half of the cylinder from geometric stagnation (0 deg) to about 70 deg downstream from the stagnation point. The $Nu/Re^{0.5}$ values over the entire measurement region increases with an increase in free-stream turbulence. Stagnation point heat transfer is enhanced up to 50 percent for Tu = 7.1 percent over low turbulence level of Tu = 1 percent. The enhancement for Tu = 4.1 percent is about 30 percent. The $Nu/Re^{0.5}$ values decreases with increase in angle from stagnation. The Frössling theoretical solution for zero turbulence is also shown for comparison. Results from Mehendale et al. (1991) are also presented for comparison. Turbulence levels used in the study by Mehendale et al. (1991) were 0.75, 5.07, and 9.67 percent. Their results agree well with the present results closer to the leading edge. However, farther from the leading edge, the present results are lower than those from Mehendale et al. (1991).

Figure 4(*b*) compares the stagnation point heat transfer results from the present study with established correlations by Smith and Keuthe (1966), Kestin and Wood (1971), and Lowery and Vachon (1975). The present data agree most closely with the Kestin and Wood correlation. Comparison with other two correlations is not good at $Tu\ Re^{1/2}$ values over 20. All the three correlations are close to each other at low $Tu\ Re^{1/2}$ values. In the present study, the Reynolds number is constant and the free-stream turbulence is varied to obtain different $Tu\ Re^{1/2}$ values.

Film Cooling. Figure 5 presents the detailed $Nu/Re^{0.5}$ distributions for the three blowing ratios for both coolants at Tu = 1 percent. For both coolants, an increase in blowing ratio produces higher $Nu/Re^{0.5}$ values. For low blowing ratio of 0.4, the $Nu/Re^{0.5}$ values are higher near the top edge of the film holes. As blowing ratio increase, the $Nu/Re^{0.5}$ values are higher downstream of the entire hole. The coolant has limited interaction with the mainstream for low blowing ratios. However, as blowing ratios increase, the interaction with mainstream increases, producing more turbulent mixing, thus enhancing downstream heat transfer coefficients. The $Nu/Re^{0.5}$ distributions for the same blowing ratio for both coolants appear similar. However, the higher density coolant produces slightly lower $Nu/Re^{0.5}$ values due to lower momentum flux ratio (I).

Figure 6 presents the detailed film effectiveness distributions at the three blowing ratios for both coolants at Tu = 1 percent. Effectiveness in the axial direction along the hole decreases with an increase in blowing ratio. However, effectiveness appears to be highest for M = 0.8 with CO_2 injection. It is evident that

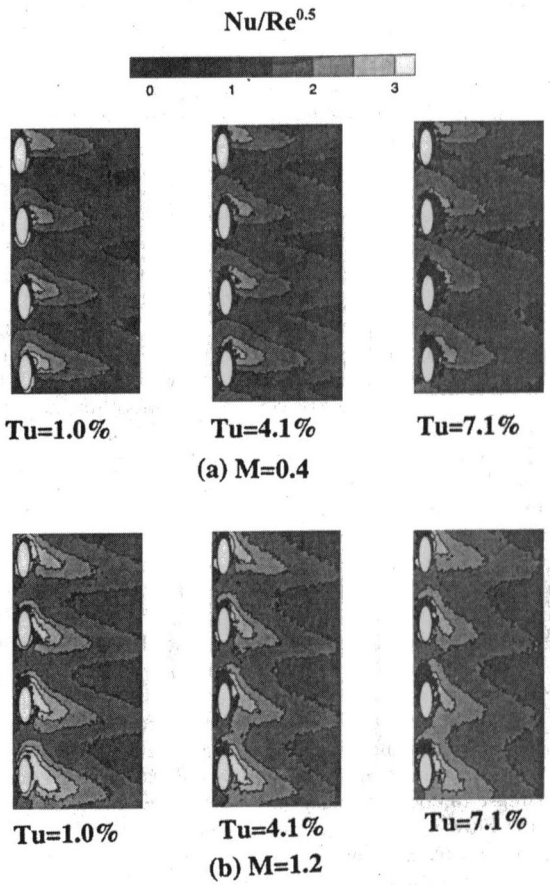

Fig. 8 Effect of free-stream turbulence on detailed $Nu/Re^{0.5}$ distributions for air injection

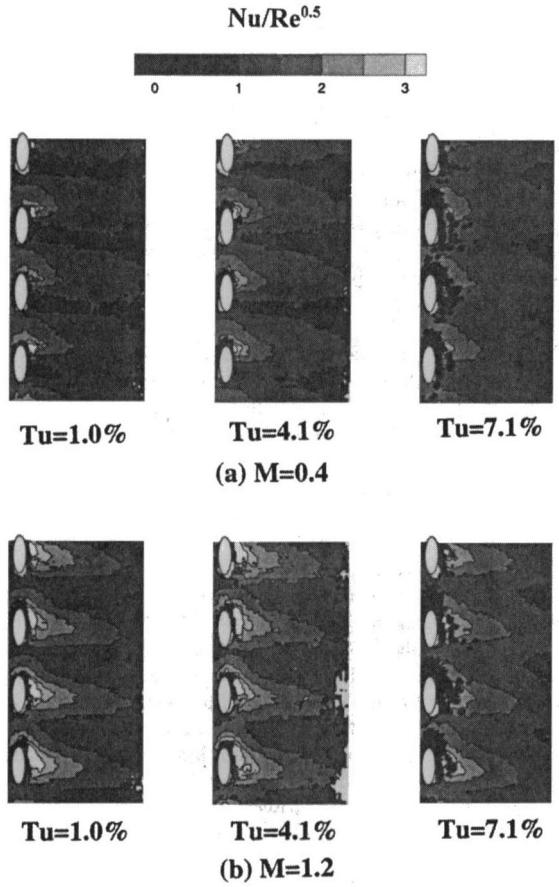

Fig. 9 Effect of free-stream turbulence on detailed Nu/Re$^{0.5}$ distributions for CO_2 injection

the coolant streaks show more angle away from the mainstream as blowing ratio increases. At higher blowing ratios, coolant jets have a higher momentum into the mainstream, which may cause the angled coolant streaks. Higher density coolant (CO_2) provides higher effectiveness near the hole at a blowing ratio of $M = 0.8$ compared to lower density coolant (air). However, at $M = 0.4$, air provides better effectiveness. Air as coolant possesses higher momentum than CO_2 at the same blowing ratio. At low blowing ratio, air has optimum momentum to provide higher effectiveness on the surface. The coolant density effect appears to be reduced at higher blowing ratios of $M = 1.2$. At higher blowing ratios, coolant jets shoot into the mainstream and disturb the thin boundary layer without providing enough protection.

Figure 7 presents the span-averaged Nu/Re$^{0.5}$ distributions for both coolants at all three blowing ratios. The momentum flux ratios (I) for each coolant at different blowing ratios are presented in the figure. Span-averaged results are presented from the upstream edge of film hole location (10 deg) to about 70 deg from leading edge stagnation point. The Nu/Re$^{0.5}$ values are high at the hole location and decrease downstream for all blowing ratios and both coolants. Far downstream (70 deg), the effect of film injection is reduced and Nu/Re$^{0.5}$ values are closer to a value of 1.0. The no-grid turbulence case for smooth surface is also presented for comparison. An increase in blowing ratio produces an increase in Nu/Re$^{0.5}$ values for both coolants. An increase in coolant density produces lower Nu/Re$^{0.5}$ values for same blowing ratio. CO_2 as coolant has lower momentum flux ratio compared to air at the same blowing ratio. The coolant-to-mainstream momentum flux ratio is also an important parameter in film cooling situations. Higher density coolant is heavier than the oncoming mainstream fluid. This reduces coolant jet to mainstream interaction, thus reducing turbulent mixing, which in turn produces lower heat transfer coefficients compared to a coolant with the same density as mainstream. Figure 7 also presents the span-averaged film effectiveness distributions for all three blowing ratios and both coolants. Results are presented from the upstream edge of film hole location. Effectiveness value decrease slightly with increase in distance from hole location. An increase in blowing ratio produces lower film effectiveness for air injection. However, the effect of blowing ratio for an increase from $M = 0.8$ to $M = 1.2$ does not produce much variation for $\overline{\eta}$ values with air as coolant. It should be noted that the detailed film effectiveness distributions at the two blowing ratios are different. CO_2 as coolant provides highest effectiveness at $M = 0.8$. Film effectiveness with CO_2 as coolant is lower than for air as coolant at blowing ratios of 0.4. However, at higher blowing ratios ($M = 1.2$), the effect of coolant density disappears. Both air and CO_2 produces similar $\overline{\eta}$ values for $M = 1.2$.

Effect of Free-Stream Turbulence. Free-stream turbulence is also an important parameter that effects airfoil leading edge film effectiveness and heat transfer coefficients. Figure 8 presents the detailed Nu/Re$^{0.5}$ distributions for air injection at blowing ratios of 0.4 and 1.2 under increased free-stream turbulence. Two higher levels of turbulence at 4.1 and 7.1 percent are presented for both blowing ratios. Free-stream turbulence does not appear to significantly affect the Nu/Re$^{0.5}$ distributions downstream of injection. Free-stream turbulence intensity may be lower than the large-scale turbulence generated immediately downstream of film holes by coolant–mainstream

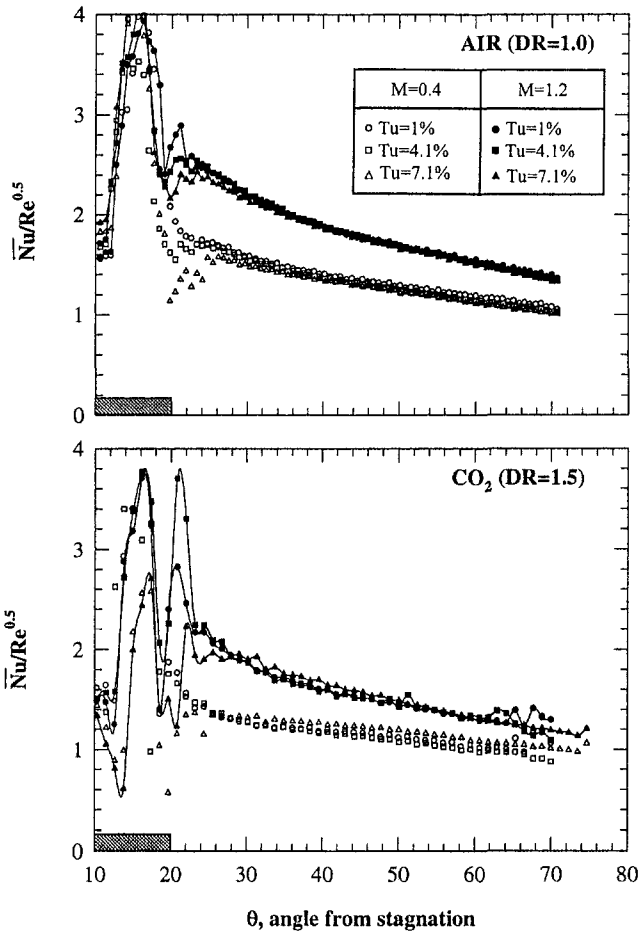

Fig. 10 Effect of free-stream turbulence on span-averaged Nu/Re$^{0.5}$ distributions for air and CO_2 injection

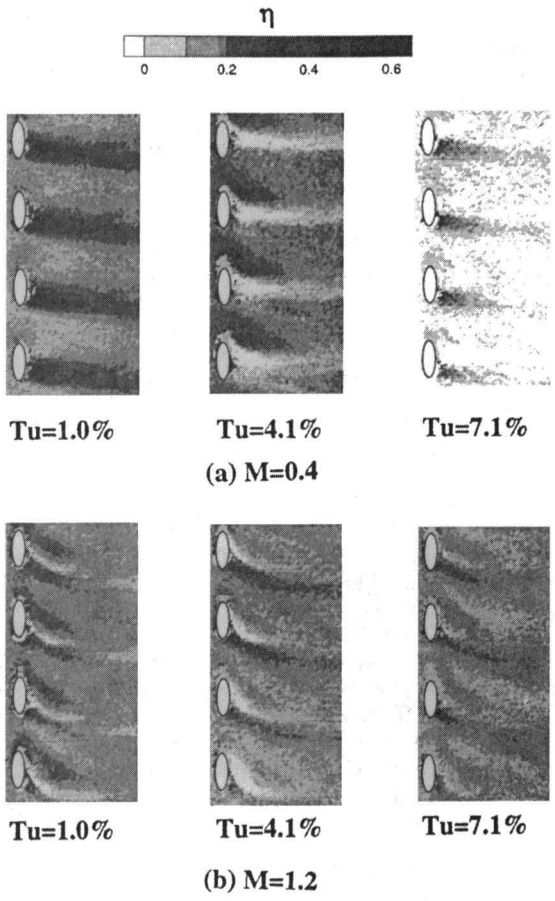

Fig. 11 Effect of free-stream turbulence on detailed film effectiveness distributions for air injection

mixing. This may be the reason for the small effect of free-stream turbulence on heat transfer coefficients.

Figure 9 presents the detailed $Nu/Re^{0.5}$ distributions for CO_2 injection at blowing ratios of 0.4 and 1.2 under increased free-stream turbulence. Two higher levels of turbulence at 4.1 and 7.1 percent are presented for both blowing ratios. Free-stream turbulence does not seem to alter the $Nu/Re^{0.5}$ distributions significantly for both blowing ratios as in the case for air injection. However, an increase in free-stream turbulence appears to reduce the spanwise variations downstream compared to the no-grid case (Tu = 1 percent) for both blowing ratios. Higher free-stream turbulence enhances coolant–mainstream mixing, which may be the reason for reduced spanwise variations of Nusselt numbers.

Figure 10 presents the span-averaged $Nu/Re^{0.5}$ distributions for both air and CO_2 injection under the effects of increase free-stream turbulence. It can be seen that free-stream turbulence has little effect for most of the surface for both coolants at both blowing ratios. However, in the region immediately (1 hole diameter) downstream of the holes, the free-stream turbulence causes significant variations of span-averaged Nusselt number values.

Figure 11 presents detailed film effectiveness distributions for air injection at blowing ratios of 0.4 and 1.2 under increased free-stream turbulence. Free-stream turbulence reduces film effectiveness significantly for M = 0.4 (I = 0.16). Higher free-stream turbulence breaks down low-momentum coolant jets (I = 0.16) and decreases surface protection. The reduction in the film effectiveness is clearly evident in the detailed distributions. At higher blowing ratio of 1.2 (I = 1.44), the effect of free-stream turbulence is not so significant. However, the effectiveness is slightly reduced immediately downstream of injection. There is more uniform effectiveness over the entire surface at higher free-stream turbulence. The stronger momentum jets at M = 1.2 (I = 1.44) are not affected significantly by free-stream turbulence as in the case for M = 0.4.

Figure 12 presents the detailed film effectiveness distributions for CO_2 injection at blowing ratios of 0.4 and 1.2 under increased free-stream turbulence. Free-stream turbulence reduces film effectiveness significantly for M = 0.4 from Tu = 1 to Tu = 7.1 percent. Higher free-stream turbulence breaks down coolant jet structure (I = 0.107) at low blowing ratio. At higher blowing ratio of 1.2 (I = 0.96), the effect of free-stream turbulence is not so significant with more uniform effectiveness over the entire surface at higher free-stream turbulence. Effectiveness downstream of the hole is reduced with an increase in free-stream turbulence.

Figure 13 presents the span-averaged film effectiveness distributions for both air and CO_2 injection under the effects of increase free-stream turbulence. For a low blowing ratio of 0.4, the film effectiveness value drops significantly with an increase in free-stream turbulence for air and CO_2 injection. The free-stream turbulence effect is not so significant at M = 1.2 for both coolants. There is a slight reduction in the region immediately downstream of the holes. But the effectiveness values are not affected by an increase in free-stream turbulence at such high blowing ratios.

Local Nusselt numbers (Nu) with film injection are normalized by local Nusselt numbers (Nu_0) without film injection. The local Nusselt number ratios (Nu/Nu_0) are regionally averaged to produce a single spatially averaged Nusselt number ratio for each blowing ratio for each coolant at each free-stream turbulence. The spatial averaging is done for the spanwise length encompassing four-hole spacing as shown in the detailed

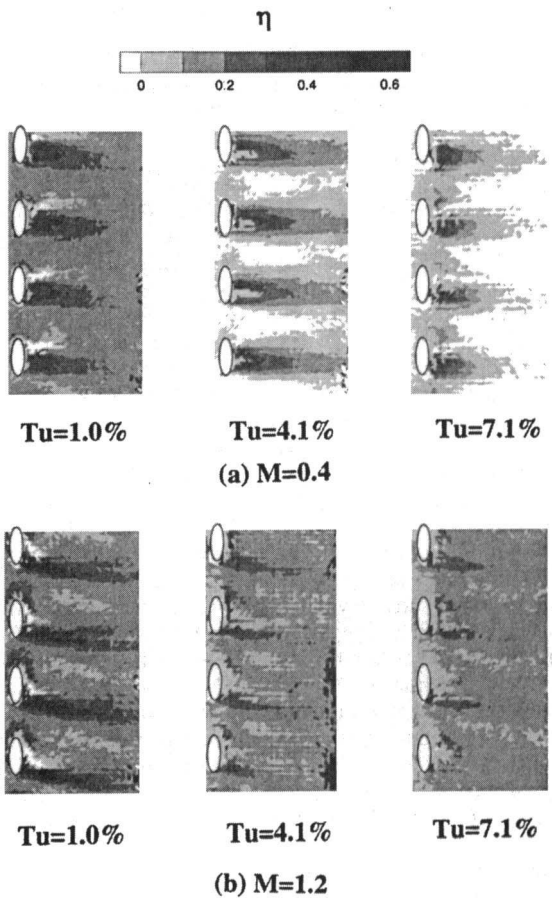

Fig. 12 Effect of free-stream turbulence on detailed film effectiveness distributions for CO_2 injection

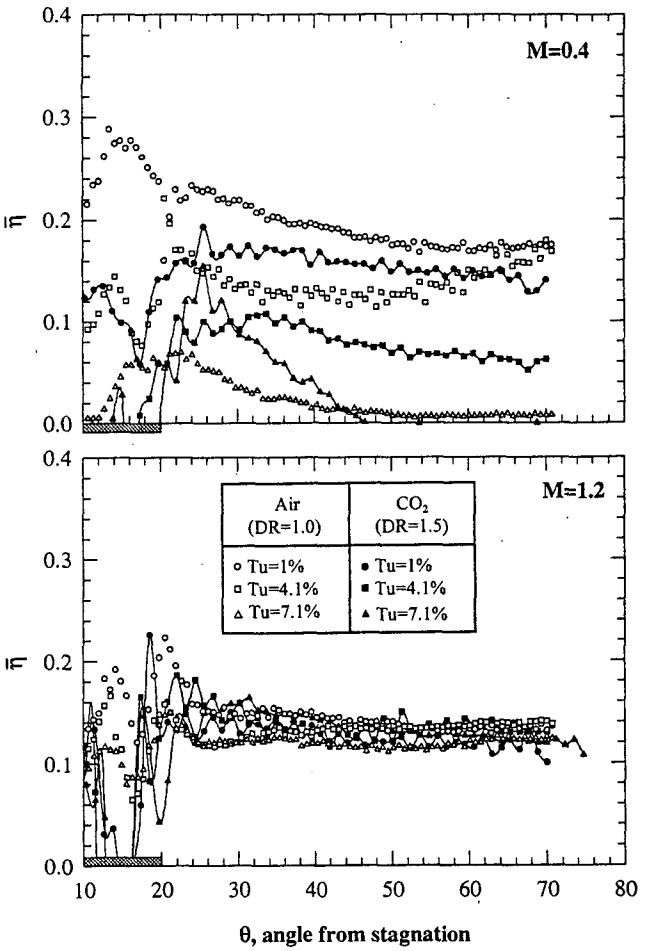

Fig. 13 Effect of free-stream turbulence on span-averaged film effectiveness distributions for air and CO_2 injection

distributions and for the axial distance from 20 to 70 deg (downstream of injection hole) from leading edge. Similarly, the local film effectiveness values are averaged over the same region to produce a single spatially averaged film effectiveness. The spatially averaged Nusselt number ratios and film effectiveness values are plotted against the momentum flux ratios in Fig. 14. The open symbols represent I values with air injection and closed symbols represent I values with CO_2 injection. The Nusselt numbers with film injection are normalized by Nusselt number without film injection at the same free-stream turbulence intensity. The Nusselt number ratios show a continuing increase with an increase in momentum flux ratio. With increasing I, there is more coolant-to-mainstream interaction causing higher heat transfer coefficients downstream of injection. This may be the reason for the increase in Nusselt number ratio with increasing I. With an increase in free-stream turbulence, Nusselt number ratio at the same I value decreases. As indicated earlier, Nusselt number downstream of injection (Nu) are not affected by increases in free-stream turbulence intensity. However, Nusselt numbers without film injection (Nu_0) increase with an increase in free-stream turbulence intensity. This is the reason for lower Nusselt number ratios for higher free-stream turbulence intensity. Film effectiveness values at low turbulence (1.0 percent) increase from $I = 0.1$ to a peak at $I = 0.16$ and then decrease to $I = 0.96$ and are maintained at about same level at $I = 1.44$. With an increase in free-stream turbulence intensity, film effectiveness at low I decreases significantly. At low I, film effectiveness is very low at $Tu = 7.1$ percent. At high I ($I > 0.96$), free-stream turbulence has little effect on film effectiveness. The high-momentum jets are not easily broken down by higher free-stream turbulence as in the case for low-momentum jets. The results obtained from this study using two different coolants at same blowing ratios correlate well with the dependent parameter I. From the results, it can be interpreted that momentum flux ratio can be used a parameter to correlate the effects of coolant density and coolant blowing ratio.

Conclusions

Detailed Nusselt number and film effectiveness distributions are presented on a cylindrical leading edge model with film cooling. The effects of higher coolant density and higher free-stream turbulence are focused.

1 Smooth surface (without film holes) heat transfer coefficient is enhanced up to 30 percent for $Tu = 4.1$ percent and up to 50 percent for $Tu = 7.1$ percent over a $Tu = 1$ percent.

2 Increase in blowing ratio increases Nusselt numbers downstream of injection. Effectiveness for air injection is higher at low blowing ratio $M = 0.4$ and decreases with an increase in blowing ratio. Effectiveness for CO_2 injection is highest at $M = 0.8$. Higher heat transfer coefficient region does not necessarily correspond to high film effectiveness as seen in the detailed distributions.

3 Increase in coolant density causes a decrease in heat transfer coefficients at all blowing ratios. Air provides better effectiveness at low blowing ratios. Higher density coolant (CO_2) provides highest effectiveness at $M = 0.8$. However, at even higher blowing ratios, an increase in coolant density has little effect on film effectiveness distributions.

4 Higher free-stream turbulence has only a small effect on Nusselt numbers at all blowing ratios for both coolants. However, higher free-stream turbulence reduces film effectiveness significantly at $M = 0.4$ for both coolants but has little effect on film effectiveness for $M = 1.2$.

5 Overall averaged Nusselt number ratios for film injection show a continual increase with increase in coolant-to-mainstream momentum flux ratio. However, overall averaged film

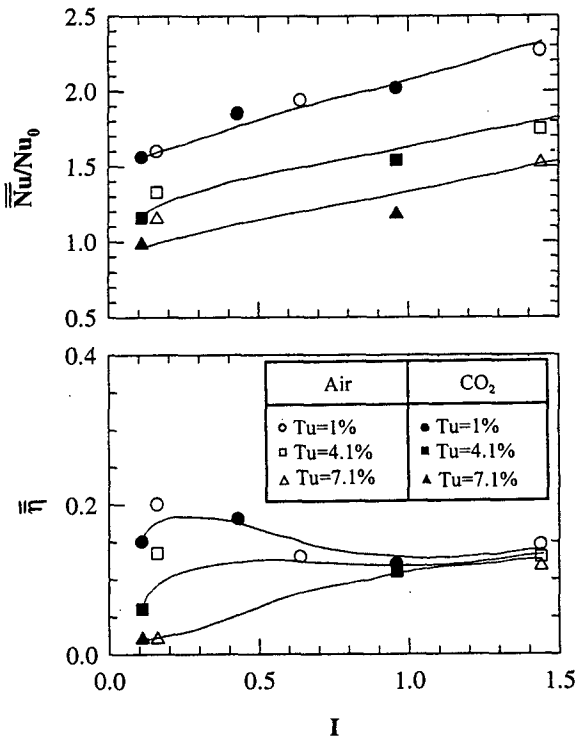

Fig. 14 Variation of spatially averaged Nusselt number ratio and film effectiveness with momentum flux ratio

effectiveness varies with increasing momentum flux ratios. Momentum flux ratio may be used to correlate the results obtained for different coolant densities and coolant blowing ratios.

Acknowledgments

This paper was prepared with the support of the NASA-Lewis Research Center under grant number NAG3-1656. The NASA technical team is Dr. Phil Poinsatte and Dr. Raymond Gaugler. Their support is greatly appreciated.

References

Bonnice, M. A., and L'Ecuyer, M. R., 1983, "Stagnation Region Gas Cooling—Effects of Dimensionless Coolant Temperature," NASA CR-168197.

Ekkad, S. V., Zapata, D., and Han, J. C., 1997a, "Heat Transfer Coefficients Over a Flat Surface With Air and CO_2 Injection Through Compound Angle Holes Using a Transient Liquid Crystal Image Method," ASME JOURNAL OF TURBOMACHINERY, Vol. 119, pp. 580–586.

Ekkad, S. V., Zapata, D., and Han, J. C., 1997b, "Film Effectiveness Over a Flat Surface With Air and CO_2 Injection Through Compound Angle Holes Using a Transient Liquid Crystal Image Method," ASME JOURNAL OF TURBOMACHINERY, Vol. 119, pp. 587–593.

Funazaki, K., Yokota, M., Yamawaki, S., 1997, "The Effect of Periodic Wake Passing on Film Effectiveness of Discrete Cooling Holes Around the Leading Edge of a Blunt Body," ASME JOURNAL OF TURBOMACHINERY, Vol. 119, pp. 292–301.

Karni, J., and Goldstein, R. J., 1990, "Surface Injection Effect on Mass Transfer From a Cylinder in Crossflow: A Simulation of Film Cooling in the Leading Edge Region of a Turbine Blade," ASME JOURNAL OF TURBOMACHINERY, Vol. 112, pp. 418–427.

Lee, J. S., Ro, S. T., and Seo, H. J., 1994, "Mass Transfer Effects of Free-Stream Turbulence and Horseshoe Vortex Formed at the Upstream Edge of Film Cooling Jets About a Cylindrical Surface," ASME Paper No. 94-GT-18.

Kestin, J., and Wood, R. T., 1971, "The Influence of Turbulence on Mass Transfer From Cylinders," ASME *Journal of Heat Transfer,* Vol. 93, pp. 321–327.

Lowery, G. W., and Vachon, R. I., 1975, "The Effect of Turbulence on Heat Transfer From Heated Cylinders," *International Journal of Heat and Mass Transfer,* Vol. 18, pp. 1229–1242.

Luckey, D. W., and L'Ecuyer, M. R., 1976, "Stagnation Region Gas Film Cooling—Spanwise Angled Coolant Injection," Thermal Sciences and Propulsion Center, Purdue University, W. Lafayette, IN, Technical Report No. TSPC-TR-76-2.

Mehendale, A. B., Han, J. C., and Ou, S., 1991, "Influence of High Mainstream Turbulence on Leading Edge Heat Transfer," ASME *Journal of Heat Transfer,* Vol. 113, pp. 843–850.

Mehendale, A. B., and Han, J. C., 1992, "Influence of High Mainstream Turbulence on Leading Edge Film Cooling Heat Transfer," ASME JOURNAL OF TURBOMACHINERY, Vol. 114, pp. 707–715.

Mick, W. J., and Mayle, R. E., 1988, "Stagnation Film Cooling and Heat Transfer, Including Its Effect Within the Hole Pattern," ASME JOURNAL OF TURBOMACHINERY, Vol. 110, pp. 66–72.

Ou, S., Mehendale, A. B., and Han, J. C., 1992, "Influence of High Mainstream Turbulence on Leading Edge Film Cooling Heat Transfer: Effect of Film Hole Row Location," ASME JOURNAL OF TURBOMACHINERY, Vol. 114, pp. 716–723.

Ou, S. and Han, J. C., 1992, "Influence of Mainstream Turbulence on Leading Edge Film Cooling Heat Transfer Through Two Rows of Inclined Film Slots," ASME JOURNAL OF TURBOMACHINERY, Vol. 114, pp. 724–733.

Salcudean, M., Gartshore, I., Zhang, K., and Barnea, Y., 1994, "Leading Edge Film Cooling of a Turbine Blade Model Through Single and Double Row Injection: Effects of Coolant Density," ASME Paper No. 94-GT-2.

Smith, M. C. and Keuthe, A. M., 1966, "Effects of Turbulence on Laminar Skin Friction and Heat Transfer," *Physics of Fluids,* Vol. 9, pp. 2337–2344.

Effect of Unsteady Wake on Detailed Heat Transfer Coefficient and Film Effectiveness Distributions for a Gas Turbine Blade

H. Du[1]

J. C. Han

S. V. Ekkad[2]

Turbine Heat Transfer Laboratory,
Department of Mechanical Engineering,
Texas A&M University,
College Station, TX 77843-3123

Unsteady wake effects on detailed heat transfer coefficient and film cooling effectiveness distributions from a gas turbine blade with film cooling are obtained using a transient liquid crystal technique. Tests were performed on a five-blade linear cascade at a axial chord Reynolds number of 5.3×10^5 at cascade exit. Upstream unsteady wakes are simulated using a spoke-wheel type wake generator. The test blade has three rows of film holes on the leading edge and two rows each on the pressure and suction surfaces. Air and CO_2 were used as coolants to simulate different coolant-to-mainstream density ratio effect. Coolant blowing ratio for air injection is varied from 0.8 to 1.2 and is varied from 0.4 to 1.2 for CO_2. Results show that Nusselt numbers for a film-cooled blade are much higher compared to a blade without film injection. Particularly, film injection causes earlier boundary layer transition on the suction surface. Unsteady wakes slightly enhance Nusselt numbers but significantly reduce film cooling effectiveness on a film-cooled blade compared with a film-cooled blade without wakes. Nusselt numbers increase slightly but film cooling effectiveness increases significantly with an increase in blowing ratio for CO_2 injection. Higher density coolant (CO_2) provides higher effectiveness at higher blowing ratios ($M = 1.2$) whereas lower density coolant (Air) provides higher effectiveness at lower blowing ratios ($M = 0.8$).

Introduction

A continuing trend towards higher gas turbine inlet temperatures has resulted in higher heat loads on turbine components. Hence, sophisticated cooling techniques must be employed to cool the components to maintain the performance requirements. Film cooling through discrete holes is used as a method of external cooling on turbine blades. Many studies have presented heat transfer measurements on turbine blades with film cooling. Nirmalan and Hylton (1990) and Camci and Arts (1990) studied heat transfer coefficients on film cooled turbine blades. Takeishi et al. (1992) compared the film cooling effectiveness values for a stationary cascade under 4 percent mainstream turbulence intensity and for a rotor blade using the heat–mass transfer analogy. Ito et al. (1978) and Haas et al. (1992) studied the effect of coolant density on film cooling effectiveness on turbine blades under low mainstream turbulence levels.

The effect of unsteady wakes produced by upstream vane trailing edges has a strong effect on rotor blade surface heat transfer distributions. Several studies have focused on the effect of unsteady wakes on the downstream blade heat transfer coefficient distributions without film cooling. They all reported that unsteady wakes enhanced turbine blade heat transfer and caused earlier and longer laminar–turbulent boundary layer transition on the suction surface. Few studies have focused on the effect of unsteady wakes on film cooled turbine blades. Abhari and Epstein (1994) conducted heat transfer experiments on a film-cooled transonic turbine stage in a short-duration turbine facility. They measured steady and time-resolved, chordwise heat flux distributions at three spanwise locations. They concluded that film cooling reduces the time-averaged heat transfer by about 60 percent on the suction surface compared to the uncooled rotor blade. However, the effect is relatively low on the pressure surface. Ou et al. (1994) and Mehendale et al. (1994) simulated unsteady wake conditions over a linear turbine blade cascade with film cooling. They studied the effects of unsteady wake on a model turbine blade with multiple-row film cooling using air and CO_2 as coolants. They measured heat transfer coefficients and film cooling effectiveness at discrete locations using thin foil heating and multiple thermocouples. They concluded that heat transfer coefficients increase and film cooling effectiveness values decrease with an increase in unsteady wake strength. They also concluded that the higher density (CO_2) coolant provides better film cooling effectiveness at higher blowing ratios than lower density coolant (air). The present study uses a transient liquid crystal technique to measure detailed heat transfer coefficient and film cooling effectiveness distributions on a turbine blade under the effect of upstream unsteady wakes. Detailed heat transfer coefficient and film cooling effectiveness distributions are obtained in the near-hole region and over the entire blade surface. Such detailed distributions were not obtained by the previous studies using thin foil-thermocouple measurement technique.

A few previous studies have measured detailed heat transfer coefficients on turbine blades without film cooling. Martinez-Botas et al. (1995) presented detailed heat transfer coefficient distributions on a non-film cooled blade in an annular transonic cascade using the transient liquid crystal technique. Hoffs et al.

[1] Present address: Schlumberger Ltd., SPT Center, Rosharon, TX.

[2] Present address: Louisiana State University, Mechanical Engineering Dept., Baton Rouge, LA.

Contributed by the International Gas Turbine Institute and presented at the 42nd International Gas Turbine and Aeroengine Congress and Exhibition, Orlando, Florida, June 2–5, 1997. Manuscript received International Gas Turbine Institute February 1997. Paper No. 97-GT-166. Associate Technical Editor: H. A. Kidd.

(1997) measured heat transfer coefficients in a linear cascade without film cooling using a transient liquid crystal technique and compared the results with measurements using the naphthalene sublimation mass transfer technique. Du et al. (1997a) applied the transient liquid crystal technique for heat transfer coefficient measurement on a turbine blade without film cooling under the effects of upstream unsteady wakes with trailing edge coolant ejection at various free-stream turbulence conditions. Vedula and Metzger (1991) presented a transient liquid crystal technique for detailed measurements of both heat transfer coefficients and film cooling effectiveness, over a flat surface with one row of simple angle injection holes. Ekkad et al. (1997a, b) presented detailed heat transfer coefficient and film cooling effectiveness distributions on a flat surface with different compound angle injections and two coolant densities. Based on the same technique, Du et al. (1997b) reported the detailed film cooling measurements over a film cooled turbine blade under steady, low free-stream turbulence conditions (i.e., no upstream unsteady wakes). The present study uses a similar transient liquid crystal technique (Ekkad et al., 1997a, b; Du et al., 1997b) to measure detailed heat transfer coefficient and film cooling effectiveness distributions on a film cooled turbine blade with air and CO_2 injection under the effect of upstream unsteady wakes. It is very important to study the effect of upstream unsteady wakes on the turbine blade film cooling performance. The detailed heat transfer coefficient and film cooling effectiveness distributions provide better understanding of both unsteady wakes and film cooling effects on a turbine blade, particularly in the near-hole region.

Experimental Apparatus

Figure 1 shows the schematic of the test section and camera locations. The test apparatus consists of a low-speed wind tunnel with an inlet nozzle, a linear turbine blade cascade with the test blade in the center, and a suction type blower. The wind tunnel is designed to accommodate for the 107.49 deg turn of the blade cascade. The mean velocity increases 2.5 times from inlet of the cascade to exit. The test apparatus is described in detail by Ou et al. (1994). A spoked wheel type wake generator, similar to the one used by Ou et al. (1994), simulated the upstream unsteady wake. The wake generator has 32 rods, each 0.63 cm in diameter, to simulate the trailing edge of an upstream vane. The wake Strouhal number is adjusted by controlling the rod rotation speed (N). The error caused by using nonparallel rotating rods with a linear blade cascade was small and is discussed by Ou et al. (1994). The liquid crystal color change time is measured using a high-precision image processing system. The system consists of four cameras individually connected to a color frame grabber board in the PC and a monitor. Software is used to measure the time of color change of liquid crystals. During one test, only one camera is operational. Hence, we require four different runs with four different camera locations to measure one set of data for a particular condition. Details on the image processing system are presented by Ekkad et al. (1997a). The image processing system consists of an RGB camera, monitor and a PC with color frame grabber board.

The blade configuration, scaled up five times, produces a velocity distribution typical of an advanced high pressure turbine blade row. The cascade has five blades, each with an axial chord length of 17 cm and radial span of 25.2 cm. The blade spacing is 17.01 cm at the cascade inlet and the throat-to-blade span ratio is 0.2. Figure 2 presents the film cooled turbine blade model. There are five cavities used to supply coolant to different film hole rows on the blade surface. The first cavity supplies coolant to the three leading edge film hole rows. Each of the other four cavities supplies coolant to each row on the pressure and suction surfaces. Flow rate into each cavity is controlled using a flowmeter. The coolant flow from each flowmeter is passed through a solenoid-controlled three-way diverter valve before the flow enters the coolant cavity inside the blade. Each solenoid-controlled valve is connected to a switch that triggers the coolant flow into the cavities at the instant the transient test is initiated. The blade film hole configuration is shown in the figure. Details of the blade film hole configurations are presented by Ou et al. (1994). Figure 2 also shows a three-dimensional view of the pressure and suction surfaces of the test blade. The liquid crystal coated surface area is 15.2 cm wide and the data acquisition area is 7.6 cm wide along the midspan region of the test blade. In the experiment, the test blade surface is heated uniformly using a heater box. The heater box has the blade shape and is slightly larger than the test blade. The insides of the heater box are instrumented with thin foil heaters and controlled using several variacs to provide a near uniform surface temperature. The heater box is lowered to completely cover

Nomenclature

C_x = blade axial chord length = 17 cm
D = film hole diameter
d = wake generator rod diameter
DR = coolant-to-mainstream density ratio = ρ_c/ρ_m
h = local heat transfer coefficient
I = coolant to mainstream momentum flux ratio = $\rho_c V_c^2/\rho_m V^2$
k = thermal conductivity of blade material = 0.159 W/m-°C
k_{air} = thermal conductivity of cascade inlet mainstream air
L = length of film injection hole
M = coolant-to-mainstream mass flux ratio or blowing ratio = $\rho_c V_c/\rho_m V$
N = speed of rotating rods
n = number of rods on wake generator
Nu = local Nusselt number based on axial chord = hC_x/k_{air}
$\overline{\text{Nu}}$ = spanwise-averaged Nusselt number
PL = streamwise length on the pressure surface = 25.6 cm
P = film hole pitch
Re = Reynolds number based on exit velocity and axial chord = $V_2 C_x/\nu$
S = wake Strouhal number = $2\pi Ndn/(60V_1)$
SL = streamwise length on the suction surface = 33.1 cm
t = liquid crystal color change time
T_c = coolant temperature
T_f = film temperature
T_i = initial temperature of blade surface
T_m = mainstream temperature
T_w = liquid crystal color change from green to red
Tu = free-stream turbulence intensity
$\tilde{Tu}$ = ensemble-averaged turbulence intensity
V = local mainstream velocity along the blade pressure or suction surface
$V(t)$ = instantaneous velocity at cascade inlet
V_1 = cascade inlet velocity
V_2 = cascade exit velocity
V_c = coolant hole exit velocity
$\tilde{V}$ = ensemble-averaged cascade inlet velocity
VR = coolant-to-mainstream velocity ratio = V_c/V
X = streamwise distance from blade leading edge
α = thermal diffusivity of blade material = 0.135×10^{-6} m^2/s
η = local film cooling effectiveness
$\overline{\eta}$ = spanwise-averaged film cooling effectiveness
ν = kinematic viscosity of cascade inlet mainstream air
ρ_c = coolant density
ρ_m = mainstream flow density

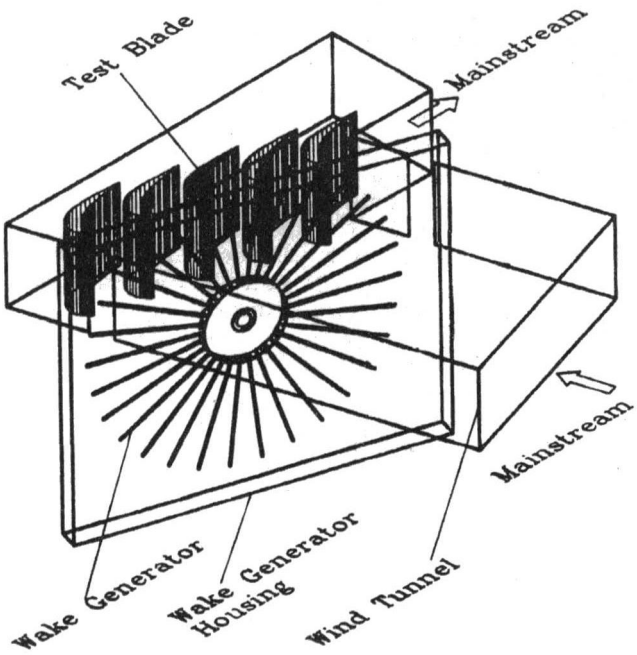

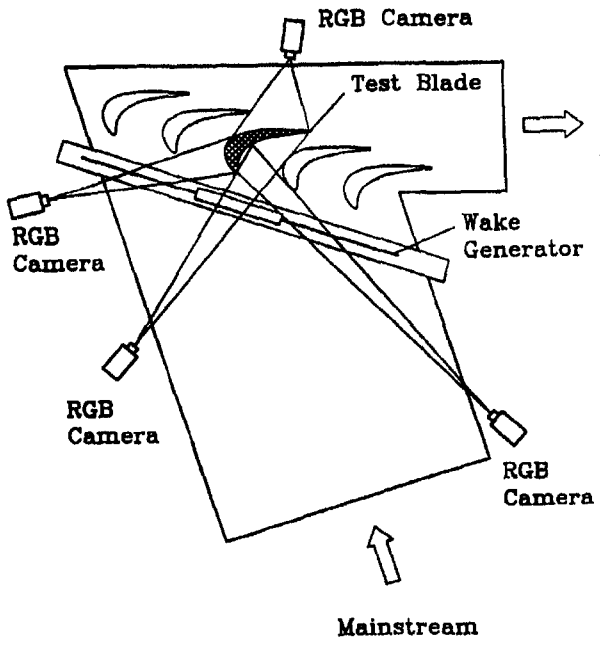

Fig. 1 Schematic of test section and camera locations

the test blade during heating. The heater box is raised completely to expose the test blade to the mainstream during the transient test. The blade surface temperature is monitored using embedded thermocouples during heating. The uniformity of surface temperature with heating is within ±1.2°C. An interpolation scheme was used to reduce the temperature variation further in the initial surface temperature to within ±0.2°C. In the present study, the blade surface is heated to a temperature above liquid crystal blue color (37.2°C). The mainstream air is turned on by starting the suction-type blower. When the blower reaches the stable test flow conditions, the heater box is raised to expose the hot blade to the room temperature mainstream air, within 0.1 seconds. When the heater box completely clears the blade height, the liquid crystal data acquisition system is automatically triggered.

Data Analysis

A vertically oriented single hot-wire was used to measure the instantaneous velocity profile under the effects of passing wakes at the blade cascade inlet. The velocity and turbulence intensity are time dependent and periodic. Due to this periodic nature of the wake passing and shedding, the analysis of the unsteady random signal indicates that its behavior cannot be characterized by time averaging only. The phase-averaged (or

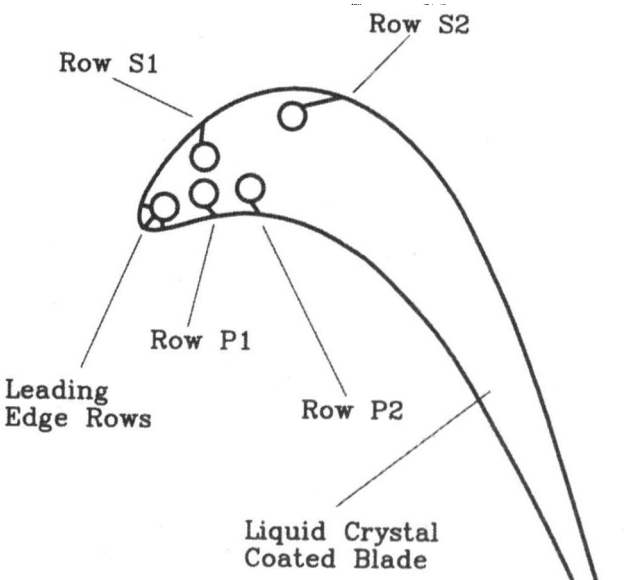

Film Hole Location	P/D	L/D	Axial Angle	Radial Angle	Tangential Angle
LE	7.31	2.7	90°	27°	—
S1	4.13	7.6	—	90°	45°
S2	5.71	12.8	—	90°	30°
P1	6.79	4.2	—	32°	55°
P2	5.00	6.7	—	35°	50°

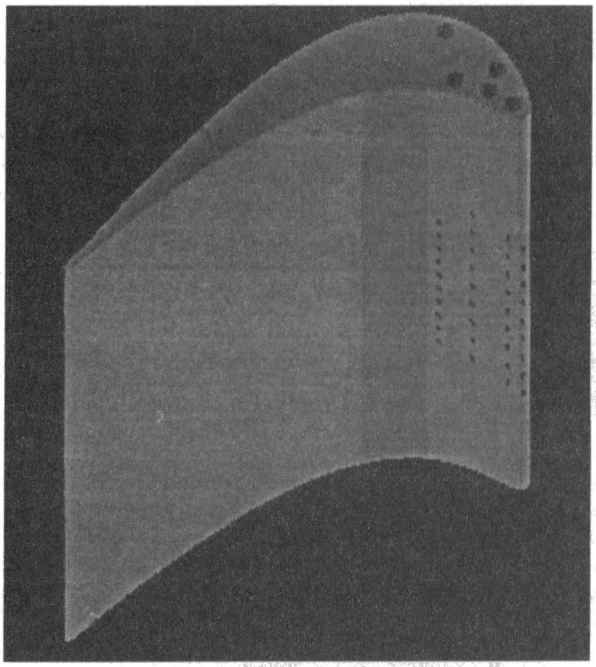

Fig. 2 Test blade geometry with film injection holes

ensemble-averaged) method was used to obtain the time-dependent periodic velocity and turbulence intensity. The ensemble-averaged velocity, $\tilde{V}$, is obtained by dividing each rod-passing period into a certain number of bins (100) and entering data from the selected number of the period into each bin. The ensemble-averaged velocity for each bin is then simply the sum of all the entering data for that bin divided by the selected number of periods (100). The ensemble-averaged turbulence intensity, $\tilde{T}u$, for the flow is obtained from the root-mean-square (rms) value of the fluctuation of the velocity with respect to the ensemble-averaged velocity, divided by the ensemble-averaged velocity.

A transient liquid crystal technique was used to measure the detailed heat transfer coefficients and film cooling effectiveness on the blade surface. The technique is similar to the one described by Ekkad et al. (1997a, b). A one-dimensional transient conduction model into a semi-infinite solid with convective boundary condition is assumed. The solution for surface temperature is obtained as

$$\frac{T_w - T_i}{T_m - T_i} = \left[1 - \exp\left(\frac{h^2\alpha t}{k^2}\right) \text{erfc}\left(\frac{h\sqrt{\alpha t}}{k}\right)\right] \quad (1)$$

where T_w is the wall temperature when liquid crystals change to red from green (32.7°C) at time t, T_i is the initial surface temperature, T_m is the oncoming mainstream flow temperature, and α and k are the thermal diffusivity and conductivity of the blade material, respectively. The heat transfer coefficient is obtained from Eq. (1). For film cooling tests, the mainstream temperature (T_m) in Eq. (1) is replaced by the local film temperature (T_f), which is a mixture of the coolant (T_c) and mainstream temperatures. The film temperature is defined in terms of η, which is the film cooling effectiveness:

$$\eta = \frac{T_f - T_m}{T_c - T_m}; \quad \text{or} \quad T_f = \eta T_c + (1 - \eta)T_m \quad (2)$$

For the film cooling test, we obtain an equation similar to Eq. (1)

$$\frac{T_w - T_i}{T_f - T_i} = \frac{T_w - T_i}{\eta T_c + (1 - \eta)T_m - T_i} = \left[1 - \exp\left(\frac{h^2\alpha t}{k^2}\right) \text{erfc}\left(\frac{h\sqrt{\alpha t}}{k}\right)\right] \quad (3)$$

Two similar transient tests are run to obtain the heat transfer coefficient (h) and film cooling effectiveness (η). In the first test, the blade surface is heated and the coolant and mainstream temperatures are nearly the same. In this case, there is only one unknown, h, in the equation. For the second test, the coolant is heated to a temperature close to blade initial temperature. The calculated local heat transfer coefficient from the first test is substituted in the equation to obtain the local film cooling effectiveness. The methodology is described in detail by Ekkad et al. (1997a, b). This equation is solved at each point (57,000 points) on the blade surface to obtain the detailed heat transfer coefficient and film cooling effectiveness distributions.

The experimental uncertainty in the measurement of the local heat transfer coefficient (h), based on Kline and McClintock's (1953) methodology, is about ±4.5 percent. The individual uncertainties of all the parameters in Eq. (1) have been included. The uncertainty in the film cooling effectiveness measurement includes the additional uncertainties in heat transfer coefficient measurement and was estimated to be about ±6.8 percent. The major contributor to uncertainty is the liquid crystal color change time (t) measured by the image processing system. It should be noted that the uncertainty in the immediate vicinity of the hole (less than one diameter around the hole) and close to blade trailing edge could be as high as ±17 percent due to invalidation of the semi-infinite model assumption. The uncertainty in the velocity measurement using the single hot-wire was estimated to be ±2 percent.

Results and Discussion

Experiments were performed at a cascade exit Reynolds number of 5.3×10^5. The corresponding flow velocity at the cascade exit was 50 m/s. Two different coolants, air and CO_2, are used to simulate density ratios of $DR = 1.0$ and $DR = 1.5$, respectively. For air injection, the blowing ratio was varied from 0.8 to 1.2 and for CO_2 injection, the blowing ratio was varied from 0.4 to 1.2. Tests are run for no rod, no wake case and a case with wake Strouhal number of 0.1. Table 1 lists the test conditions.

Flow Measurements. Figure 3 presents the local-to-exit velocity ratio (V/V_2) distribution around the blade. A pressure tap instrumented blade was used to measure the surface static pressure distributions which was then converted to local mainstream velocity distribution around the blade (Ou et al., 1994). Figure 3 also presents the instantaneous velocity ($V(t)$), ensemble-averaged velocity ($\tilde{V}$), and ensemble-averaged turbulence ($\tilde{T}u$) profiles at the cascade inlet for Strouhal number, $S = 0.1$. The instantaneous velocity profile shows the periodic unsteady fluctuations caused by the upstream passing wakes. The unsteady wakes are actually velocity deficiencies caused by the blockage of mainstream flow by the rotating rods. The ensemble-averaged velocity distribution shows the time-dependent mean velocity defect caused by the upstream passing wakes. The ensemble-averaged turbulence intensity profiles shows that intensity could be as high as 20 percent inside the wake. The time mean averaged turbulence intensity is about 10.4 percent.

Film Cooling Measurements

Effect of Unsteady Wake. Figure 4 presents the detailed Nusselt number distributions on the blade suction and pressure surfaces for cases 1–4. Case 1 is for a smooth surface (no film holes) without rods ($S = 0$); case 2 is for a smooth surface with $S = 0.1$; case 3 is for a film cooled turbine blade with air injection at $M = 0.8$ and no rods ($S = 0$); case 4 is for a film cooled turbine blade with air injection at $M = 0.8$ and $S = 0.1$.

Effect on Suction Surface Nusselt Number. For a smooth surface without wakes (case 1), the Nusselt numbers drop rapidly from the leading edge to about $X/SL = 0.5$ on the suction surface and then increase due to boundary layer transition to turbulent flow. For a smooth surface with wakes (case 2), the Nusselt numbers decrease along the suction side but transition occurs ($X/SL = 0.25$) earlier for this case than for case 1. Also the spanwise variation in the Nusselt number distribution in the transition region decreases. For a blade with film cooling (case 3), Nusselt numbers are higher than for case 1 comparing only the effect of film cooling. On the suction surface, Nusselt numbers are higher downstream of injection from the leading edge. High Nusselt number streaks are obtained along the film cooling holes. Nusselt numbers decrease toward the first film hole row S1. Nusselt numbers are higher along the holes immediately

Table 1 Test conditions

Case No.	S	Coolant	M	VR	DR	I
1	No Wake	None				
2	0.1	None				
3	No Wake	Air	0.8	0.8	1.0	0.64
4	0.1	Air	0.8	0.8	1.0	0.64
5	0.1	Air	1.2	1.2	1.0	1.44
6	0.1	CO_2	0.4	0.27	1.5	0.11
7	0.1	CO_2	0.8	0.53	1.5	0.42
8	0.1	CO_2	1.2	0.80	1.5	0.96

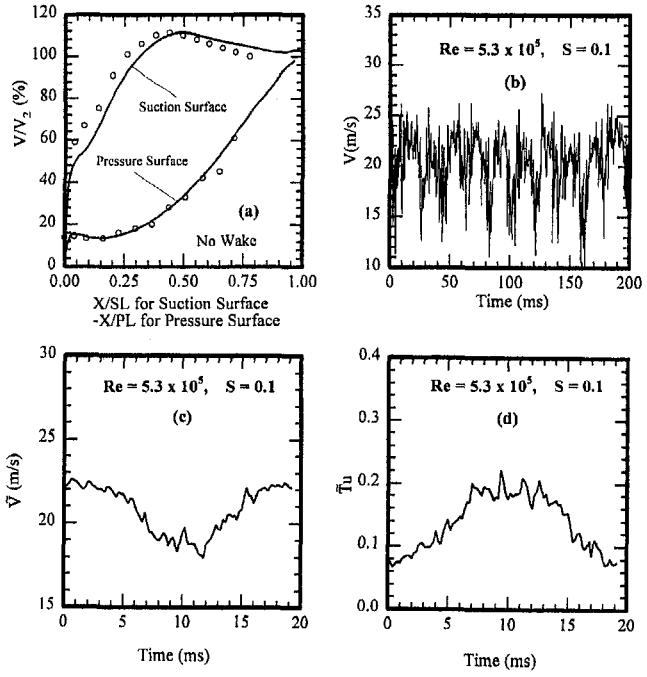

Fig. 3 Local-to-exit velocity ratio (V/V_2) distributions on the test blade; profiles for $V(t)$, $\bar{V}$, $\tilde{T}u$, under wake effect at cascade inlet

downstream of injection from S1 row. Between the film holes of S1 row, Nusselt numbers are not enhanced over case 1. Downstream of film hole row S2, Nusselt numbers are significantly higher than for both cases 1 and 2. Some streaks of high Nusselt numbers are observed immediately downstream between the film holes from S2 row. Film injection may cause transition to occur even earlier than for case 2 (smooth blade with unsteady wake condition). Further addition of an unsteady wake to the film cooled blade (case 4) does not appear to cause a significant effect on the suction surface over case 3. The Nusselt number distributions are similar with slight variations downstream of injection row S2. It appears that the unsteady wake has little effect on Nusselt numbers, which are already enhanced by film injection. Comparing cases 2 and 4 for $S = 0.1$, it can be seen that film injection enhances Nusselt numbers significantly after injection hole rows S1 and S2.

From the detailed distributions, it can be noted that the high Nusselt number streaks downstream of the hole row S2 are misaligned after the gap of missing data. This, however, is not true in the real experiment as the jet effect is evident along the hole downstream of injection as in the case for hole row S1. The misalignment between the two sets of data on the suction surface could be caused by two different experiments on the two areas. This misalignment has been adjusted to show true spanwise averaged distributions.

Effect on Pressure Surface Nusselt number. For case 1, the Nusselt numbers drop rapidly to about $X/PL = -0.15$ and increases slightly over the entire surface. Nusselt numbers are enhanced with the addition of wake (case 2) over the entire pressure surface. For case 3, film injection has little effect immediately downstream of leading edge row injection. However, Nusselt numbers are enhanced between the leading edge row and first row P1 over case 1. Downstream of rows P1 and P2, film injection enhances Nusselt numbers over case 1. Compared to case 2, Nusselt numbers for case 3 are not affected significantly by film injection as in the case for suction surface. The effect of film injection on the pressure surface is more in the region immediately downstream of injection. Nusselt numbers for case 3 are lower than for case 2 in the region far away from P2 ($-0.35 < X/PL < -0.6$). Since the boundary layer on the pressure surface is thicker than on the suction surface, the effect on Nusselt numbers due to film injection is lower. Nusselt numbers for case 4 are not significantly different from case 3 except in the region $-0.35 < X/PL < -0.6$, where Nusselt numbers for case 4 are higher. This region is far away from injection holes. It may be concluded that this may be due to unsteady wake effect. Comparing cases 2 and 4 for same $S = 0.1$, it may be noticed that film injection has some additional effect on

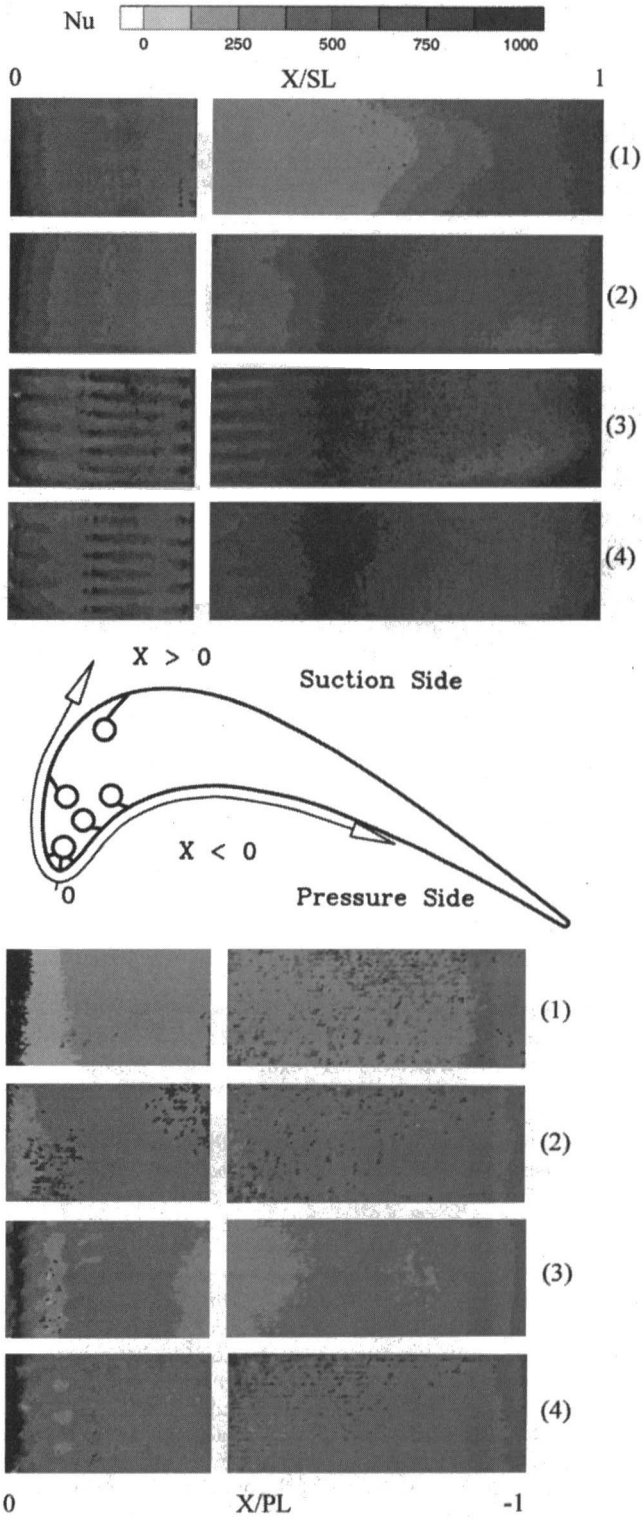

Fig. 4 Effect of unsteady wake on detailed Nusselt number distributions for air injection (cases 1–4); $M = 0.8$

pressure surface Nusselt numbers downstream for leading edge film row.

Nusselt numbers with film injection are significantly enhanced due to the boundary layer disturbance cause by injection. Earlier studies on film cooling have shown that film injection can create local turbulence intensities as high as 15–20 percent depending on blowing ratio. With such high local turbulence, heat transfer coefficients downstream of injection are significantly enhanced as seen in the figure. Further addition of unsteady wake elevates free-stream turbulence. This addition in free-stream turbulence has only a slight effect on blade surface Nusselt numbers already greatly enhanced by the high turbulence produced by jet–mainstream interactions. Also, the local jet-mainstream boundary layer interaction causes earlier transition on the suction surface and higher heat transfer coefficients.

Figure 5 presents the spanwise-averaged Nusselt number distribution for cases 1–4. The Nusselt number distribution for case 1 are the lowest on both pressure and suction surfaces. Transition on suction surface occurs at about $X/SL = 0.55$. For case 2, Nusselt numbers are higher than for case 1. Transition location on the suction surface moves upstream to $X/SL = 0.25$. With film injection (cases 3 and 4), the boundary layer transition location moves farther upstream to immediately downstream of the first row on the suction surface (S1 at $X/SL = 0.15$). Nusselt numbers are enhanced with addition of film injection without unsteady wake (case 3). On the suction surface, Nusselt numbers with film injection are much higher than for the smooth surface with unsteady wake (case 2). Boundary layer is disturbed by film injection downstream of row S1. This causes higher heat transfer coefficients immediately downstream of injection and causes the boundary layer to undergo transition to turbulence. The transitional boundary layer is further disturbed by the second row S2. Nusselt numbers are enhanced downstream of both rows S1 and S2 on the suction surface. Based on the results, it can be concluded that boundary layer transition with film injection begins around $X/SL = 0.15$ (around row S1). Nusselt numbers are significantly affected by film injection on the suction surface. However, further addition of unsteady wake does not significantly affect the Nusselt number distribution with film injection (case 4 versus case 3). On the pressure surface, unsteady wake with $S = 0.1$ (case 2) enhances Nusselt numbers up to 35 percent at $X/PL = -0.5$ over the no rod, no wake case (case 1). It is evident that unsteady wake has a significant effect on Nusselt numbers on the pressure surface for a smooth surface blade. For case 3, Nusselt numbers are enhanced in the injection region by film injection over a smooth surface. However, further downstream

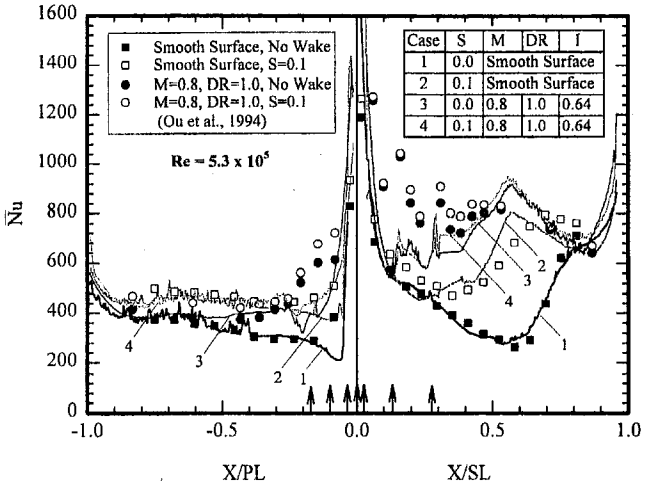

Fig. 5 Effect of unsteady wake on spanwise-averaged Nusselt number distributions for air injection (cases 1–4); $M = 0.8$

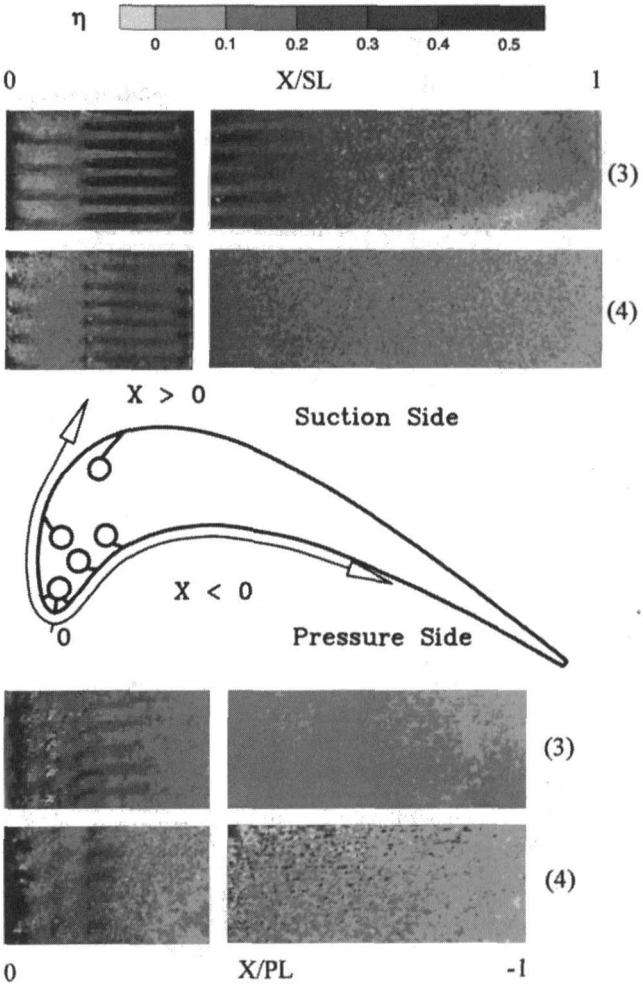

Fig. 6 Effect of unsteady wake on detailed film cooling effectiveness distributions for air injection (cases 3 and 4); $M = 0.8$

the effect is dissipated. Unsteady wake imposed on film injection (case 4) does not seem to have a significant effect on the pressure surface over a surface without film injection but with unsteady wake.

The present results are compared to results for the same cases from Ou et al. (1994). The results for the smooth surface blade without or with wake are in good agreement with the present data. However, the Nusselt numbers for the film injection cases do not agree well in the film hole regions on the pressure and suction surfaces. Ou et al. (1994) presented much higher Nusselt numbers downstream of injection hole on both pressure and suction surfaces. Ou et al. (1994) measured four locations in the spanwise direction at every axial location. Based on the analysis, it appears that the heat loss estimation using thin-foil-thermocouple technique might be underestimated during the study, which may be the reason for the overprediction of Nusselt numbers near the film hole region.

Figure 6 presents the detailed film cooling effectiveness distributions for air injection at $M = 0.8$ for cases 3 and 4.

Effect on Suction Surface Film Cooling Effectiveness. For case 3, film cooling effectiveness immediately downstream of leading edge holes is very high but drops rapidly. The leading edge holes are located in the high-curvature region. The coolant protection might be dissipating rapidly. This may be the reason for the rapid drop in effectiveness. Effectiveness is high along the holes for row S1. The film streaks are clearly evident downstream of the injection holes. The film streaks extend up to the next hole row S2. However, the film cooling effectiveness

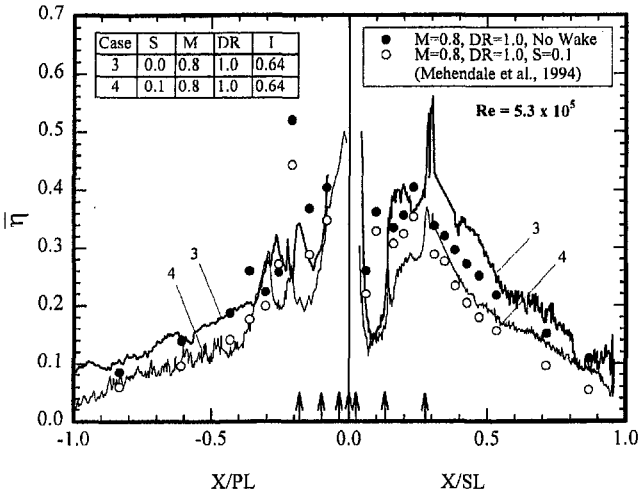

Fig. 7 Effect of unsteady wake on spanwise-averaged film cooling effectiveness distributions for air injection

between the holes is very low due to lack of spanwise mixing of jets. Effectiveness downstream of injection from row S2 is also streaklike along the holes. However, the streaks are shorter and the jets appear to coalesce a little distance downstream. This may be due to two reasons. One is the high curvature of the blade in this region. Another reason may be due to the boundary layer transition to turbulence in this region (Fig. 4). Effectiveness is higher than 0.2 up to $X/SL = 0.7$. For the case with unsteady wake (case 4), the turbulence levels in the free stream are higher. On the suction surface leading edge, effectiveness is reduced compared to case 3. The oncoming free stream disturbed by passing wakes might cause the jets to breakdown. Effectiveness along the holes for hole row S1 is also significantly reduced due to the unsteady wake effect. The streaks of higher effectiveness are still evident. However, the effectiveness levels are much lower. Downstream of hole row S2, the unsteady wake reduces effectiveness significantly. It may be important to note here that unsteady wake imposed on film injection has very small effect on Nusselt numbers on the suction surface, but the effect on film cooling effectiveness is significant.

Effect on Pressure Surface Film Cooling Effectiveness. For case 3, effectiveness is again very high immediately downstream of leading edge row injection. However, the concave curvature can cause the jets to protect the surface better in this region. There is no significant drop in effectiveness after injection on the pressure surface. Also, the row P1 is closer to the leading edge rows. Effectiveness is very high in the hole region and drops to about 0.2–0.3 immediately downstream of injection. Effectiveness is high around the hole region for row P2 also. However, the values drop below 0.2 after $X/PL = -0.3$. This may be due to film dilution. For case 4 on the pressure surface, the effect of unsteady wake has slightly lesser effect on the film cooling effectiveness in the injection hole region. The film cooling effectiveness in the hole region is slightly reduced. Further downstream, the effect shows reduced effectiveness. Effectiveness drops below 0.2 immediately downstream of row P2.

Although the addition of unsteady wake has a very small effect on heat transfer coefficients with film injection, the effect is significant on the film cooling effectiveness distributions. Without unsteady wake, the film cooling jets protect the surface better with limited mixing with the mainstream. Addition of unsteady wake causes disturbances in the mainstream, which result in more mixing between the mainstream and coolant jets and reduce protection of the surface by the coolant jets. This causes significantly reduced film cooling effectiveness with unsteady wake.

Figure 7 presents the spanwise-averaged film cooling effectiveness distributions for cases 3 and 4. Effectiveness is higher for case 3 compared to case 4 over the entire turbine blade surface. Effectiveness on the suction surface near the leading edge is high immediately downstream of injection and decreases rapidly and again increases for rows S1 and S2. Effectiveness

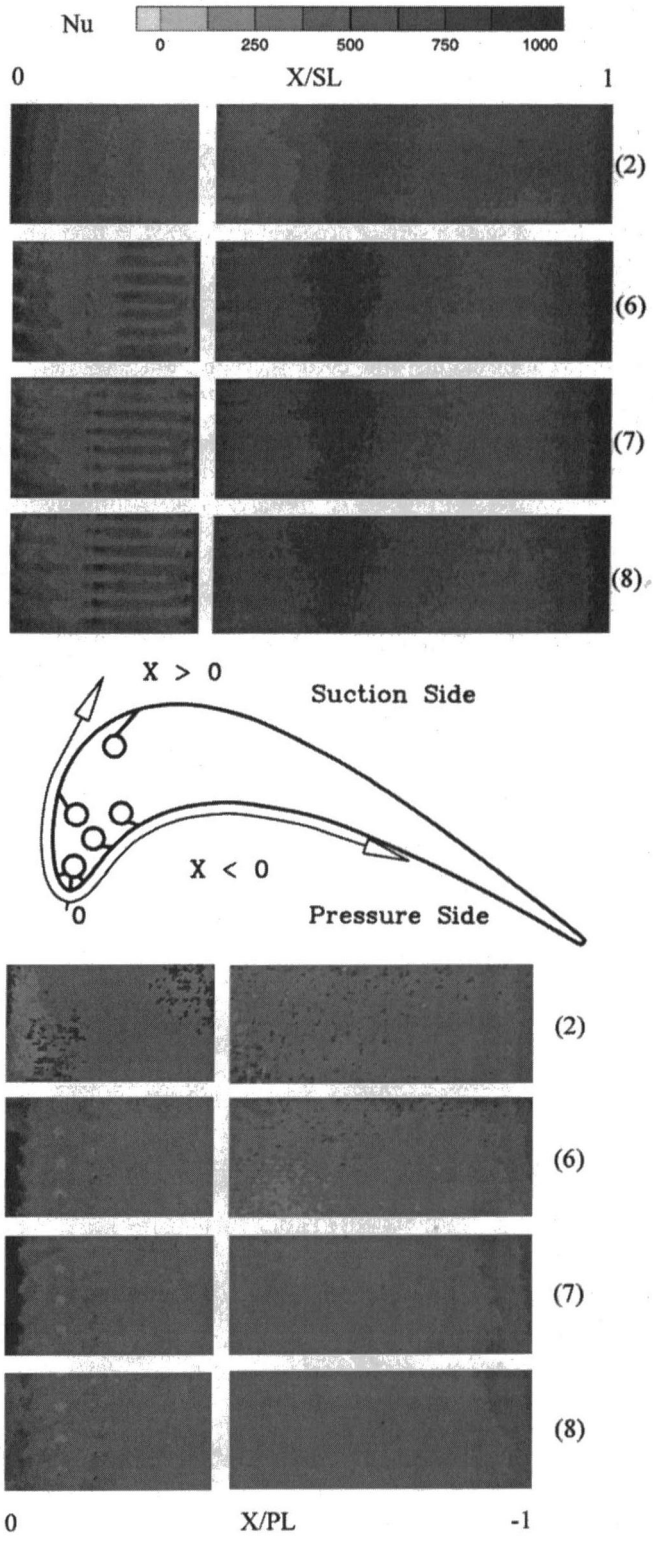

Fig. 8 Effect of blowing ratio on detailed Nusselt number distributions for CO_2 injection at $S = 0.1$ (cases 6–8)

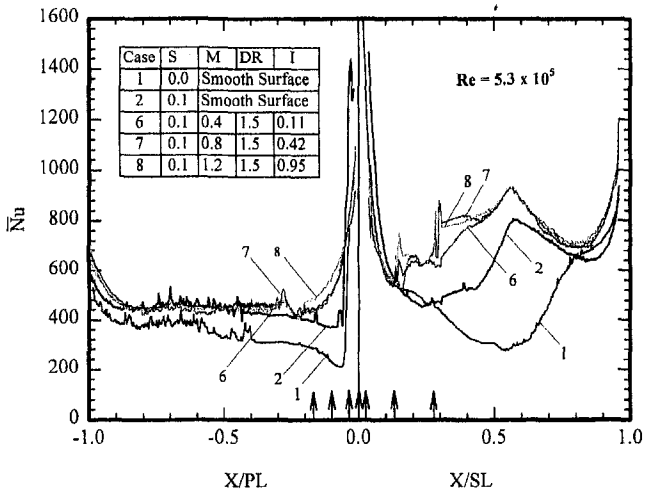

Fig. 9 Effect of blowing ratio on spanwise-averaged Nusselt number distributions for CO_2 injection at $S = 0.1$ (cases 6–8)

is as high as 0.55 immediately downstream of row S2. Further downstream effectiveness decreases gradually. On the pressure side, effectiveness is high near the leading edge, decreases downstream with locally high effectiveness immediately downstream of the injection row, P1 and P2. Effectiveness is lower on the pressure surface compared to that for the suction surface after the second row of holes. The present results are compared to results for the same cases from Mehendale et al. (1994). The data are closer away from the injection holes, but in the injection region, there are significant differences in the effectiveness levels. This might be due to heat gain in the thermocouples due to the coolant heating to obtain film cooling effectiveness in Mehendale et al. (1994) study. The effect is more significant for the locations closer to the film hole rows.

Effect of Blowing Ratio. Figure 8 presents the effect of blowing ratio on detailed Nusselt number distributions for a given wake condition, $S = 0.1$. Blowing ratio is varied from 0.4 to 0.8 to 1.2 (cases 6–8) for CO_2 injection ($DR = 1.5$). The case for smooth surface with $S = 0.1$ is also presented (case 2). On the suction surface, Nusselt numbers, downstream of injection, slightly increase with an increase in blowing ratio. This is true downstream of leading edge film row and row S1. Downstream of row S2, the blowing ratio effect is very small. This may be due to boundary layer transition to turbulence in this region. An increase in blowing ratio does not seem to significantly affect the Nusselt numbers, which are already significantly high due to the boundary layer transition. On the pressure surface, the detailed Nusselt number distributions show very little effect of an increase in blowing ratio. An increased blowing ratio causes increase in jet penetration and lesser cumulative effects. The thick boundary layer on the pressure surface does not seem to be further affected by the increasing coolant blowing.

Figure 9 presents the spanwise-averaged Nusselt number distributions for the same cases as for Fig. 8 (case 2, cases 6–8). The no rod, no wake case is also shown for comparison. On the suction surface, film injection ($M = 0.4$, case 6) enhances Nusselt numbers and causes earlier transition than for a smooth surface (case 2) as explained earlier. However, there is very little additional effect of blowing ratio (cases 7 and 8 for $M = 0.8$, 1.2) on the Nusselt number distributions except in the regions immediately downstream of injection rows S1 and S2. On the pressure surface also, the effect of blowing ratio is very little except in the film injection region. In the film injection region on both surfaces, the Nusselt numbers are slightly higher with increasing blowing ratio.

Figure 10 presents detailed film cooling effectiveness distributions for the effect of blowing ratio under an unsteady wake condition of $S = 0.1$ with CO_2 injection ($DR = 1.5$) for cases 6–8. It can be observed that effectiveness increases with an increase in blowing ratio on the suction surface. On the suction surface, effectiveness streaks downstream of injection holes become stronger with an increase in blowing ratio. Effectiveness is as high as 0.2 at $X/SL = 0.5$ for a high blowing ratio of 1.2. Effectiveness streaks are not seen for row S2. Effectiveness downstream of row S2 appears to be affected by boundary layer transition causing the jets to coalesce downstream of injection. Effectiveness immediately downstream of the leading edge holes on the pressure surface increase significantly with an increase in blowing ratio. Effectiveness streaks are not evident on the pressure surface. However, at $M = 1.2$, effectiveness appears to be higher around the holes with small streaks. An increase in blowing ratio for CO_2 injection produces increased

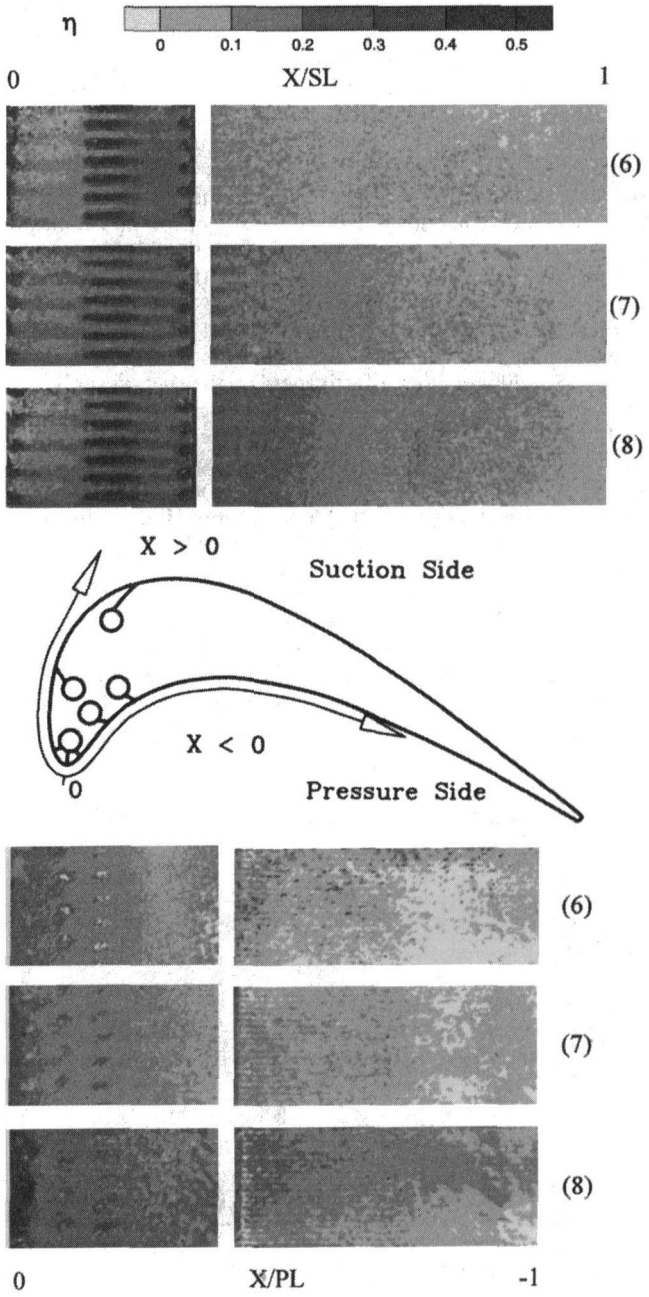

Fig. 10 Effect of blowing ratio on detailed film cooling effectiveness distributions for CO_2 injection at $S = 0.1$ (cases 6–8)

effectiveness on the blade surface. More coolant is injected into the boundary layer with an increase in blowing ratio providing more protection and thus higher effectiveness.

Figure 11 presents the spanwise-averaged film cooling effectiveness distributions for cases 6–8. Effectiveness increases with increase in blowing ratio on the suction surface. Effectiveness drops rapidly downstream of leading edge holes on the suction surface, then increases immediately downstream of hole row S1, drops again, and increases immediately downstream of hole row S2 and then decreases gradually toward the trailing edge for all three blowing ratios. Effectiveness decreases gradually over the entire pressure surface for all three blowing ratios. Effectiveness is similar for $M = 0.4$ and 0.8 on the pressure surface.

Effect of Coolant Density. Figure 12 presents effect of coolant density on spanwise-averaged Nusselt number distributions for $M = 0.8$ and $M = 1.2$ for an unsteady wake condition of $S = 0.1$ (cases 4, 5, 7, 8). Air injection simulates a density ratio of 1.0 whereas CO_2 injection simulates a density ratio of 1.5. Nusselt numbers on both the surfaces are not affected significantly by coolant density. Film injection enhances Nusselt numbers over the entire surface and causes earlier boundary layer transition on the suction surface, as indicated earlier. Increase in coolant density affects Nusselt numbers immediately downstream of injection holes. Higher density coolant produces higher Nusselt numbers downstream of injection at the same blowing ratio. Nusselt numbers downstream of injection are greatly enhanced by film injection over the blade surface. Change in coolant density ratio has little effect on the already high Nusselt numbers.

Figure 13 presents the spanwise-averaged film cooling effectiveness distributions for the same cases as for Fig. 12 (cases 4, 5, 7, 8). Film cooling effectiveness on the suction surface is higher for higher density coolant for a higher blowing ratio ($M = 1.2$). Since CO_2 is heavier (lower momentum flux ratio I), the coolant jets tend to stay closer to the surface and provide better protection compared to air. Air jets also possess higher momentum than CO_2 at same blowing ratio. Higher effectiveness is obtained at $M = 1.2$ for CO_2 injection whereas higher effectiveness is obtained at $M = 0.8$ for air injection on the suction surface. On the pressure surface, CO_2 injection at $M = 0.8$ produces the lowest effectiveness. Air injection provides higher effectiveness closer to the leading edge. However, CO_2 injection at $M = 1.2$ produces highest effectiveness after row P2. On the pressure surface also, effectiveness is higher for $M = 1.2$ for CO_2 injection compared to $M = 0.8$ and is higher at

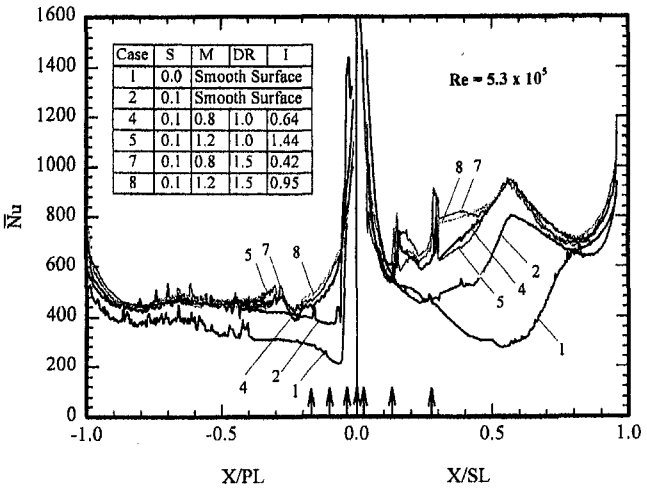

Fig. 12 Effect of coolant density on spanwise-averaged Nusselt number distributions at $S = 0.1$

$M = 0.8$ for air injection compared to $M = 1.2$ for same coolant. Heavier coolant (CO_2) stays closer to boundary layer and protects better. At low blowing ratio of 0.8, air has higher momentum ($I = 0.64$) than CO_2 ($I = 0.42$) and protects the surface better. At $M = 1.2$, air possesses very high momentum ($I = 1.44$) and coolant jets blow into the mainstream and do not provide better protection than CO_2 ($I = 0.96$).

Conclusions

Detailed Nusselt number and film cooling effectiveness distributions on a turbine blade with film cooling are presented under the effects of upstream unsteady wakes. Results are presented at a cascade exit Reynolds number of 5.3×10^5 for cases without and with wake. Film injection was provided through three rows on the leading edge and two rows each on the pressure and suction surfaces using air ($DR = 1.0$) and CO_2 ($DR = 1.5$) as coolants. The blowing ratio for both coolants was varied from 0.4 to 1.2. The conclusions based on the experimental results are:

1 Detailed Nusselt number and film cooling effectiveness distributions using the transient liquid crystal technique provide better understanding of the film cooling process. Results are

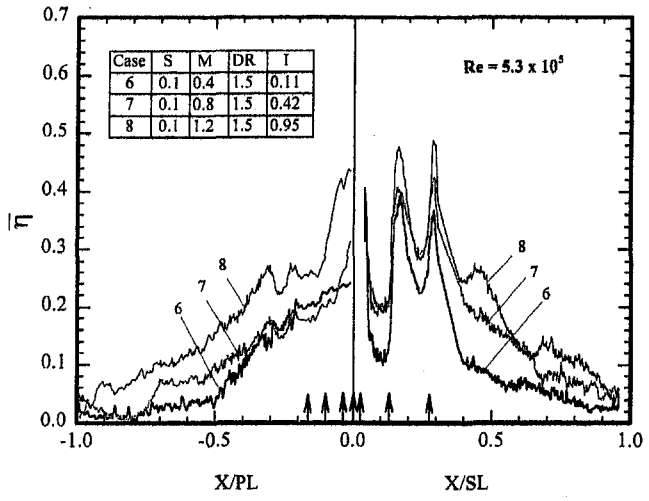

Fig. 11 Effect of blowing ratio on spanwise-averaged film cooling effectiveness distributions for CO_2 injection at $S = 0.1$ (cases 6–8)

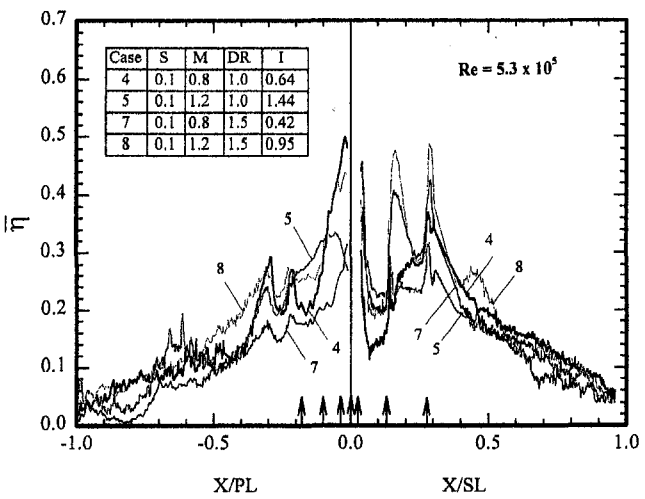

Fig. 13 Effect of coolant density on spanwise-averaged film cooling effectiveness distributions at $S = 0.1$

obtained in the near film hole region, which is difficult using the thin foil-thermocouple method.

2 Nusselt numbers are significantly enhanced for a film cooled blade compared to a non-film cooled blade. Film injection also causes earlier boundary layer transition on the suction surface. Higher effectiveness is obtained on the suction surface with strong film streaks along the holes compared to that on the pressure surface.

3 Unsteady wake slightly enhances Nusselt numbers but significantly reduces film cooling effectiveness on a film-cooled blade surface as compared to a film-cooled blade without unsteady wake.

4 For a film cooled blade, Nusselt numbers increase slightly with an increase in blowing ratio particularly in the region immediately downstream of injection. Film cooling effectiveness significantly increases with an increase in blowing ratio for CO_2 injection.

5 Nusselt numbers are not significantly affected by coolant density except in the regions immediately downstream of injection where CO_2 provides higher Nusselt number than air injection. Film cooling effectiveness is higher at higher blowing ratios ($M = 1.2$) for CO_2 injection than air. However, air provides higher effectiveness at $M = 0.8$.

Acknowledgments

This paper was prepared with the support of the NASA-Lewis Research Center under grant number NAG3-1656. The NASA technical team is Dr. Philip E. Poinsatte and Dr. Raymond Gaugler. Their support is greatly appreciated.

References

Abhari, R. S., and Epstein, A. H., 1994, "An Experimental Study of Film Cooling in a Rotating Transonic Turbine," ASME JOURNAL OF TURBOMACHINERY, Vol. 116, pp. 63–70.

Camci, C., and Arts, T., 1990, "An Experimental Convective Heat Transfer Investigation Around a Film-Cooled Gas Turbine Blade," ASME JOURNAL OF TURBOMACHINERY, Vol. 112, pp. 497–503.

Du, H., Ekkad, S. V., and Han, J. C., 1997a, "Effect of Unsteady Wake With Trailing Edge Coolant Ejection on Detailed Heat Transfer Coefficient Distributions for a Gas Turbine Blade," ASME *Journal of Heat Transfer*, Vol. 119, pp. 242–248.

Du, H., Han, J. C., and Ekkad, S. V., 1997b, "Detailed Film Cooling Measurements Over a Gas Turbine Blade Using a Transient Liquid Crystal Image Technique," ASME HTD-Vol. 350, pp. 245–254.

Ekkad, S. V., Zapata, D., and Han, J. C., 1997a, "Heat Transfer Coefficients Over a Flat Surface With Air and CO_2 Injection Through Compound Angle Holes Using a Transient Liquid Crystal Image Method," ASME JOURNAL OF TURBOMACHINERY, Vol. 119, pp. 580–586.

Ekkad, S. V., Zapata, D., and Han, J. C., 1997b, "Film Effectiveness Over a Flat Surface With Air and CO_2 Injection Through Compound Angle Holes Using a Transient Liquid Crystal Image Method," ASME JOURNAL OF TURBOMACHINERY, Vol. 119, pp. 587–593.

Haas, W., Rodi, W., and Schönung, B., 1992, "The Influence of Density Difference Between Hot and Coolant Gas on Film Cooling by a Row of Holes: Predictions and Experiments," ASME JOURNAL OF TURBOMACHINERY, Vol. 114, pp. 747–755.

Hoffs, A., Bolcs, and Harasagama, S. P., 1997, "Transient Heat Transfer Experiments in a Linear Cascade Via an Insertion Mechanism Using a Liquid Crystal Technique," ASME JOURNAL OF TURBOMACHINERY, Vol. 119, pp. 9–13.

Ito, S., Goldstein, R. J., and Eckert, E. R. G., 1978, "Film Cooling of a Gas Turbine Blade," ASME *Journal of Engineering for Power*, Vol. 100, pp. 476–481.

Kline, S. J., and McClintock, F. A., 1953, "Describing Uncertainties in Single Sample Experiments," *Mechanical Engineering*, Vol. 75, Jan., pp. 3–8.

Martinez-Botas, R. F., Lock, G. D., and Jones, T. V., 1995, "Heat Transfer Measurements in an Annular Cascade of Transonic Gas Turbine Blades Using a Transient Liquid Crystal Technique," ASME JOURNAL OF TURBOMACHINERY, Vol. 117, pp. 425–431.

Mehendale, A. B., Han, J. C., Ou, S., and Lee, C. P., 1994, "Unsteady Wake Over a Linear Turbine Blade Cascade With Air and CO_2 Film Injection: Part II—Effect on Film Effectiveness and Heat Transfer Distributions," ASME JOURNAL OF TURBOMACHINERY, Vol. 116, pp. 730–737.

Nirmalan, V., and Hylton, L., 1990, "An Experimental Study of Turbine Vane Heat Transfer With Leading Edge and Downstream Film Cooling," ASME JOURNAL OF TURBOMACHINERY, Vol. 112, pp. 477–487.

Ou, S., Han, J. C., Mehendale, A. B., and Lee, C. P., 1994, "Unsteady Wake Over a Linear Turbine Blade Cascade with air and CO_2 Film Injection: Part I—Effect on Heat Transfer Coefficients," ASME JOURNAL OF TURBOMACHINERY, Vol. 116, pp. 721–729.

Takeishi, K., Aoki, S., Sato, T., and Tsukagoshi, K., 1992, "Film Cooling on a Gas Turbine Rotor Blade," ASME JOURNAL OF TURBOMACHINERY, Vol. 114, pp. 828–834.

Vedula, R. J., and Metzger, D. E., 1991, "A Method for Simultaneous Determination of Local Effectiveness and Heat Transfer Distributions in Three-Temperature Convection Situations," ASME Paper No. 91-GT-345.

Heat Transfer in a Rotating Cavity With a Peripheral Inflow and Outflow of Cooling Air

I. Mirzaee[1]

X. Gan[2]

M. Wilson

J. M. Owen

Department of Mechanical Engineering,
University of Bath,
Bath BA2 7AY, United Kingdom

This paper describes a combined computational and experimental study of the heat transfer in a rotating cavity with a peripheral inflow and outflow of cooling air for a range of rotational speeds and flow rates. Measurements are made in a purpose-built rig, with one of the two rotating discs heated, and computations are conducted using an axisymmetric elliptic solver incorporating the Launder-Sharma low-Reynolds-number $k-\epsilon$ turbulence model. Measured values of the tangential component of velocity, V_ϕ, exhibit Rankine-vortex behaviour which is not accurately modelled by the computations. Both computed and measured values of the radial component of velocity, V_r, confirm the recirculating nature of the flow. In the outflow region, agreement between computed and measured values of V_r is mainly good, but in the inflow region the computations exhibit a "peaky" distribution which is not shown by the measurements. The measured and computed Nusselt numbers show that Nu increases as the magnitudes of the flow rate and the rotational speed increase. The computed Nusselt numbers (allowing for the effects of conduction through and radiation to the unheated disk) reproduce the measured trends but tend to underestimate the experimental values at the larger radii.

1 Introduction

In some gas turbine designs, the cooling air for the rotating turbine disks is supplied through a stationary casing at the periphery of the disks, as shown in Fig. 1. The air enters the annular rotating cavity between the disks through nozzles in the stationary casing and leaves through the small clearances between the disks and the casing.

A combined computational and experimental study of the turbulent flow in this system was conducted by Gan et al. (1996), and some of the computed streamlines are shown in Fig. 2. The computations are shown for rotational Reynolds numbers of $\mathrm{Re}_\phi = 3.75 \times 10^5$ and 1.5×10^6, and for nondimensional flow rates of $C_w = -1500$ and -3000, where the negative sign is used to indicate that the inlet flow is radially inward. The four cases correspond to values of the turbulent flow parameter, λ_T, between -0.0172 and -0.104, which are representative of the values used in the internal cooling-air systems of engines. (For a free disk, the nondimensional flow rate entrained by one side of the disk, C_{wfd}, is given by $C_{wfd} = 0.219\ \mathrm{Re}_\phi^{0.8}$; a value of $|\lambda_T| = 0.219$ therefore corresponds to the free-disk entrainment rate. Further discussion of the turbulent flow parameter is given by Owen and Rogers (1989, 1995).) For the computations, the flow entered the system radially, without swirl, in the midplane ($z/s = 0.5$); the outlet flow was split equally between the clearances at $z = 0$ and $z = s$. The gap ratio was $G = 0.30$, and the inner-to-outer radius ratio was $a/b = 0.5$.

It can be seen from Fig. 2 that there is recirculating flow, symmetric about the midplane. The radial extent of the recirculation zone, which increases as $|\lambda_T|$ increases, is governed by two effects: (*i*) the shear exerted by the stationary peripheral casing on the rotating air in the cavity; (*ii*) the exchange of angular momentum between the incoming air and the rotating air.

Computations and measurements of the velocity showed that there is radial outflow in thin boundary layers on the disk and radial inflow in the core between the boundary layers. In the core, the tangential component of velocity, V_ϕ, is invariant with z, and the measured values of V_ϕ conform to a combined free and forced vortex, or Rankine vortex (see Owen and Rogers, 1995), where

$$\frac{V_\phi}{\Omega r} = Ax^{-2} + B \tag{1}$$

and the coefficients A and B depend on C_w and Re_ϕ. The computations were unable to capture this Rankine-vortex behavior; deficiencies in the turbulence model were believed to be responsible.

This paper describes a combined computational and experimental study of heat transfer in the system described above. In addition, a modified version of the turbulence model is used to obtain improved computations of the velocity, and these are compared with measurements of $V_\phi/\Omega r$. The experimental apparatus is described in Section 2 and the computational method in Section 3. Comparisons between the computations and measurements are given in Section 4, and the conclusions are presented in Section 5.

2 Experimental Apparatus

A simple diagram of the rotating-disk rig is shown in Fig. 3. Details of the apparatus and instrumentation used for the velocity measurements are given by Gan et al. (1996) and only the salient features of the rig and details of the heat transfer instrumentation are described here.

The disks were 762 mm in diameter spaced an axial distance of 113 mm apart ($G = 0.30$), and the inner cylinder was 382 mm in diameter ($a/b = 0.5$). Disk 1, which could be heated, was made from steel, and disk 2, which provided optical access for the LDA measurements, was made from transparent polycarbonate. The surfaces of the outer stationary casing and the inner rotating cylinder were insulated with Rohacell, a lightweight

[1] Present address: Department of Mechanical Engineering, University of Urmia, Urmia, Iran.

[2] Present address: European Gas Turbines Ltd, Whetstone, Leicester LE8 6LH, United Kingdom.

Contributed by the International Gas Turbine Institute and presented at the 42nd International Gas Turbine and Aeroengine Congress and Exhibition, Orlando, Florida, June 2–5, 1997. Manuscript received at ASME Headquarters February 1997. Paper No. 97-GT-136. Associate Technical Editor: H. A. Kidd.

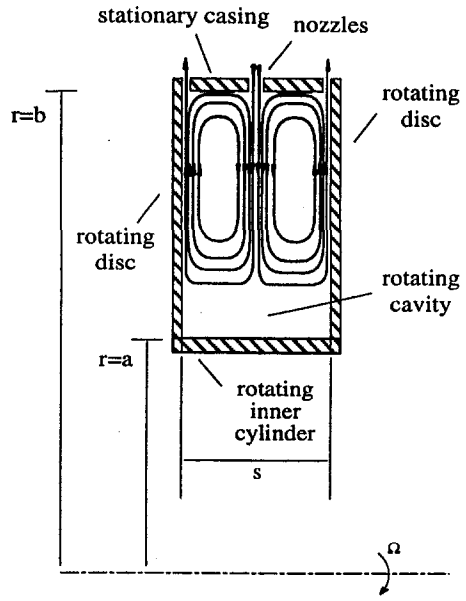

Fig. 1 Rotating cavity with a peripheral flow of cooling air

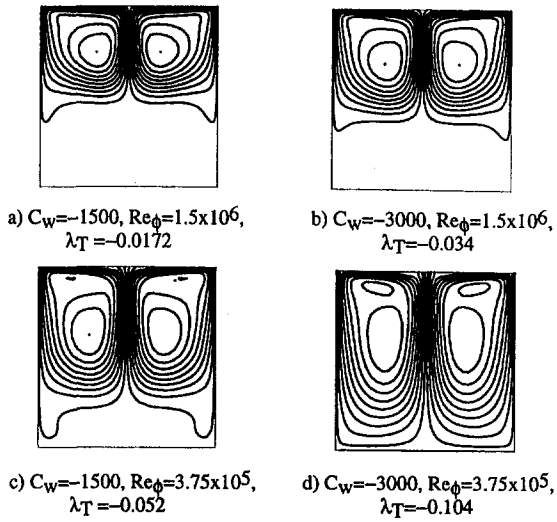

Fig. 2 Computed streamlines (from Gan et al., 1996)

foam with a thermal conductivity of $k \approx 0.03$ W/mK. The disks and inner cylinder could be rotated up to 1500 rpm by a 15 kW thyristor-controlled electric motor.

The back face of disk 1 was heated to around 100°C by thyristor-controlled stationary radiant heaters with a total output up to 21 kW. The front face was coated with a fiberglass mat, 1 mm thick, that contained ten thermocouples and ten fluxmeters. This instrumented disk had been calibrated and tested by Gan et al. (1996) in their experiments on contrarotating disks, and the interested reader is referred to that paper for further details. The signals from the thermocouples and fluxmeters were taken out through a silver/silver graphite slipring unit, and the voltages were measured by a computer-controlled data-logger and digital voltmeter with a resolution of ± 1 μV.

Air was supplied to the cavity through 39 equispaced nozzles of 11.3 mm diameter, the axis of each nozzle being on a radial line in the midplane of the cavity. The air left the system symmetrically through the two clearances between the stationary casing and the rotating disks; each radial clearance was approximately 1 mm. The inlet and outlet flow rates were measured by orifice plates made to British Standards (BS 1042). The difference between the measured inlet flow rate and the sum of the two outlet flow rates was less than 6 percent of the inlet value.

For the velocity measurements made by Gan et al. (1996), the roughness of the Rohacell layer on the inner and outer cylindrical surfaces was believed to be a possible contributory factor in the poor agreement between the computed and measured values of $V_\phi/\Omega r$. For those tests, the average roughness of the Rohacell was approximately 30 μm. In later tests, the roughness of the outer cylindrical surface was reduced by coating the Rohacell with varnish, which was subsequently polished; this reduced the average roughness to 8 μm. (Computational results were used to confirm that the thickness of the viscous sublayer was greater than 8 μm, so that the varnished surface was considered to be "aerodynamically smooth.") The velocity measurements described below were made with the (new) smooth surfaces, but the heat transfer measurements were made with the (original) rough surfaces.

3 Computational Model

Computations were carried out using an axisymmetric elliptic multigrid solver, incorporating the Launder–Sharma low-Reynolds-number $k-\epsilon$ turbulence model. Incompressible, steady flow was assumed, and full details of the primitive-variables solution were given by Wilson et al. (1997). Gan et al. (1996)

Nomenclature

a, b = inner, outer radius of disk
A, B = constants in Eq. (1)
$C_{\epsilon 2}$ = turbulence model coefficient (Appendix A)
C_{gs} = correction coefficient (Appendix A)
C_w = nondimensional mass flow rate = $m/\mu b$
G = gap ratio = s/b
h = heat transfer coefficient
k = turbulent kinetic energy, thermal conductivity
m = mass flow rate
Nu = Nusselt number = $qr/k(T_s - T_{ref})$
q = heat flux from heated disk to air
r = radial coordinate
Re_ϕ = rotational Reynolds number = $\rho\Omega b^2/\mu$
Ri_{gs} = Richardson number (Appendix A)
s = axial gap between disks
T = static temperature
U_τ = friction velocity = $\sqrt{(\tau_w/\rho)}$
V_r, V_ϕ, V_z = time-averaged velocities in r, ϕ, z directions
x = nondimensional radius = r/b
y = distance normal to wall
$y+$ = wall-distance Reynolds number = $\rho U_\tau y/\mu$
z = axial coordinate
ϵ = turbulent energy dissipation rate
λ_T = turbulent flow parameter = $C_w Re_\phi^{-0.8}$
μ = dynamic viscosity
ρ = density
τ_w = total wall shear stress
ϕ = tangential coordinate
Ω = angular speed of disks

Subscripts

eff = effective value
fd = free-disk value
s = disk surface
ref = reference value

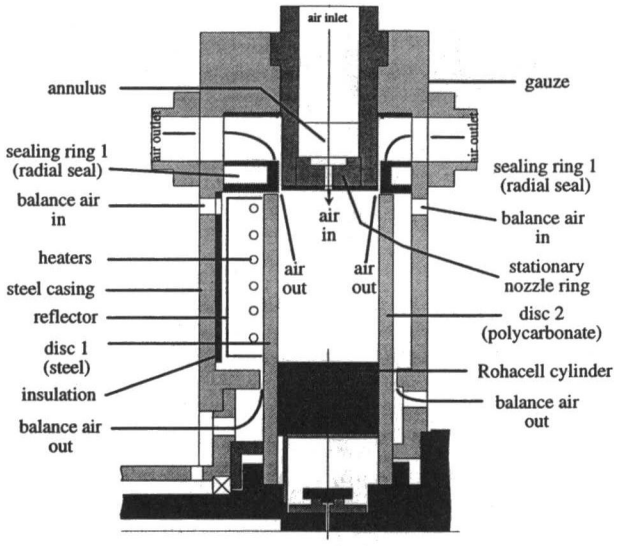

Fig. 3 Rotating cavity rig (from Gan et al., 1996)

described the computational model used to study the fluid dynamics of the peripheral flow problem. The same model was used for the present work, and only a brief summary will be given in addition to a description of the thermal model. Gan et al. (1996) noted that the prediction of tangential velocity distributions might be improved by the use of a Richardson-number-based correction to the $k-\epsilon$ turbulence model. A correction of this type is described in Appendix A, and results from the basic and modified models are presented in section 4.

A polynomial fit to measured temperatures was used to provide the radial temperature distribution of the heated disk for each case, and the insulated cylindrical surfaces were assumed to be adiabatic. As the unheated polycarbonate disk provided optical access for the LDA measurements, it could not be insulated and its temperature was not measured. The interior (cavity-side) surface temperature of the polycarbonate disk was estimated by calculating the heat flux through the disk, assuming that its exterior face behaved as a free disk. This was believed to be representative of conditions in the rig, and details of this calculation are given in Appendix B. The influence of the unheated disk temperature on computed Nusselt numbers was investigated by repeating each calculation with an adiabatic assumption for the disk. The results are discussed in section 4.

The disk speed, inlet mass flow rate, and inlet air temperature were all prescribed from experimental data. A circumferential slot in the outer casing was used to represent the cooling air inlet in the computational model. The slot was located midway between the disks and matched the flow area of the inlet nozzles in the rig. The air entered the system with uniform radial velocity, and the axial and tangential velocity components were zero. The mass flow rates out of the system, at the clearances adjacent to the top of each disk, were equal, and a uniform radial velocity was imposed to ensure mass balance between the inflow and outflows. Zero normal derivative conditions were applied for other variables. No-slip boundary conditions were used for the velocity components parallel to walls. The 89 × 89 axial by radial grid was the same as that described by Gan et al. (1996).

The measured disk heat transfer rates include the radiative heat flux between the heated disk and other surfaces (the inner and outer cylinders and the unheated disk). In earlier work, Chen et al. (1997) estimated the radiative flux by assuming that the unheated disk was at the inlet temperature of the cooling air, and corrected the measured Nusselt numbers for comparison with convective heat transfer predictions. In the present work, a surface-to-surface radiation model was included in the computations, so that predictions of total Nusselt numbers (including both convective and radiative heat flux) could be compared directly with the measurements. All the surfaces were treated as opaque, gray, and diffuse, with temperatures taken from the convective heat transfer predictions. The radiation model is described in detail by Karabay (1996).

4 Comparison Between Computation and Experiment

4.1 Velocity Distributions. Figure 4 shows the variation of $V_\phi/\Omega r$ with x^{-2}. On these axes, a straight line represents a Rankine vortex; see Eq. (1). It can be seen that the experimental data (which were obtained for a "smooth" casing) are closely approximated by Eq. (1); this was also the case for the data obtained by Gan et al. (1996) for the "rough" casing. The basic Launder–Sharma model fails to capture the Rankine-vortex behavior, particularly at smaller values of $|\lambda_T|$. The Richardson correction, discussed in Section 3, produces some improvements, but the agreement between computations and experiment cannot be regarded as good.

Figure 5 shows the variation of $V_r/\Omega r$ with z/s for three different cases. The experimental data for the "rough" and "smooth" casings are shown together with the computations with and without the Richardson correction. It can be seen that roughness has comparatively little effect on the measured values of V_r and that the Richardson correction has little effect on the computed values. Both computations and measurements show that there is radial outflow in thin boundary layers on the disks and inflow in the core between the boundary layers. The strength of the recirculation, as denoted by the magnitude of $V_r/\Omega r$, decreases as x decreases.

For the results in Fig. 5(a), where $C_w = 0$, the agreement between the computations and measurements is reasonable. For Figs. 5(b) and 5(c), where $|C_w| > 0$, the agreement between the computations and the measurements for radial outflow is mainly good, but the computed radial inflow exhibits a "peaky" distribution that is not shown in the measurements. It should be remembered that the computations are for axisymmetric flow, and the air enters the system through a circular slot in the centre of the stationary casing. In the experiments, the air enters through discrete holes, which may increase mixing and reduce the "peakiness" shown by the computations. It is also possible that the computed peakiness may be caused by deficiencies in the turbulence model.

The measured radial velocity profiles at $x = 0.85$ and $x = 0.75$ show some asymmetry for $\lambda_T = 0$ and $\lambda_T = -0.034$ (see Figs. 5(a, b). Additional computational work has suggested that the radial inflow tends to be unstable at these conditions, giving rise to unsteady flow. The highest flow rate case, $|\lambda_T| = 0.104$, is more symmetric (see Fig. 5(c)).

4.2 Heat Transfer Results. Figures 6 to 9 show the computed and measured variations of temperatures and Nusselt numbers with the nondimensional radius x. T_{ref} was taken to be the measured air temperature at inlet to the system.

Figure 6 shows the results for $C_w = -1500$, $\text{Re}_\phi = 3.75 \times 10^5$, $\lambda_T = -0.052$. The variation of temperature with x is shown in Fig. 6(a) and the Nusselt numbers in Fig. 6(b). Referring to Fig. 6(a), the fitted temperatures on the heated disk were used as boundary conditions for the numerical solution of the energy equation, as discussed in Section 3. For the unheated disk, two assumptions were used: (i) The disk was assumed to be adiabatic; (ii) the disk was assumed to be conducting, with radiation from the heated to the unheated disks.

Figure 6(a) shows that the temperature of the "conducting disk" is lower than that of the "adiabatic disk," and Fig. 6(b) shows that the "conducting-disk" assumption causes a significant increase in the Nusselt numbers on the heated disk. The increased heat flux from the heated disk occurs as a result of both increased convection to a cooler fluid and radiation from

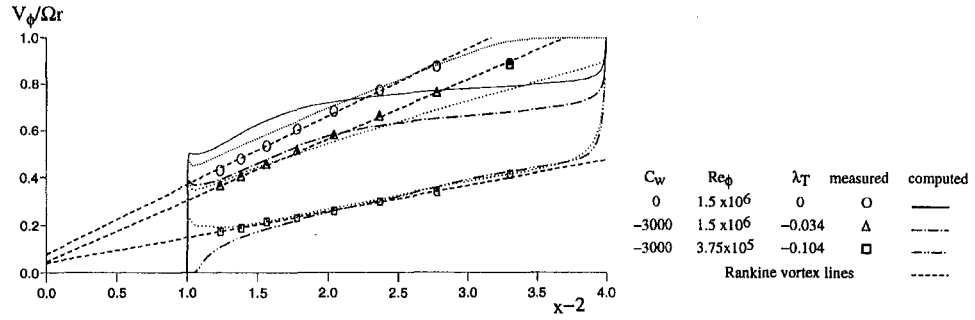

Fig. 4 Variation of $V_\phi/\Omega r$ with x^{-2} for z/s = 0.8: · · · · · · · Launder–Sharma model with Richardson-number correction

the heated to the unheated disk. (Radiation, which was not included in the adiabatic-disk case, accounts for most of the increased heat flux for the conducting-disk case in Figs. 6 to 9.) The computed Nusselt numbers for the conducting-disk case are slightly lower than, but show a similar distribution to, the measured values.

Figure 7 shows the results for $C_w = -1500$, $\mathrm{Re}_\phi = 1.5 \times 10^6$, $\lambda_T = -0.017$: The flow rate is the same as for Fig. 6 but the rotational speed is higher. The agreement between the computed values of Nu (for the conducting-disk case) and the measured values is reasonable although the computations tend to underestimate the measurements, particularly at the larger values of x. Comparing Figs. 6 and 7, it can be seen that increasing Re_ϕ causes an increase in the magnitude of Nu over most of the disk.

Figure 8 shows the results for $C_w = -3000$, $\mathrm{Re}_\phi = 3.75 \times 10^5$, $\lambda_T = -0.104$: The rotational speed is the same as for Fig. 6 but the flow rate is higher. Again, the computed values of Nu tend to underestimate the measured values, particularly at the larger values of x. Comparing Figs. 6 and 8, it can be seen that increasing $|C_w|$ causes an increase in the magnitude of Nu.

Figure 9 shows the results for $C_w = -3000$, $\mathrm{Re}_\phi = 1.5 \times 10^6$, $\lambda_T = -0.034$: The flow rate is the same as for Fig. 8 but the rotational speed is higher. Again, it can be seen that the computed values of Nu exhibit the experimental trends but tend to underestimate the magnitude of Nu at the larger values of x.

Considering Figs. 6 to 9 as a whole, the following conclusions can be drawn. The magnitude of Nu increases as Re_ϕ and $|C_w|$ increase. The computed values of Nu for the conducting-disk case are in better agreement with the experimental data than those for the adiabatic-disk case. The computed values show variations of Nu with x, C_w, and Re_ϕ similar to those shown by the experimental data, but the computed values tend to underestimate the measured values, particularly at the larger values of x. A possible reason for this underestimate of Nu is that the measurements were made with a "rough" casing (see Section 2), and the effects of roughness were not modeled in the computations.

5 Conclusions

A combined computational and experimental study of the flow and heat transfer in a rotating cavity with a peripheral inflow and outflow of cooling air has been conducted for rotational Reynolds numbers up to $\mathrm{Re}_\phi = 1.5 \times 10^6$ and flow rates up to $|C_w| = 3000$.

The measured values of $V_\phi/\Omega r$ show a Rankine-vortex behavior that is not accurately captured by the computations. The use of a "Richardson correction" in the Launder–Sharma low-Reynolds-number $k-\epsilon$ turbulence model improves the agreement between the computed and measured values of $V_\phi/\Omega r$.

The measured and computed values of $V_r/\Omega r$ confirm the recirculating nature of the flow, with radial outflow in the boundary layers on the disk and inflow in the core between the boundary layers. Agreement between computations and measurements in the outflow region is mainly good, but the compu-

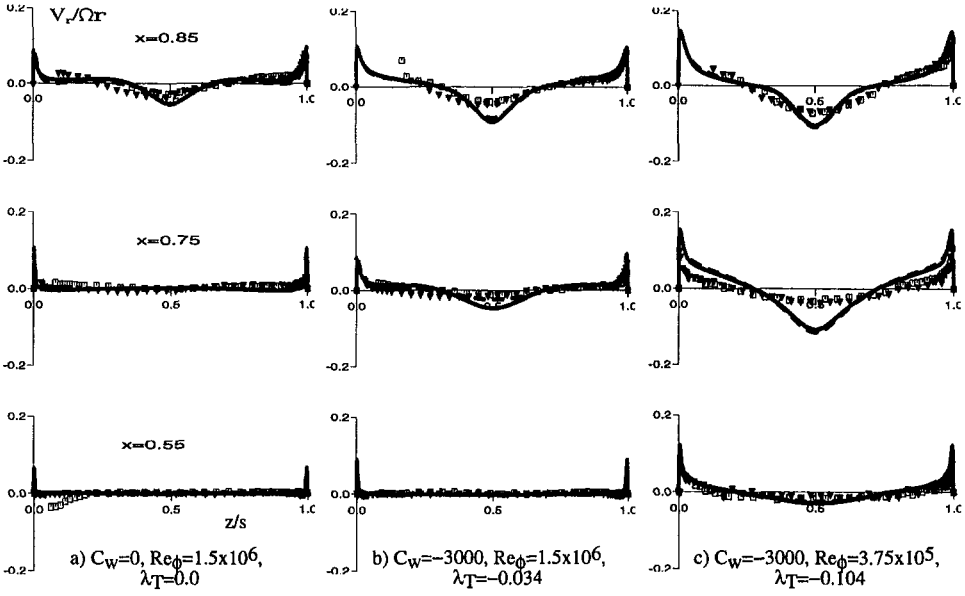

Fig. 5 Variation of $V_r/\Omega r$ with z/s; □ measured (smooth outer casing); —— computed, without Richardson number correction; ▼ measured (rough outer casing); — — – computed, with Richardson number correction

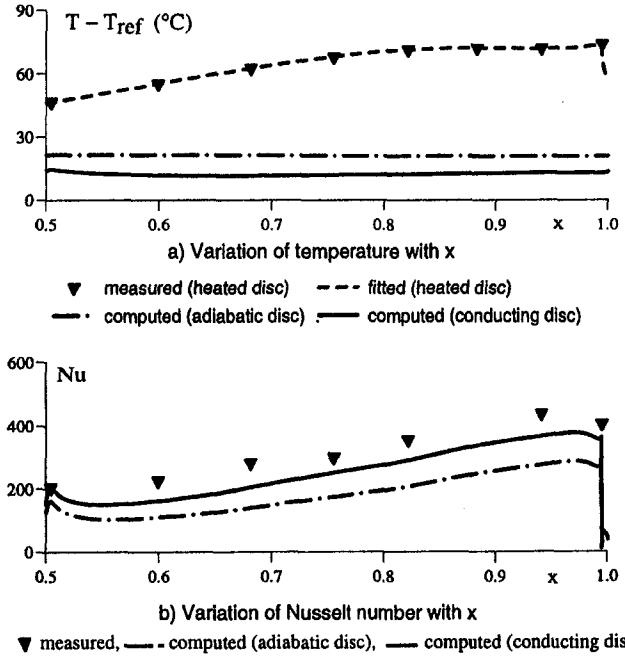

Fig. 6 Variation of temperatures and Nusselt numbers with x: C_w = −1500, $Re_\phi = 3.75 \times 10^5$, $\lambda_T = -0.052$

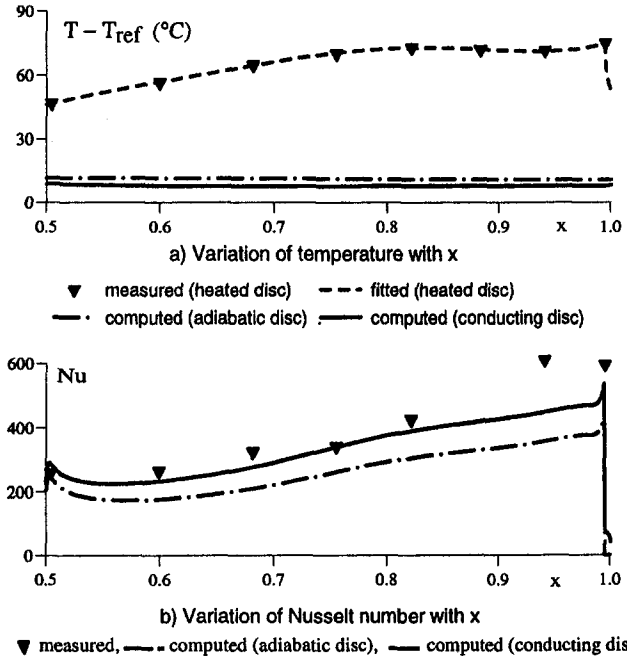

Fig. 8 Variation of temperatures and Nusselt numbers with x: C_w = −3000, $Re_\phi = 3.75 \times 10^5$, $\lambda_T = -0.104$

tations exhibit a "peaky" distribution in the inflow region that is not shown in the measurements. This peaky distribution is attributed to the axisymmetric assumption made in the computations and to possible deficiencies in the turbulence model.

The measured and computed Nusselt numbers show that Nu increases as Re_ϕ and $|C_w|$ increase. The computed Nusselt numbers show the measured trends but tend to underestimate the measured values of Nu at the larger values of x. A possible reason for this underestimate is that the inner and outer cylindrical surfaces of the experimental rig were rough (which affected the tangential component of velocity) and this roughness was not allowed for in the numerical model. Deficiencies in the turbulence model, referred to above, may also have contributed to the underestimates of Nu.

Acknowledgments

The authors wish to thank BMW-Rolls Royce GmbH, the UK Engineering and Physical Sciences Research Council, and the Defence Research Agency for funding the research described in this paper.

References

Chen, J. X., Gan, X., and Owen, J. M., 1997, "Heat Transfer From Air-Cooled Contrarotating Disks," ASME JOURNAL OF TURBOMACHINERY, Vol. 119, pp. 61–67.

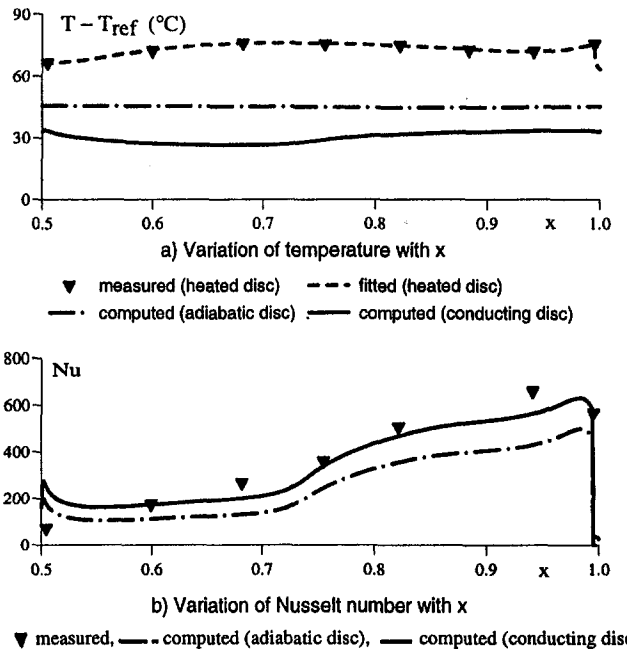

Fig. 7 Variation of temperatures and Nusselt numbers with x: C_w = −1500, $Re_\phi = 1.5 \times 10^6$, $\lambda_T = -0.017$

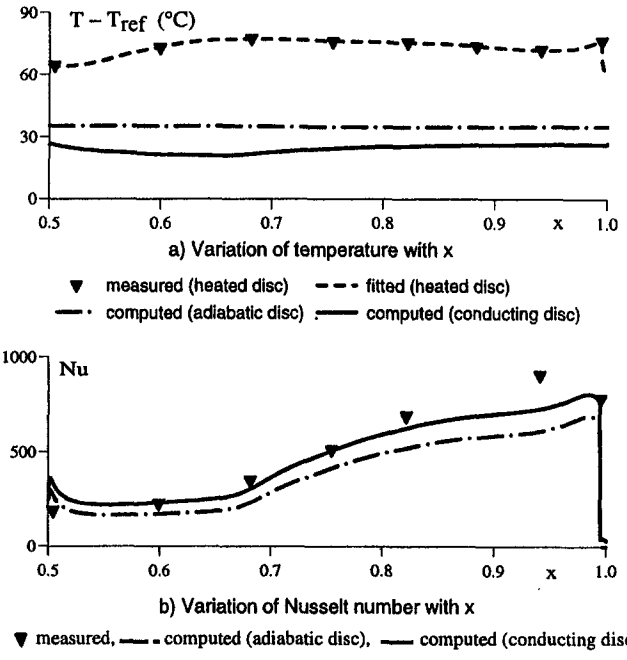

Fig. 9 Variation of temperatures and Nusselt numbers with x: C_w = −3000, $Re_\phi = 1.5 \times 10^6$, $\lambda_T = -0.034$

Gan, X., Mirzaee, I., Owen, J. M., Rees, D. A. S., and Wilson, M., 1996, "Flow in a Rotating Cavity With a Peripheral Inlet and Outlet of Cooling Air," ASME Paper No. 96-GT-309.

Karabay, H., 1996, "Radiation Heat Transfer in a Single Cavity," internal report, School of Mechanical Engineering, Bath University Report No. 60/96.

Kilic, M., 1993, "Computation of Flow Between Contra-Rotating Discs," PhD thesis, University of Bath.

Owen, J. M., and Rogers, R. H., 1989, *Flow and Heat Transfer in Rotating-Disc Systems, Vol. 1: Rotor-Stator Systems,* Research Studies Press, Taunton, UK; Wiley, New York.

Owen, J. M., and Rogers, R. H., 1995, *Flow and Heat Transfer in Rotating Disc Systems: Vol. 2: Rotating Cavities,* Research Studies Press, Taunton, UK; Wiley, New York.

Sloan, D. G., Smith, P. J., and Douglas Smoot, L., 1986, "Modeling of Swirl in Turbulent Flow systems," *Prog. Energy Combust. Sci.,* Vol. 12, pp. 163–250.

Wilson, M., Pilbrow, R., and Owen, J. M., 1997, "Flow and Heat Transfer in a Pre-swirl Rotor–Stator System," ASME JOURNAL OF TURBOMACHINERY, Vol. 114, pp. 364–373.

APPENDIX A

Richardson-Number Correction to the Launder–Sharma $k-\epsilon$ Turbulence Model

For cases of combined free and forced vortex flow, Richardson-number-based corrections have been proposed for the source term in the ϵ equation of the $k-\epsilon$ turbulence model, and several formulations have been reported in the literature (see Sloan et al., 1986) for different flow situations. In the present work, following testing of a number of previously proposed modifications, a gradient Richardson number for swirl, defined as:

$$\mathrm{Ri}_{gs} = \frac{k^2}{\epsilon^2}\frac{V_\phi}{r^2}\frac{\partial}{\partial r}(rV_\phi) \tag{A1}$$

was used to modify a source term coefficient in the transport equation for ϵ as follows:

$$C_{\epsilon 2,\mathrm{eff}} = C_{\epsilon 2}(1 - C_{gs}\mathrm{Ri}_{gs}) \tag{A2}$$

For the present study, the value of the coefficient C_{gs} was optimized numerically, and a value $C_{gs} = 0.7$ was obtained. In the basic model $C_{gs} = 0$; $C_2 = 1.92$ is the value usually taken for this empirical coefficient. In the modified model, the variation of the coefficient using Eq. (A2) was constrained by $0.1 < C_{e2,\mathrm{eff}} < 2.4$ (Sloan et al., 1986).

APPENDIX B

Conduction Model for the Unheated Disk

For steady flow, the heat flux q through the unheated disk was written as (see Fig. B1):

$$q = h_{TOT}(T_W - T_E) = k_{air}(dT/dz)_W \tag{B1}$$

where h_{TOT} is the total heat transfer coefficient, defined by:

$$h_{TOT} = \frac{1}{\dfrac{\Delta Z_{DISC}}{k_{DISC}} + \dfrac{1}{h_{EXT}}} \tag{B2}$$

The heat transfer coefficient at the exterior disk surface, h_{EXT} (Fig. B1), was deduced from the relationship $\mathrm{Nu} = 0.015\,\mathrm{Re}_\phi^{0.8}$, for heat transfer from an isothermal free disk into air (see Owen and Rogers, 1989). The values of ΔZ_{disc} and k_{disc} were taken as 10 mm and 0.2 W/mK, respectively.

The temperature gradient at the interior wall (in Eq. (B1)) was expressed using a second-order formula involving the interior surface temperature, T_w, and computed fluid temperatures (Kilic, 1993). Equation (B1) was then solved to give the interior wall temperature of the unheated disk, with the exterior temperature T_E taken to be the same as that of the cooling air at inlet.

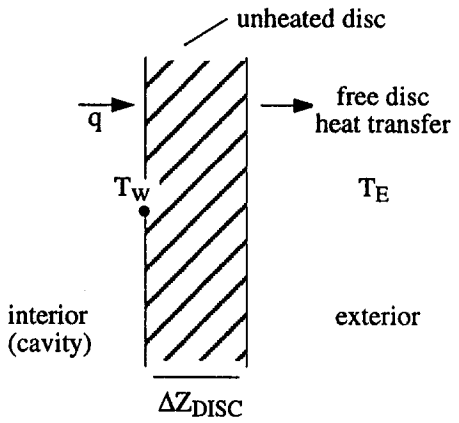

Fig. B1 Conduction model definition sketch

The Effect of Turbulence on the Heat Transfer in Closed Gas-Filled Rotating Annuli

D. Bohn

J. Gier

Institute of Steam and Gas Turbines,
Aachen University of Technology,
Aachen, Germany

Higher turbine inlet temperatures are a common measure for increasing the thermal efficiency of modern gas turbines. This development leads not only to the need for more efficient turbine blade cooling but also to the requirement for a more profound knowledge of the mechanically and thermally stressed parts of the rotor. For determining thermal stresses from the temperature distribution in the rotor of a gas turbine, one has to encounter the convective transfer in rotor cavities. In the special case of an entirely closed gas-filled rotating annulus, the convective flow is governed by a strong natural convection. Owen and other researchers have found that the presence of turbulence and its inclusion in the modeling of the flow causes significant differences in the flow development in rotating annuli with throughflow, e.g., different vortex structures. However, in closed rotating annuli there is still a lack of knowledge concerning the influence of turbulence. Based on previous work, in this paper the influence of turbulence on the flow structure and on the heat transfer is investigated. The flow is investigated numerically with a three-dimensional Navier–Stokes solver, based on a pressure correction scheme. To account for the turbulence, a low-Reynolds-number $k-\epsilon$ model is employed. The results are compared with experiments performed at the Institute of Steam and Gas Turbines. The computations demonstrate that turbulence has a considerable influence on the overall heat transfer as well as on the local heat transfer distribution. Three-dimensional effects are discussed by comparing the three-dimensional calculation with a two-dimensional calculation of the same configuration and are found to have some impact.

Introduction

The development of gas turbines that operate at higher gas temperatures in the turbine section, with a simultaneous increase of the pressure ratio, is a continuing trend to increase their thermal efficiency. This requires a careful design of the mechanically and thermally stressed parts of the gas turbine. To estimate these stresses, a proper evaluation of temperature distributions in units and components, operating in the hottest zones, is necessary. In such a zone temperature nonuniformities may lead to considerable additional stresses. Their acceptable value is also a function of the temperature level.

At present only an approximate estimation of the temperature distribution in a gas turbine rotor containing closed gas-filled enclosures (Fig. 1) is possible. In those cavities a strong, free convective flow is induced. This convection is caused by the buoyancy force corresponding to centrifugal acceleration and different temperatures of the cavity walls. Such a flow increases the heat transfer throughout the cavities considerably.

In the past many theoretical and experimental investigations have been carried out, to study the heat transfer in rotating enclosures with a throughflow of cooling fluid, e.g., Ong and Owen (1991), Farthing et al. (1992), Owen et al. (1985). For sealed cavities with a purely free convection flow, the known theoretical and experimental investigations pertain mainly to constant temperature walls, and are limited to qualitative descriptions of the convective processes. These investigations differ with respect to the direction of the heat flux in the cavity.

Most of the investigations were performed for an axially directed heat flux applied to a cylindrical rotating enclosure. For a rotating cavity with an entirely centripetal heat flux Zysina-Molozhen and Salov (1977) experimentally analyzed the influence of rotational speed and various thermal boundary conditions on heat transfer in a rotating annular enclosure. Photographs were taken, showing the flow pattern inside the enclosure. They note the absence of any regular fluid circulation contours in the cavity. Lin and Preckshot (1979) calculated the temperature, velocity, and streamline distribution for relatively low rates of acceleration.

Experimental and theoretical investigations on the heat transfer in a closed rotating cavity with a centripetally directed heat flux were carried out in a previous paper by Bohn et al. (1995). There, the feasibility of numerical prediction on the flow and the heat transfer was shown by comparison of the numerical results with the experimental data. It was also found that the flow inside the cavity might be unstable. However, these computations were conducted only with the assumption of laminar flow inside the cavity.

There are a number of publications on the numerical simulation of turbulent flows in cavity configurations with throughflow and rotor–stator systems. For turbulence modeling most authors use variations of low-Reynolds $k-\epsilon$ models, e.g., Ho et al. (1996), Gan et al. (1996), and Iacovides et al. (1996). There are other approaches, too, like Reynolds-stress modeling, e.g., Iacovides et al. (1996) and Izenson et al. (1995), and multiple scale $k-\epsilon$ models (Guo and Rhode, 1996).

Nevertheless, there is still a lack of knowledge concerning the influence of turbulence in closed rotating cavities operating under conditions valid for gas turbines.

To assess this influence, in this paper a closed rotating annulus with a 45 deg segmentation is used for the numerical study (Fig. 2). The computations are compared to experimental data gathered for the same model cavity and reported by Bohn et al. (1995) and Gorzelitz (1994). For a description of the experimental setup, please refer to Bohn et al. (1995, 1996). Additionally, effects of three dimensionality are examined.

Contributed by the International Gas Turbine Institute and presented at the 42nd International Gas Turbine and Aeroengine Congress and Exhibition, Orlando, Florida, June 2–5, 1997. Manuscript received at ASME Headquarters February 1997. Paper No. 97-GT-242. Associate Technical Editor: H. A. Kidd.

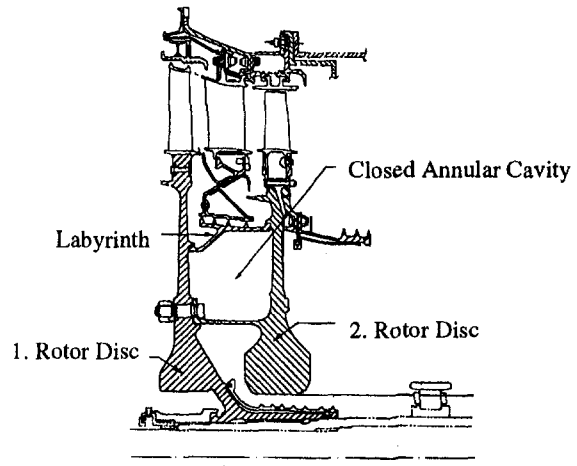

Fig. 1 Rotating enclosure in a rotor

The segmented annulus is chosen, because it requires considerably less computational effort and exhibits a much more stable flow structure, which is important for analyzing the basic effects.

By analyzing the basic conservation equations of mass, momentum, and energy (see below) it can be demonstrated that

$$\mathrm{Nu} = f(\mathrm{Ra}, \mathrm{Re}, \mathrm{Pr}, H/r_m, b/r_m) \tag{1}$$

The Nusselt number (Nu) is defined as the ratio of the heat flux throughout the cavity to that flux that would occur in solid-body rotation without any motion relative to a co-rotating frame of reference; thus, Nu is equal to unity for no convection and is greater than unity when convection takes place. The rotational Reynolds number (Re) has its origin in the Coriolis force terms in the momentum equations. In contrast to the case of an axially directed heat flux its influence is relatively small for the centripetal heat flux (Bohn et al., 1996). Because of the relatively little influence of the Coriolis forces in the segmented cavity, the calculated point of operation of $\mathrm{Ra} = 1.64 \times 10^9$ is expected to be in the turbulent flow regime ($\mathrm{Ra} > 10^9$). The rotational Rayleigh number (Ra) is the product of the Grashof number and the Prandtl number and is related to the buoyancy term in the radial momentum equation. The Prandtl number (Pr) is a combination of fluid properties and does not change significantly due to temperature variations.

Numerical Procedure

The flow in the rotating cavity is described by the Navier–Stokes conservation equations for mass (Eq. (2)), momentum (Eq. (3)), and energy (Eq. (4)). In common tensor form, these equations read:

Table 1 Constants of the employed turbulence model

$\mathrm{Pr}_{t,h}$	$\mathrm{Pr}_{t,k}$	$\mathrm{Pr}_{t,\varepsilon}$	C_1	C_2	C_μ
0,9	1	1,217	1,44	1,92	0,09

$$\nabla \cdot (\rho \vec{v}) = 0 \tag{2}$$

$$\nabla \cdot (\rho \vec{v} h_t) - \nabla \cdot \left(\frac{\lambda}{c_p} + \frac{\mu_t}{\mathrm{Pr}_t} \right) \nabla h_t = 0 \tag{3}$$

$$\nabla \cdot (\rho \vec{v} \otimes \vec{v}) - \nabla \cdot (\mu_{\mathrm{eff}} \nabla \vec{v}) = -\nabla (p + \tfrac{2}{3}k) + \nabla (\mu_{\mathrm{eff}} (\nabla \vec{v})^T) \tag{4}$$

Some important assumptions should be mentioned in this regard. Equations (2)–(4) are valid for a compressible, steady-state flow. In case of turbulent flow all primitive variables are density-weighted averaged (Favre-averaging). A cylindrical coordinate system (z, r, φ) has been used, in which $r = 0$ identifies the axis. In this system the Nabla operator becomes:

$$\nabla = \partial/\partial z + \partial/\partial r + 1/r \partial/\partial \varphi$$

The computations of the rotating cavity are carried out within a rotating frame of reference. This results in additional centrifugal and Coriolis force terms in the momentum equations and the energy equation.

Turbulence Effects. The eddy viscosity hypothesis has been used to take turbulence effects into account, hence the effective viscosity μ_{eff} is the sum of the laminar viscosity μ and the turbulent viscosity μ_t. Two additional equations for the turbulent kinetic energy k (Eq. (5)) and the dissipation rate ϵ (Eq. (6)) have to be solved to calculate the turbulent viscosity, which is not a fluid property, but depends on the flow field. The low-Reynolds version of Launder and Sharma (1974) has been used:

$$\nabla \cdot (\rho \vec{v} k) - \nabla \cdot \left(\left(\mu + \frac{\mu_t}{\mathrm{Pr}_t} \right) \nabla k \right) = \mu_{\mathrm{eff}} \nabla \vec{v} \cdot (\nabla \vec{v} + (\nabla \vec{v})^T) - \frac{2}{3} \nabla \cdot \vec{v} (\mu_{\mathrm{eff}} \nabla \cdot \vec{v} + \rho k) - \rho \epsilon - 2\mu (\nabla k^{1/2})^2 \tag{5}$$

Nomenclature

a = thermal diffusivity
b = distance between axial side walls
c_p = specific heat at constant pressure
$\mathrm{Gr} = r_m \cdot \omega^2 \cdot \Delta T \cdot L^3 \cdot \rho^2 / T_m \cdot \mu^2$ = Grashof number
H = distance between outer and inner cylindrical wall
h_t = total enthalpy
k = turbulent kintic energy
L = length
$\mathrm{Nu} = \dot{q}/\dot{q}_\lambda$ = Nusselt number
$\mathrm{Pr} = \mu \cdot c_p/\lambda = \mu/\rho \cdot a$ = Prandtl number
p = pressure
$\dot{q}$ = heat flux from the hot to the cold wall
$\dot{q}_\lambda$ = heat transfer by conduction alone
r = radius
R = gas constant
$\mathrm{Ra} = \mathrm{Gr} \cdot \mathrm{Pr}$ = Rayleigh number
$\mathrm{Re} = \rho \cdot \omega \cdot r_m \cdot L/\mu$ = Reynolds number
T = temperature
ΔT = temperature difference between hot and cold walls
(z, r, φ) = axial, radial, circumferential coordinates
v = velocity vector
α = section angle
ϵ = turbulence dissipation
λ = thermal conductivity
μ = dynamic viscosity
ρ = density
ω = angular velocity of the cavity
C = const

Subscripts

i = inner
m = arithmetical mean
max = maximum
min = minimum
o = outer

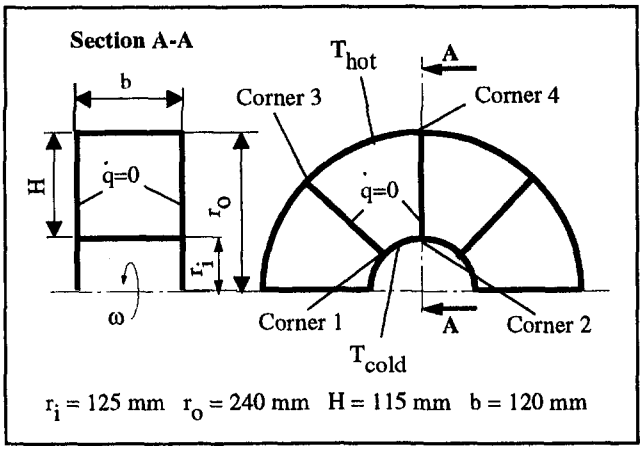

Fig. 2 Dimensions of the annular cavity

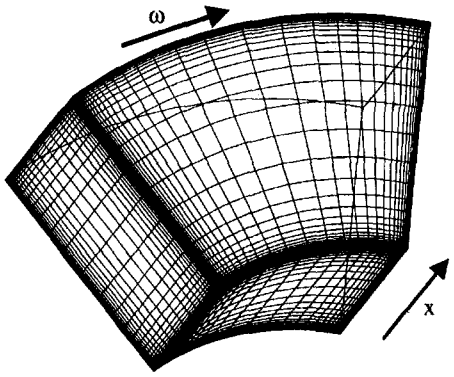

Fig. 3 Three-dimensional computational grid

$$\nabla\cdot(\rho\vec{v}\epsilon) - \nabla\cdot\left(\left(\mu + \frac{\mu_t}{\mathrm{Pr}_{t,\epsilon}}\right)\nabla\epsilon\right)$$

$$= C_1\frac{\epsilon}{k}\cdot\left(\mu_{\mathrm{eff}}\nabla\vec{v}\cdot(\nabla\vec{v} + (\nabla\vec{v})^T) - \frac{2}{3}\nabla\cdot\vec{v}(\mu_{\mathrm{eff}}\nabla\cdot\vec{v} + \rho k)\right)$$

$$- C_2 f_2\rho\frac{\epsilon^2}{k} + 2\frac{\mu\mu_t}{\rho}(\nabla\nabla\vec{v})^2 \quad (6)$$

$$\mu_t = C_\mu f_\mu\rho\frac{k^2}{\epsilon} \quad (7)$$

The model involves a damping of the effective viscosity (Eq. (7)) when the local turbulent Re number is low. Also, the source terms of the k and ϵ equation are modified. The empirical functions f_μ and f_2 are defined by:

$$f_\mu = \exp\left(\frac{-3.4}{(1 + 0.02\ \mathrm{Re}_t)^2}\right) \quad (8)$$

$$f_2 = 1 - 0.3\exp(-\mathrm{Re}_t^2) \quad (9)$$

where the local turbulent Reynolds number is given by:

$$\mathrm{Re}_t = \frac{\rho k^2}{\mu\epsilon} \quad (10)$$

The Launder–Sharma model is used because it allows the calculation of μ_t without any explicit dependence of the model functions from the wall distance. This is an important feature for a closed configuration like the rotating cavity. The model is widely used for transitional as well as fully turbulent flows. The constants in the model are given by Table 1.

The set of equations is closed by the ideal gas law.

$$\rho = \frac{p}{RT} \quad (11)$$

Numerical Scheme. A modern fully implicit Finite-Volume scheme has been used for solving the set of partial differential Eqs. (2) – (6) numerically. The SIMPLEC pressure-correction (Van Doormal and Raithby, 1984) algorithm is adapted on a nonstaggered grid, while avoiding the chequerboard oscillations by using the improved Rhie–Chow (1985) interpolation method. For the diffusion terms a central differencing scheme is used, while the advection terms are discretized by hybrid differencing in which central differencing is used if the mesh Peclet number is less than

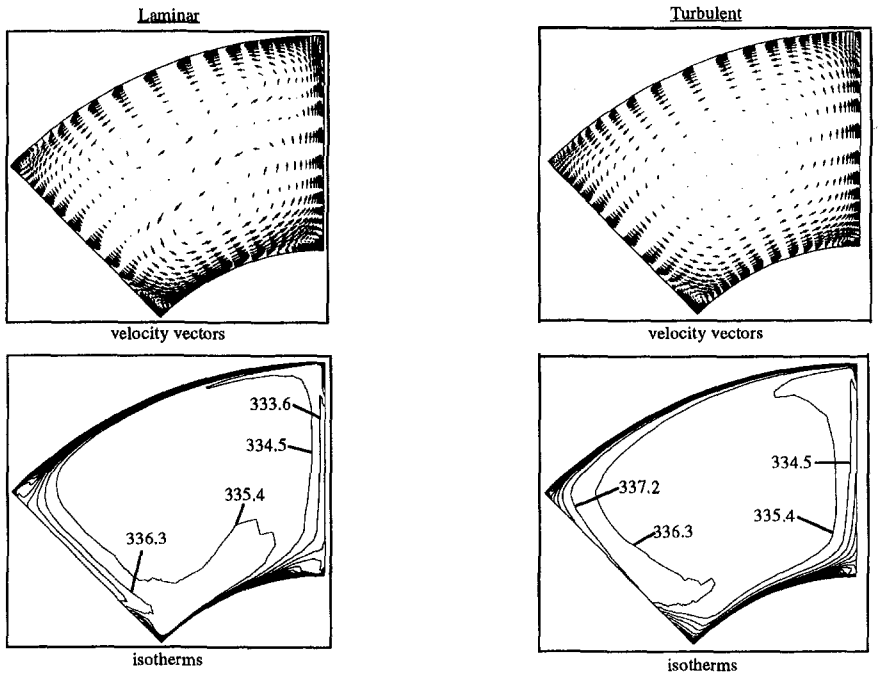

Fig. 4 Velocity vectors and isotherms [K] in the cavity (three-dimensional case, middle section: $x/b = 0.5$)

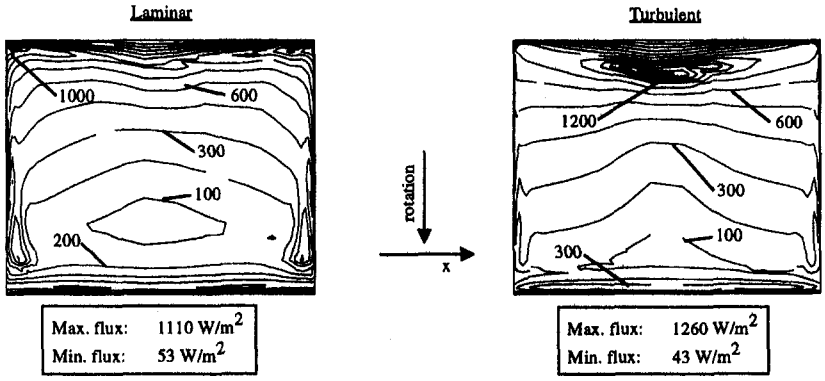

Fig. 5 Isolines of heat flux through inner cylinder wall (cold wall)

2, and upwind differencing, if the mesh Peclet number is greater than 2.

Boundaries and Mesh. In Fig. 2 the calculated cavity is shown schematically. The computational domain and boundary conditions are equivalent to an experimental setup reported by Bohn et al. (1995, 1996).

The domain consists of an annulus segmented into eight 45 deg segments. These are divided from each other by insulating walls. The outer wall is heated up to a constant temperature of 346.5 K and the hub is cooled down to a constant temperature of 320 K. All other walls are assumed to be adiabatic. At the walls the velocity (within the frame of reference) is zero. The Rayleigh number is 1.638×10^9 and the rotational Re number is 2.151×10^5. The calculation has been started with zero velocities and three different initial temperature distributions (constant, linear profile, partly linear profile) converging to the same results.

The computational mesh has been refined once, resulting in only slight differences. The results in this paper are all taken from the finer mesh, which consists of 38 cells in radial, 30 cells in axial, and 34 cells in circumferential direction with a total of 38,760 cells. It is shown in Fig. 3. In the two-dimensional calculation, the axial direction is discretized with one cell and at the axial walls periodicity is assumed giving a purely two-dimensional flow in the same cavity.

Both meshes are refined in the boundary layer region, giving a y^+_{max} for the near-wall nodes at the heated and cooled wall of 0.4 and on the other walls of 1.

Results

Influence of Turbulence. By comparing computations of the rotating cavity for laminar and turbulent flow, using exactly the same boundary conditions, one may assess the influence of turbulence in this type of flow. Both computations were converged for several orders of magnitude ensuring steady-state flow. The difference between the integral heat flux into the cavity and out of the cavity was negligible (<4 percent). The

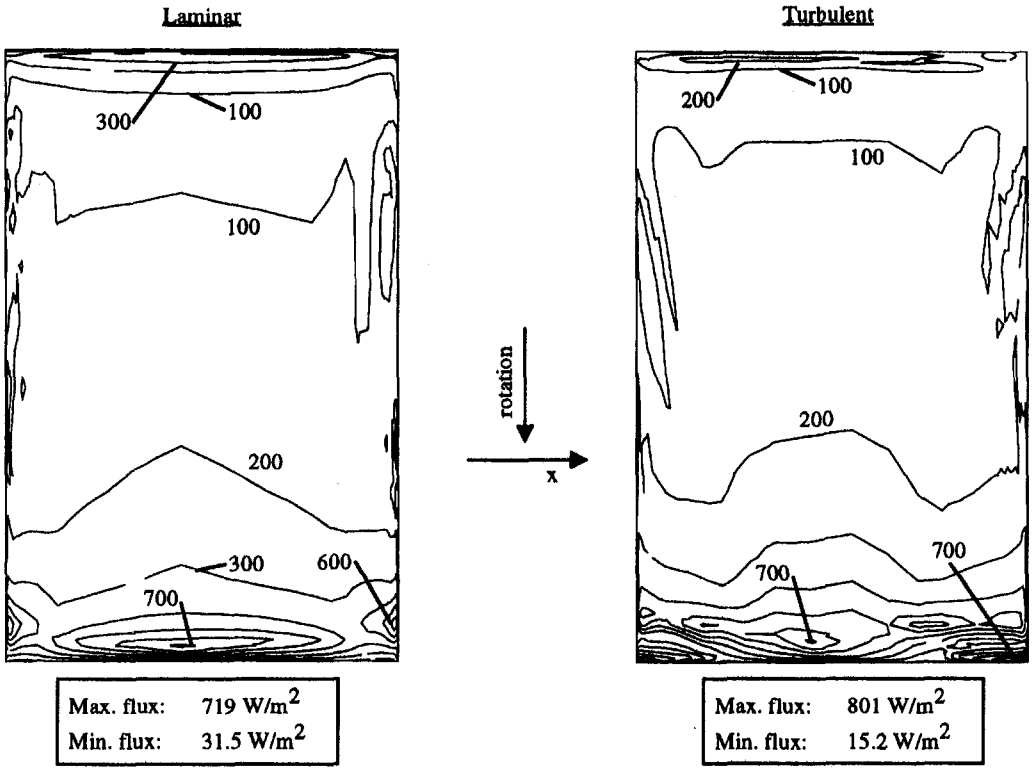

Fig. 6 Isolines of heat flux through outer cylinder wall (hot wall)

maximum turbulence degree, calculated with the maximum velocity in the cavity, is located in corners 1 and 3 and exceeds 5 percent. Looking at the velocity inside the rotating cavity, some significant differences become obvious (Fig. 4). The vector length is scaled exactly equal in both figures. The maximum velocity of the laminar flow is 1.09 m/s compared to 0.89 m/s for the turbulent one. This difference is due to the increased effective viscosity in the turbulent flow, consisting of the sum of the molecular and the turbulent viscosities. This viscosity increase dampens the fluid motion through increased shear within the flow.

That mechanism also causes the two vortices embedded in the large main vortex, which transports the hot air from the outer wall to the inner wall and the cold air from the inner to the outer wall, to exist only in the laminar case. In the turbulent case there is only a little fluid motion in the center region, which is consistent with the Taylor–Proudman theorem. While the velocity profiles in the laminar flow exhibit a significant maximum velocity near the segmentation walls with a decreasing velocity gradient toward the cavity center, the increased shear in the turbulent case damps this maximum. Therefore, the flow is faster in the region between the maximum velocity and the center. This leads to a different form of the corner vortex in corner 1.

Although turbulence generally damps these vortices, which can also be seen in the size of the other three corner vortices, corner vortex 1 is larger in the turbulent case. This is due to the flatter velocity profile in the segmentation wall boundary layer. In the layer near the segmentation wall, the laminar flow has more momentum. For this reason it is not as quickly redirected as in the turbulent case. Hence, it impinges the inner cylindrical wall at an angle closer to 90 deg. This is the reason for the heat flux maximum (Fig. 5) being closer to the wall in the laminar case. Because of the turbulence-intensified energy exchange, the maximum heat flux is still larger for the turbulent flow, though. At the outer cylindrical wall this effect is also present, but not as distinct as at the inner wall.

It is striking that the vortices are larger in the corners adjacent to the inner cylindrical wall than at the outer wall for both flow regimes, the laminar and the turbulent flow. This behavior can be attributed to the concave–convex shape of the cylindrical walls. At both corners at the inner wall the angle of impingement is less than 90 deg and is becoming smaller the nearer the flow particles are to the cavity center. This is due to the convex wall shape.

At the outer wall, which is concave, the angle of impingement is much closer to 90 deg and is hardly becoming smaller for flow particles closer to the cavity center. This inhibits larger vortices. For the local heat flux distribution on the cylindrical walls this means that the flux maximum is closer to the segmentation wall as can be seen by comparing Figs. 5 and 6.

If one compares the ratio of the local heat flux maximum and minimum on the cylindrical side walls, one realizes that this ratio is approximately 50 percent higher for the turbulent flow than for the laminar one. The reason obviously is the increased heat flux for the turbulent flow in the region of impingement to the cylindrical wall, which in effect leads to smaller temperature gradients further downstream, resulting in a further decreased flux.

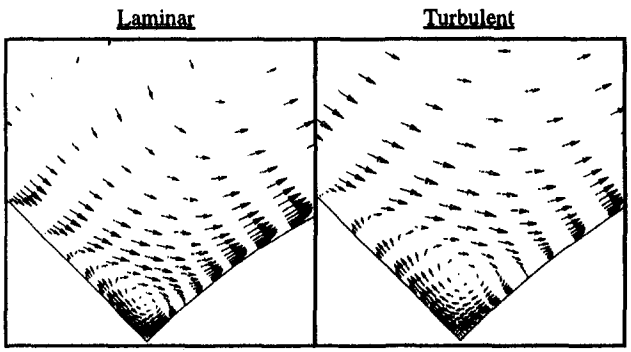

Fig. 7 Velocity vectors in the cavity (three-dimensional case, middle section: $x/b = 0.5$)

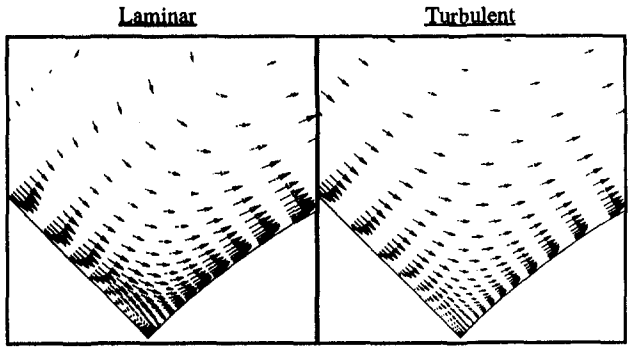

Fig. 8 Velocity vectors near the axial side wall (three-dimensional case, $x/b = 0.987$)

The buoyancy effects not only cause the fluid motion in this rotating cavity, but they also strongly influence the flow structure details. In the turbulent case the corner vortices 2 and 4 are significantly damped while the vortices in corners 1 and 3 (Fig. 2) are slightly larger compared to the laminar flow. Obviously the vortices in corners 1 and 3 are not only driven by the main flow but also by the density gradients within these vortices. For example, for corner vortex 1 (Fig. 7) the air is cooled down at the inner cylindrical wall, so the fluid particles in the corner vortex near the segmentation wall are cooler and thereby denser than those on the main flow side of the vortex. In combination with the centrifugal acceleration field, this induces buoyant forces driving this vortex additionally.

Due to the increased heat exchange, the air is cooled down further in the turbulent case, increasing the buoyant driving force and offsetting the effect of the turbulence induced higher shear forces. This explains the large extension of the corner vortices in corners 1 and 3 (Fig. 2) in radial direction. In the region nearer to the axial side walls, this corner vortex is further damped due to the proximity of the side wall, which causes additional shear stresses. That is the reason this vortex is more strongly damped in the turbulent case (Fig. 8). Here the shear stresses are stronger than the buoyant forces.

In the turbulent case the flow is slowed down further than the laminar one in the boundary layer. This not only becomes obvious through Fig. 8, but also through the effect of the slowdown on the heat transfer, which can be seen in the three-dimensional wall temperature distribution in Fig. 9. In the turbulent case, the convection in the flow direction is smaller compared to the effective temperature diffusivity due to the decreased velocity. This results in a stronger temperature gradient in the radial direction in the corner region between the segmentation wall and the axial side wall.

Looking at the resulting integral heat flux through the cavity, one realizes that the Nu number is approximately 10 percent higher for the case of turbulent flow (Table 2). This indicates that the heat flux enhancing effect of the turbulent motion is stronger than the convective flow damping effect of the increased shear.

Table 2 Integral Nusselt numbers in cavity for different cases

	experiment	3D laminar	3D turbulent	2D turbulent
Nu	34.0	36.8	40.0	41.1

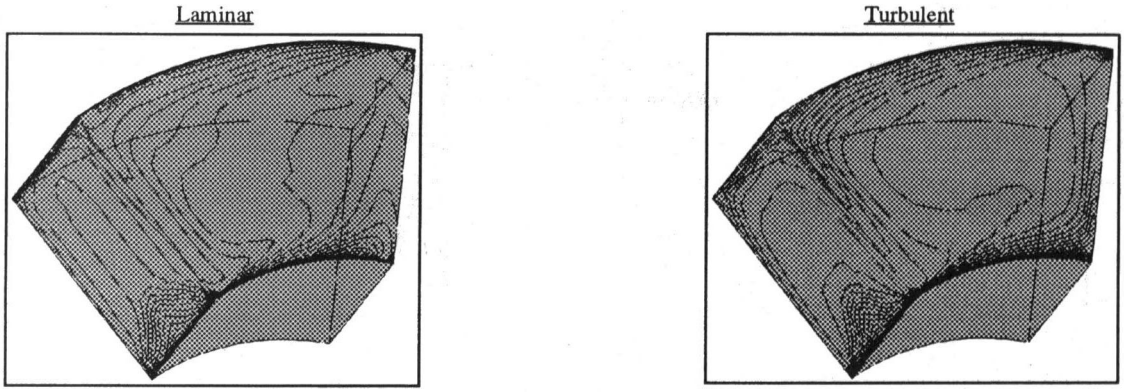

Fig. 9 Isotherms on the walls of the rotating cavity

Bohn et al. (1995, 1996) have estimated that because of the not perfectly adiabatic side walls the Nu number obtained from experiment underestimates the real value between 10 and 20 percent. This means the flux in the turbulent calculation, which is 17 percent higher than the experimental value, lies well within the experimental range.

Comparison Between Two-Dimensional and Three-Dimensional Calculation. As described in the previous subsection, the flow structure in the rotating cavity is a product of a complex interaction between buoyancy and viscous forces. Because of the long computation time required to converge this strongly buoyant flow to steady state, it is interesting to examine what can be achieved by a two-dimensional approach. In addition, the role of the three dimensionality can be investigated. Therefore, the same cavity has been discretized exactly as in the three-dimensional case with only one cell layer in axial direction and periodicity as boundary condition at the axial side walls.

In this approach the flow exhibits the same main flow features as the large main vortex but without the effects caused by the axial side walls. The only major difference in this concern is the vortex in corner 3. In the two-dimensional calculation this vortex is considerably larger than in the three-dimensional one (Fig. 10).

The similar flow structures in the two-dimensional case and in the middle plane in the three-dimensional case are consistent with comparisons of the heat flux intensity on the cold wall. As one can see in Fig. 11, the difference is negligible. However, in the proximity of the axial side walls the heat flux is considerably smaller. Here the viscous damping of the flow already has a significant effect. The integral Nusselt number therefore is somewhat higher in the two-dimensional case (Table 2). At the outer cylindrical wall the heat flux intensity maximum is shifted toward the middle in two-dimensional case, which is due to the larger extension of the vortex in corner 3. Its absolute value is the same as in the three-dimensional case.

This means that the three dimensionality of the buoyancy-induced flow in the examined rotating cavity does not have a very large impact on the overall heat flux. However, there are significant differences concerning the local heat flux distribution. In a real machine setup, these differences, and especially the differences in circumferential direction, which for the present moderate Ra number of 1.638×10^9 amount to a ratio of 29.3, will cause differences in the wall temperature. These temperature differences increase thermal stresses in the rotor.

Summary and Conclusions

Investigations have been carried out on the convective heat transfer in a closed rotating annulus with 45 deg segmentation and with a purely radial heat flux imposed. While the inner and the outer cylindrical walls were held at a constant temperature, the side walls were thermally insulated.

For this configuration two- and three-dimensional calculations were performed for a moderately high Ra number and compared to experimental data. It was found out that turbulence could be successfully simulated for this Ra number.

By comparing the laminar and the turbulent simulation, it was found that the heat exchange intensifying effect of the turbulent motion on the heat transfer is stronger than the convective flow motion damping effect of turbulence, leading to a net increase in heat transfer through turbulence. Turbulence is also responsible for a significant increase in the ratio of the local maximum and minimum heat transfer intensity on the cylindrical walls.

In addition to the effects of turbulence, it is also shown that, although the three dimensionality of the flow has only little

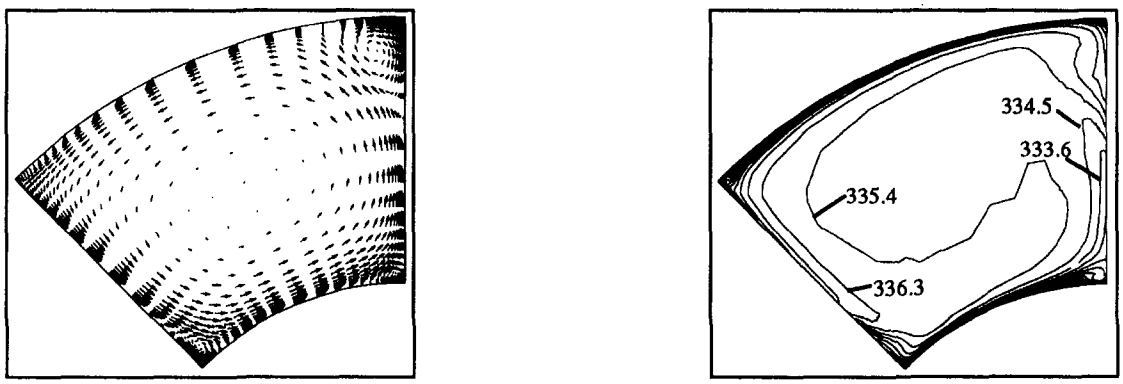

Fig. 10 Velocity vectors and isotherms [K] in the two-dimensional calculation

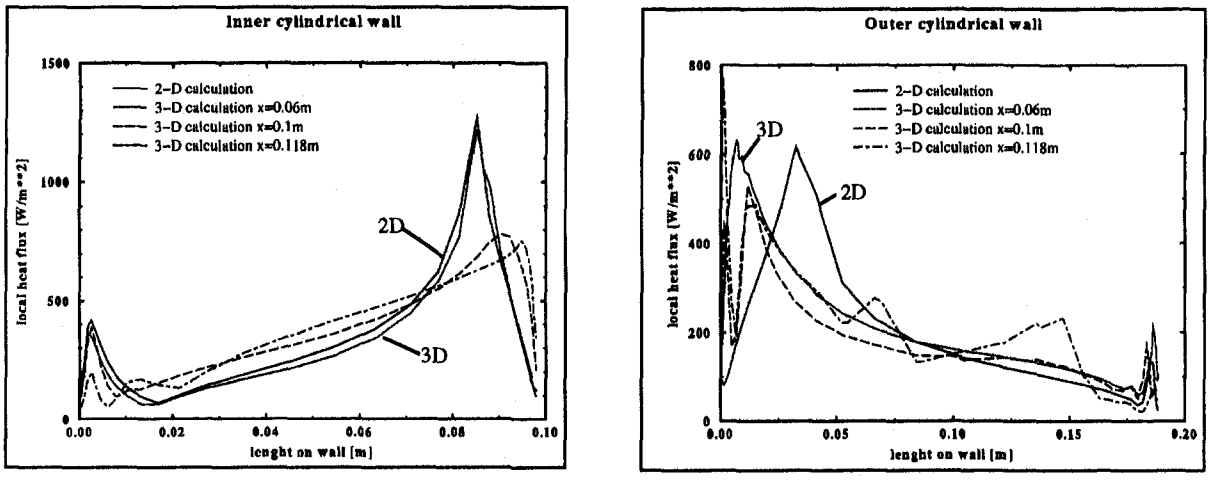

Fig. 11 Comparison of heat flux across the cylindrical walls (x = 0.06 m ⇒ x/b = 0.5; x = 0.118 m ⇒ x/b = 0.987)

impact on the overall heat transfer in the cavity, there exist considerable differences in the local heat transfer in the proximity of the side walls. Temperature differences caused by the large heat flux inhomogeneities in the local heat flux intensity should be considered for the design of modern high-temperature gas turbines.

Further investigations should extend these results to other points of operation, i.e., different Ra numbers as well as to the unsectored rotating annulus, in which additional aspects of the flow stability occur.

References

Bohn, D., Deuker, E., Emunds, R., and Gorzelitz, V., 1995, "Experimental and Theoretical Investigations of Heat Transfer in Closed Gas-Filled Rotating Annuli," ASME JOURNAL OF TURBOMACHINERY, Vol. 117, pp. 175–183.

Bohn, D., Emunds, R., Gorzelitz, V., and Krüger, U., 1996, "Experimental and Theoretical Investigations of Heat Transfer in Closed Gas-Filled Rotating Annuli II," ASME JOURNAL OF TURBOMACHINERY, Vol. 118, pp. 11–19.

Farthing, P. R., Long, C. A., Owen, J. M., and Pincombe, J. R., 1992, "Rotating Cavity With Axial Throughflow of Cooling Air: Heat Transfer," ASME JOURNAL OF TURBOMACHINERY, Vol. 114, pp. 229–236.

Gan, X., Mirzaee, I., Owen, J. M., Rees, D. A. S., and Wilson, M., 1996, "Flow in a Rotating Cavity With a Peripheral Inlet and Outlet of Cooling Air," ASME Paper No. 96-GT-309.

Gorzelitz, V., 1994, "Experimentelle Untersuchung des Wärmetransportes in geschlossenen kreisringförmigen rotierenden Hohlräumen," PhD-thesis, Aachen University of Technology.

Guo, Z., and Rhode, D. L., 1996, "Assessment of Two and Three-Scale $k-\epsilon$ Models for Rotating Cavity Flows," ASME JOURNAL OF TURBOMACHINERY, Vol. 118, pp. 826–834.

Ho, Y. H., Forry, J. M., Hendricks, R. C., and Steimetz, B. M., Athavale, M. M., 1996, "Numerical Simulation of Secondary Flow in Gas Turbine Disc Cavities, Including Conjugate Heat Transfer," ASME Paper No. 96-GT-67.

Iacovides, H., Nikas, K. S., and Te Braak, M. A. F., 1996, "Turbulent Flow Computations in Rotating Cavities Using Low-Reynolds-Number Models," ASME Paper No. 96-GT-159.

Izenson, M., Kennedy, M. R., and Sirukudi, J. R., 1995, "Turbulent Flow Computations for Turbine Disc Cavity Flows," ASME Paper No. 95-GT-192.

Launder, B. E., and Sharma, B. T., 1974, "Application of the Energy Dissipation Model of Turbulence to the Calculation of Flow Near a Spinning Disc," *Lett. Heat and Mass Transfer 1,* pp. 131–138.

Lin, T. Y., and Preckshot, G. W., 1979, "Steady State Laminar Natural Convection in a Rotating Annulus," *Studies in Heat Transfer, A Festschrift for E.R.G. Eckert,* Hemesphere Publishing Corporation, pp. 219–246.

Ong, C. L., and Owen, J. M., 1991, "Prediction of Heat Transfer in a Rotating Cavity With a Radial Outflow," ASME JOURNAL OF TURBOMACHINERY, Vol. 113, pp. 115–122.

Owen, J. M., Pincombe, J. R., and Rogers, R. H., 1985, "Source-Sink Flow Inside a Rotating Cylindrical Cavity," *J. Fluid Mech.,* Vol. 155, pp. 233–265.

Rhie, C. M., and Chow, W. L., 1983, "Numerical Study of the Turbulent Flow Past an Airfoil With Trailing Edge Separation," *AIAA Journal,* Vol. 21, pp. 1527–1532.

Van Doormal, J. P., and Raithby, G. D., 1984, "Enhancements of the SIMPLE Method for Predicting Incompressible Fluid Flows," *Num. Heat Transfer,* Vol. 7, pp. 147–163.

Zysina-Molozhen, I. M., and Salov, N. N., 1977, "Heat Exchange and Flow Regime of Liquids in a Closed Rotating Annular Cavity," *Soviet-Aeronautics,* Vol. 20, No. 1, pp. 39–43.

Low-Aspect-Ratio Rib Heat Transfer Coefficient Measurements in a Square Channel

M. E. Taslim

G. J. Korotky

Mechanical, Industrial and Manufacturing Engineering Department, Northeastern University, Boston, MA 02115

Cooling channels, roughened with repeated ribs, are commonly employed as a means of cooling turbine blades. The increased level of mixing induced by these ribs enhances the convective heat transfer in the blade cooling cavities. Many previous investigations have focused on the heat transfer coefficient on the surfaces between these ribs and only a few studies report the heat transfer coefficient on the rib surfaces themselves. The present study investigated the heat transfer coefficient on the surfaces of round-corner, low-aspect-ratio (AR_{rib} = 0.667) ribs. Twelve rib geometries, comprising three rib height-to-channel hydraulic diameters (blockage ratios) of 0.133, 0.167, and 0.25 as well as three rib spacings (pitch-to-height ratios) of 5, 8.5, and 10 were investigated for two distinct thermal boundary conditions of heated and unheated channel walls. A square channel, roughened with low-aspect-ratio ribs on two opposite walls in a staggered manner and perpendicular to the flow direction, was tested. An instrumented copper rib was positioned either in the middle of the rib arrangements or in the furthest upstream location. Both rib heat transfer coefficient and channel friction factor for these low-aspect-ratio ribs were also compared with those of square ribs, reported previously by the authors. Heat transfer coefficients of the furthest upstream rib and that of a typical rib located in the middle of the rib-roughened region of the passage wall were also compared.

Introduction

Various cooling methods have been developed over the years to ensure that the turbine blade metal temperatures are maintained at a level consistent with airfoil design life. The objective in turbine blade cooling is to achieve maximum internal heat transfer coefficients while minimizing the coolant flow rate. One such method is to route coolant air through serpentine channels within the airfoil and convectively remove heat from the blade. The coolant is then ejected either at the tip of the blade, through the cooling slots along the trailing edge, or through film holes on the airfoil surface. Heat transfer coefficients in the cooling passages can be increased by roughening the walls of the passage. One such method, used over the past 25 years in internal cooling passages, is to mount ribs on the channel walls. These ribs, also called turbulators, increase the level of mixing of the cooler channel core air with the warmer air close to the channel wall and also restart the boundary layer, thereby enhancing the cooling capability of the passage.

Geometric parameters such as channel aspect ratio (AR), rib height-to-passage hydraulic diameter (e/D_h) or blockage ratio, rib angle of attack (α), the manner in which the ribs on opposite walls are positioned relative to one another (in-line, staggered, criss-cross, etc.), rib pitch-to-height ratio (S/e) and rib shape (round versus sharp corners, fillets, rib aspect ratio (AR_{rib}), and skewness toward the flow direction) have pronounced effects on both local and overall heat transfer coefficients. Some of these effects have been studied by different investigators such as Abuaf et al. (1986), Burggraf (1970), Chandra (1988), Chandra and Han (1989), Han (1984), Han et al. (1978, 1985, 1992), Metzger et al. (1983, 1988, 1990), Taslim et al. (1988a, b, 1991a, b, 1994, 1996), and Webb et al. (1971). Considerable heat transfer coefficient data are available on the passage surface between the ribs. However, the heat transfer coefficients on the surface of the ribs themselves have not been investigated to the same extent.

In small aircraft engines with small cooling passages and relatively large ribs, the rib surfaces comprise a significant portion of the passage heat transfer area. Therefore, an accurate account of the heat transfer coefficient on the rib surfaces is critical in the overall design of the blade cooling system. The objective of this investigation was (while isolating the ribs from the wall surface thermally) to measure the overall heat transfer coefficient on the rib surface and to study the effects that pitch-to-height ratio (S/e), blockage ratio (e/D_h), and rib streamwise location (furthest upstream position or in the middle of the channel rib-roughened portion) have on the rib surface heat transfer coefficient for a channel aspect ratio (AR) of one (a square cross-sectional channel).

Among those investigations dealing with the measurement of heat transfer coefficients on the ribs are the following. Solntsev et al. (1973) experimentally investigated heat transfer in the vicinity of sudden two- and three-dimensional steps of circular and square cross-sectional areas mounted on a flat surface in an open channel. Enhancements in heat transfer coefficients on the step surfaces and in its vicinity are reported for a range of Reynolds numbers (based on the step height) between 10^4 and 10^5.

Berger and Hau (1979) performed an experimental study of flow over square ribs in a circular pipe using an electrochemical analogue technique to measure mass/heat transfer on the ribs as well as on the wall surface between them. For a blockage ratio (e/d) of 0.0364, they varied the rib pitch-to-height ratio from 3 to 10 for a range of Reynolds numbers between 10,000 and 25,000. At the Reynolds number of 10^4, they showed en-

Contributed by the International Gas Turbine Institute and presented at the 42nd International Gas Turbine and Aeroengine Congress and Exhibition, Orlando, Florida, June 2–5, 1997. Manuscript received International Gas Turbine Institute February 1997. Paper No. 97-GT-388. Associate Technical Editor: H. A. Kidd.

hancements, compared to smooth channels, in mass (heat) transfer on the rib surfaces on the order of 4.4 and 5.2 for pitch-to-height ratios of 10 and 7, respectively.

Metzger et al. (1988) used a thermal transient technique to examine the contribution of the rib heat transfer to the overall heat transfer of a rib-roughened wall with variations in rib angle of attack and in pitch. Square sharp-corner ribs with a blockage ratio of 0.14 were mounted on one of the wider sides of a 0.154 aspect ratio rectangular channel. The main conclusions were that heat transfer on the sharp-corner rib surface significantly contributed to the overall rib-roughened wall heat transfer (h_{rib}/h_{floor} of around 2) and this contribution mainly depended on the rib pitch-to-height spacing, with very little effect from the rib angle.

Lockett and Collins (1990) used a holographic interferometry technique to measure heat transfer coefficients in a 0.25 aspect ratio channel. Square ribs, with sharp and round top corners, representing a blockage ratio $e/D_h = 0.067$ and a pitch-to-height ratio 7.2, were mounted on one of the wider sides of the channel and perpendicular to the flow direction. They reported overall enhancements in rib heat transfer of up to 2.24 for the channel Reynolds number of 7400.

Liou et al. (1991) performed numerical and experimental investigations of turbulent flow in a rectangular channel with an aspect ratio of 4. The channel was roughened with square sharp-cornered ribs on the two wider sides in an in-line arrangement perpendicular to the flow direction. The rib blockage ratio, e/D_h, was 0.081 and four pitch-to-height ratios of 5, 10, 15, and 20 were examined at a fixed Reynolds number of 33,000. Two-dimensional Navier–Stokes equations in elliptic form in conjunction with the $k-\epsilon$ turbulence model were solved numerically and a holographic interferometry technique was used in the experimental part. They reported a heat transfer enhancement of 3.1 on the rib surface.

Sato et al. (1992) investigated the flow characteristics and heat transfer in a rectangular channel with a total of 20 square ribs on two opposite walls in staggered, in-line, and quarter-pitch-shift arrangements. The channel aspect ratio was 0.2 and the ribs, mounted on the two wider sides of the channel, had a blockage ratio of 0.12. Details of the flow and heat transfer over a typical rib-roughened section (including the rib surface) far downstream of the first rib were presented. They concluded that, among the three rib arrangements, staggered ribs produced the highest enhancement in heat transfer coefficients on the rib and floor surfaces.

Dawes (1994) solved the three-dimensional Navier–Stokes equations in a rotating serpentine coolant passage of cylindrical geometry roughened with square sharp-corner ribs. Rib blockage, e/d, and pitch-to-height ratios were 0.2 and 10, respectively. Local heat transfer coefficients (both rib and floor) were compared with other numerical and experimental works.

Liou and Hwang (1993) also used the holographic interferometry technique to measure the heat transfer coefficient and friction factor in a 0.25 aspect ratio rectangular channel with three rib shapes including a square rib geometry mounted on two wider sides in an in-line arrangement perpendicular to the flow direction. For a blockage ratio of 0.08, they tested four rib pitch-to-height ratios of 8, 10, 15, and 20 for Reynolds numbers between 7800 and 50,000. The heat transfer coefficient was measured on the rib surfaces as well as the wall surface between the ribs. They reported overall heat transfer coefficient enhancements on the order of 2.2 and 2.7 for semicylindrical and square ribs, respectively.

Taslim and Wadsworth (1997) investigated rib surface-averaged heat transfer coefficients in a square channel. Thirteen rib geometries including three blockage ratios (0.133, 0.167, 0.25) and four pitch-to-height ratios (5, 7.5, 8.5, 10) were tested. Sharp-corner ribs were mounted on two opposite walls of the channel at a 90 deg angle with respect to the flow direction in a staggered arrangement. A major conclusion of their study was that the rib surface-averaged heat transfer coefficient was much higher than that for the area between the ribs (h_{floor}). Therefore, the contribution of the ribs to the overall heat transfer in a rib-roughened passage is significant. They showed that for a typical rib arrangement the $h_{rib}A_{rib}$ can be as high as 33 to 53 percent of $h_{overall}A_{total}$. Other conclusions were that (*a*) for sharp-edge ribs, a pitch-to-height ratio of 8.5 produced the highest rib heat transfer coefficients, and (*b*) heat transfer coefficients on ribs in the furthest upstream position were lower than that on the midchannel ribs.

Korotky and Taslim (1998) tested twelve rib geometries in a square channel. The ribs with an aspect ratio of one and typical castable rounded top corners were mounted perpendicular to the flow direction in a staggered arrangement. Rib surface-averaged heat transfer coefficients as well as the channel friction factors were reported. They concluded that the general effects

Nomenclature

a = channel height (Fig. 1)
b = channel width = a
A = channel cross-sectional area without ribs = a^2
A_{floor} = wall heat transfer area between two ribs
A_{rib} = rib total heat transfer area (three sides)
A_{total} = total heat transfer area = $A_{rib} + A_{floor}$
AR = channel aspect ratio = $b/a = 1$
AR_{rib} = rib aspect ratio = e/w
D_h = hydraulic diameter based on the smooth square cross section = $4A/P = a$
e = rib height
$\bar{f}$ = Darcy friction factor = $\Delta P(D_h/L)/(1/2\rho U_m^2)$
$\bar{f}_s$ = Darcy friction factor in an all-smooth-wall channel
h_{floor} = average heat transfer coefficient on the wall surface between a pair of ribs
$h_{overall}$ = overall average heat transfer coefficient on a rib and on the wall surface between a pair of ribs
h_{rib} = rib average heat transfer coefficient = $q/(T_s - T_m)$
h_{smooth} = average heat transfer coefficient in a smooth channel
i = current through the heater inside the copper rib
k = air thermal conductivity
L = length of the rib-roughened portion of the test section
m = air mass flow rate
$\overline{Nu}$ = rib average Nusselt number = $h_{rib}D_h/k$
$\overline{Nu}_s$ = average Nusselt number in a smooth channel = $h_{smooth}D_h/k$
P = channel perimeter without ribs
Pr = Prandtl number
q = net heat flux from the copper rib three surfaces = $(vi - Q_{loss})/A_{rib}$
Q_{loss} = heat losses from the copper rib by radiation and conduction
Re = Reynolds number = $\rho U_m D_h/\mu$
r = rib top corner radius
S = rib pitch (center-to-center)
T_f = film temperature = 0.5 $(T_s + T_m)$
T_m = calculated air mixed mean temperature at copper rib location
T_s = copper rib surface temperature
U_m = air mean velocity
v = voltage drop across the heater inside the copper rib
w = rib width (Fig. 1)
X = distance between the instrumented rib and test section entrance (Fig. 1)
α = flow angle of attack
μ = air dynamic viscosity
ΔP = pressure drop across the rib-roughened portion of the test section
ρ = air density

of rounding the rib top corners were a decrease in heat transfer coefficient (relative to sharp-corner ribs) for the midstream ribs and an increase in heat transfer coefficient for the ribs in the furthest upstream position.

The casting process employed in the manufacture of turbine blades puts severe limitations on the size and shape of the ribs, especially in small engines. These limitations stem from a wide range of issues associated with the casting of very small turbine blades including the evidence of the molten materials to improperly fill the cast-core grooves forming the final ribs. To alleviate this "non-fill" difficulty, the more desirable square ribs are replaced by wider (low-aspect-ratio) ribs, which are consistently castable. However, this results in some deterioration in the heat transfer coefficients on the wall surface between ribs (Taslim and Spring, 1994). In addition to the "non-fill" problem, dimensional tolerances alone represent a significant deviation in heat transfer behavior for ribs in small airfoils. As blade dimensions in modern small engines are reduced, rib dimensions must follow suit. However, there is a minimum practical limit to the rib size (0.254 mm). There also is a minimum limit to the associated dimensional tolerances (0.05 mm–0.076 mm). Thus, for a rib with a cast height of $e = 0.254 \pm 0.076$ mm, the rib height can potentially vary ±30 percent. For small airfoils, where a 0.254 mm rib represents a high blockage ratio, ±30 percent in rib height can yield significant variations in the heat transfer coefficients on the rib surfaces as well as the friction factor in the blade cooling passes. It is the main objective of the present work to investigate the effects of these dimensional tolerances.

Test Sections

Figure 1 shows schematically the layout and cross-sectional area of a typical test section. Rib geometry details are shown in Table 1. All test sections, with a length of 1.1684 m, had a square 38.1 mm by 38.1 mm cross-sectional area. Three walls of these channels were made of 12.7-mm-thick clear acrylic plastic. The fourth wall, on which two etched-foil heaters and an instrumented copper rib were mounted and all measurements were taken, was made of a 76.2-mm-thick machinable polyurethane slab. Eighteen rectangular ribs with an aspect ratio of 0.667 and round top corners were symmetrically staggered on

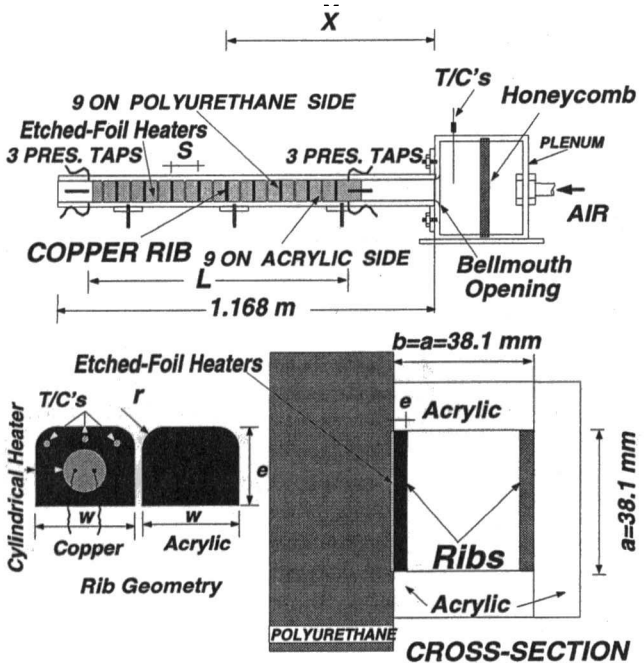

Fig. 1 Schematic of a typical test section

the polyurethane wall and its opposite acrylic wall (nine on each) at 90 deg angle of attack to the air flow. The entrance region of all test sections was left smooth to simulate the cooling passage in the dovetail region of a gas turbine blade. All ribs but one were machined out of acrylic plastic. The instrumented rib on which all measurements were taken was machined out of copper. Inside this copper rib, a 60-Ohm cylindrical electric heater was installed using a highly conductive silver glue. The heater, which ran the full length of the rib, was mounted as centrally as possible. Also installed in the copper rib were three calibrated thermocouples to measure the surface temperature. These three thermocouples were equally spaced over the length of the rib with their beads close to the rib top surface. Their temperature readings were found to be the same within a fraction of a degree. For data reduction, the average of the three temperatures was used. Copper rib end surfaces had no contact with the channel side walls and its top and side surfaces were polished to minimize the radiational heat losses to the unheated walls. Ribs were laid on the polyurethane wall using a special double-stick 0.05-mm-thick tape with minimal temperature deformation characteristics. Rib heat transfer coefficient measurements were performed for two distinct rib streamwise locations. First, the copper rib was mounted in the middle of the rib-roughened portion of the channel (fifth rib of nine) with the desired rib pitch-to-height ratio. Second, the copper rib was moved to the furthest upstream position and the other eight ribs were mounted downstream of it. Table 1 shows the rib location from the channel entrance, X, for each geometry. Two 38.1 mm by 279.4 mm custom-made etched-foil heaters with a thickness of 0.15 mm were placed on the polyurethane wall abutting both sides of the copper rib using the same special double-stick tape. The test section was covered on all sides by 50-mm-thick styrofoam sheets to minimize the heat losses to the environment. Surface heat flux in the test section was generated by the heaters through a custom-designed power supply unit. Each heater was individually controlled by a variable transformer.

Static pressure taps were mounted on all three acrylic plastic walls of the test section to measure the pressure drop across the rib-roughened portion of the test section, as shown in Fig. 1. A contact micromanometer with an accuracy of 0.025 mm of water column measured the pressure differences between the static pressure taps. A critical venturimeter, with choked flow for all cases tested, measured the total mass flow rate entering the test section. The reported friction factor, $\bar{f}$, is the overall channel (two ribbed walls and two smooth walls) friction factor and does not include the smooth inlet and exit sections. Details of the experimental apparatus and test procedures are reported by Korotky (1994).

The radiational heat loss from the heated rib (and wall) to the unheated walls (less than 0.7 percent of the net input power) as well as losses to ambient air (less than 0.05 percent of the net input power) were calculated when heat transfer coefficients were evaluated. Air properties for Nusselt and Reynolds number calculations are based on the local film temperature, T_f, for all cases. Air mixed mean temperature, T_m, was calculated using the energy balance from the test section inlet to the instrumented copper rib location. For the cases in which the foil heaters on the channel wall were off, this temperature was checked against the reading of a thermocouple hanging in the test section above the copper rib. The reported heat transfer coefficients are the average of the rib three surfaces and not the wall surfaces between the ribs. Experimental uncertainties, following the method of Kline and McClintock (1953), were determined to be ±8 and ±6 percent for the heat transfer coefficient and friction factor, respectively.

Results and Discussion

Figure 2 shows rib-averaged Nusselt number versus channel Reynolds number for the first rib geometry corresponding to a

Table 1 Geometric specifications

Test	e(mm)	r/e	e/Dh	S/e	X (cm)	X/Dh	Remarks
1	9.525	0.25	0.25	5	57.4	15	Midstream
2	9.525	0.25	0.25	8.5	57.4	15	Midstream
3	9.525	0.25	0.25	10	57.4	15	Midstream
4	9.525	0.25	0.25	8.5	24.89	10.4	Upstream
5	6.35	0.25	0.167	5	57.4	15	Midstream
6	6.35	0.25	0.167	8.5	57.4	15	Midstream
7	6.35	0.25	0.167	10	57.4	15	Midstream
8	6.35	0.25	0.167	8.5	35.81	9.4	Upstream
9	5.08	0.197	0.133	5	57.15	15	Midstream
10	5.08	0.197	0.133	8.5	57.15	15	Midstream
11	5.08	0.197	0.133	10	57.15	15	Midstream
12	5.08	0.197	0.133	8.5	39.62	10.4	Upstream
AR = 1, ARrib= e/w =0.667, α = 90 ° Staggered for all Geometries							

blockage ratio, e/D_h, of 0.25 and a pitch-to-height ratio, S/e, of 8.5. With a constant air inlet temperature of 22°C, the copper rib temperature is varied from 43.3°C to 76.7°C with no apparent change in the measured heat transfer coefficient. This lack of effect of the copper surface temperature on heat transfer coefficient continued for all geometries examined. Furthermore, this insensitivity of the measured heat transfer coefficient to the rib surface temperature supports the accuracy of accounting for the conduction losses to the walls and radiational losses from the heated copper rib to the unheated surrounding walls. In those tests labeled "Heated Wall," the foil heaters laid on the wall surface between the ribs as well as the cylindrical heater inside the copper rib were turned on. The "Unheated Wall" tests, however, are referred to those in which only the cylindrical heater inside the copper rib was turned on. A maximum difference of 4.7 percent in heat transfer coefficient was measured between the cases of heated and unheated wall. This maximum corresponded to the lowest tested Reynolds number as seen in Fig. 2. At higher Reynolds numbers, however, the difference was well below the experimental uncertainties, indicating that, for most test points, the thermal boundary layer initiated by the foil heaters, being interrupted repeatedly by the ribs, did not affect the heat transfer coefficient. It would appear that the mixing phenomenon was the dominant driving force for the high levels of heat transfer coefficient. As for having only one heated wall, El-Husayni et al. (1991) showed that heat transfer coefficient in a rib-roughened channel varied less than ±8 percent (was insensitive) as the number of channel heated walls varied from one to two and to four. Thus the present tests with one heated wall and an uncertainty of ±5 percent support this conclusion. The Dittus–Boelter (1930) correlation for an all-smooth-wall channel ($\overline{Nu}_s = 0.023\ Re^{0.8}\ Pr^{0.4}$) is also plotted in Fig. 2. With this correlation, the enhancement (relative to smooth walls) in rib-averaged heat transfer coefficients is readily evaluated.

Figures 3 and 4 show rib-averaged Nusselt number and friction factor, respectively, versus channel Reynolds number for the biggest rib geometry of $e/D_h = 0.25$. To investigate the effects pitch-to-height ratios have on rib heat transfer and channel overall friction factor, three pitch-to-height ratios of 5, 8.5, and 10 (geometries 1–3 in Table 1) were tested. For comparison, results of square ribs with rounded top corners (Korotky and Taslim, 1998) are plotted. Also shown in Fig. 3 are the rib heat transfer results for an S/e of 8.5 when the instrumented copper rib was mounted in the furthest upstream position (geometry 4 in Table 1). Several observations are made. First, the heat transfer coefficient for the furthest upstream rib was considerably lower than that for the rib in the middle of the rib-roughened region. This behavior indicated that upstream ribs and those staggered on the opposite wall contribute significantly to the very high level of heat transfer enhancement of downstream ribs by interrupting the flow and diverting its direction, thus promoting high levels of mixing. Second, low-aspect-ratio ribs produced lower Nusselt numbers than those of square ribs in the midstream position. This was expected, especially for high-blockage-ratio ribs such as these. Reported data by Taslim and Spring (1994) and other investigators have shown that, when the rib aspect ratio decreases, the heat transfer coefficient on the surface between the ribs decreases apparently due to

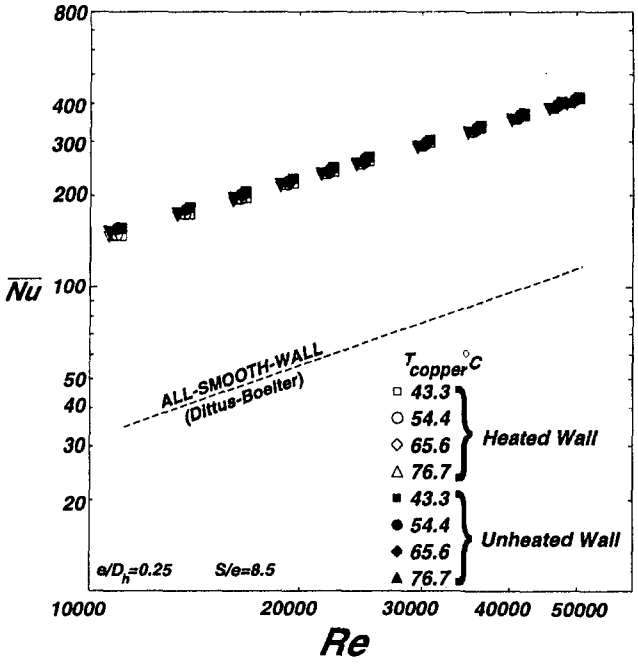

Fig. 2 Rib-averaged Nusselt number for a range of rib surface temperatures

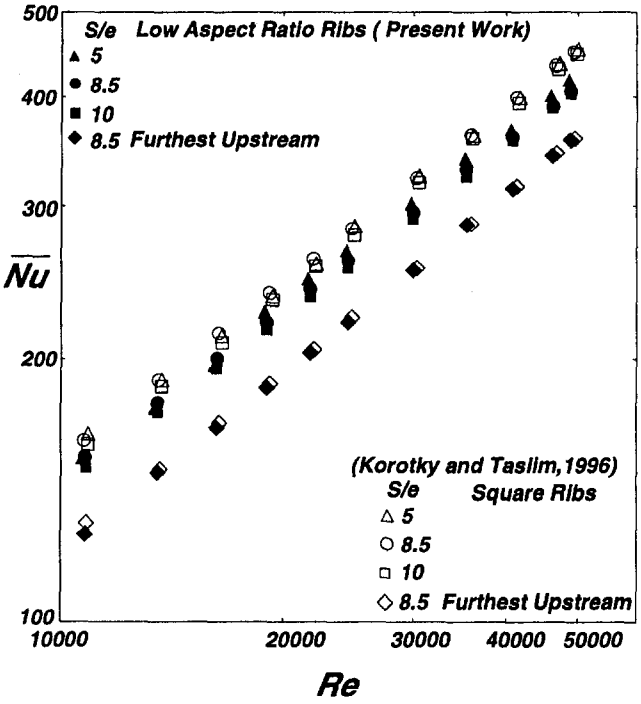

Fig. 3 Rib-averaged Nusselt number for a range of pitch-to-height ratios for $e/D_h = 0.25$

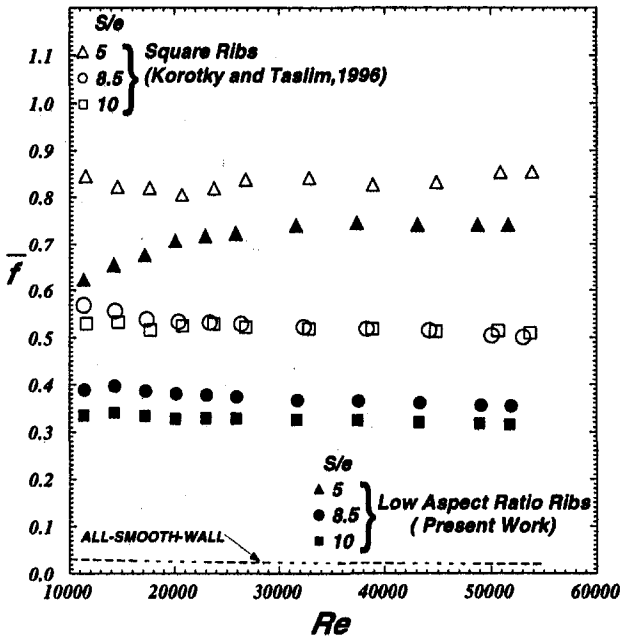

Fig. 4 Channel-averaged friction factor for a range of pitch-to-height ratios, $e/D_h = 0.25$

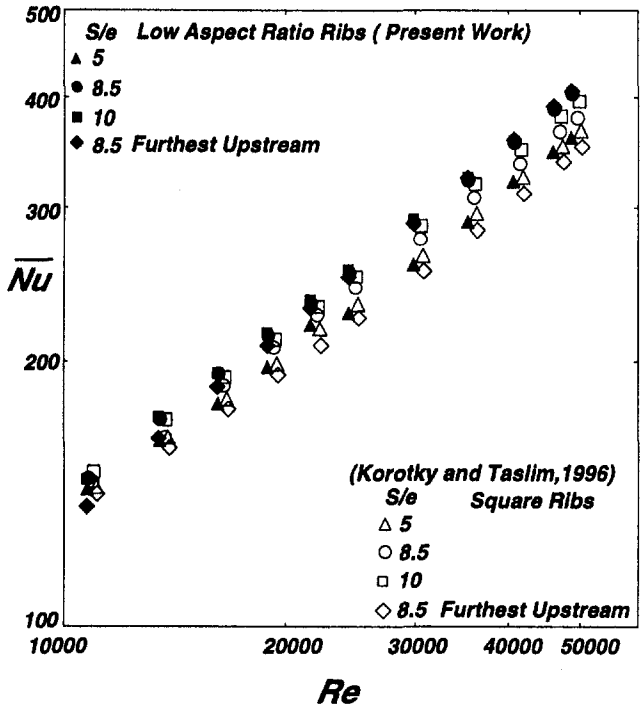

Fig. 5 Rib-averaged Nusselt number for a range of pitch-to-height ratios for $e/D_h = 0.167$

lower levels of mixing of the warmer near-wall air with the core air. At the same time, the contribution of the low-aspect-ratio ribs on the opposite wall to the flow interruption is somewhat reduced. It is speculated that, for the same reasons, the heat transfer coefficients on the rib surfaces also decrease when the rib aspect ratio decreases. The low-aspect-ratio ribs in the furthest upstream position produced Nusselt numbers very close to those by square ribs. This behavior, which was observed for the highest blockage ratio, could only be attributed to a better flow adherence to the rib surfaces, which, in turn, increases the heat transfer coefficient. Third, the rib heat transfer coefficient for these high-blockage ribs (both square and low-aspect-ratio ribs) was nearly insensitive to the pitch-to-height ratio. Effects of rib spacing on Nusselt number for this and the other two blockage ratios for a typical Reynolds number will be discussed later. We will see that the heat transfer coefficients for the smaller ribs are more sensitive to the rib spacing. As expected, the low-aspect-ratio ribs produce lower pressure drops and consequently lower friction factors compared to the square ribs. This pattern, which exists for the other two rib geometries as well, is apparently due to a lower form drag for the low-aspect-ratio ribs. The friction factor increased as the pitch-to-height ratio decreased since a lower rib spacing corresponds to more ribs per unit length of the channel.

The next series of four tests, shown in Figs. 5 and 6, corresponded to an intermediate rib blockage ratio of 0.167, three of which (test geometries 5–8 in Table 1) were performed again for pitch-to-height ratios of 10, 8.5, and 5 with the instrumented copper rib mounted in the middle of the rib-roughened region. The fourth test represents the heat transfer results when copper rib was mounted in the furthest upstream position (geometry 8 in Table 1). In the furthest upstream position and the lowest Reynolds number tested, the square ribs show higher heat transfer coefficients than those of low-aspect-ratio ribs. However, as the Reynolds number increases, the trend reverses itself. A better flow adherence to the low-aspect-ratio ribs at high Reynolds numbers is believed to be the reason for this behavior. Also for the midchannel streamwise location, the low-aspect-ratio ribs are superior to the square corner ribs. It is only at $S/e = 5$ that the heat transfer performances of the two types of ribs are comparable. The friction factor trends for these tests are similar to those of $e/D_h = 0.25$, i.e., (a) lower pressure drops (friction factors) for the low-aspect-ratio ribs and (b) the pitch-to-height ratio of 5 producing a higher friction factor than those of 8.5 and 10.

The next four tests, shown in Figs. 7 and 8, corresponded to the lowest rib blockage ratio of 0.133. The first three tests (geometries 9–11 in Table 1) were performed for pitch-to-height ratios of 10, 8.5, and 5 with the instrumented copper rib mounted in the middle of the rib-roughened region. The fourth test represents the heat transfer results for the copper rib mounted in the furthest upstream position (geometry 12 in Table

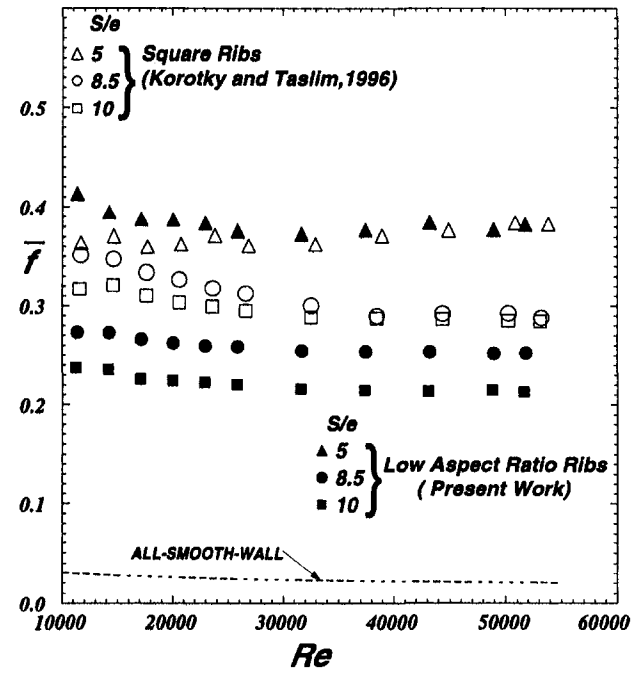

Fig. 6 Channel-averaged friction factor for a range of pitch-to-height ratios, $e/D_h = 0.167$

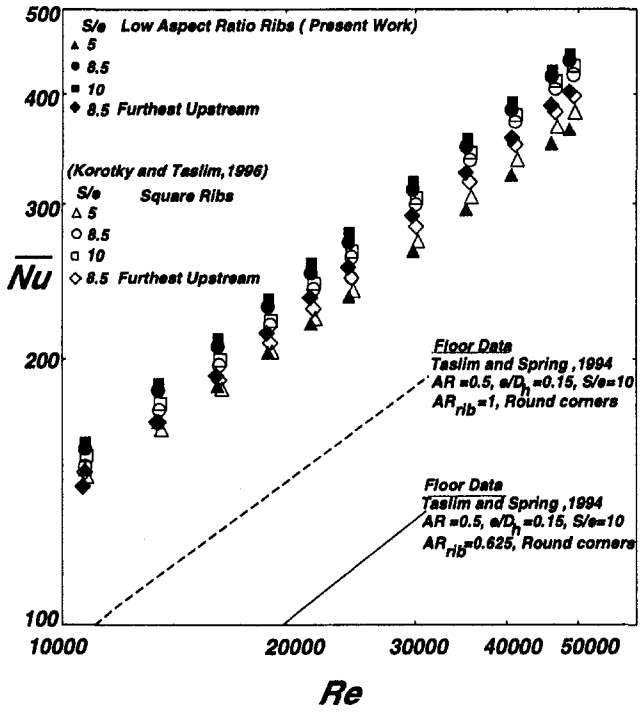

Fig. 7 Rib-averaged Nusselt number for a range of pitch-to-height ratios for $e/D_h = 0.133$

1). The solid and dashed lines represent the heat transfer results for the area between a pair of ribs reported by Taslim and Spring (1994). These were the closest geometries that could be found in open literature. Several observations are made. The rib surface-averaged Nusselt numbers are much higher than those for the area between the ribs (Nu_{floor}) and, therefore, have a significant contribution to the overall heat transfer coefficient on a rib-roughened surface, especially in small blades where the rib surface area is a significant portion of the total heat transfer area. Low-aspect-ratio rib heat transfer results for this lowest blockage ratio tested are, for most Reynolds numbers, higher than those of square ribs. Only when they are close to each other at $S/e = 5$ and in the higher range of Reynolds numbers are the heat transfer coefficients below the square rib results. Again, the low-aspect-ratio ribs in the furthest upstream position produced a higher heat transfer coefficient than that of square ribs in the same position. The heat transfer enhancements for the furthest upstream rib were comparable to those of mid-stream ribs. This is an indication that the contribution of the staggered ribs on the opposite wall to the copper rib heat transfer coefficient, caused by the diversion of flow toward the ribs on the opposite wall, is less significant for these low blockage ratio ribs. For both the low-aspect-ratio and the square ribs, the Nusselt numbers corresponding to the pitch-to-height ratio of 5 fell below the furthest upstream rib results. This behavior indicates that, compared with high blockage ratio ribs, these low blockage ratio ribs on opposite walls are less effective in redirecting the flow and promoting high levels of mixing. The low-aspect-ratio effects on the friction factor are more significant than those on the heat transfer as shown in Fig. 8. This behavior is also observed for the heat transfer coefficient on the surface between the ribs by other investigators.

Figure 9 combines the heat transfer results of all low-aspect-ratio rib geometries for all pitch-to-height ratios. In contrast with the heat transfer coefficient on the area between a pair of ribs, which is highly affected by the blockage ratio, the rib surface-averaged heat transfer coefficient did not show as strong of a dependence on blockage ratio, especially for $S/e = 10$. However, as ribs were brought closer by reducing the pitch-to-height ratio, rib heat transfer coefficient was more and more affected by the blockage ratio. It is seen that smaller ribs positioned at pitch-to-height ratios of 8.5 and 10 produced the highest rib heat transfer coefficients. Not benefiting from the effects of the ribs on the opposite wall as much as the higher blockage ratio ribs do, it is speculated that this behavior is due to the change of flow pattern over different ribs. In other words, for the bigger ribs, recirculating bubbles may form on both the back and top surfaces of the rib, reducing the contribution of the rib top surface to heat transfer, known to be major for square ribs with sharp corners by all investigators mentioned above. For the smallest rib, however, the top surface is in contact with the core air, thus higher heat transfer coefficients are produced.

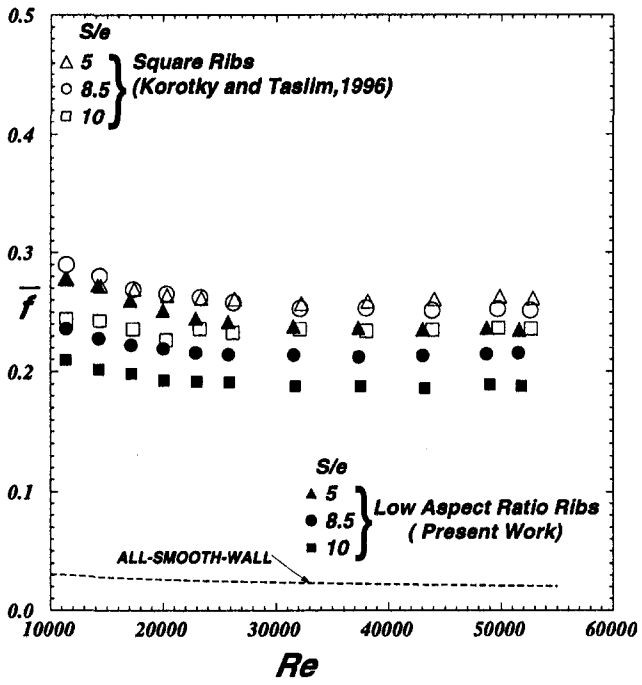

Fig. 8 Channel-averaged friction factor for a range of pitch-to-height ratios, $e/D_h = 0.133$

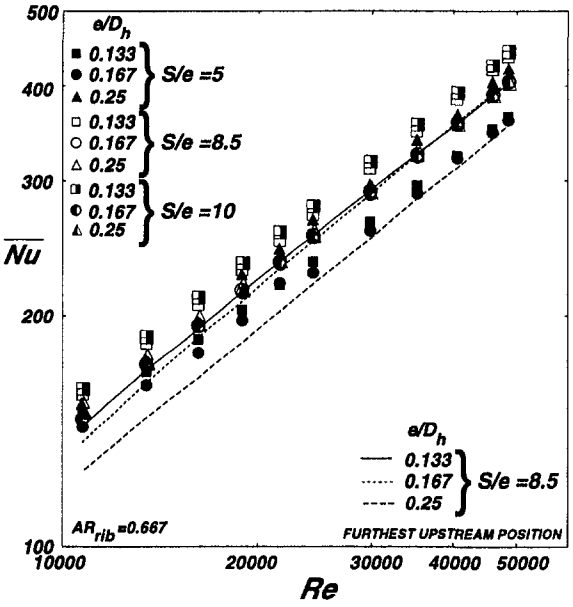

Fig. 9 Rib-averaged Nusselt number for all blockage and pitch-to-height ratios

For clarity, the three lines in Fig. 9 represent the low-aspect-ratio rib results in the furthest upstream position. The two smaller rib geometries produced heat transfer coefficients comparable to their counterparts in the midstream position while the biggest rib geometry ($e/D_h = 0.25$) in the furthest upstream position was inferior to those in the midstream position. This behavior may be attributed to a better flow adherence to rib surfaces for those cases of smaller, more streamlined, low-aspect-ratio ribs.

A pitch-to-height ratio of 5 was the least desirable spacing from both friction factor (as evidenced by Fig. 10) and heat transfer point of views. Only for the largest blockage ratio and in the higher range of Reynolds numbers, the heat transfer coefficient for the pitch-to-height ratio of 5 was higher than those for the other two rib spacings. But it was, however, accompanied by the highest friction factor measured for all these geometries. Friction factors for all low-aspect-ratio ribs are shown in Fig. 10. Several observations are made. First, ribs positioned too close to each other produced the highest friction factor with the highest blockage ratio, producing a friction factor almost three times that of the smallest rib geometry. As was mentioned previously, a lower pitch-to-height ratio corresponds to more ribs per channel length, which results in a higher pressure drop. A high level of form drag contributes to the very high friction factor for the biggest rib. Second, channel friction factor increases with rib blockage ratio and decreases with rib spacing, a known behavior documented by many investigators.

Figure 11 shows the variation of Nusselt number with the rib spacing for the three rib blockage ratios tested. The results are for a typical blade passage Reynolds number of 30,000 and for the ribs in the midstream position. The same results for the square ribs are also included for comparison. Nusselt number increases with the pitch-to-height ratio for the two smaller ribs while the rib with the highest blockage ratio shows a slight decrease. Similar to the square rib results, it appears that for the low-aspect-ratio ribs, especially the two smaller blockage ratios, the optimum spacing is 10 and possibly greater. Low rib spacing resembles a cavity-driven flow between the ribs that causes a decrease in the heat transfer coefficient (Metzger et al., 1988).

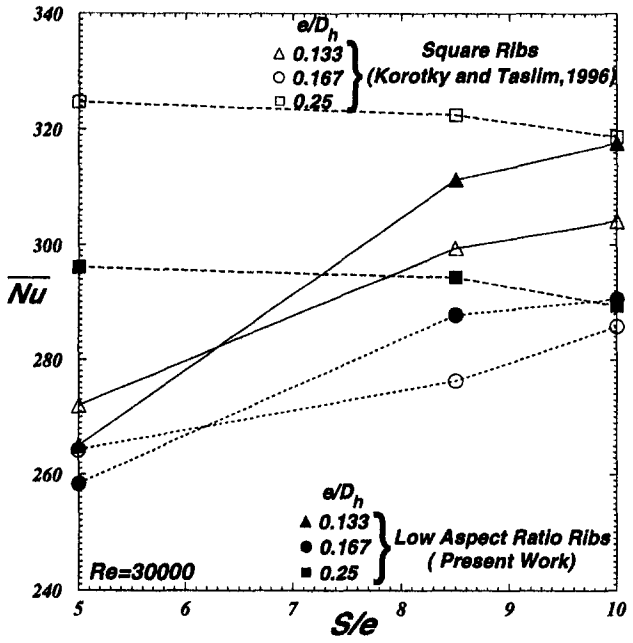

Fig. 11 Rib-averaged Nusselt number versus pitch-to-height ratio for all blockage ratios

Finally, Fig. 12 shows the thermal performances of all geometries tested. The thermal performance based on the same pumping power was derived by Gee and Webb (1980) as $(\mathrm{Nu}/\mathrm{Nu}_s)/(\bar{f}/\bar{f}_s)^{1/3}$, where $\bar{f}_s$ is the all-smooth-wall friction factor from Moody (1944). It should be noted that the thermal performances reported here do not include the contribution of the heat transfer coefficient on the surface area between the ribs, h_{floor}. Thermal performance data for the surface area between the ribs are reported by Taslim et al. (1996) and can be combined with the present data to determine the overall thermal performances. It is seen that as the blockage ratio increases, the rib

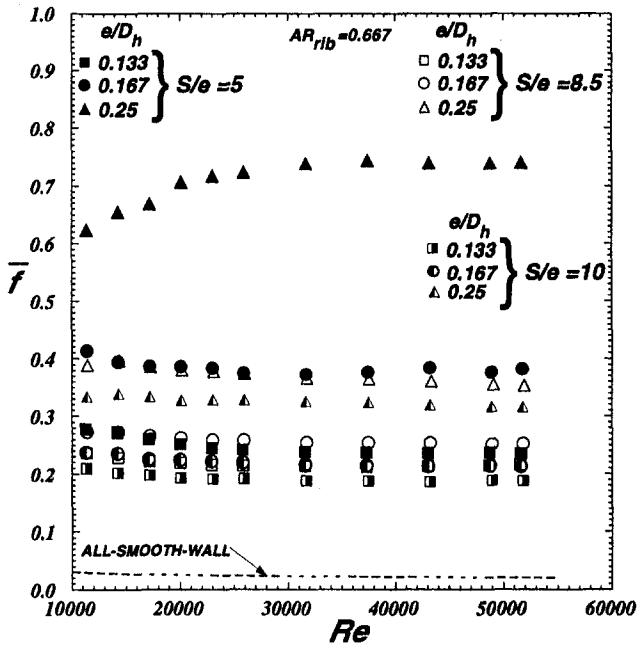

Fig. 10 Channel-averaged friction factor for all blockage and pitch-to-height ratios

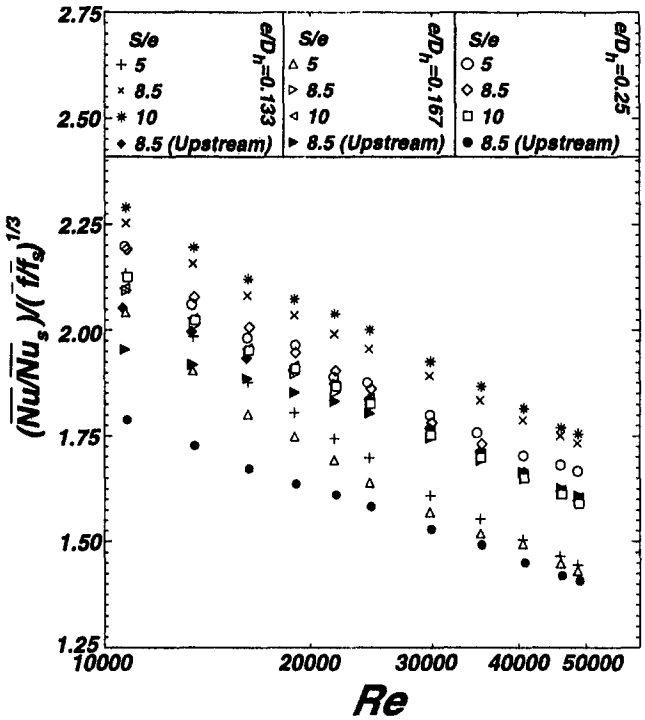

Fig. 12 Rib thermal performances of the twelve geometries

thermal performance decreases. For the blockage ratios of 0.167 and 0.25, the furthest upstream ribs had the lowest thermal performances. This was expected since, for the same channel average friction factor, the furthest upstream rib had a lower heat transfer coefficient than that in the middle of the rib-roughened region. For the small ribs, however, the pitch-to-height ratio of 5 showed the lowest thermal performance.

Conclusions

A total of twelve low-aspect-ratio rib geometries representing three blockage ratios in a practical range for small aircraft engines and at three pitch-to-height ratios were tested for heat transfer and pressure loss variations. The results were compared with those of square ribs reported previously. From this study, it was concluded that:

1 For the geometries tested, the rib average heat transfer coefficient was much higher (as high as two times) than that for the area between the ribs, reported by the first author as well as other investigators. For high blockage ribs with large heat transfer areas, commonly used in small gas turbines, the rib heat transfer is a significant portion of the overall heat transfer in the cooling passages.

2 High-blockage-ratio ($e/D_h = 0.25$) ribs were insensitive to the pitch-to-height ratio. For the medium and low blockage ratios, the pitch-to-height ratio of 5 produced the lowest heat transfer coefficient. Results of the other two pitch-to-height ratios were very close, with the results of $S/e = 10$ slightly (2 percent at most) higher than those of $S/e = 8.5$.

3 The thermal performance decreased with the blockage ratio. While the smallest rib geometry at a pitch-to-height ratio of 10 had the highest thermal performance, thermal performance of high blockage ribs at a pitch-to-height ratio of 5 was the lowest.

4 The general effects of low-aspect-ratio ribs were a decrease in channel friction factor for all rib geometries, a decrease in the rib heat transfer coefficient for the highest rib blockage ratio ($e/D_h = 0.25$) and a heat transfer increase for the medium ($e/D_h = 0.167$) and smallest ($e/D_h = 0.133$) blockage ratios.

References

Abuaf, N., Gibbs, R., and Baum, R., 1986, "Pressure Drop and Heat Transfer Coefficient Distributions in Serpentine Passages With and Without Turbulence Promoters," *Proc. Eighth International Heat Transfer Conference,* Tien, C. L., Carey, V. P., and Ferrel, J. K., eds., pp. 2837–2845.

Berger, F. P., and Hau, K.-F., 1979, "Local Mass/Heat Transfer Distribution on Surfaces Roughened With Small Square Ribs," *Int. J. Heat Mass Transfer,* Vol. 22, pp. 1645–1656.

Burggraf, F., 1970, "Experimental Heat Transfer and Pressure Drop With Two Dimensional Turbulence Promoters Applied to Two Opposite Walls of a Square Tube," *Augmentation of Convective Heat and Mass Transfer,* A. E. Bergles and R. L. Webb, eds., ASME, pp. 70–79.

Chandra, P. R., Han, J. C., and Lau, S. C., 1988, "Effect of Rib Angle on Local Heat/Mass Transfer Distribution in a Two-Pass Rib-Roughened Channel," ASME JOURNAL OF TURBOMACHINERY, Vol. 110, pp. 233–241.

Chandra, P. R., and Han, J. C., 1989, "Pressure Drop and Mass Transfer in Two-Pass Ribbed Channels," AIAA *Journal of Thermophysics,* Vol. 3, No. 3, pp. 315–319.

Colburn, 1933, "A Method of Correlating Forced Convection Heat Transfer Data and a Comparison With Fluid Friction," *Trans. AIChE,* Vol. 29, pp. 174–210.

Dawes, W. N., 1994, "The Solution-Adaptive Numerical Simulation of the 3D Viscous Flow in the Serpentine Coolant Passage of a Radial Inflow Turbine Blade," ASME JOURNAL OF TURBOMACHINERY, Vol. 116, pp. 141–148.

Dittus, F. W., and Boelter, L. M. K., 1930, University of California, Berkeley, CA, *Publications in Engineering,* Vol. 2, pp. 443.

El-Husayni, H. A., Taslim, M. E., and Kercher, D. M., 1991, "An Experimental Investigation of Heat Transfer Coefficients in a Spanwise Rotating Channel With Two Opposite Rib-Roughened Walls," ASME JOURNAL OF TURBOMACHINERY, Vol. 113, pp. 75–82.

Gee, D. L., and Webb, R. L., 1980, "Forced Convection Heat Transfer in Helically Rib-Roughened Tubes," *Int. J. Heat Mass Transfer,* Vol. 23, pp. 1127–1136.

Han, J. C., Glicksman, L. R., and Rohsenow, W. M., 1978, "An Investigation of Heat Transfer and Friction for Rib Roughened Surfaces," *Int. J. Heat Mass Transfer,* Vol. 21, pp. 1143–1156.

Han, J. C., 1984, "Heat Transfer and Friction in Channels With Two Opposite Rib-Roughened Walls," ASME *Journal of Heat Transfer,* Vol. 106, pp. 774–781.

Han, J. C., Park, J. S., and Lei, C. K., 1985, "Heat Transfer Enhancement in Channels With Turbulence Promoters," ASME *Journal of Engineering for Gas Turbines and Power,* Vol. 107, pp. 628–635.

Han, J. C., Zhang, Y. M., and Lee, C. P., 1992, "Influence of Surface Heat Flux Ratio on Heat Transfer Augmentation in Square Channels With Parallel, Crossed, and V-Shaped Angled Ribs," ASME JOURNAL OF TURBOMACHINERY, Vol. 114, pp. 872–880.

Kline, S. J., and McClintock, F. A., 1953, "Describing Uncertainty in Single-Sample Experiments," *Mechanical Engineering,* Vol. 75, Jan., pp. 3–8.

Korotky, G. J., 1994, "An Experimental Investigation of the Rib Surface-Averaged Heat Transfer Coefficient in a Square Passage Roughened With Rounded Ribs of Two Aspect Ratios," MS Thesis, Mechanical Engineering Dept., Northeastern University, Boston, MA.

Korotky, G. J., and Taslim, M. E., 1998, "An Experimental Investigation of the Rib Surface-Averaged Heat Transfer Coefficient in a Square Passage Roughened With Rounded Ribs of Two Aspect Ratios," ASME JOURNAL OF TURBOMACHINERY, Vol. 120, pp. 376–385.

Liou, T. M., Hwang, J. J., and Chen, S. H., 1991, "Turbulent Heat Transfer and Fluid Flow in a Channel With Repeated Rib Pairs," *Proc. ASME/JSME Thermal Eng.,* Vol. 3, pp. 205–212.

Liou, T. M., and Hwang, J. J., 1993, "Effects of Ridge Shapes on Turbulent Heat Transfer and Friction in a Rectangular Channel," *Int. J. Heat Mass Transfer,* Vol. 36, pp. 931–940.

Lockett, J. F., and Collins, M. W., 1990, "Holographic Interferometry Applied to Rib-Roughness Heat Transfer in Turbulent Flow," *Int. J. Heat Mass Transfer,* Vol. 33, pp. 2439–2449.

Metzger, D. E., Fan, C. S., and Pennington, J. W., 1983, "Heat Transfer and Flow Friction Characteristics of Very Rough Transverse Ribbed Surfaces With and Without Pin Fins," *Proc. ASME–JSME Thermal Engineering Joint Conference,* Vol. 1, pp. 429–436.

Metzger, D. E., Chyu, M. K., and Bunker, R. S., 1988, "The Contribution of On-Rib Heat Transfer Coefficients to Total Heat Transfer From Rib-Roughened Surfaces," *Transport Phenomena in Rotating Machinery,* J. H. Kim, ed., Hemisphere Publishing Co.

Metzger, D. E., Fan, C. S., and Yu, Y., 1990, "Effects of Rib Angle and Orientation on Local Heat Transfer in Square Channels With Angled Roughness Ribs," *Compact Heat Exchangers: A Festschrift for A. L. London,* Hemisphere Publishing Co., pp. 151–167.

Moody, L. F., 1944, "Friction Factors for Pipe Flow," *Trans. ASME,* Vol. 66, p. 671.

Sato, H., Hishida, K., and Maeda, M., 1992, "Characteristics of Turbulent Flow and Heat Transfer in a Rectangular Channel With Repeated Rib Roughness," *Exp. Heat Transfer,* Vol. 5, pp. 1–16.

Solntsev, V. P., Luzhanskii, B. E., and Kryukov, V. N., 1973, "An Investigation of Heat Transfer in the Turbulent Separation Zones in the Vicinity of Sudden Steps," *Heat Transfer—Soviet Research,* Vol. 5, No. 2, pp. 122–128.

Taslim, M. E., and Spring, S. D., 1988a, "An Experimental Investigation of Heat Transfer Coefficients and Friction Factors in Passages of Different Aspect Ratio Roughened With 45° Turbulators," *Proc. ASME National Heat Conference,* Houston, TX.

Taslim, M. E., and Spring, S. D., 1988b, "Experimental Heat Transfer and Friction Factors in Turbulated Cooling Passages of Different Aspect Ratios, Where Turbulators Are Staggered," Paper No. AIAA-88-3014.

Taslim, M. E., and Spring, S. D., 1994, "Effects of Turbulator Profile and Spacing on Heat Transfer and Friction in a Channel," AIAA *J. Thermophysics and Heat Transfer,* Vol. 8, No. 3, pp. 555–562.

Taslim, M. E., Rahman, A., and Spring, S. D., 1991a, "An Experimental Investigation of Heat Transfer Coefficients in a Spanwise Rotating Channel With Two Opposite Rib-Roughened Walls," ASME JOURNAL OF TURBOMACHINERY, Vol. 113, pp. 75–82.

Taslim, M. E., Bondi, L. A., and Kercher, D. M., 1991b, "An Experimental Investigation of Heat Transfer in an Orthogonally Rotating Channel Roughened With 45° Criss-Cross Ribs on Two Opposite Walls," ASME JOURNAL OF TURBOMACHINERY, Vol. 113, pp. 346–353.

Taslim, M. E., Li, T., and Kercher, D. M., 1996, "Experimental Heat Transfer and Friction in Channels Roughened With Angled, V-Shaped, and Discrete Ribs on Two Opposite Walls," ASME JOURNAL OF TURBOMACHINERY, Vol. 118, pp. 1–9.

Taslim, M. E., and Wadsworth, C. M., 1997, "An Experimental Investigation of the Rib Surface-Averaged Heat Transfer Coefficient in a Rib-Roughened Square Passage," ASME JOURNAL OF TURBOMACHINERY, Vol. 119, pp. 381–389.

Webb, R. L., Eckert, E. R. G., and Goldstein, R. J., 1971, "Heat Transfer and Friction in Tubes With Repeated-Rib-Roughness," *Int. J. Heat Mass Transfer,* Vol. 14, pp. 601–617.

Prediction of the Becalmed Region for LP Turbine Profile Design

V. Schulte
BMW Rolls-Royce GmbH,
15827 Dahlewitz, Germany

H. P. Hodson
Whittle Laboratory,
Cambridge University
Engineering Department,
Madingley Road,
Cambridge CB3 ODY, United Kingdom

Recent attention has focused on the so-called "becalmed region" that is observed inside the boundary layers of turbomachinery blading and is associated with the process of wake-induced transition. Significant reductions of profile loss have been shown for high lift LP turbine blades at low Reynolds numbers due the effects of the becalmed region on the diffusing flow at the rear of the suction surface. In this paper the nature and the significance of the becalmed region are examined using experimental observations and computational studies. It is shown that the becalmed region may be modeled using the unsteady laminar boundary layer equations. Therefore, it is predictable independent of the transition or turbulence models employed. The effect of the becalmed region on the transition process is modeled using a spot-based intermittency transition model. An unsteady differential boundary layer code was used to simulate a deterministic experiment involving an isolated turbulent spot numerically. The predictability of the becalmed region means that the rate of entropy production can be calculated in that region. It is found to be of the order of that in a laminar boundary layer. It is for this reason and because the becalmed region may be encroached upon by pursuing turbulent flows that for attached boundary layers, wake-induced transition cannot significantly reduce the profile loss. However, the becalmed region is less prone to separation than a conventional laminar boundary layer. Therefore, the becalmed region may be exploited in order to prevent boundary layer separation and the increase in loss that this entails. It is shown that it should now be possible to design efficient high lift LP turbine blades.

Introduction

In a modern civil engine, the LP turbine operates at subsonic Mach numbers and usually consists of several stages so that the associated weight and cost are large. Furthermore, their efficiency strongly influences the specific fuel consumption. There is a significant incentive for improving the aerodynamic design of this component.

Due to the large aspect ratios in LP turbines, the profile loss is by far the largest portion of the total. The magnitude of profile loss depends upon the development of the airfoil boundary layers. Changes in the process of boundary layer transition and separation can alter the profile loss significantly for the same profile shape at different operating conditions. Consequently the search for further improvements in loading and efficiency of LP turbines should consider the details of the processes of boundary layer transition and separation.

The performance targets of modern LP turbine blading concern not only efficiency, but also weight and manufacturing costs. It is desirable to use fewer blades per blade row so that an individual blade has to carry a greater aerodynamic load. Increased lift coefficients can only be realized if the pressure distribution has regions of significant diffusion on the suction surface. This inevitably increases the risk of laminar separation. In order to avoid significant deterioration in efficiency due to large separation bubbles (or even non-reattached separation), the concept of controlled boundary layer design has been introduced in industry (Hourmouziadis, 1989).

To date, LP turbines have been designed using steady flow assumptions. However, it is now well known that that the boundary layers on turbomachinery blades are by no means steady (e.g., Hodson et al., 1994; Halstead et al., 1997; Banieghbal et al., 1995). The turbulence associated with the wakes shed by upstream blade rows is responsible for much of the unsteady nature of the transition process. It is now known that the profile loss in the turbine can be either higher (Hodson, 1984) or lower (Schulte and Hodson, 1998) than in a steady-state cascade test. Schulte and Hodson (1998) show that at typical LPT Reynolds numbers ($Re = 0.8–3 \times 10^5$) the wake-passing induces periodic transition. The wakes do not create turbulent flow but patches of bypass transition within the boundary layer where turbulent spots appear, grow, and coalesce to form turbulent patches. So-called "becalmed regions" trail the turbulent spots/patches as they move over the blade surface.

The becalmed region is a laminar-like region with a very full velocity profile that follows after the turbulent flow. Initially it is associated with a high wall shear stress (similar to that of the turbulent flow) that then relaxes back to a laminar value (Seifert, 1994; Cumpsty et al., 1995; Halstead et al., 1997; Schulte, 1995; Gostelow et al., 1997). Whereas the transitional/turbulent patches tend to increase losses, the becalmed regions tend to reduce losses compared to the undisturbed boundary layer as it is present in steady-state cascade tests. It is the trade off between these two effects that is important for the loss. The trade off depends mainly upon the Reynolds number, the wake-passing frequency and the wake strength, and the pressure distribution of the blades.

Schulte and Hodson (1998) showed that for high lift blading at low Reynolds numbers, when a large suction side separation bubble exists, the loss in the turbine may be significantly lower than in the steady flow cascade test. Consequently the beneficial effect of the becalmed region outweighs the detrimental effect of the transitional patches.

Having recognized the potential to design efficient high lift blading even at very low Reynolds numbers by exploiting the effect of the becalmed regions, it is now necessary to set up

Contributed by the International Gas Turbine Institute and presented at the 42nd International Gas Turbine and Aeroengine Congress and Exhibition, Orlando, Florida, June 2–5, 1997. Manuscript received at ASME Headquarters February 1997. Paper No. 97-GT-398. Associate Technical Editor: H. A. Kidd.

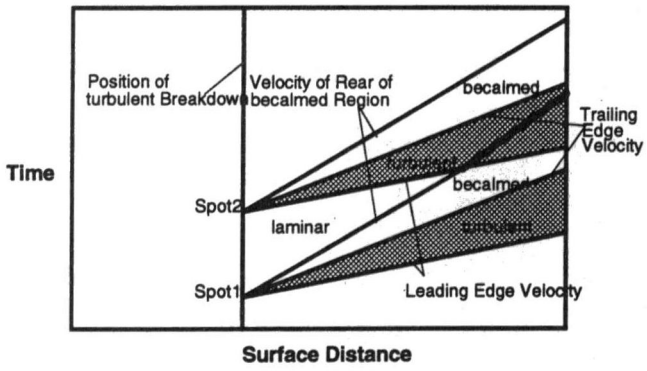

Fig. 1 Schematic of steady flow transition situation showing two individual turbulent spots

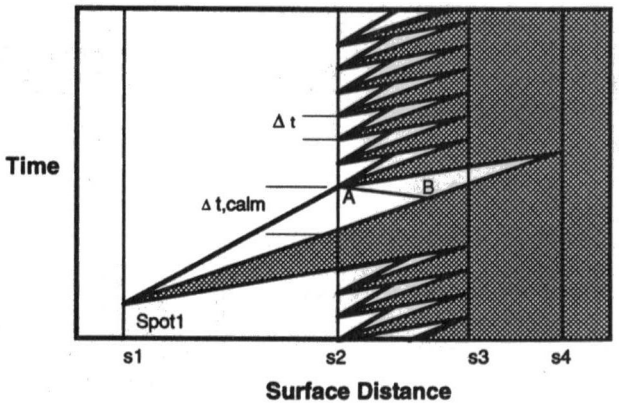

Fig. 2 Schematic of (unsteady) transition situation with one turbulent spot being formed upstream of others

design criteria and develop predictive tools that account for the mechanisms of unsteady transition including the becalmed regions.

The present paper explores the significance of the becalmed region and presents a transition model allowing for the effects of the becalmed regions. The model is validated and consequences for the design of LP turbines are discussed.

Modeling of the Becalmed Region

Becalmed regions behind isolated turbulent spots were first found by Schubauer and Klebanoff (1955). They provided an explanation for the existence of the becalmed regions that was linked to the existence of Tollmien–Schlichting waves. This was recently discredited by Schulte (1995) and Gostelow et al. (1997). The effect of the becalmed regions on the unsteady wake-induced transition process was first illustrated by Pfeil et al. (1983).

The lack of susceptibility to small disturbances within a becalmed region means that turbulent spots can probably not form inside a becalmed region and boundary layer separation is probably prevented or delayed within them. On the other hand, the becalmed region will be terminated (made turbulent) by other turbulent spots that move into it from behind. For transition in steady external flow turbulent spots only form in the vicinity of a single streamwise position according to the hypothesis of Narasimha (1957). Hence, the becalmed region does not have a noticeable effect, since spots do not form anyway within their domain of influence. This process is illustrated in the simplified distance–time (s–t) diagram of Fig. 1.

Only the unsteady scenario gives rise to a visible effect of the becalmed regions. Figure 2 illustrates this using another simplified distance–time diagram. For some reason (e.g., wake passing) spot 1 has been formed at position s1 upstream of the position of turbulent breakdown (s2) for the otherwise undisturbed flow. Along this line spots form at a rate given by $1/\Delta t$. This gives rise to the natural transition process being completed at the position s3. The becalmed region of spot 1 inhibits spot production at position s2 for the time Δt_{calm}. Therefore the disturbed (unsteady) transition process is only completed at position s4.

Finally it has to be recognized that the susceptibility of the becalmed region to various disturbances will probably vary with streamwise distance. It might therefore happen that the becalmed region has weakened sufficiently to allow spots to form along, say a line AB in Fig. 2. There is evidence that this happens, especially in compressors, where wake-induced transitional/turbulent patches seem to form further upstream and travel a longer distance until they reach the position of natural transition (e.g., Halstead et al., 1997).

In summary, the probability that a becalmed region is able to inhibit spot production and separation seems to be very high as is the probability that it is terminated (made turbulent) by neighboring turbulent spots that move into it.

Following these arguments, a probability-based (spot-based) intermittency model that includes the effects of becalmed regions is derived in the appendix. The intermittency distribution obtained as described in the appendix only models the becalmed region in terms of its effect on the transition process by way of its effect on the spot production rate. No specific model to account for the ability of the becalmed region to suppress separation is included. This is unnecessary because, as the next section will show, the becalmed region is modeled by the unsteady laminar boundary layer equations.

Numerical Simulation of the Becalmed Region

Unsteady Differential Boundary Layer Code and Implementation of the Intermittency Model. The following calculations are performed with an adaptation of the well proven unsteady differential boundary layer code by Cebeci and Carr (1978). A similar version of the code has previously been used by Addison and Hodson (1992). The code employs an eddy-viscosity turbulence model. The current version is only able to calculate attached boundary layers.

Nomenclature

A = area
Re_2 = Reynolds number at exit based on chord
Re_{th} = momentum thickness Reynolds number
S = absolute entropy
s = streamwise coordinate
$\%s$ = fraction surface length
T = temperature
t = time
U_∞ = free-stream velocity
u = streamwise velocity component
Y_p = suction surface boundary loss coefficient
y = surface normal coordinate
μ = molecular viscosity
ν = kinematic viscosity
ρ = density

Subscripts

eff = effective
lam = laminar
tr = transition
turb, t = turbulent
$\hat{}$ = time mean

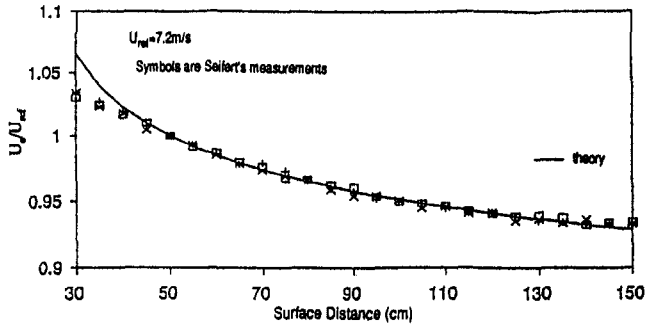

Fig. 3 Velocity distribution of Seifert's flat plate test case (Seifert, 1994)

The code has been adapted to enable it to calculate unsteady transitional boundary layers (including becalmed regions). This is done by calculating an unsteady intermittency distribution prior to the calculation with the boundary layer code. The calculated intermittency distribution is then prescribed for the boundary layer calculation. The intermittency distribution is used to weigh the eddy viscosity according to

$$\upsilon_{\text{eff}}(s, y, t) = \upsilon_{\text{lam}} + \tilde{\gamma}(s, t)\upsilon_{\text{turb}}(s, y, t), \qquad (1)$$

where $\upsilon_{\text{turb}}(s, y, t)$ is determined using the instantaneous velocity profiles.

The intermittency distribution used in Eq. (1) is determined in a separate routine and combines correlations for transition onset and the initial spot production rate with the intermittency model outlined in the appendix. Details of the correlations used for transition onset, the spot production rate, and the shape of the dependence volume can be found in Addison and Hodson (1992) and Schulte (1995). These are omitted here, because they are not needed for the simulation of the deterministic experiment described in the following section.

Numerical Simulation of a Deterministic Experiment. The experiment conducted by Seifert (1994) was simulated numerically in order to validate the model of the becalmed regions that has been introduced above. Seifert investigated an individual artificially generated turbulent spot that moves through an initially laminar and then transitional boundary layer. His test case consists of a flat plate with an imposed adverse pressure gradient simulating the rear part of the suction surface of a turbine blade. The velocity distribution as measured and predicted by Seifert is shown in Fig. 3. In undisturbed flow the transition onset is located at approximately 70%s. Downstream of this the boundary layer is transitional and reaches a fully turbulent state by the trailing edge. Time-resolved measurements of the velocity profiles at various streamwise stations utilizing a single hot-wire were presented. The velocity profiles are ensemble averaged.

Using the velocity distribution of Seifert's plate and specifying the measured location of transition onset and a suitable spot production rate in the intermittency model (see appendix), the *undisturbed* boundary layer development of the test case could be matched using the current boundary layer prediction system.

In the spot-disturbed case, an individual turbulent spot was triggered at 20%s. This was simulated using the intermittency routine by specifying that the spots are created at 20%s. This resulted in an intermittency distribution as shown in Fig. 4. Inside the spot affected region the intermittency is unity. The becalmed region suppresses spot-production completely for some time at 70%s. Otherwise the intermittency distribution is as in the undisturbed case downstream of 70%s.

In this simulation of an individual turbulent spot, the spot is assumed to be identical to the a completely turbulent spanwise strip. Hence, in order to implement the effect of the individual turbulent spot on the intermittency distribution, an integration of the volumes of dependence, as outlined in the model in the appendix, is not necessary. The intermittency can simply be set to unity within the volume of propagation of the turbulent spot and the spot production rate can simply be set to zero in the volume of propagation of the spot and its becalmed region. Since the measurements of Seifert have been taken in the plane of symmetry of the turbulent spot, the results can effectively be treated as if they were obtained from a fully turbulent strip that has been triggered at the same streamwise position. The velocities of the leading and trailing edge of the turbulent spot are taken as $0.88U_\infty$ and $0.5U_\infty$, respectively. These are well-accepted zero pressure gradient values that are also confirmed in Seifert's experiment. The velocity of the rear of the becalmed region was set to the generally quoted value of $0.3U_\infty$.

Figure 5(a) shows the variation in time of the integral boundary layer parameters at the trailing edge for the measurements and the predictions. Selected measured and predicted instantaneous (ensemble averaged in the case of the measurements) velocity profiles are shown in Fig. 5(b). At this position (trailing edge) the undisturbed boundary layer is fully turbulent, so the intermittency is unity. The intermittency is shown in Fig. 5(a). It is not possible to identify the leading edge of the turbulent spot, since the intermittency is unity before the spot arrives, but it is possible to identify the trailing edge of the spot. After the spot has passed, the intermittency drops to zero for the duration of the becalmed region. This happens approximately between t = 370 ms and t = 600 ms for the measurements and the predictions. In the case of the measurements the jump from unity to zero and the jump from zero to unity is not as sharp as for the predictions. However, the fact that the measurements show zero intermittency for approximately the same time interval as the predictions is important. It shows that the basis of the presented model concerning the effect of the becalmed region on the transition process, namely that no spots form inside the becalmed region, but that spots can move into it, appears fundamentally correct.

There is a second aspect of the becalmed region that has, as mentioned above, not been explicitly modeled in the intermittency model. This is the specific velocity profile of the becalmed region and its possible ability to suppress laminar separation. Whereas the effect of the becalmed region on the transition process, which has been modeled, can be seen from the intermittency factor, the specific velocity profiles of the becalmed region can be inferred from the integral boundary layer parameters in Fig. 5(a) and are also shown in Fig. 5(b).

The comparison of measurements and predictions in Fig. 5(a) and Fig. 5(b) reveals that more than just the main features of the integral boundary layer parameters and the velocity profiles could be predicted. This in particular refers to the region of the becalmed region between t = 370 ms and t = 600 ms, where the intermittency factor is zero and therefore the turbulence model is not active. The becalmed region is merely an unsteady response of the boundary layer to the almost instant vanishing of the turbulent stresses after a turbulent region has passed. Therefore the becalmed region is predictable by simulat-

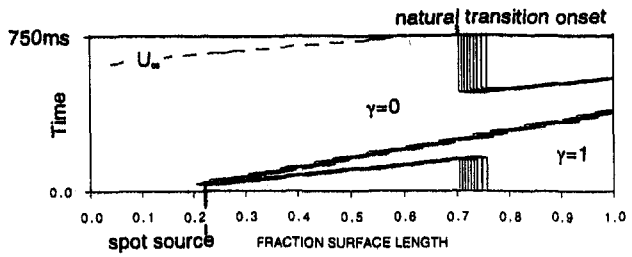

Fig. 4 Simulated unsteady intermittency distribution of Seifert's test case (individual spot triggered at 20%s)

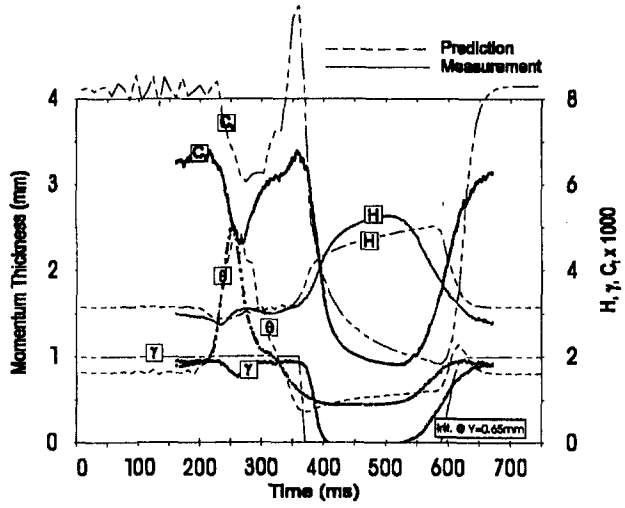

Fig. 5(*a*) Measured and predicted variation in time of integral boundary layer parameters at trailing edge for Seifert's test case

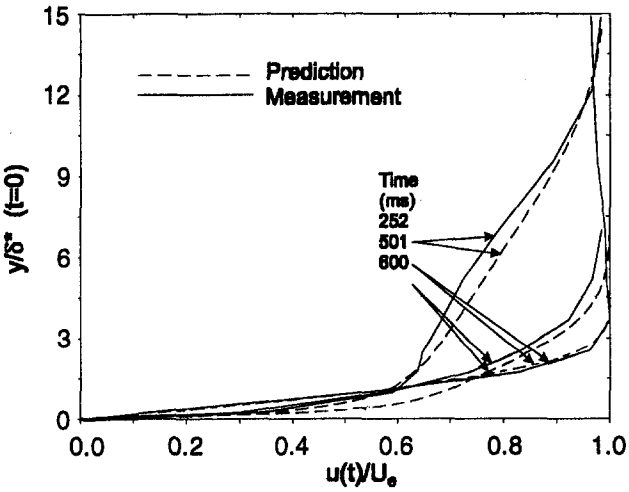

Fig. 5(*b*) Measured and predicted instantaneous velocity profiles at the trailing edge for Seifert's test case

ing the rapid vanishing of the turbulent stresses. It is concluded that the becalmed region is modeled by the *unsteady laminar* boundary layer equations and is therefore predictable by any unsteady boundary layer or Navier–Stokes solver independent of any turbulence modeling. Its effect on the transition process however needs to be either modeled in conjunction with an eddy viscosity model and the present intermittency model or can perhaps be predicted by higher order turbulence models, which have some inherent capability of predicting transition. The other main effect of the becalmed region, the suppression or delay of laminar separation, is automatically accounted for by the unsteady boundary layer or Navier–Stokes equations and can be predicted (see below).

The details of the flow shown in Fig. 5(*a*) are discussed using the example of the skin friction coefficient. The small differences in the absolute magnitude of the skin friction are very likely to be caused by the difficulties in extracting the skin friction coefficient from the hotwire measurements. The changes in skin friction and the qualitative character of the curve are well predicted. After the arrival of the turbulent spot the skin friction coefficient starts to drop at approximately $t = 230$ ms. It arrives at a local minimum at about $t = 270$ ms, which is a short period after the displacement and the momentum thickness had their peak values (approximately $t = 250$ ms). The lower skin friction in the spot affected region is due to the turbulent boundary layer inside the spot having grown for a longer time than the surrounding undisturbed turbulent boundary layer. Therefore the high momentum and displacement thickness, which are also caused by the "long grown" turbulent boundary layer inside the turbulent spot almost coincide with a minimum in skin friction (see also Cumpsty et al., 1995).

As the turbulent spot leaves the measurement station, the skin friction rises to a peak at $t = 370$ ms. This is where the intermittency drops from unity to zero and where the momentum and displacement thickness have their minima. This peak in skin friction at the trailing edge of the turbulent spot and the beginning of the becalmed region is caused by the overshooting velocity close to the wall. This is because once the turbulent stresses disappear, the low velocity in the outer part of the boundary layer rapidly increases toward the laminar value (in the becalmed region). This also affects the fluid in the inner part of the boundary layer, which is also accelerated by shear forces and causes the high velocity gradient in the inner boundary layer region. This in turn causes the minima in displacement and momentum thickness, which relate to a very transient very steep velocity gradient close to the wall at this instant in time. After the overshoot in the near-wall region, the velocity close to the wall reduces at a much slower rate towards the value of an undisturbed laminar boundary layer. The velocity profile closely follows the form $U^+ = Y^+$, as noted by Cumpsty et al. (1995), for the period of the becalmed region. After the peak the skin friction rapidly reduces to a very low value that it possesses throughout the becalmed region from approximately $t = 400$ ms to $t = 600$ ms. The minimum is reached at the end of the becalmed region at approximately $t = 600$ ms. When the intermittency rises from zero to unity at the end of the becalmed region the skin friction rises to the undisturbed turbulent value.

Entropy Generation in the Becalmed Region

Calculation of the Dissipation in the Becalmed Region. The previous section presented measurements and predictions of the variation in time of the integral boundary layer parameters and the skin friction coefficient for Seifert's test case. The low value of skin friction and the low momentum thickness within the becalmed region that were noted above suggest that the entropy generation within this region is low.

From the conservation of entropy it can be shown (Denton, 1990) that the rate of entropy production per unit surface area is given by

$$\dot{S} = \frac{1}{T}\int_0^\delta \mu_t \left(\frac{\partial u}{\partial y}\right)^2 dy. \tag{2}$$

The nondimensional dissipation coefficient is then defined by

$$C_d = \frac{T\dot{S}}{\rho U_\infty^3} \tag{3}$$

The dissipation coefficient has been evaluated for Seifert's test case. The prediction performed in order to evaluate the dissipation coefficient differs in one point from the prediction in the previous section that simulated the experiment. The undisturbed boundary layer has been taken as fully turbulent from 70%*s*, so that the intermittency factor is always zero or unity. This simplification was introduced so that the effect of "turbulent wetted area" could be assessed.

Figure 6 shows a distance–time diagram of the dissipation coefficient for this calculation. The leading edge area is signified by high entropy production. This is expected from the laminar boundary layer theory because the Reynolds number is very low at the leading edge. The origin of the turbulent spot is located at approximately 17%*s* and $t = 25$ ms. The area enclosed by the leading edge and the trailing edge trajectory of the spot exhibits a dissipation coefficients that is predominantly between

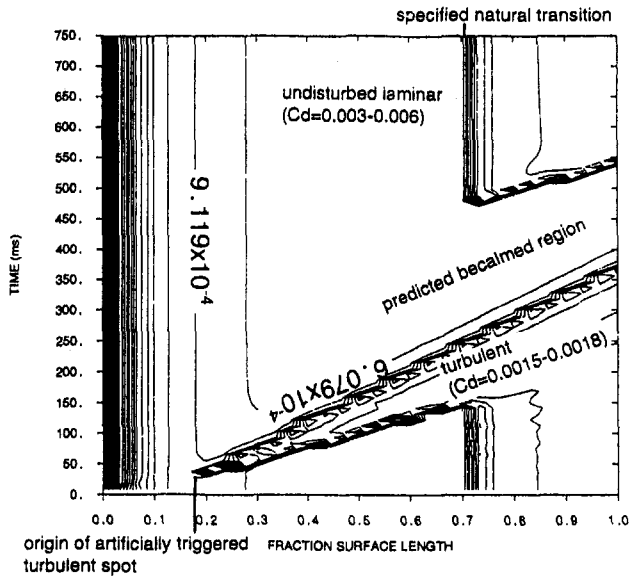

Fig. 6 Contours in the distance–time diagram of dissipation coefficient for an individual turbulent spot triggered at 17%s and a (undisturbed) fully turbulent boundary layer from 70%s

0.0015 and 0.0018. The undisturbed fully turbulent boundary layer downstream of 72%*s* has dissipation coefficients that range from 0.0015 to 0.0021. The most important observation, however, is that the dissipation coefficient in the becalmed region is on the same low level as that of the normal laminar boundary layer at the same Reynolds-number. The values range between 0.0003 and 0.0006. The becalmed region only generates as much entropy as a laminar boundary layer, but it is not as susceptible to transition or separation.

The "Wetted Area" Assumption. A striking feature of Fig. 6 is that downstream of 20%*s*, the dissipation coefficient of the laminar boundary layer and the becalmed region is almost constant (around 0.0005) and independent of surface position. The same applies for the dissipation coefficient in the turbulent boundary layer of the undisturbed boundary layer and inside the spot affected area. The value ranges around 0.0018. This is in line with the general observation that in a Reynolds number range where laminar or turbulent boundary layers can exist (momentum thickness Reynolds number between 200 and 700), the dissipation coefficient of either state is only very weakly dependent on the momentum thickness Reynolds number (Truckenbrodt, 1973).

These observations allow us to postulate that any increase in loss is directly proportional to the additional "turbulent wetted area" caused by the wakes. This hypothesis leads to a simplified quantitative assessment of losses generated in unsteady boundary layers. It presumes that any unit of surface covered by turbulent flow generates the same amount of entropy regardless of surface position and time. Furthermore, it is assumed that any unit of surface covered by laminar or becalmed flow generates the same amount of entropy regardless of surface distance and time. The wetted area assumption allows to draw conclusions about, for example, the relative increase in loss in a wake-induced unsteady boundary layer in relation to the loss generated by a completely laminar boundary layer simply by relating the ratios of the areas in the distance–time space that are covered by turbulent respectively laminar flows. Hodson (1989) used a similar approach to derive a correlation that relates the blade profile loss to the reduced frequency of the wake passing for *attached* boundary layers. That correlation did not account for the effect of the becalmed region because the data it was validated against did not suggest that this was important.

Schulte (1995) showed that for attached boundary layers no significant loss reduction due to the effect of the becalmed regions is possible. This is because the additional loss generated by, for example, a wake-induced turbulent patch in an otherwise laminar boundary layer will always almost compensate for the loss reduction due to the associated becalmed region in an otherwise turbulent boundary layer. This can also be seen from Fig. 6, if one now imagines that the turbulent region (fully turbulent spanwise band) is the result of a narrow passing wake rather then an individual turbulent spot. As a function of wake-passing frequency, the loss will be almost constant at low frequency and then rise linearly with frequency once the succeeding wake-induced turbulent patches start to cut off the preceding becalmed regions.

Separated Boundary Layers and High Lift LP Turbine Blading

Up to now, the prediction of the unsteady transition process in separated boundary layers with the above method presented is not possible. This is because not enough is known about the interaction of the becalmed region with the transition process in a separation bubble. Turbulent spots are not necessarily involved in separation bubble transition and hence the extension of Emmons spot-based model (see appendix) might not adequately describe the process.

Schulte and Hodson (1996) showed that for a high lift LP turbine cascade blade, the becalmed regions, which were caused by simulated wake passing, significantly reduced the loss compared to a no-wake case. This is because the suction surface boundary layer of the high lift blade separates if there are no wakes present. Figure 7 is taken from Schulte and Hodson. It was observed that in a separated boundary layer the becalmed region was not terminated by intruding spots from separated flow transition (supporting the above suspicion), so enhancing the effect of the becalmed region. Also, the loss associated with the separation can be very high at low Reynolds numbers, so that the gain due to the becalmed region, which keeps the boundary layer attached, is larger than the loss due to the additional turbulent flow upstream of the separation.

Schulte and Hodson (1998) also found that an optimum wake-passing frequency exists. The optimum frequency corresponds to the situation sketched in the distance–time diagram of Fig. 7. Figure 7 represents a first crude model of the interaction of the becalmed region with the transition process in the separation region. This will certainly have to be refined in the future. One may assume that no grossly (and "lossy") separated flow exists for this situation. Although the flow cannot be predicted using the presented intermittency routine, the loss may at least be estimated from the "wetted area" assumption.

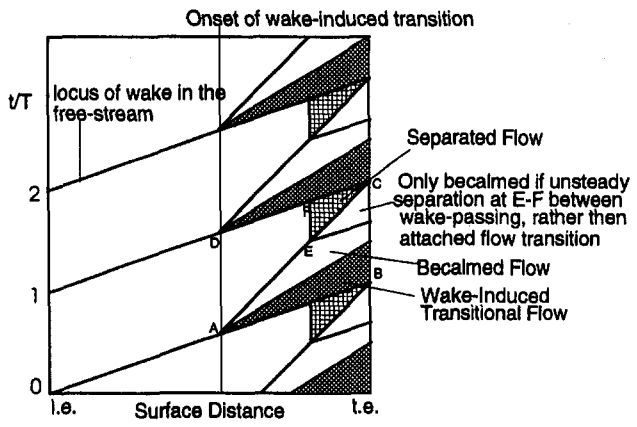

Fig. 7 Schematic distance–time diagram showing effect of becalmed region on a separated boundary layer and illustrating optimum wake-passing frequency

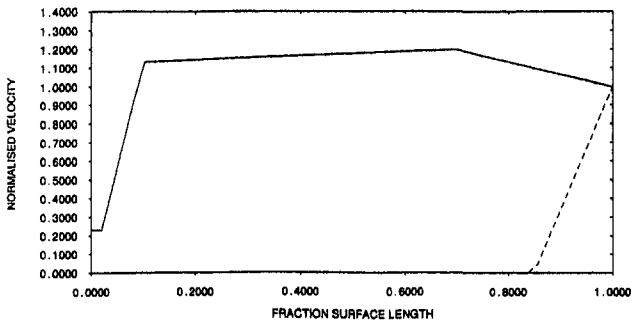

Fig. 8 Example of generic velocity distribution used for parametric design study

In Fig. 7 one can treat the becalmed region as laminar (as suggested by Fig. 6) as well as the small separated area (which is assumed to be justified, since the separation bubble will take some time to gain the shape it would adopt if no wakes were present, see Schulte, 1995). The region marked "transitional" will be assumed to be fully turbulent. The reduced frequency will be assumed to be fixed at the optimum value that corresponds to the situation of Fig. 7 (this is representative for LP turbines). Then the area ratios in Fig. 7 yield the relation

$$\frac{Y_p - Y_{p,\text{lam}}}{Y_{p,\text{turb}} - Y_{p,\text{lam}}} = \frac{A_{\text{turb}}}{A_{ABCD}} \tag{4}$$

for the suction surface boundary loss coefficient. Assuming the well-accepted zero pressure gradient values of $1.0U_\infty$ for the leading edge propagation speed of a turbulent patch, $0.5U_\infty$ for the trailing edge, and $0.33U_\infty$ for the rear of the becalmed region, the boundary layer loss coefficient approximates to

$$Y_p \cong Y_{p,\text{lam}} + 0.25(Y_{p,\text{turb}} - Y_{p,\text{lam}}) \tag{5}$$

where $Y_{p,\text{turb}}$ is the loss generated by a fully turbulent boundary layer from the onset of wake-induced transition and $Y_{p,\text{lam}}$ is the loss of a completely laminar boundary layer.

Equation (4) can now be used to perform a parametric design study. For this purpose generic velocity distributions of the type shown in Fig. 8 are produced. They feature different back surface diffusion and Zweifel-lift coefficients. Wake-induced transition (fully turbulent) is assumed to take place at $\text{Re}_{\text{th}} = 200$. This is before the start of laminar separation in all cases. In order to evaluate the boundary layer loss coefficient, the values for $Y_{p,\text{turb}}$ and $Y_{p,\text{lam}}$ must be found.

The value of $Y_{p,\text{turb}}$ can simply be found by performing a steady boundary layer calculation and specifying transition where $\text{Re}_{\text{th}} = 200$. This will give a value for the momentum thickness at the trailing edge, which represents the loss generated in the boundary layer. This can be converted into a loss coefficient by dividing by the pitch (which is proportional to the Zweifel-lift coefficient in incompressible flow).

The value of $Y_{p,\text{lam}}$ can be found by performing an unsteady calculation with the present boundary layer code by specifying an intermittency distribution of the type shown in Fig. 4. This merely serves the purpose to generate some laminar (becalmed flow) at the trailing edge in order to extract a laminar value of the momentum thickness at the trailing edge. This is possible if the simulated becalmed region suppresses the laminar separation that would otherwise be predicted by the code. The momentum thickness at the trailing edge at the rear of the becalmed region (where it has almost relaxed to the undisturbed value) will be taken as an indicator of the loss that would be generated if the boundary layer were completely laminar (or becalmed). This momentum thickness will be converted into a loss coefficient in the same way as the turbulent momentum thickness.

The results of the study are presented in Fig. 9. The study has been performed at $\text{Re}_2 = 130{,}000$ (which is representative of a low Reynolds number LPT environment). The results of the study are the points labeled as "unsteady wake-passing." There is an optimum lift coefficient calculated, which is of the order of traditional optimum Zweifel-lift coefficients. For the five cases with the highest lift coefficients, the boundary layer code predicts laminar separation, if no transition or unsteady wake passing is specified. If an unsteady calculation is performed with the unsteady intermittency distribution as an input, then the code predicts the boundary layer to stay attached inside the becalmed region. This confirms the earlier statement that the ability of the becalmed region to suppress separation is predictable. At even higher lift and diffusion coefficients (not shown here), the becalmed region separated.

The most important observation from Fig. 9 is that at relative lift values above 1.16 (where laminar separation occurs if there is no transition, thick dotted line) the unsteady wake passing cases show a significantly *reduced rise* in loss compared to the relative loss evaluated from a simulation without unsteady wake passing (assuming a fully turbulent boundary layer from onset of laminar separation). The difference in absolute level of the two loss curves is not claimed to be accurate, since in reality the no-wake case features a separated rather than a fully turbulent boundary layer. At this low Reynolds number the loss for the separated boundary layer in the no-wake case is likely to be even higher as the calculated fully turbulent loss. This is indicated by the measured data from the high lift LP turbine blade from Schulte and Hodson (1998), where the data point with wake passing has been fitted to the calculations in order to compare the relative increase of the loss if there is no wake passing.

The results show that high lift blading, owing to the becalmed regions, has more potential than for example a steady-state cascade test or numerical study would suggest. A 15 percent increase in lift (from 1.16 to 1.34) only results in 7 percent increase in boundary layer loss when wake passing effects are present, while it results in approximately 21 percent increase in boundary loss from steady state considerations.

The real benefit of high lift blading is of course application specific and must take the reduction of blade numbers (weight and manufacturing cost) into account. This should for many aircraft engine applications lead to the result that a slight increase of profile loss is perfectly acceptable (Curtis et al., 1996). In order to estimate the magnitude of increased profile loss, studies of the type presented in this paper accounting for the effect of the becalmed region may be performed.

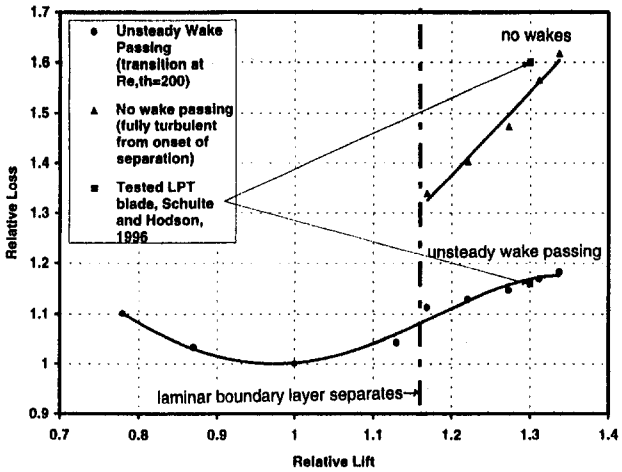

Fig. 9 Numerical design study using model of Fig. 7 and wetted area assumption showing suction surface loss only ($\text{Re}_2 = 1.3 \times 10^5$, $\text{Re}_{\text{th,tr}} = 200$)

Conclusions

1 The becalmed region that trails wake-induced turbulent patches inside boundary layers is an unsteady boundary layer feature modeled by the *laminar* unsteady boundary layer equations. It is therefore predictable independent of any turbulence modeling.

2 The effect of the becalmed region on the transition process can be modeled using a probability-based intermittency approach, similar to the Emmons model.

3 The entropy generation inside the becalmed region is on the same level as in a conventional laminar boundary layer.

4 The becalmed region is less prone to separation than a conventional laminar boundary layer.

5 The loss of an attached boundary layer cannot be significantly reduced due to unsteady wake passing, despite the beneficial effect of the becalmed region.

6 Design criteria for high lift blading may be derived from the "wetted area assumption." The loss of higher lift blading subjected to unsteady wake-passing does not rise to the same extend as for steady fully turbulent or separated boundary layers.

Acknowledgments

During his time at the Whittle Laboratory, the first author was in receipt of grants from the Engineering and Physical Sciences Research Council of the UK, the Cambridge University Engineering Department, and the Flughafen Frankfurt Main Stiftung.

References

Addison, J. S., and Hodson, H. P., 1992, "Modeling of Unsteady Transitional Boundary Layers," ASME JOURNAL OF TURBOMACHINERY, Vol. 114, pp. 580–589.

Banieghbal, M. R., Curtis, E. M., Denton, J. D., Hodson, H. P., Huntsman, I., Schulte, V., Harvey, N. W., and Steele, A. B., 1995, "Wake Passing in LP Turbine Blades," presented at the AGARD conference, Derby, UK, pp. 8.5.–12.5.

Cebeci, T., and Carr, L. W., 1978, "A Computer Program for Calculating Laminar and Turbulent Boundary Layers for Two Dimensional Time Dependent Flows," NASA TM 78470, Mar.

Cumpsty, N. A., Dong, Y., Li, Y. S., 1995, "Compressor blade boundary layers in the presence of wakes," ASME Paper No. 95-GT-443.

Curtis, E. M., Hodson, H. P., Banieghbal, M. R., Denton, J. D., and Howell, R. J., 1997, "Development of blade profiles for low pressure turbine applications," ASME JOURNAL OF TURBOMACHINERY, Vol. 119, pp. 531–538.

Denton, J. D., 1990, "Entropy generation in turbomachinery flows," 7th Cliff Garrett Turbomachinery Award Lecture, SAE Paper No. 902011.

Emmons, H. W., 1951, "The laminar-turbulent transition in a boundary layer—Part 1," *Journal of Aerospace Science,* Vol. 18, No. 7, pp. 490–498.

Gostelow, J. P., Walker, G. J., Solomon, W. J., Hong, G., and Melwani, N., 1997, "Investigation of the calmed region behind a turbulent spot," ASME JOURNAL OF TURBOMACHINERY, Vol. 119, pp. 802–809.

Halstead, D. E., Wisler, D. C., Okiishi, T. H., Walker, G. J., Hodson, H. P., and Shin, H., 1997, "Boundary layer development in axial compressors and turbines," JOURNAL OF TURBOMACHINERY, Vol. 119, Part 1: pp. 114–127; Part 2: pp. 426–445; Part 3: pp. 225–237; Part 4: pp. 128–139.

Hodson, H. P., 1984, "Boundary Layer and Loss Measurements on the Rotor of an Axial Flow Turbine," ASME *Journal of Engineering for Gas Turbines and Power,* Vol. 106, No. 2.

Hodson, H. P., 1989, "Modelling Unsteady Transition and Its Effects on Profile Loss," *Proc. AGARD Conf. PEP 74a on Unsteady Flows in Turbomachines,* AGARD CP 468; also ASME JOURNAL OF TURBOMACHINERY, Vol. 112, Oct. 1990, pp. 691–701.

Hodson, H. P., Huntsman, I., and Steele, A. B., 1994, "An investigation of boundary layer development in a multistage LP turbine," ASME JOURNAL OF TURBOMACHINERY, Vol. 116, pp. 375–383.

Hourmouziadis, J., 1989, "Aerodynamic Design of Low Pressure Turbines," AGARD Lecture Series, 167.

Narasimha, R., 1957, "On the Distribution of Intermittency in the Transition Region of a Boundary Layer," *Journal of Aerospace Science,* Vol. 24, pp. 711–712.

Pfeil, H., Herbst, R., and Schröder, Th., 1983, "Investigation of laminar-turbulent transition of boundary layers distributed by wakes," ASME *Journal of Engineering for Power,* Vol. 105, Jan.

Schubauer, G. B., and Klebanoff, P. S., 1955, "Contributions on the Mechanics of Boundary Layer Transition," NACA TN 3489 (1955) and NACA Rep. 1289 (1956).

Schulte, V., 1995, "Unsteady Separated Boundary Layers in Axial-Flow Turbomachinery," PhD Dissertation, Cambridge University.

Schulte, V., and Hodson, H. P., 1998, "Unsteady wake-induced boundary layer transition in high lift LP turbines," ASME JOURNAL OF TURBOMACHINERY, Vol. 120, pp. 28–35.

Seifert, A., 1994, "The turbulent spot as a stabilising agent of a transitional boundary layer," submitted for publication in the *Journal of Fluid Mechanics.*

Truckenbrodt, E., 1973, "Neuere Erkenntnisse über die Berechnung von Strömumgsgrenzschichten mittels einfacher Quadraturformeln," Part I, *Ing. Arch.* 43, 9–25 (1973), Part II, *Ing. Arch.* 43 136–144 (1974).

APPENDIX

Consider the (x, z, t)-space as sketched in Fig. A1. The x and z coordinates are the streamwise and spanwise coordinates of a boundary layer and t is the time coordinate. The figure shows by analogy with a figure from Emmons (1951) a section of the dependence volume of a turbulent spot $V_{dep1}(x, z, t)$ and in addition that of a turbulent spot and its becalmed region $V_{dep2}(x, z, t)$. The dependence volume $V_{dep1}(x, z, t)$ comprises all those points in the (x, z, t)-space that could have been the origin of a turbulent spot that made the point $P(x, z, t)$ turbulent. Its shape is determined by the streamwise and spanwise growth rates of turbulent spots. The dependence volume $V_{dep2}(x, z, t)$ contains all those points in the (x, z, t)-space that could have been the origin of a turbulent spot that made the point $P(x, z, t)$ turbulent *or* becalmed. Its shape is determined by the streamwise and spanwise growth rates of turbulent spots and becalmed regions. The intersection with the x–z plane shows the plan view of a turbulent spot (simplified triangular shape ABC) and its becalmed region ($BDEC$).

The probability, that the flow at a given point $P(x, z, t)$ in the (x, z, t)-space is turbulent was given by Emmons (1951) by the expression

$$\gamma(x, z, t) = 1 - \exp\left[- \iiint_{V_{dep1}(x,z,t)} g(x_0, z_0, t_0) dx_0 dz_0 dt_0 \right]. \tag{A1}$$

Here $g(x, z, t)$ denotes the spot production rate, which is a function of space and time. The spot production rate at any given point $P_0(x_0, z_0, t_0)$ is defined as the number of spots formed in an infinitesimal volume $dV_0 = dx_0 dz_0 dt_0$ at point $P_0(x_0, z_0, t_0)$.

The expression (A1) is derived for the (x, z, t)-space. It is generally valid for steady and unsteady flows. In order to be able to calculate the intermittency (probability) $\gamma(x, z, t)$ one needs to specify the spot production function $g(x, z, t)$ and one needs the geometry of the volume of dependence, which is governed by the spreading angles and the propagation rates of a turbulent spot. It was concluded above that spot production is inhibited by a becalmed region following a turbulent spot, as

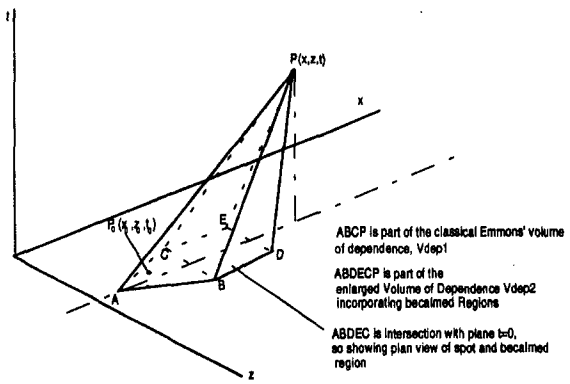

Fig. A1 Schematic of dependence volumes of a turbulent spot and its becalmed region

it is underneath the turbulent spot itself. This was sketched in Fig. 2.

Following this argument, the formation of a turbulent spot and a becalmed region at point $P_0(x_0, z_0, t_0)$ inside the enlarged volume of dependence $V_{dep2}(x, z, t)$ (as sketched in Fig. A1) renders the spot production function $g(x, z, t)$ at point $P(x, z, t)$ equal to zero. Not all spots formed in the enlarged volume of dependence will pass through $P(x, z, t)$ but if the spots do not their becalmed regions will. Consequently, the spot production function inside the enlarged volume of dependence $V_{dep2}(x, z, t)$ has an effect on the spot production function $g(x, z, t)$ at some $P(x, z, t)$. Therefore, the spot production rate $g(x, z, t)$ has an effect on the spot production at downstream locations. To take proper account of the effect of becalmed regions, one needs an expression to correct the distribution of the spot production rate $g(x, z, t)$, which can then be used in Emmons' expression (A1) to calculate the intermittency.

The desired expression can be derived by using the same principle as that used to derive Eq. (A1). The probability, that point $P(x, z, t)$ in Fig. A1 is turbulent *or* becalmed is by analogy with Eq. (A1) given by

$$p_{tc}(x, z, t) = 1 - \exp\left[- \iiint_{V_{dep2}(x,z,t)} g_{cor}(x_0, z_0, t_0) dx_0 dz_0 dt_0 \right] \quad (A2)$$

The corrected spot production function $g_{cor}(x_0, z_0, t_0)$ within the volume of dependence $V_{dep2}(x, z, t)$ is assumed to be known at this stage of the analysis. The probability $p_{tc}(x, z, t)$ also corresponds to the probability that the spot production function $g(x, z, t)$ at point $P(x, z, t)$ is zero. The initially specified probability that a spot forms at $P(x, z, t)$ is given by $g(x, z, t)dxdzdt$. The corrected probability that a spot forms at $P(x, z, t)$ is the initial probability times the probability that $P(x, z, t)$ is neither turbulent nor becalmed. This yields

$$g_{cor}(x, z, t)dxdzdt = g(x, z, t)dxdzdt \cdot (1 - p_{tc}(x, z, t)) \quad (A3)$$

Substituting Eq. (A2) into Eq. (A3) one obtains

$$g_{cor}(x, z, t) = g(x, z, t) \cdot \exp\left[- \iiint_{V_{dep2}(x,z,t)} g_{cor}(x_0, z_0, t_0) dx_0 dz_0 dt_0 \right] \quad (A4)$$

for the corrected spot production rate at point $P(x, z, t)$. After the entire distribution of the corrected spot production rate $g_{cor}(x, z, t)$ has been found, it can then be used in Eq. (A1) instead of $g(x, z, t)$ to calculate the distribution of the intermittency. The calculation can proceed by marching downstream from a starting position where the spot production rate is negligible.

In practice, the omission of the correction of the spot production function (Eq. (A4)) does not have any relevance for steady flow transition, because Narasimha's concentrated breakdown hypothesis states that the spot production rate is zero downstream of the breakdown position.

The presented extension of Emmons' theory to calculate the intermittency has to be applied if one wants to take account of the becalmed regions in unsteady flow transition.

Direct Full Surface Skin Friction Measurement Using Nematic Liquid Crystal Techniques

D. R. Buttsworth

S. J. Elston

T. V. Jones

Department of Engineering Science,
University of Oxford,
Parks Road,
Oxford, United Kingdom

New techniques for the direct measurement of skin friction using nematic liquid crystal layers are demonstrated. Skin friction measurements can be made using a molecular rotation time technique or an equilibrium orientation technique. A mathematical model describing the molecular dynamics of the nematic liquid crystal layer has been introduced. Theoretical results from the proposed mathematical model are in excellent agreement with the current experimental measurements. It is thus demonstrated that the present model captures the essential physics of the nematic liquid crystal measurement techniques. Estimates based on the variance of the liquid crystal calibration data indicate that skin friction measurements to within ±4 percent should certainly be possible. The techniques offer the considerable advantage of simplicity, without any compromise on the accuracy, relative to other surface shear stress measurement techniques. The full surface measurement capacity of the equilibrium orientation technique is demonstrated by measuring the skin friction distribution around a cylindrical obstruction in a fully developed laminar flow.

Introduction

Skin friction (otherwise known as surface shear stress) is a key parameter of interest in both fundamental and applied aerodynamics investigations. Skin friction measurements can provide an insight into the physics of complex flow fields, and can also identify the contribution of the viscous drag to the overall loss production in aerodynamic configurations. Furthermore, skin friction measurements can also be used to validate computational fluid dynamics predictions.

It is therefore not surprising that many skin friction measurement techniques have already been developed. Detailed reviews of these methods can be found elsewhere (Winter, 1977; Fernholz et al., 1996; Hanratty and Campbell, 1996). Briefly however, the majority of the previous methods are *indirect* techniques in that a parameter other than the skin friction (e.g., heat transfer) is actually measured. Indirect techniques then rely on assumptions that relate the measured parameter to the skin friction. *Direct* skin friction measurement techniques avoid such assumptions, and are therefore to be preferred, particularly in complex flows where these assumptions break down. Direct methods include floating element (Marshakov et al., 1996), oil film (Tanner and Blows, 1976; Bandyopadhyay and Weinstein, 1991), and liquid crystal techniques (Bonnet et al., 1989; Reda et al., 1994, 1996). Of these techniques, only the liquid crystal method described by Reda et al. (1996), which relies on the color change response of cholesteric liquid crystal, has been developed to give quantitative *full surface* skin friction measurements. However, the physics of this liquid crystal technique is not well understood, and furthermore, the practical implementation of this technique is very complicated.

The focus of the current paper is a simple and direct full surface skin friction measurement technique that utilizes the wave guiding properties of nematic liquid crystals (e.g., Walton, 1990; Jones and Walton, 1991; Jones, 1992). With the nematic liquid crystal skin friction method, a surface layer of nematic liquid crystal is initially aligned approximately perpendicular to the anticipated flow direction. The application of the flow causes the molecules to rotate, forming a twisted structure, which alters the orientation of the polarized light that is transmitted through the layer. Walton (1990) found that the rotation time of the nematic liquid crystal (as indicated by the rise time of the transmitted light intensity) varies inversely with the applied shear stress. In subsequent investigations, it was found that, under relatively low shear stress conditions, the liquid crystal director at the fluid interface did not fully align with the flow direction, but adopted an equilibrium orientation that was also a function of the applied shear stress. Neither the rotation time technique nor the equilibrium orientation technique has yet been applied or developed to full potential. Therefore, the aim of the present work is to extend the development of these nematic liquid crystal techniques and demonstrate the potential for skin friction measurements.

Nematic Liquid Crystal Technique

General Arrangement. The liquid crystal layer is prepared by first painting polyvinyl alcohol (PVA) onto the surface of interest (usually perspex or glass). Once the PVA is dry, the layer is unidirectionally rubbed with a velvet cloth. The PVA is rubbed at an angle roughly perpendicular to the anticipated flow direction. It appears probable that this rubbing process aligns the long polymer molecules at the PVA surface with the stroke direction through a localized melting and shearing process. Nematic liquid crystals are then painted onto the surface. The surface treatment of the PVA layer causes the nematic liquid crystal molecules, being relatively long rodlike molecules, to align with the direction of the rubbing. In the absence of external forces, the liquid crystal director throughout the entire thickness of the layer, thus lies approximately parallel to the direction in which the PVA layer was rubbed. (The director indicates the mean molecular orientation, i.e., the direction of the "rod.")

A schematic illustration of the nematic liquid crystal skin friction technique is given in Fig. 1. Plane polarized light with an orientation parallel to the surface alignment direction passes though the liquid crystal layer and, provided the flow has not yet been initiated, the light also passes through the liquid crystal layer with minimal distortion. The liquid crystal is viewed through another polarizer that is usually oriented perpendicular

Contributed by the International Gas Turbine Institute and presented at the 42nd International Gas Turbine and Aeroengine Congress and Exhibition, Orlando, Florida, June 2–5, 1997. Manuscript received at ASME Headquarters February 1997. Paper No. 97-GT-397. Associate Technical Editor: H. A. Kidd.

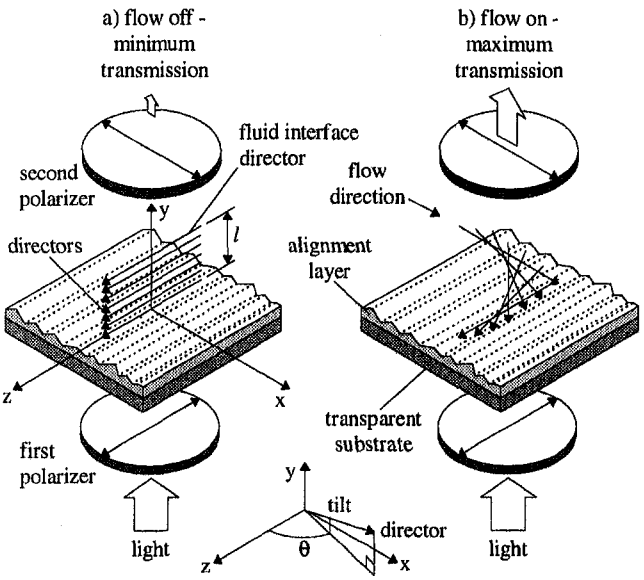

Fig. 1 Illustration of the liquid crystal technique

to the polarization plane of the illumination light. When the flow is initiated, the molecules attempt to align with the flow direction, but because the molecules are strongly anchored at the solid interface by the surface treatment, a twisted structure forms. Because the liquid crystal layer is much thicker than the wavelength of the polarized light, the twisted layer is able to guide the plane of polarization of the light through the twisted structure. As the liquid crystal layer reorients due to the applied shear stress, a change in transmitted light intensity can be observed through the second polarizer.

Streamwise Layer Motion. When a shear stress is suddenly applied to the exposed surface of the liquid crystal, the layer attempts to move in the direction of the applied shear. For a layer of sufficient thickness, the streamwise acceleration may be approximated by the diffusion equation for an isotropic fluid (White, 1991, p. 149),

$$\frac{\partial^2 u}{\partial y^2} = \frac{1}{\nu}\frac{\partial u}{\partial t} \tag{1}$$

subject to the boundary and initial conditions,

$$\left(\frac{\partial u}{\partial y}\right)_{y=l} = \frac{\tau_w}{\mu} \quad \text{for} \quad t > 0 \tag{2}$$

$$u(0, t) = 0 \tag{3}$$

$$u(y, 0) = 0 \tag{4}$$

The solution of this problem can be written (from the solution of an analogous heat transfer problem, Carslaw and Jaeger, 1959, p. 113),

$$\frac{u}{\tau_w l/\mu} = \frac{y}{l} - \frac{8}{\pi^2}\sum_{n=0}^{\infty}\frac{(-1)^n}{(2n+1)^2}\cdot e^{-[(2n+1)^2\pi^2/4][\nu t/l^2]}\sin\left(\frac{(2n+1)\pi}{2}\frac{y}{l}\right) \tag{5}$$

Equation (5) predicts that the velocity at the fluid interface (i.e., at $y = l$) is within 1 percent of the steady value at a time given by

$$t \approx 1.78\frac{l^2}{\nu} \tag{6}$$

Thus, at a similar time, the velocity distribution within the layer approaches the steady (linear) velocity profile,

$$u = \frac{\tau_w y}{\mu} \tag{7}$$

For the work described in the current paper, the kinematic viscosity of the liquid crystal was around 580×10^{-6} m$^2\cdot$s^{-1} (at 20°C), and the thickness of the layer is estimated to be around 10 μm. Thus, the steady velocity profile was set up approximately 0.3 μs from the application of the flow (using Eq. (6)). In the present investigation, the molecular reorientation due to the applied shear stress was on the order of 1 s, and hence, the velocity profile establishment time in the liquid crystal layer is insignificant. The surface shear stresses generated in the present experiments were generally less than 4 Pa. Thus, the maximum surface velocity of the layer would have been around 7×10^{-5} m$\cdot$s^{-1}, which is an insignificant fraction of the air flow velocities used in the present experiments (on the order of 10 m$\cdot$s^{-1}). Hence, the downstream movement of the

Nomenclature

a = duct height
b = duct width
c = function of du/dy, tilt angle, and viscosity coefficients, Pa
$C = cl^2/K$ = nondimensional value of c
K = elastic constant, N
l = thickness of liquid crystal layer
n = dummy variable used in summation (in Eq. (5))
Δn = birefringence
p = pressure, Pa
t = time, usually measured relative to the air flow start or stop
T = nondimensional time $= Kt/\mu l^2$
u = velocity
x = streamwise coordinate (in the direction of the duct length)
y = vertical coordinate (in the direction of the duct height)
Y = nondimensional distance through layer $= y/l$
z = transverse coordinate (in the direction of the duct width)
θ = angle of liquid crystal director
λ = wavelength of light
μ = dynamic viscosity, Pa$\cdot$s
ν = kinematic viscosity $= \mu/\rho$, m$^2\cdot$s^{-1}
ρ = density, kg$\cdot$m^{-3}
σ = standard deviation
τ_w = skin friction (surface shear stress), Pa

Subscripts

1, 3 = elastic constants for liquid crystal material
63.2 = time constant based on an angle change of $(1 - e^{-1}) \times 100$ percent
10–90 = rotation time based on intensity change between 10 and 90 percent

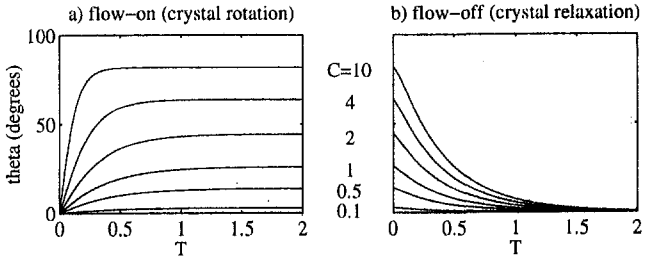

Fig. 2 Theoretical prediction of the fluid interface director dynamics

liquid crystals did not have a measurable effect on the surface shear stress generated by the air flow.

Molecular Rotation. The surface treatment orients the liquid crystal director perpendicular to the anticipated flow direction and anchors the liquid crystal molecules at the solid interface in that direction. Furthermore, the surface treatment also imparts a small azimuthal tilt angle (of around 3 deg) to the liquid crystal molecules (Fig. 1). The liquid crystal molecules rotate when a shear stress is applied to the fluid interface because the local gradient of streamwise velocity (du/dy) exerts a torque (in the θ direction) on the tilted molecule.

A simple model for the motion of the liquid crystal director can be written as

$$\mu \frac{\partial \theta}{\partial t} = K \frac{\partial^2 \theta}{\partial y^2} + c \cdot \cos \theta \tag{8}$$

Equation (8) balances the viscous torque, which retards the rotation of the molecules, against the elastic aligning torque, and a rotation forcing-function. The forcing-function ($c \cdot \cos \theta$) is itself a function of the gradient of the streamwise velocity, the molecular tilt angle, and the various viscosities associated with the nonisotropic liquid crystal molecules. As it is presently assumed that the steady velocity profile within the liquid crystal layer is established rapidly and is also linear, the parameter c will be constant throughout the thickness of the layer and will be proportional to the applied shear stress (τ_w). In nondimensional form, Eq. (8) can be written

$$\frac{\partial \theta}{\partial T} = \frac{\partial^2 \theta}{\partial Y^2} + C \cdot \cos \theta \tag{9}$$

where

$$T = \frac{Kt}{\mu l^2} \tag{10}$$

$$Y = \frac{y}{l} \tag{11}$$

$$C = \frac{cl^2}{K} \tag{12}$$

For the present analysis, it is assumed that the molecules in contact with the solid interface are strongly anchored due to the surface alignment treatment, and that prior to the start of the flow, the liquid crystal director throughout the entire thickness of the layer is perpendicular to the flow direction. Furthermore, at the fluid interface, there is negligible torque. Thus, the appropriate boundary and initial conditions for Eq. (9) are

$$\theta(0, T) = 0 \tag{13}$$

$$\left(\frac{\partial \theta}{\partial Y}\right)_{Y=1} = 0 \tag{14}$$

$$\theta(Y, 0) = 0 \tag{15}$$

Solution of Eq. (9) was achieved using an explicit finite difference routine with 51 nodes distributed evenly throughout the layer. An investigation of solution convergence suggests that results obtained with this level of discretization are within approximately 1 percent of the actual solution.

For rapidly established air flows, there will effectively be a step change in the value of C (at $T = 0$) when the flow is initiated (since C is proportional to the applied shear stress). For various steps in the value of C, results from the finite difference solution (at $Y = 1$) are given in Fig. 2(a). (Provided the liquid crystal layer operates as a perfect wave guide, i.e., provided the twist is gentle relative to the wavelength of the light, it is the director orientation at the fluid interface, $Y = 1$, that determines the orientation of the transmitted light, and hence the intensity observed through the second polarizer.) For the same values of C, Fig. 2(b) presents results for the relaxation of the liquid crystal layer resulting from switching off the air flow, after the orientation of the liquid crystal layer has reached its steady-state distribution. Results in Fig. 2(b) were again obtained using the finite difference routine, however, this time, the initial conditions were given by the solution of

$$\frac{\partial^2 \theta}{\partial Y^2} = -C \cdot \cos \theta \tag{16}$$

subject to the boundary conditions described by Eqs. (13) and (14). Equation (16) was integrated using a high-order Runge–Kutta method.

For the flow-on and flow-off cases (Fig. 2, parts (a) and (b)) a nondimensional time constant was defined as the value of T at which the fluid interface director had changed its orientation by 63.2 percent of its equilibrium value of θ. Results from this analysis of the theoretical model are given in Fig. 3 as a function of C (which is proportional to the applied shear stress). It is clear that the time constant associated with the flow on crystal rotation is a relatively strong function of the applied shear stress (Fig. 3(a)), particularly in comparison with the flow-off crystal relaxation time constant (Fig. 3(b)). The theoretical results in Fig. 3(a) describe the rotation time shear stress measurement technique originally investigated by Walton (1990). For $C > 10$ (approximately), the theoretical rise time varies approximately with the inverse of the applied shear stress. That is, the theoretical rotation time relationship can be approximated as

$$T_{63.2} \propto \frac{1}{C} \tag{17}$$

or, converting back to dimensional parameters,

$$t_{63.2} \propto \frac{\mu}{\tau_w} \tag{18}$$

which indicates that the rotation time is also proportional to the material viscosity, but is independent of the elastic constant, and the layer thickness.

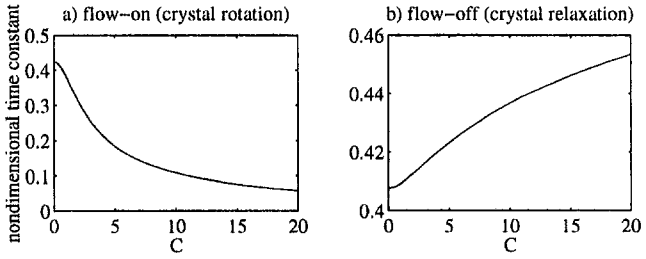

Fig. 3 Theoretical prediction of the time constant for the fluid interface director dynamics

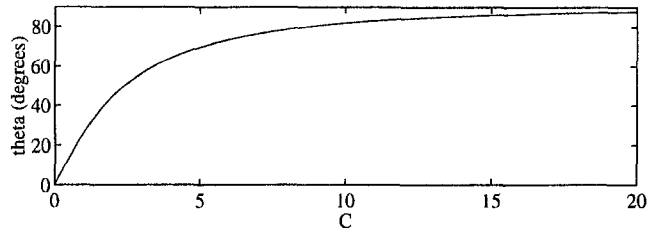

Fig. 4 Theoretical prediction of the fluid interface equilibrium orientation

In Fig. 4, theoretical results are also given for the steady-state orientation of the fluid interface director, based on the solution of Eq. (16). This figure describes the second nematic liquid crystal skin friction measurement technique, the equilibrium orientation technique. The theoretical results indicate that for shear stresses corresponding to values of $C < 10$ (approximately), the equilibrium orientation is a strong function of the applied shear stress. The equilibrium orientation technique offers advantages over the rotation time technique, in that there are no restrictions on the test flow establishment time. (For the rotation time technique, the test flow establishment time must be short relative to the rotation time constant of the liquid crystal layer.) However, with the equilibrium orientation technique, the measured intensity will be a function of the model illumination, and hence an in-situ illumination calibration will be necessary. Thus, in turn, the rotation time technique offers advantages over the equilibrium orientation technique in that the measured parameter (the orientation time) is independent of the absolute intensity of the light.

Results are presented in Fig. 5 for the equilibrium director orientation throughout the thickness of the layer (again from the solution of Eq. (16)). Since the present layer thickness was around 10 μm, the effective pitch of the twisted nematic structure will be around 40 μm (since there is approximately a quarter of a twist within the layer). For good wave guiding, a pitch significantly greater than $\lambda/\Delta n$ is generally required. Assuming $\lambda = 500$ nm and $\Delta n = 0.2$, indicates a required pitch significantly greater than 2.5 μm. Thus, at least for relatively low shear stress conditions, it appears that the liquid crystal layer performs as a reasonable wave guide. Hence, the intensity observed through the second polarizer will vary with $\sin^2 \theta$, where θ is the director orientation at the fluid interface.

Measurements in Laminar Duct Flow

The nematic liquid crystal material used in the present investigation was supplied by Merek Ltd., England, and was designated BL009. Previous surface shear stress investigations using nematic liquid crystal methods have been hampered by the low viscosity of the commonly available materials. In particular, full surface shear stress measurements using the rotation time technique were very difficult because of the video rate restriction. The viscosity of the BL009 material, which is approximately 0.083 Pa·s, was further increased by adding a small

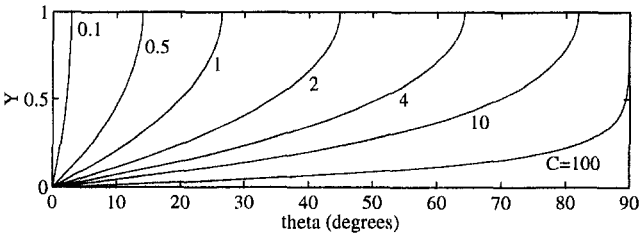

Fig. 5 Theoretical prediction of the director orientation throughout the liquid crystal layer

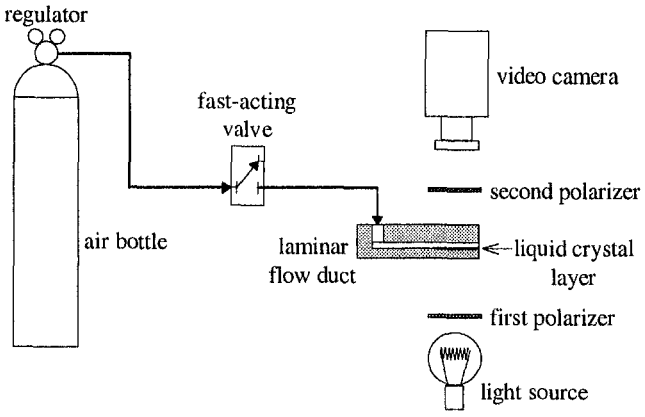

Fig. 6 Diagram of the experimental arrangement

amount of liquid crystal polymer (approximately 6.1 percent by weight) giving a mixture viscosity of approximately 0.58 Pa·s. (The liquid crystal polymer was again supplied by Merek Ltd., and was designated LCP83.)

To determine the validity of the mathematical model, measurements were obtained using the experimental arrangement shown in Figs. 6 and 7. The performance of the duct was investigated by monitoring the flow rate (using a rotameter) and taking pressure measurements at the locations shown in Fig. 7(*b*). It was determined that there was fully developed laminar flow in

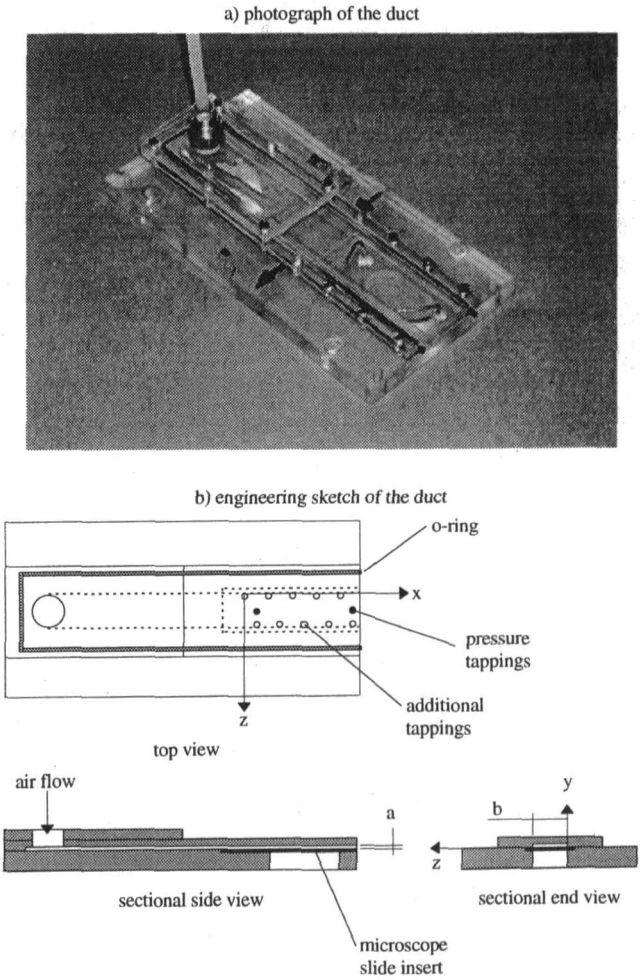

Fig. 7 Illustration of the laminar flow duct

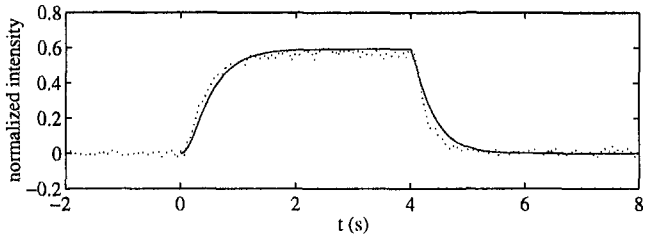

Fig. 8 Comparison of measured intensity history (broken line) and theoretical prediction (solid line)

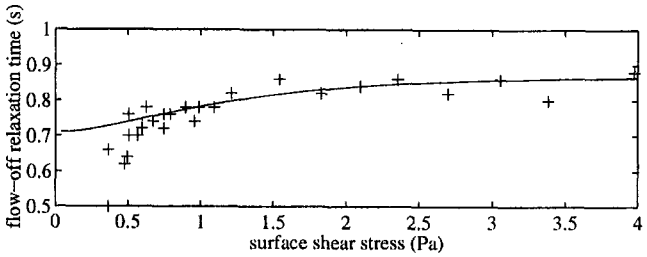

Fig. 10 Comparison of measured flow-off relaxation time (symbols) and theoretical prediction (solid line)

the duct up to a Reynolds number (based on the duct height, a) of around 1000. (The critical Reynolds number for laminar flow in a circular pipe is usually quoted as 2000, e.g., Streeter and Wylie, 1981, p. 239.) Theoretical laminar flow predictions based on solution of the two-dimensional Poisson equation indicated that for the present geometry (a = 1 mm; b = 20 mm), the skin friction along the upper and lower surfaces will be accurately given by

$$\tau_w = -\frac{a}{2}\frac{dp}{dx} \tag{19}$$

provided $0.1 < z/b < 0.9$.

Measurements of the light intensity transmitted through the second polarizer (Fig. 6) were obtained at 27 different shear stress levels by recording the video signal and later extracting the intensity level using software developed by Wang et al. (1996). A measurement of intensity from a pixel of the video signal (corresponding to an area of approximately 0.02 mm^2), representing just one of the 27 shear stress levels, is presented in Fig. 8, along with results from the mathematical model. The location of this pixel was within the region $0.1 < z/b < 0.9$ (the uniform surface shear stress region of the duct). The measured values of intensity were normalized using the measured equilibrium orientation intensity at the maximum applied shear stress, which in the present example, was a value of almost 4 Pa.

For comparison with the experimental results, normalized intensity values from the mathematical model were obtained using the value of $\sin^2\theta$, where θ is the director orientation at the fluid interface. Further comparisons between the experimental results and the mathematical model are presented in Figs. 9 to 11 (using measurements from the same pixel used in Fig. 8). The appropriate scaling used to convert the mathematical model shear stress (C) into real units was determined by fitting the theoretical equilibrium orientation results to the experimental measurements, Fig. 9, and is given by

$$\tau_w = 0.4\ C \tag{20}$$

where τ_w is measured in Pascals. Similarly, the appropriate scaling for the rotation time was determined by fitting the theoretical flow-off relaxation time result to the experimental measurements, Fig. 10, and is given by

$$t_{10\text{-}90} = 1.6T_{10\text{-}90} \tag{21}$$

where $t_{10\text{-}90}$ is measured in seconds. (Note that rotation and relaxation times are now redefined on the basis of a 10 to 90 percent rise time because experimentally, this is easier to determine than the time constant). Figure 11 compares the model for the flow-on rotation time with the experimental measurements, and uses the scaling factors determined from Figs. 9 and 10 to convert the theoretical result into real units. Thus, Fig. 11 provides a basis for an absolute comparison between the model and experimental results.

The trends predicted by the model in Figs. 9 and 10 were observed experimentally (it is inappropriate to compare the absolute levels since these experimental results were used to effectively calibrate the theoretical model). From Fig. 11, the correct trends were again predicted by the model, and furthermore, the absolute levels predicted by the theory compare favorably with the experimental results. (Figure 8, which also uses the scaling factors determined from Figs. 9 and 10, similarly demonstrates the high correlation that exists between the theoretical model and the experimental results.) It is therefore concluded that the mathematical model provides a good description of the physical processes associated with the nematic liquid crystal skin friction measurement techniques. Although the agreement between the experimental results and the theory is, on the whole, very good, it should be noted that at present, the model itself is not used to define the sensitivity of the shear stress measurement system. The actual sensitivity is determined using a curve fit to the calibration data. However, the real value of the model lies in the enhanced physical understanding that it provides. It is anticipated that the present mathematical model will aid future development and investigation of the measurement technique.

Further confirmation of the performance of the theoretical model is obtained by estimating the layer thickness using the scaling indicated by Eq. (21). Combining Eqs. (10) and (21) indicates that the layer thickness can be written

$$l \approx \sqrt{\frac{1.6K}{\mu}} \tag{27}$$

Assuming $K = 2.0 \times 10^{-11}$ N for the liquid crystal mixture (pure BL009 has elastic constants of $K_1 = 1.46 \times 10^{-11}$ N, and

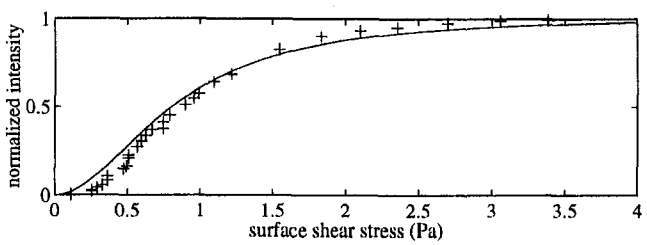

Fig. 9 Comparison of measured equilibrium orientation (symbols) and theoretical prediction (solid line)

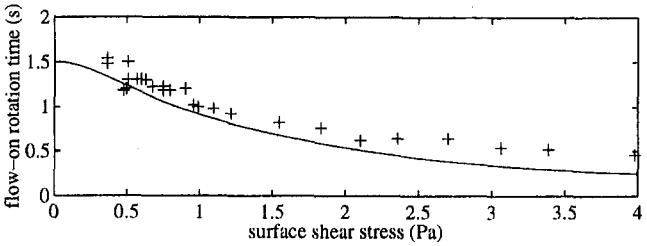

Fig. 11 Comparison of measured flow-on rotation time (symbols) and theoretical prediction (solid line)

$K_3 = 2.99 \times 10^{-11}$ N), and $\mu = 0.58$ Pa·s (which is a bulk flow viscosity for the liquid crystal mixture) suggests a layer thickness of approximately 7.4 μm. This value is in acceptable agreement with the value of 10 μm estimated from measurements of the weight and the wetted surface area of the liquid crystal layer (assuming $\rho = 1000$ kg·m^{-3}).

To determine the actual calibration of the nematic liquid crystal for the analysis of aerodynamic experiments using either the equilibrium orientation or rotation time techniques, it is possible to fit polynomials to the experimental calibration data (e.g., the experimental data presented in Figs. 9 and 11). For the equilibrium orientation data presented in Fig. 9, a second-order polynomial was fitted (in a least-squares sense) for $0.4 < \tau_w < 2$ Pa. Error estimates based on the deviation of the actual equilibrium orientation data from polynomial curve fit suggest that for any measured value of intensity, the uncertainty ($\pm 0.6745\ \sigma$) in the corresponding value of the surface shear stress is between ± 3 and ± 4 percent over this shear stress range. For the entire range of the rotation time data presented in Fig. 11, a second-order polynomial was fitted to a plot of τ_w versus $1/t_{10-90}$ (see Eq. (18)). Error estimates suggest that the uncertainty of the surface shear stress measurements varies from ± 15 at 1 Pa to ± 5 percent at 4 Pa with the rotation time measurement technique.

Full Surface Measurement Demonstration

As a demonstration of the full surface measurement capacity of the equilibrium orientation nematic liquid crystal technique developed here, a cylindrical obstruction was installed in the laminar duct as shown in Fig. 12. Prior to this experiment, every pixel in the uniform skin friction region of the liquid crystal layer ($0.1 < z/b < 0.9$) was calibrated using the unobstructed laminar flow duct (Fig. 7) at seven different values of applied shear stress. The sensitivity at each of these points was determined (as discussed previously) by fitting a second-order polynomial to the calibration measurements (transmitted light intensity versus τ_w). At a flow rate of approximately 4.6×10^{-5} m^3·s^{-1}, the liquid crystal layer was allowed to reach its equilibrium orientation. The shear stress distribution was then determined from the measured equilibrium orientation intensity, and the prior calibration. Full surface shear stress results for this experiment are given in Fig. 13.

Immediately ahead of the obstruction, the surface shear stress is relatively low due to the deceleration of the flow as it approaches the obstruction. To negotiate a path around the obstruction, the flow accelerates, and thus generates regions of high surface shear stress on either side of the obstacle. Downstream of the obstacle, an extensive wake region is clearly apparent. However, *immediately* downstream of the cylinder, a small region of relatively high shear stress appears to shadow its circumference. This region has probably arisen due to the flow between the obstacle and the liquid crystal layer (the cylinder did not fully extend across the duct height; see Fig. 12). Clearly, the flow field is significantly different from that of a simple two-dimensional flow around a cylinder, as is further evidenced by the regions of high shear stress that bound the wake flow region. However, the experiment was not conducted with the intention of performing an in-depth analysis of this particular flow field. Rather, the experiment is presented simply as a demonstration of the technique's potential.

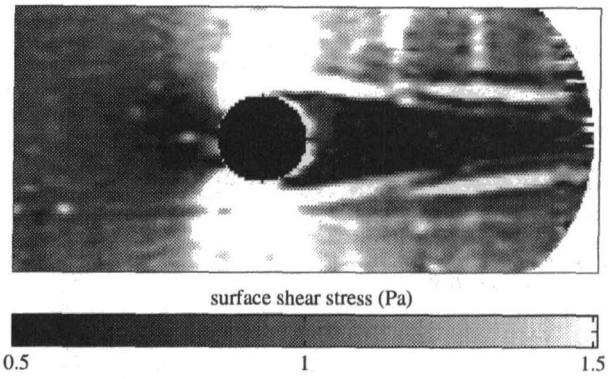

Fig. 13 Full surface skin friction distribution around the cylindrical obstruction

The cylindrical obstruction was placed centrally within the width of the duct. It is therefore reasonable to expect the observed flow field to be symmetric. The primary features of the flow field are indeed largely symmetric; however, there remain a number of localized features that are not symmetric (e.g., the apparent localized high shear stress values ahead of the obstruction). In these regions, the response of the liquid crystal did not follow the assumed second-order polynomial calibration. Such features are caused by nonuniformities within the layer due to contamination of the layer with dust particles, and imperfection in the production of the liquid crystal layer. However, application of the technique in an unfiltered flow does not necessarily represent a particular difficulty, since the contamination will be localized, and thus, only a small fraction of the data cannot be used. A similar argument can be applied to flaws arising in the production of the layer; however, it should be possible to avoid such imperfections. Techniques to improve the uniformity of the layer are currently being investigated.

In the region ahead of the cylinder, the flow direction may deviate significantly from the general flow direction and may even approach the initial orientation of the liquid crystal director. In such regions, the flow direction will have a strong influence on the magnitude of the results. Such effects have not yet been incorporated into the analysis of the intensity measurements, and therefore the quantitative validity of the measurements (Fig. 13) in this region is somewhat doubtful. Future work will include an investigation of the flow direction sensitivity of these nematic liquid crystal techniques, with a view to the development of a simple technique for full surface skin friction vector measurements.

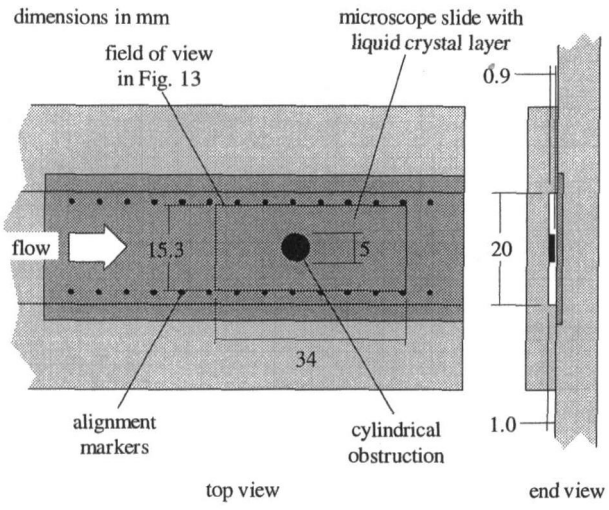

Fig. 12 Laminar flow duct configuration for the cylindrical obstruction experiments

Conclusions

It has been demonstrated that direct full surface skin friction measurements are possible with simple techniques based on the use of nematic liquid crystal. With nematic liquid crystal, direct surface shear stress measurements can be obtained using either a

rotation time technique or an equilibrium orientation technique. Both of these nematic liquid crystal techniques differ significantly from the color change approach of Reda et al. (1996) in that the measured intensity of polarized light transmitted through the layer is calibrated to determine the surface shear stress.

When a shear stress is applied to the nematic liquid crystal layer, the layer begins to flow in the direction of the applied shear. However, calculations indicate that for the viscosity and thickness of the present layers, the downstream migration will have a negligible influence on the measurements. A theoretical model for the molecular rotation dynamics has been introduced. Through comparison of the theoretical model and the present experimental measurements, it is demonstrated that the model provides a very good description of the physical layer behavior. Future assessment, development, and application of the technique will be aided by the mathematical model. The present techniques are directly sensitive to the surface shear stress; however, the viscosity of the liquid crystal is also temperature sensitive and hence, the measurement techniques are ideally applied in isothermal flows.

Based on the deviation of the nematic liquid crystal calibration results from the least-squares polynomial curve fits applied to the data, it is estimated that direct surface shear stress measurements can be made to within ± 4 percent using the present techniques. Thus, the techniques developed here offer the considerable advantage of simplicity, but do not compromise the measurement accuracy relative to other surface shear stress measurement techniques. Following the full surface calibration of the liquid crystal layer, a cylindrical obstruction was placed in the laminar flow duct. The skin friction distribution was visualized with video imaging and then quantitative full surface shear stresses were determined using the calibration data. These measurements represent the first full surface skin friction measurements using the equilibrium orientation nematic liquid crystal technique.

Future work includes the investigation of materials with higher viscosities and elastic constants so that regimes of higher skin friction can be accessed using the present techniques. (The maximum shear stress used in the present investigation of the liquid crystal layer was approximately 4 Pa.) At present, skin friction measurements are made using a light transmission arrangement; however, it is also intended to develop the technique so that the liquid crystal layer can be viewed in reflection. A full surface shear stress vector measurement technique (i.e., giving the magnitude of the shear stress and the local flow direction at the surface) can be developed through the simultaneous use of the equilibrium orientation and the rotation time techniques.

References

Bandyopadhyay, P. R., and Weinstein, L. M., 1991, "A Reflection-Type Oil-Film Skin-Friction Meter," *Experiments in Fluids,* Vol. 11, pp. 281–292.

Bonnet, P., Jones, T. V., and McDonnel, D. G., 1989, "Shear-Stress Measurement in Aerodynamic Testing Using Cholesteric Liquid Crystals," *Liquid Crystals,* Vol. 6, No. 3, pp. 271–280.

Carslaw, H. S., and Jaeger, J. C., 1959, *Conduction of Heat in Solids,* 2nd ed., Oxford University Press.

Fernholz, H. H., Janke, G., Schober, M., Wagner, P. M., and Warnack, D., 1996, "New Developments and Applications of Skin-Friction Measuring Techniques," *Meas. Sci. Technol.,* Vol. 7, pp. 1396–1409.

Hanratty, T. J., and Campbell, J. A., 1996, "Measurement of Wall Shear Stress," in: R. J. Goldstein, ed., *Fluid Mechanics Measurements,* 2nd ed., Taylor and Francis, Washington, DC, pp. 575–648.

Jones, T. V., 1992, "The Use of Liquid Crystals in Aerodynamic and Heat Transfer Testing," in: J. A. Reizes, ed., *Transport Phenomena in Heat and Mass Transfer,* Vol. 2, Elsevier, Amsterdam, pp. 1242–1273.

Jones, T. V., and Walton, T. W., 1991, "Reynolds Analogy in Film Cooling," *Proc. 10th Int. Symp. on Air Breathing Engines,* pp. 1263–1268.

Marshakov, A. V., Schetz, J. A., and Kiss, T., 1996, "Direct Measurement of Skin Friction in a Turbine Cascade," *J. Propulsion and Power,* Vol. 12, No. 2, pp. 245–249.

Reda, D. C., Muratore, J. J., and Heineck, J. T., 1994, "Time and Flow-Direction Responses of Shear-Stress-Sensitive Liquid Crystal Coatings," *AIAA J.,* Vol. 32, No. 4, pp. 693–700.

Reda, D. C., and Muratore, J. J., 1994, "Measurement of Shear Stress Vectors Using Liquid Crystal Coatings," *AIAA J.,* Vol. 32, No. 8, pp. 1576–1582.

Reda, D. C., Wilder, M. C., Farina, D. J., Zilliac, G., McCabe, R. K., Lehman, J. R., Hu, K. C., Whitney, D. J., and Deardorff, D. G., 1996, "Areal Measurements of Surface Shear Stress Vector Distributions Using Liquid Crystal Coatings," AIAA Paper No. 96-0420.

Streeter, V. L., and Wylie, E. B., 1981, *Fluid Mechanics,* 1st SI metric edition, McGraw-Hill, Singapore.

Tanner, L. H., and Blows, L. G., 1976, "A Study of the Motion of Oil Films on Surfaces in Air Flow, With Application to the Measurement of Skin Friction," *J. Physics E: Sci. Instr.,* Vol. 9, No. 3, pp. 194–202.

Walton, T. W., 1990, "Shear Induced Twist in Nematic Liquid Crystals," Department of Engineering Science Report, University of Oxford, Apr.

Wang, Z., Ireland, P. T., Jones, T. V., and Davenport, R., 1996, "A Color Image Processing System for Transient Liquid Crystal Heat Transfer Experiments," ASME JOURNAL OF TURBOMACHINERY, Vol. 118, pp. 421–432.

White, F. M., 1991, *Viscous Fluid Flow,* 2nd ed., McGraw-Hill, New York.

Winter, K. G., 1977, "An Outline of Techniques Available for the Measurement of Skin Friction in Turbulent Boundary Layers," *Prog. Aerospace Sci.,* Vol. 18, pp. 1–57.

Journal of Turbomachinery Discussion

On the Conservation of Rothalpy in Turbomachines[1]

H. B. Urbach[2] and E. Jones.[3] Professor F. A. Lyman's paper covered, among other topics, what we have called "Euler's turbomachinery equation with viscous correction." He referenced our prior work from a master's thesis (Urbach, 1987) (done under Professor Everett Jones of the University of Maryland) and an in-house report (1990), which Lyman states covers very similar ground. Although he acknowledged the priority of this earlier work, he did not reference later refinements (1991, 1993).

Lyman (1990) communicated with us to announce his own elegant integration of the differential equations of enthalpy transfer, which also leads to Euler's turbomachinery equation. He pointed out that he had reviewed the 1990 report and found a mathematical flaw. Lyman states in his paper that Urbach had "split . . . [turbomachinery flow] terms into separate axial and radial components and assumed constant axial and radial mass flow rates." Lyman argued that the latter assumption is untrue because the initial flow is essentially axial, and the effluent exits in directions either axial or radial. His Eq. (B5), referencing our report, illustrates the splitting process:

$$\rho(Dh_o/Dt) = \rho U\cdot[(W\cdot\nabla)W + 2\omega \times W] + \nabla\cdot(\tau\cdot W), \quad \text{(B5)}$$

where h_o, t, ρ, U, W, V, ω, and τ are the total specific enthalpy, time, specific density, the rotor velocity, relative velocity, absolute velocity, and angular velocity vectors and the stress tensor, respectively. The first term of the right-hand side of Eq. (B5) can be written as follows:

$$\rho U\cdot(W\cdot\nabla)W = (\rho U(W_r(\partial W_\theta/\partial r) + W_r W_\theta/r) + (W_\theta/r)(\partial W_\theta/\partial\theta) + W_z(\partial W_\theta/\partial z)), \quad \text{(B6)}$$

where the subscripts represent components of the velocity vectors. Lyman adds the steady-state continuity equation, $\nabla\cdot(\rho W) = 0$, to the first term of the right-hand side of Eq. (B5), or the left-hand side of Eq. (B6) to obtain

$$\rho U\cdot(W\cdot\nabla)W = \nabla\cdot(\rho W U W_\theta). \quad \text{(B7)}$$

Lyman used this elegant device to perform the volume integration and obtain Euler's turbomachinery equation in a single term.

Referring to Eq. (B6), we point out that the separate flow terms (which include azimuthal as well as radial and axial terms) represent an expansion of the dot product of the blade velocity, U, and the azimuthal force components of the azimuthal, radial and axial flows. (This latter statement is a correction of an error noted by Lyman). There is no nonphysical "split . . . [of the turbomachinery component flow] term into separate axial and radial components . . ." In fact, we notice three components, not two, when we recognize the azimuthal term. Lyman was correct in stating that the radial and axial flow rates are not constant, and indeed, the original integration was flawed. However, the revised integration (1991, 1993) shows that the principle is correct.

Integrating the first term over all space, one obtains the integral INT_r, thus:

$$\text{INT}_r = \iiint \rho r\omega(W_r/r)(\partial r W_\theta/\partial r)\,r dr d\theta dz = \int (\iint \rho W_r r d\theta dz)(\partial r\omega \underline{W}_\theta/\partial r)dr, \quad (1)$$

which is in the in-house Urbach (1991, 1993) reports. The underlined $\underline{W}_\theta$ is defined by the mean value theorem applied to the double integral thus:

$$\underline{W}_\theta(r) = \iint W_\theta d\theta dz/\Delta\theta\Delta z. \quad (2)$$

The double integral in the right-hand side of Eq. (1) is the radial flow at any point r:

$$m_r(r) = \iint \rho W_r r d\theta dz = m f_r(r), \quad (3)$$

where $f_r(r)$ is the fraction of radial flow at radius r. Since $f_r(r)$, and $\underline{W}_\theta(r)$ are functions of r, Eqs. (1)–(3) yield

$$\text{INT}_r = m\int f_r(r)d(U\underline{W}_U(r)). \quad (4)$$

Now the mean value theorem may be used again to take f_r, an average value of $f_r(r)$ outside the integral thus:

$$f_r = \int f_r(r)d(U\underline{W}_U(r))/\Delta_r(U\underline{W}_U). \quad (5)$$

At the lower limit of r in the integral of Eq. (5), $f_r(r)$, the radial flow vanishes if the flow enters the turbomachine through a purely axial manifold. As Lyman stated, the axial or radial-flow terms are not constant. At the exit station of a radial manifold, the value of $f_r(r)$ must be unity. However, the mean value, f_r is the flow fraction of fluid that exits the turbomachine into a radial manifold, and thus, it is an experimental *invariant* quantity. Since the radial and axial flows may be known, the mean value theorem can simplify integration in some calculations.

[1] By F. A. Lyman, published in the July 1993 issue of the ASME JOURNAL OF TURBOMACHINERY, Vol. 115, pp. 520–526.

[2] Naval Surface Warfare Center, Carderock Division, Annapolis, MD 21402-5067.

[3] Aerospace Engineering Department, University of Maryland, College Park, MD 20742-3035.

Finally the integral becomes

$$\mathrm{INT}_r = \underline{m}_r f_r[\Delta_r(U\underline{W}_U)] = \underline{m}_r \Delta_r(U\underline{W}_U). \quad (6)$$

The procedure can be applied to obtain a mean axial, $\mathrm{INT}_z = \underline{m}_z \Delta_z(U\underline{W}_U)$, and a mean azimuthal mass flow, $\mathrm{INT}_\theta = \underline{m}_\theta \Delta_\theta(U\underline{W}_U)$.

Although as Lyman noted, the original integration was erroneous in execution, it was subsequently revised, and the principle is correct. The version of our report describing this was sent to Lyman.

A quick review of the expansion components of Eq. (B6) reveals an interesting overlooked introspective. The first term of the right-hand side of Eq. (B6) represents the axial contribution of the energy transfer. Likewise, the radial component of the energy transfer involves the Coriolus force and arises from the purely radial flow term. The azimuthal component of the energy transfer, associated with purely azimuthal flow, may be identified with the energy transfer of Hero's engine, the mechanism of which drives the common garden sprinkler. The three components represent three kinds of flow, and three aspects of turbomachine energy transfer.

Lacking this introspective, Vavra (1960) stated that the mechanism of energy transfer in a turbomachine arises from the Coriolus force, which can only be associated with the radial term. But purely axial turbomachines, and the sails of sailboats, have no radial flow and yet produce significant energy transfer. Clearly, an examination of the "split" terms described above would have prevented Vavra from making such an error.

Lyman's concern with the conservation of rothalpy may also be rationalized by examination of the enthalpy, because the rothalpy is ultimately defined in terms of the enthalpy and not vice versa. Thus, following Wu (1976), the rothalpy change, Δl, is given by:

$$\Delta l = \Delta(h + W^2/2 - U^2/2) = \Delta h_o - \Delta(UV_U). \quad (7)$$

Now for a steady-state, real, total-enthalpy change, we must add the viscous work, w_{VIS}, and heat transfer, q, to the Eulerian work thus:

$$\Delta h_o = \Delta(UV_U) + w_{\mathrm{VIS}} + q, \quad (8)$$

where w_{VIS} is given by

$$w_{\mathrm{VIS}} = \iiint \nabla \cdot (\Pi' \cdot W) r dr d\theta dz, \quad (9)$$

where Π' is the stress tensor less the pressure tensor. Combining Eqs. (7) and (8), the change in the rothalpy shows that

$$\Delta l = w_{\mathrm{VIS}} + q, \quad (10)$$

and the rothalpy, although constant at any point in the steady-state frame of the rotors, is changed between the inlet and outlet surfaces, a result predicted by the rules of Cumpsty (1989), consistent with the data of the Moores (1980, 1985), and Lyman (see Lyman's introduction and detailed references, 1993) et al. Thus, it would seem logical to investigate the conservation of rothalpy through examination of the total enthalpy.

Acknowledgments

The work presented here and in previous reports was sponsored, in part, by the in-house Research Director of the Naval Surface Warfare Center, Dr. Bruce Douglas. The writers are grateful to Dr. Donald T. Knauss for his review of the manuscript.

References

Cumpsty, N. A., 1989, *Compressor Aerodynamics*, Longman Scientific & Technical, Harlow, Essex, United Kingdom.

Lyman, F. A., 1990, private communication.

Moore, J., and Moore, J. G., 1980, "Three-Dimensional Viscous Flow Calculations in Turbomachines," AGARD Conference Proceedings No. 282, *Centrifugal Compressors, Flow Phenomena, and Performance*, pp. 9-1–9-19.

Moore, J., 1985, "Performance Evaluation of Flow in Turbomachinery Blade Rows," AGARD Lecture Series No. 140, *3-D Computation Techniques Applied to Internal Flows in Propulsion Systems*, pp. 6-1–6-26.

Urbach, H. B., 1990, DTRC-PAS-90/45, 1991, DTRC-PAS-91/29, 1993, MRD-80-93-10, Internal reports of the Naval Surface Warfare Center Carderock Division.

Urbach, H. B., 1987, "Fluid Dynamics of Energy Transfer in Turbomachinery," Thesis, Aerospace Engineering Department, University of Maryland, College Park, MD.

Vavra, M. H., 1960, *Aero-Thermodynamics and Flow in Turbomachines*, Wiley, New York, p. 115.

Wu, Chung-Hua, 1976, "Three-Dimensional Turbomachine Flow Equations Expressed With Respect to Non-Orthogonal Coordinates and Methods of Solution," presented at the Third International Symposium on Air Breathing Engines, Munich.

Author's Closure

The comments of Urbach and Jones mostly concern a point that was dealt with in Appendix B of my 1993 paper. An earlier, more extended version of that appendix had been sent to Urbach in 1991, and I had thought that the question was settled. Apparently it was not, so I will try to be more explicit here.

One of the main results of my 1993 paper was Eq. (21), the rothalpy equation for a control volume. For adiabatic and steady flow in the rotor-fixed frame, that equation reduces to Eq. (33), which for comparison with Urbach and Jones is written in their notation as follows:

$$\Delta \overline{h_0} = \Delta(\overline{UV_\theta}) + w_{\mathrm{vis}} \quad (1)$$

where Δ means the change between inlet and outlet control surfaces. The overbars denote the mass-averaged value over the rotor fixed control surface, i.e.,

$$(\overline{\ }) = \frac{1}{m} \int \rho(\ ) \overrightarrow{W} \cdot \overrightarrow{dS'} \quad (2)$$

m is the mass flow rate through the rotor, and $w_{\mathrm{vis}} = P_f/m$ is the work per unit mass done on the fluid by the viscous stresses.

Urbach and Jones evidently prefer the following multiterm expression for what they call "Euler's turbomachinery equation":

$$\Delta \overline{h_0} = f_r \Delta_r(\overline{UV_\theta}) + f_z \Delta_z(\overline{UV_\theta}) + f_\theta \Delta_\theta(\overline{UV_\theta}) + w_{\mathrm{vis}} \quad (3)$$

The symbols are as defined in their comments, except they do not state that Δ_r is the change in the quantity in the parentheses between two constant-radius surfaces r_1 and r_2, and Δ_z is the change between two axial (z = const) planes. Equation (3) is the same as the result obtained by Urbach (1990, 1991, 1993), except that result has been slightly generalized by the addition of the third term on the right to account for the change in angular momentum between two azimuthal (θ = const) planes.

Obviously Eq. (1) has only one term for the change in angular momentum, whereas Eq. (3) has three. In my 1993 paper I stated that Urbach's result was incorrect and pointed out an invalid assumption he made in his 1990 report. Urbach and Jones note that I did not cite Urbach's 1991 and 1993 reports, which corrected the error but nevertheless arrived as the same result as the 1990 report. The reason I did not cite these later reports is that I did not see how the multiterm expression for the change in angular momentum could be correct. I have now convinced myself that the two results are identical, because the mass-flux-averaged integral defined by Eq. (2) can be expanded by projecting $\overrightarrow{dS'}$ onto planes of constant r', θ', and z', respectively, i.e.,

$$m\Delta(\overline{UV_\theta}) = \int \rho UV_\theta \overrightarrow{W} \cdot \overrightarrow{dS'} = \iint_{S_r} \rho UV_\theta W_r r' d\theta' dz' + \iint_{S_\theta} \rho UV_\theta W_\theta dr' dz' + \iint_{S_z} \rho UV_\theta W_z r' dr' d\theta'$$

Finally the integral becomes

$$\mathrm{INT}_r = \underline{m}_r f_r[\Delta_r(U\underline{W}_U)] = \underline{m}_r \Delta_r(U\underline{W}_U). \quad (6)$$

The procedure can be applied to obtain a mean axial, $\mathrm{INT}_z = \underline{m}_z \Delta_z(U\underline{W}_U)$, and a mean azimuthal mass flow, $\mathrm{INT}_\theta = \underline{m}_\theta \Delta_\theta(U\underline{W}_U)$.

Although as Lyman noted, the original integration was erroneous in execution, it was subsequently revised, and the principle is correct. The version of our report describing this was sent to Lyman.

A quick review of the expansion components of Eq. (B6) reveals an interesting overlooked introspective. The first term of the right-hand side of Eq. (B6) represents the axial contribution of the energy transfer. Likewise, the radial component of the energy transfer involves the Coriolus force and arises from the purely radial flow term. The azimuthal component of the energy transfer, associated with purely azimuthal flow, may be identified with the energy transfer of Hero's engine, the mechanism of which drives the common garden sprinkler. The three components represent three kinds of flow, and three aspects of turbomachine energy transfer.

Lacking this introspective, Vavra (1960) stated that the mechanism of energy transfer in a turbomachine arises from the Coriolus force, which can only be associated with the radial term. But purely axial turbomachines, and the sails of sailboats, have no radial flow and yet produce significant energy transfer. Clearly, an examination of the "split" terms described above would have prevented Vavra from making such an error.

Lyman's concern with the conservation of rothalpy may also be rationalized by examination of the enthalpy, because the rothalpy is ultimately defined in terms of the enthalpy and not vice versa. Thus, following Wu (1976), the rothalpy change, Δl, is given by:

$$\Delta l = \Delta(h + W^2/2 - U^2/2) = \Delta h_o - \Delta(UV_U). \quad (7)$$

Now for a steady-state, real, total-enthalpy change, we must add the viscous work, w_{VIS}, and heat transfer, q, to the Eulerian work thus:

$$\Delta h_o = \Delta(UV_U) + w_{\mathrm{VIS}} + q, \quad (8)$$

where w_{VIS} is given by

$$w_{\mathrm{VIS}} = \iiint \nabla \cdot (\Pi' \cdot W) r dr d\theta dz, \quad (9)$$

where Π' is the stress tensor less the pressure tensor. Combining Eqs. (7) and (8), the change in the rothalpy shows that

$$\Delta l = w_{\mathrm{VIS}} + q, \quad (10)$$

and the rothalpy, although constant at any point in the steady-state frame of the rotors, is changed between the inlet and outlet surfaces, a result predicted by the rules of Cumpsty (1989), consistent with the data of the Moores (1980, 1985), and Lyman (see Lyman's introduction and detailed references, 1993) et al. Thus, it would seem logical to investigate the conservation of rothalpy through examination of the total enthalpy.

Acknowledgments

The work presented here and in previous reports was sponsored, in part, by the in-house Research Director of the Naval Surface Warfare Center, Dr. Bruce Douglas. The writers are grateful to Dr. Donald T. Knauss for his review of the manuscript.

References

Cumpsty, N. A., 1989, *Compressor Aerodynamics*, Longman Scientific & Technical, Harlow, Essex, United Kingdom.

Lyman, F. A., 1990, private communication.

Moore, J., and Moore, J. G., 1980, "Three-Dimensional Viscous Flow Calculations in Turbomachines," AGARD Conference Proceedings No. 282, *Centrifugal Compressors, Flow Phenomena, and Performance*, pp. 9-1–9-19.

Moore, J., 1985, "Performance Evaluation of Flow in Turbomachinery Blade Rows," AGARD Lecture Series No. 140, *3-D Computation Techniques Applied to Internal Flows in Propulsion Systems*, pp. 6-1–6-26.

Urbach, H. B., 1990, DTRC-PAS-90/45, 1991, DTRC-PAS-91/29, 1993, MRD-80-93-10, Internal reports of the Naval Surface Warfare Center Carderock Division.

Urbach, H. B., 1987, "Fluid Dynamics of Energy Transfer in Turbomachinery," Thesis, Aerospace Engineering Department, University of Maryland, College Park, MD.

Vavra, M. H., 1960, *Aero-Thermodynamics and Flow in Turbomachines*, Wiley, New York, p. 115.

Wu, Chung-Hua, 1976, "Three-Dimensional Turbomachine Flow Equations Expressed With Respect to Non-Orthogonal Coordinates and Methods of Solution," presented at the Third International Symposium on Air Breathing Engines, Munich.

Author's Closure

The comments of Urbach and Jones mostly concern a point that was dealt with in Appendix B of my 1993 paper. An earlier, more extended version of that appendix had been sent to Urbach in 1991, and I had thought that the question was settled. Apparently it was not, so I will try to be more explicit here.

One of the main results of my 1993 paper was Eq. (21), the rothalpy equation for a control volume. For adiabatic and steady flow in the rotor-fixed frame, that equation reduces to Eq. (33), which for comparison with Urbach and Jones is written in their notation as follows:

$$\Delta \overline{h_0} = \Delta(\overline{UV_\theta}) + w_{\mathrm{vis}} \quad (1)$$

where Δ means the change between inlet and outlet control surfaces. The overbars denote the mass-averaged value over the rotor fixed control surface, i.e.,

$$\overline{(\ )} = \frac{1}{m} \int \rho(\ )\vec{W} \cdot \vec{dS'} \quad (2)$$

m is the mass flow rate through the rotor, and $w_{\mathrm{vis}} = P_f/m$ is the work per unit mass done on the fluid by the viscous stresses.

Urbach and Jones evidently prefer the following multiterm expression for what they call "Euler's turbomachinery equation":

$$\Delta \overline{h_0} = f_r \Delta_r(\overline{UV_\theta}) + f_z \Delta_z(\overline{UV_\theta}) + f_\theta \Delta_\theta(\overline{UV_\theta}) + w_{\mathrm{vis}} \quad (3)$$

The symbols are as defined in their comments, except they do not state that Δ_r is the change in the quantity in the parentheses between two constant-radius surfaces r_1 and r_2, and Δ_z is the change between two axial (z = const) planes. Equation (3) is the same as the result obtained by Urbach (1990, 1991, 1993), except that result has been slightly generalized by the addition of the third term on the right to account for the change in angular momentum between two azimuthal (θ = const) planes.

Obviously Eq. (1) has only one term for the change in angular momentum, whereas Eq. (3) has three. In my 1993 paper I stated that Urbach's result was incorrect and pointed out an invalid assumption he made in his 1990 report. Urbach and Jones note that I did not cite Urbach's 1991 and 1993 reports, which corrected the error but nevertheless arrived as the same result as the 1990 report. The reason I did not cite these later reports is that I did not see how the multiterm expression for the change in angular momentum could be correct. I have now convinced myself that the two results are identical, because the mass-flux-averaged integral defined by Eq. (2) can be expanded by projecting $\vec{dS'}$ onto planes of constant r', θ', and z', respectively, i.e.,

$$m\Delta(\overline{UV_\theta}) = \int \rho UV_\theta \vec{W} \cdot \vec{dS'} = \iint_{S_r} \rho UV_\theta W_r r' d\theta' dz' + \iint_{S_\theta} \rho UV_\theta W_\theta dr' dz' + \iint_{S_z} \rho UV_\theta W_z r' dr' d\theta'$$

The three double integrals on the right correspond to the first three terms on the right of Eq. (3). Note that the integrations are over three different surfaces, so that *six* such integrals would have to be evaluated unless the inlet and outlet control surfaces were surfaces on which one or two of the variables (r', θ', z') were constant. For this reason I prefer the form given in Eq. (1). Also, I maintain that the rothalpy integral equation provides a much clearer and easier way to derive the result than termwise integration of the equation for the total enthalpy. I do, however, apologize for not earlier realizing that the two different forms of the result, Urbach's and mine, are mathematically equivalent.

In conclusion, I note several misstatements in the comments of Urbach and Jones:

1 The last sentence of their second paragraph misquotes my paper. It should read "Lyman argued that the latter assumption is untrue in a *mixed flow impeller* because the initial flow is essentially axial, and the effluent exits in a direction which is *neither* axial *nor* radial." (italics added to show words omitted by Urbach and Jones).

2 This is an inconsistency in notation for the tangential component of relative velocity in their Eqs. (1), (2), (4), (5), (6)—both W_θ and W_U are used.

3 The paragraph beginning "A quick review . . ." refers to radial, axial and azimuthal components of energy transfers. First, the energy equation is a scalar equation, so referring to its *components* is meaningless. Second, their so-called "introspective" (interpretation?) of the terms in Eq. (B6) is neither a clear nor a convincing explanation of the physical meanings of these terms.

4 I strongly disagree with the implications of their statement "Lyman's concern with the conservation of rothalpy may also be rationalized by examination of the enthalpy, because the rothalpy is ultimately defined in terms of the enthalpy and not vice versa." It implies that my 1993 paper needs to be "rationalized" by recasting it in terms of enthalpy, and further, that I defined enthalpy in terms of rothalpy. It is clear from my paper that neither of these implications is true. Following Wu (1953), I defined rothalpy in terms of enthalpy (Eqs. (2) and (4) of Lyman, 1993), and I started my derivation of the differential and integral equations for the rothalpy with the equation for the total enthalpy (Eq. (5)), subsequently giving various forms of this equation (cf. Eqs. (6), (10), (12), (16)) for purposes of comparison.

5 Equation (8) is presented as if it were a basic physical law, whereas it is actually a consequence of the integral form of either the total enthalpy equation of the rothalpy equation for the special case of steady flow in rotor-fixed coordinates with no body forces (cf. Eqs. (12) and (21) of Lyman, 1993).

6 The statement immediately following Eq. (10) is incorrect—the rothalpy is *not* "constant at any point" even in the rotating frame if viscous dissipation is important. Also, the next sentence in that paragraph again implies that I did not examine the variation in total enthalpy, which is untrue (see #4 above).